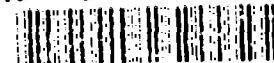


(2)

# DESIGN MANUAL FOR TWO-PHASE COMPONENTS OF SPACECRAFT THERMAL MANAGEMENT SYSTEMS

Christopher J. Crowley  
Michael G. Izenson  
James J. Barry  
Jerry L. Martin  
Rebecca S. Ent  
Javier A. Valenzuela

AD-A260 027



Creare Inc  
P.O. Box 71, Etna Road  
Hanover, NH 03755

September 1992

Final Report



APPROVED FOR PUBLIC RELEASE; DISTRIBUTION UNLIMITED.

92-30062



PHILLIPS LABORATORY  
Directorate of Space & Missile Technologies  
AIR FORCE MATERIEL COMMAND  
EDWARDS AIR FORCE BASE CA 93524-5000

PL-TR-92-3002

# DESIGN MANUAL FOR TWO-PHASE COMPONENT SPACECRAFT THERMAL MANAGEMENT SYSTEMS

Christopher J. Crowley  
Michael G. Izenon  
James J. Barry  
Jerry L. Martin  
Rebecca S. Ent  
Javier A. Valenzuela

Creare Inc  
P.O. Box 71, Etna Road  
Hanover, NH 03755

September 1992

Final Report

CLEARED  
FOR PUBLIC RELEASE

PL/PA 1 DEC 92

APPROVED FOR PUBLIC RELEASE; DISTRIBUTION UNLIMITED



PHILLIPS LABORATORY  
Directorate of Space & Missile Technology  
AIR FORCE MATERIEL COMMAND  
EDWARDS AIR FORCE BASE CA 93550

PL 92-3002



DEPARTMENT OF THE AIR FORCE  
PHILLIPS LABORATORY (AFMC)

FROM: PL/PA  
3550 Aberdeen Avenue S.E.  
Kirtland AFB, NM 87117-5776

DATE: 1 Dec 92

SUBJ: Phillips Laboratory Security Review Case Number(s): PL 92-0819

TO: OLAC-PL/PA (Ranney Adams)

1. Action on the document(s) (security review case) mentioned above has been completed with the following determination, as marked:

- ☒ CLEARED FOR OPEN PUBLICATION/PRESENTATION (NO CHANGES).
- ☐ CLEARED FOR OPEN PUBLICATION/PRESENTATION AS AMENDED. The amendments, changes, deletions, etc., denoted by the words "as amended" -- are mandatory. Words or information to be deleted are indicated inside brackets.
- ☐ CLEARED FOR OPEN PUBLICATION/PRESENTATION WITH RECOMMENDED CHANGES. The reviewers have suggested some changes which are not mandatory, indicated by the words "recommended changes."
- ☐ DISAPPROVED FOR PUBLIC RELEASE (for the following reason(s):
- ☐ CONTAINED CLASSIFIED INFORMATION
- ☐ CONTAINED TECHNOLOGY SECURITY INFORMATION DETERMINED NOT TO BE RELEASABLE TO THE PUBLIC
- ☐ RELEASE DENIED FOR OTHER AF/DOD/GOVERNMENT REASONS
- ☒ The PL project officer must notify the author/contractor about the decision on this case and send a copy of this letter with a copy of the stamped document (attached).
- ☐ OTHER: \_\_\_\_\_

2. For an explanation of the changes or denials, please see the attached document and/or letter of explanation.

3. If you have questions, please call me at (505) 846-6246.

JUDY L. JOHNSTON  
Security Review Officer

1 Atch(s)  
PL 92-0819

## NOTICE


When U.S. Government drawings, specifications, or other data are used for any purpose other than a definitely related Government procurement operation, the fact that the Government may have formulated, furnished, or in any way supplied the said drawings, specifications, or other data, is not to be regarded by implication or otherwise, or in any way licensing the holder or any other person or corporation, or conveying any rights or permission to manufacture, use or sell any patented invention that may be related thereto.


## FOREWORD

This final report was submitted by Creare Inc, Hanover NH, under SBIR Contract F04611-90-C-0004 with the OLAC, Phillips Laboratory, Edwards AFB CA 93524-7001. SBIR funding provided by the Small Business Innovative Research Program. PL Project Manager was Mary Corrigan.

This report has been reviewed and is approved for release and distribution in accordance with the distribution statement on the cover and on the SF Form 298.

  
MARY CORRIGAN,  
Project Manager

  
ROBERT M. VACEK,  
Chief, Thermal Management Branch

  
ERNEST HERRERA, Lt Col, USAF  
Chief, Space Power & Thermal Management Division

Accession For	
NTIS GRA&I	<input checked="checked" type="checkbox"/>
DTIC TAB	<input type="checkbox"/>
Unannounced	<input type="checkbox"/>
Justification	
By <i>per Notice</i>	
Distribution/	
Availability Codes	
Dist	Special
A-1	



## REPORT DOCUMENTATION PAGE

Form Approved  
OMB No. 0704-0188

1a. REPORT SECURITY CLASSIFICATION Unclassified			1b. RESTRICTIVE MARKINGS Unlimited rights		
2a. SECURITY CLASSIFICATION AUTHORITY			3. DISTRIBUTION/AVAILABILITY OF REPORT Requests for this document must be referred to: Phillips Laboratory, OL-AC PL/VTPT, Edwards AFB, CA 93523-5000		
2b. DECLASSIFICATION/DOWNGRADING SCHEDULE			5. MONITORING ORGANIZATION REPORT NUMBER(S) PL-TR-92-3002		
4. PERFORMING ORGANIZATION REPORT NUMBER(S) TM-1524					
6a. NAME OF PERFORMING ORGANIZATION Creare Inc.		6b. OFFICE SYMBOL (If applicable) ---		7a. NAME OF MONITORING ORGANIZATION Phillips Laboratory	
6c. ADDRESS (City, State, and ZIP Code) P.O. Box 71, Etna Road Hanover, NH 03755 USA				7b. ADDRESS (City, State, and ZIP Code) Edwards AFB, CA 93523-5000	
8a. NAME OF FUNDING/SPONSORING ORGANIZATION		8b. OFFICE SYMBOL (If applicable)		9. PROCUREMENT INSTRUMENT IDENTIFICATION NUMBER F04611-90-C-0004	
6c. ADDRESS (City, State, and ZIP Code)				10. SOURCE OF FUNDING NUMBERS	
				PROGRAM ELEMENT NO.	PROJECT NO.
				TASK NO.	WORK UNIT ACCESSION NO.
11. TITLE (Include Security Classification) Design Manual for Two-Phase Components of Spacecraft Thermal Management Systems					
12. PERSONAL AUTHOR(S) Crowley, Christopher J.; Izenon, Michael G.; Barry, James J.; Martin, Jerry L.; Ent, Rebecca S.; Valenzuela, Javier A.					
13a. TYPE OF REPORT Final		13b. TIME COVERED FROM 9005 TO 9208		14. DATE OF REPORT (Year, Month, Day) 92/5	
15. PAGE COUNT					
16. SUPPLEMENTARY NOTATION					
17. COSATI CODES			18. SUBJECT TERMS (Continue on reverse if necessary and identify by block number)		
FIELD	GROUP	SUB-GROUP			
20	04	---	Heat Transfer, Condensation, Space Technology,		
20	13	---	Spacecraft Components, Two-Phase Flow		
19. ABSTRACT (Continue on reverse if necessary and identify by block number)					
<p>This design manual presents methods to design and model the performance of key two-phase components in thermal management systems for spacecraft. Components for both capillary- and mechanically-pumped loops are modelled, including: forced-convection evaporators; droplet evaporators; two-phase transport lines, fittings, and tees; shear condensers; capillary condensers; and mechanical pumps. Heat pipe condensers are also included. The methods can be used for component design and sizing, analysis of component performance in system or component development tests, development and evaluation of analytical models for key phenomena, and integration with transient codes for system analysis. This manual describes in detail the analysis methods which have been used to produce software for component design. The software and methods are validated against experimental data whenever such data are available. When possible, simple design maps are presented for initial scoping calculations for sizing two-phase components.</p> <p>The basic analytical approach for these design methods is mechanistic, so that the mathematical models for component behavior are based upon the fundamental physics. Thus the methods include inherent scaling with gravity, physical size, and fluid properties. This approach allows the models to be easily upgraded as new experimental data become available and includes the ability to assess the analytical uncertainty in design calculations.</p>					
20. DISTRIBUTION/AVAILABILITY OF ABSTRACT <input checked="" type="checkbox"/> UNCLASSIFIED/UNLIMITED <input type="checkbox"/> SAME AS RPT. <input type="checkbox"/> DTIC USERS			21. ABSTRACT SECURITY CLASSIFICATION Unclassified		
22a. NAME OF RESPONSIBLE INDIVIDUAL Gary Strack			22b. TELEPHONE (Include Area Code) (505) 846-4992		22c. OFFICE SYMBOL PL/VTPT

## TABLE OF CONTENTS

<u>Section</u>	<u>Page</u>
1 INTRODUCTION TO THE DESIGN MANUAL.....	1-1
1.1 Purpose.....	1-1
1.2 Approach.....	1-1
1.3 Contents.....	1-3
1.4 Corresponding Software.....	1-3
1.5 References.....	1-3
2 TRANSPORT LINES: Flow Regime Methods.....	2-1
2.1 Summary of Flow Regime Methods and Applications.....	2-1
2.1.1 Summary of the Flow Regimes and Transitions.....	2-2
2.1.2 Summary of Regime Transition Models.....	2-5
2.2 Flow Regime Transition Methods.....	2-5
2.2.1 Equations for Flow Regime Transition Methods....	2-7
2.2.2 Modelling Uncertainties for Sensitivity Calculations.....	2-20
2.2.3 Limits of the Methods.....	2-24
2.3 Dimensionless Design Charts for Flow Regimes.....	2-24
2.4 Validation With Microgravity Flow Regime Data.....	2-32
2.4.1 Experimental Data.....	2-32
2.4.2 Comparisons with Individual Experiments.....	2-34
2.4.3 Conclusions from Microgravity Comparisons.....	2-44
2.5 References for Flow Regime Methods.....	2-46
3 TRANSPORT LINES: Pressure Drop Methods.....	3-1
3.1 Summary and Application of Pressure Drop Methods.....	3-1
3.1.1 Summary of Pressure Drop Methods.....	3-2
3.1.2 Applications.....	3-4
3.2 Pressure Drop Methods for Each Flow Regime in Pipes....	3-5
3.2.1 Equations for Pressure Drop in Pipes.....	3-5
3.2.2 Modelling Uncertainties for Sensitivity Calculations in Pipes.....	3-16
3.2.3 Limits of the Methods for Pipes.....	3-17
3.3 Pressure Drop Methods for Elbows, Tees, and Fittings...	3-18
3.3.1 Equations for Elbows, Tees, and Fittings.....	3-18
3.3.2 Modelling Uncertainties for Sensitivity Calculations in Elbows, Tees, and Fittings.....	3-24
3.4 Dimensionless Design Calculations for Pipes.....	3-24
3.5 Validation with Microgravity Pressure Drop Data.....	3-36
3.5.1 Experimental Data.....	3-37
3.5.2 Comparisons with Individual Experiments.....	3-38
3.5.3 Conclusions from Pressure Drop Comparisons.....	3-50
3.6 References for Pressure Drop Methods.....	3-52

<u>Section</u>	<u>Page</u>
4 EVAPORATORS: Forced Convection Dominated Tubes.....	4-1
4.1 Applications.....	4-1
4.2 Summary of Methods.....	4-5
4.3 Calculation Procedure for an Evaporator Tube.....	4-11
4.3.1 Boundary Conditions.....	4-11
4.3.2 Segment Calculations.....	4-15
4.3.3 Calculation of Entire Evaporator Tube.....	4-17
4.4 Heat Transfer Coefficients.....	4-17
4.4.1 Single Phase Convection.....	4-17
4.4.2 Partially-Developed Subcooled Boiling.....	4-18
4.4.3 Fully-Developed Subcooled Boiling.....	4-18
4.4.4 Saturated Boiling.....	4-19
4.5 Fluid State, Quality, and Void Fraction.....	4-19
4.5.1 Single-Phase Convection.....	4-19
4.5.2 Partially-Developed Subcooled Boiling.....	4-20
4.5.3 Fully-Developed Subcooled Boiling.....	4-20
4.5.4 Saturated Boiling.....	4-20
4.6 Pressure Drop.....	4-21
4.6.1 Single-Phase Convection.....	4-21
4.6.2 Partially-Developed Subcooled Boiling.....	4-22
4.6.3 Fully-Developed Subcooled Boiling.....	4-22
4.6.4 Saturated Boiling.....	4-23
4.6.5 Correction Factor for Curved Tubes.....	4-24
4.7 Regime Transitions.....	4-24
4.7.1 Onset of Nucleate Boiling.....	4-24
4.7.2 Onset of Significant Voiding.....	4-24
4.7.3 Bulk Saturated Conditions.....	4-25
4.7.4 Critical Heat Flux.....	4-25
4.8 Scoping Calculations and Dimensionless Design Charts...	4-28
4.8.1 Evaporator Tube Length.....	4-29
4.8.2 Forced Convection Fraction.....	4-30
4.8.3 Significance of Body Forces.....	4-32
4.8.4 Operating Limits.....	4-33
4.8.5 Pressure Losses.....	4-37
4.9 Validation with Evaporator Test Data.....	4-41
4.10 References for Forced Convection Dominated Tubes.....	4-47
5 EVAPORATORS: Droplet Impingement Cooling.....	5-1
5.1 Introduction to DIC Evaporators.....	5-1
5.1.1 DIC Process.....	5-1
5.1.2 DIC Evaporator Design.....	5-3
5.1.3 DIC Evaporator Sizing.....	5-6
5.2 Design Methods.....	5-7
5.2.1 Equations for DIC Heat Transfer.....	5-7
5.2.2 Limitations.....	5-12
5.3 Dimensionless Design Charts.....	5-12
5.4 Validation.....	5-13
5.5 References for Droplet Impingement Cooling.....	5-16

<u>Section</u>	<u>Page</u>
6 CONDENSERS: Vapor Shear.....	6-1
6.1 Applications.....	6-2
6.2 Summary of Methods.....	6-5
6.3 Calculation Procedure for a Shear Condenser Tube.....	6-10
6.3.1 Boundary Conditions.....	6-11
6.3.2 Preliminary Calculations.....	6-13
6.3.3 Segment Calculations.....	6-14
6.3.4 Calculation of the Entire Condenser Tube.....	6-17
6.3.5 Mass Flow Rate Iterations for Specified Pressure Drop.....	6-18
6.4 Condensing Heat Transfer Coefficient.....	6-19
6.4.1 Annular Flow.....	6-19
6.4.2 Slug Flow.....	6-22
6.4.3 Bubbly Flow.....	6-25
6.4.4 Single-Phase Liquid Flow.....	6-25
6.5 Void Fraction.....	6-26
6.5.1 Annular Flow.....	6-26
6.5.2 Slug Flow.....	6-27
6.5.3 Bubbly Flow.....	6-28
6.5.4 Single-Phase Liquid Flow.....	6-29
6.6 Pressure Drop.....	6-29
6.6.1 Total Pressure Drop.....	6-29
6.6.2 Pressure Drop Due to Friction.....	6-29
6.6.3 Pressure Drop Due to Body Forces.....	6-31
6.6.4 Pressure Drop Due to Fluid Acceleration.....	6-32
6.6.5 Pressure Drop Due to Taper of the Condenser Tube.....	6-32
6.7 Dimensionless Design Charts for Condensing Radiators...	6-33
6.7.1 Modelling Condensing Radiators with MICROCON....	6-33
6.7.2 Estimates for Condensing Length.....	6-38
6.7.3 Design Charts for Pressure Drop.....	6-40
6.8 Validation of Methods.....	6-44
6.8.1 Overall Conclusions for Validation.....	6-45
6.8.2 Experiments Used for Validation.....	6-45
6.8.3 Comparison of Data With MICROCON Calculations...	6-50
6.9 References for Vapor Shear Condensers.....	6-55
7 CONDENSERS: Capillary Grooves.....	7-1
7.1 Introduction.....	7-1
7.2 Pressure Gradient in Capillary Grooves.....	7-3
7.2.1 Pressure Gradient in Rectangular Grooves.....	7-6
7.2.2 Pressure Gradient in Triangular Grooves.....	7-7
7.2.3 Pressure Gradient in Trapezoidal Grooves.....	7-10
7.3 Heat Transfer Coefficients on Rectangular Fins.....	7-13
7.4 Heat Transfer Coefficients on Contoured Fins.....	7-17
7.5 Internally Drained Condenser (IDC).....	7-19
7.6 Grooved Surface Condensers.....	7-22
7.6.1 Rectangular Grooves.....	7-22
7.6.2 Triangular Grooves.....	7-23
7.6.3 Trapezoidal Grooves.....	7-26
7.7 References for Capillary Groove Condensers.....	7-29

<u>Section</u>	<u>Page</u>
8 PUMPS: Two-Phase Degradation.....	8-1
8.1 Introduction.....	8-1
8.1.1 Four Quadrant Operation.....	8-2
8.1.2 Two-Phase Effects.....	8-2
8.2 Design Methods for Pump Two-Phase Performance.....	8-5
8.2.1 Pump Scaling Relationships.....	8-5
8.2.2 Pump Dimensionless Homologous Relations.....	8-6
8.2.3 Two-Phase Multipliers.....	8-6
8.2.4 Transient Calculations.....	8-9
8.2.5 Limitations of These Methods.....	8-12
8.3 Use of Dimensionless Performance Charts.....	8-12
8.4 Validation of Design Methods.....	8-18
8.5 References for Two-Phase Degradation in Pumps.....	8-21
APPENDIX A FLUID PROPERTY ROUTINES.....	A-1
A.1 Introduction.....	A-1
A.2 Use of the DIPPR Routines.....	A-1
A.3 Error Trapping and Handling.....	A-2
A.3.1 General Error Messages.....	A-2
A.3.2 List of Routines and Specific Errors.....	A-3
A.4 Validation of Curve Fit Coefficients.....	A-6
A.5 References for Fluid Property Routines.....	A-18
APPENDIX B REFERENCES FOR DESIGN METHODS SOFTWARE.....	B-1

## LIST OF FIGURES

<u>Figure</u>		<u>Page</u>
1.1	ILLUSTRATION OF A MECHANICALLY PUMPED LOOP (MPL).....	1-2
1.2	ILLUSTRATION OF A CAPILLARY PUMPED LOOP (CPL).....	1-2
2.1	ILLUSTRATING FLOW PATTERNS (REGIMES) OF INTEREST.....	2-3
2.2	SAMPLE FLOW REGIME MAP IN SUPERFICIAL VELOCITY COORDINATES.....	2-4
2.3	SAMPLE FLOW REGIME MAP IN MASS FLUX AND QUALITY COORDINATES.....	2-4
2.4	ILLUSTRATING FORCE BALANCE FOR STRATIFIED FLOW REGIME TRANSITION BASED UPON A FLOW INSTABILITY CRITERION.....	2-7
2.5	ILLUSTRATING FORCE BALANCE FOR STRATIFIED FLOW REGIME TRANSITION BASED UPON A SURFACE TENSION CRITERION.....	2-11
2.6	EXAMPLE FLOW REGIME MAPS FOR UPWARDLY INCLINED PIPES AT 1g.....	2-13
2.7	EXAMPLE FLOW REGIME MAPS FOR DOWNWARDLY INCLINED PIPES AT 1g.....	2-14
2.8	EXAMPLE FLOW REGIME MAPS AS A FUNCTION OF ACCELERATION.....	2-15
2.9	EXAMPLE FLOW REGIME MAPS AT SMALL DIAMETER.....	2-16
2.10	ILLUSTRATING FORCE BALANCE FOR SLUG-TO-BUBBLY FLOW REGIME TRANSITION BASED UPON TURBULENCE.....	2-17
2.11	EXAMPLE FLOW REGIME MAPS IN MASS FLUX COORDINATES AS A FUNCTION OF ACCELERATION.....	2-21
2.12	SENSITIVITY OF FLOW REGIME TRANSITIONS TO KEY MODELLING PARAMETERS.....	2-22
2.13	LOGIC FOR FLOW REGIME DETERMINATION.....	2-26
2.14	DIMENSIONLESS MAP FOR STRATIFIED REGIME TRANSITION AT SMALL DIAMETER ( $B_0 < 100$ ).....	2-27
2.15	DIMENSIONLESS MAP FOR STRATIFIED REGIME TRANSITION BASED UPON KELVIN-HELMHOLTZ INSTABILITY.....	2-27
2.16	DIMENSIONLESS MAP FOR BUBBLY REGIME TRANSITION BASED UPON TURBULENCE.....	2-30
2.17	DIMENSIONLESS MAP FOR BUBBLY REGIME TRANSITION BASED UPON CRITICAL VOID FRACTION.....	2-31
2.18	DIMENSIONLESS MAP FOR ANNULAR REGIME TRANSITION.....	2-32
2.19	COMPARISON WITH CHEN ET AL. (1988) MICROGRAVITY DATA.....	2-35
2.20	COMPARISON WITH CHEN ET AL. (1988) GROUND TEST DATA.....	2-35
2.21	COMPARISON WITH COLIN ET AL. (1991) MICROGRAVITY DATA.....	2-36
2.22	COMPARISON WITH CROWLEY ET AL. (1991) MICROGRAVITY DATA.....	2-37
2.23	COMPARISON WITH CROWLEY ET AL. (1991) GROUND TEST DATA.....	2-37
2.24	COMPARISON WITH DUKLER ET AL. (1987) MICROGRAVITY LEARJET DATA.....	2-39
2.25	COMPARISON WITH DUKLER ET AL. (1987) MICROGRAVITY DROP TOWER DATA.....	2-39
2.26	COMPARISON WITH HILL-BEST (1991) MICROGRAVITY DATA ( $D = 8.8$ mm).....	2-40
2.27	COMPARISON WITH HILL-BEST (1991) MICROGRAVITY DATA ( $D = 11.1$ mm).....	2-40

Figure		Page
2.28	SENSITIVITY OF COMPARISON WITH HILL-BEST DATA TO CRITICAL LIQUID FRACTION ( $D = 8.8$ mm).....	2-41
2.29	SENSITIVITY OF COMPARISON WITH HILL-BEST DATA TO CRITICAL LIQUID FRACTION ( $D = 11.1$ mm).....	2-41
2.30	COMPARISON WITH HILL-BEST (1991) DATA DURING "LEVEL FLIGHT" ( $D = 8.8$ mm).....	2-42
2.31	COMPARISON WITH LEE-BEST (1987) MICROGRAVITY DATA.....	2-43
2.32	COMPARISON WITH REZKALLAH (1991) MICROGRAVITY DATA (Data Set #1).....	2-43
2.33	SENSITIVITY OF COMPARISON WITH REZKALLAH (1991) DATA TO CRITICAL LIQUID FRACTION (Data Set #1).....	2-44
3.1	GEOMETRIES AND FLOW REGIMES FOR PRESSURE DROP CALCULATIONS.....	3-2
3.2	DIMENSIONLESS PLOT OF LIQUID FRACTION FOR THE ANNULAR FLOW REGIME.....	3-26
3.3	DIMENSIONLESS PLOT OF TWO-PHASE MULTIPLIER FOR THE ANNULAR FLOW REGIME.....	3-26
3.4	DIMENSIONLESS PLOT OF LIQUID FRACTION FOR THE STRATIFIED FLOW REGIME.....	3-29
3.5	DIMENSIONLESS PLOT OF TWO-PHASE MULTIPLIER FOR THE STRATIFIED FLOW REGIME.....	3-29
3.6	DIMENSIONLESS PLOT OF LIQUID FRACTION FOR THE SLUG FLOW REGIME.....	3-31
3.7	DIMENSIONLESS PLOT OF TWO-PHASE MULTIPLIER FOR THE SLUG FLOW REGIME.....	3-31
3.8	DIMENSIONLESS PLOT OF LIQUID FRACTION FOR HOMOGENEOUS FLOW.....	3-34
3.9	DIMENSIONLESS PLOT OF TWO-PHASE MULTIPLIER FOR HOMOGENEOUS FLOW.....	3-34
3.10	DIMENSIONLESS PLOT OF LIQUID FRACTION FOR THE BUBBLY FLOW REGIME.....	3-35
3.11	DIMENSIONLESS PLOT OF TWO-PHASE MULTIPLIER FOR THE BUBBLY FLOW REGIME.....	3-35
3.12	PRESSURE DROP COMPARISONS FOR CHEN ET AL. (1989) MICROGRAVITY DATA IN THE ANNULAR FLOW REGIME.....	3-40
3.13	PRESSURE DROP COMPARISONS FOR CHEN ET AL. (1989) MICROGRAVITY DATA IN THE SLUG FLOW REGIME.....	3-40
3.14	PRESSURE DROP COMPARISONS FOR CHEN ET AL. (1989) GROUND TEST DATA IN THE STRATIFIED FLOW REGIME.....	3-41
3.15	FRICTION FACTOR COMPARISONS FOR COLIN ET AL. (1991) MICROGRAVITY DATA IN THE BUBBLY AND SLUG FLOW REGIMES.....	3-41
3.16	PRESSURE DROP COMPARISONS WITH THE DESIGN METHOD FOR HILL AND BEST (1991) MICROGRAVITY DATA IN THE ANNULAR AND SLUG FLOW REGIMES.....	3-43
3.17	PRESSURE DROP COMPARISONS WITH THE WALLIS CORRELATION FOR HILL AND BEST (1991) MICROGRAVITY DATA IN THE ANNULAR FLOW REGIME.....	3-43

Figure		Page
3.18	PRESSURE DROP COMPARISONS WITH REZKALLAH AND MITCHELL (1991) MICROGRAVITY DATA IN THE SLUG FLOW REGIME.....	3-44
3.19	PRESSURE DROP COMPARISONS WITH REZKALLAH AND MITCHELL (1991) MICROGRAVITY DATA IN THE BUBBLY FLOW REGIME.....	3-45
3.20	PRESSURE DROP COMPARISONS WITH CROWLEY ET AL. (1991) GROUND TEST DATA IN THE ANNULAR FLOW REGIME ( $G = 175 \text{ kg/m}^2\text{-s}$ ).....	3-45
3.21	PRESSURE DROP COMPARISONS WITH CROWLEY ET AL. (1991) GROUND TEST DATA IN THE ANNULAR FLOW REGIME ( $G = 100 \text{ kg/m}^2\text{-s}$ ).....	3-46
3.22	PRESSURE DROP COMPARISONS WITH CROWLEY ET AL. (1991) GROUND TEST DATA IN THE SLUG FLOW REGIME.....	3-46
3.23	PREDICTED REGIME MAP FOR LEE (1991) TEST CONDITIONS AT $D = 15.8 \text{ mm}$ .....	3-47
3.24	PRESSURE DROP COMPARISONS WITH LEE (1991) DATA AT $D = 15.8 \text{ mm}$ .....	3-48
3.25	PREDICTED REGIME MAP FOR LEE (1991) TEST CONDITIONS AT $D = 21.1 \text{ mm}$ .....	3-49
3.26	PRESSURE DROP COMPARISONS WITH LEE (1991) DATA AT $D = 21.1 \text{ mm}$ ( $G = 65 \text{ kg/m}^2\text{-s}$ ).....	3-49
3.27	PRESSURE DROP COMPARISONS WITH LEE (1991) DATA AT $D = 21.1 \text{ mm}$ ( $G = 95 \text{ kg/m}^2\text{-s}$ ).....	3-50
4.1	STRAIGHT TUBE EVAPORATOR.....	4-3
4.2	SPIRAL COIL EVAPORATOR.....	4-4
4.3	HELICAL COIL EVAPORATOR.....	4-4
4.4	FLOW BOILING REGIMES (COLLIER, 1981).....	4-7
4.5	FORCES ON AN ELEMENTAL CONTROL VOLUME.....	4-10
4.6	FLOWCHART FOR EVAPORATOR CALCULATIONS.....	4-13
4.7	EXAMPLE OF ITERATION BEHAVIOR FOR CONSTANT WALL TEMPERATURE BOUNDARY CONDITION (R-11 Fluid, $T_{\text{sat}} = 351 \text{ K}$ )...	4-14
4.8	DESIGN CHART FOR EVAPORATOR TUBE LENGTH.....	4-29
4.9	DESIGN CHART FOR FORCED CONVECTION HEAT TRANSFER.....	4-32
4.10	DESIGN CHART FOR $Bo_{\text{ucc}}$ (Shah, 1987).....	4-34
4.11	DESIGN CHART FOR $Bo_o$ in LCC (Shah, 1987).....	4-34
4.12	DESIGN CHART FOR $F_x$ IN LCC (Shah, 1987).....	4-35
4.13	DIMENSIONLESS FRICTIONAL PRESSURE DROP IN THE EVAPORATOR....	4-38
4.14	DIMENSIONLESS PRESSURE DROP DUE TO BODY FORCES IN THE EVAPORATOR.....	4-38
4.15	DIMENSIONLESS PRESSURE DROP DUE TO FLUID ACCELERATION IN THE EVAPORATOR.....	4-39
4.16	COMPARISON OF FCEVAP RESULTS WITH CREARE GROUND TEST DATA FOR WALL SUPERHEAT.....	4-42
4.17	COMPARISON OF FCEVAP RESULTS WITH CREARE GROUND TEST DATA FOR PRESSURE DROP.....	4-43
4.18	CRITICAL HEAT FLUX PREDICTED FOR CREARE TESTS ( $G = 168 \text{ kg/m}^2\text{-s}$ , Power = 739 W).....	4-44
4.19	COMPARISON OF WALL AND FLUID TEMPERATURES FOR SUNDSTRAND SFE.....	4-46
4.20	COMPARISON OF PRESSURE DROPS FOR SUNDSTRAND SFE.....	4-46



Figure		Page
5.1	DROPLET IMPINGEMENT COOLING CONCEPT.....	5-2
5.2	DROPLET IMPACT, SPREADING, AND EVAPORATION.....	5-3
5.3	TRANSIENT TEMPERATURE RESPONSE IN SOLID.....	5-4
5.4	EXAMPLE DROPLET IMPINGEMENT COOLING EVAPORATOR CONFIGURATIONS.....	5-5
5.5	THIN FILM SPOT PACKING ARRANGEMENTS.....	5-8
5.6	TRANSIENT WALL HEAT TRANSFER SOLUTION.....	5-11
5.7	VARIATION OF DROPLET SPREAD RATIO WITH IMPACT PARAMETERS (YANG, 1975).....	5-14
5.8	SIMULTANEOUS EFFECT OF SOLID, LIQUID AND EVAPORATION RESISTANCES ON THE EVAPORATION TIME.....	5-15
5.9	VARIATIONS OF PEAK WALL SUPERHEAT WITH HEAT TRANSFER RESISTANCE.....	5-15
5.10	VALIDATION COMPARISON OF DESIGN METHODS VERSUS CREARE DIC DATA.....	5-16
6.1	THERMAL MODEL FOR A CONDENSING RADIATOR.....	6-3
6.2	THERMAL MODEL FOR AN INTERFACE CONDENSER.....	6-4
6.3	A SINGLE TUBE IN A SHEAR CONDENSER.....	6-6
6.4	QUALITY AND VOID FRACTION PROFILES IN A SHEAR CONDENSER.....	6-8
6.5	PRESSURE DROP PROFILES IN A SHEAR CONDENSER.....	6-10
6.6	STEPS IN A CONDENSER TUBE CALCULATION.....	6-12
6.7	SLUG FLOW REGIME.....	6-23
6.8	ANGLE BETWEEN CONDENSING FLOW AND BODY FORCES.....	6-27
6.9	SECTION OF A CONDENSING RADIATOR PANEL.....	6-34
6.10	ANALYSIS OF HEAT TRANSFER IN A RADIATOR PANEL.....	6-37
6.11	DESIGN MAPS FOR PRESSURE DROPS IN SHEAR CONDENSERS.....	6-42
6.12	LTV's AMMONIA SHEAR CONDENSER.....	6-46
6.13	SHEAR CONDENSER TEST SPECIMEN AND COOLING ARRANGEMENT.....	6-46
6.14	SUNDSTRAND TEST FACILITY.....	6-48
6.15	CREARE TEST FACILITY.....	6-48
6.16	BAE ET AL. TEST FACILITY.....	6-49
6.17	AMMONIA INTERFACE HEAT EXCHANGER (Fredley and Warren, 1990).....	6-49
6.18	COMPARISON WITH LTV CONDENSER DATA.....	6-51
6.19	COMPARISON WITH SUNDSTRAND DATA.....	6-51
6.20	COMPARISON OF HEAT TRANSFER CALCULATIONS WITH CREARE DATA...	6-52
6.21	COMPARISON OF PRESSURE DROP CALCULATIONS WITH CREARE DATA...	6-52
6.22	COMPARISON WITH BAE ET AL., RUN 2.....	6-54
6.23	COMPARISON WITH BAE ET AL., RUN 6.....	6-54
6.24	COMPARISON WITH HEAT TRANSFER DATA FROM AN AMMONIA INTERFACE HEAT EXCHANGER.....	6-55
7.1	HEAT TRANSFER IN A RECTANGULAR GROOVE.....	7-2
7.2	GROOVE GEOMETRY STRONGLY AFFECTS THE FRICTION IN A CAPILLARY GROOVE.....	7-2
7.3	GEOMETRY FOR A RECTANGULAR GROOVE.....	7-4
7.4	DIMENSIONLESS VELOCITY PROFILES IN RECTANGULAR GROOVE.....	7-4
7.5	DIMENSIONLESS VELOCITY PROFILES IN TRIANGULAR GROOVE.....	7-5
7.6	DIMENSIONLESS VELOCITY PROFILES IN TRAPEZOIDAL GROOVE.....	7-5

Figure		Page
7.7	DIMENSIONLESS PRESSURE GRADIENT IN RECTANGULAR GROOVES.....	7-8
7.8	PRESSURE DROP IN RECTANGULAR GROOVES.....	7-8
7.9	GEOMETRY FOR A TRIANGULAR GROOVE.....	7-9
7.10	DIMENSIONLESS PRESSURE GRADIENT IN TRIANGULAR GROOVES.....	7-11
7.11	GEOMETRY FOR A TRAPEZOIDAL GROOVE.....	7-11
7.12	DIMENSIONLESS PRESSURE GRADIENT IN TRAPEZOIDAL GROOVES.....	7-13
7.13	GEOMETRY FOR A FLAT TOP FIN.....	7-14
7.14	FLAT TOP FIN HEAT TRANSFER COEFFICIENT VERSUS FIN PITCH.....	7-15
7.15	FLAT TOP FIN HEAT TRANSFER COEFFICIENT VERSUS MENISCUS ANGLE	7-16
7.16	GEOMETRY FOR THE CONTOURED FIN.....	7-17
7.17	CONTOURED FIN HEAT TRANSFER COEFFICIENT VERSUS FIN PITCH....	7-19
7.18	GEOMETRY FOR AN INTERNALLY DRAINED CONDENSER.....	7-20
7.19	DIMENSIONLESS HEAT TRANSFER PER GROOVE FOR A RECTANGULAR GROOVE.....	7-24
7.20	DIMENSIONLESS HEAT TRANSFER RATE PER GROOVE FOR A TRAPEZOIDAL GROOVE.....	7-28
8.1	FOUR QUADRANT CHARACTERISTICS FOR TYPICAL CENTRIFUGAL PUMP.....	8-3
8.2	OPERATING ZONES OF TYPICAL CENTRIFUGAL PUMP.....	8-4
8.3	PUMP HEAD CHARACTERISTICS.....	8-7
8.4	PUMP TORQUE CHARACTERISTICS.....	8-8
8.5	HEAD DEGRADATION MULTIPLIER CURVE.....	8-10
8.6	TORQUE DEGRADATION MULTIPLIER CURVE.....	8-10
8.7	ELEMENTS OF PUMP DYNAMICS.....	8-11
8.8	SINGLE-PHASE HEAD.....	8-14
8.9	TWO-PHASE HEAD.....	8-14
8.10	HEAD DEGRADATION MULTIPLIER.....	8-14
8.11	CHOICE OF HEAD CHARACTERISTIC CURVES.....	8-15
8.12	CHOICE OF TORQUE CHARACTERISTIC CURVES.....	8-15
8.13	SINGLE-PHASE TORQUE.....	8-17
8.14	TORQUE DEGRADATION MULTIPLIER.....	8-17
8.15	SCHEMATIC OF EPRI/CREARE TWO-PHASE PUMP TEST FACILITY.....	8-19
8.16	COMPARISON OF PREDICTED RESULTS WITH TEST DATA FOR PUMP HEAD.....	8-20
A.1	LIQUID DENSITY.....	A-8
A.2	GAS DENSITY.....	A-9
A.3	LIQUID SPECIFIC HEAT.....	A-10
A.4	GAS SPECIFIC HEAT.....	A-11
A.5	HEAT OF VAPORIZATION.....	A-12
A.6	SURFACE TENSION.....	A-13
A.7	GAS VISCOSITY.....	A-14
A.8	LIQUID VISCOSITY.....	A-15
A.9	LIQUID THERMAL CONDUCTIVITY.....	A-16
A.10	VAPOR PRESSURE.....	A-17

## LIST OF TABLES

<u>Table</u>	<u>Page</u>
1.1	SUMMARY OF DESIGN METHODS AND APPLICATIONS..... 1-4
2.1	SUMMARY OF RECOMMENDED METHODS FOR FLOW REGIME TRANSITIONS..... 2-6
2.2	DIMENSIONLESS GEOMETRY PARAMETERS FOR SLUG-TO-STRATIFIED FLOW REGIME TRANSITION..... 2-9
2.3	SUMMARY OF PARAMETER VALUES FOR FRICTION FACTOR CALCULATION..... 2-28
2.4	SUMMARY OF EXPERIMENTAL DATA FOR FLOW REGIME METHOD VALIDATION..... 2-33
3.1	METHODS FOR PRESSURE DROP CALCULATIONS IN STRAIGHT PIPES.... 3-3
3.2	PRESSURE DROP METHODS IN PIPING COMPONENTS..... 3-4
3.3	DRIFT-FLUX PARAMETERS FOR THE SLUG FLOW REGIME..... 3-13
3.4	DRIFT-FLUX PARAMETERS FOR THE BUBBLY FLOW REGIME..... 3-14
3.5	CONTRACTION COEFFICIENTS..... 3-22
3.6	VALIDATION COMPARISONS FOR PRESSURE DROP METHODS..... 3-37
3.7	SUMMARY OF PRESSURE DROP COMPARISONS WITH DESIGN METHODS FOR PIPES..... 3-51
4.1	HEAT TRANSFER AND FLOW REGIMES..... 4-8
4.2	SUMMARY OF EVAPORATOR CALCULATIONS..... 4-12
4.3	SUMMARY OF TRANSITION CALCULATIONS..... 4-12
4.4	COMPARISON OF FCEVAP CALCULATIONS WITH FOSTER-MILLER DATA... 4-45
6.1	THERMAL BOUNDARY CONDITIONS FOR SHEAR CONDENSER ANALYSIS.... 6-11
6.2	FLOW BOUNDARY CONDITIONS FOR SHEAR CONDENSER ANALYSIS..... 6-13
6.3	EMPIRICAL COEFFICIENTS FOR $f_i/f_{wg}$ ..... 6-20
6.4	CALCULATED PRESSURE DROP DEPENDS STRONGLY ON $f_i/f_{wg}$ ..... 6-43
8.1	SCALING RELATIONSHIPS FOR CENTRIFUGAL PUMPS..... 8-5
A.1	AVAILABLE FLUIDS..... A-1
A.2	FLUID PROPERTY DATA FILE FOR AMMONIA (NH3.DAT)..... A-2
A.3	VALID TEMPERATURE RANGES OF FLUID PROPERTY CORRELATIONS.... A-3

## NOMENCLATURE

Symbol	Description	Units
$a$	magnitude of acceleration vector	(m/s <sup>2</sup> )
$a_{11}, a_{12}, a_{13}$	constants in equation to calculate drainage hole pitch for internally drained condensers	
$A$	cross-sectional area of flow channel or radiator surface	(m <sup>2</sup> )
$A, B, C, D$	constants in $f_i/f_{wg}$ correlation	
$A, B, C, D, E$	coefficients in fluid property calculations	
$A_c$	condenser area	(m <sup>2</sup> )
$A_g^*$	dimensionless cross-section occupied by gas phase in stratified flow	
$A_l^*$	dimensionless cross-section occupied by liquid phase in stratified flow	
$A_m$	reduction in cross-sectional flow area due to the meniscus	(m <sup>2</sup> )
$A_o$	cross-sectional flow area with flat meniscus	(m <sup>2</sup> )
$A_r$	ratio of solid to liquid thermal resistance in a DIC evaporator	
$b$	coefficient in empirical equation for $f_i/f_{wg}$	
$b$	exponent in LCC correlation for critical heat flux	
$b$	one-half the pitch between condenser tubes in a radiating panel	(m)
$B$	two-phase loss coefficient	
$B$	radiator fin parameter	(m <sup>-1</sup> )
$B_r$	ratio of evaporation to liquid film thermal resistance in a DIC evaporator	
$Bo$	Bond number, $aD^2(\rho_l - \rho_g)/\sigma$	
$Bo$	boiling number	
$Bo_{CHF}$	boiling number at CHF	
$Bo_{LCC}$	boiling number for LCC (CHF)	
$Bo_{UCC}$	boiling number for UCC (CHF)	
$Bo_0$	boiling number evaluated at zero quality	
$c$	exponent in LCC correlation for critical heat flux	
$c_{pl}$	specific heat capacity of liquid phase	(J/kg-K)
$c_s$	specific heat of solid wall material	(J/kg-K)
$C$	contraction coefficient	
$C_{11}, C_{12}, C_{21}, C_{22}$	constants in calculation of heat transfer in triangular and trapezoidal grooves	(-)
$C_a$	coefficient in $f_i/f_{wg}$ correlation	
$C_b$	bearing and windage torque coefficient	(N-m)
$C_e$	constant in equation for entrained liquid fraction (Eq. 3-2)	
$C_f$	frictional torque coefficient	(N-m)
$C_g$	coefficient in friction factor model for gas phase	
$C_l$	coefficient in friction factor model for liquid phase	
$C_o$	bubble distribution coefficient in drift-flux model	
$C_{ob}$	drift flux coefficient for bubbly flow regime	
$C_{os}$	drift flux coefficient for slug flow regime	
$(dP/dz)_a$	pressure gradient due to acceleration (phase change)	(Pa/m)
$(dP/dz)_f$	frictional pressure gradient	(Pa/m)
$(dP/dz)_g$	pressure gradient due to body forces	(Pa/m)

Symbol	Description	Units
$(dP/dz)_t$	total pressure gradient	(Pa/m)
$d$	diameter of droplet	(m)
$d$	depth of drainage groove	(m)
$D$	diameter of thin film spot in a DIC evaporator	(m)
$D$	diameter of pipe	(m)
$D$	drainage hole diameter	(m)
$D$	pump dimension	(m)
$D_{coil}$	effective diameter of coil	(m)
$D_g^*$	dimensionless hydraulic diameter for gas phase in stratified flow	
$D_g^*$	flat meniscus hydraulic diameter	(m)
$D_h$	actual meniscus hydraulic diameter	(m)
$D_h$	hydraulic diameter in heated (evaporator) tube	(m)
$D_{ht}$	hydraulic diameter for heat transfer	(m)
$D_i$	diameter of the vapor core in annular flow	(m)
$D_l^*$	dimensionless hydraulic diameter for liquid phase in stratified flow	
$D_{pd}$	hydraulic diameter for pressure drop	(m)
$E$	enhancement factor for forced convection	
$E_d$	fraction of liquid flow entrained as droplets	
$E_f$	fraction of wall heat flux to fluid heating	
$E_{fc}$	fraction of total heat transfer in saturated boiling due to forced convection	
$E_{ls}$	fraction of liquid contained in the liquid slugs	
$f$	Darcy friction factor $\Delta P = f \frac{L}{D} \frac{\rho v^2}{2}$	(-)
$f_{coil}$	correction factor for coil pressure drop	
$f_i$	friction factor at gas-liquid interface	
$f_{wg}$	wall friction factor for single-phase gas	
$f_{wl}$	wall friction factor for single-phase liquid	
$F$	multiplier for Reynolds number in saturated boiling model	
$F$	view factor for a radiator	
$F_a$	constant used to estimate mass flux in a condenser	(m <sup>3</sup> /kg)
$F_e$	entrance effect factor in CHF correlation	
$F_f$	constant used to estimate mass flux in a condenser	(m <sup>3</sup> /kg)
$F_g$	Froude number for gas phase, $j_g \rho_g^{0.5} / [aD(\rho_l - \rho_g)]^{0.5}$	(m/s <sup>2</sup> )
$F_x$	quality factor in CHF correlation	
$F_1$	factor in CHF correlation	
$F_2$	factor in CHF correlation	
$F_2$	factor in calculation of condensing Nusselt number	
$F_3$	factor in CHF correlation	
$Fr$	Froude number	
$g$	gravitational acceleration on earth (= 9.8 m/s <sup>2</sup> )	(m/s <sup>2</sup> )
$G$	mass flux	(kg/m <sup>2</sup> -s)
$G_c$	mass flux of vapor during condensation	(kg/m <sup>2</sup> -s)
$G_{est}$	estimated mass flux in a condenser	(kg/m <sup>2</sup> -s)
$h$	enthalpy	(J/kg)
$h$	normalized pump head	(-)
$h_{av}$	average heat transfer coefficient in the slug flow regime	(W/m <sup>2</sup> -K)

Symbol	Description	Units
$h_b$	actual heat transfer coefficient in a fin	(W/m <sup>2</sup> -K)
$h_c$	heat transfer coefficient for condensation	(W/m <sup>2</sup> -K)
$h_{cb}$	one-dimensional conduction heat transfer coefficient	(W/m <sup>2</sup> -K)
$h_{dic}$	average heat transfer coefficient for droplet impingement cooling	(W/m <sup>2</sup> -K)
$h_{fb}$	uniform wall temperature heat transfer coefficient	(W/m <sup>2</sup> -K)
$h_{fc}$	heat transfer coefficient in forced convection	(W/m <sup>2</sup> -K)
$h_{fg}$	latent heat of vaporization	(J/kg)
$h_{fg}$	latent heat of vaporization	(J/kg)
$h_l$	liquid level in pipe for stratified flow regime	(m)
$h_{nb}$	heat transfer coefficient in nucleate boiling	(W/m <sup>2</sup> -K)
$h_{nb}$	coefficient in nucleate boiling model	(W/m <sup>2</sup> -K <sup>2</sup> )
$h_{tp}$	total two-phase heat transfer coefficient	(W/m <sup>2</sup> -K)
$h_{1\phi}$	normalized single-phase pump head	(-)
$h_{2\phi}$	normalized two-phase pump head	(-)
$h_2$	heat transfer coefficient on secondary side of condensing interface heat exchanger	(W/m <sup>2</sup> -K)
$h^*$	dimensionless liquid level in stratified pipe flow	(m)
$H$	heated perimeter in evaporator tube	(m)
$H$	contoured fin height	(m)
$H$	pump head	(N-m/kg)
$H_l$	total liquid fraction	
$H_{lf}$	liquid fraction in the film for annular flow	
$H_r$	rated pump head	(N-m/kg)
$I$	pump moment of inertia	(kg-m <sup>2</sup> )
$j$	total volumetric flux or mixture velocity ( $j_g + j_l$ )	(m/s)
$j_g$	gas phase volumetric flux ( $Q_g/A$ ) or superficial velocity	(m/s)
$j_l$	liquid phase volumetric flux ( $Q_l/A$ ) or superficial velocity	(m/s)
$j_{icut}$	cutoff criterion for liquid phase superficial velocity (Eq. 2-13)	(m/s)
$Ja$	Jakob number, $c_{pl}(T_{sat} - T_f)/h_{fg}$	
$k$	coefficient for drift velocity in drift-flux model or coefficient for turbulence in slug-to-bubbly flow regime transition model	
$k_b$	drift flux coefficient for bubbly flow regime	
$k_{fin}$	thermal conductivity of a radiator fin	(W/m-K)
$k_l$	thermal conductivity of liquid phase	(W/m-K)
$k_s$	thermal conductivity of solid wall material	(W/m-K)
$k_s$	drift flux coefficient for slug flow regime	
$k_{spl}$	single-phase loss coefficient	
$k_w$	thermal conductivity of solid wall material	(W/m-K)
$K$	phase slip coefficient	
$K$	groove friction coefficient $K = f Re$	(-)
$K_g$	Kutateladze number for gas phase, $j_g \rho_g^{0.5} / [g \sigma (\rho_l - \rho_g)]^{0.25}$	
$L$	length	(m)
$L$	fin half pitch	(m)
$L_b$	length of a Taylor bubble in the slug flow regime	(m)
$L_c$	condensing length	(m)

<u>Symbol</u>	<u>Description</u>	<u>Units</u>
$L_c$	groove length	(m)
$L_s$	length of a liquid slug	(m)
$L_{sc}$	length of subcooled region in the evaporator	(m)
$L_{ss}$	distance into wall beyond thermal oscillations	(m)
$L_{sub}$	subcooled length in a condenser	(m)
$L_{tot}$	length of gas bubble plus liquid slug	(m)
$L_{tot}^*$	total length of condenser ( $L_{tp} + L_{sp}$ )	(m)
$L^*$	dimensionless length of evaporator ( $L/D_h$ )	
$m$	exponent in friction factor model for gas phase	
$m_g$	magnitude of spacecraft acceleration	(g's)
$m_o$	fraction of cross-section occupied by liquid film	
$\dot{m}$	condensate flow rate per unit groove length	(kg/m)
$\dot{m}_{vap}$	mass flow rate of vapor	(kg/s)
$\dot{m}_{tot}$	total mass flow rate	(kg/s)
$M$	surrounding a bubble in the slug flow regime	
$M_h$	ratio of superficial phase velocities, $j_l/j_g$	(-)
$MW$	pump head degradation multiplier	(kg/kg-mole)
$n$	molecular weight	
$n$	exponent in friction factor model for liquid phase	
$n$	exponent in UCC CHF correlation	(-)
$n$	the number of active radiating sides on a radiator panel (1 or 2)	
$N$	pump rotational speed	(rad/s)
$N_r$	rated pump rotational speed	(rad/s)
$N_s$	pump specific speed	(-)
$N_t$	total number of turns in coil	(-)
$N_\beta$	pump torque degradation multiplier	(-)
$Nu$	Nusselt number	(-)
$Nu_b$	Nusselt number for bubbles in slug flow regime	
$Nu_c$	Nusselt number for condensation	
$Nu_{fc}$	Nusselt number in forced convection heat transfer	
$Nu_{lo}$	Nusselt number calculated for liquid-only flow	
$Nu_{nb}$	Nusselt number in nucleate boiling heat transfer	
$Nu_s$	Nusselt number for liquid in a slug	
$Nu_{sp}$	Nusselt number in single-phase forced convection heat transfer	
$Nu_{tp}$	Nusselt number in nucleate boiling heat transfer	
$p$	power	(Watts)
$p$	pressure	(Pa)
$P$	power	(Watts)
$P$	pressure	(Pa)
$P$	drainage hole pitch	(m)
$P_{crit}$	critical pressure	(Pa)
$P_i$	tube internal perimeter	(m)
$P_r$	reduced pressure ( $P/P_{crit}$ )	
$P_{sat}$	saturation pressure	(Pa)
$P_x$	external perimeter of a condensing tube	(m)

Symbol	Description	Units
$\Delta P^*$	dimensionless pressure drop	
$\Delta P_a$	pressure drop due to acceleration (phase change)	(Pa)
$\Delta P_a^*$	dimensionless pressure drop due to acceleration	
$\Delta P_{ae}$	pressure drop due to acceleration (phase change) in two-phase region of evaporator	(Pa)
$\Delta P_{coil}$	evaporator pressure drop including coiling effects	(Pa)
$\Delta P_{evap}$	total pressure drop in evaporator ( $\Delta P_p + \Delta P_{sp}$ )	(Pa)
$\Delta P_f$	frictional pressure drop	(Pa)
$\Delta P_{fe}$	frictional pressure drop in two-phase region of evaporator	(Pa)
$\Delta P_{fe}^*$	dimensionless frictional pressure drop in two-phase region of evaporator	
$\Delta P_g$	pressure drop due to body forces	(Pa)
$\Delta P_{ge}$	pressure drop due to body forces in two-phase region of evaporator	(Pa)
$\Delta P_{ge}^*$	dimensionless pressure drop due to body forces in two-phase region of evaporator	
$\Delta P_{sat}$	difference between saturation pressures at fluid and heated wall temperatures	(Pa)
$\Delta P_{sp}$	pressure drop in single-phase region of evaporator or condenser	(Pa)
$\Delta P_t$	pressure drop due to taper	(Pa)
$\Delta P_{t'}$	pressure drop in a mixing tee	(Pa)
$\Delta P_{tot}$	total pressure drop in a shear condenser	(Pa)
$\Delta P_{tp}$	total pressure drop in two-phase region of evaporator or condenser	(Pa)
Pe	Peclet number	
Pr <sub>l</sub>	Prandtl number of the liquid phase, $c_{p1}\mu_1/k_1$	
q	total evaporator heat load	(W)
q	normalized pump flow rate	(-)
q <sub>sp</sub>	total heat transferred in the single-phase regime	(W)
q	linear rate of heat transfer	(W/m)
q"	heat flux	(W/m <sup>2</sup> )
q" <sub>CHF</sub>	critical heat flux (CHF)	(W/m <sup>2</sup> )
q" <sub>env</sub>	absorbed orbital average heat flux	(W/m <sup>2</sup> )
q" <sub>fc</sub>	portion of wall heat flux attributed to forced convection boiling	(W/m <sup>2</sup> )
q" <sub>lcc</sub>	value of CHF calculated by LCC	(W/m <sup>2</sup> )
q" <sub>max</sub>	maximum wall heat flux in the evaporator	(W/m <sup>2</sup> )
q" <sub>sub</sub>	portion of wall heat flux attributed to subcooled boiling	(W/m <sup>2</sup> )
q" <sub>ucc</sub>	value of CHF calculated by UCC	(W/m <sup>2</sup> )
Q	pump volumetric flow rate	(m <sup>3</sup> /s)
Q <sub>c</sub>	condensation rate	(W)
Q <sub>r</sub>	rated pump flow rate	(m <sup>3</sup> /s)
r <sub>b</sub>	radius of bubble at the onset of nucleate boiling	(m)
r <sub>crit</sub>	radius of vapor bubble at ONB	(m)
r <sub>i</sub>	inner radius of coil (at tube centerline)	(m)
r <sub>o</sub>	outer radius of coil (at tube centerline)	(m)
R	radius of curvature of a pipe bend	
R <sub>1</sub> , R <sub>2</sub>	radii of curvature of the menisci on the fin top and groove	(m)



Symbol	Description	Units
$R_c$	thermodynamic ratio in high vapor shear condenser	
$R_{ev}$	thermodynamic ratio in forced convection evaporator	
$R_{evap}$	thermal resistance due to evaporation	(m <sup>2</sup> -K/W)
$R_g$	gas constant for the vapor phase	(J/kg-K)
$R_g^*$	void fraction parameter for calculating stratified flow transition (Table 2.2)	
$R_l^*$	liquid fraction parameter for calculating stratified flow transition (Table 2.2)	
$R_p$	ratio of pressure drop to maximum pressure drop	(-)
$\hat{R}_p$	pressure drop ratio which corresponds to a receding meniscus	(-)
$Re$	flow Reynolds number	(-)
$Re_b$	effective Reynolds number in nucleate boiling	
$Re_d$	Reynolds number for a liquid droplet ( $= \rho_l V d / \mu_l$ )	
$Re_f$	Reynolds number for liquid phase, based on inlet velocity, $GD/\mu_l$	
$Re_g$	Reynolds number for gas phase, based on actual velocity, $\rho_g Du_g / \mu_g$	
$Re_{gs}$	Reynolds number for gas phase, based on superficial velocity, $\rho_g Dj_g / \mu_g$	
$Re_{jc}$	two-phase Reynolds number based on flow in the vena contracta	
$Re_{jd}$	two-phase Reynolds number based on downstream conditions	
$Re_{jp}$	two-phase Reynolds number based on pipe flow	
$Re_{ju}$	two-phase Reynolds number based on upstream conditions	
$Re_l$	Reynolds number for liquid phase, based on inlet velocity, $GD/\mu_l$	
$Re_{lm}$	Reynolds number based on mixture density	
$Re_{lo}$	Reynolds number calculated for liquid-only flow ( $GD_l/\mu_l$ )	
$Re_{ls}$	Reynolds number for liquid phase, based on superficial velocity, $\rho_l Dj_l / \mu_l$	
$Re_m$	Reynolds number for a homogeneous two-phase mixture	
$Re_s$	Reynolds number of liquid in a slug	
$Re_{tp}$	two-phase Reynolds number, based on mixture velocity, $\rho_m Dj / \bar{\mu}$	
$S$	suppression factor in saturated boiling model	
$S$	contoured fin surface length	(m)
$S_g^*$	dimensionless perimeter in contact with gas phase for stratified flow	
$S_l^*$	dimensionless contact length between gas and liquid phases for stratified flow	
$S_l^*$	dimensionless perimeter in contact with liquid phase for stratified flow	
$S_t$	wetted perimeter	(m)
$St$	Stanton number, $Nu/Re_f Pr_l$	
$t$	time	(sec)
$t_{drop}$	time between droplets in a DIC evaporator	(s)

Symbol	Description	Units
$t_{eff}$	effective one-dimensional wall thickness	(m)
$t_{evap}$	evaporation time for the liquid film in a DIC evaporator	(s)
$t_{fin}$	radiator fin thickness	(m)
$t_w$	thickness of condenser wall	(m)
$T$	pump torque	(N-m)
$T_b$	bearing and windage torque	(N-m)
$T_{crit}$	critical temperature	(K)
$T_f$	fluid temperature	(K)
$T_f$	frictional torque	(N-m)
$T_r$	radiator temperature for condenser	(K)
$T_r$	rated pump torque	(N-m)
$T_{sat}$	saturation temperature	(K)
$T_{sub}$	temperature of subcooled liquid	(K)
$T_v$	vapor temperature	(K)
$T_w$	wall temperature	(K)
$T_{wi}$	temperature at the inside wall of a condenser tube	(K)
$T_{wonb}$	wall temperature in evaporator at ONB transition	(K)
$T_{wx}$	average effective radiating temperature	(K)
$T_2$	temperature of heat sink for radiation	(K)
$T_2$	temperature on secondary (coolant) side of condenser	(K)
$TR$	reduced temperature ( $TR = T/T_{crit}$ )	(-)
$\Delta T_{CHF}$	wall superheat at CHF	(K)
$\Delta T_{eff}$	effective wall superheat	(K)
$\Delta T_f$	change in fluid temperature due to heat input	(K)
$\Delta T_{peak}$	peak wall superheat	(K)
$\Delta T_{sat}$	difference between saturation and fluid temperatures ( $T_{sat} - T_f$ )	(K)
$\Delta T_{sub}$	difference between wall and saturation temperatures ( $T_w - T_{sat}$ )	(K)
$\Delta T_w$	temperature difference between tube inner and outer surfaces	(K)
$u_{bo}$	velocity of a vapor bubble in the condenser	(m/s)
$u_f$	actual velocity of liquid phase ( $j_l/(1-\alpha)$ ),	(m/s)
$u_g$	actual velocity of vapor phase ( $j_g/\alpha$ ),	(m/s)
$U_g^*$	ratio of total pipe area to area occupied by gas phase	
$U_l^*$	ratio of total pipe area to area occupied by liquid phase	
$v$	velocity	(m/s)
$v_{fg}$	difference between liquid and gas phase specific volume ( $v_g - v_l$ )	(m <sup>3</sup> /kg)
$v_g$	gas phase specific volume	(m <sup>3</sup> /kg)
$v_l$	liquid phase specific volume	(m <sup>3</sup> /kg)
$v^*$	dimensionless velocity	(-)
$V$	droplet velocity in a DIC evaporator	(m/s)
$V_e$	critical velocity for onset of liquid entrainment	(m/s)
$V_g$	flow velocity averaged over the actual cross-section	(m/s <sup>2</sup> )
$V_g^o$	flow velocity averaged over the full groove area	(m/s <sup>2</sup> )
$V_s$	velocity of liquid slugs	(m/s)
$V_\infty$	bubble velocity for drift flux model in bubbly regime	(m/s)

Symbol	Description	Units
$w$	mass flow rate	(kg/s)
$W$	groove characteristic length	(m)
$W_c$	condenser width	(m)
$W_f$	terminal groove side length	(m)
$We$	Weber number	
$We_j$	Weber number, based on mixture velocity, $\rho^l D_j^2 / \sigma$	
$x$	quality (fraction of two-phase mass flow which is vapor)	
$x$	groove coordinate in x-direction	(m)
$x_{ief}$	effective inlet quality for CHF	
$x_{in}$	inlet evaporator quality	
$x_o$	quality at evaporator outlet or condenser inlet	
$x_s$	quality at transition from annular to slug flow	
$x_t$	quality at the transition from annular to slug flow	
$X$	Martinelli parameter	
$X_a$	Martinelli parameter in the annular flow regime	
$X_s$	Martinelli parameter in the slug flow regime	
$X_{tt}$	Martinelli parameter assuming turbulent gas and liquid phases	
$\Delta x$	change in quality	
$y$	groove coordinate in y-direction	(m)
$Y$	Shah's correlating parameter	
$Y$	dimensionless acceleration vector parameter	
$Y_a$	acceleration vector parameter for the annular flow regime	
$Y_s$	acceleration vector parameter in the slug flow regime	
$z$	arbitrary position or length coordinate	(m)
$z$	groove longitudinal coordinate	(m)
$z_{eff}$	effective distance from inlet for CHF	(m)
$z_{sp}$	distance from beginning of single-phase region in the condenser	(m)
$z^*$	dimensionless length increment, $z^* = z/D$	
$\Delta z$	segment length	(m)

#### Greek

$\alpha$	void fraction	(-)
$\alpha$	groove half angle for triangular grooves	(°)
	groove aspect ratio for rectangular and trapezoidal grooves	(-)
$\alpha_c$	critical void fraction defining a flow regime transition	
$\alpha_f$	terminal aspect ratio for meniscus height	(-)
$\alpha_l$	liquid fraction (fraction of two-phase volumetric flow which is liquid)	
$\alpha_{lc}$	critical liquid fraction	
$\alpha_o$	initial aspect ratio for meniscus height	(-)
$\alpha_s$	thermal diffusivity of solid wall material ( $k/\rho_s C_s$ )	(m <sup>2</sup> /s)
$\beta$	ratio of calculated to input heat flux in evaporator	
$\beta$	droplet spread ratio in a DIC evaporator ( $= d/D$ )	
$\beta$	normalized pump torque	(-)
$\beta_{1\phi}$	normalized single-phase pump torque	(-)

Symbol	Description	Units
$\beta_{2\phi}$	normalized two-phase pump torque	(-)
$\gamma$	wetted area fraction in a DIC evaporator	
$\gamma$	meniscus contact angle	(°)
$\gamma_t$	terminal meniscus contact angle	(°)
$\gamma_o$	initial meniscus contact angle	(°)
$\delta$	film thickness	(m)
$\delta_o$	thickness of liquid film at condenser inlet	(m)
$\delta_0$	initial film thickness in a DIC evaporator	(m)
$\delta(t)$	film thickness	(m)
$\delta^+$	dimensionless film thickness	
$\epsilon$	emissivity of radiator surface	
$\epsilon_r$	pipe wall roughness	(m)
$\eta$	radiating fin efficiency	
$\eta$	ratio of evaporation time to time between droplets in a DIC evaporator	
$\eta$	fin efficiency	(-)
$\theta$	angle between acceleration vector and flow direction	(°)
	0° = colinear (downflow on earth)	
	90° = perpendicular (horizontal on earth)	
	180° = opposing (upflow on earth)	
$\theta$	groove base angle for the trapezoidal groove	(°)
$\theta_{\text{evap}}$	dimensionless evaporation time	
$\lambda$	dimensionless fluid property parameter, $\mu_1^2/D\rho_1\sigma$	
$\mu$	dynamic viscosity of liquid	(kg/m-s)
$\mu_g$	gas phase viscosity	(kg/m-s)
$\mu_l$	liquid phase viscosity	(kg/m-s)
$\mu_m$	viscosity of a two-phase mixture	(kg/m-s)
$\mu_w$	liquid viscosity at wall temperature	(kg/m-s)
$\bar{\mu}$	average viscosity of two-phase mixture	(kg/m-s)
$\nu$	kinematic viscosity of liquid	(m <sup>2</sup> /s)
$\nu_l$	kinematic viscosity of the liquid phase	(m <sup>2</sup> /s)
$\rho$	density of liquid	(kg/m <sup>3</sup> )
$\rho_c$	density of two-phase mixture in droplet flow	(kg/m <sup>3</sup> )
$\rho_c^*$	ratio of droplet mixture density to gas density ( $\rho_c/\rho_g$ )	
$\rho_g$	gas phase density	(kg/m <sup>3</sup> )
$\rho_l$	liquid phase density	(kg/m <sup>3</sup> )
$\rho_{ls}$	mixture density in the liquid slugs	(kg/m <sup>3</sup> )
$\rho_m$	density of two-phase mixture	(kg/m <sup>3</sup> )
$\rho_m$	mixture density of two-phase fluid	(kg/m <sup>3</sup> )
$\rho_r$	rated pump fluid density	(kg/m <sup>3</sup> )
$\rho_s$	density of the solid wall	(kg/m <sup>3</sup> )
$\rho^*$	ratio of phase densities, $\rho_l/\rho_g$	
$\sigma$	surface tension	(N/m)
$\sigma_o$	Stefan-Boltzmann constant	(W/m <sup>2</sup> -K <sup>4</sup> )
$\tau$	wall shear stress	(Pa)
$\tau_i$	shear stress at gas-liquid interface	(Pa)
$\tau_w$	wall shear stress	(Pa)
$\phi$	wall heat flux in evaporator	(Watts/m <sup>2</sup> )

<u>Symbol</u>	<u>Description</u>	<u>Units</u>
$\phi^2$	empirical factor which multiplies the calculated heat flux in the slug flow regime	
$\phi_{go}^2$	two-phase multiplier, ratio of two-phase to single-phase gas pressure gradient	
$\phi_{tp}$	two-phase multiplier for pressure losses	
$\omega$	normalized pump speed	(-)

### Subscripts

b	bend
c	vena contracta
crit	critical value of a parameter which corresponds to a flow regime transition
d	downstream
fa	friction in annular flow (refers to a pressure gradient)
fb	friction in bubbly flow (refers to a pressure gradient)
fdb	fully developed boiling
fsl	friction in slug flow (refers to a pressure gradient)
fst	friction in stratified flow (refers to a pressure gradient)
ga	body forces in annular flow (refers to a pressure gradient)
gb	body forces in bubbly flow (refers to a pressure gradient)
gst	body forces in stratified flow (refers to a pressure gradient)
gsl	body forces in slug flow (refers to a pressure gradient)
i	insert
i	inlet
in	inlet
lcc	local conditions correlation
o	exit
onb	onset of nucleate boiling
p	pipe
spl	single-phase liquid
ta	total gradient in annular flow (refers to a pressure gradient)
tb	total gradient in bubbly flow (refers to a pressure gradient)
tsl	total gradient in slug flow (refers to a pressure gradient)
tst	total gradient in stratified flow (refers to a pressure gradient)
tx	total gradient in regime x (refers to a pressure gradient)
u	upstream
ucc	upstream conditions correlation

# 1 INTRODUCTION TO THE DESIGN MANUAL

## 1.1 Purpose

This design manual presents methods to design and model the performance of key two-phase components in thermal management systems for spacecraft. Figures 1.1 and 1.2 are schematic illustrations of mechanically pumped and capillary pumped two-phase thermal loops. The key components of these loops include:

- Evaporators
- Transport lines
- Condensers
- Mechanical pumps

Condensers in heat pipes are also addressed by the capillary condenser methods.

The analysis methods presented here apply to various approaches to these components. Each method concerns a fundamental and general unit of the system component — for example, a single tube in a forced convection evaporator or shear condenser. These methods can be used for:

- Component design and sizing,
- Analysis of component performance in system or component development tests,
- Development and evaluation of analytic models for key phenomena, and
- Integration with transient codes for system analysis.

As an example of the integration with transient codes, the flow regime methods described here in Section 2 have already been implemented in the recent releases of SINDA/FLUINT (Cullimore et al., 1987) and ESATAN/FHTS (Stock et al., 1991).

## 1.2 Approach

The basic analytical approach in each method presented here is mechanistic. That is, the models of the components are based upon fundamental physics rather than empirical relationships such as correlations. Thus, these models include the inherent scaling of the results with gravity, physical size, and fluid properties. In these mechanistic models, correlating elements are at a secondary level of detail, for example as modelling parameters describing interfacial friction relationships for the pressure drop, in contrast to a direct empirical correlation of pressure drop. This provides a basic structure to the models which does not change, though values of the modelling parameters can be later refined as experimental data become available.

The analysis approach also includes the ability to assess the analytical uncertainty. That is, ranges of the modelling parameters which correspond to physical limits are identified. An example is a smooth gas-liquid interface to describe the interfacial friction relationship in a pressure drop model. The designer can assess the sensitivity of his results to the range of uncertainty in these modelling parameters. On that basis, he can determine whether further refinement of a particular model is important or unnecessary in his application.

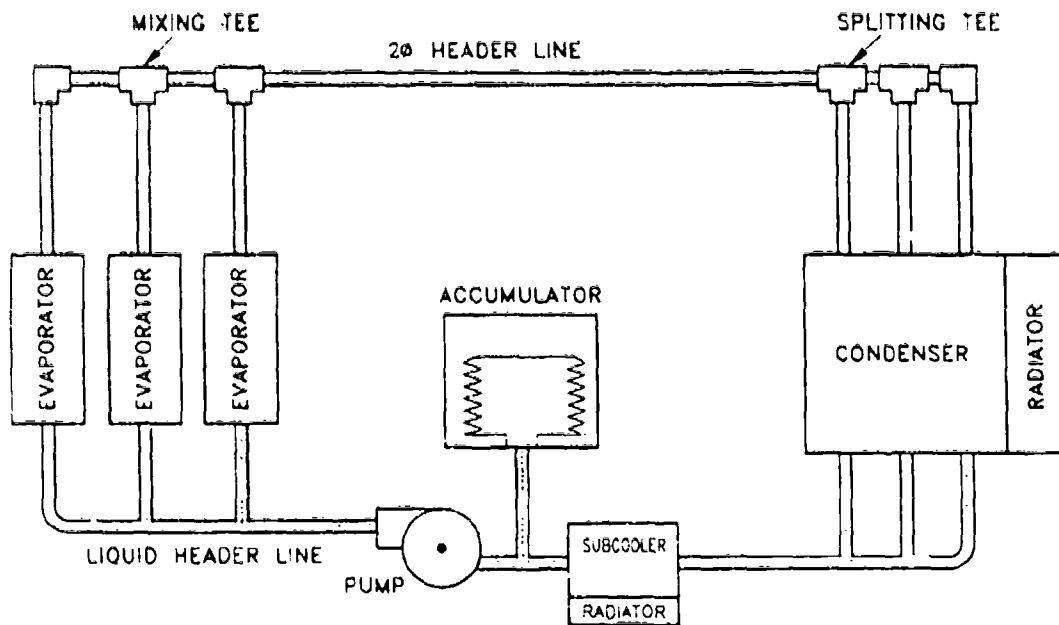


Figure 1.1. ILLUSTRATION OF A MECHANICALLY PUMPED LOOP (MPL)

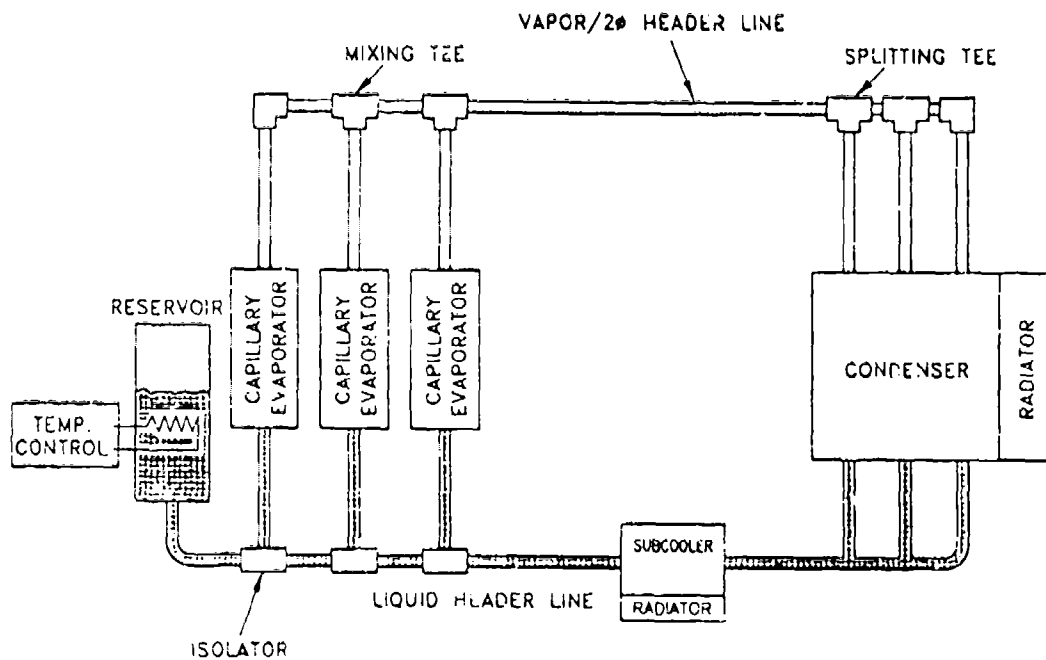


Figure 1.2. ILLUSTRATION OF A CAPILLARY PUMPED LOOP (CPL)

Simple design maps are presented where feasible. These can be used for initial scoping calculations in sizing two-phase components.

Finally, the design methods have been validated against experimental data to the extent that data are available. Each section of this report presents the validation comparisons performed with each model. In some areas, the validation is extensive. In others, additional work can be identified. In this way, the work described here can focus additional microgravity experimental research on the key issues.

### 1.3 Contents

Table 1.1 summarizes the design methods included in this report. The methods have been significantly upgraded and expanded compared with an earlier version of the design manual (Crowley and Izenzon, 1989). The table lists the nine topics addressed, the function of the design method, and the application to specific components of two-phase thermal management systems. Each section of the design manual deals with one of these areas.

### 1.4 Corresponding Software

Table 1.1 also identifies a corresponding software item for each topic (section) in this manual. References for this software are listed in Appendix B of this manual. Validation of these programs by comparison with experimental data is presented in the corresponding chapter of this manual. The software generally consists of small (100 kB or less) easy-to-use programs, written in standard FORTRAN, which are readily transportable to various personal computers. Executable versions for IBM DOS and compatibles as well as Macintosh IIci computers with math coprocessors are available, and the source code can be readily compiled on other hardware. Persons interested in obtaining the software should contact the authors.

### 1.5 References

Crowley, C.J. and Izenzon, M.G.; "MICROGRAVITY TWO PHASE-FLOW AND HEAT TRANSFER", AL-TR-89-026, Prepared by Creare Inc., Hanover, NH, Prepared for Phillips Laboratory (OL-AC PL/VTPT), Edwards AFB, CA, Contract F04611-88-C-0050, October, 1989.

Cullimore, B.A., Goble, R.G., Jensen, C.L., and Ring, S.G.; "SINDA '85/FLUINT SYSTEMS IMPROVED NUMERICAL DIFFERENCING ANALYZER AND FLUID INTEGRATOR"; Version 2.1, User's Manual, MCR-86-594, Prepared for NASA JSC, Contract No. NAS9-17448, Prepared by Martin-Marietta Aerospace Corp., Denver, CO, Nov., 1987.

Stock, N.J., Kirtley, C.J., and Stroom, C.J.M.; "ESATAN - CURRENT STATUS AND FUTURE DEVELOPMENTS"; ESA SP-324. Presented at the 4th European Symposium on Space Environmental Control Systems, Florence, Italy, 21-24 Oct., 1991.



Table 1.1. SUMMARY OF DESIGN METHODS AND APPLICATIONS

Topic	Application	Function	Design Manual Section	Software	Software Reference
Flow Regimes	Transport Line (MPL or CPL)	Map flow regime transitions or determine the flow regime for given liquid and vapor phase flow rates.	2	MICROREG	PL-TR-92-3003, Vol. 1
Pressure Drop	Transport Line (MPL or CPL)	Calculate pressure drop and void fraction for specified flow rates: <ul style="list-style-type: none"> <li>• straight pipes (annular, slug, bubbly, and stratified regimes)</li> <li>• bends and elbows</li> <li>• tees</li> <li>• fittings (expansions and contractions)</li> </ul>	3	MICROP	PL-TR-92-3003, Vol. 2
Forced Convection Heat Transfer	Evaporator (MPL)	Determine boiling flow characteristics for a given wall heat flux or wall temperature in (1) straight and (2) coiled tubes.	4	FCEVAP	PL-TR-92-3003, Vol. 3
Evaporation Heat Transfer	Evaporator (MPL or CPL)	Calculate wall heat transfer for droplet impingement cooling with evaporation of thin liquid films.	5	DROPEVAP	PL-TR-92-3003, Vol. 4
High Vapor Shear Condensation	Shear Condenser (MPL or CPL)	Determine condensing flow pressure drops and heat transfer characteristics for straight and tapered tube flow channels, with convection or radiation boundary conditions.	6	MICROCON	PL-TR-92-3003, Vol. 5
Capillary Condensation	CPL Condenser, Heat Pipe or Interface HX	Calculate the friction factor and pressure gradient in a capillary groove of rectangular, triangular, or trapezoidal geometry.	7	MICROCAP	PL-TR-92-3003, Vol. 6
Capillary Condensation	CPL Condenser, Heat Pipe or Interface HX	Calculate the local heat transfer coefficient in a groove of rectangular, triangular, or trapezoidal geometry with flat or curved fin tops.	7	MICROCAP	PL-TR-92-3003, Vol. 6
Capillary Condensation	Interface HX (MPL or CPL)	Calculate the local heat transfer coefficient on a curved capillary (Gregorig type) surface.	7	MICROCAP	PL-TR-92-3003, Vol. 6
Two-Phase Pumps	Mechanical Pump (MPL)	Calculate the multiphase degradation of two-phase pumps for steady or transient operation.	8	PUMPS	PL-TR-92-3003, Vol. 7

## **2 TRANSPORT LINES: Flow Regime Methods**

Most two-phase thermal management systems for spacecraft include gas and liquid flow in the transport line between the evaporator and condenser components or in the condenser/radiator component. Mechanically pumped systems permit two-phase flow at the evaporator exit. Others, such as capillary pumped loops (CPLs) or droplet impingement cooling (DIC) devices, have single-phase flow at the evaporator exit, but two-phase flow occurs downstream in the transport line because heat losses lead to condensate formation between the evaporator and the condenser.

The purpose of this section of the design manual is to provide methods for determining the two-phase flow regime in piping. Knowledge of the flow regime is crucial to the calculation of the pressure drop and void fraction. (See Section 3 of this design manual.) Void fraction – or liquid inventory – is especially important when calculating transient system behavior.

Section 2.1 summarizes the flow regime methods and discusses their applications.

Section 2.2 describes the methods and presents the basic equations behind each of three flow regime transition boundaries which define the four flow regime domains. The equations include sufficient detail that the designer can recreate the flow regime maps shown here, either in dimensional or dimensionless form. The software called MICROREG (Crowley, 1992) developed on this project uses the methods and equations presented in this section.

Section 2.3 presents dimensionless design maps for the flow regime determination. The user does not need to know the details of the theory and can determine the flow regime quickly by hand using the procedures described in this section. The designer approaches the flow regime calculations with knowledge of the phase flow rates, physical geometry, and fluid conditions. The designer can then calculate a few dimensionless parameters, plot points on simple maps, and determine the flow regime very quickly.

Finally, Section 2.4 compares the flow regime maps for the recommended design methods against data from various microgravity experiments.

A key feature of the design methods recommended here is that they are applicable to a wide range of acceleration levels, including earth gravity and microgravity, and all "inclinations". The upper limit on the acceleration level would be the point where fluid properties vary significantly across the flow channel due to hydrostatic pressures. Once the flow regime is selected from four possible choices, the pressure drop specific to that regime can then be calculated (see Section 3).

### **2.1 Summary of Flow Regime Methods and Applications**

A particular flow pattern occurs only for limited ranges of gas and liquid flow. The gas/liquid flows which mark the transition from one regime to another are called regime transitions. Regime transitions are calculated using mechanistic models for the dominant forces which shape the flow patterns.

### 2.1.1 Summary of the Flow Regimes and Transitions

Figure 2.1 illustrates the four primary flow patterns of interest for two-phase flow in pipes. The patterns include:

- Stratified,
- Slug,
- Annular, and
- Bubbly.

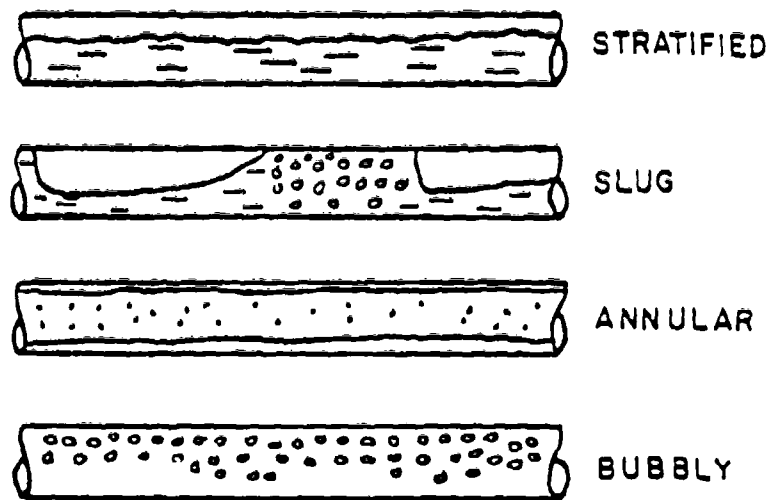
These patterns are referred to as "flow regimes":

- In the annular regime the vapor flows as a continuous gas core, and the liquid flows as a thin film on the wall of the pipe. This is perhaps the most important flow regime for thermal management systems in microgravity.
- In the stratified regime body forces due to gravity segregate the gas and liquid phases. Liquid flows near the bottom of the pipe and the gas flows near the top. This regime does not occur in a "vertical" pipe on the ground. On a spacecraft, the acceleration must have a strong component perpendicular to the axis of the pipe for this flow regime to occur. Often, the flow conditions of interest produce stratified flow at earth gravity, but annular flow in microgravity for the same conditions.
- In the slug regime, the vapor forms long bubbles so that the vapor phase is not continuous in the axial (flow) direction, but is separated by liquid slugs. Vapor bubbles many pipe diameters in length occur and may be either asymmetrical or symmetrical with respect to the central axis of the pipe.
- In the bubbly regime, the vapor flows as discrete bubbles within the liquid phase.

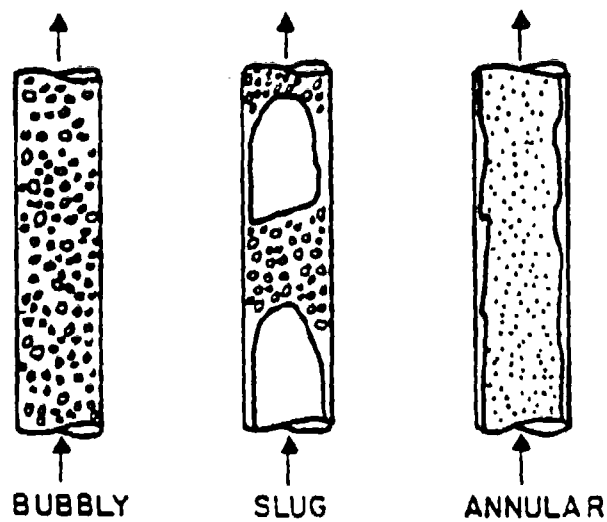
The key to determining the flow regime is to first identify the dominant forces acting on the fluid. Balances between the dominant forces are then used to describe the boundaries (the transitions) between the four flow patterns described above. Three flow regime transitions:

- Stratified to nonstratified,
- Slug to bubbly, and
- Slug to annular.

bound the four flow regimes. These three transitions depend upon different balances of forces. Figures 2.2 and 2.3 show sample flow regime maps in coordinates of superficial velocity (Figure 2.2) and mass flux and quality (Figure 2.3) for earth gravity. Both maps display the three regime boundaries and the regions corresponding to each of the four flow regimes.



#### HORIZONTAL GAS LIQUID FLOWS



#### VERTICAL GAS LIQUID FLOWS

Figure 2.1. ILLUSTRATING FLOW PATTERNS (REGIMES) OF INTEREST

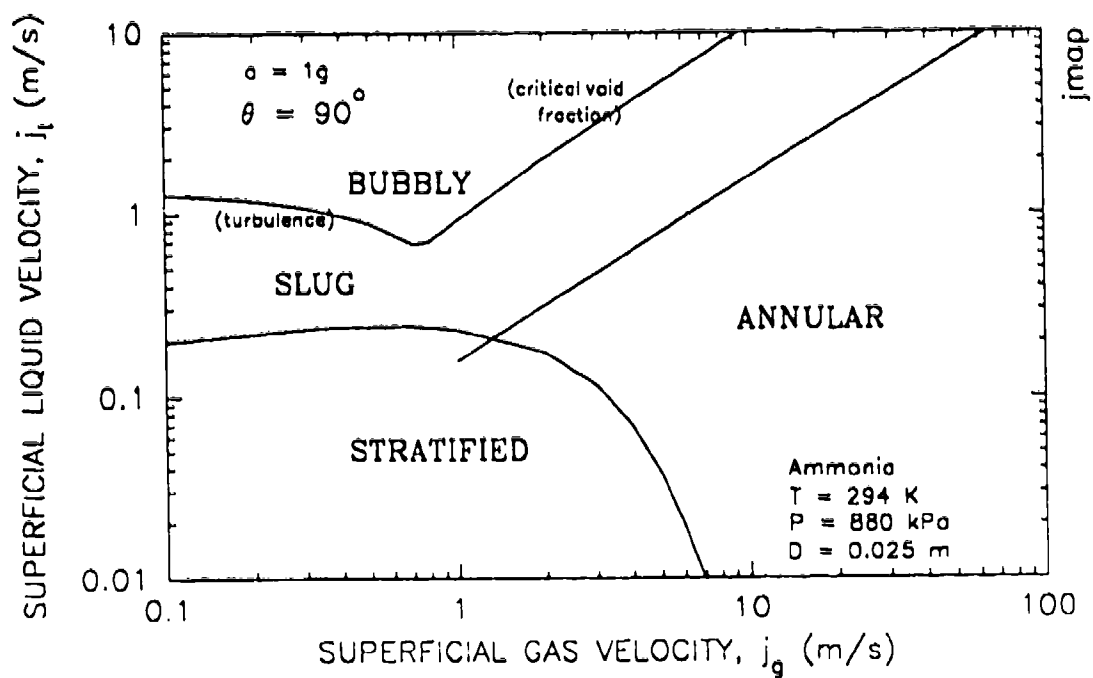


Figure 2.2. SAMPLE FLOW REGIME MAP IN SUPERFICIAL VELOCITY COORDINATES

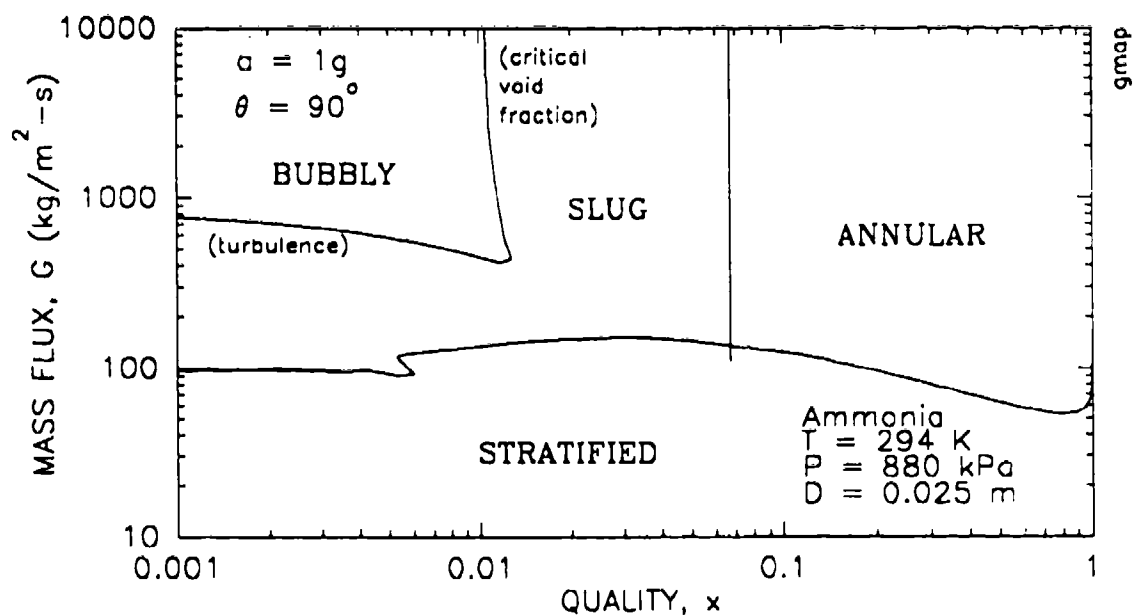


Figure 2.3. SAMPLE FLOW REGIME MAP IN MASS FLUX AND QUALITY COORDINATES

### 2.1.2 Summary of Regime Transition Models

This design manual uses mechanistic models for each of these flow regime transitions. In contrast to empirical correlations, the mechanistic approach considers the governing physics for each transition. Therefore the mechanistic models should scale well with all acceleration magnitudes (g-levels) and directions. The three basic forces and force balances to consider in the determination of the flow regimes include:

- Balance of buoyancy and inertia forces,
- Balance of surface tension and inertia forces, and
- Balance of surface tension and buoyancy forces.

The dimensionless Froude number, Weber number, and Bond number represent these three force balances, respectively. Models for regime transitions which consider the balances of buoyancy and inertia forces include Taitel and Dukler (1976), Barnea (1986), and Dukler et al. (1987). Models which consider the balances involving surface tension include Lee and Best (1987) and Barnea et al. (1983).

There is a tendency in current literature to draw a distinction between flow regime models for earth gravity and for microgravity. However, based upon the experimental evidence presented thus far, we find that the models developed for earth-gravity conditions reduce to the appropriate limits for microgravity conditions without resorting to separate models. Reddy Karri (1988) and Revankar (1989) provide examples for selected flow regime transitions. In this design manual, all of the significant regime transitions at earth gravity scale properly to microgravity conditions, hence a single set of flow regime transitions applies at all acceleration levels and angles between the body force and the flow direction. Table 2.1 summarizes the models recommended for the design manual.

To determine the flow regime using these models, the basic data supplied by the designer should include: the fluid properties, the pipe size, the acceleration (magnitude and direction), and the volumetric flow rates of the gas and the liquid phases.

The methods in this section apply to adiabatic flow in pipes of uniform, circular cross-section. Alternate geometries such as square or rectangular channels must be treated separately. The methods also assume that the liquid phase wets the material of the wall. If the liquid does not wet the wall surface (such as mercury in a glass tube for example), then the flow regimes and pressure drop models may be different than described here.

Extensive comparisons against experimental data validate the flow regime methods at earth gravity in various flow orientations ranging from vertical upward to vertical downward. The models for each orientation reduce to the same model under microgravity conditions and compare well with the available microgravity data.

## 2.2 Flow Regime Transition Methods

This section describes in detail the analytical equations used for each of the flow regime transitions. Design maps can be generated by plotting the equations presented in this section. The software package MICROREG, prepared on this project, calculates the regime transitions necessary to plot the flow regime maps, and also determines the flow regime for input flow conditions. The Software Maintenance Manual (Crowley, 1992) describes the computer program and its use.

Table 2.1. SUMMARY OF RECOMMENDED METHODS FOR FLOW REGIME TRANSITIONS						
TRANSITION CRITERION:	RECOMMENDED MODEL	APPROACH	KEY MODEL PARAMETER FOR UNCERTAINTY	BASELINE VALUE OF MODEL PARAMETER	RANGE OF UNCERTAINTY FOR MODEL PARAMETER	
1. STRATIFIED-TO-NONSTRATIFIED:	BASELINE	BALANCE $\left[ \frac{\text{gas inertia}}{\text{buoyancy}} \right]$	INTERFACIAL SHEAR $\left[ \frac{f_1}{f_{wg}} \right]$	5	1 to 10	
	DOWNFLOW CUTOFF	STABILITY OF FALLING FILM	--	--	--	
	SMALL DIAMETER ( $B_o < 100$ )	BALANCE $\left[ \frac{\text{buoyancy}}{\text{surf. tens.}} \right]$	--	--	--	
2. SLUG-TO-BUBBLY:	TURBULENCE	BALANCE $\left[ \frac{2\phi \text{ inertia}}{\text{buoyancy}} \right]$	TURBULENCE COEFFICIENT ( $\kappa$ )	1.14	0.725 to 3.7	
	MAXIMUM VOID FRACTION	MAXIMUM PACKING OF VAPOR BUBBLES	CRITICAL VGID FRACTION ( $\alpha_c$ )	0.40	0.30 to 0.52	
			BUBBLE DISTRIBUTION PARAMETER, $C_o$	1.2	1.0 to 1.2	
3. SLUG-TO-ANNULAR:	BASELINE	"NEUTRAL STABILITY" or	INTERFACIAL SHEAR COEFFICIENT $[1 + C_a (1 - \alpha)]$	$Ca = 75$	0 to 75	
		"PHYSICAL BLOCKAGE"	CRITICAL LIQUID FRACTION ( $\alpha_{lc}$ )	0.24	0.24 to 0.40	

Stratified to Nonstratified Transition

This flow regime transition consists of two parts. The first uses a balance between buoyancy and inertial forces (Kelvin-Helmholtz instability) that applies to all except very small tubes. The second considers a balance between buoyancy and surface tension forces that comes into play for very small diameter tubes – a few millimeters in diameter. The Bond number must be less than about 100 for the second case to matter. Since the Bond number also becomes small as the acceleration decreases, this transition also needs to be considered for larger pipes under microgravity conditions.

**Basic Transition Model.** This transition from stratified flow (to slug or annular flow) involves the simultaneous solution of two equations. One equation is a dimensionless two-phase momentum equation for a separated flow, and the other represents a dimensionless transition criterion.

The dimensionless transition criterion in this model is based upon a balance between gas inertia and buoyancy in the gas and liquid phases. Figure 2.4 illustrates the concept. At a certain critical gas flow rate the pressure drop created by the gas flow over a wave (the Bernoulli effect) lifts the wave in a stratified flow to the top of the pipe. The theory for this regime transition model involves a balance between inertial and buoyancy forces, represented by the Froude number for the gas phase, and a critical gas flow rate determines the transition criterion. The methodology, based upon the work of Taitel-Dukler (1976), approximates the criterion for wave growth detailed by more complex models (Crowley, Wallis, and Barry, 1992).

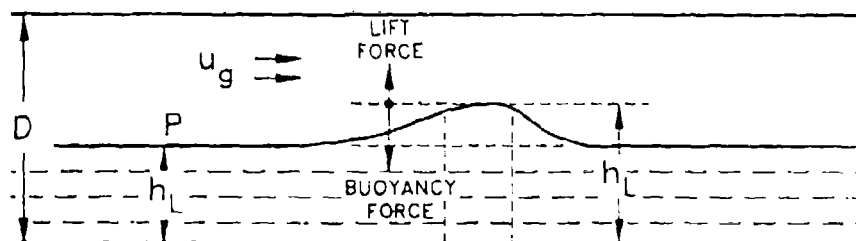


Figure 2.4. ILLUSTRATING FORCE BALANCE FOR STRATIFIED FLOW REGIME TRANSITION BASED UPON A FLOW INSTABILITY CRITERION



To calculate this transition in the design method, the dimensionless Froude number for the gas phase:

$$F_g = \frac{\rho_g j_g^{0.5}}{[m_g g D (\rho_l - \rho_g)]^{0.5}} \quad (2-1)$$

is calculated from the superficial gas velocity  $j_g$ , where

$F_g$  is the Froude number for the gas phase (-),  
 $m_g$  is the magnitude of the acceleration (-),  
 $g$  is the acceleration of earth gravity (9.8 m/s<sup>2</sup>),  
 $D$  is the pipe diameter (m),  
 $\rho_l$  is the liquid phase density (kg/m<sup>3</sup>), and  
 $\rho_g$  is the gas phase density (kg/m<sup>3</sup>).

The dimensionless Froude number is used in the following equation:

$$F_g = [1-h^*] \left[ \frac{1}{R_g^*} \right] \left[ \frac{A_g^*}{dA_l^*/dh^*} \right]^{0.5} \quad (2-2)$$

to determine the corresponding dimensionless liquid level  $h^*$  in the pipe. Table 2.2 defines the three dimensionless geometric parameters on the right hand side of this equation. Each is a function of the liquid level, so solving Equation 2-2 iteratively in the range  $0 < h^* < 1.0$  determines the liquid level. (Note that the original reference for this Equation (Taitel-Dukler, 1976) contains a typographical error for the exponent of the  $R_g^*$  parameter. The equation shown here is correct.)

The gas velocity,  $j_g$ , is then used to calculate a Reynolds number for the gas phase by:

$$Re_{gs} = (\rho_g D j_g / \mu_g) \quad (2-3)$$

where

$\rho_g$  is the gas phase density (kg/m<sup>3</sup>),  
 $j_g$  is the superficial velocity of the gas phase (m/s),  
 $D$  is the pipe diameter (m), and  
 $\mu_g$  is the gas phase viscosity (kg/m-s).

Then a gas phase friction factor:

$$f_{wg} = C_g Re_{gs}^{-m} \quad (2-4)$$

is calculated, where the coefficient  $C_g$  and the exponent  $m$  are:

$$C_g = 0.046 \quad (2-5a)$$

$$m = 0.2 \quad (2-5b)$$

if  $Re_{gs} \geq 1500$ . This is the Blasius (1913) equation for the turbulent friction factor in a smooth pipe. If  $Re_{gs} < 1500$ , then:

**Table 2.2. DIMENSIONLESS GEOMETRY PARAMETERS FOR SLUG-TO-STRATIFIED FLOW REGIME TRANSITION**

$$h^* = h_1/D$$

$$A_1^* = \frac{1}{4} \left\{ \pi - \cos^{-1}(2h^* - 1) + (2h^* - 1)[1 - (2h^* - 1)^2]^{\frac{1}{2}} \right\}$$

$$A_g^* = \frac{1}{4} \left\{ \cos^{-1}(2h^* - 1) - (2h^* - 1)[1 - (2h^* - 1)^2]^{\frac{1}{2}} \right\}$$

$$S_1^* = [\pi - \cos^{-1}(2h^* - 1)]$$

$$S_g^* = [\cos^{-1}(2h^* - 1)]$$

$$S_1^* = [1 - (2h^* - 1)^2]^{\frac{1}{2}} = (dA_1^*/dh^*)$$

$$R_1^* = [\pi/4A_1^*] = 1/(1-\alpha)$$

$$R_g^* = [\pi/4A_g^*] = 1/\alpha$$

$$D_1^* = \frac{4A_1^*}{S_1^*}$$

$$D_g^* = \frac{4A_g^*}{[S_g^* + S_1^*]}$$

$$C_g = 16 \quad (2-6a)$$

$$m = 1.0 \quad (2-6b)$$

Using these coefficients in Equation 2-4 models laminar flow of the gas phase.

After calculating the friction factor, a dimensionless parameter defined by:

$$Y = - \left[ \frac{m_g g (\rho_l - \rho_g) \cos \theta}{\left[ \frac{4f_{wg}}{D} \right] \left[ \frac{\rho_g j_g^2}{2} \right]} \right] \quad (2-7)$$

is calculated, where

$\theta$  is the angle between the body force and the direction of fluid flow in the pipe ( $^\circ$ ).

The other parameters are defined above.

The parameter Y is then used in a dimensionless two-phase momentum equation to determine another dimensionless parameter (the Martinelli parameter, X) related to the liquid flow rate:

$$X^2 = \frac{\left[ (R_g^* D_g^*)^{-m} (R_g^*)^2 \right] \left[ \frac{S_g^*}{A_g^*} + \left[ \frac{f_i}{f_{wg}} \right] \left[ \frac{S_l^*}{A_l^*} + \frac{S_l^*}{A_g^*} \right] \right]}{\left[ R_l^* D_l^* \right]^{-n} (R_l^*)^2 (S_l^* / A_l^*)} - 4Y \quad (2-8)$$

Table 2.2 summarizes the dimensionless geometry parameters (starred parameters in Equation 2-8) as a function of the dimensionless liquid level  $h^*$  determined using Equation 2-2. The parameter  $(f_i / f_{wg})$  is a constant representing the shear at the gas-liquid interface and has a recommended value of  $f_i / f_{wg} = 5$ .

The liquid velocity can then be calculated from the definition of the parameter  $X^2$  by:

$$j_l = \frac{\left[ X^2 \left[ \frac{4C_g}{D} \right] \left[ \frac{\rho_g D j_g}{\mu_g} \right]^{-m} \left[ \frac{\rho_g j_g^2}{2} \right] \right]^{1/(2-n)}}{\left[ \frac{4C_l}{D} \right] \left[ \frac{\rho_l D}{\mu_l} \right]^{-n} \left[ \frac{\rho_l}{2} \right]} \quad (2-9)$$

Equations 2-8 and 2-9 are first used with the assumption that the liquid flow is turbulent, and:

$$C_l = 0.046 \quad (2-10a)$$

$$n = 0.2 \quad (2-10b)$$

to calculate the superficial liquid velocity at the transition  $j_l$ .

The Reynolds number for the liquid phase:

$$Re_{ls} = (\rho_l D j_l / \mu_l) \quad (2-11)$$

is then evaluated. If  $Re_{ls} \geq 1500$ , the flow is turbulent, and the superficial liquid velocity calculated by Equation 2-9 is the transition velocity. However, if  $Re_{ls} < 1500$ , then the liquid flow is laminar, and the parameters X and  $j_l$  in Equations 2-8 and 2-9 are recalculated with:

$$C_l = 16 \quad (2-12a)$$

$$n = 1.0 \quad (2-12b)$$

**Cutoff Model.** For the special case of small angles ( $0^\circ < \theta < 20^\circ$ ), a cutoff may be invoked. This cutoff (Barnea et al., 1982) recognizes that stratified flow cannot be maintained in downflow in a nearly vertical pipe. The cutoff criterion for the maximum superficial liquid velocity is:

$$j_{lcut} = [(m_g g D / f_{wl}) (\sin \theta) (1 - h^*)] \quad (2-13)$$

As long as the value of  $j_l$  from Equation 2-9 is less than this cutoff value, then that value of  $j_l$  is used as the transition. If  $j_l > j_{lcut}$ , then the transition value is limited to the cutoff value ( $j_l = j_{lcut}$ ).

**Transition for Small Pipe Diameters.** The model described so far applies to pipes at large enough size that buoyancy and inertial effects dominate. Barnea, Luninski, and Taitel (1983) studied very small pipes (4 to 12 mm diameter) and found that capillary (surface tension) forces can cause a transition to slug flow where stratified flow would be predicted based upon the model described above. This could be important in determining the flow regime in the condenser tubes of two-phase radiators in ground tests. Thermal management systems such as the space station Active Thermal Control System (ATCS) and various capillary pumped loops use tubes in this size range.

Barnea et al. suggest that the transition occurs at a dimensionless liquid level given by:

$$h^* = \left[ 1 - \frac{\pi}{2(4 - \pi)^{0.5} Bo^{0.5}} \right] \geq (1 - \pi/4) \quad (2-14)$$

where Bo is the Bond number:

$$Bo = \left[ \frac{m_g g D^2 (\rho_l - \rho_g)}{\sigma} \right] \quad (2-15)$$

which balances surface tension and buoyancy.

The criterion in Equation 2-14 is based upon a force balance pictured in Figure 2.5. It results in a constant liquid (or void) fraction which depends upon the value of the Bond number. This dimensionless liquid level is also subject to the limit that  $h^* \geq (1 - \pi/4)$  or  $h^* \geq 0.215$ , at which point there is insufficient liquid available to form the slugs. By Equation 2-14, the limit of  $h^* = 0.215$  occurs if  $Bo < 4.7$ . At  $Bo \approx 100$ , the value of  $h^* = 0.83$ , which is a high enough liquid level that this transition is unimportant compared with Kelvin-Helmholtz instability in the basic Taitel-Dukler (1976) transition, and it can be neglected.

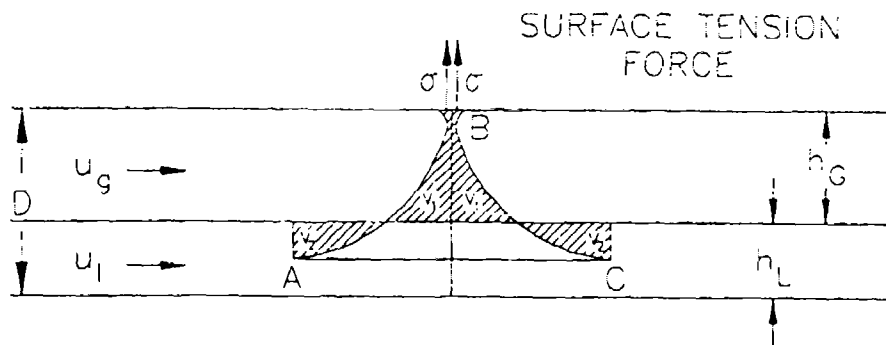


Figure 2.5. ILLUSTRATING FORCE BALANCE FOR STRATIFIED FLOW REGIME TRANSITION BASED UPON A SURFACE TENSION CRITERION

Since the criterion is a dimensionless liquid level, the solution procedure for the superficial liquid velocity at the transition is similar to the solution for the basic model. The geometric parameters (Table 2.2) are solved with  $h^*$  given by Equation 2-14. Then, the liquid velocity at the transition is found by solving Equations 2-8 through 2-12.

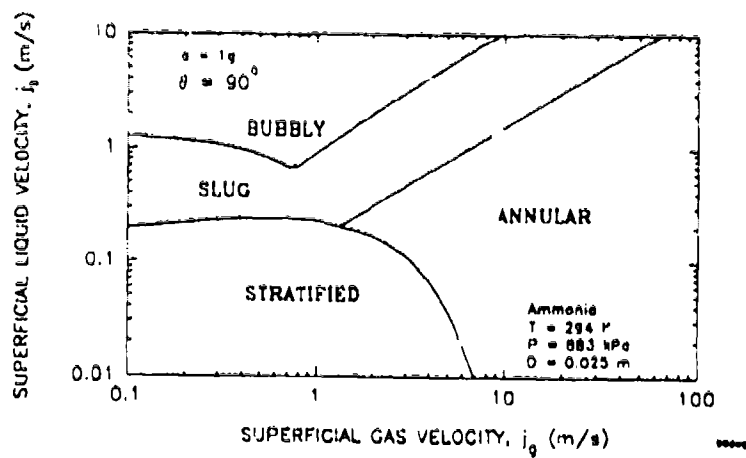
Characteristics of the Stratified to Nonstratified Transition Boundary. For each value of  $j_g$  assumed, the corresponding transition value of  $j_l$  can be calculated, so this transition boundary can be plotted as  $(j_g, j_l)$  pairs on a flow regime map. (Alternatively, if  $h^*$  is assumed, the corresponding  $j_g$  can be found from Equations 2-1 and 2-2 first.) Figures 2.6 and 2.7 plot all of the flow regime transitions at earth gravity ( $a = 1$ ) for upflow (Figure 2.6) and downflow (Figure 2.7). Focusing on the transition from stratified flow, which is given by the Taitel-Dukler model in these figures, the range of the stratified flow regime shrinks as the flow direction and the body force oppose each other more (Figure 2.6, corresponding to upflow on the ground). The stratified regime expands as the flow direction and the body force become colinear (Figure 2.7b, corresponding to downflow on earth), but it also disappears in vertical downflow (Figure 2-7c) because of the Barnea et al. (1982) cutoff. Extensive comparisons with test data on earth show that these characteristics represent the actual data very well for a wide range of pipe sizes and fluid properties.

Figure 2.8 shows the effect of the magnitude of the acceleration on the results. The stratified region diminishes with reduced gravity. In fact, the stratified flow regime occurs at liquid velocities of little practical interest at acceleration levels lower than  $10^{-2}g$  to  $10^{-3}g$ , which is the level achieved in aircraft flying microgravity parabolas.

For the pipe size used in Figures 2.6 through 2.8 ( $D = 25.4$  mm), the transition criterion given by Equation 2-14 is out of the range of the flow regime maps. Figure 2.9 presents flow regime maps for pipes at 4 and 10 mm diameter with air and water. The dotted line marks the transition boundary for the small diameter pipes. An additional region of slug flow appears, which would alternatively be a stratified region if the model for small diameter tubes did not apply. These maps agree with data presented by Barnea et al. (1983) to justify this model.

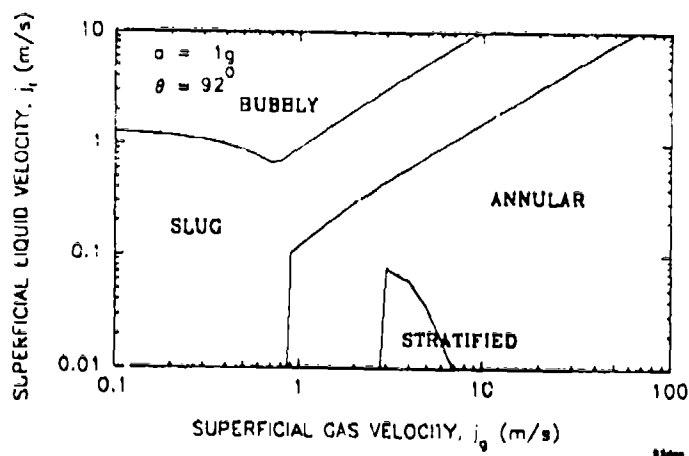
#### Slug to Bubbly Flow Regime Transition

This flow regime transition can occur by two mechanisms. The first mechanism balances the inertia (turbulence) of the two phase flow and buoyancy (Figure 2.10). High turbulent mixing can overcome the buoyant segregation of gas and liquid, resulting in a bubbly flow. A limiting criterion, and the second mechanism for this transition, is the maximum "packing" of bubbles in the pipe. The void fraction can only be so large before the bubbles touch and coalesce into large bubbles in a slug flow pattern.



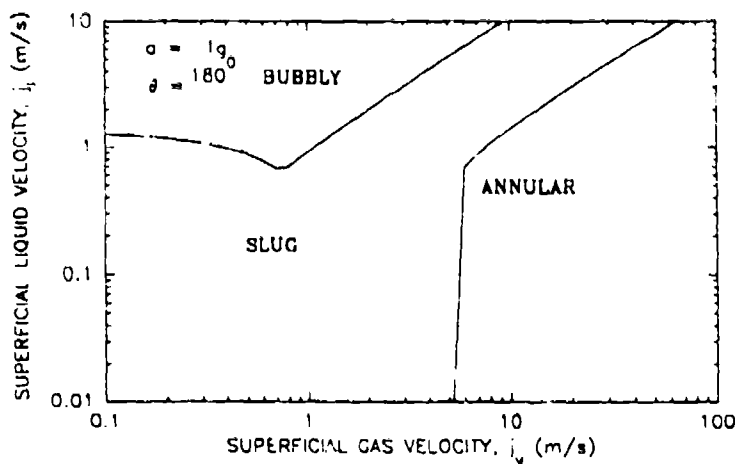
2.6a

(a) Horizontal



2.6b

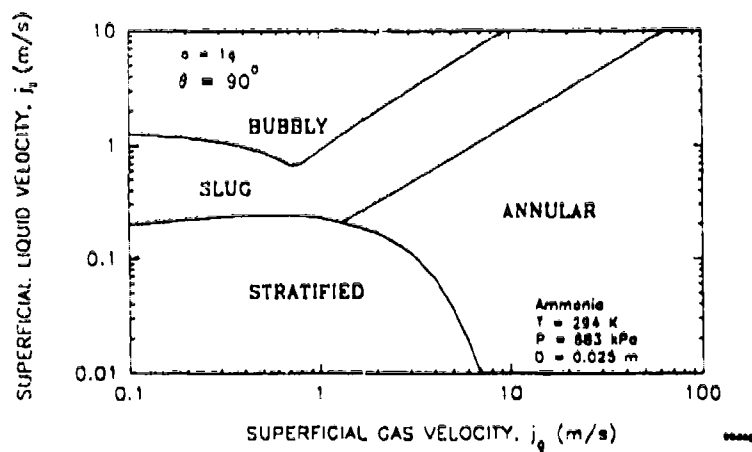
(b)  $2^\circ$  Upslope



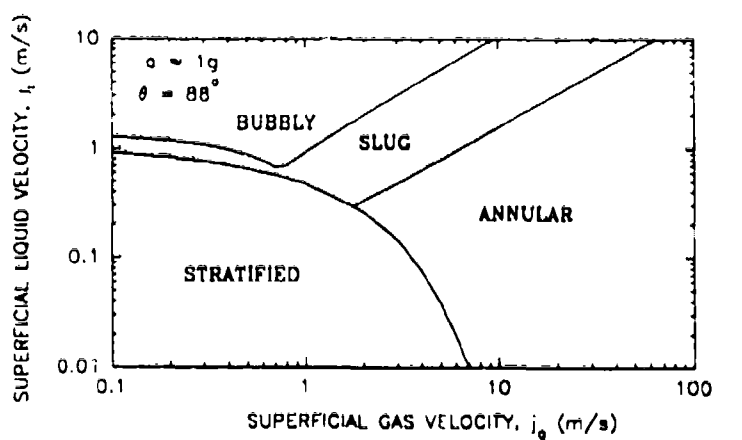
2.6c

(c) Vertical  
Upward

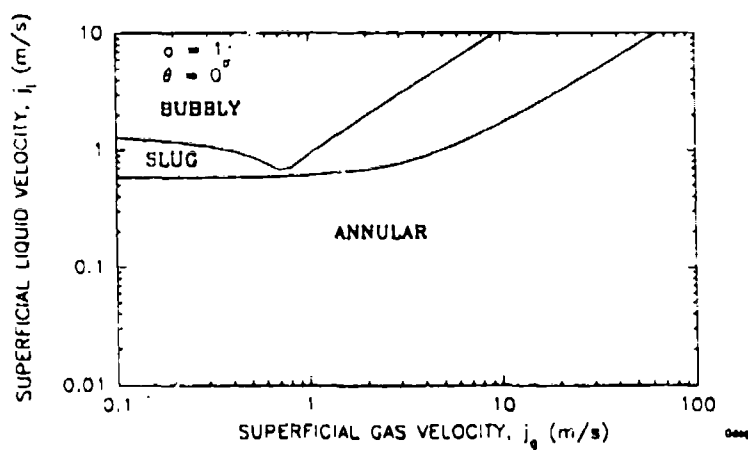
Figure 2.6. EXAMPLE FLOW REGIME MAPS FOR UPWARDLY INCLINED PIPES AT  $1g$



2.7a  
(a) Horizontal

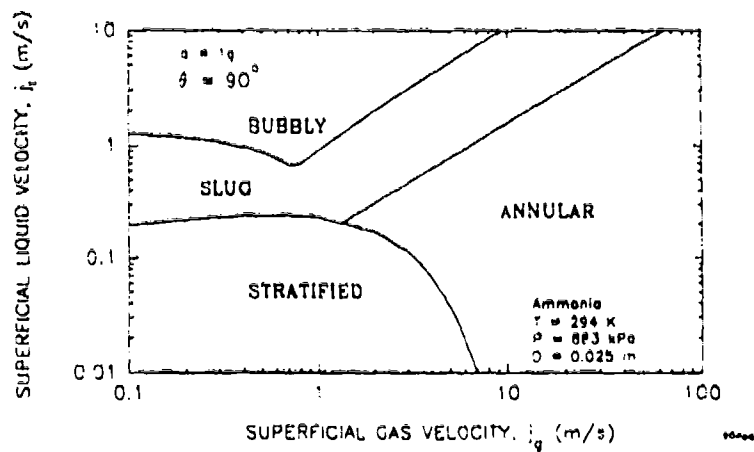


2.7b  
(b)  $2^\circ$  Downslope

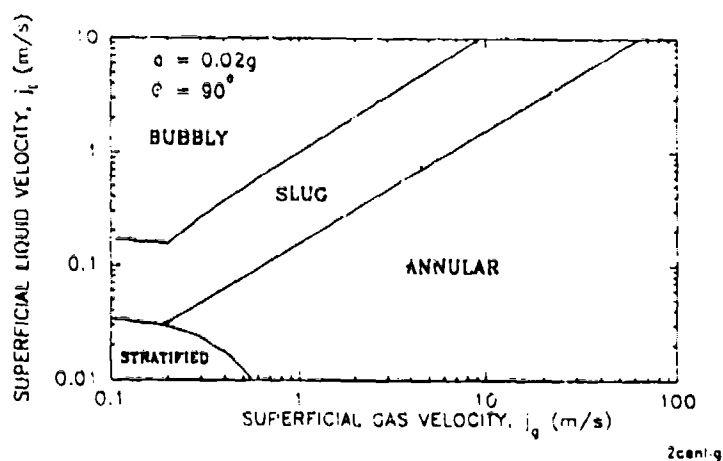


2.7c  
(c) Vertical  
Downward

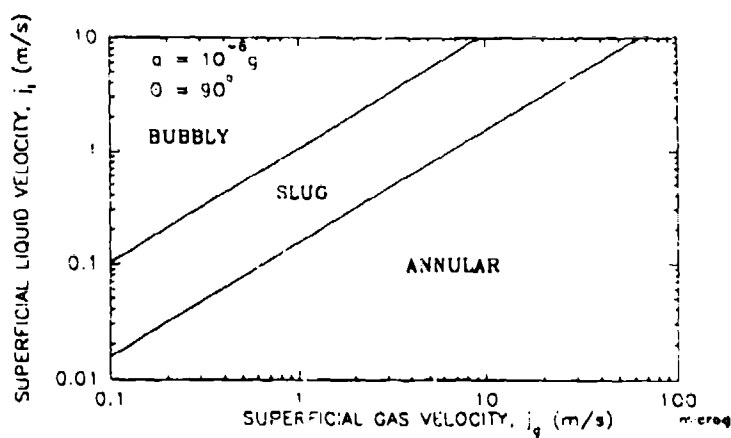
Figure 2.7. EXAMPLE FLOW REGIME MAPS FOR DOWNWARDLY INCLINED PIPES AT  $1g$



2.8a  
(a) Earth Gravity



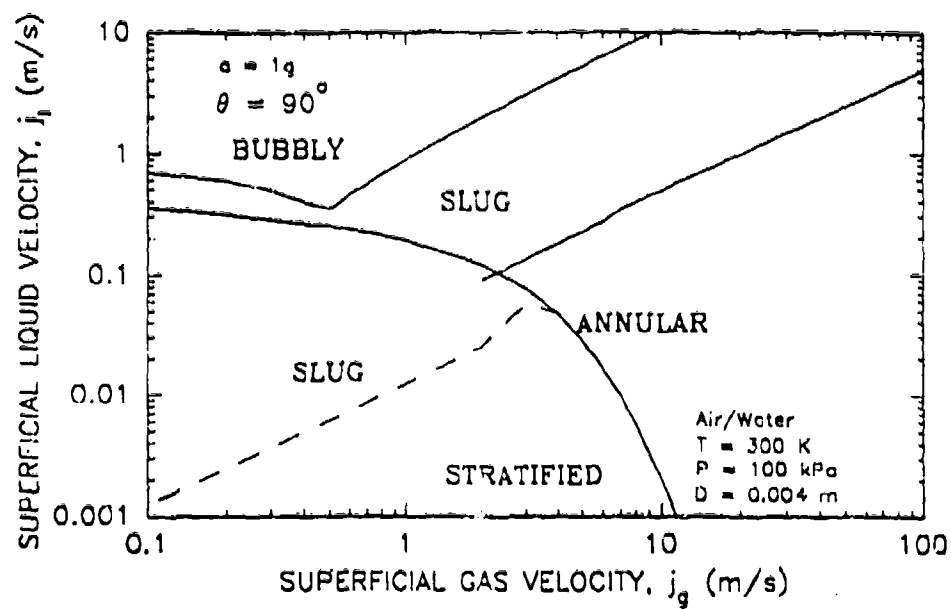
2.8b  
(b) KC-135 Gravity



2.8c  
(c) Microgravity

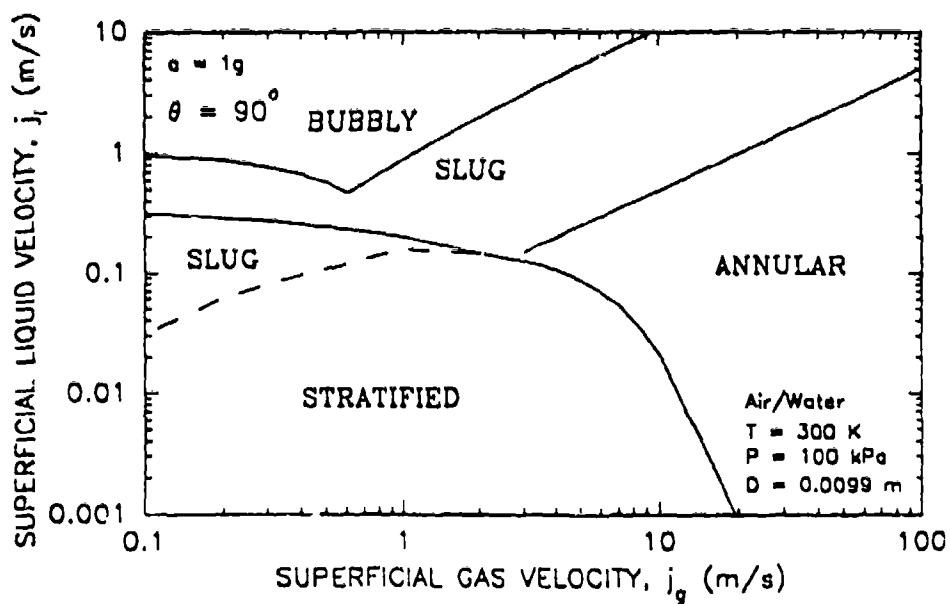
Figure 2.8. EXAMPLE FLOW REGIME MAPS AS A FUNCTION OF ACCELERATION





(a) 4mm Diameter

4mm



(b) 9.85 mm Diameter

10mm

Figure 2.9. EXAMPLE FLOW REGIME MAPS AT SMALL DIAMETER

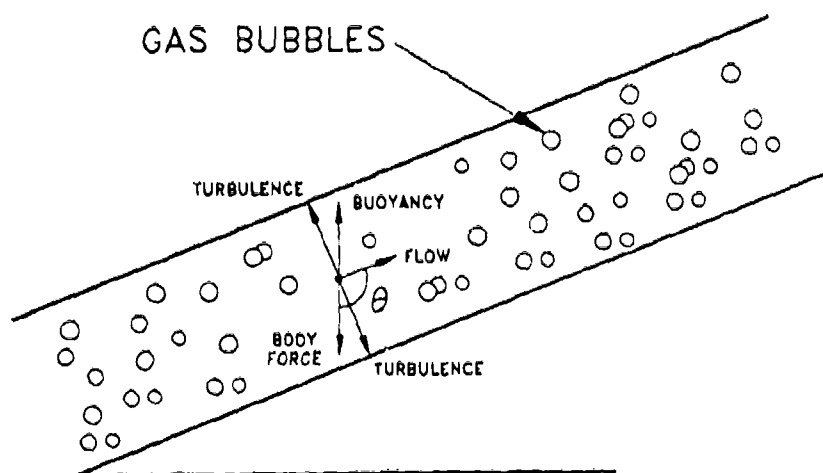


Figure 2.10. ILLUSTRATING FORCE BALANCE FOR SLUG-TO-BUBBLY FLOW REGIME TRANSITION BASED UPON TURBULENCE

**Turbulence Criterion.** Barnea (1986) suggests that turbulent mixing causes bubbly flow at a critical value of the two-phase Weber number:

$$We_j = \left[ \frac{0.6k}{f_{wl}^{0.4}} \right]^{1.67} Bo^{0.835} \quad (2-16)$$

where

$We_j$  is a two-phase Weber number,  
 $Bo$  is the Bond number (defined in Equation 2-15),  
 $f_{wl}$  is a friction factor with a value of  $\approx 0.005$ , and  
 $k$  is a constant in the range of 0.725 to 3.7 (Barnea, 1986). (Taitel et al. (1980) recommend a value of  $k = 1.14$ ).

The Weber number can therefore be calculated directly from known quantities.

The definition of the two-phase Weber number,

$$We_j = \left[ \frac{\rho_l D j^2}{\sigma} \right] = \left[ \frac{\rho_l D (j_g + j_l)^2}{\sigma} \right] \quad (2-17)$$

can be rewritten to solve for the superficial liquid velocity:

$$j_l = \left[ \frac{We_j \sigma}{\rho_l D} \right]^{0.5} - j_g \quad (2-18)$$

Equation 2-18, with Equation 2-16, can be used to map the slug to bubbly transition (based upon turbulence) as  $(j_g, j_l)$  pairs by selecting a range of values of  $j_g$  and calculating the corresponding  $j_l$  values.

**Maximum Void Fraction Criterion.** The second criterion for the slug to bubbly transition comes from a basic drift-flux equation (Zuber-Findlay, 1965) for bubbly flow:

$$\frac{j_g}{\alpha_c} = C_o(j_g + j_l) + 1.41 \left[ \frac{m_g g \sigma (\rho_l - \rho_g)}{\rho_l^2} \right]^{0.25} \quad (2-19)$$

where

- $\alpha_c$  is a critical value of the void fraction for maximum packing of the bubbles. Dukler et al. (1987) recommend a value of  $\alpha_c = 0.45$ , though other recommended values range from 0.3 to 0.52 (Taitel-Dukler, 1976).
- $C_o$  is a constant typically near 1.2.

Equation 2-19 can be written to solve for the superficial liquid velocity as:

$$j_l = \left[ \frac{1}{C_o \alpha_c} - 1 \right] j_g - \left[ \frac{1.41}{C_o} \right] \left[ \frac{m_g g \sigma (\rho_l - \rho_g)}{\rho_l^2} \right]^{0.25} \quad (2-20)$$

Similarly to Equation 2-18, values of  $(j_g, j_l)$  pairs at the transition boundary can be determined by varying  $j_g$  across an appropriate range of values.

**Characteristics of the Slug to Bubbly Regime Transition Boundary.** The transition from slug to bubbly flow regimes is mapped by selecting the pair of coordinates with the higher value of  $j_l$  for a given value of  $j_g$ . Said another way, for the flow regime map, the transition criterion with a higher liquid velocity at a given gas velocity (Equation 2-18 or 2-20) takes precedence in the flow regime transition. The portion of the transition with a negative slope corresponds to the turbulence model (Equation 2-18), and the portion with a positive slope corresponds to the void fraction model (Equation 2-20).

Figures 2.6 and 2.7 also plot the slug to bubbly flow regime on regime maps in superficial velocity coordinates. These figures show that pipe inclination has very little effect on the transition. This is confirmed by data at earth gravity conditions (Barnea, 1986).

Figure 2.8 shows that as the magnitude of the acceleration is reduced, the portion of the transition criterion related to turbulence and body forces (Equation 2-18) disappears, and the portion of the transition related to void fraction (Equation 2-20) remains.

### Slug to Annular Flow Regime Transition

This regime transition, proposed by Barnea (1986), also consists of two parts. Both describe blockage of an annular core, but by different mechanisms. As Barnea explains, the first mechanism ("neutral stability") is an instability of the annular flow configuration, and the second occurs when the liquid film is large enough to cause blockage as a result of flow in the liquid film.

**"Neutral Stability" Criterion.** For this transition, the values of  $Re_{gs}$ ,  $C_g$ ,  $m$ ,  $f_{wg}$ , and  $Y$  are the same as calculated for the stratified to nonstratified transition in Equations 2-3 to 2-7. The next part of the solution involves the simultaneous solution of two equations. In dimensionless form, the two equations are:

$$Y = \left[ \frac{(f_i/f_{wg})}{\alpha_l(1 - \alpha_l)^{2.5}} \right] - \left[ \frac{1}{\alpha_l^3} \right] X^2 \quad (2-21)$$

$$Y = \frac{(2 - 1.5\alpha_l)}{\alpha_l^3[1 - 1.5\alpha_l]} X^2 \quad (2-22)$$

where  $\alpha_l$  is the liquid fraction,  $(1 - \alpha)$ . Equation 2-21 is the two-phase void fraction relationship for the annular flow regime (Wallis, 1969). Equation 2-22 is the transition criterion derived by Barnea (1986). The parameter  $(f_i/f_{wg})$  in Equation 2-21 represents the interfacial friction between the gas and the liquid phases. For the purpose of these design maps, the model proposed by Wallis (1969) based on tests at earth gravity is used:

$$(f_i/f_{wg}) = [1 + C_a\alpha_l] \quad (2-23)$$

where  $C_a = 75$ . An equivalent model is also used by Dukler et al. (1987) for microgravity comparisons. Various alternative models appear in the literature, but the Wallis (1969) model appears to be a reasonable limit for most data. The minimum value of  $f_i/f_{wg}$  would be unity, representing a smooth gas-liquid interface.

In this solution, the Equations 2-21 and 2-22 have been solved simultaneously to eliminate  $X^2$  and obtain  $Y$  as a function of the liquid fraction,  $\alpha_l$ . This equation is then differentiated with respect to liquid fraction ( $dY/d\alpha_l$ ) to find the point where the slope is zero ( $dY/d\alpha_l = 0$ ), which is a minima in the solution curve. The value of  $Y$  at that point is called  $Y_{crit}$ , and the corresponding value of the liquid fraction  $\alpha_{lcrit}$ . Typically,  $Y_{crit}$  has a value of about 70.

If the value of  $Y$  (from Equation 2-7) is greater than  $Y_{crit}$ , Equations 2-21 and 2-22 are solved simultaneously in the range of  $0 < \alpha_l < \alpha_{lcrit}$  to determine  $\alpha_l$  and  $X$ . Having obtained the value of  $X$ , the superficial liquid velocity at the transition,  $j_l$ , is found by using the same approach as Equations 2-9 through 2-13.

**Critical Liquid Fraction.** The second transition criterion is invoked if  $Y \leq Y_{crit}$ . (This condition is always satisfied if  $\theta \leq 90^\circ$  or  $m_g = 0$ .) Equation 2-21 is first rewritten to solve for  $X^2$ :

$$X^2 = \frac{(f_i/f_{wg})\alpha_{lc}^2}{(1 - \alpha_{lc})^{2.5}} - \alpha_{lc}^3 Y \quad (2-24)$$

This transition involves using a critical liquid fraction  $\alpha_{lc} = 0.24$  in Equation 2-24, with Equation 2-23. Having obtained the value of  $X$ , the superficial liquid velocity at the transition is found by using the same approach as Equations 2-9 through 2-13.

**Characteristics of the Slug to Annular Regime Transition Boundary.** Figures 2.6 and 2.7 also show the slug to annular transition on typical flow regime maps in  $(j_g, j_l)$  coordinates. The set of plots in Figure 2.6 shows that this transition is approximately linear (occurring at a constant liquid fraction) in a horizontal pipe at earth gravity, but the lower portion of the transition approaches a constant liquid velocity for downward inclinations (Figure 2.6c). The transition in this case is determined by the "maximum liquid fraction" model ( $Y < Y_{crit}$  and  $\alpha_l = \alpha_{lc} = 0.24$ ). Figure 2.7 shows that the lower portion of the transition approaches a

constant superficial gas velocity at large upward inclinations (Figure 2.7c). In this case, the transition is determined by the "neutral stability" model ( $Y > Y_{crit}$ ). Since the value of  $Y_{crit}$  is about 70 over a wide range of the liquid fraction (see Figure 2.18 below), this corresponds to a constant gas Froude number of about  $F_g = 1.2$ , which can be seen by solving Equation 2-7 for  $Y = 70$  and  $\theta = 180^\circ$ . Barnea (1986) shows that the trends in these figures are consistent with experimental flow regime data at earth gravity.

Figure 2.8 shows that the slug to annular transition is approximately the same under microgravity conditions as it is for a horizontal pipe at earth gravity. This is readily apparent from Equation 2-3 because the parameter  $Y$  approaches zero in the case of either small inclinations ( $\theta = 0$ ) or low acceleration level ( $m_g = 0$ ).

### Alternate Regime Map Coordinates

Simple transformations convert the flow regime maps in  $(j_g, j_l)$  coordinates as described above to quality and mass flux  $(x, G)$  coordinates:

$$G = (\rho_g j_g + \rho_l j_l) \quad (2-25)$$

$$x = \frac{\rho_g j_g}{(\rho_g j_g + \rho_l j_l)} = \left[ \frac{\rho_g j_g}{G} \right] \quad (2-26)$$

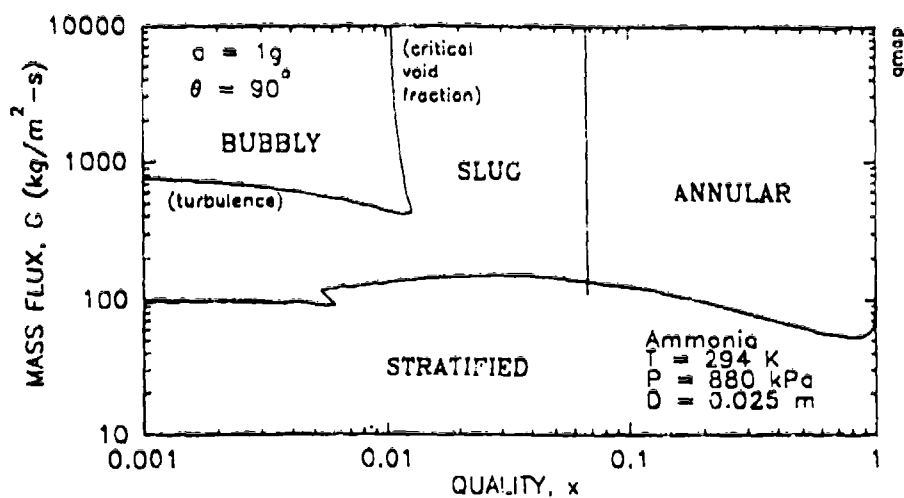
where

- $G$  is the mass flux ( $\text{kg/m}^2\text{-s}$ ), and
- $x$  is the quality (ratio of vapor mass flow rate to the total mass flow rate).

Figure 2.11 illustrates how the regime maps in Figure 2.8 appear when converted to these coordinates. It is particularly interesting to note that under microgravity conditions (Figure 2.11c), the transitions from slug to bubbly and slug to annular flow regimes appear as lines at approximately constant quality. In addition, the transition from stratified to nonstratified flow occurs at approximately constant mass flux  $G$  (Figure 2.11a), and the value of the mass flux becomes smaller at low acceleration (Figure 2.11b), before disappearing at microgravity conditions (Figure 2.11c).

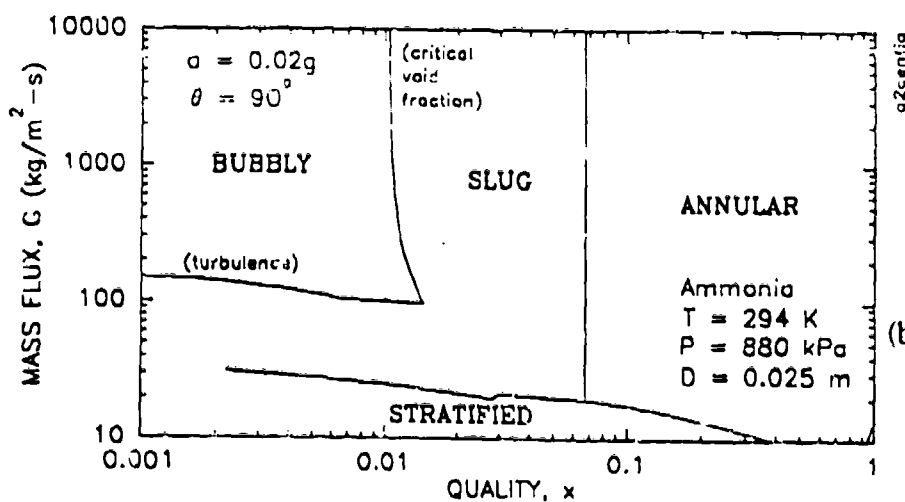
### **2.2.2 Modelling Uncertainties for Sensitivity Calculations**

Table 2.1 summarizes the key modelling parameters in each of the regime transition models. For each transition, the sensitivity of the predicted transitions to these parameters provides a measure of the uncertainty in the regime models. That is, they represent the "fuzz" in accurately locating the transitions on a regime map. Figure 2.12 illustrates the range of sensitivity encompassed by the uncertainty in each transition boundary, shown by the pairs of lines with the same style. If the predicted flow regimes for a particular design application change when these parameters are varied across the ranges of their uncertainty, and if pressure drops significantly change as a result, then the predictions should be treated cautiously. It is usually better to err on the side of predicting the regime which results in higher pressure drops.



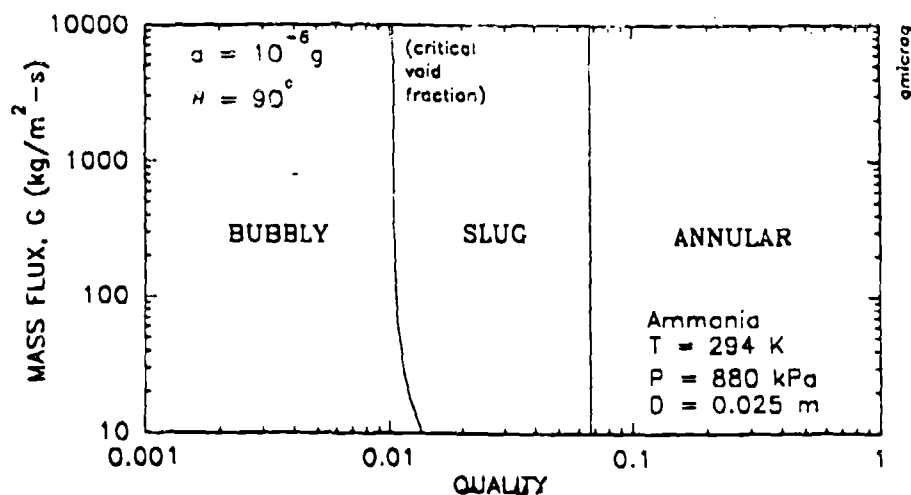
2.11a

(a) Earth Gravity



2.11b

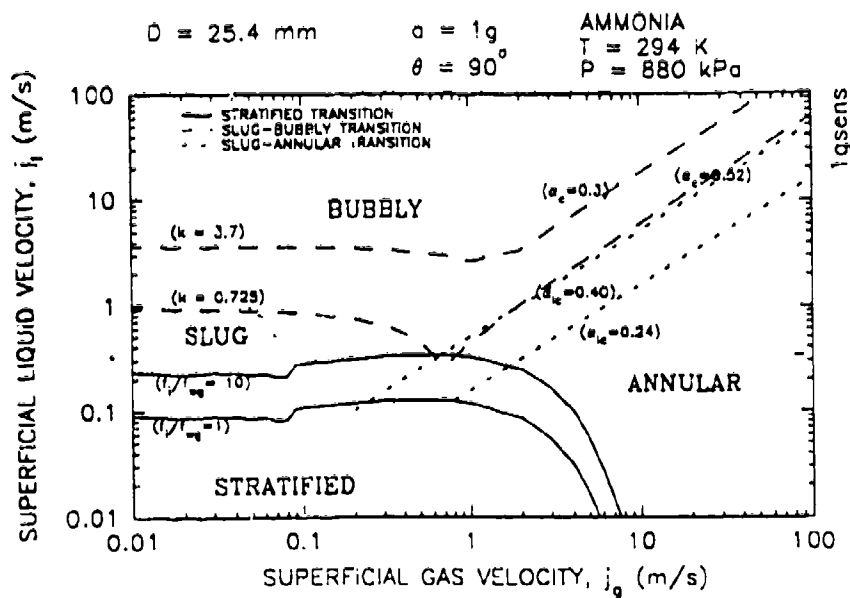
(b) KC-135 Gravity



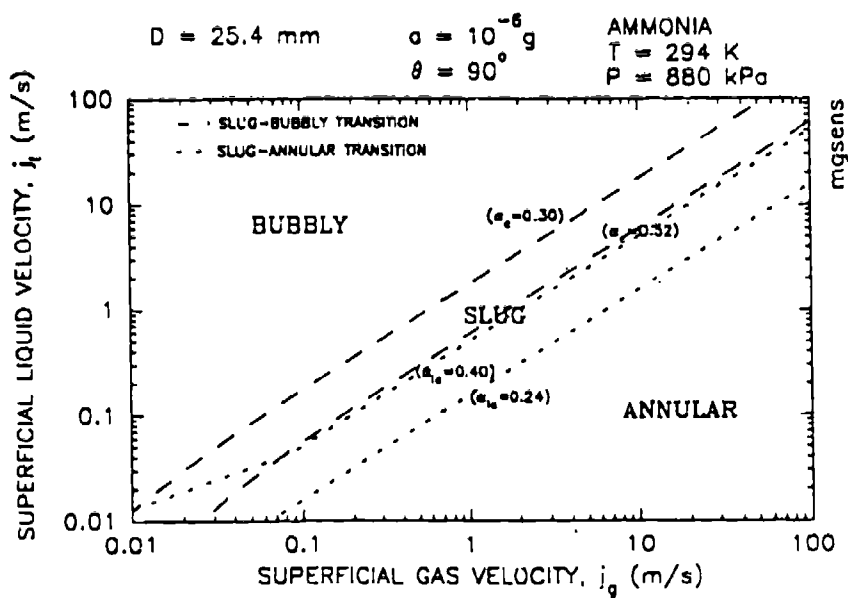
2.11c

(c) Microgravity

Figure 2.11. EXAMPLE FLOW REGIME MAPS IN MASS FLUX COORDINATES AS A FUNCTION OF ACCELERATION



(a) Earth Gravity



(b) Microgravity

Figure 2.12. SENSITIVITY OF FLOW REGIME TRANSITIONS TO KEY MODELLING PARAMETERS

For the stratified to nonstratified transition, the key modelling parameter is the interfacial shear  $f/f_{wg}$  between the gas and the liquid phases. The limiting case of  $f/f_{wg} = 1$  represents a smooth interface between the gas and the liquid. Using this value in the model tends to give the lowest superficial liquid velocities for this transition (Figure 2.12a). At the other extreme, experimental data suggest that a value of  $f/f_{wg} = 10$  bounds experimental data, providing the highest superficial liquid velocities for this transition. Unlike the lower limit, this upper limit is not mechanistic, but it does tend to bound experimental data.

Furthermore, the recommended limits also tend to bound predictions of this regime made with more detailed transition models such as the one-dimensional wave model suggested by Crowley, Wallis, and Barry (1992). While the one-dimensional wave model is even more mechanistic, its solution is quite complex. For the purposes of this design manual, the simpler approach suggested here is preferred.

For the portion of the slug to bubbly regime transition which is based upon turbulence, a coefficient  $k$  which describes the magnitude of the turbulence is the uncertainty parameter. The parameter  $k$  has been assigned a value of 1.14, though Barnea (1986) indicates that the value may range from 0.725 to 3.7. This represents a significant range of uncertainty (Figure 2-12a).

For the portion of the slug to bubbly regime transition which is based upon the maximum void fraction, there are two modelling parameters:

- The critical void fraction  $\alpha_c$ , and
- The drift-flux coefficient  $C_o$ .

The drift-flux coefficient has been hypothesized to range between 1.0 and 1.2. The value of 1.0 represents a very uniform distribution of the bubbles across the diameter of the pipe. A value of 1.2 represents a void fraction profile across the diameter. Recent data (Colin et al., 1991) support a value of  $C_o = 1.2$ , even under microgravity conditions. (Those data are described in Section 2.4.) The value of the critical void fraction has been reported to range from 0.3 to 0.52. Some uncertainty remains, and additional microgravity data are needed to select the best value for this parameter.

For the slug to annular flow regime transition, the uncertainty lies in the modelling parameters for:

- Coefficient  $C_a$  in the interfacial shear model, and
- Critical liquid fraction,  $\alpha_{lc}$ .

The values of these two parameters are intertwined, as may be seen in Equation 2-23 for the interfacial shear. Microgravity data suggest that the transition occurs at somewhat higher values of the superficial liquid velocity. This could be the result of a higher liquid fraction or higher interfacial shear coefficient in the model. (See Section 2.4.3.) Experimental data on pressure drop and void fraction at the transition would resolve this question, however no data are presently available.



### 2.2.3 Limits of the Methods

**Pipe Geometry.** The theory described in Section 2.2.1 applies to pipes which range in size from a few millimeters to a meter in diameter. The pipe diameters thus span the range of interest for thermal management systems (from a few millimeters to a few centimeters) to gas and oil pipelines.

The theory has also been developed for a pipe with circular cross-section. As a first approximation, the theory could be applied to square or rectangular cross-sections, but the models should really be modified for other geometries. The theory might easily be modified for square or rectangular cross-sections. For example, the stratified to nonstratified transition requires the derivation of several geometric parameters (see Table 2.2). For this transition, the same theory for the Kelvin-Helmholtz instability applies for rectangular cross-sections if these geometric parameters are redefined. The transition from slug to bubbly flow depends upon the drift-flux parameter  $C_0$ , which may be different in rectangular cross-sections. Data may be available for this value, though the value may not be far from the value of 1.2 suggested. For the slug to annular transition, Equations 2-21 and 2-22 would have to be rederived for the rectangular geometry. The result may not be far from the result for the circular geometry.

**Acceleration.** These transition models assume that the fluid properties are approximately constant. If the densities or surface tensions between the phases vary dramatically with small changes in pressure or temperature, as they do near the critical point for a given fluid, then this assumption breaks down. The assumption of constant fluid properties also breaks down if there is a significant gradient in the fluid properties across the diameter of the flow channel. This can occur for example in a two-phase line during launch, where the acceleration may be ten times earth gravity. The models should not be applied to high acceleration levels.

## 2.3 Dimensionless Design Charts for Flow Regimes

This section illustrates how the flow regime can be determined quickly from known conditions. The information required in order to determine the flow regime includes:

### Fluid Properties

- $\rho_l$  Liquid phase density
- $\rho_g$  Gas phase density
- $\mu_l$  Liquid phase viscosity
- $\mu_g$  Gas phase viscosity
- $\sigma$  Surface tension

### Geometry

- $D$  Pipe diameter

### Acceleration

- $a$  Magnitude of acceleration ( $= m_g g$ )
- $\theta$  Direction (angle between the body force and the flow direction)

## Flow Rates

- $j_l$  Liquid phase volumetric flux ( $Q_l/A$ )
- $j_g$  Gas phase volumetric flux ( $Q_g/A$ )

Each of the three flow regime transitions can be represented on dimensionless design maps. The dimensionless coordinates for these regime maps can be determined from the information listed above.

The order of examining the transitions is important to the determination of the flow regime, since certain regimes supersede others. The order should be:

- Stratified to Nonstratified Flow Regime Transition,
- Slug to Bubbly Flow Regime Transition, and
- Slug to Annular Flow Regime Transition.

Figure 2.13 illustrates the logic for the flow regime selection. The dimensionless design maps for flow regimes are presented and discussed in that order below. See Section 2.2.1 for the theory and equations behind these maps.

**Stratified to Nonstratified Flow Regime Transition.** To determine first whether or not the flow regime is stratified, the proposed design point is mapped on dimensionless plots of:

- Bond number,  $Bo$ , versus the Martinelli parameter,  $X$ , and
- Gas Froude number,  $F_g$ , versus the Martinelli parameter,  $X$ ,

as shown in Figures 2.14 and 2.15. These maps correspond to two transition criteria described in Section 2.2.1:

- The first is important at small pipe diameter (low Bond number) and represents a balance between buoyancy and surface tension forces, and
- The second is important at all pipe diameters and represents a balance between buoyancy and inertia forces.

The definitions of the dimensionless parameters used in the maps are:

$$Bo = \left[ \frac{m_g g D^2 (\rho_l - \rho_g)}{\sigma} \right] \quad (2-27)$$

$$F_g = \frac{j_g \rho_g^{0.5}}{[m_g g D (\rho_l - \rho_g)]^{0.5}} \quad (2-28)$$

$$X = \left[ \frac{\left[ \frac{4C_l}{D} \right] \left[ \frac{\rho_l D j_l}{\mu_l} \right]^{-n} \left[ \frac{\rho_l j_l^2}{2} \right]}{\left[ \frac{4C_g}{D} \right] \left[ \frac{\rho_g D j_g}{\mu_g} \right]^{-m} \left[ \frac{\rho_g j_g^2}{2} \right]} \right]^{0.5} \quad (2-29)$$

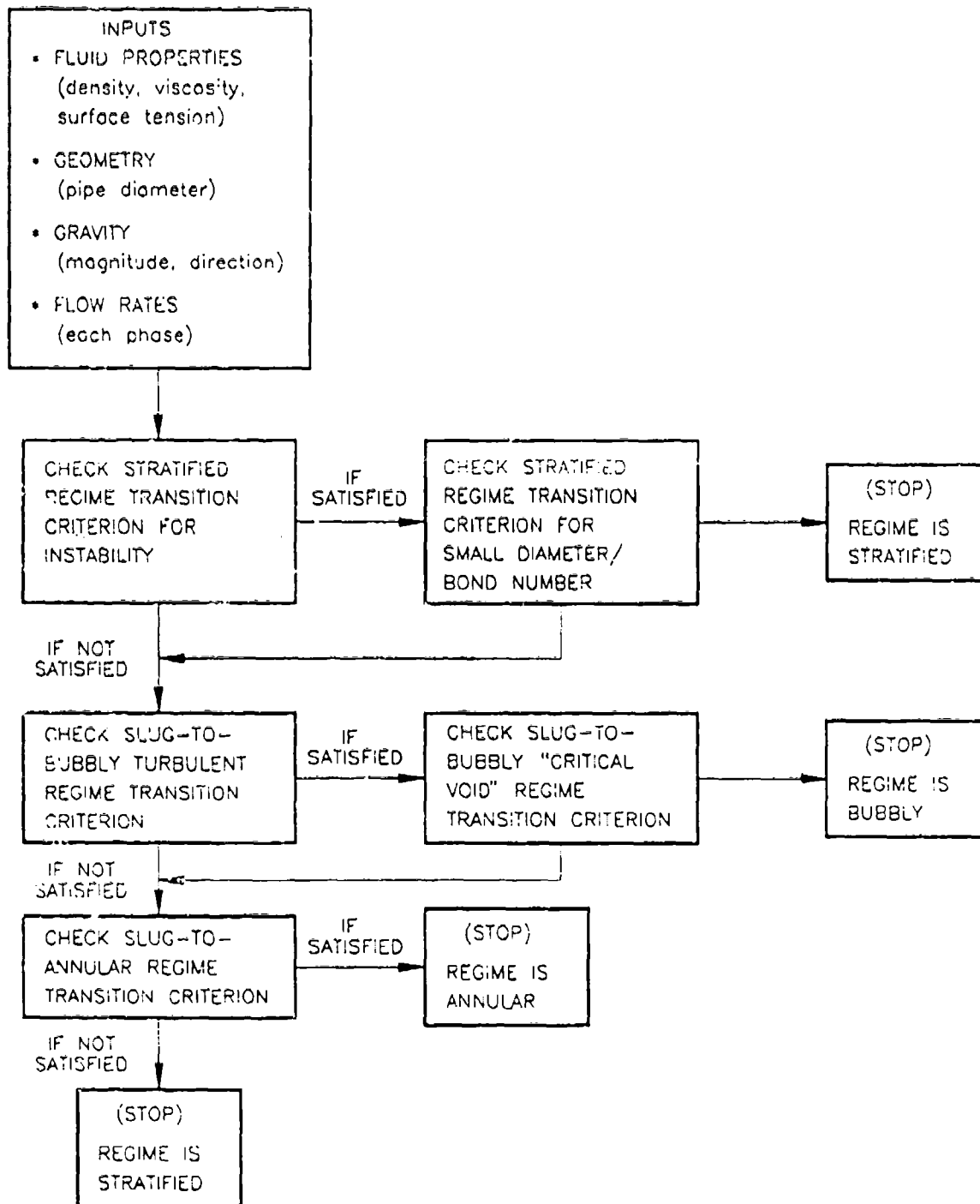
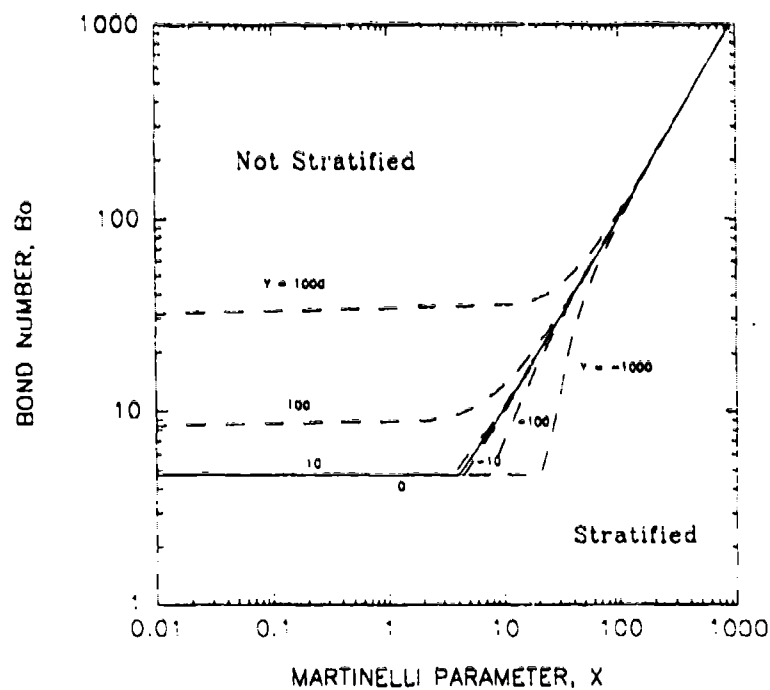
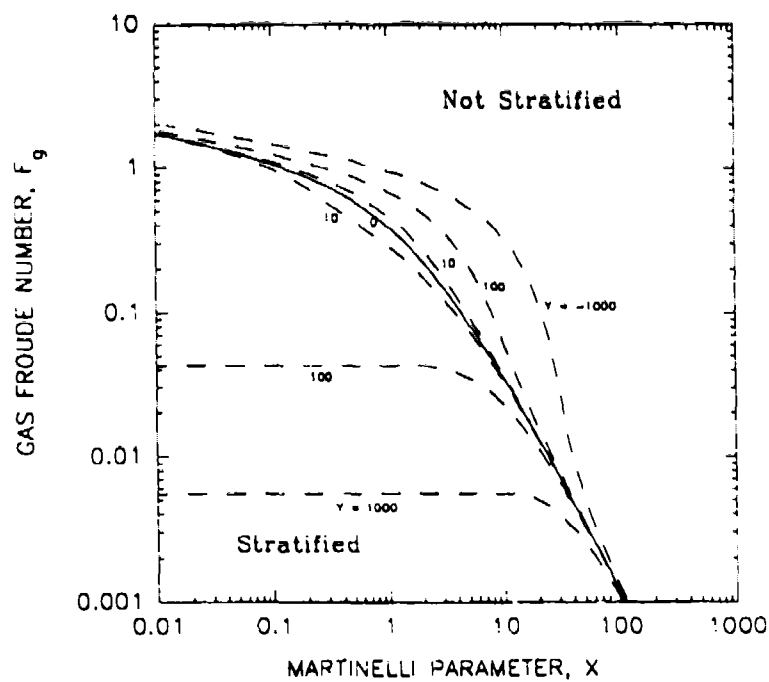


Figure 2.13. LOGIC FOR FLOW REGIME DETERMINATION



bomap

Figure 2.14. DIMENSIONLESS MAP FOR STRATIFIED REGIME TRANSITION AT SMALL DIAMETER ( $Bo < 100$ )



fgmap

Figure 2.15. DIMENSIONLESS MAP FOR STRATIFIED REGIME TRANSITION BASED UPON KELVIN-HELMHOLTZ INSTABILITY

$$Y = - \left[ \frac{m_g g (\rho_l - \rho_g) \cos \theta}{\left[ \frac{4C_g}{D} \right] \left[ \frac{\rho_g D j_g}{\mu_g} \right]^{-m} \left[ \frac{\rho_g j_g^2}{2} \right]} \right] \quad (2-30)$$

where

- Bo is the dimensionless Bond number,  
 F<sub>g</sub> is the dimensionless Froude number for the gas phase,  
 X<sup>\*</sup> is the dimensionless Martinelli parameter,  
 Y is the dimensionless pipe inclination parameter  
 g is the acceleration due to earth gravity (m/s<sup>2</sup>),  
 ρ<sub>l</sub> is the gas phase density (kg/m<sup>3</sup>),  
 ρ<sub>g</sub> is the liquid phase density (kg/m<sup>3</sup>),  
 j<sub>l</sub> is the superficial velocity of the liquid phase (m/s),  
 j<sub>g</sub> is the superficial velocity of the gas phase (m/s),  
 D is the pipe diameter (m), and  
 θ is the angle between the flow direction and the body force (°) (e.g. 0° is colinear, 90° is perpendicular, and 180° is opposing, corresponding to downflow, horizontal, and upflow on the ground).

Table 2.3 indicates how to determine the values of the friction factor coefficients C<sub>l</sub>, C<sub>g</sub>, n and m to use in Equations 2-29 and 2-30.

Table 2.3. SUMMARY OF PARAMETER VALUES FOR FRICTION FACTOR CALCULATION				
PHASE	REGIME	CRITERION	C <sub>g</sub> or C <sub>l</sub>	m or n
VAPOR	LAMINAR	$Re_{gs} = \left[ \frac{\rho_g D j_g}{\mu_g} \right] < 1500$	16	1.0
	TURBULENT	$Re_{gs} \geq 1500$	0.046	0.2
LIQUID	LAMINAR	$Re_{ls} = \left[ \frac{\rho_l D j_l}{\mu_l} \right] < 1500$	16	1.0
	TURBULENT	$Re_{ls} \geq 1500$	0.045	0.2
Note: Re = 1500 is the point where laminar and turbulent friction factors are equal in these two models.				

The procedure to check the stratified transition using Figures 2.14 and 2.15 is to first calculate the four dimensionless quantities in Equations 2-27 to 2-30. These quantities depend upon the superficial phase velocities (or volumetric flow rates)  $j_l$  and  $j_g$  of each phase and the fluid properties.

The desired operating point is first plotted on Figure 2.14 at the coordinates  $(X, Bo)$ . The line corresponding to the constant value of  $Y$  from Equation 2-30 is then located. The designer notes whether the operating point is above or below the line. The desired operating point is then plotted on the design map in Figure 2.15 at the coordinates  $(X, F_g)$ . Then the line of constant  $Y$  for the proposed design conditions is located on this map, and the designer notes whether the operating point is above or below the line. If the operating point falls below the line for the value of  $Y$  on both maps (Figures 2.14 and 2.15), then the flow regime is stratified. If the operating point falls above the line for the value of  $Y$  on either of the two maps, then the slug to bubbly flow regime transition is assessed as described below.

Note that if the acceleration level is very small, for example at microgravity conditions where  $a \approx 10^{-6} g$ , then  $Y \approx 0$ . The lines corresponding to  $Y = 0$  are highlighted in Figures 2.14 and 2.15.

**Slug to Bubbly Flow Regime Transition.** The transition from the slug to the bubbly flow regime should be examined as the second step. The slug to bubbly flow regime transition consists of two parts:

- A transition based upon fluid turbulence, and
- A transition based upon a critical void fraction,

and both of these criteria need to be checked to determine the flow regime.

Figure 2.16 is the dimensionless design map for the transition based upon turbulence. To determine the flow regime, a dimensionless Weber number:

$$We_j = \left[ \frac{\rho_l D j^2}{\sigma} \right] = \left[ \frac{\rho_l D (j_g + j_l)^2}{\sigma} \right] \quad (2-31)$$

and the dimensionless Bond number from Equation 2-27 are used, where

- $\rho_l$  is the liquid phase density ( $\text{kg/m}^3$ ),
- $\rho_g$  is the gas phase density ( $\text{kg/m}^3$ ),
- $D$  is the pipe diameter (m),
- $\sigma$  is the surface tension (N/m),
- $j_g$  is the superficial velocity of the gas phase (m/s), and
- $j_l$  is the superficial velocity of the liquid phase (m/s).

The point with coordinates  $(Bo, We_j)$  is then located on Figure 2.16. If the point is above the transition line in the figure, then the regime *may* be bubbly, but the second (void fraction) transition criterion must be checked first.

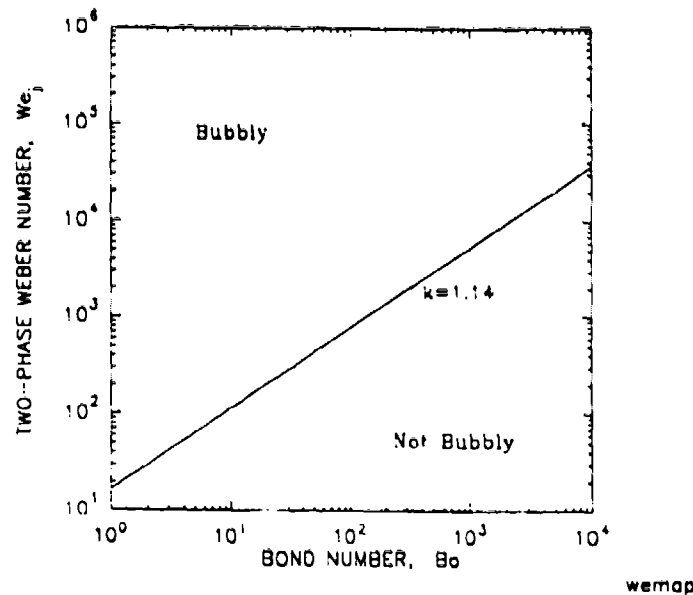


Figure 2.16. DIMENSIONLESS MAP FOR BUBBLY REGIME TRANSITION BASED UPON TURBULENCE

Equation 2-20 can be written in dimensionless form as:

$$M = \left[ \frac{1}{C_o \alpha_c} - 1 \right] - \frac{1.41}{C_o K_g \rho^*{}^{0.5}} \quad (2-32)$$

where

$$M = (j_l / j_g) \quad (2-33)$$

$$K_g = \frac{\rho_g^{0.5} j_g}{[m_g g D (\rho_l - \rho_g)]^{0.25}} \quad (2-34)$$

$$\rho^* = (\rho_l / \rho_g) \quad (2-35)$$

and the other parameters are defined above.

Figure 2.17 illustrates the second slug to bubbly flow regime transition criterion, based upon a critical void fraction. The design map in Figure 2.17 plots the dimensionless regime transition of Equation 2-32 using the parameters defined by Equations 2-33, 2-34, and 2-35. The design map uses the recommended value  $C_o = 1.2$ . The proposed operating point is plotted in Figure 2.17 at the coordinates  $(K_g - 1 \rho^{*-0.5}, M)$ . If the operating point is above the transition line, then the flow regime is bubbly. If the operating point is below this line, then the slug to annular flow regime transition needs to be evaluated as described below.

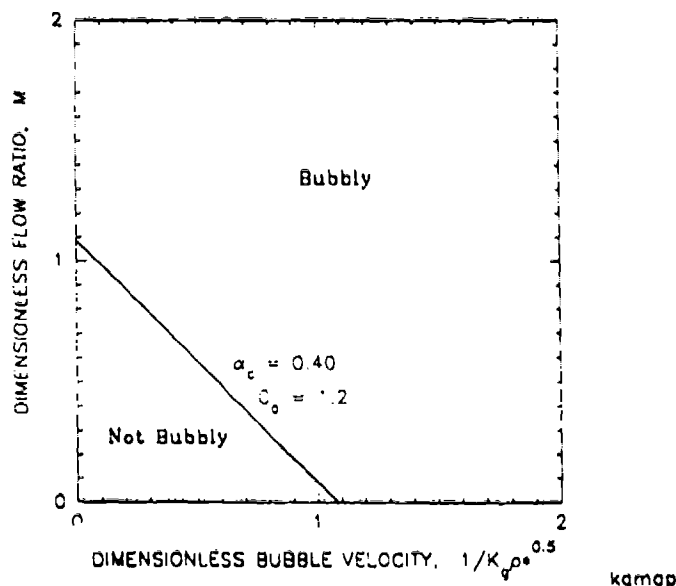


Figure 2.17. DIMENSIONLESS MAP FOR BUBBLY REGIME TRANSITION  
BASED UPON CRITICAL VOID FRACTION

**Slug to Annular Flow Regime Transition.** If the liquid fraction is varied between values of zero and the critical value,  $\alpha_{lc}$ , then Equations 2-21, 2-22, and 2-23 map out coordinates of (X, Y) as shown by the upper, U-shaped portion of the curve in the design map of Figure 2.18. Equation 2-24 with Equation 2-23 and with  $\alpha_{lc} = 0.24$  describes the line originating in the region  $Y < 0$  in Figure 2.18.

The slug to annular flow regime transition involves two of the same dimensionless groups as the stratified-to-slug transition; namely, the parameters X and Y given in Equations 2-30 and 2-31. The proposed design point is plotted on the graph of Figure 2.18, for the coordinates (X,Y). If the location of the design point is below the curve in the figure, then the flow regime is annular. If the location of the design point is above the curve in the figure, then the flow regime is slug because all of the previous regimes have been checked, and that is the only regime remaining.

It should also be noted that for microgravity conditions where  $a \approx 10^{-6}g$  the value of Y is approximately 0, so that only the X coordinate is important. That is, the point can be plotted as (X,0). If  $Y \approx 0$  and the value of  $X \leq 1.47$ , then the flow regime is annular. If  $X > 1.47$ , then the flow regime is slug.



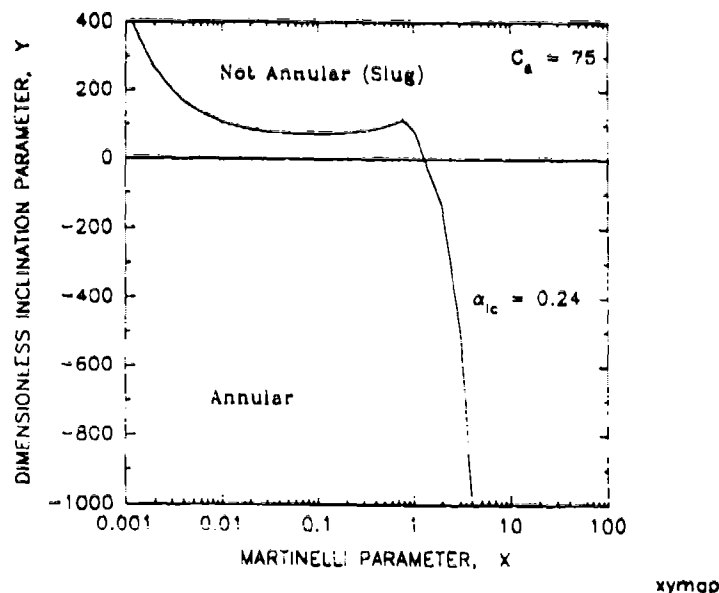


Figure 2.18. DIMENSIONLESS MAP FOR ANNULAR REGIME TRANSITION

## 2.4 Validation With Microgravity Flow Regime Data

As Barnea (1986) points out, the methods and models described here apply well at earth gravity to the full range of pipe inclinations from vertical upward, to horizontal, to vertical downward. Examples of the flow regime comparisons are given in Barnea (1986), Barnea et al. (1982) and Taitel et al. (1980). The purpose of this section is to illustrate that the same models can be applied to microgravity conditions.

### 2.4.1 Experimental Data

Table 2.4 summarizes the nine experimenters, test geometries, and range of data for microgravity tests of gas-liquid flows. Most of the experiments have been performed on aircraft which provide about 25 seconds of acceleration at about  $a \approx 0.01g$ . A few tests have been performed in drop towers which provide a few seconds of acceleration at  $0.001g$  or less.

Tube sizes range from 6 to 40 mm. This is an appropriate size range for two-phase thermal management systems at power levels from 2 kW to 25 kW. Tubes in directly condensing radiators might be somewhat smaller (only a few millimeters in diameter).

Table 2.4. SUMMARY OF EXPERIMENTAL DATA FOR FLOW REGIME METHOD VALIDATION									
Investigator	Sponsor	Test Vehicle	D (mm)	L (m)	Fluid	T (K)	P (kPa)	Acceleration (g's)	$\rho/\rho_s$
1. Chen et al. (1988)	NASA JSC	KC-135	15.8	1.83	R-114	337	643	0.01, 1	29
2. Colin et al. (1991)	CNES/ESA	Zero G	40	3.17	A/W	300	100	0.01, 1	860
3. Crowley et al. (1991)	PL/STPP	KC-135	6.34	1.0	R-11	350	460	0.01, 1	51
4. Dukler et al. (1987)	NASA/LeRC	Drop Tower Learjet	5.52 12.7	0.457 1.06	A/W A/W	300 300	100 100	0.001 0.01	860
5. Dukler et al. (to be published)	NASA/LeRC	Learjet	12.7	1.06	A/W A/Glycerine	300	130	0.01, 0.17	860
6. Heppner et al. (1975)	NASA/MSFC	KC-135	25.4	0.508	A/W	300	130	0.01, 1	860
7. Hill & Best (1991) Reinarts et al. (1991)	PL/STPP	KC-135	8.7, 11.1	1.2	R-12	300	680	0.01, 1	34
8. Lee & Best (1987) Kechnik et al. (1987)	NASA JSC	KC-135	6.0	?	A/W	300	100	0.01	860
9. Rezakallah (1991)	CSA	KC-135	9.52	1.09	A/W	300	100	0.01, 1	860

The fluids used in the tests include primarily air/water combinations and several types of Freon refrigerants. No microgravity data are available for ammonia, heat transfer fluid most likely to be used for thermal management systems on satellites or manned spacecraft. With these fluids, the ratio of the liquid density to the gas density ranges from 30 (R-12) to 900 (air/water). This density ratio is an important criterion in the flow regime transitions which depend upon void fraction. For comparison, ammonia has a density ratio of about 88 at room temperature. At a density ratio of 50 to 100, experiments with Freon R-11 come the closest to matching this value.

Effects of surface tension are not strong in the existing analytical models. Only a relatively small range of surface tension has been studied experimentally – from 0.018 N/m with Freon to 0.050 N/m with air and water. This bounds the surface tension of ammonia, which is about 0.023 N/m.

#### 2.4.2 Comparisons with Individual Experiments

This section describes the comparisons between the design manual methods and the experiments listed in Table 2.4. The MICROREG software (Crowley, 1992) has been used in the comparisons.

Chen et al. (1988). These flow regime data were obtained with Freon R-114, nominally at a constant mass flux ( $G \approx 200 \text{ kg/m}^2\text{-s}$ ). The heat input was varied at constant mass flux in order to vary the quality from about 5% to 86%.

These microgravity data provide information about the transition between the slug and annular flow regimes. Figure 2.19 shows that the observed transition lies very close to the calculated transition. The observed transition is in the range of the transition curve governed by the critical void fraction and the interfacial shear model. The baseline interfacial shear model (Wallis, 1969) and the baseline liquid fraction  $\alpha_{lc} = 0.24$  work well for these data.

Chen et al. also provide complementary flow regime observations at 1g (Figure 2.20). For the mass flux chosen, many data previously in the slug flow regime at 0.01g (Figure 2.19) are in the stratified flow regime at 1g (Figure 2.20). Data at the highest vapor velocities remain in the annular flow regime. The observed data for the stratified to nonstratified regime transition lie right on the borderline with respect to the transition from stratified flow. A slightly larger value of the interfacial shear ( $f_i/f_{wg}$ ) would predict these data well.

Colin et al. (1991). This experiment primarily studied the transition between the bubbly and slug flow regimes. The measured transition occurs at approximately a constant void fraction of  $\alpha_c = 0.2$  (Figure 2.21).

The predicted transition between slug and bubbly flow regimes has two parts: one at a constant void fraction of about 0.40, and the other – based upon turbulence – has a negative slope with respect to liquid velocity. For the portion of the transition at constant void fraction, these data suggest a lower critical void fraction as the transition criterion. The authors attribute the lower void fraction for the transition in the data to the larger pipe diameter (40 mm) and the short length of the test section, suggesting that entrance effects may play a role in the results observed in these tests.

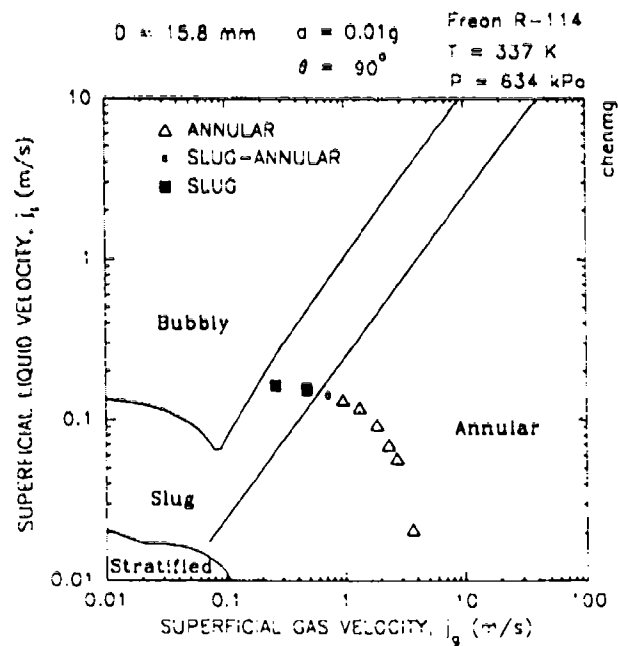


Figure 2.19. COMPARISON WITH CHEN ET AL. (1988) MICROGRAVITY DATA

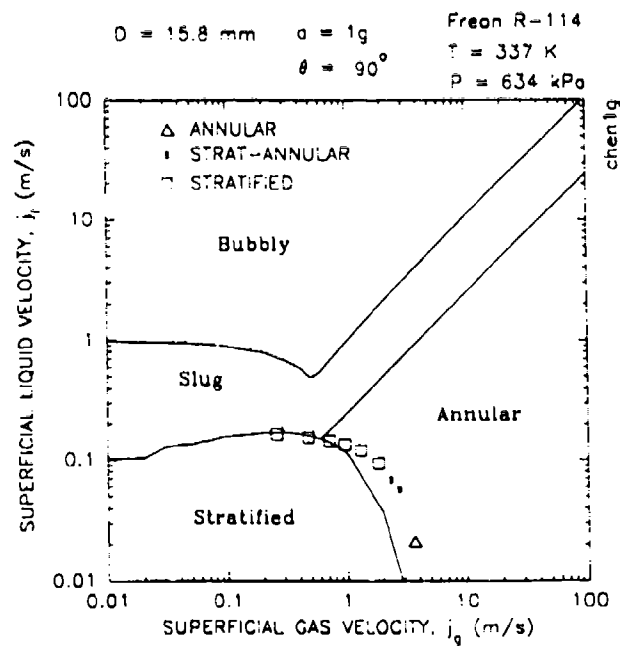


Figure 2.20. COMPARISON WITH CHEN ET AL. (1988) GROUND TEST DATA

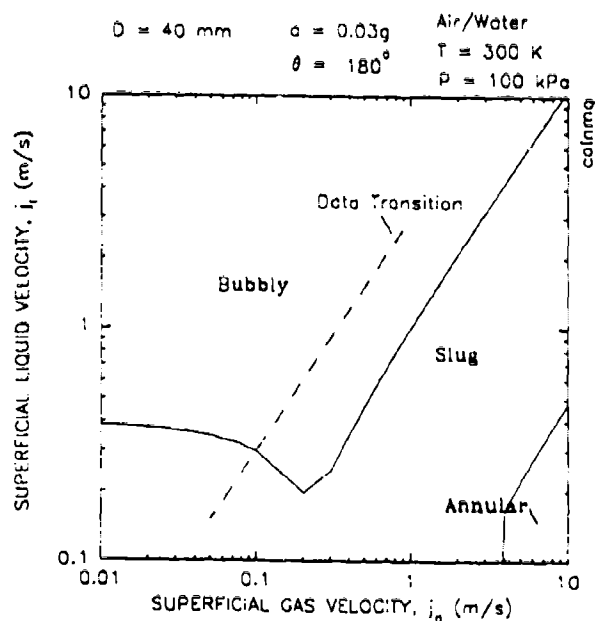


Figure 2.21. COMPARISON WITH COLIN ET AL. (1991)  
MICROGRAVITY DATA

For the portion of the transition based on turbulence, the comparisons may suggest that this transition boundary disappears (moves to lower liquid velocity) more rapidly with decreasing acceleration than is shown by the analysis. On the other hand, the calculated transition would be at liquid velocities lower than the data range if the actual acceleration level achieved is only slightly less than the reported average value of  $a = 0.03g$ . The authors suggest that this may be the case.

Crowley et al. (1991). Figure 2.22 shows the limited data obtained at  $0.01g$  in these experiments. Measured data in the annular flow regime intrude across the transition boundary to slightly higher liquid velocities than is predicted by the analysis. This suggests that the part of the analytical transition at constant liquid fraction should be moved to a higher value of the liquid fraction in order to include these data. One observed data point in the slug flow regime lies right on the border between the slug and bubbly flow regimes, but provides insufficient information to make any conclusions about that transition.

Figure 2.23 presents the complementary  $1g$  data (horizontal) for this experiment. With respect to the stratified to nonstratified transition, the interfacial shear should be lower than the baseline value ( $f_i/f_{wg} = 5$ ) in order to match the measured transition. A value near unity matches the data. The transition between the slug and annular flow regimes matches the observed regimes well.

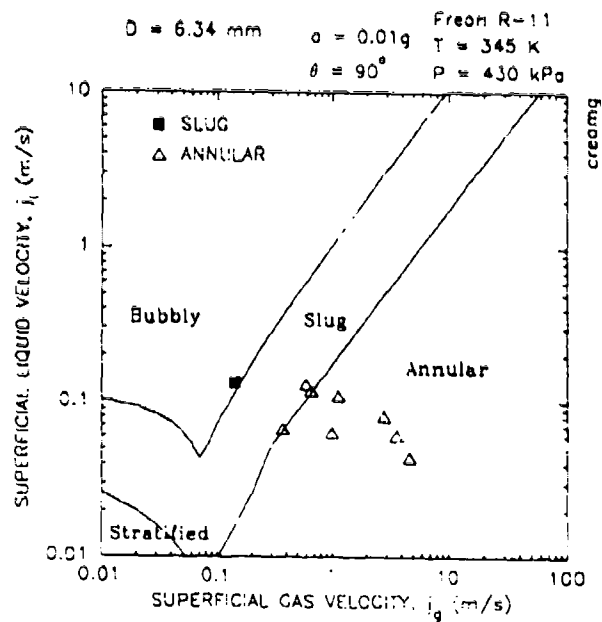


Figure 2.22. COMPARISON WITH CROWLEY ET AL. (1991) MICROGRAVITY DATA

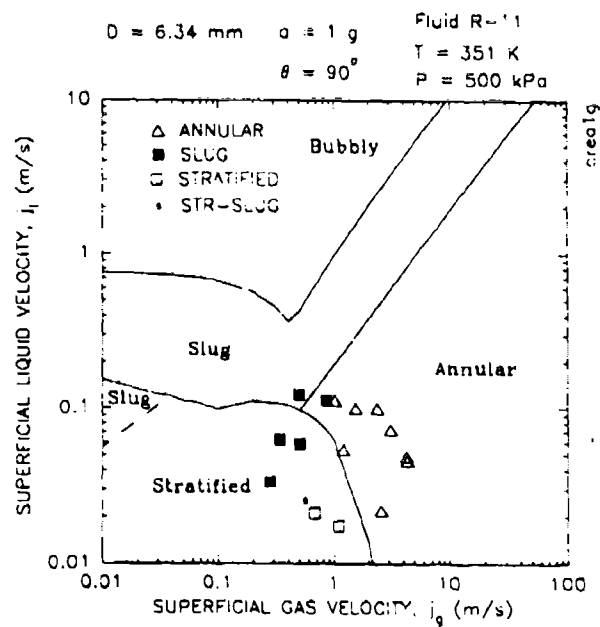


Figure 2.23. COMPARISON WITH CROWLEY ET AL. (1991) GROUND TEST DATA

Dukler et al. (1987). Experiments by Dukler et al. have been performed in a NASA Learjet as well as the Lewis Research Center drop tower facilities. Figures 2.24 and 2.25 present the comparisons for these sets of data. Figures 2.24 and 2.25 both show that the transition from bubbly to slug flow is adequately predicted by the analysis. Figure 2.24 shows that the transition between the slug and annular flow regimes might lie at higher liquid flow rate (or liquid fraction), similar to the data from Crowley et al.

Dukler et al. have obtained additional flow regime observations in the Learjet, including data at an intermediate acceleration of 0.17g (representing the gravity level on Mars) and data with air/glycerine. Those data have not yet been published. However, the initial comments of reviewers with access to both the MICROREG software and the data report that the portion of the slug to bubbly transition based upon turbulence is questionable at intermediate accelerations.

Heppner et al. (1975). As reported in an earlier version of the design manual (Crowley and Izenon, 1989), the lack of information about these data precludes meaningful comparisons.

Hill and Best (1991). Figures 2.26 and 2.27 show the microgravity data from these experiments at 8.8 and 11.1 mm tube sizes, respectively. The preponderance of the data are in the annular flow regime. The comparisons in these two figures suggest, as do previous data, that the transition between slug and annular flow regimes occurs at slightly greater liquid velocity (or liquid fractions) than is calculated. Figures 2.28 and 2.29 show that the critical liquid fraction in this transition must be increase to  $\alpha_{lc} \approx 0.40$  in order to bound the observed data in the annular flow regime. This is a minimum value, since there are no data in the slug flow regime at higher liquid velocities.

For some cases which are nominally under the same conditions where annular flow is observed, however, the flow regime is reported to be slug or slug-annular transition instead of annular. There may be a reason to neglect these few observations which are not in annular flow. The reason is that there is a large uncertainty in the gas flow rate for those cases (taken on a certain flight date), and they may actually lie at significantly lower gas velocities than reported here. Additional microgravity data are expected to be available from this facility.

Complementary flow regime observations have been obtained during the periods of the KC-135 flight profile between the microgravity parabolas. Nominally, these conditions were expected to correspond to horizontal, ground test data. The data are mainly observed to be in the stratified flow regime (Figure 2.30), with the transition from stratified to slug flow at a superficial liquid velocity of  $j_l \approx 0.6$ . Analytical predictions indicate that the data should be predominantly in the slug flow regime, even at the highest value of the interfacial shear. The predicted transition from stratified to slug flow is significantly lower, at  $j_l \approx 0.1$ . This result – where the transition is not bounded by the range of uncertainty in interfacial shear – is contrary to the preponderance of stratified data in the literature. Even the more comprehensive one-dimensional wave theory (Crowley, Wallis, and Barry, 1992) fails to account for this difference, as shown by the dashed transition line in the figure. The result suggests that the test section was probably not level during the observation period, but had a slight upward slope of several degrees or more. True ground test data are presently being obtained in this facility which should answer this question.

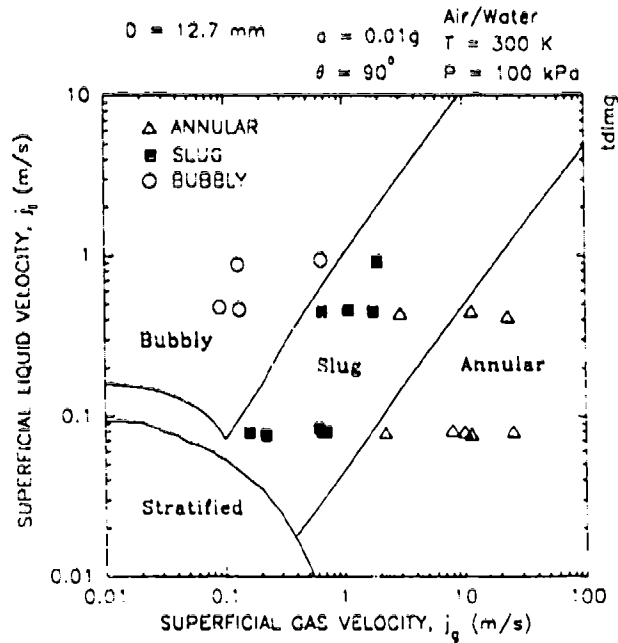


Figure 2.24. COMPARISON WITH DUKLER ET AL. (1987)  
MICROGRAVITY LEARJET DATA

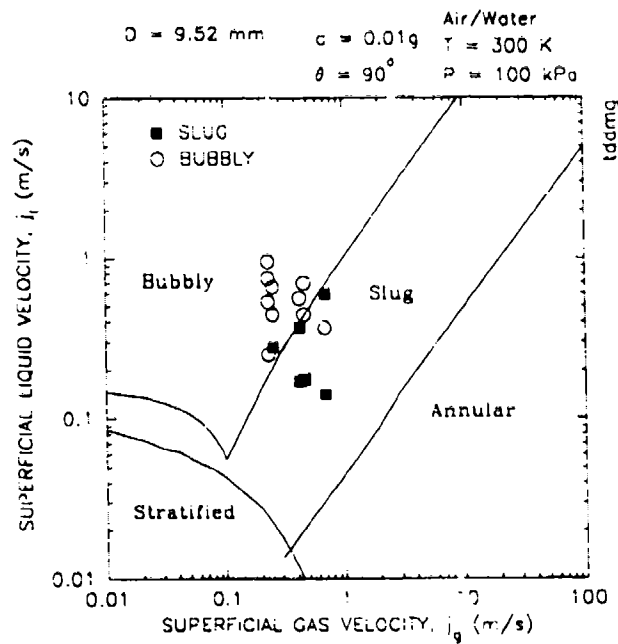


Figure 2.25. COMPARISON WITH DUKLER ET AL. (1987)  
MICROGRAVITY DROP TOWER DATA



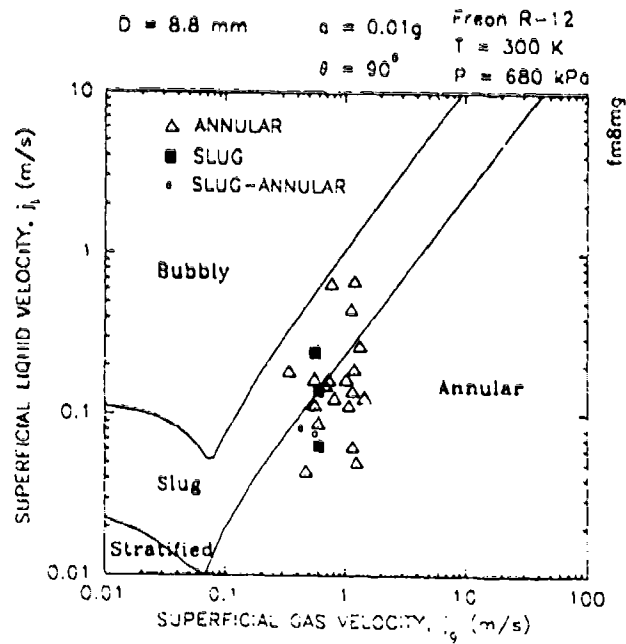


Figure 2.26. COMPARISON WITH HILL-BEST (1991) MICROGRAVITY DATA ( $D \approx 8.8 \text{ mm}$ )

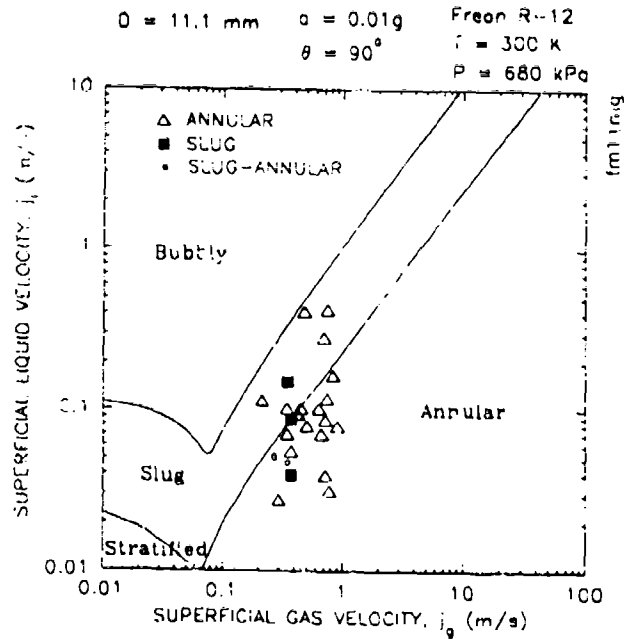


Figure 2.27. COMPARISON WITH HILL-BEST (1991) MICROGRAVITY DATA ( $D = 11.1 \text{ mm}$ )

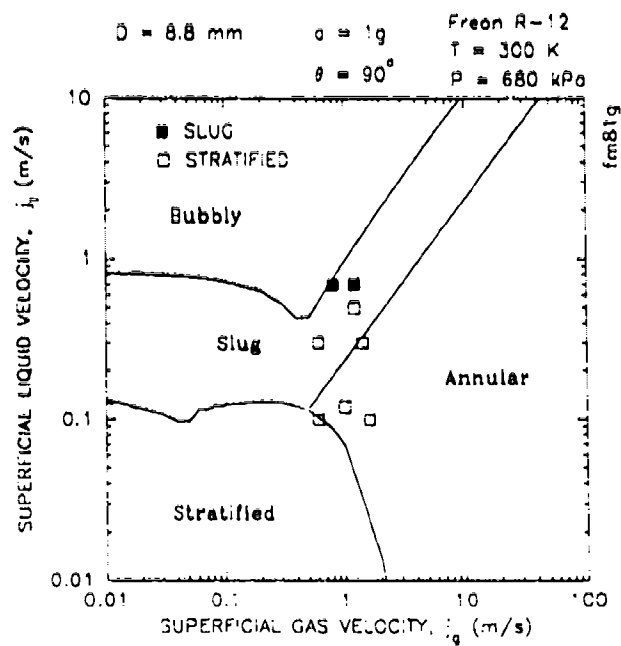


Figure 2.28. SENSITIVITY OF COMPARISON WITH HILL-BEST DATA  
 TO CRITICAL LIQUID FRACTION ( $D = 8.8 \text{ mm}$ )

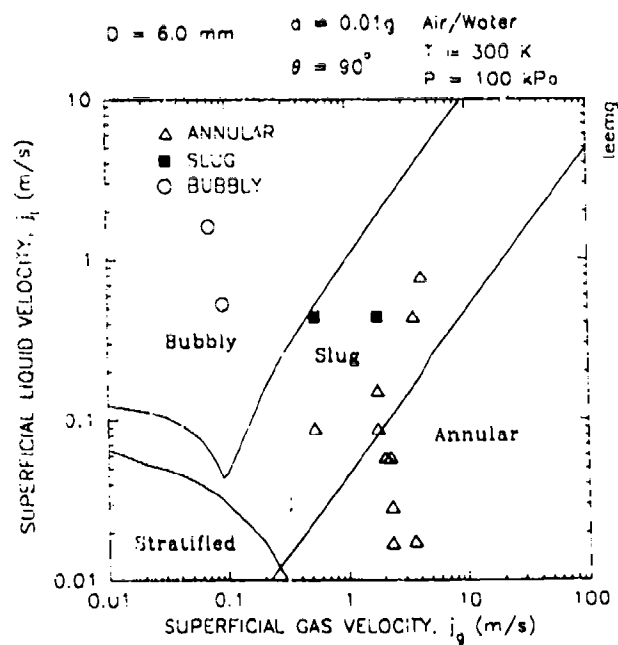


Figure 2.29. SENSITIVITY OF COMPARISON WITH HILL-BEST DATA  
 TO CRITICAL LIQUID FRACTION ( $D = 11.1 \text{ mm}$ )

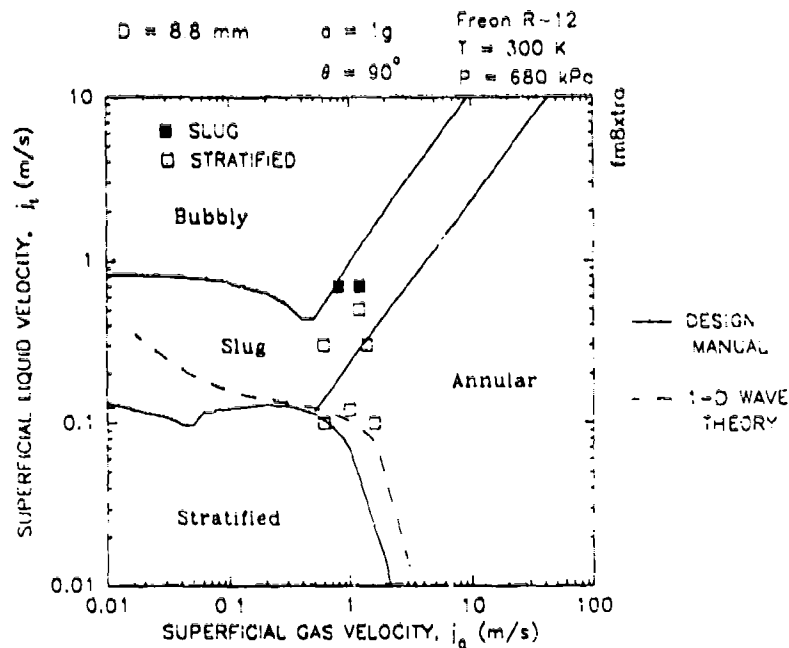


Figure 2.30. COMPARISON WITH HILL-BEST (1991) DATA DURING "LEVEL FLIGHT" ( $D = 8.8 \text{ mm}$ )

Lee and Best (1987). The data from Lee and Best (Figure 2.31) provide some information on both the slug to bubbly and slug to annular regime transitions at low gravity. The predicted transition from slug to bubbly flow lies correctly between the data observed to be in the bubbly and the slug flow regimes. Because of the limited number of data points, however, it is difficult to pinpoint this transition. Like data from Hill and Best described above, these data also suggest that the part of the transition based upon void fraction occurs at higher liquid velocities (higher liquid fraction) for the slug to annular transition.

Rezkaiah (1991). The experimental data from the University of Saskatchewan (Figure 2.32) show that:

- For the part of the slug to bubbly transition based upon a critical void fraction, the model agrees with the results from the Dukler model ( $\alpha_c = 0.40$ ).
- For the part of the slug to annular transition based upon a critical void fraction, a somewhat larger liquid fraction than is included in the model ( $\alpha_{lc} = 0.24$ ) is needed to match these data. Figure 2.33 shows that a value of  $\alpha_{lc} \approx 0.40$ , which matches the Hill-Best data (Figures 2.28 and 2.29), may be slightly too large to compare well with these data.

Further microgravity data are also expected from this facility.

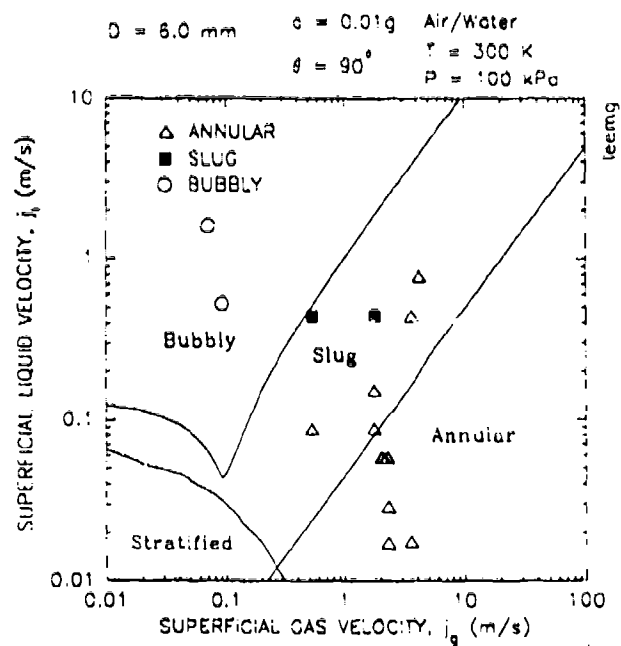


Figure 2.31. COMPARISON WITH LEE-BEST (1987) MICROGRAVITY DATA

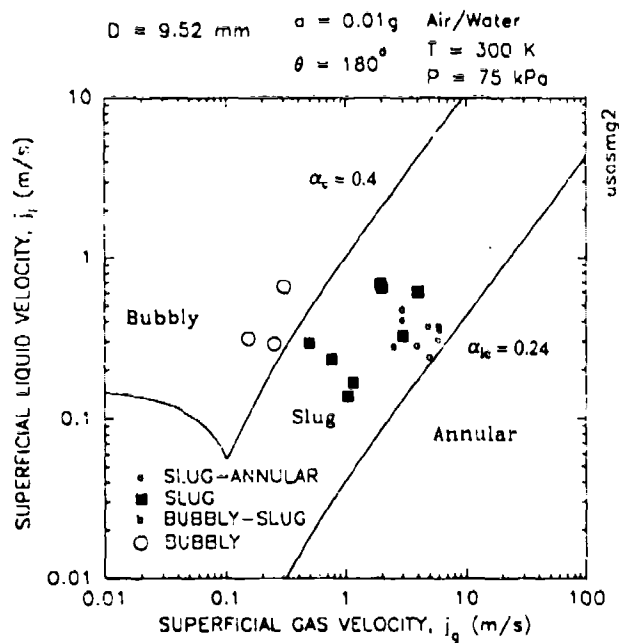


Figure 2.32. COMPARISON WITH REZKALLAH (1991) MICROGRAVITY DATA (Data Set #1)

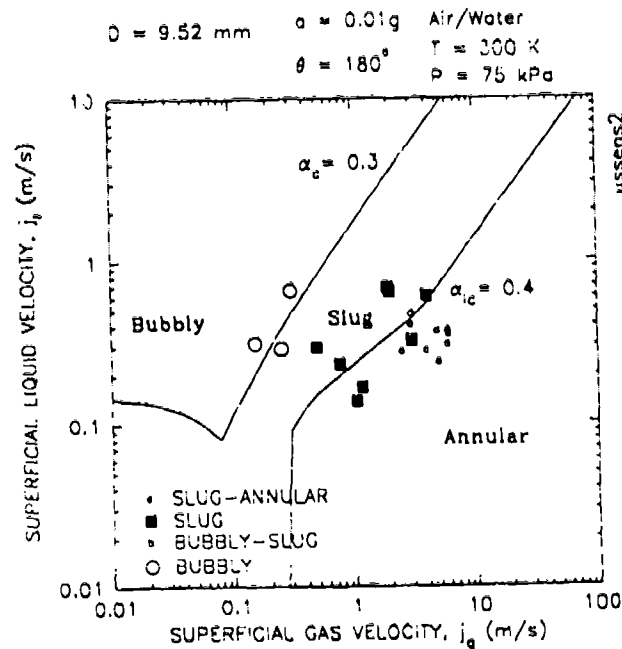


Figure 2.33. SENSITIVITY OF COMPARISON WITH REZKALLAH (1991) DATA TO CRITICAL LIQUID FRACTION (Data Set #1)

#### 2.4.3 Conclusions from Microgravity Comparisons

This section summarizes general conclusions about the comparisons of the design manual methods against the microgravity data with respect to each of the three transitions.

##### Slug to Annular Transition

Comparisons between the data and the design manual methods suggest that:

- A slight modification is needed for the part of the transition which occurs at critical liquid fraction,  $\alpha_{lc}$ . The effect can be bounded by a constant value between 0.24 and 0.4 in the model, but needs further verification through experiments.
- A cutoff model developed by Lee (1987) involving surface tension does not compare well with the available data and has not been included here (see the discussion below).

**Constant Void Fraction.** For the part of this transition based upon critical liquid fraction, several experiments (Crowley, Dukler, Hill-Best, Lee-Best, and Rezkallah) suggest that this transition occurs at higher liquid velocity than calculated in the baseline model. In the discussion of Section 2.4.2, this is referred to as an indication that the transition occurs at a higher critical liquid fraction for simplicity. The actual situation is more complicated. Since the calculated liquid fraction is determined by the relationship for the interfacial shear (see Equation 2-23), the same result can be achieved by either:

- Increasing the liquid fraction while retaining the interfacial shear relationship, or
- Modifying the interfacial shear relationship to increase the interfacial friction at a given liquid fraction.

It is necessary to have liquid fraction measurements corresponding to the flow regime data in order to decide whether the first or second approach is correct. Until liquid fraction measurements are available to refine the approach, the upper limit for the modelling parameter of critical liquid fraction can be extended from  $\alpha_{lc} = 0.24$  to  $\alpha_{lc} = 0.40$  in the analysis to represent this uncertainty.

**Special Cutoff Based Upon Surface Tension.** Lee and Best (1987) suggested a slug to annular transition criterion based upon surface tension forces. Many of these experiments indicate that as a minimum the cutoff is predicted at much too high a gas velocity. This cutoff has been considered here, but ultimately not validated for use in the design manual.

### Slug to Bubbly Transition

The comparisons for this transition suggest that:

- The range of critical void fraction might be extended to lower void fraction (at least for larger pipes) in the portion of the model based on void fraction.
- That the portion of the model based upon turbulence is either inappropriate at these tube sizes or disappears more quickly as the acceleration level is reduced.

**Constant Void Fraction.** For the part of this transition based upon a critical void fraction, the data from tubes less than 40 mm in diameter indicate that the transition is predicted well at the baseline value of  $\alpha_c = 0.40$  in the model. Only the data from Colin et al. at the 40 mm tube size suggest that the transition should be at a lower void fraction of  $\alpha_c = 0.2$ . This may be attributable to the short length of the test section, according to the authors.

**Turbulence Model.** For the part of this transition based upon turbulence, experimental data suggest that the transition drops to low liquid velocities more quickly as the acceleration level is reduced than the model predicts. (See the data by Colin et al.) For the most part, this transition is of no consequence at microgravity conditions. Data at intermediate acceleration levels (representing lunar and Mars gravity) are expected from NASA LeRC. These data should be used to validate the methods for this transition when they become available.

### Stratified to Nonstratified Transition

The model correctly predicts that the stratified transition lies below the range of the data obtained at 0.01g. No change to the models is needed.

The transition from the stratified to nonstratified regimes only matters in the comparisons at about 1g. The range of interfacial shear given in the model causes the data to be bounded for the transitions.

Note: For applications at earth gravity, the stratified to slug portion of the transition is generally predicted very well. The stratified to annular portion of the transition is not always predicted very well — especially in the region where stratified, annular, and slug regimes meet. Stratified flow tends to extend to higher gas velocities than given by the model in observations near this point. (This is evident in the pressure drop comparisons as well, where the pressure drop is given by the stratified model at the regime boundary — approximately  $F_g \approx 1$  and by the annular model only when  $F_g \approx 3$ .) This is not important for space tests, but might be important in ground tests of the equipment. (See the discussion of ground tests in Section 3.5.2.)

## 2.5 References for Flow Regime Methods

Barnea, D., Shoham, O. and Taitel, Y.; "*Flow Pattern Transition for Downward Inclined Two Phase Flow: Horizontal to Vertical*"; Chemical Engrg. Science, V37(5), 1982, pp. 735-746.

Barnea, D., Luninski, Y. and Taitel, Y.; "*Flow Patterns in Horizontal and Vertical Two Phase Flow in Small Diameter Pipes*"; Canadian J. of Chem. Eng., V61, October 1983, pp. 617-620.

Barnea, D.; "*Transition from Annular Flow and From Dispersed Bubble Flow — Unified Models for the Whole Range of Pipe Inclinations*"; Int. J. Multiphase Flow, V12(5), 1986, pp. 733-744.

Barnea, D.; "*A Unified Model for Predicting Flow-Pattern Transitions for the Whole Range of Pipe Inclinations*"; Int. J. Multiphase Flow, V13(1), 1987, pp. 1-12.

Blasius, H.; "*Das Aehnlichkeitsgesetz Bei Reibungsvorgangen in Flussigkeiten*"; Vid-Forschungsh., V131, 1913.

Chen, I.-Y. and Downing, R.S.; "*A Reduced Gravity Flight Experiment: Observed Flow Regimes and Pressure Drops of Vapor and Liquid Flow in Adiabatic Piping*"; AIChE Symp. Series, V84(263), 1988, pp. 203-216.

Colin, C., Fabre, J. and Dukler, A.E.; "*Gas-Liquid Flow at Microgravity Conditions — I. Dispersed Bubble and Slug Flow*"; Int. J. Multiphase Flow, V17(4), 1991, pp. 533-544.

Crowley, C.J. and Sam, R.G.; "*MICROGRAVITY EXPERIMENTS WITH A SIMPLE TWO-PHASE THERMAL SYSTEM*"; PL-TR-91-1059, Prepared by Creare, Inc., Hanover, NH, Prepared for Phillips Laboratory (PL/VTTP), Kirtland AFB, New Mexico, Contract F29601-88-C-0066, 1991.

Crowley, C.J.; "MICROREG PROGRAM: FLOW REGIMES IN MICROGRAVITY"; PL-TR-92-3003, Volume 1, Prepared by Creare, Inc., Hanover, NH, Prepared for Phillips Laboratory (OL-AC PL/VTPT), Edwards AFB, California, Contract F04611-90-C-0004, May 1992.

Crowley, C.J. and Izenson, M.G.; "MICROGRAVITY TWO-PHASE FLOW AND HEAT TRANSFER", AL-TR-89-026, Prepared by Creare Inc., Hanover, NH, Prepared for Astronautics Laboratory, Edwards AFB, California, Contract F04611-88-C-0050, October 1989.

Crowley, C.J., Wallis, G.B. and Barry, J.J.; "Validation of a One-Dimensional Wave Model for the Stratified to Slug Flow Regime Transition, with Consequences for Wave Growth and Slug Frequency"; *Int. J. Multiphase Flow*, V18(2), 1992, pp. 249-271.

Dukler, A.E., Fabre, J.A., McQuillen, J.B. and Vernon, R.; "Gas Liquid Flow at Microgravity Conditions: Flow Patterns and Their Transitions"; ASME Heat Transfer Division Vol. 83, Presented at ASME Annual Meeting, 13-18 December, 1987, Boston, Massachusetts.

Heppner, D.B., King, C.D. and Littles, J.W.; "Zero-G Experiments in Two-Phase Fluids Flow Regimes"; ASME Paper 75-ENAS-24, Presented at the Intersociety Conference on Environmental Systems, 21-24 July, 1975, San Francisco, California.

Hill, W.S. and Best, F.R.; "DEFINITION OF TWO PHASE FLOW BEHAVIORS FOR SPACECRAFT DESIGN"; AFK-0062-FM-8933-418, Prepared by Foster-Miller, Inc., Waltham, Massachusetts, Prepared for Air Force Phillips Laboratory (PL/VTPP), Contract F29601-88-C-0062, June 1991.

Kachnik, L., Lee, D. Best, F.R. and Faget, N.; "A Microgravity Boiling and Convective Condensation Experiment"; ASME Paper 87-WA/HT-12, Presented at ASME Winter Annual Meeting, 13-18 December, 1987, Boston, Massachusetts.

Lee, D. and Best, F.R.; "THERMOHYDRAULIC AND FLOW REGIME ANALYSIS FOR CONDENSING TWO PHASE FLOW IN A MICROGRAVITY ENVIRONMENT"; Doctoral Thesis, Texas A&M University, December, 1987.

Reddy Karri, S.B. and Mathur, V.K.; "Two-Phase Flow Regime Map Predictions Under Microgravity"; R&D Notes, *AIChE J.*, V34(1), January 1988, pp. 137-139.

Reinarts, T.R., Best, F.R., Miller, K.M. and Hill, W.S.; "Definition of Two-Phase Flow Behaviors for Spacecraft Design"; Proceedings of the Eighth Symposium on Space Nuclear Power Systems, M.S. El-Genk and M.D. Hoover, Eds., 6-10 January, 1991, Albuquerque, New Mexico.

Revankar, S.T.; "Flow Regime Map for Gas-Liquid Flow in Channel at Microgravity Condition"; Sixth Symposium on Space Nuclear Power Systems, Transactions, Albuquerque, New Mexico, CONF-890103, January 8-12, 1989.

Rezkallah, K.; "Final Report on Software Evaluation", Private communication to C.J. Crowley, Creare Inc., from the Department of Mechanical Engineering, U. of Saskatchewan, Saskatoon, Saskatchewan, October 24, 1991.



Taitel, Y. and Dukler, A.E.; "A Model for Predicting Flow Regime Transitions in Horizontal and Near Horizontal Gas-Liquid Flow"; AIChE J., V22(1), January 1976, pp. 47-55.

Taitel, Y. and Dukler, A.E.; "Brief Communication - A Theoretical Approach to the Lockhart-Martinelli Correlation for Stratified Flow"; Int. J. Multiphase Flow, V2, 1976, pp. 591-595.

Taitel, Y., Barnea, D. and Dukler, A.E.; "Modeling Flow Pattern Transitions for Steady Upward Gas-Liquid Flow in Vertical Tubes"; AIChE J., V26(3), May 1980, pp. 345-354.

Wallis, G.B.; One-Dimensional Two-Phase Flow; McGraw-Hill Book Company, New York, New York, 1969.

Zuber, N. and Findlay, J.A.; "Average Volumetric Concentration in Two-Phase Flow Systems"; J. Heat Transfer, Trans. ASME, V87(4), November 1965, pp. 453-468.

### **3 TRANSPORT LINES: Pressure Drop Methods**

This section of the design manual provides methods to calculate the two-phase pressure drop in piping. Knowledge of the flow regime is crucial to the calculation of the pressure drop and void fraction in pipes, and Section 2 of the manual covers the flow regime determination for pipe components. Pressure drop methods for bends or elbows, tees, and fittings are also included here.

Section 3.1 summarizes the methods and discusses the applications.

Section 3.2 describes the methods and presents the basic equations for each of the calculations. Calculation methods are available for the following components

- Pipes (various flow regimes),
- Bends and elbows,
- Mixing tees, and
- Fittings (expansions, contractions and short inserts)

The companion software called MICROP (Crowley, et al., 1992) developed on this project uses the methods and equations presented in this section.

Section 3.3 summarizes the information which the designer must have in hand in order to estimate the pressure drop. This section also presents dimensionless parameters and graphs which can be used to quickly calculate void fraction and pressure gradient for a specific flow regime in pipes. This section is set up so that the user does not need to know the details of the theory or the equations. The designer approaches the calculations with knowledge of the flow regime, the phase flow rates, physical geometry, and fluid conditions. Simple dimensionless parameters are used to determine a void fraction or a two-phase multiplier on plots. The pressure gradient is then calculated by using this information in explicit equations.

Finally, Section 3.4 compares the pressure drop and void fraction calculations for the recommended design methods against data from various microgravity experiments and ground based experiments with ammonia.

The design methods recommended here apply to a wide range of acceleration levels, including earth gravity and microgravity, and all "inclinations". The upper limit on the acceleration level would be the point where fluid properties vary significantly across the flow channel due to pressure gradients caused by large body forces. Once the flow regime is selected from four possible choices (see Section 2), the pressure drop specific to that regime can then be calculated by the methods presented in this section.

#### **3.1 Summary and Application of Pressure Drop Methods**

Pressure drop methods have been developed for a variety of basic flow components. These components are found in the adiabatic transport lines in two-phase thermal management systems.

### 3.1.1 Summary of Pressure Drop Methods

Figure 3.1 shows the pipe, elbow, tee, and fitting components which can be modelled. To calculate the pressure drop in a straight pipe component, the flow regime must first be determined from among the four possible regimes:

- Annular,
- Slug,
- Bubbly, or
- Stratified.

The sketches for straight pipes in Figure 3.1 illustrate these four flow regimes. (Section 2 describes them in greater detail and provides the methods to determine the regime.)

The three general geometries for fittings are:

- Abrupt expansion,
- Abrupt contraction, or
- Short insert.

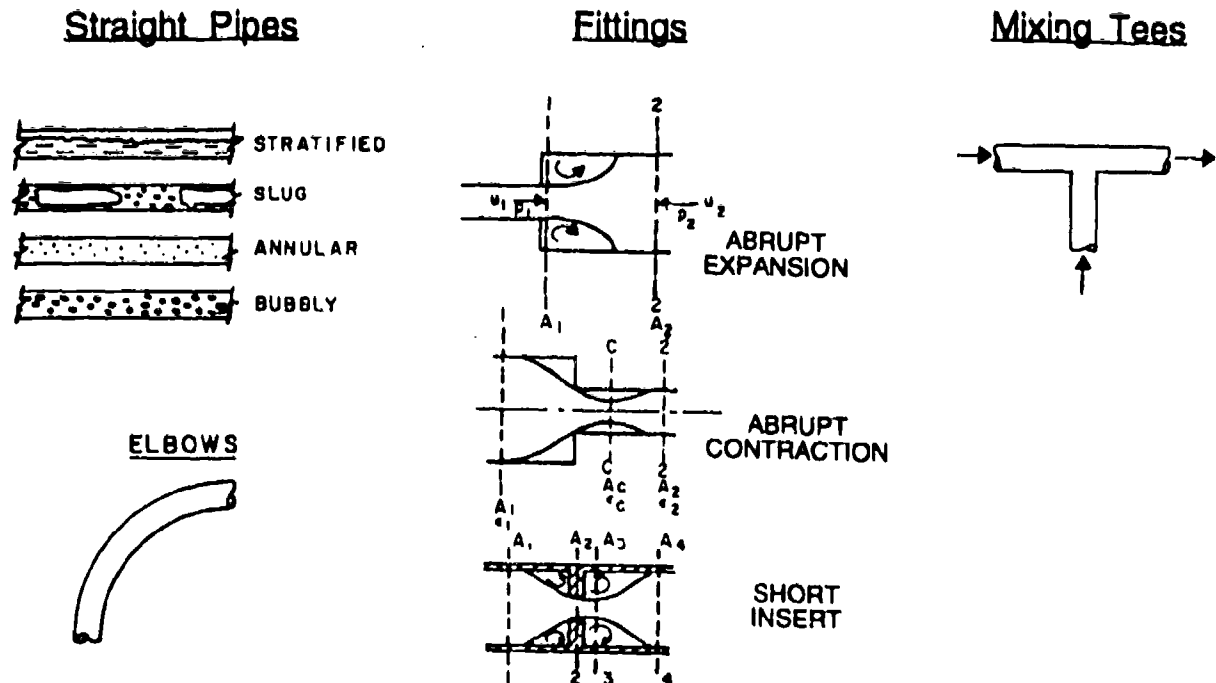


Figure 3.1. GEOMETRIES AND FLOW REGIMES FOR PRESSURE DROP CALCULATIONS

Table 3.1 summarizes the main features of the recommended models for pressure gradient and void fraction in pipes. The model used for each of the flow regimes is mechanistic. In contrast to empirical correlations, which abound in the two-phase flow literature, the mechanistic approach considers the governing physics in the momentum balances, therefore the mechanistic models should scale well over a range of acceleration magnitudes (g-levels).

These are not the only mechanistic modelling approaches in the literature. Generally, alternate mechanistic models can be derived at various levels of detail for each of the four flow regimes. Modelling approaches used include:

- Homogeneous,
- Drift flux, and
- Separated (also called Two Fluid).

The models recommended here use whichever approach suffices for design purposes. Table 3.1 shows that the mechanistic models for the slug and the bubbly flow regimes are based upon a "drift flux" approach and that the models for the annular and stratified flow regimes are based upon a "separated" approach. For more detailed information on the background, the reference texts on two-phase flow modelling by Wallis (1969) and Collier (1986) are recommended reading.

Table 3.1. METHODS FOR PRESSURE DROP CALCULATIONS IN STRAIGHT PIPES					
FLOW REGIME	RECOMMENDED MODEL	APPROACH	KEY PARAMETER FOR UNCERTAINTY	BASELINE VALUE OF KEY PARAMETER	RANGE OF UNCERTAINTY FOR KEY PARAMETER
ANNULAR	HEWITT (1982) WALLIS (1969)	SEPARATED FLUIDS	INTERFACIAL FRICTION $C_s$ $b$	$1 + C_s(1-\alpha)^b$ Chen    Wallis 6.81    75 0.39    0	0 to 75 0 to 1
	LILES-MAHAFFY (1986)		ENTRAINMENT FRACTION ( $E_d$ )	0	0 to (model)
STRATIFIED	TAITEL-DUKLER (1976)	SEPARATED FLUIDS	INTERFACIAL FRICTION	5	1 to 10
	LILES-MAHAFFY (1976)		ENTRAINMENT FRACTION ( $E_d$ )	0	0 to (model)
SLUG	WALLIS (1969)	DRIFT-FLUX	DISTRIBUTION PARAMETER ( $C_0$ )	1.3	1.0 to 1.3
			DRIFT FLUX COEFFICIENT ( $k$ )	0.35	0 to 0.5
BUBBLY	WALLIS (1969)	DRIFT-FLUX	DISTRIBUTION PARAMETER ( $C_0$ )	1.2	1.0 to 1.2
			DRIFT-FLUX COEFFICIENT ( $k$ )	1.4	0 to 1.4

Table 3.2 summarizes the methods used to calculate pressure drop in the other types of components: elbows, tees, and fittings. In several instances – elbows, tees, and abrupt contractions – a homogeneous two-phase model is used. For abrupt expansions and short inserts, a separated model approach is used. The table lists the references for these models as well.

### 3.1.2 Applications

Most two-phase thermal management systems for spacecraft include gas and liquid flow in the transport line between the evaporator and condenser components or in the condenser/radiator component. Mechanically pumped systems permit two-phase flow at the evaporator exit. Others, such as capillary pumped loops (CPLs) or droplet impingement cooling (DIC) devices, have single-phase flow at the evaporator exit, but two-phase flow occurs downstream in the transport line because heat losses lead to condensate formation between the evaporator and the condenser.

Table 3.2. PRESSURE DROP METHODS IN PIPING COMPONENTS					
	COMPONENT				
	Bends and Elbows	Tees	Abrupt Expansion	Abrupt Contraction	Short Inserts
Approach	Homogeneous	Homogeneous	Separated	Homogeneous	Separated
Recommended Model	Chisholm (1980)	Rohsenow-Hartnett-Ganic (1985)	Hussain-Weisman (1975)	Hussain-Weisman (1975) and Tapucu et al. (1989)	Harshe-Hussain-Weisman (1976)
Key Uncertainty	Single Phase Loss Coefficient	---	Slip Model Coefficients	---	Slip Model Coefficients
Limit or Range	0.6 to 2.0	---	Homogeneous	---	Homogeneous

For space systems operating under microgravity conditions, the annular flow regime is probably the most common in pipes. This is because the annular flow regime occurs at flow qualities above  $x \approx 0.05$ . Flow qualities at the evaporator exit typically approach 1.0 in order to take maximum advantage of the latent heat of vaporization of the liquid, which is the main purpose for using two-phase systems in the first place. The slug and bubbly flow regimes will be less common during steady-state operation because they occur at low flow qualities. Slug and bubbly flows may be encountered at turndown conditions, during startup and shutdown, or in short regions of high-shear condensers and evaporators. The stratified flow regime may appear during ground testing, or when the acceleration level is relatively large (greater than 0.1g).

The methods in this section apply to adiabatic flow in pipes and fittings. Alternate geometries such as square or rectangular channels could be treated by similar methods, but are not included here. The methods also assume that the liquid phase wets the material of the pipe wall. If the liquid does not wet the wall surface (such as mercury in a glass tube for example), then the flow regime may be different than the regimes considered here, and the pressure drop models will differ accordingly.

The recommended models for pressure drop in pipes have been extensively compared against experimental data at earth gravity in various flow orientations ranging from vertical upward to vertical downward. In the absence of gravity, the hydrostatic component of the pressure gradient becomes negligible, and the frictional component dominates, so the models reduce to the appropriate limits under microgravity conditions.

### 3.2 Pressure Drop Methods for Each Flow Regime in Pipes

This section presents the detailed analytical equations and solution methods used to calculate the void fraction and the pressure gradient in each of the four flow regimes. See Figure 3.1 for sketches of the flow regimes.

#### 3.2.1 Equations for Pressure Drop in Pipes

**Annular Flow Regime.** The references by Wallis (1969) and Hewitt (1982) describe the derivation of the basic model for the annular flow regime. In the separated approach used in this regime, individual momentum balances are first written for each of the gas and liquid phases. These equations are then subtracted to derive the void fraction equation and added to derive the pressure gradient equation for this regime.

The first step in the calculation process for this flow regime is to determine if entrainment occurs, and if so, the value of the entrainment fraction. First, calculate the critical velocity,  $V_e$ , for onset of liquid entrainment by:

$$V_e = (2.5 \times 10^{-4}) \left[ \frac{\rho_l}{\rho_g} \right]^{0.5} \left[ \frac{\sigma}{\mu_g} \right] \quad (3-1)$$

where

$\rho_l$  is the density of the liquid phase ( $\text{kg/m}^3$ ),  
 $\rho_g$  is the density of the gas phase ( $\text{kg/m}^3$ ),  
 $\sigma$  is the surface tension ( $\text{N/m}$ ), and  
 $\mu_g$  is the viscosity of the gas phase ( $\text{kg/m}\cdot\text{s}$ ).

Wallis (1969) provides this critical velocity equation.

Then calculate the fraction of the liquid flow,  $E_d$ , in the form of entrained droplets:

$$E_d = 1 - \exp \left[ C_e \left( \frac{V_c - j_g}{V_c} \right) \right] \quad (3-2)$$

where

$V_c$  is the critical velocity by Equation 3-1,  
 $C_e$  is a coefficient with a value  $0 < C_e < 0.23$ , and  
 $j_g$  is the superficial velocity of the gas phase ( $\text{m/s}$ ).

Liles and Mahaffy (1986) derived this relationship to represent the fraction of liquid which is in the form of entrained droplets. Values of  $E_d$  less than zero should not be allowed.

Next calculate the density of the gas/liquid droplet core as a homogeneous mixture:

$$\rho_c^* = \left( \frac{\rho_c}{\rho_g} \right) = \left[ E_d \left( \frac{\rho_l j_l}{\rho_g j_g} \right) + 1 \right] \quad (3-3)$$

where

$E_d$  is the fraction of liquid entrained as droplets from Equation 3-1 (-),  
 $\rho_c$  is the density of the two-phase mixture ( $\text{kg/m}^3$ ), and  
 $j_l$  is the superficial velocity of the liquid phase ( $\text{m/s}$ ).

Note that if the rate of liquid entrainment,  $E_d$ , is zero, the density of the core flow is the same as the gas density  $\rho_g$ .

The basic equation for the liquid fraction in the film for the annular flow regime is:

$$X_a^2 (1 - E_d)^{1.8} - \left( \frac{f_l}{f_{wg}} \right) \left[ \frac{H_{lf}^2}{(1 - H_{lf})^{2.5}} \right] + Y_a H_{lf}^3 = 0 \quad (3-4)$$

where the dimensionless Martinelli parameter,  $X_a$ , is

$$X_a = \left[ \frac{4f_{wl}(\rho_l j_l^2 / 2D)}{4f_{wg}(\rho_g j_g^2 / 2D)} \right]^{1/2} \quad (3-5)$$

In Equation 3-5 the new parameters include:

$f_{wl}$  is the friction factor at the wall-liquid interface (-),  
 $f_{wg}$  is the friction factor at a wall-gas interface (-), and  
 $D$  is the pipe diameter (m).

The dimensionless parameter,  $Y_a$ , is:

$$Y_a = - \left[ \frac{m_g g (\rho_l - \rho_g) (\cos \theta)}{4 f_{wg} (\rho_g j_g^2 / 2D)} \right] \quad (3-6)$$

where

$m_g$  is the magnitude of the acceleration (-),  
 $g$  is the acceleration of earth gravity (m/s<sup>2</sup>), and  
 $\theta$  is the angle between the flow direction and the acceleration (°).

And the recommended model for the interfacial friction factor ratio, ( $f_i/f_{wg}$ ), is:

$$\left[ \frac{f_i}{f_{wg}} \right] = (1 + C_a H_{if}^b) \quad (3-7)$$

$C_a$  and  $b$  are coefficients having the values and the ranges noted in Table 3.1. Values of these coefficients which correspond to models suggested by Wallis (1969) and Chen et al. (1989) are included in the table. The interfacial friction is the key modelling parameter in the annular flow regime.

To evaluate  $X_a$  in Equation 3-5, the friction factors must be evaluated. To determine the wall-liquid friction factor, first calculate the Reynolds number for the liquid phase:

$$Re_l = \left[ \frac{\rho_l D j_l}{\mu_l} \right] (1 - E_d) \quad (3-8)$$

where  $\mu_l$  is the viscosity of the liquid phase (kg/m-s).

If the Reynolds number,  $Re_l$ , is greater than 1500, then:

$$f_{wl} = 0.25 \left[ -2.0 \log \left\{ \frac{(\epsilon_r/D)}{3.7} + \left[ \frac{5.02}{Re_l} \right] \log \left[ \frac{(\epsilon_r/D)}{3.7} + \frac{13}{Re_l} \right] \right\} \right]^{-2} \quad (3-9)$$

where  $(\epsilon_r/D)$  is the dimensionless roughness of the pipe. This friction factor model for turbulent flow closely approximates the Colebrook friction factor relationship. Suggested by Zigrang and Sylvester (1982), this model avoids the iterative approach needed to solve the Colebrook form of the friction factor equation. If the Reynolds number for the liquid phase is less than 1500 ( $Re_l < 1500$ ), however, then:

$$f_{wl} = 16(Re_l)^{-1.0} \quad (3-10)$$



which is the standard equation for the friction factor in laminar flow. The Reynolds number of 1500 has been selected for the transition because it is the point where the friction factors in Equations 3-9 and 3-10 are equal.

To evaluate  $X_a$  in Equation 3-5 and  $Y_a$  in Equation 3-6, a friction factor for the gas phase interacting with a smooth wall (liquid interface) is calculated. For the gas phase, the Reynolds number is

$$Re_g = \left[ \frac{\rho_g D_{if}}{\mu_g} \right] \left[ \frac{1}{1-H_{lf}} \right]^{\frac{1}{2}} \quad (3-11)$$

If the Reynolds number for the gas phase,  $Re_g$ , is greater than 1500, then:

$$f_{wg} = 0.25 \left[ -2.0 \log \left\{ \frac{(\epsilon/D)}{3.7} - \left[ \frac{5.02}{Re_g} \right] \log \left[ \frac{(\epsilon/D)}{3.7} + \frac{13}{Re_g} \right] \right\} \right]^2 \quad (3-12)$$

but if  $Re_g < 1500$ , then:

$$f_{wg} = 16(Re_g)^{-1.0} \quad (3-13)$$

Laminar flow of the gas phase is unlikely for the conditions of interest to spacecraft thermal management systems.

Equations 3-4 through 3-13 must be solved iteratively to determine the liquid holdup in the annular liquid film,  $H_{lf}$ . These equations are solved by systematically varying the liquid holdup,  $H_{lf}$ , until the basic holdup equation (Equation 3-4) is solved. Since values of  $H_{lf}$  must lie in the range from zero to unity (and will tend to lie closer to zero), a simple bisectional search method is recommended. A tolerance of  $1 \times 10^{-7}$  is recommended for the value of  $H_{lf}$  to achieve convergence.

With the liquid fraction in the film and the fraction of liquid entrained determined, the total liquid fraction is:

$$H_l = H_{lf} + \left[ \frac{E_d J_l}{E_d J_l + J_g} \right] (1-H_{lf}) \quad (3-14)$$

which is the sum of the liquid fraction in the annular film and in the form of entrained droplets. Note that the total liquid fraction,  $H_l$ , is the same as the liquid fraction in the film,  $H_{lf}$ , if there is zero liquid entrainment ( $E_d = 0$ ). The void fraction is therefore:

$$\alpha = (1 - H_l) \quad (3-15)$$

The frictional component of the pressure pressure gradient is:

$$\left[ \frac{dP}{dz} \right]_{fa} = - \left[ 2f_{wl} \left[ \frac{\rho_l J_l^2}{D} \right] \left[ \frac{1-E_d}{H_{lf}} \right]^2 \right] \quad (3-16)$$

and the component of the pressure gradient due to body forces (gravity) is:

$$\left(\frac{dP}{dz}\right)_{ga} = m_g g [H_{lf} \rho_l + (1-H_{lf}) \rho_c] (\cos \theta) \quad (3-17)$$

The total pressure gradient is the sum of the individual components above:

$$\left(\frac{dP}{dz}\right)_{ta} = \left(\frac{dP}{dz}\right)_{fa} + \left(\frac{dP}{dz}\right)_{ga} \quad (3-18)$$

Equations 3-16, 3-17, and 3-18 can normally be applied over most of the range of interest. However, as the liquid fraction approaches very small values ( $H_{lf} < 0.002$ ), it is recommended that the total pressure gradient be calculated using the gas phase equation alone, as follows:

$$\left(\frac{dP}{dz}\right)_{ta} = - \left[ 4f_{wg} \left(\frac{f_i}{f_{wg}}\right) \left(\frac{\rho_{lg}}{2D}\right)^2 \left(\frac{1}{1-H_{lf}}\right)^{5/2} \right] + [m_g g \rho_c (\cos \theta)] \quad (3-19)$$

More complicated models could be written for the annular flow regime, involving liquid droplet entrainment and deposition. For most cases of interest to thermal management systems, liquid droplet entrainment should not be significant. The effect of liquid droplet entrainment on the pressure gradient is relatively small in any event.

**Stratified Flow Regime.** The approach to the model for the stratified flow regime is similar to that used for the annular regime. This regime should not occur in microgravity, but often occurs in ground tests. Taitel and Dukler (1976) first developed this approach for the stratified flow regime, although the form was first proposed by Lockhart and Martinelli in the 1950s. Like the annular flow regime, separate momentum equations are written for the gas and liquid phases. The main difference compared with the annular flow model is in the geometric parameters which describe the interfaces between each fluid phase and the wall and also between the liquid and vapor phases. The equations for each phase are subtracted to derive the void fraction relationship and added to derive the two-phase momentum equation and the pressure gradient.

First, the possible liquid entrainment is calculated using the same model as for the annular flow regime. Equations 3-1, 3-2, and 3-3 are used to calculate the critical gas velocity, entrainment fraction, and density of the homogeneous flow of gas and liquid droplets.

For the stratified flow regime, the basic holdup equation is:

$$X_s^2 \left[ \left( R_l^* \right)^2 \left( \frac{S_l^*}{A_l} \right) (1 - E_d)^2 \right] - \left( R_g^* \right)^2 \left[ \left( \frac{S_g^*}{A_g} \right) + \left( \frac{f_i}{f_{wg}} \right) \left( \frac{S_i^*}{A_g} + \frac{S_i^*}{A_l} \right) \right] + 4Y_s = 0 \quad (3-20)$$

where the Martinelli parameter,  $X_s$ , in stratified flow is:

$$X_s = \left[ \frac{4f_{wl}(\rho_l j_l^2/2D)}{4f_{wg}(\rho_g j_g^2/2D)} \right]^{0.5} \quad (3-21)$$

The dimensionless pipe slope parameter,  $Y_s$ , is:

$$Y_s = - \left[ \frac{m_g g (\rho_l - \rho_g) (\cos \theta)}{4f_{wg}(\rho_g j_g^2/2D)} \right] \quad (3-22)$$

The interfacial friction factor ratio ( $f_l/f_{wg}$ ) in Equation 3-20 has a constant value in the range  $1 < f_l/f_{wg} < 10$  and a recommended value of 5. Table 2.2 of Section 2 defines the dimensionless geometric parameters in Equation 3-20 as functions of the dimensionless height of the liquid in the pipe  $h^*$ .

To evaluate the parameter  $X_s$  in Equation 3-21, the friction factor at the wall-liquid interface must be calculated. First determine the Reynolds number for the liquid phase:

$$Re_l = \left[ \frac{\rho_l D_{j_l}}{\mu_l} \right] R_l^* D_l^* (1 - E_d) \quad (3-23)$$

If the Reynolds number,  $Re_l$ , is greater than 1500, then:

$$f_{wl} = 0.25 \left[ -2.0 \log \left\{ \frac{(\epsilon_r/D)}{3.7} - \left[ \frac{5.02}{Re_l} \right] \log \left[ \frac{(\epsilon_r/D)}{3.7} + \frac{13}{Re_l} \right] \right\} \right]^{-2} \quad (3-24)$$

using the Zigrang-Sylvester (1982) equation, but if the Reynolds number,  $Re_l$ , is less than 1500, then:

$$f_{wl} = 16(Re_l)^{-1.0} \quad (3-25)$$

for the laminar regime in the liquid phase. (See the notes in the section on the annular flow regime above concerning these friction factor models.)

To evaluate the parameter  $X_s$  in Equation 3-20 and  $Y_s$  in Equation 3-21, the friction factor at the wall-gas interface must be calculated. The first step is to determine the gas phase Reynolds number:

$$Re_g = \left[ \frac{\rho_g D_{j_g}}{\mu_g} \right] R_g^* D_g^* \quad (3-26)$$

If  $Re_g \geq 1500$ , then:

$$f_{wg} = 0.25 \left[ -2.0 \log \left\{ \frac{(\epsilon_r/D)}{3.7} - \left[ \frac{5.02}{Re_g} \right] \log \left[ \frac{(\epsilon_r/D)}{3.7} + \frac{13}{Re_g} \right] \right\} \right]^{-2} \quad (3-27)$$

If  $Re_g < 1500$ , then:

$$f_{wg} = \frac{16(Re_g)^{-1.0}}{3-10} \quad (3-28)$$

The dimensionless liquid level,  $h^*$ , which satisfies Equations 3-19 through 3-28, must be determined by an iterative approach. To solve these equations iteratively, the value of the liquid level  $h^*$  is varied until both sides of the holdup equation (Equation 3-19) are equal. There is only a single solution for downward inclinations or horizontal flows. Since values of  $h^*$  must lie in the range from zero to unity (and will tend to be less than 0.5), a simple bisectional search method could be used. (Due to the cylindrical geometry of the pipe cross-section, there is a possibility of multiple (three) solutions for certain cases with small upward inclinations in the stratified flow regime.)

Once the value of  $h^*$  which satisfies the equations is found, the liquid fraction,  $H_{lf}$ , in the stratified layer is determined from the geometric parameter,  $R_1^*$ , by:

$$H_{lf} = \left[ 1/R_1^* \right] \quad (3-29)$$

When entrainment occurs, the total liquid fraction,  $H_l$ , is the sum of the fraction in the liquid film and the entrained liquid:

$$H_l = H_{lf} + \left[ \frac{E_d j_l}{E_d j_l + j_g} \right] (1 - H_{lf}) \quad (3-30)$$

and the void fraction is:

$$\alpha = (1 - H_l) \quad (3-31)$$

Once the liquid fraction has been determined, calculating the pressure gradient is straightforward. The frictional component of the pressure gradient is:

$$\left[ \frac{dP}{dz} \right]_{fst} = - \left[ 2f_{wl} \left[ \frac{\rho_l j_l^2}{\pi D} \right] \left[ R_1^* \right]^2 \left[ S_1^* \right] (1 - E_d)^2 \right] - \left[ 2f_{wg} \left[ \frac{\rho_g j_g^2}{\pi D} \right] \left[ R_g^* \right]^2 \left[ S_g^* \right] \right] \quad (3-32)$$

The component of the pressure gradient due to body forces (gravity) is:

$$\left[ \frac{dP}{dz} \right]_{gst} = m_g g [H_{lf} \rho_l + (1 - H_{lf}) \rho_g] (\cos \theta) \quad (3-33)$$

The total pressure gradient is therefore:

$$\left[ \frac{dP}{dz} \right]_{tst} = \left[ \frac{dP}{dz} \right]_{fst} + \left[ \frac{dP}{dz} \right]_{gst} \quad (3-34)$$

Because it is difficult to achieve numerical accuracy in the calculations when the liquid fraction approaches the limits of zero or unity, the liquid phase or the gas phase momentum equations are used in these limits. If the liquid holdup,  $H_{lf}$ , is greater than 0.99, then the momentum equation for the liquid phase is used:

$$\begin{aligned} \left(\frac{dP}{dz}\right)_{\text{tst}} = & - \left[ f_{wl} \left( \frac{\rho_l j_l^2}{2D} \right) \left[ R_l^{*2} \right] \left[ \frac{S_l^*}{A_l^*} \right] \right] \\ & + \left[ f_{wg} \left( \frac{f_l}{f_{wg}} \right) \left( \frac{\rho_g j_g^2}{2D} \right) \left[ R_g^{*2} \right] \left[ \frac{S_l^*}{A_l^*} \right] \right] + [m_g g \rho_l (\cos \theta)] \end{aligned} \quad (3-35)$$

If the liquid fraction,  $H_{lf}$ , is less than 0.01, then the momentum equation for the gas phase is used:

$$\left(\frac{dP}{dz}\right)_{\text{tst}} = - (f_{wg}) \left( \frac{\rho_g j_g^2}{2D} \right) \left[ R_g^{*2} \right] \left[ \left[ \frac{S_g^*}{A_g^*} \right] + \left( \frac{f_l}{f_{wg}} \right) \left[ \frac{S_l^*}{A_g^*} \right] \right] + [m_g g \rho_c (\cos \theta)] \quad (3-36)$$

**Slug Flow Regime.** The model for void fraction in the slug flow regime is based upon a drift flux approach (Wallis, 1969; Zuber and Findlay, 1965), which requires an empirical relationship between the void fraction and the flow rates of each phase. First, the velocity of the slugs is calculated using the drift flux equation:

$$V_s = C_{os}(j_g + j_l) + k_s \left[ \frac{m_g g D (\rho_l - \rho_g)}{\rho_l} \right]^{0.5} \quad (3-37)$$

where

$C_{os}$  is a constant typically near 1.3 (see Table 3.3), and  
 $k_s$  is a constant whose value is given in Table 3.3.

The other parameters have been defined previously. The values in Table 3.3 have been selected based upon our review of almost two dozen experiments.

The void fraction is then calculated by:

$$\alpha = \left[ \frac{j_g}{V_s} - \frac{(1-E_{ls})[V_s(j_g + j_l)]}{V_s} \right] = (1 - H_l) \quad (3-38)$$

where  $E_{ls}$  is the fraction of liquid contained in the liquid slugs. Typically, a value of  $E_{ls} = 0.75$  is assumed. The density of the two-phase liquid and gas mixture in the liquid slugs is then:

$$\rho_{ls} = [(1 - E_{ls})\rho_g + E_{ls}\rho_l] \quad (3-39)$$

Table 3.3. DRIFT-FLUX PARAMETERS FOR THE SLUG FLOW REGIME		
ANGLE $\theta$ BETWEEN FLOW DIRECTION AND BODY FORCE VECTOR ( $^\circ$ )	DISTRIBUTION PARAMETER $C_{os}$	$k_s$
$90^\circ \leq \theta \leq 180^\circ$	1.3	0.35
$\theta = 90^\circ$	1.3	0
$0^\circ < \theta \leq 90^\circ$	1.0	-0.35

Next calculate a two-phase Reynolds number for the liquid slugs by:

$$Re_{lm} = \left[ \frac{\rho_{ls} D (j_g + j_l)}{\mu_l} \right] \quad (3-40)$$

and use this value to calculate the friction factor for the slug flow regime. If the Reynolds number,  $Re_{lm}$  is greater than 1500, then:

$$f_{wl} = 0.25 \left[ -2.0 \log \left\{ \frac{(\epsilon_s/D)}{3.7} - \left[ \frac{5.02}{Re_{lm}} \right] \log \left\{ \frac{(\epsilon_s/D)}{3.7} + \frac{13}{Re_{lm}} \right\} \right\} \right]^{-2} \quad (3-41)$$

using the Zigrang-Sylvester (1982) equation for turbulent flow, but if  $Re_{lm} < 1500$ , then:

$$f_{wl} = 16(Re_{lm})^{-1.0} \quad (3-42)$$

for laminar flow. (See the notes on these friction factor models in the discussion of the annular flow regime above.)

The basic modelling approach for the pressure gradient assumes homogeneous flow, as suggested by Wallis (1969). To calculate the frictional component of the pressure gradient, use:

$$\left( \frac{dP}{dz} \right)_{fsl} = - \left[ \frac{2f_{wl}\rho_{ls}(j_g + j_l)^2}{D} \right] (1 - \alpha) \quad (3-43)$$

To calculate the portion of the pressure gradient due to body forces (gravity), use:

$$\left( \frac{dP}{dz} \right)_{gs} = m_g g [(1 - \alpha)\rho_l + \alpha\rho_g](\cos \theta) \quad (3-44)$$

The total pressure gradient is therefore:

$$\left[ \frac{dP}{dz} \right]_{tsl} = \left[ \frac{dP}{dz} \right]_{tsl} + \left[ \frac{dP}{dz} \right]_{gs} \quad (3-45)$$

More complicated models could be written for the slug flow regime also. These models would involve asymmetric gas bubbles or corrections for long gas bubbles. Models with as many as 17 parameters have been developed (Fernandes, 1982). For microgravity flow conditions, these detailed models are probably unnecessary.

**Bubbly Flow Regime.** The drift flux approach is also used to calculate the void fraction in the bubbly flow regime. As in the slug flow regime, the equation for the pressure gradient assumes homogeneous flow, as suggested by Wallis (1969). The empirical drift flux model used with the homogeneous pressure gradient equation is based on extensive research.

The void fraction for the bubbly flow regime has this form (Zuber and Findlay, 1965):

$$\alpha = \left[ \frac{j_g}{C_{ob}(j_g + j_l) + k_b V_\infty} \right] = (1 - H_l) \quad (3-46)$$

in which the drift flux approach is used to model the flow rate and void fraction relationship. In Equation 3-46,

$C_{ob}$  is a constant typically near 1.2 (Table 3.4),  
 $k_b$  is a constant whose value is given in Table 3.4.

Table 3.4. DRIFT-FLUX PARAMETERS FOR THE BUBBLY FLOW REGIME		
ANGLE $\theta$ BETWEEN FLOW DIRECTION AND BODY FORCE VECTOR ( $^\circ$ )	DISTRIBUTION PARAMETER $C_{ob}$	$k_b$
$90^\circ \leq \theta \leq 180^\circ$	1.2	1.4
$\theta = 90^\circ$	1.2	0
$0^\circ < \theta \leq 90^\circ$	1.0	0

and the other parameters have been defined previously. The values of  $C_o$  and  $k$  are based upon work by Mishima and Ishii (1984), Harmathy (1960), Zuber and Hench (1962), and Martin (1973) for swarms of bubbles flowing in a liquid. The velocity,  $V_\infty$ , is:

$$V_\infty = \left[ \frac{m_g g \sigma (\rho_l - \rho_g)}{\rho_l^2} \right]^{0.25} \quad (3-47)$$

The two-phase Reynolds number for the bubbly flow regime is:

$$Re_{lm} = \left[ \frac{\rho_l D (j_g + j_l)}{\mu_l} \right] \quad (3-48)$$

and the friction factor is calculated by the Zigrang-Sylvester (1982) equation for turbulent flow if  $Re_{lm} \geq 1500$ :

$$f_{wl} = 0.25 \left[ -2.0 \log \left\{ \frac{(\epsilon_r/D)}{3.7} - \left[ \frac{5.02}{Re_{lm}} \right] \log \left[ \frac{(\epsilon_r/D)}{3.7} + \frac{13}{Re_{lm}} \right] \right\} \right]^{-2} \quad (3-49)$$

If  $Re_{lm} < 1500$ , then:

$$f_{wl} = 16(Re_{lm})^{-1.0} \quad (3-50)$$

for laminar flow. (See the notes on these friction factor models in the discussion of the annular flow regime above.)

The frictional component of the pressure gradient is:

$$\left[ \frac{dP}{dz} \right]_{fb} = - \left[ \frac{2f_{wl}(j_g + j_l)(\rho_g j_g + \rho_l j_l)}{D} \right] \quad (3-51)$$

The component of the pressure gradient due to body forces (gravity) is:

$$\left[ \frac{dP}{dz} \right]_{gb} = m_g g [(1 - \alpha)\rho_l + \alpha\rho_g](\cos \theta) \quad (3-52)$$

and the total pressure gradient is therefore:

$$\left[ \frac{dP}{dz} \right]_{tb} = \left[ \frac{dP}{dz} \right]_{fb} + \left[ \frac{dP}{dz} \right]_{gb} \quad (3-53)$$

More complicated models could be written for the bubbly flow regime, involving determining the sizes of vapor bubbles and calculating the interfacial forces on gas bubbles. For bubbly flow under most conditions, the simple drift flux model is adequate.



**Pressure Drop.** To calculate the pressure drop in the section of pipe, multiply the total pressure gradient by the pipe length:

$$\Delta p = L \left[ \frac{dP}{dz} \right]_{tx} \quad (3-54)$$

where  $L$  is the length of the pipe section and the 'x' subscript in the  $(dP/dz)$  term indicates the total pressure gradient for the appropriate flow regime.

### 3.2.2 Modelling Uncertainties for Sensitivity Calculations in Pipes

Table 3.1 summarizes the key modelling parameters in each of the four pipe flow regimes. For each transition, the sensitivity of the predicted pressure gradient and void fraction to these parameters provides a measure of the uncertainty in the calculations obtained using these models.

**Annular or Stratified Flow Regime.** For the annular flow regime, the key modelling parameters are:

- The interfacial friction factor (shear) ratio  $f_i/f_{wg}$ , and
- The entrainment fraction  $E_d$ , which depends upon the coefficient  $C_e$ .

The interfacial friction, which depends upon the coefficients  $C_a$  and  $b$ , is the key modelling parameter in the annular flow regime. It represents the major uncertainties in the modelling of pressure drop and void fraction. The minimum possible value of this parameter is unity ( $f_i/f_{wg} = 1$ , with  $C_a = 0$  and  $b = 0$  in Equation 3-7), representing a smooth interface between the gas and the liquid phases. Maximum values of the liquid fraction and minimum values of the pressure gradient are obtained using this limit. Wallis (1969) suggested a model where the coefficients are  $C_a = 75$  and  $b = 1$ . This model tends to represent an upper limit to the pressure drop calculations (see Section 3.5), providing the minimum values of the liquid fraction and the maximum values of the pressure gradient. The model suggested by Chen et al. (1989) is intermediate to these two limits.

In the stratified flow regime, the interfacial friction factor ratio is treated as a constant in the range from 1 to 10. The lower limit of  $f_i/f_{wg} = 1$  again represents a smooth gas-liquid interface. The value of  $f_i/f_{wg} = 10$  represents an upper limit based upon experimental data comparisons. More detailed models (Laurinat et al., 1984) have been suggested, but the recommended value of  $f_i/f_{wg} = 5$  compares well with experimental data.

The entrainment coefficient,  $C_e$ , determines the magnitude of liquid entrainment,  $E_d$ , in the calculations. A value of  $C_e = 0$  represents no entrainment. A maximum value of  $C_e = 0.23$  is suggested. For the range of conditions of interest to thermal management systems, the value of this coefficient has only a small effect on the pressure gradient or the void fraction.

Slug and Bubbly Flow Regimes. The uncertainty in the slug and bubbly flow regimes is represented by:

- The velocity distribution parameter,  $C_o$ , and
- The drift flux coefficient,  $k$ ,

in each regime.

The velocity distribution parameter models nonuniformity of the velocity profile across the pipe cross section. In the bubbly flow regime, this parameter is typically given a value of  $C_{ob} = 1.2$  (Table 3.4). Recent experiments by Colin et al. (1991) appear to confirm that this value is also valid for microgravity conditions. A value of  $C_{os} = 1.3$  is typically assigned to the slug flow regime (Table 3.3).

The drift flux coefficient represents the fact that, due to buoyancy, the vapor bubbles in these flow regimes tend to move at a velocity slightly different than the velocity of the two-phase mixture. (Which explains the origin of the term 'drift flux'.) In horizontal pipes on the ground or under microgravity conditions, this drift velocity and the coefficient are zero. In vertical pipes on the ground, the drift flux value is about  $k = 1.4$  in the bubbly flow regime and  $k = 0.35$  in the slug flow regime.

Limiting values of  $C_o = 1$  and  $k = 0$  represent a completely homogeneous two-phase flow. This gives the largest pressure gradient and the largest void fraction in each of these regimes.

### 3.2.3 Limits of the Methods for Pipes

Pipe Geometry. The theory described in Section 3.2.1 applies to pipes which range in size from a few millimeters to a meter in diameter. The pipe diameters thus span the range of interest for thermal management systems on spacecraft (from a few millimeters to a few centimeters) to gas and oil pipelines on earth.

The only caveat to this wide application is for large pipes in the slug flow regime. Thorough study of the slug flow regime in gas and oil pipelines (Crowley and Sam, 1986) has led to special models for slug flow which take into account the asymmetry in the flow pattern introduced by the effects of buoyancy. The models recommended by Crowley, Barry, and Rothe (1990) should be used for large pipes in the slug flow regime.

The theory for each flow regime has also been developed for a pipe with circular cross-section. As a first approximation, the theory could be applied to square or rectangular cross-sections, but the models should really be modified for the other geometries. For example, the theory for the annular flow regime should be rederived by starting with the basic momentum equations for the liquid and gas phases, using new relationships for the geometric parameters. For the stratified flow regime, all that is needed is to redefine the geometric parameters that appear in Table 2.2. For the slug and bubbly flow regimes, the void fraction relationships need to be include a drift flux coefficient (parameter  $k$ ) representative of the new geometry, and that value can be determined experimentally. The pressure gradient models for the slug and bubbly flow regimes can be used directly, with the new values of the void fraction.

**Acceleration.** These models for pressure drop and void fraction assume that the fluid properties are approximately constant across the pipe cross-section. If the densities or surface tensions between the phases vary dramatically with small changes in pressure or temperature, as they do near the critical point for a given fluid, then this assumption breaks down. The assumption of constant fluid properties also breaks down if there is a significant gradient in the fluid properties across the diameter of the flow channel. This can occur for example in a two-phase line during launch, where the acceleration may be ten times earth gravity. The models should not be applied to high acceleration levels.

### 3.3 Pressure Drop Methods for Elbows, Tees, and Fittings

This section presents the detailed equations to calculate the pressure losses due to two-phase flow in elbows, tees, and fittings.

#### 3.3.1 Equations for Elbows, Tees, and Fittings

**Bends and Elbows.** The pressure drop method for bends and elbows is based upon the homogeneous modelling approach suggested by Chisholm (1980). The bend or elbow is treated as a stepwise loss, like a component such as a valve. The first step is to determine the equivalent single-phase loss coefficient,  $k_{spl}$ , which depends upon the curvature of the bend. Typical values are:

<u>Bend</u>	<u><math>k_{spl}</math></u>
Close	2.2
Standard	0.9
Medium	0.75
Long	0.60

The designations close, standard, medium and long refer to the radius of curvature of the bend relative to the diameter of the pipe and may be found in typical textbooks on fluid flow. The designations are qualitative and must be interpreted by the designer. When in doubt, the loss coefficient for the standard case should be used.

Then, calculate the equivalent pressure drop in single-phase flow by:

$$\Delta p_{spl} = k_{spl} \left[ \frac{G^2}{2\rho_l} \right] \quad (3-55)$$

where

$G$  is the total mass flux  $G = (j_g \rho_g + j_l \rho_l)$  ( $\text{kg}/\text{m}^2\text{-s}$ ),  
 $\rho_l$  is the liquid phase density ( $\text{kg}/\text{m}^3$ ).

Determine a two-phase loss coefficient:

$$B = \left[ 1 + \frac{2.2}{k_{spl}[2 + (R/D)]} \right] \quad (3-56)$$

where

R is the radius of curvature of the bend or elbow (m), and  
D is the diameter of the pipe (m).

Then calculate the two-phase multiplier:

$$\phi_{tp} = 1 + [(\rho_l/\rho_g) - 1][Bx(1 - x) + x^2] \quad (3-57)$$

where

$\rho_g$  is the gas phase density ( $\text{kg/m}^3$ ), and  
x is the flow quality  $x = (\rho_g j_g / G)$  (-).

Finally, calculate the pressure loss in the bend:

$$\Delta p_b = \phi_{tp} \Delta P_{spl} \quad (3-58)$$

**Mixing Tee.** Figure 3.1 shows that two fluid streams are assumed to mix together in a single outlet stream in a mixing tee. A homogeneous approach to the modelling of a mixing tee suggested by Rohsenow, Hartnett, and Ganic (1985) is used.

First, calculate the single-phase pressure drop:

$$\Delta p_{spl} = B \left[ \frac{G^2}{2\rho_l} \right] \quad (3-59)$$

where

B is the single-phase loss coefficient. For tees,  $B = 1.6$ ,  
G is the total mass flux;  $G = (j_g \rho_g + j_l \rho_l)$  in the branch of the tee where both streams have mixed (Figure 3.1) ( $\text{kg/m}^2\text{-s}$ ), and  
 $\rho_l$  is the liquid phase density ( $\text{kg/m}^3$ ).

Next calculate the two-phase multiplier:

$$\phi_{tp} = \{1 + Bx[(\rho_l/\rho_g) - 1]\} \quad (3-60)$$

where

$\rho_g$  is the gas phase density ( $\text{kg/m}^3$ ), and  
x is the quality of the mixed flow;  $x = (\rho_g j_g / G)$  (-).

Finally, calculate the pressure loss in the tee:

$$\Delta p_t = \phi_{tp} \Delta P_{spl} \quad (3-61)$$

Note that this homogeneous model does not take into account the flow regime which occurs upstream in each of the branches or the flow regime in the branch where mixing has occurred. The modelling of mixing in tees is one area where additional research is needed in order to provide more accurate models.

Abrupt Expansion. The model for an abrupt expansion uses a separated flow model. Hussain and Weisman (1975) developed the model used here.

First calculate the area ratio:

$$\gamma = (A_d/A_u) = (D_d/D_u)^2 \quad (3-62)$$

where

$A_u$  is the upstream (smaller) area ( $m^2$ ),  
 $A_d$  is the downstream (larger) area ( $m^2$ ),  
 $D_u$  is the upstream diameter (m), and  
 $D_d$  is the downstream diameter (m).

At this point, a choice is made whether to use the baseline separated flow approach to the analysis or to use a homogeneous approach as a limiting case. Pressure drops using the homogeneous approach will be conservative estimates. If the homogeneous model is selected, then the void fraction relationship is:

$$\alpha_u = \alpha_d = \left[ 1 + \left[ \frac{\rho_g}{\rho_l} \right] \frac{(1-x)}{x} \right]^{-1} \quad (3-63)$$

where

$\alpha_u$  is the void fraction upstream of the expansion (-),  
 $\alpha_d$  is the void fraction downstream of the expansion (-),  
 $\rho_g$  is the density of the gas phase ( $kg/m^3$ ),  
 $\rho_l$  is the density of the liquid phase ( $kg/m^3$ ),  
 $x$  is the quality upstream of the expansion ( $x = \rho_g j_g / G$ ) (-), and  
 $G$  is the mass flux upstream of the expansion ( $G = \rho_g j_g + \rho_l j_l$ ) ( $kg/m^2-s$ ).

The separated flow model provides a more realistic predictions of the pressure drop. The upstream and downstream void fractions are then:

$$\alpha_u = \left[ \frac{1}{1 + K_u} \right] \left[ 1 + \left[ \frac{\rho_g}{\rho_l} \right] \frac{(1-x)}{x} \right]^{-1} \quad (3-64)$$

and:

$$\alpha_d = \left[ \frac{1}{1 + K_d} \right] \left[ 1 + \left[ \frac{\rho_g}{\rho_l} \right] \frac{(1-x)}{x} \right]^{-1} \quad (3-65)$$

where

$K_u$  is a phase slip coefficient upstream of the expansion (-), and  
 $K_d$  is a phase slip coefficient downstream of the expansion (-).

The upstream coefficient,  $K_u$ , is a function of a two-phase Reynolds number upstream of the expansion:

$$Re_{ju} = \frac{\rho_l(j_g + j_l)}{\mu_l} \quad (3-66)$$

and the downstream coefficient,  $K_d$ , is a function of a two-phase Reynolds number downstream of the expansion:

$$Re_{jd} = \frac{\rho_l(j_g + j_l)}{\mu_l \gamma} \quad (3-67)$$

The functional relationship to determine these coefficients,  $K_x = f(Re_x)$ , is:

$$K_x = \begin{cases} 1.0 & \text{if } Re_{jx} \leq 10^3 \\ 1 - 0.38 \log_{10}(Re_{jx})^{-3} & \text{if } 10^3 < Re_{jx} \leq 10^4 \\ 0.62 - 0.3 \log_{10}(Re_{jx})^{-4} & \text{if } 10^4 < Re_{jx} \leq 10^5 \\ 0.32 - 0.143 \log_{10}(Re_{jx})^{-5} & \text{if } 10^5 < Re_{jx} \leq 5 \times 10^5 \\ 0.22 & \text{if } Re_{jx} > 5 \times 10^5 \end{cases} \quad (3-68)$$

This represents a fit to the relationship derived by Hughmark (1962) for the void fraction in two-phase flows.

The two-phase pressure drop in the expansion is then:

$$\Delta p_e = \left[ \frac{G^2 \gamma^2}{\rho_l} \right] \left\{ \left[ x^2 \left[ \frac{\rho_l}{\rho_g} \right] \left[ \frac{1}{\alpha_u \gamma} - \frac{1}{\alpha_d} \right] \right] + \left[ (1-x)^2 \left[ \frac{1}{(1-\alpha_u) \gamma} - \frac{1}{(1-\alpha_d)} \right] \right] \right\} \quad (3-69)$$

**Abrupt Contraction.** A homogeneous approach is a good model for abrupt contractions. Hussain and Weisman (1975) developed the basic model used here, but ideas contributed by Tapucu et al. (1989) have also been incorporated.

First, calculate the area ratio:

$$\gamma = A_u/A_d = (D_u/D_d)^2 \quad (3-70)$$

where

$A_u$  is the upstream (larger) area ( $m^2$ ),  
 $A_d$  is the downstream (smaller) area ( $m^2$ ),  
 $D_u$  is the upstream diameter (m), and  
 $D_d$  is the downstream diameter (m).

Next estimate the contraction coefficient,  $C$ , from Table 3.5. The contraction coefficient is the ratio between the cross-sectional area at the vena contracta ( $A_c$ ) and the cross-sectional area of the pipe downstream of the contraction ( $A_d$ ). Table 3.5 can be represented by this equation:

$$C = 0.61668 + 0.083119\gamma^{-1} - 0.097439\gamma^{-2} + 0.1$$

Table 3.5. CONTRACTION COEFFICIENTS	
$1/\gamma$	$C = A_c/A_d$
0	0.617
0.1	0.624
0.2	0.632
0.3	0.643
0.4	0.659
0.5	0.681
0.6	0.712
0.7	0.755
0.8	0.813

The two-phase pressure drop across the contraction is:

$$\Delta p_c = \left[ \frac{G^2}{2\gamma} \right] \left[ \left( \frac{1}{C} - 1 \right)^2 + (1 - \gamma)^2 \right] \left[ \frac{1}{\rho_g} + \frac{(1 - x)}{\rho_l} \right] \quad (3-72)$$

**Short Insert.** The model for the short insert is a combination of the models for the abrupt expansion and the abrupt contraction. Harshe, Hussain, and Weisman (1976) derived this model for the short insert.

First, calculate the area ratio:

$$\gamma = A_i/A_p = (D_i/D_p)^2 \quad (3-73)$$

where

- $A_i$  is the cross-sectional area of the insert ( $m^2$ ),
- $A_p$  is the cross-sectional area of the pipe, assumed to be the same upstream or downstream of the insert ( $m^2$ ),
- $D_i$  is the diameter of the insert (m), and
- $D_p$  is the diameter of the pipe.

Just as for the abrupt contraction, the contraction coefficient  $C$  is then estimated from:

$$C = 0.61668 + 0.083119\gamma - 0.097439\gamma^2 + 0.37458\gamma^3 \quad (3-74)$$

Like the abrupt expansion, a choice must be made whether to 1) use the baseline separated flow approach to the analysis, or 2) use a homogeneous approach as a limiting case. Pressure drops using the homogeneous approach will be conservative estimates. If the homogeneous model is selected, then the void fraction relationship is:

$$\alpha_c = \alpha_p = \left[ 1 + \left[ \frac{\rho_g}{\rho_l} \right] \frac{(1 - x)}{x} \right]^{-1} \quad (3-75)$$

where

- $\alpha_c$  is the void fraction in the vena contracta (-),
- $\alpha_p$  is the void fraction in the pipe (-),
- $\rho_g$  is the density of the gas phase (kg/m<sup>3</sup>),
- $\rho_l$  is the density of the liquid phase (kg/m<sup>3</sup>),
- $x$  is the quality upstream of the insert ( $x = \rho_g j_g / G$ ) (-), and
- $G$  is the mass flux upstream of the insert ( $G = \rho_g j_g + \rho_l j_l$ ) (kg/m<sup>2</sup>-s).

The separated flow model provides a more realistic prediction of the pressure drop. Then the void fractions are:

$$\alpha_c = \left[ \frac{1}{1 + K_c} \right] \left[ 1 + \left[ \frac{\rho_g}{\rho_l} \right] \frac{(1 - x)}{x} \right]^{-1} \quad (3-76)$$

and:

$$\alpha_p = \left[ \frac{1}{1 + K_d} \right] \left[ 1 + \left[ \frac{\rho_g}{\rho_l} \right] \frac{(1 - x)}{x} \right]^{-1} \quad (3-77)$$

where

- $K_c$  is a phase slip coefficient in the vena contracta downstream of the insert (-), and
- $K_p$  is a phase slip coefficient in the pipe (-).

The phase slip coefficient,  $K_c$ , is a function of a two-phase Reynolds number in the vena contracta:

$$Re_{jc} = \frac{\rho_l (j_g + j_l)}{\mu_l} \quad (3-78)$$

and the phase slip coefficient,  $K_p$ , is a function of a two-phase Reynolds number in the pipe:

$$Re_{jp} = \frac{\rho_l (j_g + j_l)}{\mu_l} \quad (3-79)$$

The functional relationship to determine these coefficients,  $K_x = f(Re_x)$ , is:

$$K_x = \begin{cases} 1.0 & \text{if } Re_{jx} \leq 10^3 \\ 1 - 0.38 \log_{10}(Re_{jx})^{-3} & \text{if } 10^3 < Re_{jx} \leq 10^4 \\ 0.62 - 0.3 \log_{10}(Re_{jx})^{-4} & \text{if } 10^4 < Re_{jx} \leq 10^5 \\ 0.32 - 0.143 \log_{10}(Re_{jx})^{-5} & \text{if } 10^5 < Re_{jx} \leq 5 \times 10^5 \\ 0.22 & \text{if } Re_{jx} > 5 \times 10^5 \end{cases} \quad (3-80)$$

This represents a fit to the relationship derived by Hughmark (1962) for the void fraction in two-phase flows.



Calculate the average void fraction:

$$\bar{\alpha} = (\alpha_c + \alpha_p)/2 \quad (3-81)$$

Then the two-phase pressure drop in the short insert is:

$$\begin{aligned} \Delta p_i = & \left[ \frac{G^2}{2\rho_l \gamma^2 C^2} \right] \left\{ x^2 \bar{\alpha} \left[ \frac{\rho_l}{\rho_g} \right] \left[ \left( \frac{1}{\alpha_c} \right)^2 - \left( \frac{\gamma C}{\alpha_p} \right)^2 \right] \right. \\ & + (1-x)^2 (1-\bar{\alpha}) \left[ \frac{1}{(1-\alpha_c)^2} - \frac{\gamma^2 C^2}{(1-\alpha_p)^2} \right] \\ & \left. - 2\gamma C \left[ x^2 \left[ \frac{\rho_l}{\rho_g} \right] \left[ \frac{1}{\alpha_c} - \frac{\gamma C}{\alpha_p} \right] + (1-x)^2 \left[ \frac{1}{1-\alpha_c} - \frac{\gamma C}{1-\alpha_p} \right] \right\} \quad (3-82) \end{aligned}$$

### 3.3.2 Modelling Uncertainties for Sensitivity Calculations in Elbows, Tees, and Fittings

**Bends and Elbows.** The discussion of the model for bends and elbows in Section 3.3.1 includes a table where a single-phase loss coefficient must be selected for different curvatures of the elbow. The default value of the coefficient for a standard elbow is  $k_{spl} = 0.9$ . The tabulated values range from 0.6 to 2.0, so this represents the range of the uncertainty in this parameter.

**Mixing Tees.** Because the model is homogeneous, no uncertainty parameters are included for tees.

**Fittings.** Uncertainty in the models for the fittings is represented by selection of the options for:

- Homogeneous modelling, or
- Slip modelling using the Hughmark correlation.

Slip modelling using the Hughmark correlation provides realistic pressure drop estimates. The homogeneous model will give conservative results for the pressure drop calculation, tending to overestimate the pressure drop.

### 3.4 Dimensionless Design Calculations for Pipes

This section shows how to obtain quick estimates of the void fraction and the pressure gradient in pipes. In addition to the flow regime, the information required to calculate these quantities includes:

#### Fluid Properties

$\rho_l$	Liquid phase density
$\rho_g$	Gas phase density
$\mu_l$	Liquid phase viscosity
$\mu_g$	Gas phase viscosity
$\sigma$	Surface tension

## Geometry

D     Pipe diameter  
L     Pipe length

## Acceleration

a     Magnitude of acceleration ( $\approx m_g g$ )  
 $\theta$      Direction (angle between the body force due to acceleration and the flow direction)

## Flow Rates

$j_l$      Liquid phase volumetric flux ( $Q_l/A$ )  
 $j_g$      Gas phase volumetric flux ( $Q_g/A$ )  
 $j$      The total volumetric flux ( $j_g + j_l$ )  
G     The total mass flux ( $\rho_l j_l + \rho_g j_g$ )

See the section below for the annular, stratified, slug, or bubbly flow regime as appropriate.

**Annular Flow Regime.** The procedure to calculate the pressure gradient in the annular flow regime under microgravity conditions is:

- 1.) Calculate the dimensionless Martinelli parameter, X, in Equation 3-83 (below).
- 2.) Obtain the void fraction from Figure 3.2.
- 3.) Obtain the two-phase multiplier for the frictional portion of the pressure gradient from Figure 3.3.
- 4.) Calculate the total pressure gradient with Equation 3-88 (below).

The dimensionless Martinelli parameter for the annular flow regime is:

$$X = \frac{\left[ \left( \frac{4C_l}{D} \right) \left( \frac{\rho_l D j_l}{\mu_l} \right)^{-n} \left( \frac{\rho_l j_l^2}{2} \right) \right]^{0.5}}{\left[ \left( \frac{4C_g}{D} \right) \left( \frac{\rho_g D j_g}{\mu_g} \right)^{-m} \left( \frac{\rho_g j_g^2}{2} \right) \right]} \quad (3-83)$$

where

X     is the dimensionless Martinelli parameter,  
 $\rho_l$      is the gas phase density ( $\text{kg/m}^3$ ),  
 $\rho_g$      is the liquid phase density ( $\text{kg/m}^3$ ),  
 $j_l$      is the superficial velocity of the liquid phase (m/s),  
 $j_g$      is the superficial velocity of the gas phase (m/s),  
 $\mu_l$      is the viscosity of the liquid phase (kg/m-s),  
 $\mu_g$      is the viscosity of the gas phase (kg/m-s), and  
D     is the pipe diameter (m).

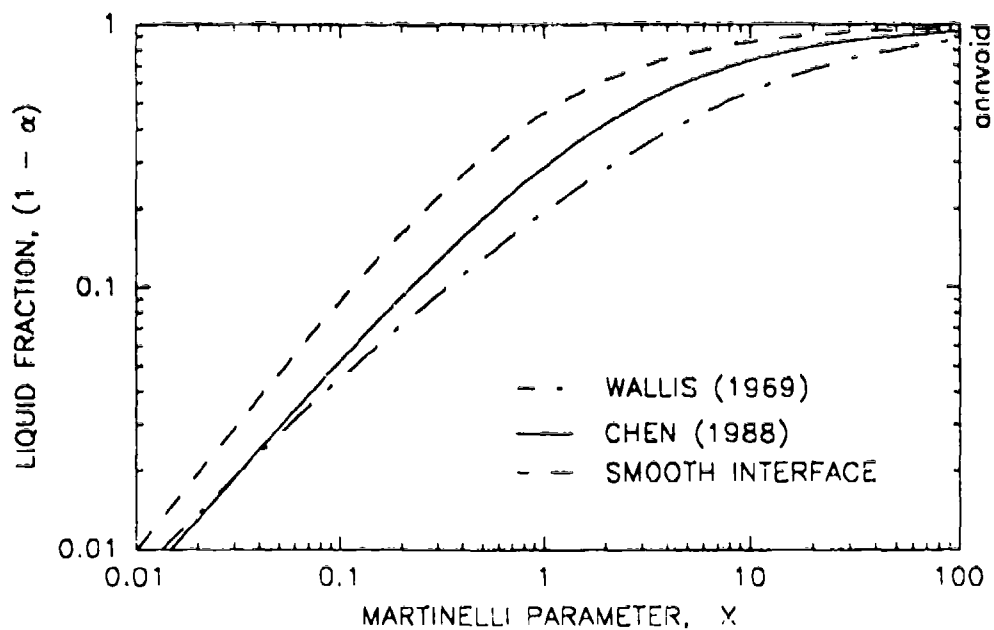


**Figure 3.2. DIMENSIONLESS PLOT OF LIQUID FRACTION FOR THE ANNULAR FLOW REGIME**

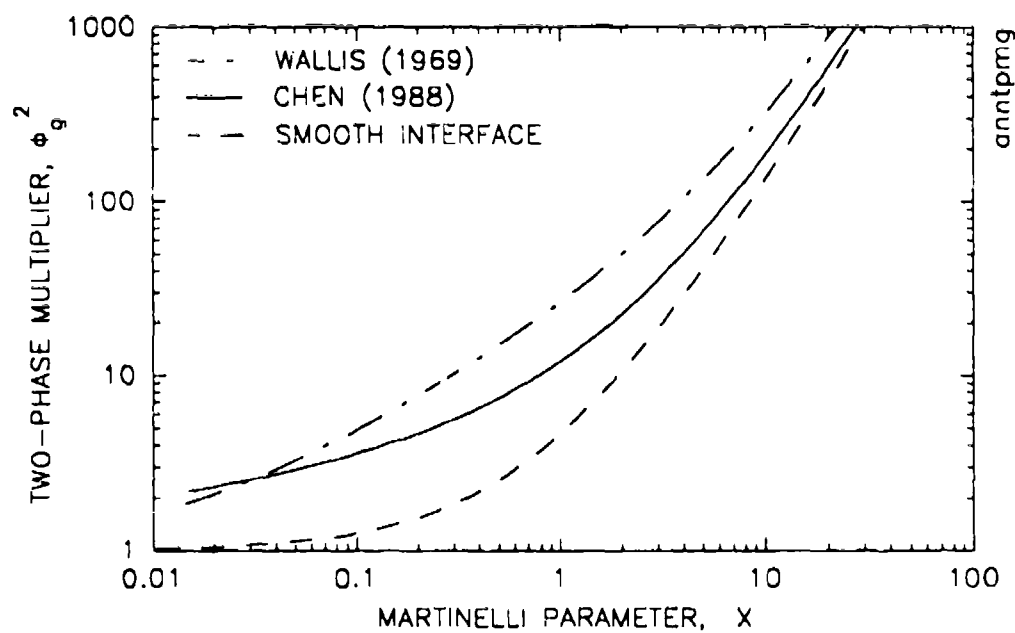


**Figure 3.3. DIMENSIONLESS PLOT OF TWO-PHASE MULTIPLIER FOR THE ANNULAR FLOW REGIME**

Table 2.3 indicates how to determine the values of the friction factor coefficients  $C_l$ ,  $C_g$ ,  $n$  and  $m$  to use in Equation 3-83.

Figure 3.2 shows the liquid fraction,  $H_{lf} = (1 - \alpha)$ , as a function of the Martinelli parameter,  $X$  (Equation 3-83). The curves plotted in Figure 3.2 represent the holdup equation for the annular flow regime:

$$X^2 = \left[ \frac{f_l}{f_{wg}} \right] \left[ \frac{H_{lf}^2}{(1-H_{lf})^{5/2} H_{lf}} \right] \quad (3-84)$$

which is the same as Equation 3-4 with the following assumptions:

- No entrainment ( $F_d = 0$ ),
- Microgravity conditions or horizontal pipes ( $Y_a \approx 0$ ),
- Friction factors for smooth-walled pipes:
  - $f_{wl} = C_l Re_l^{-n}$
  - $f_{wg} = C_g Re_g^{-m}$ , and
- $X_a = X$ .

The three curves shown in Figure 3.2 represent different assumptions about interfacial shear between the gas and liquid phases. The assumptions are:

- Smooth interface ( $C_a = 0$  in Equation 3-7),
- Chen et al. model ( $C_a = 6.81$ ,  $b = 0.39$  in Equation 3-7), and
- Wallis model ( $C_a = 75$ ,  $b = 1$  in Equation 3-7).

The smooth interface and Wallis (1969) models are limiting cases for most data. The Chen et al. (1989) model provides the best estimate of the liquid fraction for thermal management applications.

Figure 3.3 plots a two-phase multiplier for the annular flow regime as a function of the Martinelli parameter,  $X$ . The two-phase multiplier is defined as the ratio of the frictional pressure gradient in the annular flow regime to the equivalent pressure gradient as if single-phase (vapor) flowed in the pipe. That is,

$$\phi_g^2 = \frac{\left[ \frac{dP}{dz} \right]_{fa}}{\left[ \frac{4C_g}{D} \right] \left[ \frac{\rho_g D j_g}{\mu_g} \right]^{-m} \left[ \frac{\rho_g j_g^2}{2} \right]} \quad (3-85)$$

where  $(dP/dz)_{fa}$  is the frictional pressure gradient in two-phase flow given by Equation 3-16 and the other parameters are defined above. Using Equations 3-16 and 3-85, with the same assumptions given for Equation 3-84, the two-phase multiplier is:

$$\phi_g^2 = \frac{X^2}{H_{lf}^2} = \frac{X^2}{(1 - \alpha)^2} \quad (3-86)$$

This is the basis of the Equation plotted in Figure 3.3. The same assumptions for the interfacial shear modelling as Figure 3.2 are used.

Once the frictional two-phase multiplier is determined, the total pressure gradient is calculated by:

$$(dP/dz)_{ta} = -\phi_g^2 \left[ \frac{4C_g}{D} \right] \left[ \frac{\rho_g D j_g}{\mu_g} \right]^{-m} \left[ \frac{\rho_g j_g^2}{2} \right] + m_g g[(1 - \alpha)\rho_l + \alpha\rho_g](\cos \theta) \quad (3-87)$$

This is the basic pressure gradient equation for a separated (two-fluid) flow. In Equation 3-87, the first term on the right hand side is the frictional component, and the second term is the component due to the body force (gravity).

**Stratified Flow Regime.** The procedure for calculating the void fraction and the pressure gradient in the stratified flow regime is the same as for the annular flow regime, only the figures used to estimate the void fraction and the two-phase multiplier are different. The procedure to calculate the pressure gradient in the stratified flow regime is:

- 1.) Calculate the dimensionless Martinelli parameter,  $X$ , in Equation 3-83.
- 2.) Obtain the void fraction,  $\alpha$ , from Figure 3.4.
- 3.) Obtain the frictional two-phase multiplier,  $\phi_g^2$ , from Figure 3.5.
- 4.) Calculate the total pressure gradient with Equation 3-91 (below).

With the same assumptions made for the void fraction equation (Equation 3-84) as in the annular flow regime, the void fraction relationship for the stratified flow regime (Equation 3-20) becomes:

$$X^2 = \frac{[(R_g^* D_g^*)^{-m} (R_g^*)^2] \left[ \frac{S_g^*}{A_g^*} + \left( \frac{f_i}{f_{wg}} \right) \left( \frac{S_l^*}{A_l^*} + \frac{S_g^*}{A_g^*} \right) \right]}{[R_l^* D_l^*]^{-n} (R_l^*)^2 (S_l^* / A_l^*)} \quad (3-88)$$

The Martinelli parameter,  $X$ , is given by Equation 3-83. The "starred" parameters in Equation 3-88 are the dimensionless geometric parameters for the stratified flow regime. Table 2.2 summarizes these parameters as a function of the dimensionless liquid level and shows how they are related to the void fraction. The values of the parameters  $n$  and  $m$  are determined from the Reynolds numbers for the liquid and gas phases. Table 2.3 provides the equations necessary to determine these values. This is the basis of Equation 3-88, which is plotted in Figure 3.4.

Just as in the annular flow regime, the parameter  $(f_i/f_{wg})$  represents the interfacial friction, which is the key modelling parameter. Various empirical correlations have been proposed for this relationship in the stratified flow regime, but most data lie between values of 1 and 10 for this parameter. In this design manual a constant value of  $(f_i/f_{wg}) = 5$  is recommended for stratified flow. This selection is based upon extensive work by the authors reviewing alternative modelling approaches and specific models representing the interfacial shear in stratified flows at high gas densities. Figure 3.4 plots the void fraction for the limiting and best estimate values of the interfacial friction.

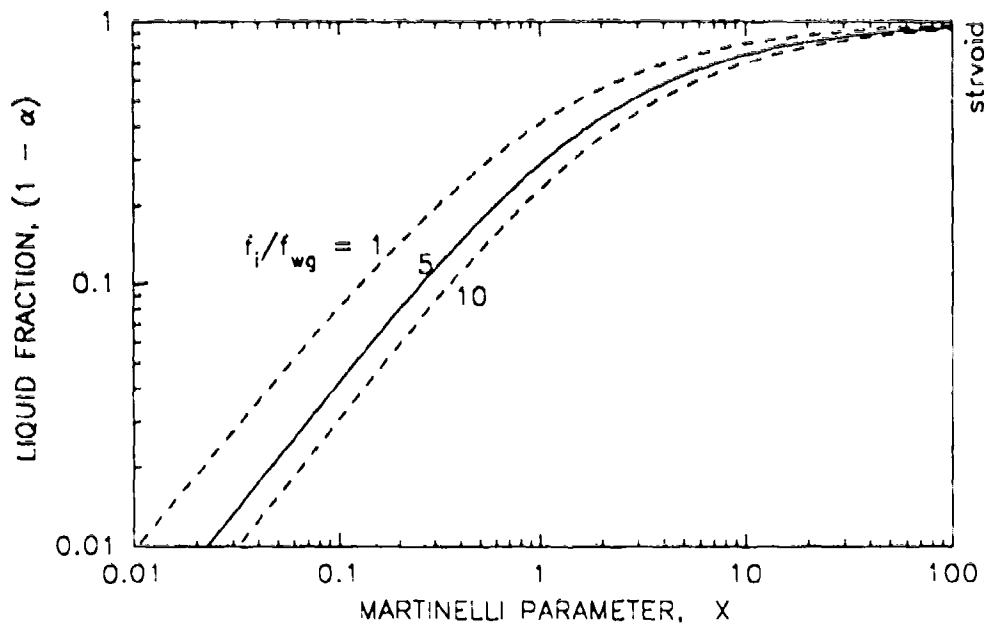


Figure 3.4. DIMENSIONLESS PLOT OF LIQUID FRACTION FOR THE STRATIFIED FLOW REGIME

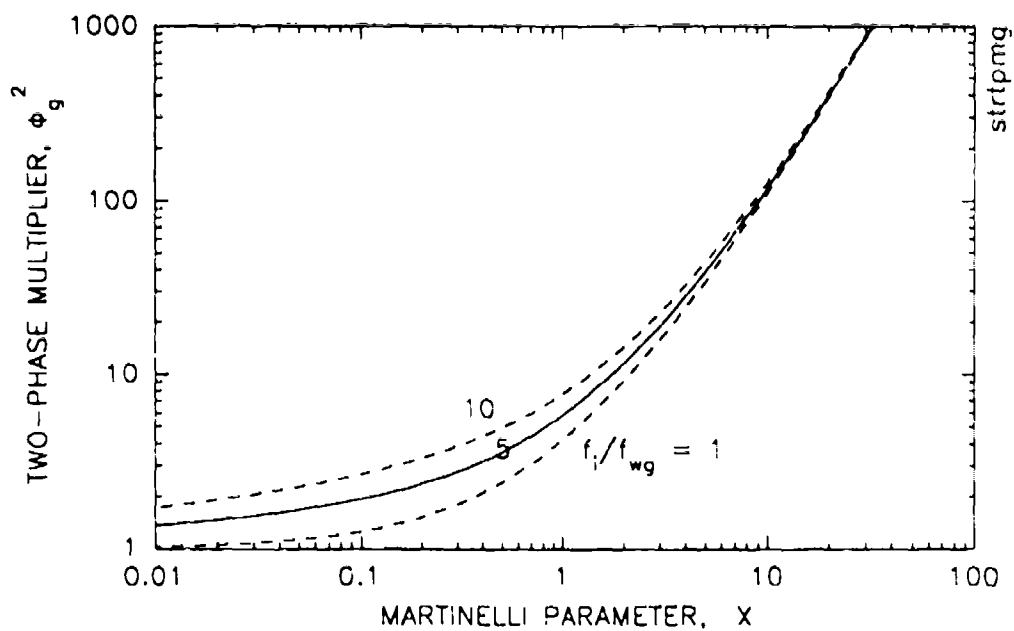


Figure 3.5. DIMENSIONLESS PLOT OF TWO-PHASE MULTIPLIER FOR THE STRATIFIED FLOW REGIME

Figure 3.5 shows the two-phase multiplier for stratified flow. The two-phase multiplier is defined as:

$$\phi_g^2 = \frac{\left[ \frac{dP}{dz} \right]_{\text{st}}}{\left[ \frac{4C_g}{D} \right] \left[ \frac{\rho_g D j_g}{\mu_g} \right]^{-m} \left[ \frac{\rho_g j_g^2}{2} \right]} \quad (3-89)$$

Using Equation 3-89 and the equation for the frictional component of the pressure gradient (Equation 3-22), the two-phase multiplier in the stratified flow regime becomes:

$$\phi_g^2 = \left[ \frac{1}{\pi} \right] \left[ X^2 (R_1^*)^2 (S_1^*) + (R_g^*)^2 (S_g^*) \right] \quad (3-90)$$

Since the dimensionless geometric parameters  $R_1^*$ ,  $R_g^*$ ,  $S_1^*$  and  $S_g^*$  are related to the void fraction, which in turn is a function of the parameter  $X$  by Equation 3-88, this allows the two-phase multiplier to be plotted as a function of the parameter  $X$  in Figure 3.5.

The dimensional equation for the total pressure gradient in the stratified flow regime is:

$$\begin{aligned} (dP/dz)_{\text{st}} = & - \phi_g^2 \left[ \frac{4C_g}{D} \right] \left[ \frac{\rho_g D j_g}{\mu_g} \right]^{-m} \left[ \frac{\rho_g j_g^2}{2\pi} \right] \\ & + m_g g [(1 - \alpha)\rho_l + \alpha\rho_g] (\cos \theta) \end{aligned} \quad (3-91)$$

which is derived from Equations 3-32, 3-33, and 3-34 using the definition in Equation 3-89.

Defining the two-phase multipliers for the annular and the stratified flow regimes in the manner shown allows a comparison of the void fractions and the pressure drops in the two regimes. Comparison of Figures 3.2 and 3.4 shows that the void fraction tends to be somewhat greater in the stratified flow regime. Comparison of Figures 3.3 and 3.5 shows that the two-phase multiplier, and hence the frictional pressure gradient, tends to be significantly greater in the annular flow regime. (This is due to the increased interfacial area in the annular flow regime.)

**Slug Flow Regime.** The procedure to calculate the pressure gradient in the slug or bubbly flow regime is:

- 1.) Calculate the dimensionless parameters  $X$  and  $\rho^*$  in Equations 3-92 and 3-93 (below).
- 2.) Obtain the void fraction,  $\alpha$ , from Figure 3.6.
- 3.) Obtain the two-phase multiplier,  $\phi_g^2$ , from Figure 3.7.
- 4.) Calculate the pressure gradient with Equation 3-97 (below).

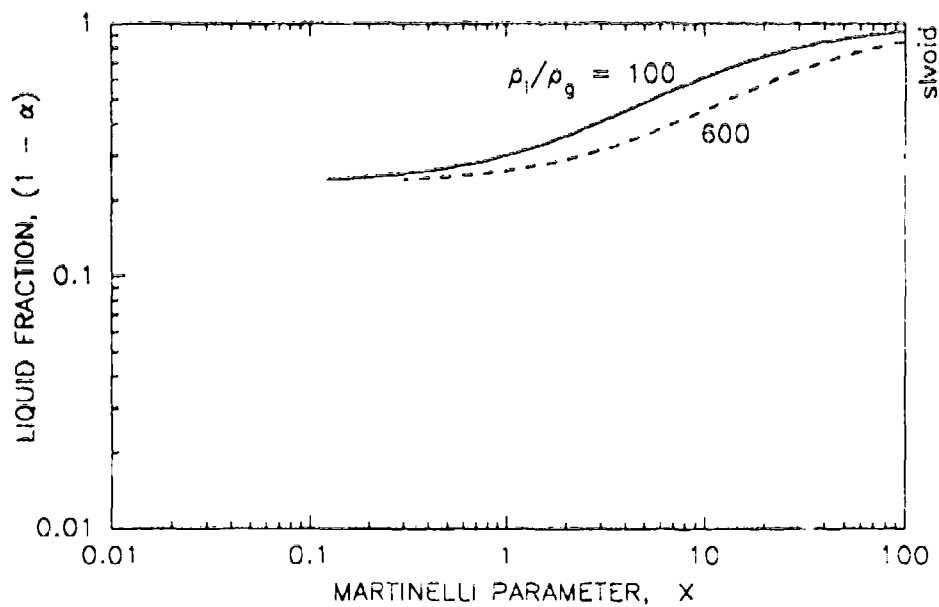


Figure 3.6. DIMENSIONLESS PLOT OF LIQUID FRACTION FOR THE SLUG FLOW REGIME

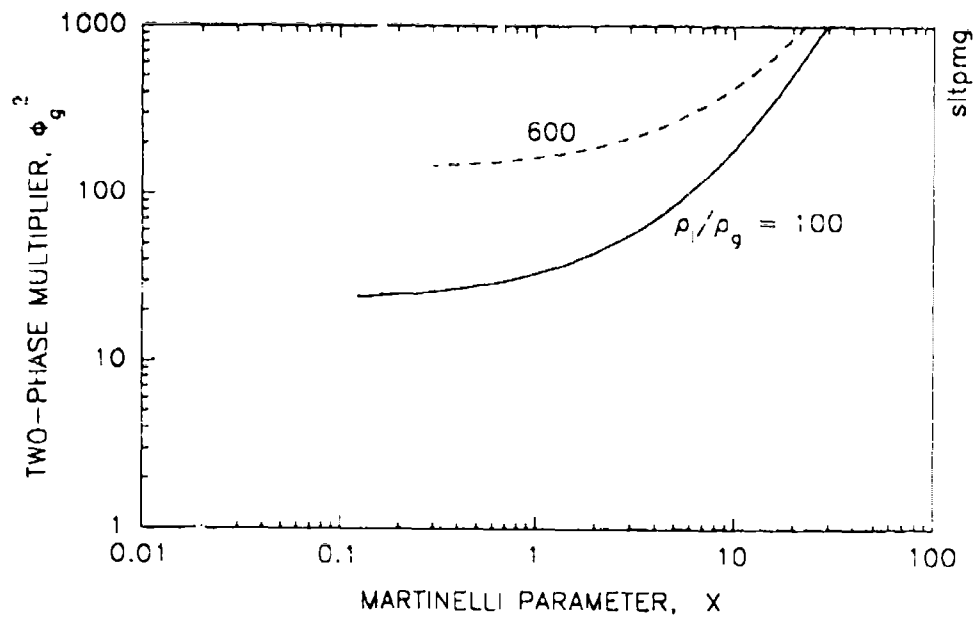


Figure 3.7. DIMENSIONLESS PLOT OF TWO-PHASE MULTIPLIER FOR THE SLUG FLOW REGIME



First calculate the dimensionless parameters  $X$  and  $\rho^*$  as follows:

$$X = \frac{\rho_l j_l^2}{\rho_g j_g^2} \quad (3-92)$$

$$\rho^* = (\rho_l / \rho_g) \quad (3-93)$$

where

$j_l$  is the superficial velocity of the liquid phase (m/s),  
 $j_g$  is the superficial velocity of the gas phase (m/s),  
 $\rho_g$  is the density of the gas phase ( $\text{kg/m}^3$ ), and  
 $\rho_l$  is the density of the liquid phase ( $\text{kg/m}^3$ ).

Note that the parameter  $X$  in Equation 3-92 is similar to the Martinelli parameter in Equation 3-83. By assuming that the friction factors for the gas and liquid phases are equal, Equation 3-83 reduces to the simpler form in Equation 3-92. This simplification allows the void fraction and pressure gradient in the slug flow regime to be presented in terms of parameters similar to the annular and stratified flow regimes.

Figure 3.6 shows the void fraction in the slug flow regime as a function of these dimensionless parameters. Assuming 1) microgravity conditions or horizontal pipes ( $m_g \cong 0$  or  $\cos \theta \cong 0$ ), and 2) no gas is contained within the liquid slugs ( $E_{ls} = 0$ ), the void fraction relationship in Equations 3-37 and 3-38 simplifies to:

$$\alpha = C_{os} \left[ 1 + \left( \frac{j_l}{j_g} \right) \left( \frac{\rho_g}{\rho_l} \right)^{0.5} \right]^{-1} = C_{os} \left[ 1 + \frac{X}{\rho^{*0.5}} \right]^{-1} \quad (3-94)$$

which is the equation plotted in Figure 3.6, using the recommended value  $C_{os} = 1.3$ . Lines for a range of density ratios  $\rho^*$  are included in this plot.

Figure 3.7 shows the two-phase multiplier for the slug flow regime. The two-phase multiplier in the slug flow regime is:

$$\phi_g^2 = \frac{\left[ \frac{dP}{dz} \right]_{fs1}}{\left[ \frac{4C_g}{D} \right] \left[ \frac{\rho_g D j_g}{\mu_g} \right]^{-m} \left[ \frac{\rho_g j_g^2}{2} \right]} \quad (3-95)$$

Then the two-phase multiplier is:

$$\phi_g^2 = [X^2 + \rho^{*0.5} X + \rho^*](1 - \alpha) \quad (3-96)$$

which is the equation used to plot the graphs in Figure 3.7.

The pressure gradient in the slug flow regime is then evaluated from:

$$\begin{aligned} (dP/dz)_{sl} = & - \phi_g^2 \left[ \frac{4C_g}{D} \right] \left[ \frac{\rho_g D j_g}{\mu_g} \right]^{-n} \left[ \frac{\rho_g j_g^2}{2} \right] \\ & + m_g g [(1 - \alpha)\rho_l + \alpha\rho_g] (\cos \theta) \end{aligned} \quad (3-97)$$

where the parameters  $C_g$  and  $n$  are determined using Table 2.3. The first term on the right hand side of this equation is the frictional component of the pressure gradient, and the second term is the component due to body forces (gravity). Note that if the magnitude of the acceleration becomes small, as it would under microgravity conditions, then only the frictional component remains.

Figures 3.8 and 3.9 illustrate the modelling uncertainty for the slug flow regime. The key uncertainty in the void fraction relationship of Equation 3-94 is the value of the parameter  $C_{os}$ . The limiting case of  $C_{os} = 1.0$  represents a homogeneous flow. This is the relationship plotted in Figure 3.8. This limit maximizes the void fraction in the slug (or bubbly) flow regime. Compared with the liquid fractions calculated for  $C_o = 1.3$  (Figure 3.6), the homogeneous model predicts lower liquid fractions at low values of the Martinelli parameter,  $X$ . For slug flow,  $X$  typically lies in the range  $1 < X < 10$ . Figure 3.9 shows the corresponding two phase multiplier. Void fraction values will be higher and the pressure gradient will be lower using the homogeneous approach. The magnitude of the effect is about 30% on the void fraction and 30% on both pressure gradient components.

**Bubbly Flow Regime.** The procedure to calculate the pressure gradient in the slug or bubbly flow regime is:

- 1.) Calculate the dimensionless parameters  $X$  and  $\rho^*$  in Equations 3-92 and 3-93.
- 2.) Obtain the void fraction,  $\alpha$ , from Figure 3.10.
- 3.) Obtain the two-phase multiplier,  $\phi_g^2$ , from Figure 3.11.
- 4.) Calculate the pressure gradient by Equation 3-101 (below).

This procedure is very similar to the procedure for the slug flow regime.

Figure 3.10 plots the void fraction relationship for the bubbly flow regime as a function of the dimensionless parameters  $X$  and  $\rho^*$ . Assuming microgravity conditions or horizontal pipes ( $m_g \equiv 0$  or  $\cos \theta \equiv 0$ ), the void fraction relationship for the bubbly flow regime in Equation 3-46 simplifies to:

$$\alpha = C_{ob} \left[ 1 + \left( \frac{j_l}{j_g} \right) \left( \frac{\rho_g}{\rho_l} \right)^{0.5} \right]^{-1} = C_{ob} \left[ 1 + \frac{X}{\rho^{*0.5}} \right]^{-1} \quad (3-98)$$

which is the equation plotted in Figure 3.10, using the recommended value  $C_{ob} = 1.2$ . Lines for a range of density ratios  $\rho^*$  are included in this plot.

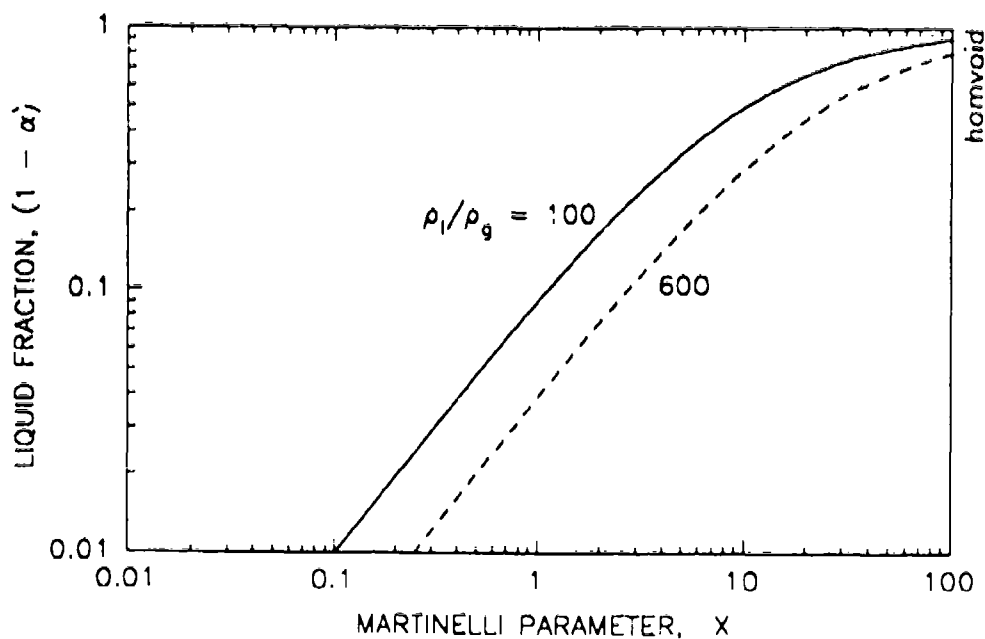


Figure 3.8. DIMENSIONLESS PLOT OF LIQUID FRACTION FOR HOMOGENEOUS FLOW

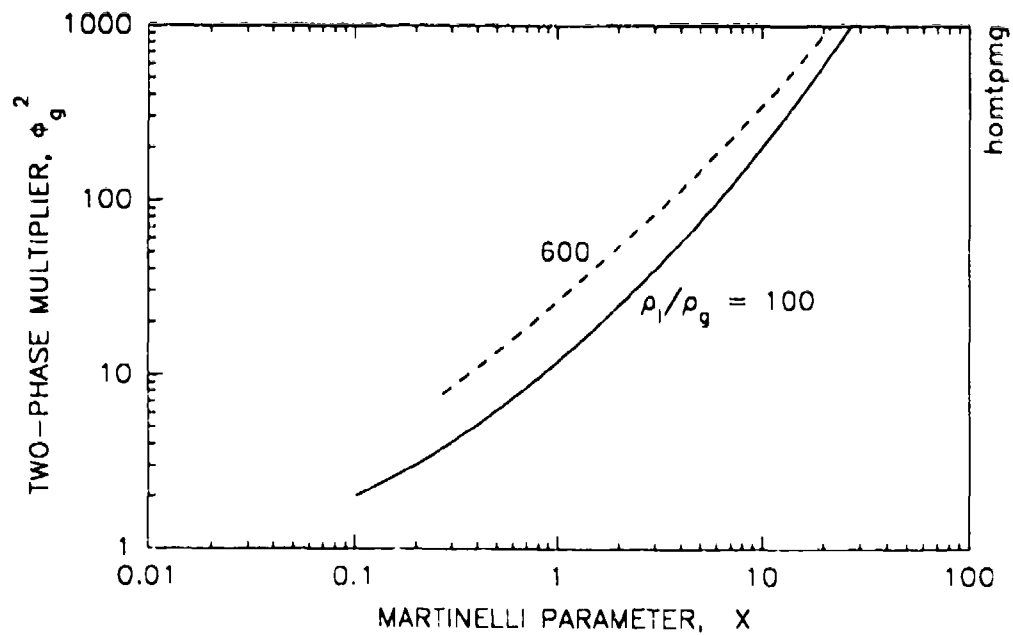


Figure 3.9. DIMENSIONLESS PLOT OF TWO-PHASE MULTIPLIER FOR HOMOGENEOUS FLOW

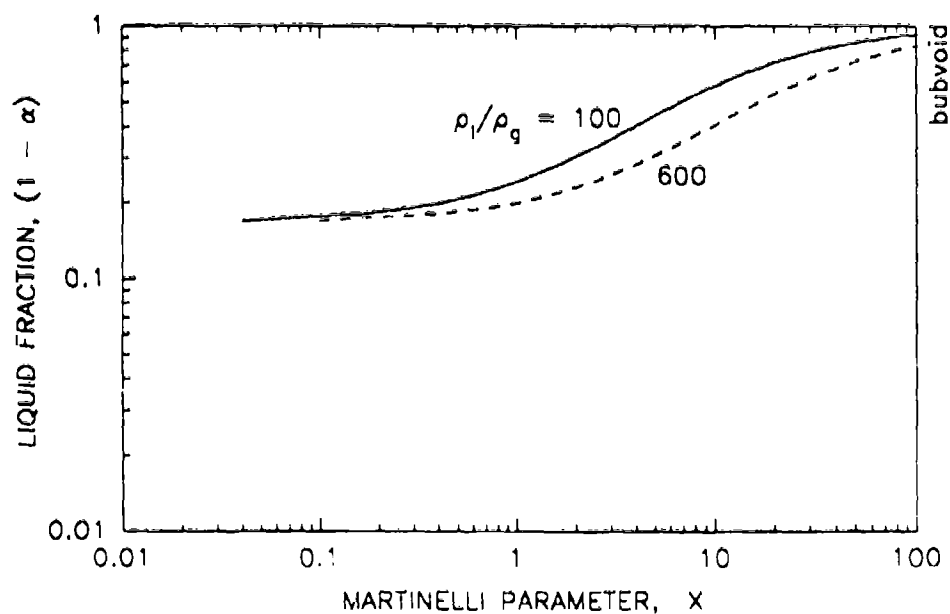


Figure 3.10. DIMENSIONLESS PLOT OF LIQUID FRACTION FOR THE BUBBLY FLOW REGIME

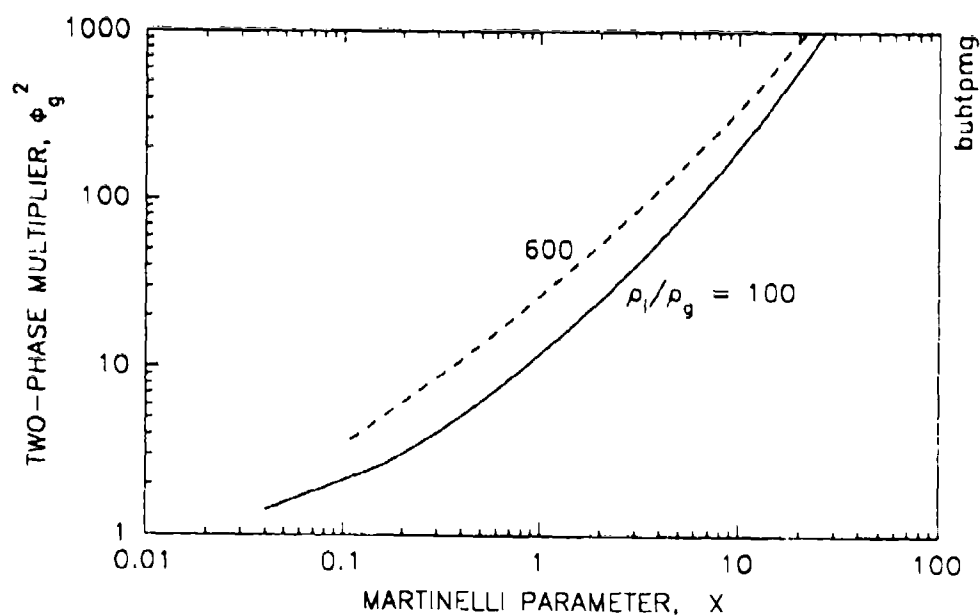


Figure 3.11. DIMENSIONLESS PLOT OF TWO-PHASE MULTIPLIER FOR THE BUBBLY FLOW REGIME

Figure 3.11 shows the two-phase multiplier for the bubbly flow regime. The two-phase multiplier in the bubbly flow regime is:

$$\phi_g^2 = \left[ \frac{\left[ \frac{dP}{dz} \right]_{fb}}{\left[ \frac{4C_g}{D} \right] \left[ \frac{\rho_g D j_g}{\mu_g} \right]^{-n} \left[ \frac{\rho_g j_g^2}{2} \right]} \right] \quad (3-99)$$

If  $\rho_g j_g \ll \rho_l j_l$ , then the two-phase multiplier can be written as:

$$\phi_g^2 = [X^2 + \rho^{*0.5} X] \quad (3-100)$$

which is the equation used to plot the graphs in Figure 3.11.

The pressure gradient in the bubbly flow regime is calculated by:

$$\begin{aligned} (dP/dz)_{fb} = & - \phi_g^2 \left[ \frac{4C_g}{D} \right] \left[ \frac{\rho_g D j_g}{\mu_g} \right]^{-n} \left[ \frac{\rho_g j_g^2}{2} \right] \\ & + m_g g [(1 - \alpha)\rho_l + \alpha\rho_g] (\cos \theta) \end{aligned} \quad (3-101)$$

where the parameters  $C_g$  and  $n$  are determined using Table 2.3. The first term on the right hand side of this equation is the frictional component of the pressure gradient, and the second term is the component due to body forces (gravity). Note that if the magnitude of the acceleration becomes small, as it would under microgravity conditions, then only the frictional component remains.

The key uncertainty in the drift flux relationship of Equation 3-98 is the value of the parameter  $C_{ob}$ . Like the slug flow regime, the limiting case of  $C_{ob} = 1.0$  represents a homogeneous flow, i.e. no drift flux. So Figures 3.8 and 3.9 represent the limiting case for both the bubbly and the slug flow regimes. The void fraction and pressure gradient values obtained from using Figures 3.8 and 3.9 in place of Figures 3.10 and 3.11 illustrate the range of the uncertainty. In bubbly flow, the Martinelli parameter  $X$  is typically greater than 10. The magnitude of the uncertainty is about 20% in the void fraction. This does not affect the frictional component of the pressure gradient at all, but does affect the body force component by 20%.

### 3.5 Validation with Microgravity Pressure Drop Data

This section validates the mechanistic pressure drop models by comparing calculations with data from microgravity tests. Microgravity data are available for pipes from four experiments. Data from two ground tests of spacecraft thermal management systems have also been included in the comparisons. Section 2.4 presents flow regime maps and comparisons for the experiments in which the flow regime has been observed. No microgravity data are available at this time for pressure drops in elbows, tees, or fittings.

### 3.5.1

### Experimental Data

**Completed Experiments.** Table 3.6 summarizes the experimenters, test geometries, and range of data for tests of gas-liquid flows for spacecraft thermal management systems. All of the microgravity tests have been performed on aircraft which provide about 25 seconds of acceleration at about 0.01g. No pressure drop data are available for long-term microgravity conditions. Two ground tests relevant to spacecraft thermal management systems are compared.

Pipe sizes in the experiments range from 6 to 40 mm. This is an appropriate size range for two-phase thermal management systems at power levels from 2kW to 25 kW. Tubes in directly condensing radiators might be somewhat smaller, probably only a few millimeters in diameter. Section 6 includes pressure drop and heat transfer comparisons with condenser data in these small tubes.

The test fluids include primarily air/water ("A/W" in Table 3.6) combinations and several types of Freon refrigerants. No microgravity data are available for ammonia, which is the heat transfer fluid most likely to be used for thermal management systems on radar satellites or the space station. However, ground tests (Lee, 1991) with ammonia have now been performed and are included in the comparisons here. With the fluids tested, the ratio of the liquid density to the gas density ranges from 30 (R-12) to 1000 (air/water). This density ratio is an important criterion in determining the flow regime and the pressure drop. For comparison, ammonia has a density ratio of about 88 at room temperature.

Table 3.6. VALIDATION COMPARISONS FOR PRESSURE DROP METHODS

Investigator	Sponsor	Test Vehicle	D (mm)	L (m)	Fluid	T (K)	P (kPa)	a (g's)	$\rho_l/\rho_g$
<b>MICROGRAVITY EXPERIMENTS</b>									
1. Chen et al. (1989)	NASA JSC	KC-135	15.8	1.83	R-114	337	643	0.01, 1	29
2. Colin et al. (1991)	CNES/ESA	Zero G	40	3.17	A/W	300	100	0.01, 1	860
3. Dukler et al. (to be published)	NASA/LeRC	Learjet	12.7	1.06	A/W A/Glycerine	300	130	0.01, 0.17	360
4. Hill & Best (1991); Reinarts et al. (1991)	PL/STPP	KC-135	8.7, 11.1	1.2	R-12	300	680	0.01, 1	33
5. Rezkallah and Mitchell (1991)	CSA	KC-135	9.52	1.09	A/W	300	100	0.01, 1	1000
<b>GROUND TESTS ONLY</b>									
A. Crowley et al. (1991)	PL/STPP	Ground	6.34	1.0	R-11	350	460	1	51
B. Lee (1991)	NASA JSC	Ground	15.8 17.9 21.1	3.048 4.572 5.791	NH <sub>3</sub>	294	883	1	88

Effects of surface tension are not strong in the existing analytical models. Only a relatively small range of surface tension has been studied experimentally – from 0.018 N/m with Freon to 0.070 N/m with air and water. This range includes the surface tension of ammonia, which is about 0.023 N/m.

Void Fraction Measurements. Because of the intimate relationship between void fraction and pressure drop – which is different in each pipe flow regime – a better test of the design methods would be to have simultaneous void fraction and pressure drop measurements. Ongoing experiments at:

- University of Houston (Dukler et al.), and
- University of Saskatchewan (Rezkallah et al.)

intend to provide void fraction data in the future. However, in all of the experiments reported thus far and considered here, only the pressure drop data have been reported.

Microgravity Data for Fittings. No microgravity data in elbows, tees, or fittings is available for data comparisons. However, ongoing experiments at:

- University of Saskatchewan (Rezkallah et al.), and
- NASA Lewis Research Center (McQuillen et al.)

are expected to provide some experimental data on pressure drop for these components.

Other Experiments. Other plans for experiments include:

- Variation of fluid properties, such as viscosity (U. of Saskatchewan and U. of Houston),
- Collection of experimental data under long term microgravity conditions (Air Force Phillips Laboratory, STARS Rocket flight test article), and
- Collection of two-phase data in support of the space station Active Thermal Control System Design (Texas A&M University, under sponsorship of NASA Johnson Space Center and using the test facility built and tested by Foster-Miller Inc.).

These experiments will provide additional opportunities to use and validate the pressure drop methods presented in this section.

### 3.5.2 Comparisons with Individual Experiments

This section describes the comparisons between the design manual methods and the experiments listed in Table 3.6. The MICROP software (Crowley et al., 1992) has been used in the comparisons.

### Microgravity Experiments

Chen et al. (1989). Chen et al. obtained flow regime data with Freon R-114 at a mass flux of approximately 200 kg/m<sup>2</sup>-s. The heat input was varied at this constant mass flux in order to vary the quality from about 5% to 86%. These data illustrate the pressure drop in the annular and the slug flow regimes in microgravity and in the stratified flow regime at 1g.

Figures 3.12 and 3.13 plot the experimental microgravity data and the analysis comparisons in the annular and slug flow regimes, respectively. Chen et al. developed a correlation for the interfacial friction factor ratio in the annular flow regime:

$$\text{CHEN} \quad (f_i/f_{wg}) = [1 + 6.81(1 - \alpha)^{0.39}] \quad (3-102)$$

which fits these data well, as shown in Figure 3.12. The limiting cases for a smooth interface,

$$\text{SMOOTH} \quad (f_i/f_{wg}) = 1 \quad (3-103)$$

and a correlation by Wallis (1969),

$$\text{WALLIS} \quad (f_i/f_{wg}) = [1 + 75(1 - \alpha)] \quad (3-104)$$

are shown for comparison. These models, which represent the range of uncertainty in the pressure drop calculations, bound the data. The model with a smooth interface underpredicts the pressure drop by about a factor of three. The Wallis model overpredicts the pressure drop by about a factor of two. Figure 3.13 shows that the recommended design methods predict the pressure drop well in the slug flow regime. Note that the reported accuracy of the transducer used to make the pressure drop measurements is 0.33 kPa (0.05 psi), so that the pressure drop data in the slug flow regime and at low quality in the annular flow regime have a large uncertainty associated with them.

Chen et al. also provide complementary pressure drop data in the same facility at earth gravity. At 1g, stratified flow occurs at all values of the quality. Figure 3.14 presents the 1g data in the stratified flow regime. Comparison with the data in the annular flow regime (Figure 3.12) shows that the pressure drop is about a factor of two smaller in the stratified flow regime. Figure 3.14 also compares these data with the recommended design methods for the stratified flow regime. The recommended model uses a value of  $f_i/f_{wg} = 5$  for the interfacial friction factor ratio, which agrees well with the data. The figure also shows the limiting cases of  $f_i/f_{wg} = 1$  (smooth interface) and  $f_i/f_{wg} = 10$ , which bound the experimental data. Note again that the accuracy of the pressure drop measurements is about 0.33 kPa, so these data all have a large uncertainty.

Colin et al. (1991). This comparison demonstrates that the homogeneous approach to modelling the pressure drop in both the slug and bubbly flow regimes (Section 3.2.1) is valid under microgravity conditions. The experiment addressed the bubbly and slug flow regimes and the transition between them. Figure 3.15 plots a two-phase friction factor derived from the experimental pressure drop measurements versus a two-phase Reynolds number. The two-phase Reynolds number,  $Re_{inv}$  is defined by Equations 3-40 and 3-48 in the design methods for the bubbly and the slug flow regimes. The two-phase friction factor,  $f_{wi}$ , is equivalent to the friction factor derived by solving Equations 3-43 and 3-51. The analytical line shown in Figure 3.15 is the Blasius correlation:

$$f_{wi} = 0.079 Re_{inv}^{-0.25} \quad (3-105)$$



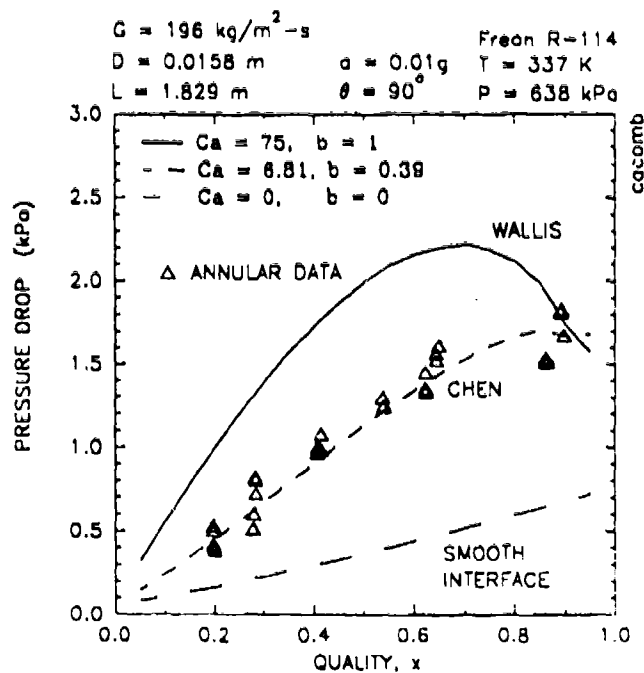


Figure 3.12. PRESSURE DROP COMPARISONS FOR CHEN ET AL. (1989) MICROGRAVITY DATA IN THE ANNULAR FLOW REGIME

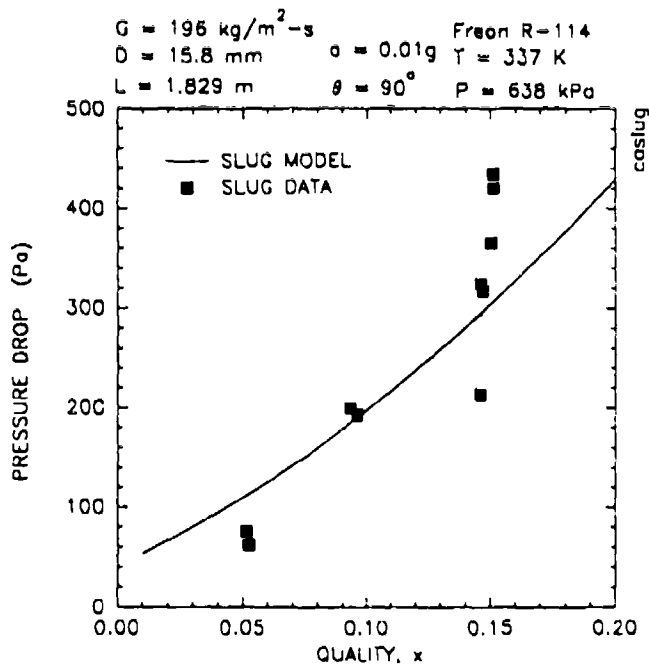


Figure 3.13. PRESSURE DROP COMPARISONS FOR CHEN ET AL. (1989) MICROGRAVITY DATA IN THE SLUG FLOW REGIME

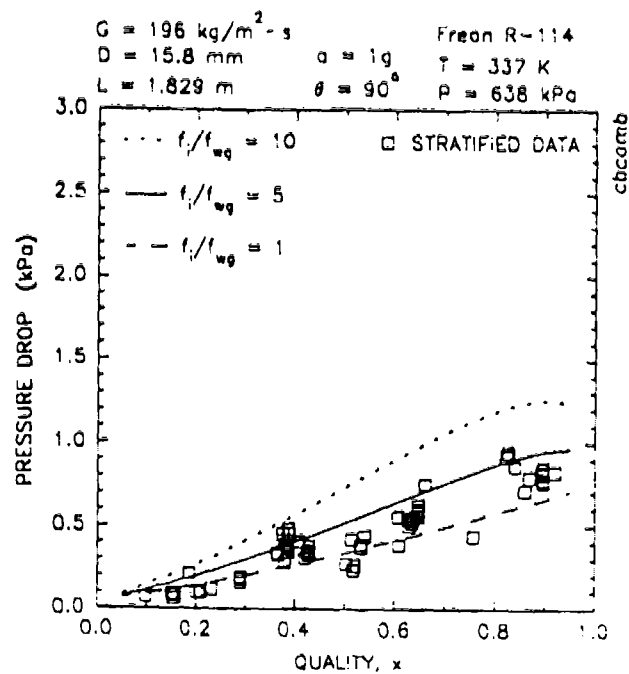


Figure 3.14. PRESSURE DROP COMPARISONS FOR CHEN ET AL. (1989)  
GROUND TEST DATA IN THE STRATIFIED FLOW REGIME

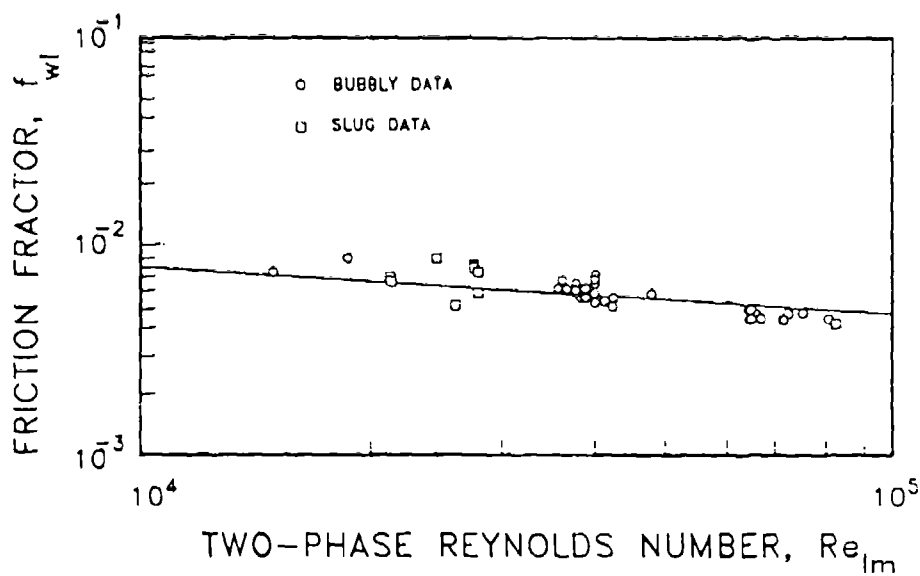


Figure 3.15. FRICTION FACTOR COMPARISONS FOR COLIN ET AL. (1991)  
MICROGRAVITY DATA IN THE BUBBLY AND SLUG FLOW REGIMES

The Zigrang-Sylvester model recommended here (Equation 3-41 or 3-49) compares within 2% of the values predicted by Equation 3-105 when the roughness ( $\epsilon_r/D$ ) is equal to 0.

Hill and Best (1991). This comparison shows that the interfacial shear depends on more than just the local void fraction. Hill and Best obtained microgravity data for Freon R-12 flowing in 8.7 and 11.1 mm diameter tubes. The data lie primarily in the annular flow regime under microgravity conditions. Many of the measured pressure drops in the 11.1 mm tube are about as large as the uncertainty of  $\pm 0.124$  kPa estimated in Appendix E of the reference. Since the measured pressure drops in the 8.7 mm tube are about three times larger than in the larger tube and therefore have less uncertainty, comparisons with those data are presented here. In this set of data, the data are a random collection of flow conditions, so no trends can be plotted with superficial velocity, mass flux, or quality. For that reason, Figure 3.16 plots the data as a calculated pressure drop versus a measured value for the data set. There are a few data points in the slug flow regime, which agree quite well with the pressure drops calculated by the design method. Most of the data lie in the annular flow regime, however, and the calculated pressure drop using the baseline model (Chen correlation) for the annular flow regime underpredicts the pressure drop by about a factor of two. Figure 3.17 shows that the pressure drop predicted using the Wallis correlation in the model for the annular flow regime predicts these data much better.

In the reference, it is reported that test data in this facility have been obtained at the same test conditions during the periods between microgravity parabolas, which are nominally 1g in level flight. Those data are in the stratified flow regime rather than the annular flow regime, but it has been reported that the pressure drops are the same as the microgravity data. Tabulated data for these tests are not included in the data files supplied with the reference. However, if the pressure drop is calculated using the design methods for stratified flows, the calculated pressure drops are about a factor of two smaller than the calculated values for the annular flow regime plotted in Figure 3.16 and about a factor of four smaller than the calculated values shown in Figure 3.17. Thus, the measured pressure drops would be about two to four times larger than what would be expected. It is likely that body forces contributed to these pressure drop measurements. Flow regime tests (Section 2.4.2) further support this hypothesis that the aircraft and the test section were not level. The question can be resolved with ground tests, which are currently being performed.

Rezkallah and Mitchell (1991). This comparison shows that the design methods scale well to very high density ratios. The University of Saskatchewan has obtained microgravity data with air and water (at about 75 kPa) in a tube 9.52 mm in diameter. Figure 3.18 compares the calculated and measured pressure drops for data in the slug flow regime and in the intermediate flow regimes between slug and bubbly or slug and annular. (Data for the flight series listed as Day 3 in the reference are shown.) The data in the slug flow regime (solid squares) and the transition region between slug and bubbly flow regimes (symbol b) agree very well with the pressure drops calculated using the design methods for the slug flow regime. Data points in the transition region between slug and annular flow (symbol a) show some pressure drops which are about 30% greater than the values calculated using the model for the slug flow regime. Using the model for the annular flow regime, these data are underpredicted by a factor of two. Thus, pressure drop data agree with the flow regime observations that these data are between slug and annular flow regimes and that a fully developed annular flow pattern has not been achieved.

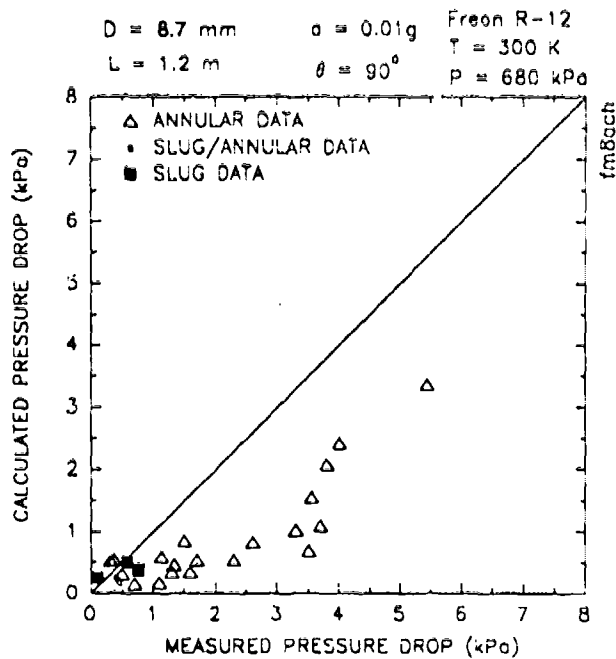


Figure 3.16. PRESSURE DROP COMPARISONS WITH THE DESIGN METHOD FOR HILL AND BEST (1991) MICROGRAVITY DATA IN THE ANNULAR AND SLUG FLOW REGIMES

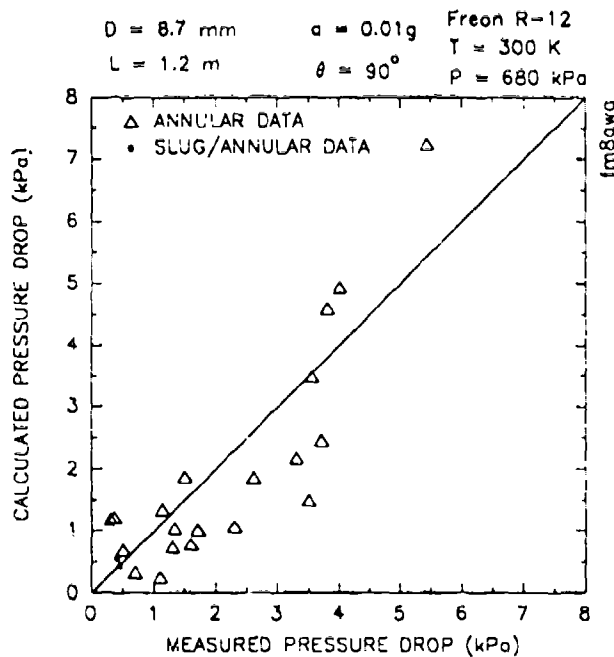
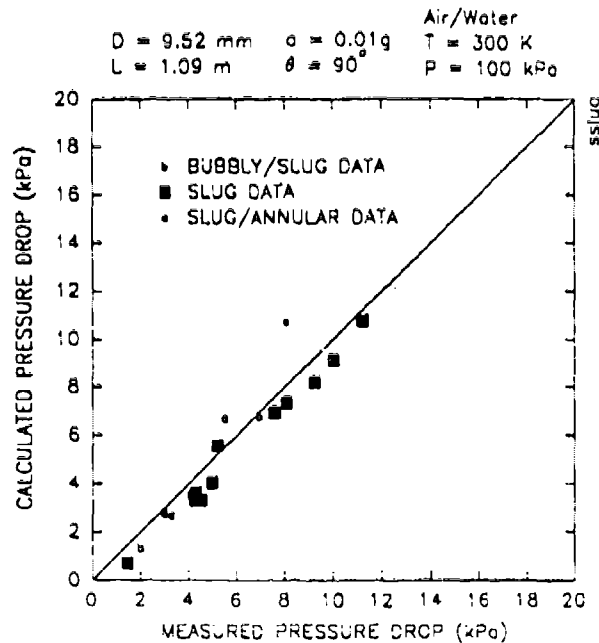


Figure 3.17. PRESSURE DROP COMPARISONS WITH THE WALLIS CORRELATION FOR HILL AND BEST (1991) MICROGRAVITY DATA IN THE ANNULAR FLOW REGIME



**Figure 3.18. PRESSURE DROP COMPARISONS WITH REZKALLAH AND MITCHELL (1991) MICROGRAVITY DATA IN THE SLUG FLOW REGIME**

Figure 3.19 compares the few data points in the bubbly flow regime (open circles) and the data in the transition region between bubbly and slug flow regimes (symbol b) with the pressure drop model for the bubbly flow regime. Although the data are limited, the measured data and the model agree very well.

#### Ground Tests Only

Crowley et al. (1991). Crowley et al. measured the pressure drop in a 6.34 mm diameter tube with Freon R-11. At a mass flux of  $175 \text{ kg/m}^2\text{-s}$ , most of the data lie in the annular flow regime, and Figure 3.20 compares the measured pressure drop with the predictions by the various interfacial shear models, similar to the comparisons presented in Figure 3.12. For the most part, the measured pressure drops lie between the predictions of the model with the Chen and Wallis correlations for the interfacial friction. At a mass flux of  $100 \text{ kg/m}^2\text{-s}$  (Figure 3.21), the measured pressure drops are much smaller than at the higher mass flux. Measured data tend to lie between the predictions of the Chen correlation and the limiting case of a smooth interface ( $f/f_{wg} = 1$ ). Note however that these data have a large uncertainty associated with them ( $\pm 0.2 \text{ kPa}$ ). So, the data in Figure 3.20 might be considered more reliable.

A few data points have also been obtained in the slug flow regime for each of the two mass fluxes. These points occur at low quality ( $x < 0.10$ ) and at low pressure drops. Figure 3.22 shows that the limited data agree with the design methods for the stratified flow regime.

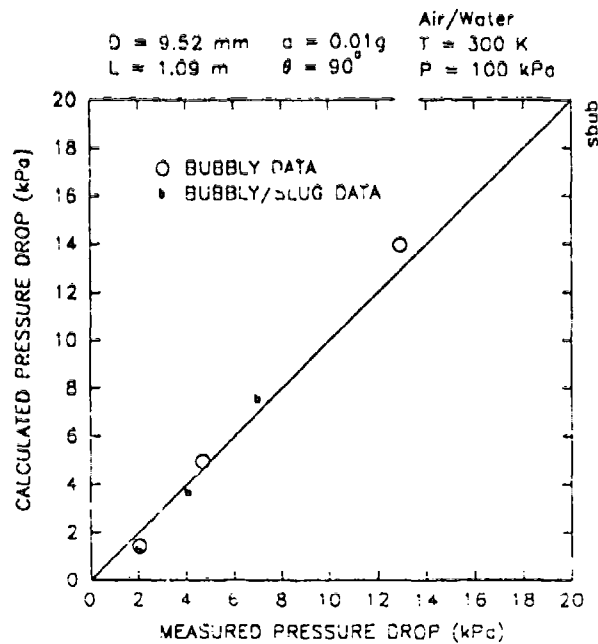


Figure 3.19. PRESSURE DROP COMPARISONS WITH REZKALLAH AND MITCHELL (1991) MICROGRAVITY DATA IN THE BUBBLY FLOW REGIME

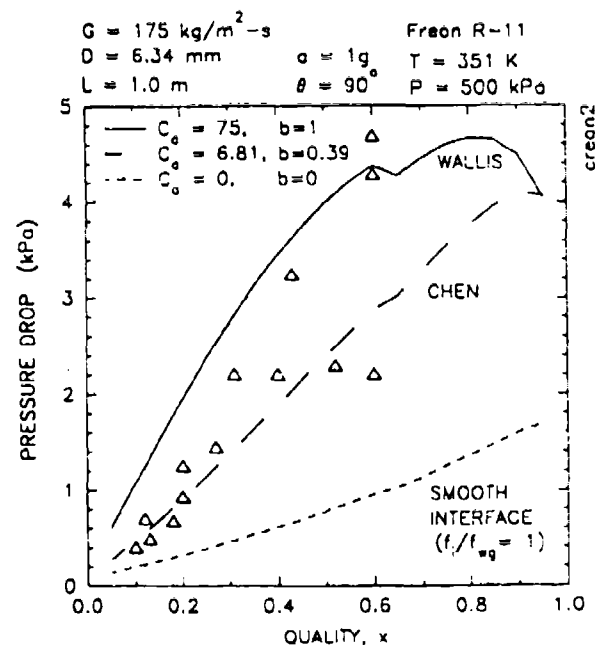


Figure 3.20. PRESSURE DROP COMPARISONS WITH CROWLEY ET AL. (1991) GROUND TEST DATA IN THE ANNULAR FLOW REGIME ( $G = 175 \text{ kg/m}^2\text{-s}$ )

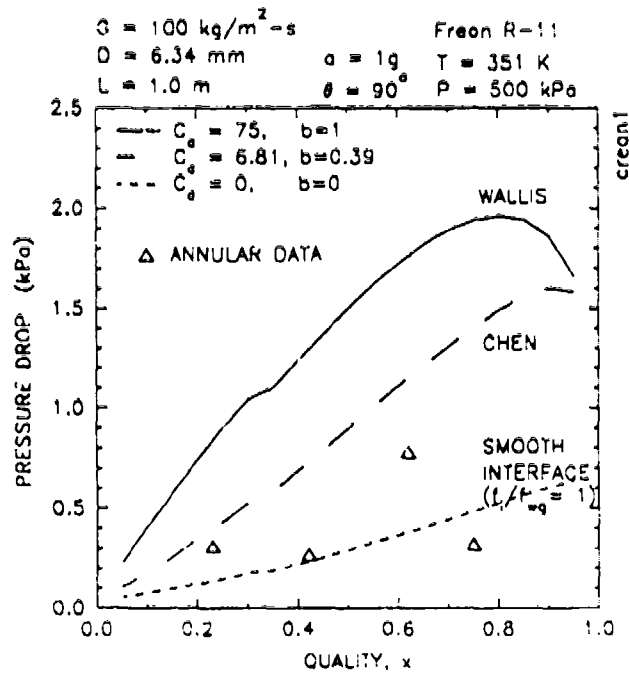


Figure 3.21. PRESSURE DROP COMPARISONS WITH CROWLEY ET AL. (1991)  
 GROUND TEST DATA IN THE ANNULAR FLOW REGIME  
 $(G = 100 \text{ kg/m}^2\text{-s})$

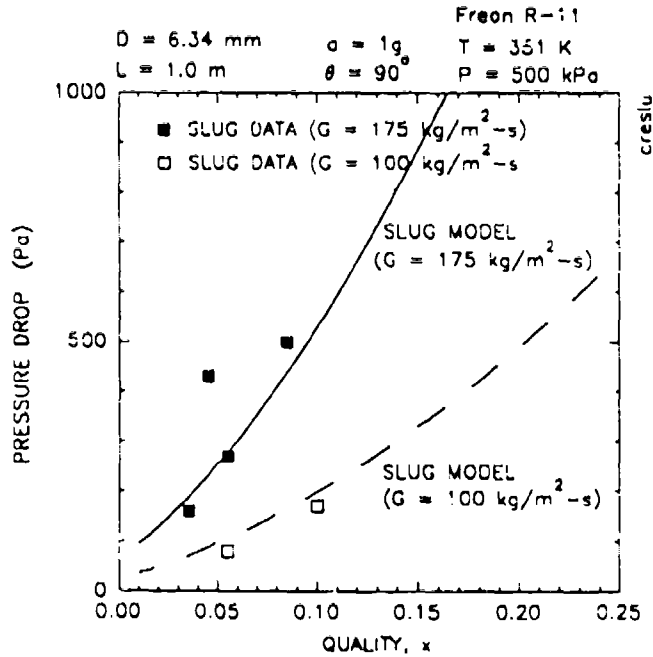


Figure 3.22. PRESSURE DROP COMPARISONS WITH CROWLEY ET AL. (1991)  
 GROUND TEST DATA IN THE SLUG FLOW REGIME

Lee (1991). McDonnell Douglas Space Systems Co. is obtaining data to support the design of Space Station Freedom. While only preliminary ground tests have been performed thus far (at McDonnell Douglas in Houston, Texas), space experiments are planned for the future. These data are particularly interesting because they have been obtained with ammonia at pressures and temperatures typical of thermal management systems for spacecraft. These experiments report only the measured pressure drop; no corresponding flow regime observations or void fraction measurements are available.

Figure 3.23 calculates the flow regimes in these tests. The figure shows where the test conditions lie on a map of predicted flow regimes in mass flux versus quality coordinates. These test conditions correspond to pressure drops measured in a 15.8 mm pipe. The mass flux is approximately constant at 90 kg/m<sup>2</sup>-s, with the quality varied in the range of 0.09 to 0.9 by increasing or decreasing the heat input. Data points at  $x < 0.1$  are predicted to lie in the stratified flow regime.

Figure 3.24 plots the pressure drop data for the 15.8 mm pipe. On this plot, the symbols for the data show the predicted flow regime on the map in Figure 3.23, since the flow regime has not been observed. The measured pressure drops agree with the model for stratified flow at a quality less than 0.4. The measured pressure drops agree with the annular flow model (using the Chen correlation) for quality values greater than 0.6. A transition region occurs in the range  $0.4 < x < 0.6$ , where the pressure drop values lie between the two models.

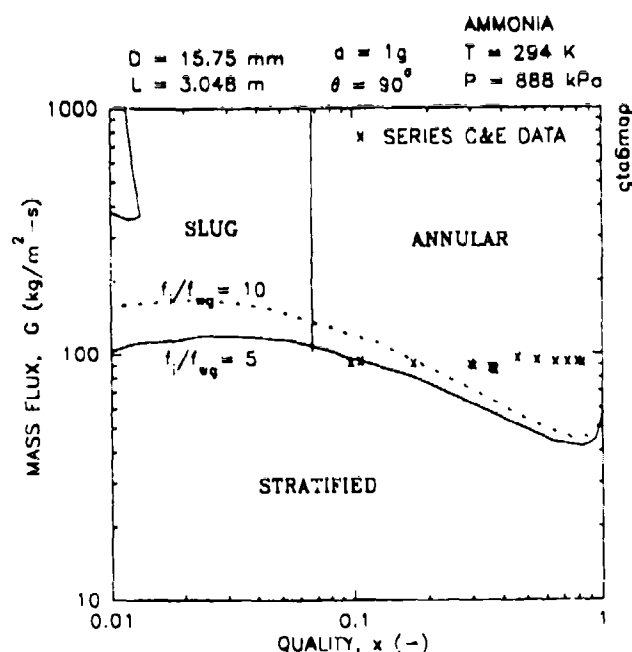


Figure 3.23. PREDICTED REGIME MAP FOR LEE (1991)  
 TEST CONDITIONS AT  $D = 15.8 \text{ mm}$



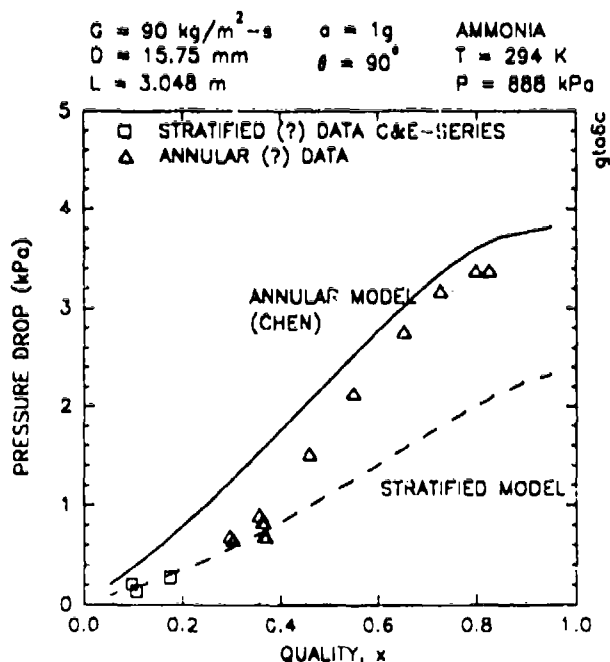


Figure 3.24. PRESSURE DROP COMPARISONS WITH LEE (1991)  
 DATA AT  $D = 15.8 \text{ mm}$

Figure 3.25 plots the corresponding flow regime map at a 21.1 mm tube size, which is the largest size tested. The transition from stratified to annular flow is predicted to occur at about twice the value of the quality as in the smaller tube (Figure 3.23). Also notice that the mass flux of  $65 \text{ kg/m}^2\text{-s}$  lies very close to the predicted transition boundary between stratified and annular flow regimes even at the highest value of the quality tested, about  $x = 0.7$ . Figures 3.26 and 3.27 shows that the measured pressure drop data agree closely with the model for the stratified flow regime across the range of quality tested at both mass fluxes. These data therefore suggest that the flow pattern is still much closer to the stratified than the annular regime for all of these data, which is not surprising given that the test conditions lie close to the transition (Figure 3.25) and the transition boundary is somewhat uncertain.

The tests at these two pipe sizes illustrate the uncertainty and risk that accrues when operating at conditions near the flow regime transition, such as between stratified and annular flow regimes. Under microgravity conditions, all of the data would be in the annular flow regime (the stratified flow regime would effectively disappear), and therefore pressure drops might be twice as large in the larger pipe than they are on the ground. (Compare the predictions for the annular and stratified regimes in Figure 3.26 or 3.27.)

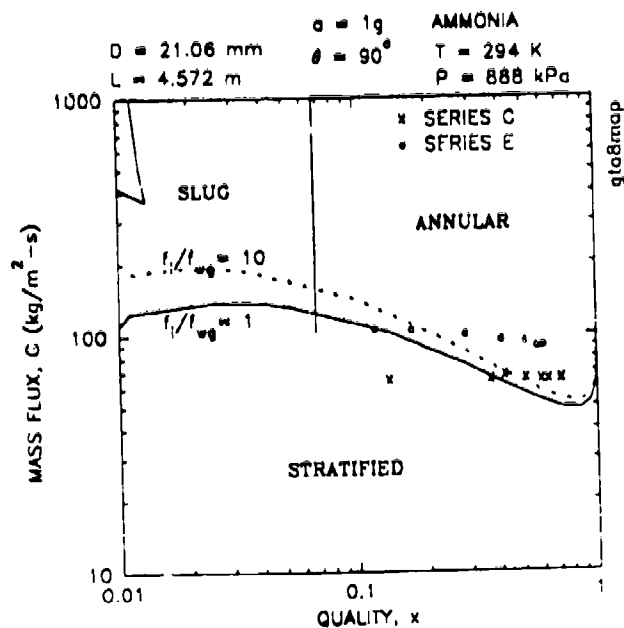


Figure 3.25. PREDICTED REGIME MAP FOR LEE (1991)  
TEST CONDITIONS AT  $D = 21.1 \text{ mm}$

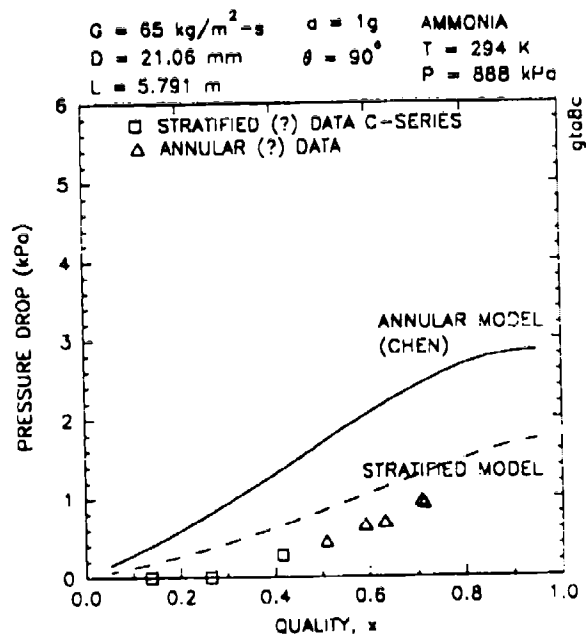


Figure 3.26. PRESSURE DROP COMPARISONS WITH LEE (1991)  
DATA AT  $D = 21.1 \text{ mm}$  ( $G = 65 \text{ kg}/\text{m}^2\text{-s}$ )

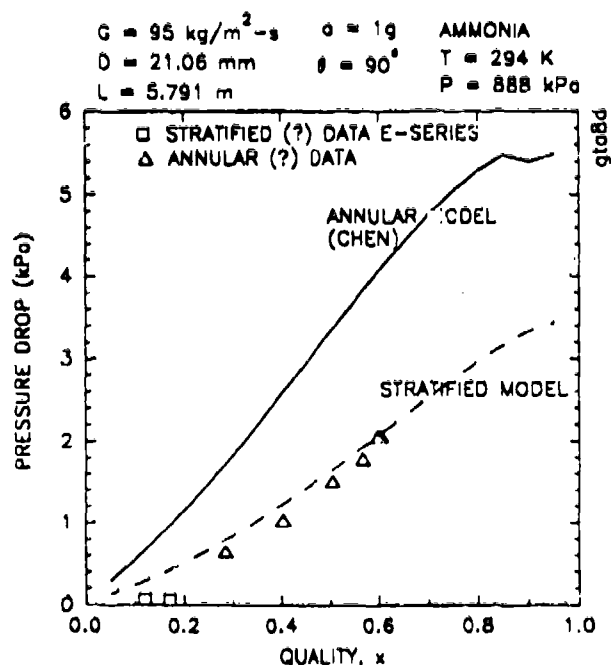


Figure 3.27. PRESSURE DROP COMPARISONS WITH LEE (1991)  
DATA AT  $D = 21.1 \text{ mm}$  ( $G = 95 \text{ kg/m}^2\text{-s}$ )

### 3.5.3 Conclusions from Pressure Drop Comparisons

Table 3.7 summarizes the conclusions from the pressure drop comparisons presented in Section 3.5.2.

**Annular Flow Regime.** The experimental data show that the pressure drop in the annular flow regime is predicted by the separated flow model in the range bounded by the Chen et al. and Wallis correlations for the interfacial friction. The microgravity data of Chen et al. and the ground test data with ammonia by McDonnell Douglas Space System Co. support the Chen et al. model. Data from the experiments by Hill and Best with air and water support the Wallis model. Data from the experiments by Crowley et al. lie between the two models.

**Slug Flow Regime.** Experimental data show that the pressure drop in the slug flow regime is predicted very well by the recommended drift flux model. The data from Colin et al. and Rezkallah and Mitchell show excellent agreement with the predictions.

**Bubbly Flow Regime.** Experimental data show that the pressure drop in the bubbly flow regime is predicted very well by the recommended drift flux model. The data from Colin et al. and Rezkallah and Mitchell also show excellent agreement with the predictions.

Table 3.7. SUMMARY OF PRESSURE DROP COMPARISONS WITH DESIGN METHODS FOR PIPES					
ACCELERATION	EXPERIMENT	ANNULAR REGIME	SLUG REGIME	BUBBLY REGIME	STRATIFIED REGIME
MICROGRAVITY	Chen (1989)	<ul style="list-style-type: none"> <li>Bounded by Wallis (1969) and Smooth Interface Shear Models</li> </ul>	<ul style="list-style-type: none"> <li>Good Comparisons</li> </ul>	(No Data)	N.A.
	Colin (1991)	<ul style="list-style-type: none"> <li>Intermediate Best-fit Model Proposed</li> <li>(No Data)</li> </ul>	<ul style="list-style-type: none"> <li>Good Comparisons</li> </ul>	<ul style="list-style-type: none"> <li>Good Comparisons</li> </ul>	N.A.
	Hill and Best (1991)	<ul style="list-style-type: none"> <li>Agreed with Wallis (1969) Interface Shear Model</li> </ul>	<ul style="list-style-type: none"> <li>Good Comparison (Limited Data)</li> </ul>	(No Data)	N.A.
	Rezkallah and Mitchell (1991)	<ul style="list-style-type: none"> <li>(No Data)</li> </ul>	<ul style="list-style-type: none"> <li>Good Comparisons</li> </ul>	<ul style="list-style-type: none"> <li>Good Comparison (Limited Data)</li> </ul>	N.A.
GROUND TESTS	Chen (1989)	<ul style="list-style-type: none"> <li>(No Data)</li> </ul>	<ul style="list-style-type: none"> <li>(No Data)</li> </ul>	(No Data)	<ul style="list-style-type: none"> <li>Data Bounded by Shear Model Range</li> </ul>
	Crowley (1991)	<ul style="list-style-type: none"> <li>Bounded by Wallis and Chen Shear Models</li> </ul>	<ul style="list-style-type: none"> <li>Good Comparison (Limited Data)</li> </ul>	(No Data)	(No Data)
	Lee (1991)	<ul style="list-style-type: none"> <li>Agree with Chen Shear Model for Well-Developed Annular Flow</li> </ul>	<ul style="list-style-type: none"> <li>(No Data)</li> </ul>	(No Data)	<ul style="list-style-type: none"> <li>Agree with Stratified Shear Model at Low Quality</li> </ul>

**Stratified Flow Regime.** In general, the model and the data correctly show that the stratified flow regime does not occur under microgravity conditions – only in the ground tests. Data lie between the predictions of the separated flow model with the recommended value for the interfacial friction ( $f_i/f_{wg} = 5$ ) and a smooth gas-liquid interface. The data from Chen et al. and McDonnell Douglas (discussed as examples in this report) support this conclusion, and it is also true for many other ground tests in the stratified flow regime (e.g. Crowley and Sam, 1986).

The only disagreement is with the data reported by Hill and Best, where pressure drops in the stratified regime are two to four times greater than expected. However this discrepancy is likely to be due to the fact that the aircraft was not actually in level flight during those tests.

### 3.6 References for Pressure Drop Methods

Chen, I.-Y., Downing, R.S., Keshock, E. and Al-Sharif, M.M.; "An Experimental Study and Prediction of a Two-Phase Pressure Drop in Microgravity"; AIAA Paper 89-0074, Presented at the AIAA 27th Aerospace Science Meeting, Reno, Nevada, 9-12 January, 1989.

Chisholm, D.; "Brief Communications – Two-Phase Flow in Bends"; Int. J. Multiphase Flow, V6, August 1980, pp. 363-367.

Collier, J.G.; Convective Boiling and Condensation; Second Edition, McGraw-Hill Book Company, New York, New York, 1986.

Colin, C., Fabre, J. and Dukler, A.E.; "Gas-Liquid Flow at Microgravity Conditions – I. Dispersed Bubble and Slug Flow"; Int. J. Multiphase Flow, V17(4), 1991, pp. 533-544.

Crowley, C.J. and Sam, R.G.; "INVESTIGATION OF TWO-PHASE FLOW IN HORIZONTAL AND INCLINED PIPES AT LARGE PIPES SIZE AND HIGH GAS DENSITY"; Creare TN-399, Prepared for the Pipeline Research Committee, American Gas Association, Project PR 172-507, Catalog #L51509, Prepared by Creare, Inc., Hanover, New Hampshire, February 1986.

Crowley, C.J., Barry, J.J. and Rothe, P.H.; "STATE OF THE ART METHODS FOR MULTIPHASE FLOW PIPELINES"; Creare TN-477, Prepared for the Pipeline Research Committee, American Gas Association, Project PR-172-904, Catalog #L51611, Prepared by Creare Inc., Hanover, New Hampshire, August 1989.

Crowley, C.J. and Sam, R.G.; "MICROGRAVITY EXPERIMENTS WITH A SIMPLE TWO-PHASE THERMAL SYSTEM"; PL-TR-91-1059, Prepared for Air Force Phillips Laboratory (PL/STPP), Contract F29601-88-C-0066, Prepared by Creare Inc., Hanover, New Hampshire, 1991.

Crowley, C.J., Wallis, P.N. and Ent, R.S.; "MICROP PROGRAM: PRESSURE DROPS IN MICROGRAVITY"; PL-TR-92-3003, Volume 2, Prepared for Air Force Phillips Laboratory (OL-AC PL/VTPT), Contract F04611-90-C-0004, Prepared by Creare Inc., Hanover, New Hampshire, May 1992.

Fernandes, R.C.; "Hydrodynamic Model for Gas-Liquid Slug Flow in Vertical Tubes"; AIChE J. V29(6), November 1983, pp. 981-989.

Harmathy, T.Z.; "Velocity of Large Drops and Bubbles in Media of Infinite or Restricted Extent"; AIChE J., V6(2), 1960, pp. 281-288.

Harshe, B., Hussain, A. and Weisman, J.; "TWO-PHASE PRESSURE DROP ACROSS RESTRICTIONS AND OTHER ABRUPT AREA CHANGES"; NUREG-0062, Prepared for U.S. Nuclear Regulatory Commission, Contract AT (49-24)-0179, Prepared by University of Cincinnati, Cincinnati, Ohio, April 1976.

Hewitt, G.R.; Flow Regimes: Chapter 2.1, Handbook of Multiphase Systems, G. Hetsroni, ed., Washington D.C., Hemisphere Publishing Corp., 1982.

Hill, W.S. and Best, F.R.; "DEFINITION OF TWO PHASE FLOW BEHAVIORS FOR SPACECRAFT DESIGN"; AFK-0062-FM-8933-418, Prepared for Air Force Phillips Laboratory (PL/STPP), Contract F29601-88-C-0062, Prepared by Foster-Miller, Inc., Waltham, Massachusetts, June 1991.

Hughmark, G.A.; "Holdup in Gas-Liquid Flow"; Chem. Engrg. Prog., V58(4), 1962, pp. 62-65.

Hussain, A. and Weisman, J.; "TWO-PHASE PRESSURE DROP ACROSS ABRUPT AREA CHANGES"; Report C00 2152-15, Prepared for U.S. Nuclear Regulatory Commission, Contract AT-11-1-2152, Prepared by University of Cincinnati, Cincinnati, Ohio, January 1975.

Kachnik, L., Lee, D., Best, F. and Faget, N.; "A Microgravity Boiling and Convective Condensation Experiment"; ASME 87-WA/HT-12, Presented at ASME Winter Annual Meeting, Boston, Massachusetts, 13-18 December 1987.

Laurinat, J.E., Hanratty, T.J. and Dallman, J.C.; "Pressure Drop and Film Height Measurements for Annular Gas-Liquid Flow"; Int. J. Multiphase Flow, V10(3), June 1984, pp. 341-356.

Lee, D.Y.; "GTA TEST-FLOW REGIME ANALYSIS"; A95-J849-DYL-M-9103340, Prepared by McDonnell-Douglas Space Systems Co., 2 August, 1991.

Liles, D.R. and Mahaffy, J.H.; "TRAC-PF1/MOD1: AN ADVANCED BEST-ESTIMATE COMPUTER PROGRAM FOR PRESSURIZED WATER REACTOR THERMAL-HYDRAULIC ANALYSIS"; NUREG/3858, LA-10157-MS, Prepared for the U.S. Nuclear Regulatory Commission, Prepared by Los Alamos National Laboratory, Los Alamos, New Mexico, July 1986.

Martin, C.S.; "Vertically Downward Two Phase Slug Flow"; J. Fluids Engrg., Trans. ASME, V98(4), December 1976, pp. 715-722.

Martin, C.S.; "Transition from Bubbly to Slug Flow of a Vertically Downward Air Water Mixture"; Flow Studies in Air and Water Pollution; R.E.A. Arndt et al., eds., ASME Symposium, Atlanta, Georgia, June 1973, ASME Publ. I-1, 1973, pp. 49-60.

Mishima, K. and Ishii, M.; "Flow Regime Transition Criteria for Upward Two-Phase Flow in Vertical Tubes"; Int. J. Heat Mass Transfer, 27(5), May 1984, pp. 723-738.

Reinarts, T.R., Best, F.R., Miller, K.M., and Hill, W.S.; "*Definition of Two-Phase Flow Behaviors for Spacecraft Design*"; Proceedings of the Eighth Symposium on Space Nuclear Power Systems, M.S. El-Genk and M.D. Hoover, eds., 6-10 January 1991, Albuquerque, New Mexico.

Rezkallah, K. and Mitchell, D.R.; "EVALUATION OF THE SOFTWARE PACKAGES MICROP AND MICROREG"; University of Saskatchewan, Saskatoon, Canada, 23 October, 1991.

Rohsenow, W.P., Hartnett, J.P. and Ganic, E.N., Handbook of Heat Transfer Fundamentals; Second Edition, McGraw-Hill Book Company, New York, New York, 1985.

Taitel, Y. and Dukler, A.E.; "*Brief Communication - A Theoretical Approach to the Lockhart-Martinelli Correlation for Stratified Flow*"; Int. J. Multiphase Flow, V2, 1976, pp. 591-595.

Tapucu, A., Teyssedou, A., Troche, N. and Merilo, M.; "*Pressure Losses Caused by Area Changes in a Single-Channel Flow Under Two-Phase Flow Conditions*"; Int. J. Multiphase Flow, V15(1), 1989, pp. 51-64.

Wallis, G.B.; One-Dimensional Two-Phase Flow; McGraw-Hill Book Company, New York, New York, 1969.

Zigrang, D.J. and Sylvester, N.D.; "*Explicit Approximations to the Solution of Colebrook's Friction Factor Equation*"; AIChE Journal, V28, May 1982, p. 514.

Zuber, N. and Hench, J.; "STEADY STATE AND TRANSIENT VOID FRACTION OF BUBBLING SYSTEMS AND THEIR OPERATING LIMIT. PART I. STEADY STATE OPERATION"; 62GL100, General Electric Co., San Jose, California, 1962.

Zuber, N. and Findlay, J.A.; "*Average Volumetric Concentration in Two-Phase Flow Systems*"; J. Heat Transfer, Trans. ASME, V87(4), November 1965, pp. 453-468.

## 4 EVAPORATORS: Forced Convection Dominated Tubes

Evaporators are common components in two-phase spacecraft thermal management systems, providing the sink for heat rejection by the thermal loads of spacecraft systems. This section of the design manual considers evaporators based on forced convection dominated tubes. In this type of evaporator, subcooled liquid enters at the inlet side of the tube and is evaporated by heat transferred through the tube walls. Vapor or a two-phase mixture of vapor and saturated liquid exit the tube. To make the evaporator insensitive to the acceleration level of the spacecraft, the evaporator is designed so that heat transfer by forced convection dominates nucleate boiling. Since the physical mechanisms of nucleate boiling (e.g., bubble growth and detachment) can be sensitive to body forces and forced convection is not, a forced convection evaporator will not be sensitive to the acceleration level of the spacecraft.

This section of the design manual presents methods for predicting the heat transfer and pressure drop characteristics of forced convection evaporators. Methods focus on a single evaporator tube. The wall temperature or heat flux, flow quality and void fraction, and pressure drop components are computed over the length of the evaporator tube. The methods described here are implemented in the companion FCEVAP software (Barry et al., 1992).

Section 4.1 discusses applications of the evaporator design methods, focusing on predicting performance of different geometrical configurations.

Section 4.2 summarizes the analysis approach and methods. The calculation strategy is based on breakup of the tube into segments. For each segment, the methods predict heat transfer and pressure losses for the appropriate flow regime.

Section 4.3 presents the overall calculation methodology, concentrating on the stepwise procedure used to traverse the evaporator tube from entrance to exit.

Sections 4.4, 4.5, 4.6, and 4.7 give the detailed equations for the calculations. For each regime, the equations for heat transfer coefficient, quality and void fraction, pressure drop, regime transition, and critical heat flux are listed.

Dimensionless design charts are presented in Section 4.8. These charts may be used for quick scoping calculations of evaporator heat transfer and pressure drop.

Section 4.9 describes validation calculations performed using the methods. Predicted results for heat transfer and pressure loss compare well with available test data.

### 4.1 Applications

The design methods presented here apply to the fluid and thermal design of forced convection evaporators. These evaporators may have various geometries depending on the type and geometry of the heat source that must be cooled. The following paragraphs discuss application of the design methods to:

- Straight tube evaporators,
- Spiral coil evaporators,
- Helical coil evaporators,
- Tubes of noncircular cross section.



The application of the methods to interpretation of test data is also discussed.

**General Design Considerations.** Design of a forced convection evaporator involves a number of important and sometimes conflicting tradeoffs. Typically the design proceeds in an iterative fashion, with an initial set of design parameters undergoing modification as all of the physical effects are accounted for. The methods described in this manual can predict these effects.

In each of the geometries, the flow area  $A$  and hydraulic diameter of the tube,  $D_h$ , are typically fixed by the mass flux,  $G$ , and the total heat removal,  $q$ . Mass flux is usually selected based on heat transfer, flow regime, and pressure drop considerations. As discussed in Section 4.2, heat transfer by forced convection dominates nucleate boiling at sufficiently high mass fluxes. For reduced gravity (low acceleration) applications, it is important to operate in the forced convection dominated regime since nucleate boiling relies to some extent on body forces. Sufficiently high mass fluxes also guarantee operation in non-stratified flow regimes (see Section 2), so that operation is insensitive to acceleration in other components. High mass fluxes, however, also result in larger pressure drops. A balance must be struck between pumping requirements and insensitivity to acceleration.

An overall energy balance on the evaporator tube relates the flow area to the mass flux and total heat removal by:

$$A = \frac{q}{Gh_{fg}\Delta x} \quad (4-1)$$

where  $\Delta x$  represents the change in quality over the length of the tube and  $h_{fg}$  is the latent heat of vaporization. (Note that negative qualities are defined for subcooled liquids.) If a target exit quality is known and a suitable mass flux has been selected, Equation 4-1 relates the flow area,  $A$ , to the total heat load,  $q$ .

The tube diameter can be directly computed from the flow area  $A$ . The procedures for noncircular tubes are discussed below.

**Design of Straight Tube Evaporators.** Figure 4.1 illustrates the straight tube evaporator geometry. Straight tube geometries are common in many applications. In a multiple pass heat exchanger design, for example, the design methods may be applied to individual straight sections alone or as an approximation of the total tube length. Straight tube evaporators frequently appear in experimental facilities due to their straightforward construction and simpler modelling requirements.

With the diameter of the tube known from the overall flow rate and heat load, the designer must specify the length of the evaporator to meet goals for temperature and size. The length determines the heat flux and the wall temperature, since the diameter and heat load are fixed. High heat fluxes reduce the size of the evaporator but result in higher wall temperatures and may approach physical operating limits like critical heat flux. This design manual provides methods for computing the heat transfer coefficient and wall temperature along the length of the evaporator. Comparison of the maximum wall temperature to design limits is one important design criteria. The design methods also predict the critical heat flux. If critical heat flux is exceeded, heat transfer occurs by inefficient film boiling, resulting in high wall temperatures.

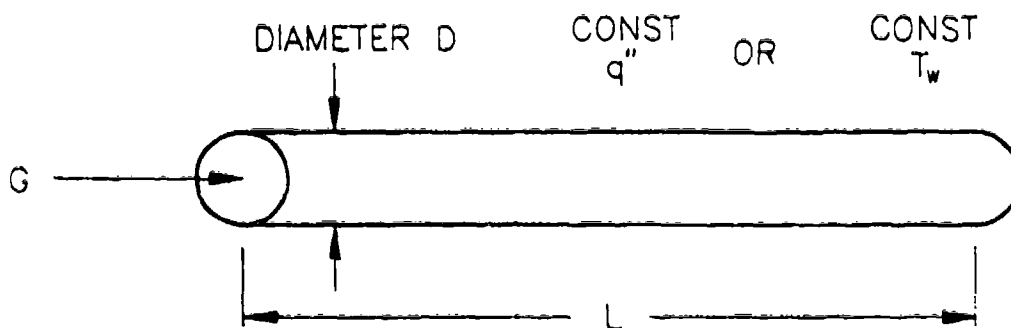


Figure 4.1. STRAIGHT TUBE EVAPORATOR

The design methods also predict the pressure drop in the evaporator tube. Large pressure drops result in large pumping power requirements, usually a scarce resource on spacecraft. Pressure drops can be reduced by lowering the mass flux and/or increasing the tube diameter.

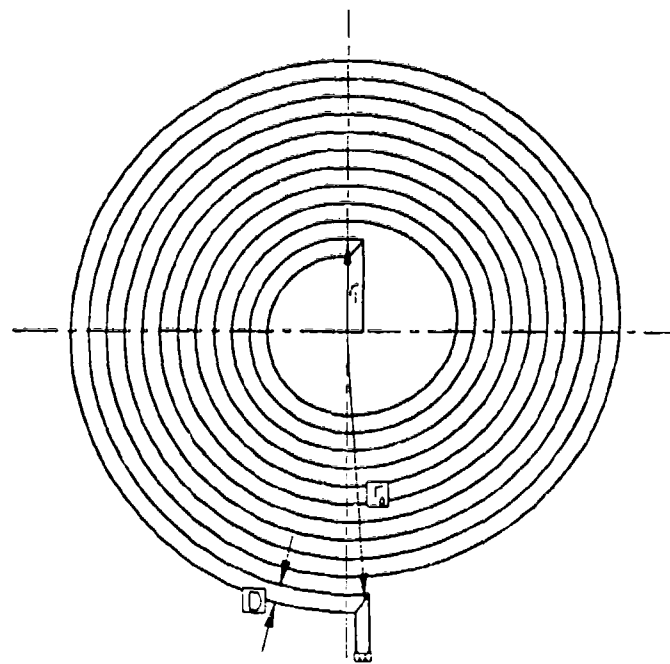
**Design of Spiral Coil Evaporators.** Figure 4.2 shows an evaporator of the flat spiral coil variety. This configuration is commonly found in cold plate applications. Heat transfer surfaces are fastened to one or both sides of the flat coil. Subcooled liquid may be introduced into either the inner or outer ends of the spiral. In practice, the inner-to-outer and outer-to-inner flow directions may behave very similarly (Niggemann et al., 1985).

Design of the spiral coil evaporator is quite similar to the straight tube. The uncoiled length of the evaporator tubing determines the heat flux. Note that for a spiral coil, the heat flux is normally applied only to the faces (cold plates) of the coil. In the design methods presented here, the heat flux is defined at the entire tube periphery (as in a straight tube). This heat flux is calculated from the cold plate heat flux by a simple geometry conversion. The inner and outer radius of the spiral are determined primarily by mechanical and manufacturing considerations. The bent tube must not have kinking or excessive distortion of the cross section.

The design methods include a correction factor that accounts for the increased pressure drop expected in a spiral coil compared to a straight tube of the same length. The methods for heat transfer and fluid state remain the same as for a straight tube. The effects of flow redistribution caused by the centrifugal forces are not considered. As shown by the data comparisons of Section 4.9, this appears to be a valid approximation.

**Design of Helical Coil Evaporators.** Figure 4.3 shows a helical coil evaporator. Such an evaporator could be used to "wrap" a heat source for example. Alternatively, two coils could be intermeshed or a coil could be placed in a bath to form a fluid-fluid heat exchanger.

In the design methods, a helical coil evaporator is treated in the same way as a spiral coil, i.e., a helix is treated as a degenerate spiral. The inner and outer radii are set equal, and all of the same equations are applied. This is an approximation if the coils of the helix are widely spaced along its axis. As with the spiral coil, flow redistribution due to centrifugal forces is not accounted for by the methods.



SPIRAL COIL

**Figure 4.2. SPIRAL COIL EVAPORATOR**

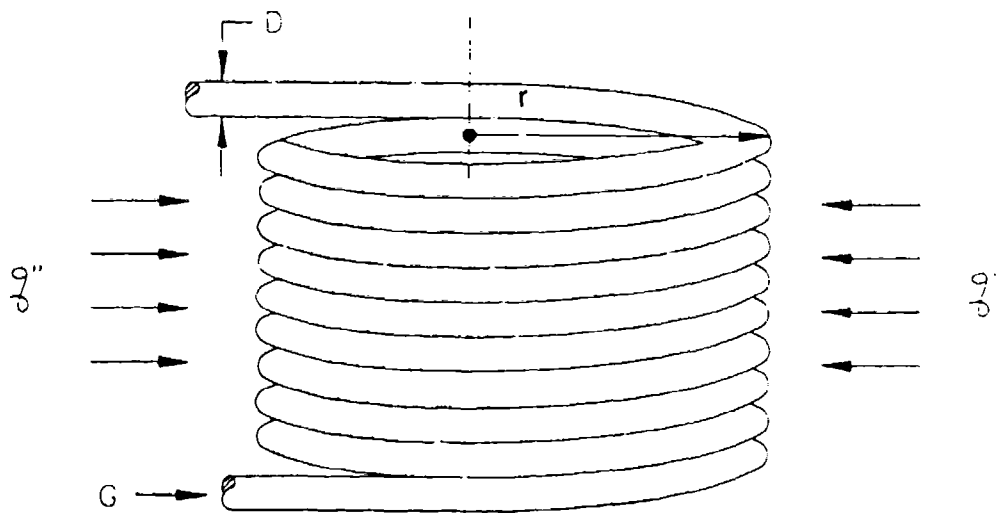


**Figure 4.3. HELICAL COIL EVAPORATOR**

**Noncircular Cross Sections.** The design methods have been formulated to handle noncircular tube cross sections in a simple and straightforward way. Two general types of noncircular cross sections may be considered.

For many noncircular cross sections, the hydraulic diameter approach is valid. These cases require no modification to the methods or to the companion software, only changes in input parameters. The input to the calculations includes the flow area, heated perimeter, and two hydraulic diameters. To apply the methods to a noncircular cross section, these parameters must be calculated using the appropriate geometric formulas. Two hydraulic diameters may be used: one for heat transfer and one for pressure drop. For heat transfer, the hydraulic diameter is defined using the heated perimeter,  $H$ :

$$D_{ht} = \frac{4A}{H} \quad (4-2)$$

For pressure drop, the wetted perimeter,  $S_t$ , is used instead:

$$D_{pd} = \frac{4A}{S_t} \quad (4-3)$$

The definition of two hydraulic diameters improves the flexibility of the methods. In most cases of interest, the two hydraulic diameters are equal,  $D_{ht} = D_{pd}$ . For simplicity, the hydraulic diameter is referred to as simply  $D_h$  in the remainder of this section, with the implicit requirement that the appropriate definition be applied in cases where the wetted and heated perimeters differ.

In cases where the hydraulic diameter approach is not valid, the design methods are formulated so that appropriate substitute correlations may be inserted.

**Interpretation of Test Data.** The design methods may be applied to interpretation of evaporator test data as well as evaporator design. The test article geometry and test conditions are used as the inputs, and performance of the test is predicted. Comparison of the predictions with measured data may yield insights into the performance of the evaporator or the validity of the design models.

## 4.2 Summary of Methods

The design methods described here predict the thermal and pressure loss performance of forced convection evaporators. Typically, the key results of the calculations will be predictions for the wall temperature and pressure drop in the evaporator tube. Various boundary conditions and heat transfer and flow regimes are included. The following paragraphs outline the capabilities of the methods.

**Boundary Conditions.** The design methods accommodate two general thermal boundary conditions: constant wall heat flux and constant wall temperature. A constant wall heat flux condition generally applies for constant heat loads that are independent of temperature, such as the heat dissipation of electronic equipment or instruments. Constant wall temperature boundary conditions typically apply in cases where heat is being transferred from another fluid medium as in an interface heat exchanger.

The design methods presented here are most accurate and robust for constant heat flux boundary conditions. Section 4.3.1 discusses some of the potential difficulties involved in using constant wall temperature boundary conditions.

The design methods require specification of the inlet mass flux, pressure, and quality (or subcooling). A marching technique is used to calculate heat and momentum transfer along the length of the tube to the exit. Outlet pressure and quality are determined as part of the problem solution.

**Heat Transfer and Flow Regimes.** Heat and momentum transfer occur by several mechanisms in the evaporator tube as the fluid quality increases along the tube length. The flow rates of each phase along the tube depend on the heat transfer which, in turn, depends on the flow regime. Figure 4.4 illustrates the various flow and heat transfer regimes along the length of an evaporator tube. The methods described in this manual consider the subcooled liquid through annular flow regimes and heat transfer regimes from convective heat transfer to single-phase liquid to forced convective heat transfer through the liquid film. Beyond these regimes, critical heat flux is likely.

Single-phase flow and heat transfer occur when the liquid is subcooled and the wall temperature is too low to nucleate bubbles. Standard single-phase pressure drop and heat transfer correlations apply. As the wall temperature increases, the onset of nucleate boiling (ONB) is reached, causing a transition to subcooled nucleate boiling heat transfer.

Subcooled nucleate boiling is divided into partially-developed boiling (PDB) and fully-developed boiling regimes (FDB). In PDB, small bubbles nucleate but stay attached to the wall, and there is no significant void fraction. Heat transfer correlations should account for the enhanced heat transfer resulting from the nucleate boiling, but there is no net vapor generation and the pressure drop remains single-phase. As the bulk temperature of the liquid becomes sufficiently large, the bubbles grow larger and detach from the wall, resulting in the onset of significant voiding (OSV) and transition to FDB. In FDB, both the heat transfer by nucleate boiling and the generation of vapor are modelled, and the pressure drop must be calculated using two-phase methods.

The saturated nucleate boiling regime is reached when the bulk liquid temperature reaches saturation. Heat transfer occurs by combined forced convection and nucleate boiling (although forced convection should dominate for well-designed evaporators). All of the heat transferred generates vapor, and the pressure drop has large two-phase components.

In parallel with heat transfer regimes, flow regimes must be considered. In subcooled conditions, of course, the fluid is single-phase liquid. The PDB regime is similar to single-phase liquid, perhaps with enhanced wall roughness due to the bubbles. At very low quality, typically in the FDB regime, the flow is bubbly or slug and normally modelled as a homogeneous vapor/liquid mixture. As the quality increases (in saturated boiling), the flow regime rapidly becomes annular, with a film of liquid located around the periphery of the tube.

In practice, the length of tube where single phase, PDB, and FDB take place are small, with the bulk of the length operating in the saturated boiling regime. Similarly, the bulk of the tube operates in the annular flow regime as well. As a first approximation, an evaporator can usually be modelled using only saturated boiling and annular flow correlations.

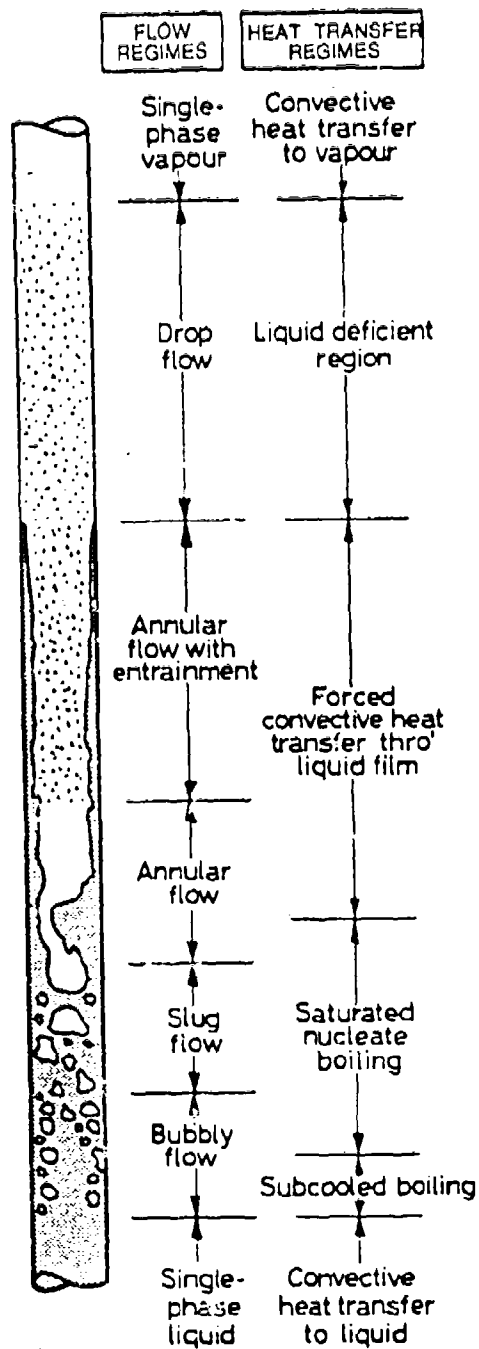


Figure 4.4. FLOW BOILING REGIMES (COLLIER, 1981)

Due to the dominance of saturated boiling and annular flow, the design methods couple heat transfer and flow regimes, as shown in Table 4.1. Heat transfer regimes are calculated from local conditions using methods described in Section 4.7. Then the corresponding flow regimes are assumed to be those listed in Table 4.1. This approach simplifies the calculation methodology significantly, while resulting in only minor modelling inaccuracy.

Depending on the heat flux level, some of the heat transfer regimes depicted in Figure 4.4 may not occur in an evaporator tube. At heat fluxes which are high relative to the liquid mass flux, various other regimes may occur, as described by Collier (1981). However, these cases represent poor evaporator designs in which the tube walls dry out and reach very high temperatures. The design methods are limited to well designed evaporators in which two-phase forced convection is the major heat transfer mechanism.

Readers who wish further background in two-phase heat transfer should consult the text by Collier (1981) or the report by Eastman (1985).

**Two-Phase Forced Convection Heat Transfer.** In saturated flow boiling, the fluid generally flows in an annular pattern with a vapor core and a liquid film on the tube wall. Vaporization occurs by two mechanisms: nucleate boiling in the liquid at the wall and evaporation at the vapor/liquid interface. Annular flow is the dominant regime for practical coolants because the void fraction is quite high even at low qualities, implying high vapor velocities over most of the tube length.

A useful concept for describing heat transfer in saturated flow boiling is the *superposition principle*. Heat transfer is treated as the sum of two components. One is due to nucleate boiling at the wall, and the other is due to forced convection heat transfer to the liquid film. Quantitatively, the total heat flux,  $q''$ , is expressed as a sum:

$$q'' = (h_{fc} + h_{nb}) \Delta T_{sat} \quad (4-4)$$

where  $h_{fc}$  is the "forced convection" heat transfer coefficient,  $h_{nb}$  is the "nucleate boiling" heat transfer coefficient, and  $\Delta T_{sat}$  is the temperature difference between the tube wall and the fluid saturation temperature.

**Table 4.1. HEAT TRANSFER AND FLOW REGIMES**

Heat Transfer Regime	Flow Regime
Single-Phase	Single-Phase
Partially-Developed Subcooled Boiling	Single-Phase
Fully-Developed Subcooled Boiling	Two-Phase Homogeneous
Saturated Flow Boiling	Two-Phase Annular

The superposition principle is the basis for an important evaporator design criterion. Since forced convection heat transfer is independent of gravity while nucleate boiling heat transfer has an uncertain gravity dependence, a design criterion for evaporators in microgravity is:

$$h_{fc} \gg h_{nb} \quad (4-5)$$

In this way operation of the evaporator is assured regardless of the spacecraft acceleration.

As shown in Section 4.4, the superposition principle can be extended to the partially- and fully-developed nucleate boiling regimes by appropriate selection of the temperature difference and by adjustments in the calculation of  $h_{fc}$  and  $h_{nb}$ .

Fluid State, Quality, and Void Fraction. As the fluid in the evaporator is heated from subcooled to saturated and then boiled, the fluid state changes. That is, the temperature, quality, and void fraction evolve. The change in fluid state depends on the heat transfer and flow regime.

In the single-phase and PDB regimes, the bulk fluid is subcooled, and any bubbles that are present are small and remain attached to the wall. The increase in fluid temperature represents the change in fluid state for these regimes. No significant voiding occurs; the quality and void fraction are zero.

In the FDB regime, a significant volume of vapor may be generated even though the bulk temperature of the fluid remains subcooled. This behavior is accounted for by partitioning the energy delivered to the fluid into two parts. One part of the energy goes to raising the fluid temperature (i.e., sensible heat) similar to the single-phase and PDB regimes. The other part of the energy generates vapor (i.e., latent heat), increasing the quality and void fraction. The design methods specify how the energy is partitioned.

The picture simplifies again in saturated boiling. Here all of the heat transfer generates vapor, and the bulk fluid remains saturated.

The relationship between void fraction and quality varies with the flow regime. In the bubbly and slug flow regimes, the quality is low. The quality and the void fraction are treated using a homogeneous model, i.e., there is no slip between the phases. As the quality rises and the flow regime changes to annular, phase slip becomes significant, and an annular flow model must be used to predict the void fraction.

Pressure Losses in Flow Boiling. The pressure drop through an evaporator determines the pumping power requirement. Generally, good heat transfer performance requires higher pressure drops, so system level tradeoffs are necessary to balance component size and pumping power.

Pressure losses in an evaporator tube are due to the phenomena illustrated in Figure 4.5, which shows the forces acting on elemental control volume in the evaporator tube. The forces are:

- Wall friction,
- Body forces, and
- Fluid acceleration.



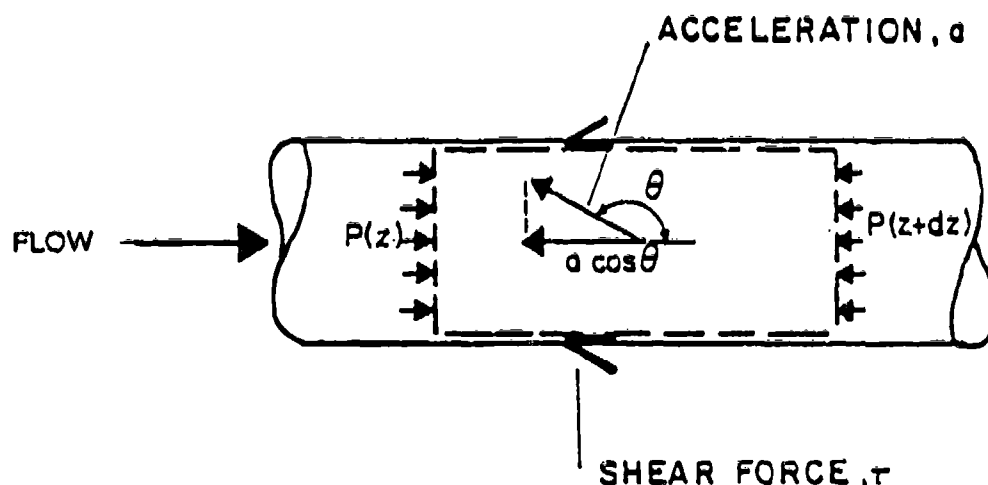


Figure 4.5. FORCES ON AN ELEMENTAL CONTROL VOLUME

The total pressure drop in the evaporator is the sum of the pressure drops due to these three components. Pressure drops due to wall friction and body forces are similar to the pressure losses in a transport line (Section 3). The difference is that the fluid changes phase in an evaporator so the effective fluid properties vary along the tube. The pressure drop due to fluid acceleration is also caused by vaporization of liquid. Since the vapor is less dense than the liquid, it must have a higher velocity. To accelerate the fluid into the vapor phase a force must be exerted on the liquid. This force is the acceleration pressure loss in the evaporator tube.

**Dimensionless Design Maps.** This design manual presents dimensionless design maps to calculate heat transfer and pressure losses in evaporator tubes (Section 4.8). The dimensionless design variables provide physical insight and the maps are suitable for scoping level design. These maps ignore the less important heat transfer and flow regimes which contribute minimally to the overall behavior of the evaporator. Instead, the maps focus on the key regimes that dominate performance. More precise estimates of the evaporator performance need to account for all the various heat transfer and flow regimes, and the design equations are provided (Sections 4.4 through 4.7) which are suitable for detailed computer calculations.

### 4.3 Calculation Procedure for an Evaporator Tube

To first order, an evaporator tube can be designed assuming only one heat transfer regime: saturated boiling. However, for final design calculations more precision is often needed, and the detailed behavior of the coolant must be considered. These calculations should consider all the possible heat transfer regimes and calculate the transition from one regime to the next.

This section presents detailed design relations. Procedures are given to generate design maps for additional cases of interest or to program computerized calculations for forced convection evaporators. The usual way to use these design relations is to first divide the evaporator tube into a number of segments within which the fluid properties are approximately constant. In each segment there are three basic calculations:

- Determine the fluid state at the segment exit,
- Calculate the wall temperature (or heat flux),
- Compute the pressure drop, and
- Check for heat transfer regime transition.

Tables 4.2 and 4.3 summarize the calculations in each of the heat transfer regimes and the transitions between them. Figure 4.6 shows schematically the sequence for performing these calculations. The sections which follow provide more detail.

The number of segments required for a design calculation varies. One hundred or so segments are often sufficient for the evaporator calculation. In general, the designer should increase the number of segments until the solution no longer changes. This assures that the solution is not dependent on the number of segments.

#### 4.3.1 Boundary Conditions

**Thermal Boundary Conditions.** Two types of thermal boundary conditions can be prescribed: constant wall heat flux and constant wall temperature. The constant wall heat flux boundary condition specifies the heat flux along the length of the evaporator, fixing the net heat load on the evaporator. The heat flux boundary condition is often used and is robust, with no iteration required for solution.

The constant wall temperature condition is somewhat less used and requires iteration in order to converge to a solution. Due to this iteration and to the sensitivity of the Gungor-Winterton (1986) flow boiling heat transfer correlation to wall temperature, the design methods are less robust and more uncertain for constant wall temperature boundary conditions.

Figure 4.7 illustrates the behavior of the design methods during iteration for constant wall temperatures. In the iteration, the heat flux is guessed, the heat transfer coefficient is computed using this guess, then the heat flux is calculated from the heat transfer coefficient and known wall temperature. If the heat fluxes are the same, the calculation ends. Otherwise, the newly calculated heat flux is used as a new guess and so on. The figure plots the behavior of the solution as the heat flux is guessed and calculated. In the plot, the iterations converge when the 45° line is reached.

Table 4.2. SUMMARY OF EVAPORATOR CALCULATIONS					
Regime	Wall Heat Transfer	Fluid Heating/ Vapor Generation	Void Fraction	Pressure* Drop	Friction Factor ( $2\phi$ Multiplier)
Single-Phase	Dittus-Boelter	Energy Balance (No vapor)	-	$1\phi$	Colebrook
Partially-Developed Boiling	Gungor & Winterton	Energy Balance (No vapor)	-	$1\phi$	Colebrook
Fully-Developed Boiling	Gungor & Winterton	Energy Balance & Gregoria-Merlini	Homogenous $2\phi$	Homogenous $2\phi$	McAdams- Colebrook
Saturated Boiling	Gungor & Winterton	Energy Balance (All Vapor)	Annular $2\phi$	Annular $2\phi$	Wallis- Colebrook
*Srinevasan et al. Correction Applied for Coiled Tubes					

Table 4.3. SUMMARY OF TRANSITION CALCULATIONS			
From	To	Transition	Model
Single-Phase	Partially-Developed Boiling	ONB Transition	Davis-Anderson
Partially-Developed Boiling	Fully-Developed Boiling	OSV Transition	Saha-Zuber
Fully-Developed Boiling	Saturated Boiling	Saturation	$T_f = T_{sat}$
Any Regime	Post-CHF	Critical Heat Flux	Shah

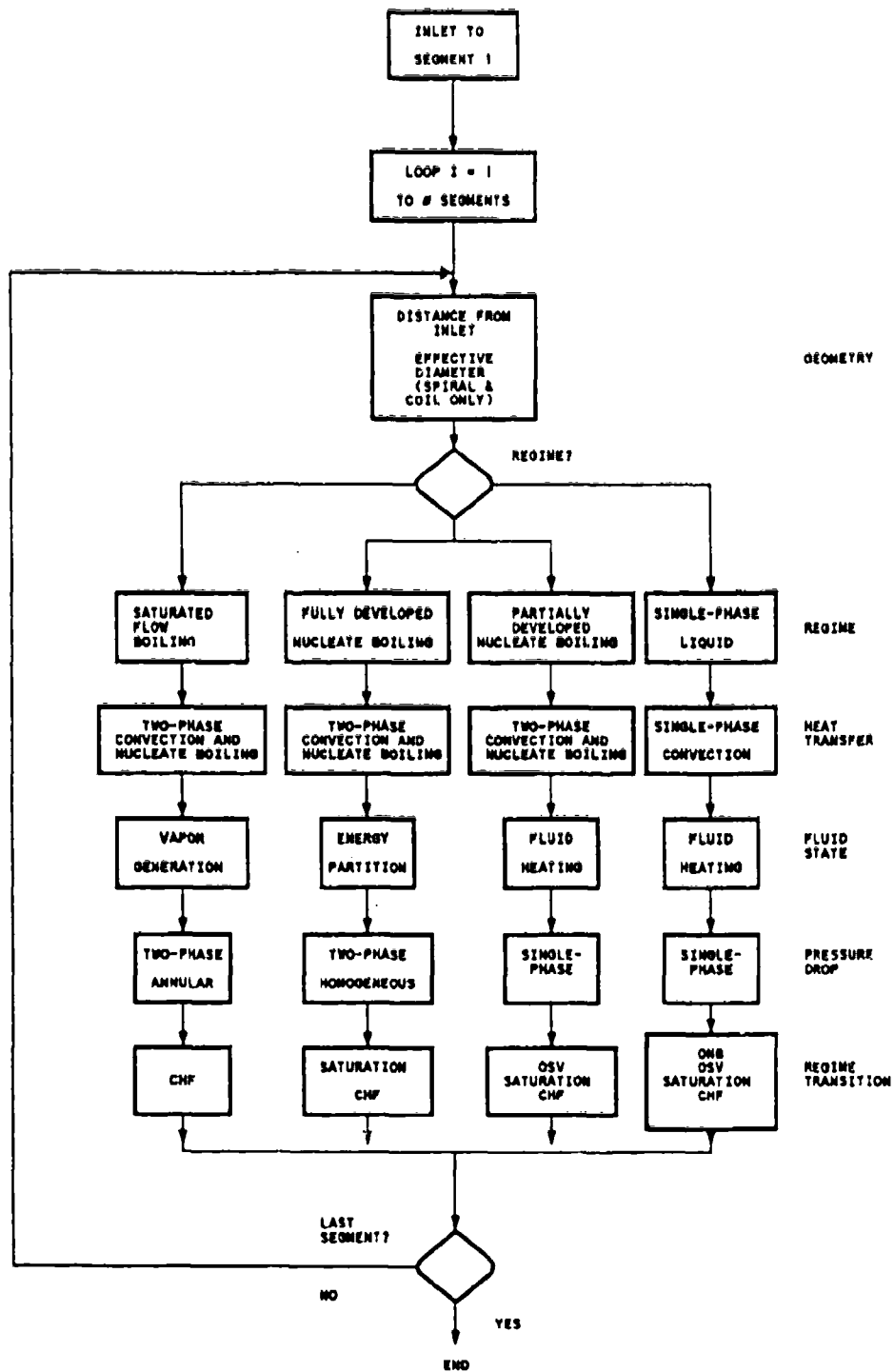
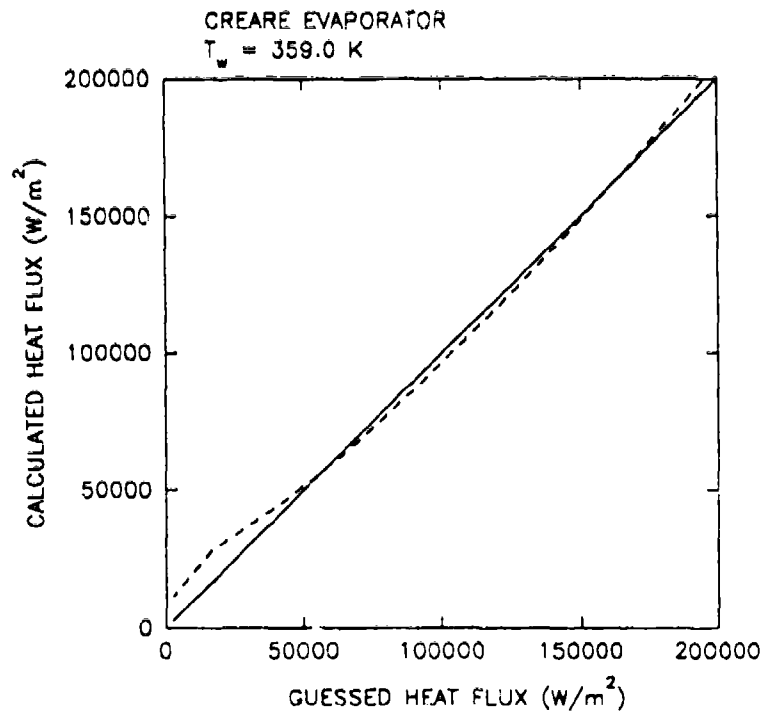
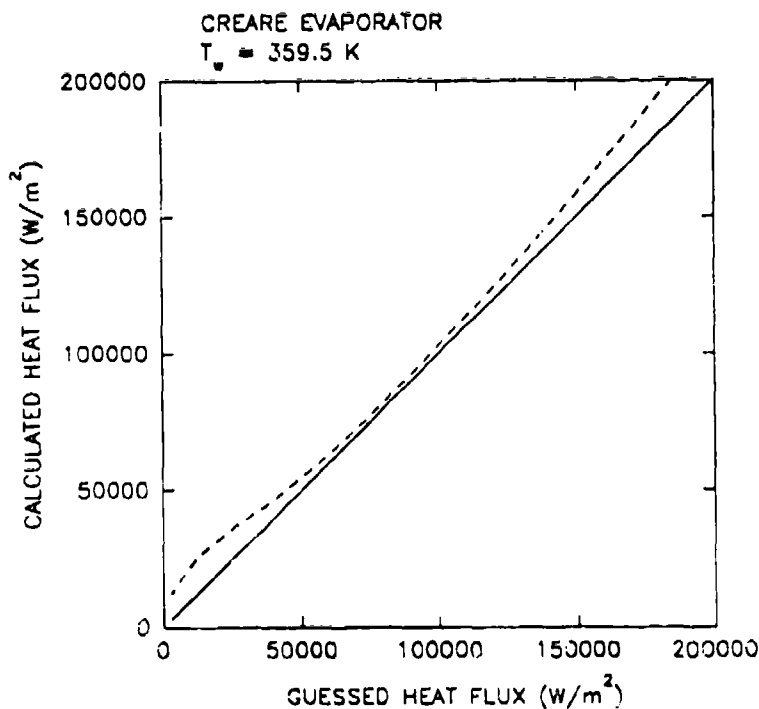


Figure 4.6. FLOWCHART FOR EVAPORATOR CALCULATIONS



a)  $T_w = 359.0 \text{ K}$ : Converges at  $q'' = 5.5 \times 10^4 \text{ W/m}^2$



b)  $T_w = 359.5 \text{ K}$ : No Convergence

Figure 4.7. EXAMPLE OF ITERATION BEHAVIOR FOR CONSTANT WALL TEMPERATURE BOUNDARY CONDITION (R-11 Fluid,  $T_{\text{sat}} = 351 \text{ K}$ )

The two examples of Figure 4.7 indicate the strong sensitivity of the heat flux on the wall temperature. Small changes in wall temperature result in large changes in heat flux. The plot also shows the uncertainty involved. The computed heat flux depends strongly on the convergence criterion selected, and the solution may not be single-valued. It is also easy to specify a wall temperature that will not result in a convergent solution.

For these reasons, the constant wall temperature boundary condition should be used cautiously. The results should be carefully reviewed, and sensitivity of the results should be checked for each case. For some situations, the problem can be reasonably recast into constant heat flux form.

**Flow Boundary Conditions.** The flow boundary conditions are set at the inlet to the evaporator. These consist of the inlet pressure, mass flux, and the inlet temperature or quality. For subcooled inlet flow, the temperature is specified (quality and void fraction are zero). For two-phase inlet flow, the methods use the specified inlet quality to compute the corresponding void fraction. The temperature is set to saturated conditions. Note that the methods assume that the flow is in the saturated boiling regime (annular flow) if the inlet quality is nonzero.

#### 4.3.2 Segment Calculations

In each segment of the evaporator, a sequence of six calculations, is performed:

- 1.) Geometry parameters,
- 2.) Regime,
- 3.) Heat transfer,
- 4.) Fluid state,
- 5.) Pressure drop, and
- 6.) Regime transition.

The following paragraphs outline these calculations.

**Geometry Parameters.** For all evaporator configurations, the distance from the inlet  $z$  is incremented by the length of the segment. In spiral and helical coil configurations, the methods also compute the position of the segment in the coil.

The total number of turns,  $N_t$ , in a spiral coil is:

$$N_t = \frac{L}{\pi(r_i + r_o)} \quad (4-6)$$

where  $L$  is the total tubing length,  $r_i$  is the inner radius of the coil, and  $r_o$  is the outer radius of the coil. (For helical coils,  $r_i = r_o$ , and the equation reduces to the formula for circumference of a circle. Recall that the design methods do not account for wide axial spacing of the helical coils.)

The effective diameter of the coil,  $D_{coil}$ , at any position,  $z$ , depends on the flow direction. The effective diameter is used later in computing a factor that accounts for additional pressure drop in curved tubing. For the inner-to-outer flow direction,

$$D_{coil} = 2 \left[ r_i^2 + \frac{(r_o - r_i)z}{\pi N_t} \right]^{0.5} \quad (4-7)$$

and for the outer-to-inner flow direction,

$$D_{\text{coil}} = 2 \left[ r_o^2 - \frac{(r_o - r_i)z}{\pi N_t} \right]^{0.5} \quad (4-8)$$

**Heat Transfer/Flow Regime.** The heat transfer/flow regime for the current segment is determined by the inlet conditions for that segment, i.e., the outlet of the previous segment or the inlet to the evaporator. The appropriate calculation sequences for heat transfer, fluid state, and pressure drop are selected based on this regime. Regime transitions that occur in the current segment set the inlet regime for the next segment.

**Heat Transfer.** The wall temperature or wall heat flux is calculated using heat transfer coefficient models and correlations for the appropriate regime. For the single-phase regime, the Dittus-Boelter (1930) correlation is used. For all other regimes the Gungor-Winterton (1986) model is applied, with appropriate definitions of the parameters. Section 4.4 presents the detailed equations for these calculations.

For constant wall heat flux boundary conditions, the heat transfer coefficient may be calculated directly. In constant wall temperature cases, the iteration scheme outlined in Section 4.3.1 is required.

**Fluid State, Quality, and Void Fraction.** For segments operating in the single-phase and PDB regimes, the design methods calculate the increase in fluid temperature based on the heat flux for the segment, its length, and its heated perimeter. For the FDB regime, the energy partition, fluid temperature increase, and vapor generation are calculated. Vapor generation alone is computed for segments operating in the saturated boiling regime. The void fraction at the end of the segment is computed using the appropriate flow regime model. Section 4.5 gives the equations for fluid state, quality, and void fraction in each regime.

**Pressure Drop.** The pressure drop calculations for each segment include the contributions of friction, acceleration, and body forces (i.e., gravity):

$$\Delta P_{\text{evap}} = \Delta P_f + \Delta P_a + \Delta P_g \quad (4-9)$$

In spacecraft applications the pressure drop due to friction is usually the largest. For single-phase and PDB regimes, single-phase friction factors are used to calculate  $\Delta P_f$ . The FDB regime uses a homogeneous model, and the saturated boiling regime implements an annular flow model. The acceleration term results from the density decrease and velocity increase that occurs in evaporators due to phase change. It will be most significant when the vapor generation rate is large. The body force term depends on the acceleration magnitude and direction.

**Regime Transitions.** Transitions between heat transfer/flow regimes are checked at the exit conditions of each segment to determine the appropriate regime for the following segment. Table 4.3 lists the regime transitions considered in the design methods.

The methods account for regime transitions in one direction only. That is, the methods properly track the transitions from single-phase to subcooled boiling to saturated boiling, but they do not follow potential reverse transitions such as PDB to single-phase. Such situations would most likely occur for evaporators with nonuniform heat flux profiles. For instance, an evaporator with a very large heat flux near the inlet, then a very low heat flux through the

remainder of the evaporator, the flow could conceivably transition to PDB, then back to single-phase convection. In general, this type of behavior would occur only within a narrow range of operating conditions and is not considered by the design methods.

The methods do allow more than one transition to occur within a single segment. The flow could pass from single-phase to saturated boiling within one segment length, for example. Generally, however, the segments in most actual calculations are short enough to prevent skipping of regimes.

Section 4.7 details the equations for the regime transition models.

### 4.3.3 Calculation of Entire Evaporator Tube

Calculation of the entire evaporator tube consists of the sequential calculation of each of the segments, proceeding from the inlet to the exit of the evaporator. Conditions in the first segment are known from the evaporator inlet conditions and will usually be single-phase liquid at a known pressure and subcooling. Exit conditions calculated for one segment become the inlet conditions for the next. When the segment calculations are complete, the results include profiles for:

- Fluid temperature,
- Saturation temperature,
- Wall temperature,
- Pressure,
- Quality, and
- Void fraction.

Overall evaporator parameters such as pressure drop can be calculated from the inlet and exit conditions or by integrating the segment results.

## 4.4 Heat Transfer Coefficients

The heat transfer coefficient is calculated using models which depend on the local heat transfer/flow regime.

### 4.4.1 Single Phase Convection

The evaporator wall temperature and heat flux in the single-phase regime are related by the single-phase heat transfer coefficient,  $h_{fc}$ :

$$q'' = h_{fc} (T_w - T_f) \quad (4-10)$$

For turbulent flow, the Dittus-Boelter equation (Collier, 1981) yields the heat transfer coefficient:

$$h_{fc} = 0.023 (k_l / D_i) (GD_w / \mu_l)^{0.8} (Pr_l)^{0.4} \quad (4-11)$$

where  $k_l$  is the thermal conductivity of the liquid and  $Pr_l$  is the Prandtl number of the liquid ( $Pr_l = \mu_l c_{pl} / k_l$ ).



#### 4.4.2 Partially-Developed Subcooled Boiling

A single heat transfer correlation is used for all three of the boiling heat transfer regimes. Changes in the definition of the temperature difference are used to account for differences in the driving forces in each regime. The correlation (Gungor and Winterton, 1986) is based on the superposition approach described in Section 4.2. Forced convection and nucleate boiling heat transfer coefficients are combined using correlated enhancement and suppression factors.

The general relation for heat transfer in flow boiling is:

$$q'' = E h_{fc} (T_w - T_f) + S h_{nb} (T_w - T_{sat}) \quad (4-12)$$

where  $E$  is the enhancement factor and  $S$  is the suppression factor. The forced convection heat transfer coefficient is computed from:

$$h_{fc} = 0.023 \left[ \frac{k_l}{D_h} \right] \left[ \frac{GD_h(1-x)}{\mu_l} \right]^{0.8} (Pr_l)^{0.4} \quad (4-13)$$

where  $x$  is the local quality. The nucleate boiling heat transfer coefficient is based on a pool boiling correlation:

$$h_{nb} = 55 P_r^{0.12} \left[ -\log(P_r) \right]^{-0.55} MW^{-0.5} q''^{0.67} \quad (4-14)$$

where  $P_r$  is the reduced pressure ( $P/P_{crit}$ ) and  $MW$  is the molecular weight of the fluid. The heat flux ( $q''$ ) must be expressed in units of  $W/m^2$  and the resulting heat transfer coefficient has units of  $W/m^2 \cdot K$ .

For subcooled boiling (PDB and FDB), the enhancement factor,  $E$ , is equal to 1. The suppression factor,  $S$ , is computed from:

$$S = \frac{1}{1 + 1.15 \times 10^{-6} E^2 \left[ \frac{GD_h(1-x)}{\mu_l} \right]^{1.17}} \quad (4-15)$$

For some applications, buoyancy forces may be important. To account for these, the Froude number,  $Fr$ , is computed by:

$$Fr = \frac{G^2}{a D_h \rho_l^2} \quad (4-16)$$

If  $Fr$  is less than 0.05, then the suppression factor (Equation 4-15) is multiplied by a factor of  $Fr^{0.5}$ .

#### 4.4.3 Fully-Developed Subcooled Boiling

In this regime, the heat transfer coefficient is determined by the same method as for PDB, using Equations 4-12 to 4-15.

#### 4.4.4 Saturated Boiling

The Gungor-Winterton correlation is again used in saturated flow boiling, but some of the parameters are adjusted. The overall heat transfer relationship for saturated boiling is the same as Equation 4-12. Since  $T_f = T_{sat}$ , the equation becomes

$$q'' = (E h_{fc} + S h_{nb}) (T_w - T_{sat}) \quad (4-17)$$

For saturated boiling, the enhancement factor,  $E$ , is calculated by:

$$E = 1 + 24,000 Bo^{1.16} + 1.37(1/X_u)^{0.86} \quad (4-18)$$

where the boiling number,  $Bo$ , and Martinelli parameter,  $X_u$ , are defined as:

$$Bo = \frac{q''}{G h_{fg}} \quad (4-19)$$

$$X_u = \left[ \frac{(1-x)}{x} \right]^{0.9} \left[ \frac{\rho_g}{\rho_l} \right]^{0.5} \left[ \frac{\mu_l}{\mu_g} \right]^{0.1} \quad (4-20)$$

If the Froude number (Equation 4-16) is less than 0.05 and the angle between the flow direction and the acceleration vector is about  $90^\circ$  (i.e., horizontal), the enhancement factor,  $E$ , (Equation 4-18) should be multiplied by this correction factor:

$$Fr^{(0.1 - 2Fr)}$$

The forced convection heat transfer coefficient,  $h_{fc}$ , nucleate boiling heat transfer coefficient,  $h_{nb}$ , and suppression factor,  $S$ , are determined in the same way as for PDB and FDB (Equations 4-13, 4-14, and 4-15, respectively).

#### 4.5 Fluid State, Quality, and Void Fraction

The change in fluid state is calculated using methods which depend on the local flow regime.

##### 4.5.1 Single-Phase Convection

In the single-phase regime all of the heat is absorbed by the liquid as sensible heat. Therefore the temperature rise,  $\Delta T_f$ , in a segment of length  $\Delta z$  is calculated from a simple energy balance:

$$\Delta T_f = \frac{H q'' \Delta z}{G c_{pl} A} \quad (4-21)$$

#### 4.5.2 Partially-Developed Subcooled Boiling

In this regime there is no net vapor generation, so that fluid heating is the same as in the single-phase regime, Equation 4-21.

#### 4.5.3 Fully-Developed Subcooled Boiling

In this regime there is a division of the heat flux between heating of the liquid towards saturation (sensible heat) and vapor generation (latent heat). Gregorio and Merlini (1968) suggest that the fraction of the heat flux,  $E_f$ , which goes to heating the fluid is:

$$E_f = 1 - \left[ 1 + (\rho_l / \rho_g) c_{pl} (T_{sat} - T_f) / h_{fg} \right]^{-1} \quad (4-22)$$

In this case the fluid temperature rise in a segment is:

$$\Delta T_f = \frac{H \Delta z}{G c_{pl} A} E_f q'' \quad (4-23)$$

Note that the bulk fluid temperature will not exceed the saturation temperature,  $T_{sat}$ . Once the liquid reaches  $T_{sat}$ , the heat transfer regime changes to saturated boiling, as discussed below.

In FDB the flow is assumed to be homogeneous, and the void fraction is a simple function of the quality and phase densities:

$$\alpha = \frac{x}{(1-x)(\rho_g / \rho_l) + x} \quad (4-24)$$

where  $x$  is a "pseudo-quality" calculated for the fraction of liquid flow  $(1-E_f)$  which is assumed to be saturated:

$$x = \frac{H(z - z_{fdb})(1-E_f)}{G A h_{fg}} q'' \quad (4-25)$$

#### 4.5.4 Saturated Boiling

In this regime, all of the heat flux generates vapor and increases the quality of the two-phase mixture. The change in quality,  $\Delta x$ , in a segment of length of  $\Delta z$  is:

$$\Delta x = \frac{H q'' \Delta z}{G h_{fg} A} \quad (4-26)$$

The flow regime in saturated boiling is assumed to be annular. If the interfacial shear ratio,  $f_i / f_{wg}$ , is known, the void fraction is related to the quality in annular flow by:

$$\left[ \frac{1-x}{x} \right]^2 = \left[ \frac{\rho_l}{\rho_g} \right] \left[ \frac{(1-\alpha)^2}{\alpha^{2.5}} \right] (f_i / f_{wg}) \quad (4-27)$$

This equation can be solved iteratively for the void fraction if an expression for  $f_i/f_{wg}$  is known. Wallis (1969) recommends the following expression for the shear ratio in annular flow:

$$f_i/f_{wg} = [1 + 75(1-\alpha)] \quad (4-28)$$

Note also that the equation used to compute  $\alpha$  (4-27) is valid only for constant friction factor  $f_{wl}$ .

## 4.6 Pressure Drop

This section presents pressure drop equations which can be used in detailed computer calculations. Most of the pressure drop occurs in the annular flow regime with saturated boiling. Here we use a separated flow model to calculate pressure losses. Homogeneous flow is assumed for the less important FDB regimes. Further information is available in Collier (1981) or Wallis (1969). Kakac (1988) has shown that this method works well for boiling systems on Earth. Figure 4.6 shows a scheme for calculating the pressure losses during the detailed heat transfer computation. Equations are provided for friction, body force and fluid acceleration pressure drops in the various heat transfer regimes of an evaporator tube.

### 4.6.1 Single-Phase Convection

Frictional component. The basic equation for the pressure drop in a segment due to wall friction is:

$$\Delta P_{fe} = f_{wl} (4/D_h) (G^2/2\rho_l) \Delta z \quad (4-29)$$

in which  $f_{wl}$  is a friction factor,  $(4/D_h)$  is the perimeter to area ratio, and  $(G^2/2\rho_l)$  is the kinetic energy per unit volume of the fluid. The friction factor,  $f_{wl}$ , depends on the liquid-only Reynolds number:

$$Re_l = \frac{GD_h}{\mu_l} \quad (4-30)$$

For  $Re_l$  less than 1500, the flow is laminar and the friction factor is calculated by:

$$f_{wl} = \frac{16}{Re_l} \quad (4-31)$$

Generally, flows in practical evaporators have large Reynolds numbers and are turbulent. If  $Re_l$  is greater than 1500, the flow is considered turbulent, and the friction factor is determined by solution of the Colebrook-White equation (1939):

$$\left[ \frac{1}{f_{wl}} \right]^{0.5} = -4.0 \log_{10} \left[ \frac{\epsilon_r/D_h}{3.7} + \frac{1.255}{Re_l} \left[ \frac{1}{f_{wl}} \right]^{0.5} \right] \quad (4-32)$$

where  $\epsilon_r$  is the wall roughness.

**Acceleration component.** In single-phase flow, no vapor is generated, and acceleration effects are negligible ( $\Delta P_{ae} = 0$ ).

**Body force component.** The pressure loss due to body forces depends on the acceleration magnitude and direction. For single-phase flow, the "gravitational" loss term is:

$$\Delta P_{ge} = - \rho_l a \cos \theta \Delta z \quad (4-33)$$

where  $a$  is the acceleration magnitude and  $\theta$  is the angle between the acceleration vector and flow direction.

#### 4.6.2 Partially-Developed Subcooled Boiling

In PDB, no vapor generation is considered, and the methods for single-phase flow (Equations 4-29 to 4-33) apply

#### 4.6.3 Fully-Developed Subcooled Boiling

**Frictional component.** For two-phase flow, the expression for single-phase friction loss (Equation 4-29) is modified for two-phase flow as follows:

$$\Delta P_{fe} = f_{wi} \phi^2 (1-x)^2 (4/D_b) (G^2/2\rho_l) \Delta z \quad (4-34)$$

Now the friction factor and kinetic energy terms are calculated as if the flow were single-phase liquid. Two-phase effects are lumped into  $\phi^2$ , which is the *two-phase multiplier*. The value of  $\phi^2$  depends on the fluid properties, the quality and the flow regime as described below.

In the FDB heat transfer regime, a homogeneous flow model is recommended to estimate the pressure drop. This model assumes that the liquid and vapor have the same velocity and that the two-phase fluid properties can be estimated by a quality-weighted average of the liquid and vapor properties.

McAdams (1942) recommends this value for the two-phase multiplier based upon a quality-weighted viscosity for the two-phase fluid:

$$\phi^2 = \left[ 1 + x \left( \frac{\rho_l}{\rho_g} - 1 \right) \right] \left[ 1 + x \left( \frac{\mu_l}{\mu_g} - 1 \right) \right]^{-1/4} \quad (4-35)$$

The friction factor is calculated as for single-phase liquid flow.

**Acceleration component.** Appreciable vapor is generated in FDB, resulting in an acceleration pressure loss as the flow velocity increases. From Collier (1981), the acceleration loss for homogeneous two-phase flow in a segment is:

$$\Delta P_{ae} = G^2 \left[ \frac{1}{\rho_g} - \frac{1}{\rho_l} \right] \Delta x \quad (4-36)$$

where  $\Delta x$  is the change in quality over the length of the segment.

**Body force component.** The basic equation for the pressure drop in a segment due to body forces is:

$$\Delta P_{ge} = - [ \alpha \rho_g + (1-\alpha) \rho_l ] a \cos \theta \Delta z \quad (4-37)$$

where  $\alpha$  is the void fraction calculated with Equation 4-24. (The pressure drop is positive when the inlet pressure is greater than the outlet pressure.)

#### 4.6.4 Saturated Boiling

**Frictional component.** This heat transfer regime is characterized by annular flow, and the two-phase multiplier is (Collier, 1981):

$$\phi^2 = \frac{1}{(1-\alpha)^2} \quad (4-38)$$

where  $\alpha$  is the local void fraction. Note that this expression for  $\phi^2$  differs from that used for FDB. In FDB, a homogeneous model is used where the phase velocities of the gas and liquid are equal. In the annular flow model used here, the phase velocities are not equal, with the gas flowing in a high speed core inside an annular liquid film. This fundamental difference in the flow regime causes much larger pressure drops and analysis yields the expression for  $\phi^2$  given in Equation 4-38.

Combining the annular flow multiplier with Equation 4-34, the pressure drop due to friction in a short tube segment of length  $\Delta z$  can be calculated using this expression:

$$\Delta P_{fe} = \frac{f_w}{(1-\alpha)^2} (1-x)^2 (4/D_b) (G^2/2\rho_l) \Delta z \quad (4-39)$$

**Acceleration component.** The basic equation for pressure gradient due to fluid acceleration is (Collier, 1981):

$$(dP/dz)_a = - G^2 \frac{d}{dz} \left[ \frac{x^2}{\alpha} \frac{1}{\rho_g} + \frac{(1-x)^2}{(1-\alpha)} \frac{1}{\rho_l} \right] \quad (4-40)$$

Thus the pressure drop in a pipe segment due to fluid acceleration is:

$$\Delta P_a = G^2 \Delta \left[ \frac{x^2}{\alpha} \frac{1}{\rho_g} + \frac{(1-x)^2}{(1-\alpha)} \frac{1}{\rho_l} \right] \quad (4-41)$$

where the symbol " $\Delta$ " is used to represent the value of the bracketed quantity at the tube exit minus the value at the inlet. (Once again, the pressure drop is positive when the pressure gradient is negative.) The pressure drop is independent of the segment length and depends only on the fluid quality and void fraction at the inlet and outlet of the segment.

**Body force component.** For the body force term in saturated boiling, the same equation is applied as for the FDB regime, Equation 4-37.

#### 4.6.5 Correction Factor for Curved Tubes

A correction factor is applied to the friction pressure loss component to account for the behavior in curved tubes, i.e., spiral coils and helical coils, so that:

$$\Delta P_{\text{coil}} = f_{\text{coil}} \Delta P_{fe} \quad (4-42)$$

where  $\Delta P_{fe}$  is the frictional pressure drop neglecting the effects of coiling,  $\Delta P_{\text{coil}}$  is the pressure drop including the coiling effect, and  $f_{\text{coil}}$  is the correction factor.

To calculate  $f_{\text{coil}}$  for turbulent flow, the following equation is used (Srinevasan et al., 1968):

$$f_{\text{coil}} = \left[ \text{Re}_l \left( \frac{D_{\text{coil}}}{D_u} \right)^2 \right]^{0.05} \quad (4-43)$$

which is valid for:

$$\text{Re}_l \left( \frac{D_{\text{coil}}}{D_b} \right)^2 > 6$$

#### 4.7 Regime Transitions

The three key regime transitions (ONB to OSV to saturated boiling) occur when the calculated fluid or wall temperatures reach critical values. The possible transition to critical heat flux is calculated using Shah's correlation (1987).

##### 4.7.1 Onset of Nucleate Boiling

The single-phase heat transfer regime ends when the wall temperature reaches a critical value,  $T_{\text{wobn}}$ , at which vapor bubble nucleation and subcooled nucleate boiling begins. The correlation of Davis and Anderson (1966) is recommended:

$$T_{\text{wobn}} = T_{\text{sat}} + \left[ \frac{8 \sigma q'' T_{\text{sat}}}{h_{fg} k_l \rho_g} \right]^{1/2} \quad (4-44)$$

The correlation of Frost and Dzakowic (1967), which is identical except that the second term is multiplied by  $\text{Pr}_l^{1/3}$ , is an alternate choice.

##### 4.7.2 Onset of Significant Voiding

Saha and Zuber (1974) recommend a model for the transition from partially to fully developed subcooled boiling (PDB to FDB). This model expresses the fluid subcooling at the transition as a function of the heat flux:

$$(T_{\text{sat}} - T_f)_{\text{fdb}} = (0.0022) q'' D_b / k_l \quad (4-45)$$

(when  $Re_l Pr_l < 70,000$ ), or

$$(T_{\text{sat}} - T_f)_{\text{fdb}} = (153.8) \frac{q''}{Gc_{pl}} \quad (4-46)$$

(when  $Re_l Pr_l \geq 70,000$ )

#### 4.7.3 Bulk Saturated Conditions

The FDB regime ends when saturated flow boiling begins, as indicated by:

$$T_f = T_{\text{sat}} \quad (4-47)$$

This transition depends on the fluid temperature rather than the flow regime. The design methods also assume a transition from homogeneous to annular flow at this point (see Table 4.1).

To be more precise than this, one could calculate a transition to annular flow based on the local void fraction, and this would represent the transition to two-phase forced convection heat transfer, an event distinct from transition to saturated boiling. However, the transition void fraction is exceeded almost immediately when the two-phase fluid achieves a significant positive quality. So it is acceptably accurate and simpler to assume that the homogeneous flow regime ends (and the annular flow regime begins) when the liquid reaches its saturation temperature.

#### 4.7.4 Critical Heat Flux

Critical heat flux (CHF) describes a condition in which the heat transfer mechanisms of two-phase forced convection and nucleate boiling have reached their limit. At higher heat fluxes the physical processes responsible for efficient heat transfer break down, the heat transfer coefficient becomes dramatically smaller, and the wall temperatures become correspondingly much larger. The wall temperatures may rise to such a degree that actual damage to the evaporator material results. This is why CHF is sometimes termed burnout.

CHF may occur under either single-phase or two-phase conditions, hence it provides an upper limit on evaporator performance regardless of the flow or heat transfer regime. Many aspects of CHF are still incompletely understood. Measurement and correlation of CHF behavior continues. The uncertainty in CHF prediction is substantial, and the designer should provide significant safety margins for most evaporator applications.



The Shah CHF correlation (1987) is recommended for predicting CHF. This correlation has the advantage of applying over a broad range of fluids and operating conditions. Its key disadvantage is that it does not consider body forces. The dependence of CHF on acceleration for flow boiling, however, is not well known at this time, and comprehensive correlations considering this effect are not yet available.

The Shah correlation is based on a two part approach: an upstream conditions correlation (UCC) and a local conditions correlation (LCC). Its application begins by computing a number of parameters. First, the Peclet number,  $Pe$ , is:

$$Pe = \frac{GD_h c_{pl}}{k_l} \quad (4-48)$$

where  $c_{pl}$  is the specific heat of the liquid. Next, an entrance effect factor is calculated:

$$F_e = 1.54 \cdot 0.032 \frac{z}{D_h} \quad (4-49)$$

where  $z$  is the distance from the inlet. If the value of  $F_e$  calculated by Equation 4-49 is less than 1, then  $F_e$  is set equal to 1. Following this, the boiling number,  $Bo$  (Equation 4-19), and Shah's correlating parameter,  $Y$ , are calculated:

$$Y = Pe F_e^{0.4} \left( \frac{\mu_l}{\mu_g} \right)^{0.6} \quad (4-50)$$

where  $\mu_l$  and  $\mu_g$  are the liquid and gas viscosities respectively.

Next, the effective inlet quality,  $x_{ief}$ , and effective distance from the inlet,  $z_{eff}$ , are calculated. For subcooled liquid at the inlet, the expressions for these are:

$$x_{ief} = - \frac{(T_{sat} - T_f) c_{pl}}{h_{fg}} \quad (4-51)$$

$$z_{eff} = z \quad (4-52)$$

For a two-phase mixture at the inlet of quality,  $x_{in}$ , the values are:

$$x_{ief} = 0 \quad (4-53)$$

$$z_{eff} = z + \frac{x_{in} A}{Bo H} \quad (4-54)$$

For the UCC, the critical heat flux,  $q''_{ucc}$ , is calculated by:

$$q''_{ucc} = 0.124 \left[ \frac{D_h}{z_{eff}} \right]^{0.89} \left[ \frac{10^4}{Y} \right]^n (1 - x_{ief}) G h_{fg} \quad (4-55)$$

where  $n$  is an exponent that depends on  $Y$ . For  $Y < 10^4$ ,  $n = 0$ . For  $10^4 \leq Y \leq 10^6$ ,

$$n = \left[ \frac{D_h}{z_{eff}} \right]^{0.54} \quad (4-56)$$

and for  $Y > 10^6$ ,

$$n = \frac{0.12}{(1 - x_{ief})^{0.5}} \quad (4-57)$$

The LCC value of the CHF is calculated by the following equation:

$$q''_{lcc} = F_e F_x Bo_o G h_{fk} \quad (4-58)$$

where  $F_e$  is the entrance effect factor (Equation 4-49),  $F_x$  is a quality factor, and  $Bo_o$  is the boiling number at  $x = 0$ .

The quality factor is calculated by the following equation for a two-phase mixture ( $x$  greater than 0):

$$F_x = F_3 \left[ 1 + \frac{(F_3^{-0.29} - 1)(P_r - 0.6)}{0.35} \right]^c \quad (4-59)$$

where

$$c = \begin{cases} 0 & \text{for } P_r \leq 0.6 \\ 1 & \text{for } P_r > 0.6 \end{cases}$$

$$F_3 = \left[ \frac{1.25 \times 10^5}{Y} \right]^{0.833x} \quad (4-60)$$

$$P_r = \text{critical pressure-ratio, } P/P_{crit}$$

For subcooled liquid ( $x < 0$ ), the following expression is used for  $F_x$ :

$$F_x = F_1 \left[ 1 - \frac{(1 - F_2)(P_r - 0.6)}{0.35} \right]^b \quad (4-61)$$

where

$$b = \begin{cases} 0 & \text{for } P_r \leq 0.6 \\ 1 & \text{for } P_r > 0.6 \end{cases}$$

$$F_1 = 1 + 0.0052(-x^{0.88})Y^{0.41} \quad \text{for } Y \leq 1.4 \times 10^7$$

$$F_1 = 1 + 4.425(-x^{0.88}) \quad \text{for } Y > 1.4 \times 10^7$$

$$F_2 = F_1^{-0.42} \quad \text{for } F_1 \leq 4$$

$$F_2 = 0.55 \quad \text{for } F_1 > 4$$

The criteria for selecting which of the correlations (UCC or LCC) to use is:

- $Y \leq 10^6$  use UCC value ( $q''_{CHF} = q''_{UCC}$ ),
- $Y > 10^6$  use the smaller of the two values  
( $q''_{CHF} = q''_{UCC}$  or  $q''_{LCC}$ ).

If the operating heat flux,  $q''$ , exceeds the predicted critical heat flux,  $q''_{CHF}$ , the evaporator may transition to post-CHF heat transfer and flow regimes (e.g., film boiling) that are much less efficient. The result may be large wall temperatures and possible evaporator failure.

#### 4.8 Scoping Calculations and Dimensionless Design Charts

This section presents methods for scoping calculations of the evaporator size, heat transfer, and pressure drop. It is assumed that the heat flux and the fluid conditions at the inlet are known and that the primary design goals are to achieve a desired fluid exit quality and to ensure operation independent of spacecraft acceleration. The basic procedure to meet these objectives is:

- Estimate the evaporator tube length,
- Estimate the forced convection fraction,
- Check the significance of body forces,
- Check the design for maximum heat flux and tube wall temperature, and
- Estimate the pressure drop.

Saturated boiling with annular flow is the dominant regime in an evaporator tube if the inlet subcooling of the fluid is only a few degrees. The following discussion assumes that this regime dominates the evaporator behavior. We also assume that the heat flux can be specified. For detailed design all of the heat transfer regimes must be treated explicitly, and the detailed analysis presented in Sections 4.4 to 4.7 is recommended.

The information needed in order to perform the scoping calculations includes:

##### Fluid Properties

$\rho_l$	density of liquid phase (kg/m <sup>3</sup> )
$\mu_l$	viscosity of liquid phase (kg/m-s)
$c_{pl}$	specific heat of liquid phase (J/kg-K)
$k_l$	thermal conductivity of the liquid (W/m-K)
$\rho_g$	density of vapor phase (kg/m <sup>3</sup> )
$\mu_g$	viscosity of vapor phase (kg/m-s)
$h_{fg}$	latent heat of evaporation (J/kg)
$P_{crit}$	critical pressure (Pa)
MW	molecular weight of fluid (kg/kg-mole)

### Operating Conditions

$q''$	heat flux (W/m <sup>2</sup> )
$T_{\text{sat}}$	saturation temperature (K)
$\Delta T_{\text{sub}}$	inlet subcooling (K)
$G$	mass flux (kg/m <sup>2</sup> -s)
$P$	evaporator absolute pressure (Pa)
$x_o$	evaporator outlet quality (-)
$a$	acceleration magnitude (m <sup>2</sup> /s)
$\theta$	angle between acceleration vector and flow direction (-)

### Geometry

$H$	tube heated perimeter (m)
$A$	cross-sectional flow area (m <sup>2</sup> )

#### 4.8.1 Evaporator Tube Length

Figure 4.8 is a universal design map (independent of heat transfer regime) that shows the required evaporator tube length in terms of the desired change in fluid quality and an evaporator thermodynamic ratio,  $R_{\text{ev}}$ , which is proportional to the heat flux divided by the mass flux. A compact evaporator has a large thermodynamic ratio. Unfortunately, this competes with design requirements for forced-convection dominance and low pressure drops. The optimum  $R_{\text{ev}}$  comes from a tradeoff between these objectives.

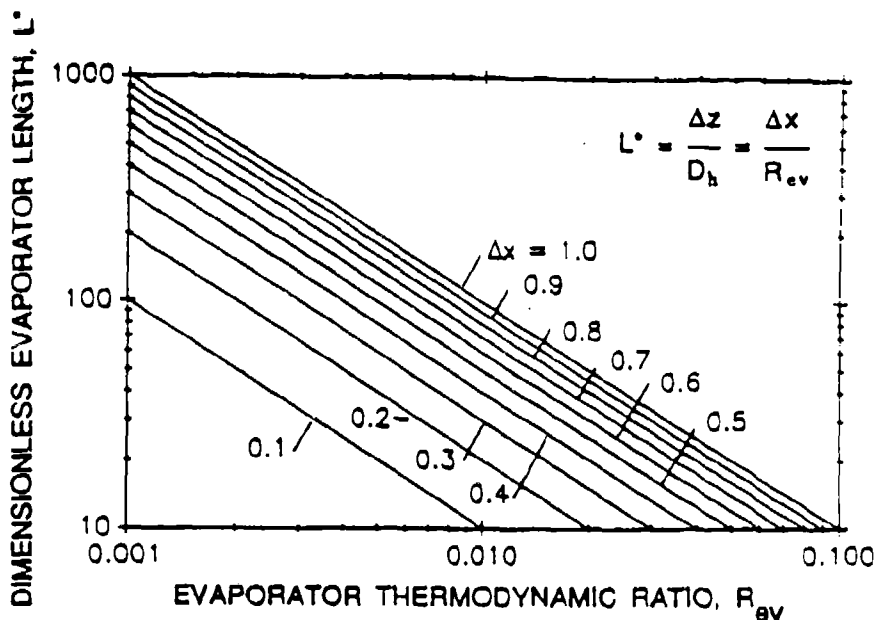


Figure 4.8. DESIGN CHART FOR EVAPORATOR TUBE LENGTH

The procedure to use this map includes three steps as described below.

- 1.) First, calculate the thermodynamic ratio,  $R_{ev}$ , for the evaporator:

$$R_{ev} \equiv \frac{4q''}{Gh_{fg}} \quad (4-62)$$

where  $q''$  is the heat flux,  $G$  is the mass flux, and  $h_{fg}$  is the latent heat of vaporization.

- 2.) Next, determine the change in fluid quality,  $\Delta x$ , that the evaporator is to produce. The inlet subcooling and exit quality, and thus the change in quality within the evaporator, are determined as part of the overall system design. If fluid enters the evaporator with a subcooling,  $\Delta T_{sub}$ , and is to exit with a quality  $x_o$ , then the change in enthalpy is:

$$\Delta h = c_{pl}\Delta T_{sub} + x_o h_{fg} \quad (4-63)$$

The change in quality in the evaporator is calculated by:

$$\Delta x \equiv \Delta h / h_{fg} \quad (4-64)$$

- 3.) Select the line which corresponds to  $\Delta x$  in Figure 4.8 and locate the point with the abscissa  $R_{ev}$ . The value of the ordinate at this point is the dimensionless tube length,  $L^*$ , which will produce the desired exit quality. The required tube length is:

$$L = L^* D_h \quad (4-65)$$

where  $L$  is the tube length (in meters) and  $D_h$  is the hydraulic diameter ( $4A/H$ ).

#### 4.8.2 Forced Convection Fraction

The evaporator design should ensure that forced convection is the dominant heat transfer mechanism. The fraction of heat transfer due to forced convection in the saturated nucleate boiling regime depends on the coolant properties, mass flux, tube hydraulic diameter, heat flux, and quality. The procedures given in this section permit the designer to estimate the forced convection and nucleate boiling heat transfer coefficients, as well as the enhancement and suppression factors. Due to the multivariate character of most of the equations, the calculations are presented primarily in terms of equations rather than design charts.

There are 9 steps to calculate the forced convection fraction:

- 1.) Select a representative fluid quality,  $x$ .
- 2.) Calculate the boiling number,  $Bo$  (Equation 4-66).
- 3.) Calculate the Martinelli parameter,  $X_{tt}$  (Equation 4-67).
- 4.) Calculate the enhancement factor,  $E$  (Equation 4-68).
- 5.) Calculate the two-phase Reynolds number,  $Re_{tp}$  (Equation 4-69).
- 6.) Determine the forced-convection heat transfer coefficient,  $h_{fc}$  (Figure 4.9 and Equation 4-70).
- 7.) Calculate the suppression factor,  $S$  (Equation 4-71).
- 8.) Calculate the nucleate boiling heat transfer coefficient,  $h_{nb}$  (Equation 4-72).
- 9.) Calculate the fraction of the heat transfer due to forced convection,  $E_{fc}$  (Equation 4-73).

These steps are described in more detail below:

1.) Select a representative fluid quality,  $x$ : The average flow quality in the channel will do. This is simply one-half the exit quality.

2.) Calculate the boiling number,  $Bo$ :

$$Bo = \frac{q''}{G h_{fg}} \quad (4-66)$$

3.) Calculate the Martinelli parameter,  $X_{tt}$ :

$$X_{tt} = \left[ \frac{(1-x)}{x} \right]^{0.9} \left[ \frac{\rho_g}{\rho_l} \right]^{0.5} \left[ \frac{\mu_l}{\mu_g} \right]^{0.1} \quad (4-67)$$

4.) Calculate the enhancement factor,  $E$ :

$$E = 1 + 24,000 Bo^{1.16} + 1.37(1/X_{tt})^{0.86} \quad (4-68)$$

5.) Calculate the two-phase Reynolds number:

$$Re_{tp} = \frac{G(1-x)D_h}{\mu_l} \quad (4-69)$$

6.) Determine the forced-convection heat transfer coefficient,  $h_{fc}$ . Use Figure 4.9 and read the value of the Nusselt number for forced convection ( $Nu_{fc}$ ) which corresponds to the two-phase Reynolds number and the liquid Prandtl number ( $Pr_l = \mu_l c_{pl} / k_l$ ). Then calculate the heat transfer coefficient:

$$h_{fc} = \frac{Nu_{fc} k_l}{D_h} \quad (4-70)$$

7.) Calculate the suppression factor,  $S$ :

$$S = \frac{1}{1 + 1.15 \times 10^{-6} E^2 Re_{tp}^{1.17}} \quad (4-71)$$

8.) Calculate the nucleate boiling heat transfer coefficient,  $h_{nb}$ :

$$h_{nb} = 55 P_r^{0.12} [-\log(P_r)]^{-0.55} MW^{-0.5} q''^{0.67} \quad (4-72)$$

where  $P_r$  is the reduced pressure ( $P/P_{crit}$ ) and  $MW$  is the molecular weight.

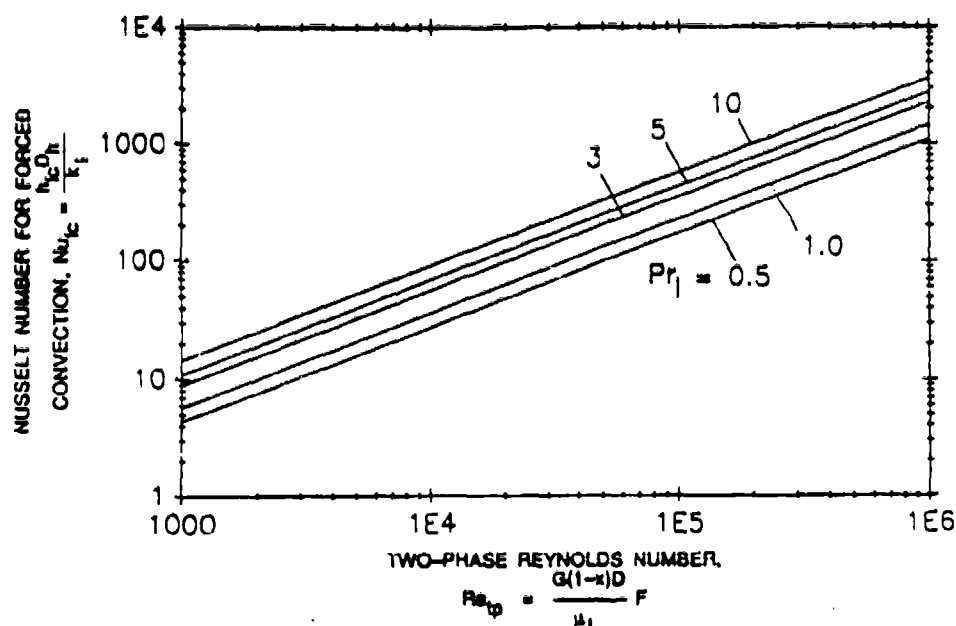


Figure 4.9. DESIGN CHART FOR FORCED CONVECTION HEAT TRANSFER

9.) Calculate the forced convection fraction: The fraction of the heat transfer due to forced convection,  $E_{fc}$ , is:

$$E_{fc} = \left[ \frac{Eh_{fc}}{Eh_{fc} + Sh_{bb}} \right] \quad (4-73)$$

This ratio should be near unity ( $E_{fc} \geq 0.9$ ) for forced convection to dominate.

#### 4.8.3 Significance of Body Forces

For evaporators which are nearly horizontal with respect to gravity (i.e., angle between flow direction and acceleration vector is  $90^\circ$ ), stratification of the flow may affect the heat transfer. As a check, the effect of buoyancy can be evaluated by calculating the Froude number:

$$Fr = \frac{G^2}{a D_b \rho_l^2} \quad (4-74)$$

where  $a$  is the spacecraft acceleration. If the Froude number lies above 0.05, the effect of buoyancy is negligible. This should be the case for well-designed evaporators.

#### 4.8.4

#### Operating Limits

There are two limits which should be checked for evaporator design. One is the critical heat flux and the other is the wall temperature. As noted in Section 4.8.2, the forced convection fraction,  $E_{fc}$ , should also be greater than 0.9 to ensure the acceleration-independence of the heat transfer.

**Wall Temperature.** The evaporator designer may be faced with temperature limits for the tube material or components which are cooled by the evaporator. To estimate the wall temperature, the designer needs the calculated heat transfer coefficients ( $h_{fc}$  and  $h_{nb}$ ) and factors ( $E$  and  $S$ ) calculated in Section 4.8.3 for determining the forced convection fraction. These are used with the heat flux to determine the wall temperature:

$$T_w = T_{sat} + \frac{q''}{Eh_{fc} + Sh_{nb}} \quad (4-75)$$

This estimate of the wall temperature corresponds to the expected wall temperature during stable saturated boiling and should be compared with the material and operating limits. Much higher wall temperatures are associated with the phenomenon of critical heat flux discussed next.

**Critical Heat Flux.** Critical heat flux (CHF) occurs when stable saturated boiling heat transfer (forced convection plus nucleate boiling) reaches its physical limits. Vapor blankets the heating surface, resulting in poor heat transfer and high wall temperatures. In general, the evaporator needs to avoid operating close to CHF to assure heat transfer performance and prevent failure.

For CHF prediction, the Shah (1987) correlation is recommended. The Shah correlation is based on a two part approach: an upstream conditions correlation (UCC) and a local conditions correlation (LCC). Its application is complex, with many equations and conditions to check. In this section a simplified version is presented, with restrictions on the range of parameters. To accommodate situations outside this range of parameters, the designer should consult the full correlation in Section 4.7.4.

To calculate the value of the critical heat flux, the following procedure is followed:

- 1.) Calculate the Peclet number,  $Pe$  (Equation 4-76).
- 2.) Calculate the entrance effect factor,  $F_e$  (Equation 4-77).
- 3.) Calculate Shah's correlating parameter,  $Y$  (Equation 4-78).
- 4.) Calculate effective inlet quality,  $x_{ief}$  (Equation 4-79).
- 5.) Determine the boiling number for UCC,  $Bo_{ucc}$ , graphically (Figure 4.10).
- 6.) Determine the boiling number at zero quality,  $Bo_o$ , graphically (Figure 4.11).
- 7.) Determine the quality factor,  $F_x$ , graphically (Figure 4.12).
- 8.) Calculate the boiling number for LCC,  $Bo_{lcc}$  (Equation 4-80).
- 9.) Select the appropriate correlation and calculate the critical heat flux,  $q''_{CHF}$ , (Equation 4-81).

These steps are described in more detail below.



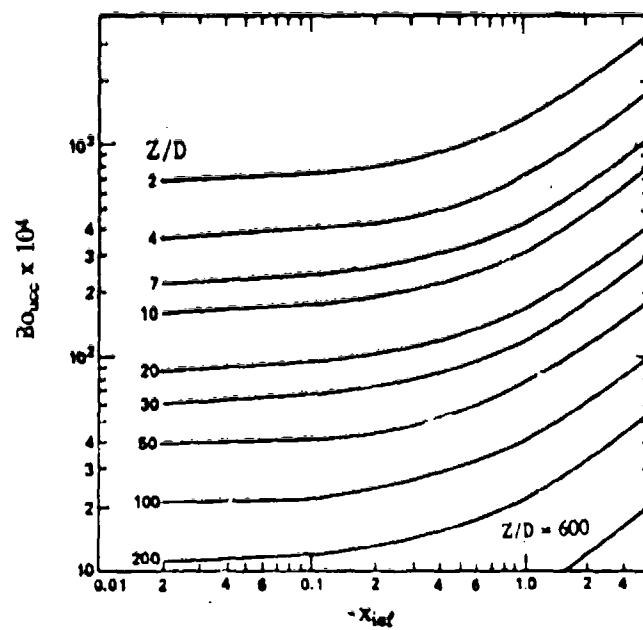


Figure 4.10. DESIGN CHART FOR  $Bo_{ucc}$  (Shah, 1987)

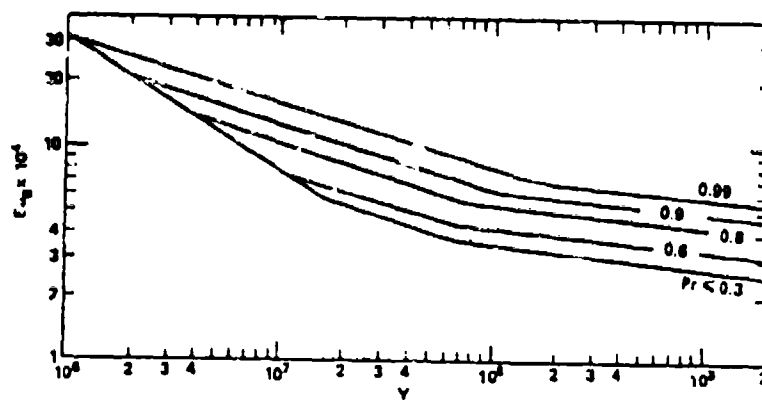
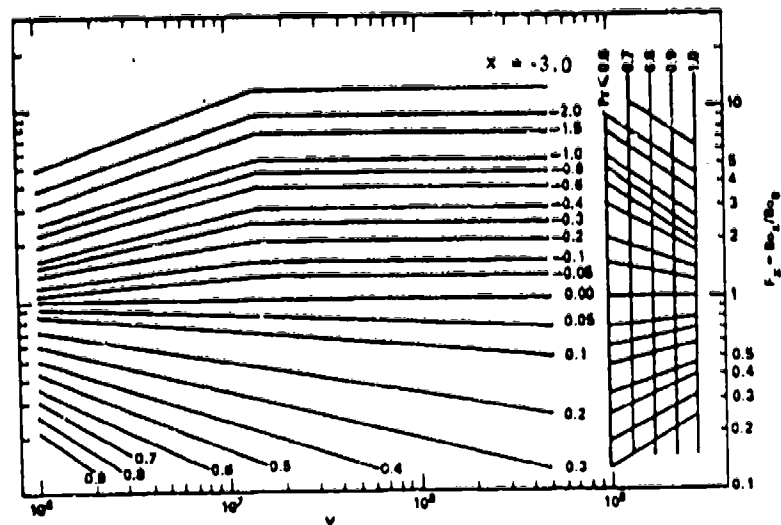


Figure 4.11. DESIGN CHART FOR  $Bo_0$  in LCC (Shah, 1987)

a) Design Chart



b) Examples of Use

Case A:

if  $Y = 10^7$ ,  $x = 0.3$   
 $P_r = 0.8$   
 then  $F_x = 0.42$

Case B:

if  $Y = 2 \times 10^7$   
 $x = -0.4$   
 and  $P_r = 0.7$   
 then  $F_x \approx 2.6$

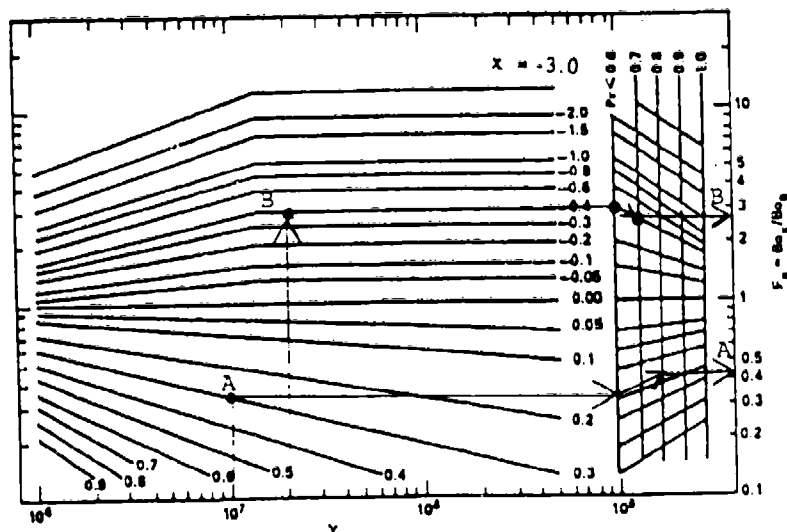


Figure 4.12. DESIGN CHART FOR  $F_x$  IN LCC (Shah, 1987)

- 1.) Calculate the Peclet number  $Pe$ :

$$Pe = \frac{GD_h c_{pl}}{k_l} \quad (4-76)$$

- 2.) Calculate the entrance effect factor:

$$F_e = 1.54 - 0.032 \frac{z}{D_h} \quad (4-77)$$

where  $z$  is the distance from the inlet. If the value of  $F_e$  calculated by Equation 4-77 is less than 1, then  $F_e$  is set equal to 1.

- 3.) Calculate Shah's correlating parameter  $Y$ :

$$Y = Pe F_e^{0.4} \left[ \frac{\mu_l}{\mu_g} \right]^{0.6} \quad (4-78)$$

- 4.) Calculate the effective inlet quality  $x_{ief}$ :

$$x_{ief} = - \frac{(T_{sat} - T_f) c_{pl}}{h_{fg}} \quad (4-79)$$

- 5.) Determine the boiling number for UCC,  $Bo_{ucc}$ , from Figure 4.10. This plot is only valid for  $Y \leq 10^4$ . For larger  $Y$ , the equations of Section 4.7.4 should be consulted.

- 6.) Determine the boiling number at zero quality,  $Bo_o$ , graphically from Figure 4.11.

- 7.) Determine the quality factor,  $F_x$ , graphically from Figure 4.12-a. First determine the ordinate which corresponds to the correlating parameter,  $Y$ , and the local quality,  $x$ , using the left-hand plot. Then modify the ordinate to account for the critical pressure ratio ( $P_r$ ) using the left-hand plot. Figure 4.12-b illustrates the procedure.

- 8.) Calculate the LCC value of the boiling number,  $Bo_{lcc}$ :

$$Bo_{lcc} = F_e F_x Bo_o \quad (4-80)$$

- 9.) Select which of the correlations (UCC or LCC) to use, depending on the value of  $Y$ :

$Y \leq 10^6$	use UCC value ( $Bo_{CHF} = Bo_{ucc}$ ).
$Y > 10^6$	use the smaller of the two values ( $Bo_{CHF} = Bo_{ucc}$ or $Bo_{lcc}$ ).

Calculate the critical heat flux from the definition of the boiling number  $Bo_{CHF}$ :

$$q''_{CHF} = Bo_{CHF} G h_{fg} \quad (4-81)$$

Compare to  $q''_{CHF}$  to the operating heat flux  $q''$ . If  $q''$  exceeds  $q''_{CHF}$ , the evaporator may transition to post-CHF regimes with adverse effects on performance or possible evaporator failure.

#### 4.8.5 Pressure Losses

This section presents design maps to estimate pressure losses in an evaporator tube. These maps assume that the major pressure losses in the tube occur in the saturated flow boiling regime. If there is a very large subcooling at the entrance to the evaporator, then there may be a significant pressure loss in the single-phase liquid regime as well. Single-phase methods can be used if that is the case.

The basic procedure to estimate the evaporator pressure drop is:

- Estimate the pressure drop due to friction in the two-phase region (Figure 4.13 and Equations 4-82 to 4-85).
- Estimate the pressure drop due to body forces in the two-phase region (Figure 4.14 and Equation 4-86).
- Estimate the pressure drop due to fluid acceleration in the two-phase region (Figure 4.15 and Equation 4-87).
- Calculate the total pressure drop in the two-phase region (Equation 4-88).
- Estimate the pressure drop in the single-phase region (Equations 4-89 and 4-90).
- Estimate the total pressure drop in the evaporator (Equation 4-91).

The following sections describe the procedure to obtain a best-estimate calculation for the pressure drop in the evaporator. The main uncertainty in these calculations is the interfacial friction between the liquid and vapor phases in the two-phase forced convection region of the evaporator. The pressure drop can be bounded by choosing high or low values for the interfacial friction.

Friction in the Two-Phase Region. The procedure to calculate the frictional pressure drop is:

- 1.) Calculate the ratio of the liquid phase density to the vapor phase density,  $\rho_l / \rho_g$ .
- 2.) Locate the curve in Figure 4.13 which corresponds to this value of the density ratio and locate the point on the curve which corresponds to the evaporator outlet quality. Call the ordinate on the map at this point  $\Delta P_{fe}^* / 4f_{wl}$ .
- 3.) Calculate  $R_{ev}$ , the thermodynamic ratio of the evaporator:

$$R_{ev} = \frac{4 q''}{G h_{fg}} \quad (4-82)$$

- 4.) Calculate  $f_{wl}$ , the friction factor for liquid-only flow through the evaporator. This friction factor is a function of  $Re_l$ , the Reynolds number for liquid-only flow:

$$Re_l = \frac{GD_b}{\mu_l} \quad (4-83)$$

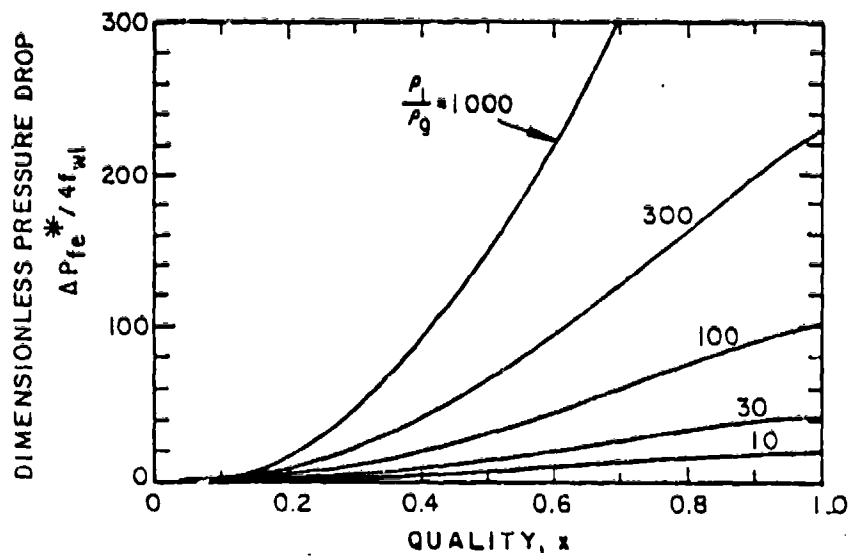


Figure 4.13. DIMENSIONLESS FRICTIONAL PRESSURE DROP IN THE EVAPORATOR

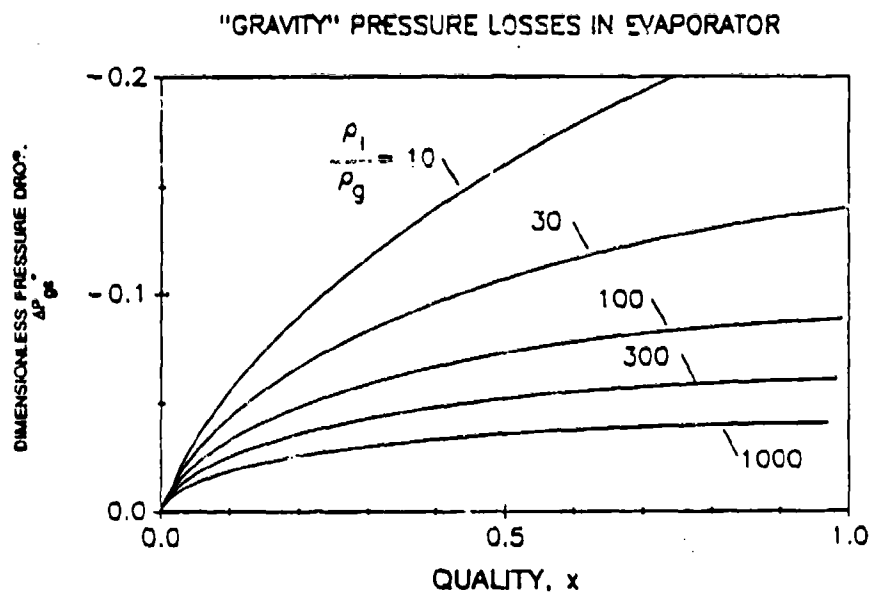
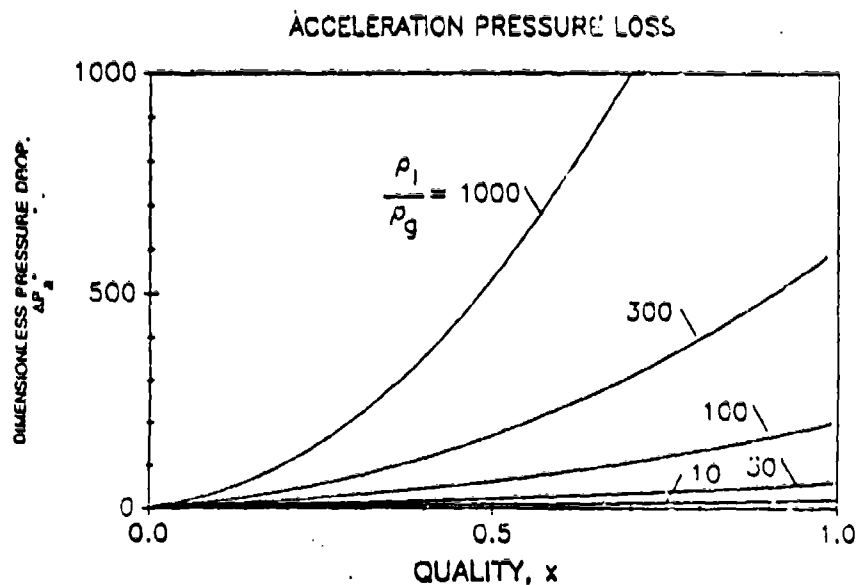


Figure 4.14. DIMENSIONLESS PRESSURE DROP DUE TO BODY FORCES IN THE EVAPORATOR



**Figure 4.15. DIMENSIONLESS PRESSURE DROP DUE TO FLUID ACCELERATION IN THE EVAPORATOR**

The liquid-only friction factor is:

$$f_{wl} = \begin{cases} \frac{16}{Re_1} & \text{for } Re_1 < 1500 \\ 0.046 Re_1^{-0.2} & \text{for } Re_1 \geq 1500 \end{cases} \quad (4-84)$$

5.) Calculate  $\Delta P_{fe}$ , the pressure drop in the two-phase section of the evaporator due to wall friction:

$$\Delta P_{fe} = 4f_{wl} \left[ \frac{G^2/2\rho_l}{Re_v} \right] \left[ \frac{\Delta P_{fe}^*}{4f_{wl}} \right] \quad (4-85)$$

**Body Forces in the Two Phase Region.** The procedure to calculate the pressure drop due to body forces is:

1.) Locate the curve in Figure 4.14 which corresponds to the liquid-to-vapor density ratio,  $\rho_l/\rho_g$ . Find the point on this curve which corresponds to the evaporator outlet quality. The ordinate of this plot is the dimensionless pressure drop  $\Delta P_{ge}^*$ .

- 2.) Calculate the dimensional pressure drop,  $\Delta P_{ge}$ :

$$\Delta P_{ge} = \left[ \frac{\rho_l D_b a \cos \theta}{R_{ev}} \right] (\Delta P_{ge}^*) \quad (4-86)$$

Acceleration in the Two-Phase Region. The procedure to calculate the pressure drop due to fluid acceleration in the evaporator is:

- 1.) Locate the curve in Figure 4.15 which corresponds to the ratio of liquid-to-vapor density,  $\rho_l/\rho_g$ . Find the point on this curve which corresponds to the evaporator outlet quality. The ordinate is the dimensionless pressure drop  $\Delta P_a^*$ .

- 2.) Calculate the dimensional pressure drop,  $\Delta P_{ae}$ :

$$\Delta P_{ae} = \left[ \frac{G^2}{2 \rho_l} \right] (\Delta P_a^*) \quad (4-87)$$

Total Pressure Drop in Two-Phase Section. The total pressure drop in the two-phase section of the evaporator,  $\Delta P_{tp}$ , is the sum of the frictional, body force, and fluid acceleration components:

$$\Delta P_{tp} = \Delta P_{fe} + \Delta P_{ge} + \Delta P_{ae} \quad (4-88)$$

Pressure Drop in the Single-Phase Liquid Section. This pressure drop will be insignificant unless the subcooling is very high. There are only two components of the pressure drop in the single-phase section: friction and body forces. The total pressure drop is easily estimated using parameters already calculated in the procedure for the two-phase section. The procedure is:

- 1.) Calculate  $L_{sc}$ , the length of the evaporator tube in which single-phase liquid flows. For these scoping calculations it is sufficient to estimate  $L_{sc}$  using this equation:

$$L_{sc} \approx \left[ \frac{G A c_{pl} \Delta T_{sub}}{H q''} \right] \quad (4-89)$$

- 2.) Estimate  $\Delta P_{sp}$ , the pressure drop in the single phase section:

$$\Delta P_{sp} = 4f_{wl} \left[ \frac{L_{sc}}{D_b} \frac{G^2}{2 \rho_l} \right] + \rho_l L_{sc} a \cos \theta \quad (4-90)$$

(Equation 4-90 can also be used for detailed calculations in which the evaporator is subdivided into many short segments.  $L_{sc}$  is simply the segment length ( $\Delta z$ ) and  $\Delta P_{sp}$  is the pressure drop in one single-phase segment.)

**Total Pressure Drop.** The total pressure drop in the evaporator tube is the sum of the pressure drops in the single-phase and two-phase sections:

$$\Delta P_{\text{evap}} = \Delta P_{\text{tp}} + \Delta P_{\text{sp}} \quad (4-91)$$

where  $\Delta P_{\text{evap}}$  represents the total pressure drop.

#### 4.9 Validation with Evaporator Test Data

The design methods for forced convection evaporators have been validated by comparison with experimental data from ground tests. For the validation calculations, companion software FCEVAP (Barry et al., 1992) employing these methods was used. Validation comparisons include data from both straight tube and spiral coil geometries.

In summary, the design methods compare well with available data. This should be qualified by noting that none of the data represented steady microgravity conditions. Wall superheat is predicted conservatively, within about 2 K over the operating range. The methods underpredict pressure drop in most cases but by less than 0.5 kPa. All of the trends predicted by the methods are in agreement with those observed.

Principal remaining areas of uncertainty include the effect of gravity on the nucleate boiling contribution to forced convection boiling heat transfer and critical heat flux.

For the validation, three useful sources of data were identified:

- Creare straight tube ground tests (Crowley and Sam, 1991),
- Sundstrand spiral coil ground tests (Niggemann et al., 1985),
- Foster-Miller straight tube ground tests (Hill and Best, 1991).

Comparisons were most extensive with the Creare and Sundstrand data. Only two data points from the Foster Miller tests were usable. The following paragraphs discuss the validation calculations in more detail for each set of data.

**Creare Data.** Ground tests of the Creare flight test system (Crowley et al., 1990) provide an extensive body of data for validation, with about 20 individual data points. The system consisted of a complete two-phase loop, with a 0.9 m long, 6.35 mm diameter evaporator. Working fluid was R-11.

Figure 4.16 compares wall superheats for three nominal mass fluxes. At mass fluxes of 175 and 100 kg/m<sup>2</sup>-s, FCEVAP predicts superheats that are about 1 to 2 K larger (10 to 30%) than the measured values. The dominant flow regime at these mass fluxes is annular flow. Calculated superheats for a mass flux of 50 kg/m<sup>2</sup>-s lie 2 to 3 K (up to a factor of two) higher than the data. Note that at 50 kg/m<sup>2</sup>-s, the majority of the data points are in the stratified flow regime.

Figure 4.17 compares measured and computed pressure drops at the same three mass fluxes. FCEVAP results again compare well with data at the higher mass fluxes, agreeing to within 0.5 kPa or better over the entire operating range. At the 50 kg/m<sup>2</sup>-s mass flux, predicted pressure drops are about half the measured values.



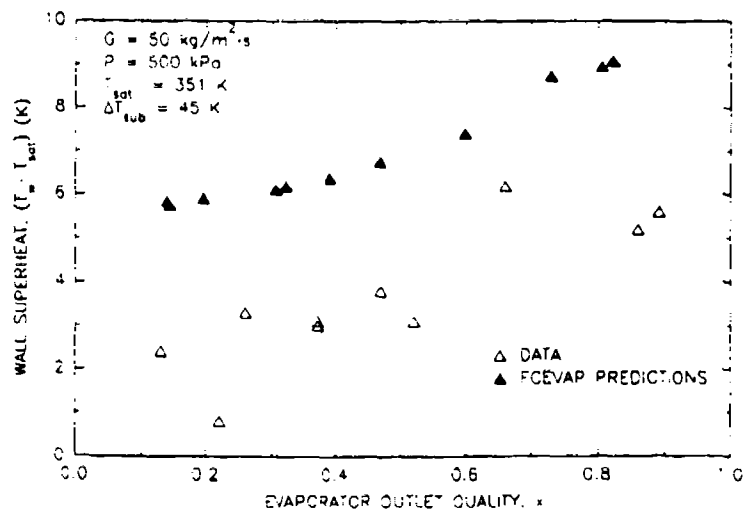
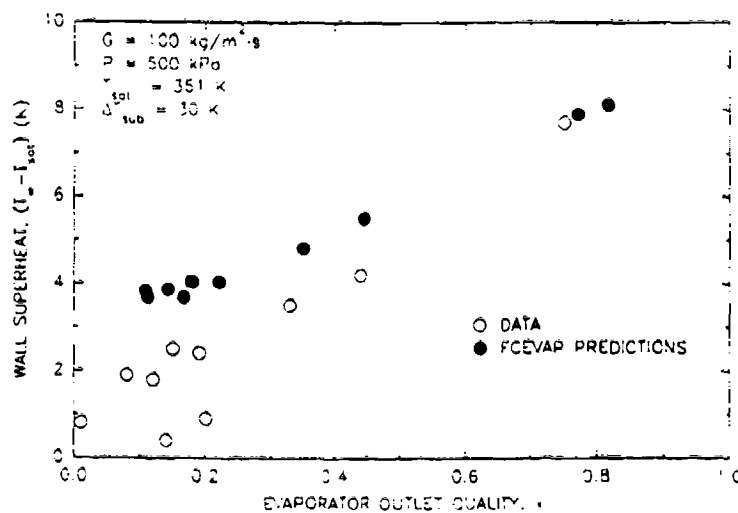
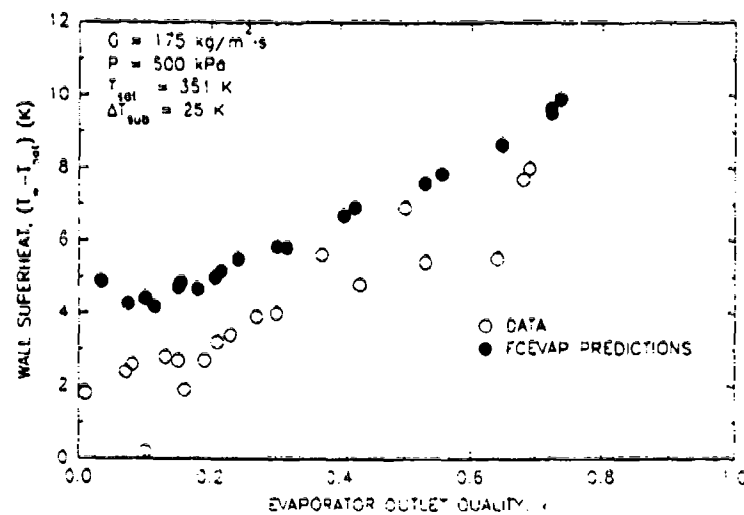


**Figure 4.16. COMPARISON OF FCEVAP RESULTS WITH CREARE GROUND TEST DATA FOR WALL SUPERHEAT**

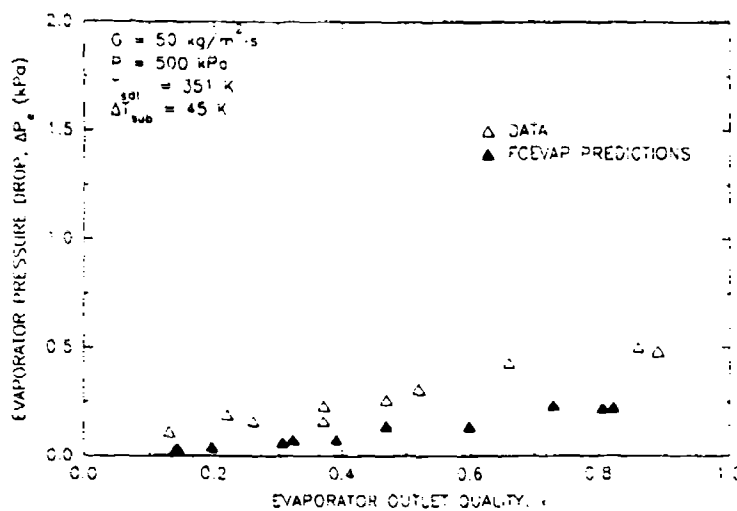
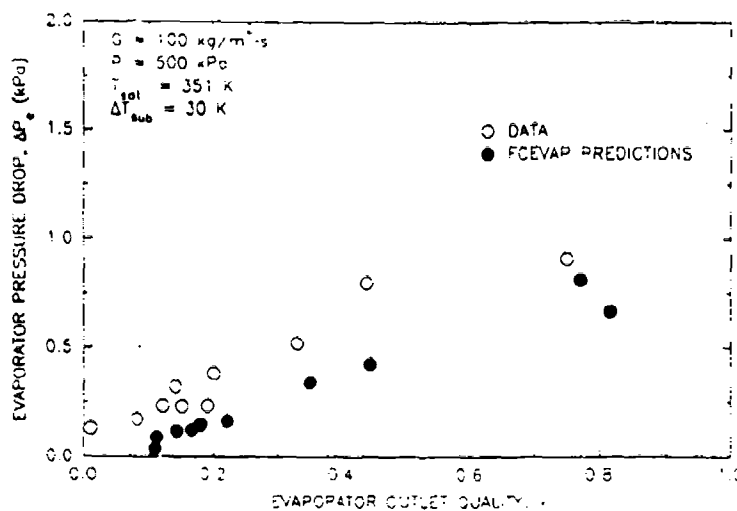
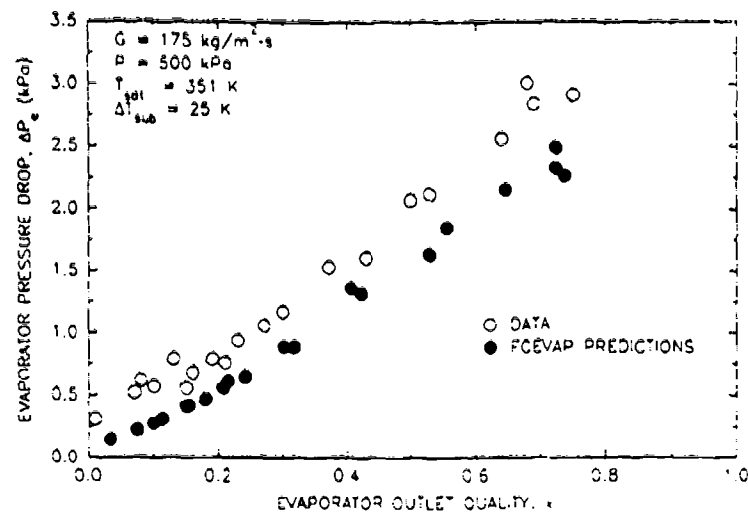


Figure 4.17. COMPARISON OF FCEVAP RESULTS WITH CREARE GROUND TEST DATA FOR PRESSURE DROP

In the tests, thermal losses from the evaporator were a significant fraction of the total power level and were estimated as part of the tests. For the comparisons of Figures 4.16 and 4.17, the full, uncorrected power was used at the 175 and 100  $\text{kg/m}^2\text{-s}$  mass fluxes, while a reduced power level (corrected for losses) was used at 50  $\text{kg/m}^2\text{-s}$ . Since FCEVAP calculations generally overpredict wall superheat and underpredict pressure drop, a tradeoff has been made. Use of the uncorrected power yields larger wall superheats (poorer agreement with these data) and higher pressure drop (better agreement with these data). The opposite, of course, occurs if the lower power values are used. At the two higher mass fluxes, either choice yields reasonable results and acceptable comparisons. For the 50  $\text{kg/m}^2\text{-s}$  mass flux, neither choice yields very good agreement with data.

In the Creare aircraft tests, the last 0.3 meter section of the evaporator operated in the film boiling regime for many of the tests at high power. As illustrated in Figure 4.18, FCEVAP predicts that critical heat flux (CHF) will be exceeded about 5 cm from the exit of the evaporator. Note that given the 20% uncertainty expected from CHF correlations, transition to film boiling at about  $z = 0.6$  meters is entirely consistent with the FCEVAP predictions.

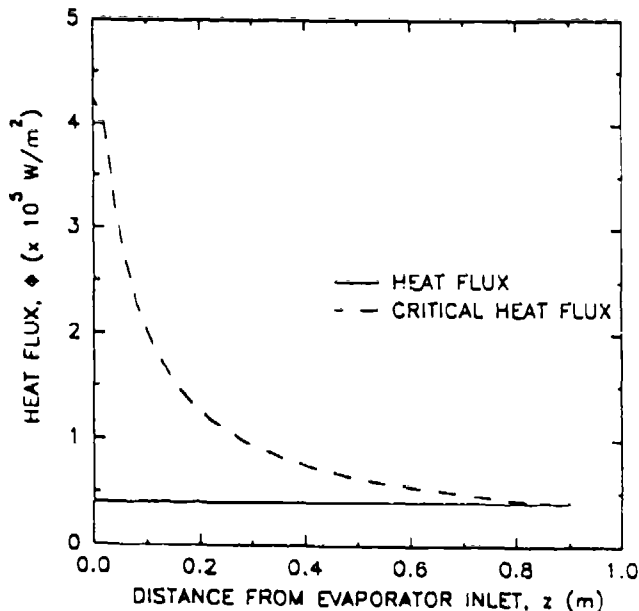


Figure 4.18. CRITICAL HEAT FLUX PREDICTED FOR CREARE TESTS  
( $G = 168 \text{ kg/m}^2\text{-s}$ , Power = 739 W)

**Sundstrand Data.** The Sundstrand swirl flow evaporator (SFE) ground test data are summarized in the report of Niggemann et al. (1985). The SFE uses a flat spiral coil of square tubing to provide a two-sided cold plate. Tests were performed with R-114 as the working fluid.

Figure 4.19 shows wall and fluid temperature versus flow length along the coil. FCEVAP calculations follow the fluid temperature very well. The predicted wall temperature agrees with measured values to within about 2 K (4°F) over the length of the evaporator. Both the calculations and the data show that wall superheat is approximately constant. There is little difference between the inner to outer and outer to inner flow directions in either the calculations or in the data.

Figure 4.20 compares measured values of the pressure drop with those predicted by FCEVAP. The calculated values lie within 30% of the data over most of the power range. Note, however, that the pressure drop data were obtained by subtracting the absolute pressure at two locations. Each transducer has an estimated uncertainty of 10 kPa. Thus, the uncertainty bands on the data of Figure 4.20 are very large, easily covering the range containing the FCEVAP predictions. The apparent differences in the data reported for the two flow directions are therefore negligible.

**Foster-Miller Data.** The aircraft data of Foster-Miller (Hill and Best, 1991) offer little meaningful comparison. In many of the tests the evaporators simply did not function and produced no data. The little data that appear to have been acquired is haphazardly organized, making it difficult to establish the actual operating conditions.

Nevertheless, calculations comparing wall heat transfer for two data points have been run. The results are summarized in Table 4.4. The computed values of the wall superheat and heat transfer coefficient lie within about 40% of the measured values. Given the uncertainties in the data and the poorly characterized operating conditions, this appears to be very good agreement.

It is important to note that the Foster-Miller data *do not* truly represent steady microgravity or reduced gravity conditions. The evaporator used on this facility had a very large thermal mass which damped the response of the evaporator to the changing operating conditions.

Table 4.4. COMPARISON OF FCEVAP CALCULATIONS WITH FOSTER-MILLER DATA				
Heat Flux (kW/m <sup>2</sup> )	Wall Superheat $\Delta T$ (K)		Heat Transfer Coefficient h (W/m <sup>2</sup> -K)	
	Data	FCEVAP	Data	FCEVAP
4.61	3.4	2.37	1350	1950
19.1	8.3	6.18	2300	3090

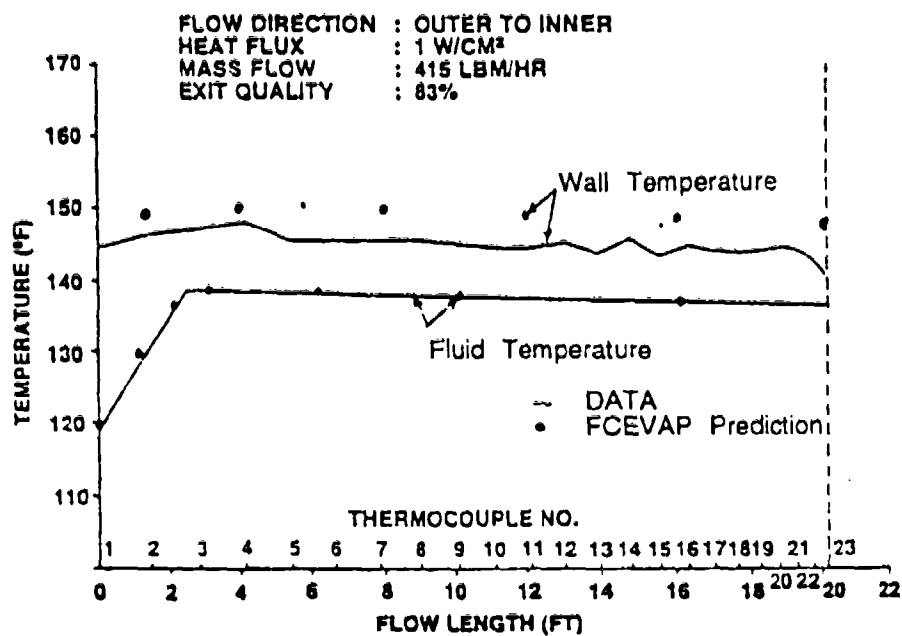


Figure 4.19. COMPARISON OF WALL AND FLUID TEMPERATURES FOR SUNDSTRAND SFE

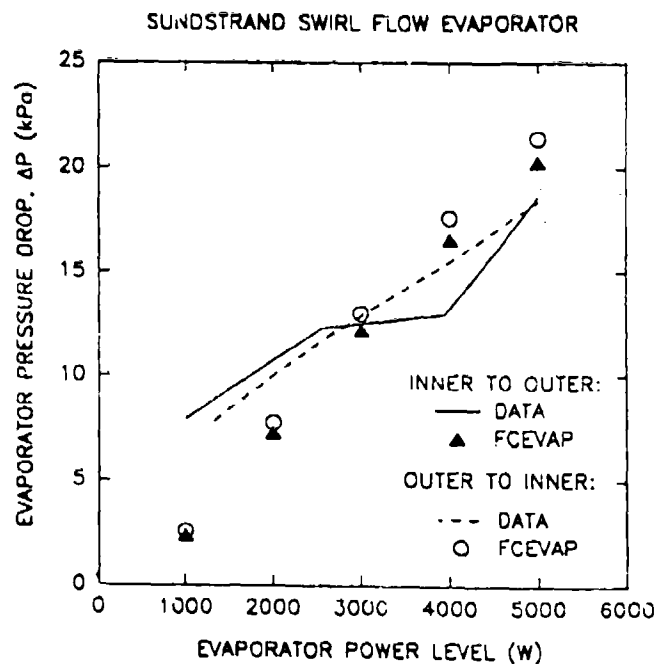


Figure 4.20. COMPARISON OF PRESSURE DROPS FOR SUNDSTRAND SFE

#### 4.10 References for Forced Convection Dominated Tubes

Barry, J.J., Ent, R.S. and Crowley, C.J.; "FCEVAP PROGRAM: FORCED CONVECTION EVAPORATORS"; Creare CPD-243, Software Maintenance Manual, Prepared for Phillips Laboratory, Edwards AFB, California, Prepared by Creare Inc., Hanover, New Hampshire, May 1992.

Colebrook, C.F.; *Turbulent Flow in Pipes, with Particular Reference to the Transition Region Between the Smooth and Rough Pipe Laws*; J. Inst. Civil Engineers London, V11, 1938-9.

Collier, J.G.; Convective Boiling and Condensation; McGraw-Hill Book Company, 2nd Edition, 1981.

Crowley, C.J. and Sam, R.G.; "MICROGRAVITY EXPERIMENTS WITH A SIMPLE TWO-PHASE THERMAL SYSTEM"; PL-TR-91-1059, Prepared for Phillips Laboratory, Kirtland AFB, Prepared by Creare Inc., Hanover, New Hampshire, December 1991.

Davis, E.J. and Anderson, G.H.; *The Incipience of Nucleate Boiling in Forced Convection Flow*; AIChE J., V12, 1966, pp. 774-780.

Dittus, F.W. and Boelter, L.M.K.; Univ. Calif. (Berkeley) Pub. Eng., Vol. 2, 1930, p. 443.

Eastman, R.E.; *Spacecraft Straight-Tube Evaporator Design*; AFWAL-TR-85-3024, 1985.

Frost, W. and Dzakowic, G.S.; *An Extension of the Method for Predicting Incipient Boiling on Commercially Finished Surfaces*; ASME Paper 67-HT-61, 1967.

Gregorio, P. and Merlini, C.; *Voids, Friction, and Vibration Associated with Localized Boiling*; AERE Trans. 1114, 1968.

Gungor, K.E., and Winterton, R.H.S.; *A General Correlation for Flow Boiling in Tubes and Annuli*; Int. J. Heat Mass Transfer, V(29), No. 3, 1986, pp. 351-358.

Hill, S.W. and Best, F.R.; "DEFINITION OF TWO-PHASE FLOW BEHAVIORS FOR SPACECRAFT DESIGN"; AFK-0062-FM-8933-418, Prepared for Air Force Phillips Laboratory, June 1991.

Kakac, S.; *Two-Phase Flow Thermal Instabilities in a Vertical Boiling Channel*; Fundamentals of Gas-Liquid Flows, E. E. Michaelides and M. P. Sharm, eds., FED Vol 72, ASME, 1988, pp. 49-56.

McAdams, W.H., et al; *Vaporization Inside Horizontal Tubes - II - Benzene-Oil Mixtures*; Trans. ASME, 64, 1942, p. 193.

Niggemann, R.E., Greenlee, W.J., Hill, D.G., Ellis, W., and Marshall, P.; *A Swirl Flow Evaporative Cold Plate*; AIAA 85-0920, AIAA 20th Thermophysics Conf., Williamsburg, Virginia, June 1985.

Saha, P. and Zuber, N.; *Point of Net Vapour and Vapour Void Fraction in Subcooled Boiling*; Proc. of 5th International Heat Transfer Conf., Tokyo, Paper B4.7, 1974.

Shah, M.M.; *Improved General Correlation for CHF during Upflow in Uniformly Heated Vertical Tubes*; Int. J. Heat Fluid Flow, V8(4), 1987, pp. 326-335.

Srinivasan, P.S., Nandapurka, S.S. and Hollard, F.A.; *Pressure Drop and Heat Transfer in Coils*; The Chemical Engineer, CE 113-119, May 1968.

Wallis, G.B.; One-Dimensional Two-Phase Flow; McGraw-Hill Book Company, 1969.

## **5 EVAPORATORS: Droplet Impingement Cooling**

This section of the design manual describes methods for sizing evaporators based on the droplet impingement cooling (DIC) technique. Design calculations for estimating heat transfer characteristics of the evaporator are explained. This manual does not include design methods for the piezoelectric droplet generator.

Section 5.1 of this manual provides an introduction to the DIC process and presents an overview of evaporator design. Operation of DIC evaporators is described, and an example sizing procedure is reviewed.

The calculation methods for predicting the heat transfer characteristics of the evaporator are presented in Section 5.2. Methods for calculating droplet spreading, heat transfer coefficient, peak wall superheat, and critical heat flux are provided. These methods are implemented in the companion DROPEVAP software (Barry, 1992).

Dimensionless design charts for quick estimates of DIC heat transfer are presented in Section 5.3. These design charts do not require the designer to know in detail the theory associated with DIC or to have software available which implements the methods.

Section 5.4 gives validation results, comparing predicted performance with test data.

### **5.1 Introduction to DIC Evaporators**

The specific DIC technique discussed in this manual has been developed by Creare for NASA. These evaporators are designed for use in two-phase thermal management systems where the gas and liquid phases are separated, i.e., where gas and liquid do not flow as a mixture. Subcooled or saturated liquid is supplied to the evaporator, and saturated vapor is produced. The DIC process provides very high heat transfer coefficients, enabling DIC evaporators to be made lightweight and compact.

The DIC technique also has important applications to cooling of high heat flux electronic components. The droplet generator may be designed to fire droplets directly at discrete components, focusing the cooling capability precisely where it is needed. Dielectric heat transfer fluids allow direct contact with electronic components.

#### **5.1.1 DIC Process**

Figure 5.1 illustrates the DIC concept. Tiny liquid droplets are produced at a high frequency by a piezoelectric transducer. The droplets strike the hot surface and spread out to form a film, then rapidly evaporate. After complete evaporation of the droplets, another set of droplets is formed by the transducer and the process repeats. If the droplets are formed at too high a frequency, evaporation of successive droplets is not completed and the solid surface floods. In DIC, all of the droplets are formed and ejected simultaneously at well defined time intervals in a fixed geometry. This is in contrast to the relatively random droplet distributions (in time, space, and size) found in spray cooling. Since inertial forces on the droplets are much larger than gravity forces, the DIC evaporator is insensitive to the acceleration (gravity) level.



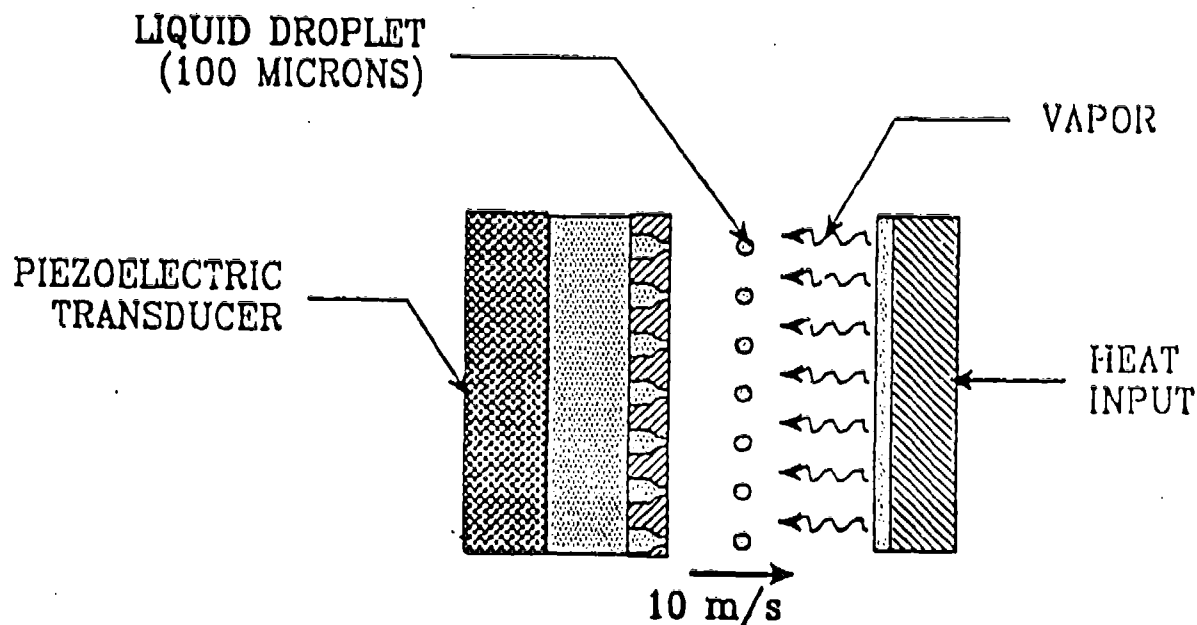


Figure 5.1. DROPLET IMPINGEMENT COOLING CONCEPT

Figure 5.2 shows the process of droplet impact and evaporation. Very high heat fluxes are achieved without nucleate boiling because the droplets form very thin films. Because the films are so thin, heat fluxes can be achieved which are substantially above the critical heat flux in flow boiling. The DIC technique breaks down when the heat flux becomes high enough to cause nucleate boiling in the thin film. Bubble nucleation and growth disrupt the thin film resulting in reduced heat transfer coefficients. For DIC, nucleate boiling is equivalent to critical heat flux.

Due to the very high heat transfer coefficients and transient nature of the DIC process, the conduction resistance and heat capacity of the solid surface must be considered in the design of DIC evaporators. Figure 5.3 illustrates the transient behavior of the solid surface temperature. The effective surface temperature is the extrapolation of the internal wall temperature profile to the surface. The actual surface temperature oscillates around this value as cold droplets impact the wall, then evaporate. The peak wall surface temperature determines whether critical heat flux is reached.

Design variables for a DIC evaporator include the droplet diameter, droplet velocity, and the time between droplets. The droplet diameter and velocity govern the spreading of the droplet. The spreading of the droplet controls heat transfer. To prevent flooding of the hot surface, a droplet must completely evaporate before the next droplet strikes. Thus, the droplet evaporation time must be less than the time interval between droplets.

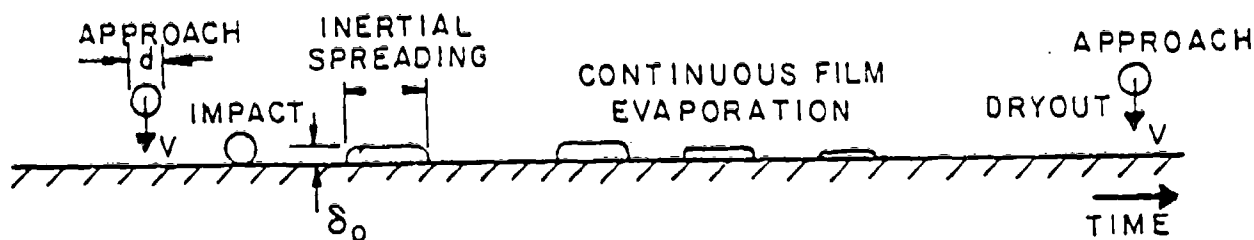


Figure 5.2. DROPLET IMPACT, SPREADING, AND EVAPORATION

The physical processes affecting heat transfer in the DIC evaporator include:

- Droplet impact and spreading,
- Film evaporation,
- Heatup of the solid surface between droplets,
- Critical heat flux (nucleate boiling).

Section 5.2 describes models for each of these processes.

### 5.1.2 DIC Evaporator Design

As shown in Figure 5.1, a DIC evaporator consists of several components. The droplet generator is comprised of the piezoelectric transducer, driver electronics, and a nozzle plate. Droplet diameter and velocity are determined by design of the generator. The droplets pass through a vapor space, then strike the hot surface of the evaporator wall. As noted earlier, the design methods presented here consider the droplet impact, spreading, and evaporation processes affecting the heat transfer characteristics of the evaporator.

A DIC evaporator may be constructed in several configurations, as shown in Figure 5.4. Planar evaporators would be suitable for such applications as cold plates. Cylindrical geometries might be more applicable to heat exchanger concepts such as fluid-fluid loop interfacing. The DIC evaporator concept can also be applied to the cooling of individual high heat flux components such as electronics components.

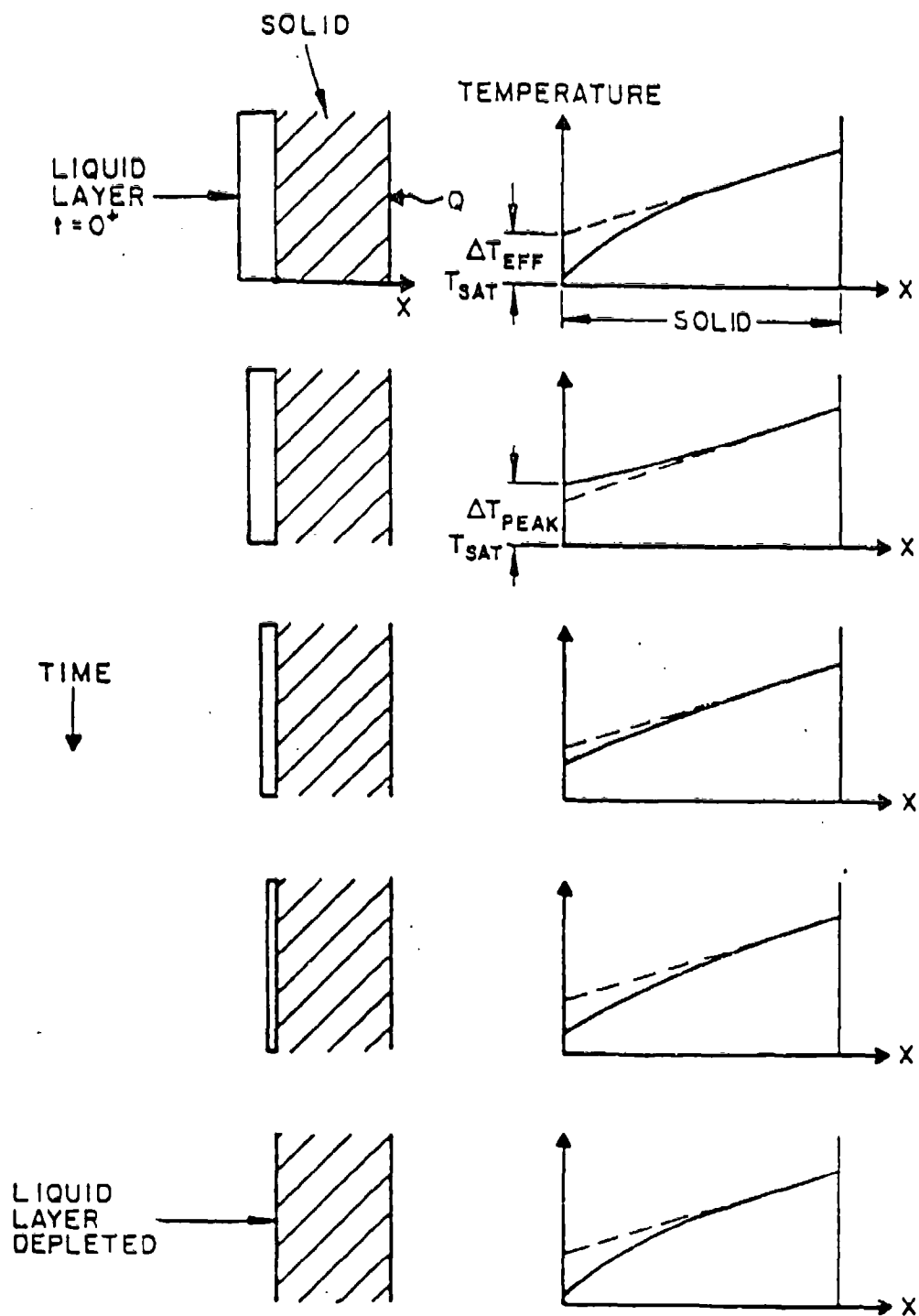


Figure 5.3. TRANSIENT TEMPERATURE RESPONSE IN SOLID

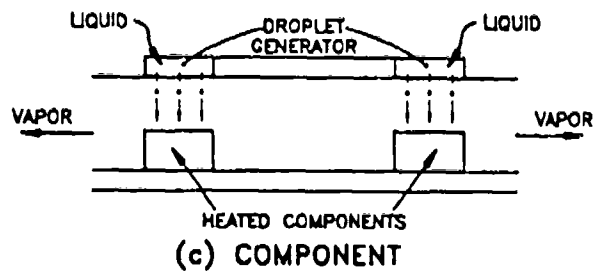
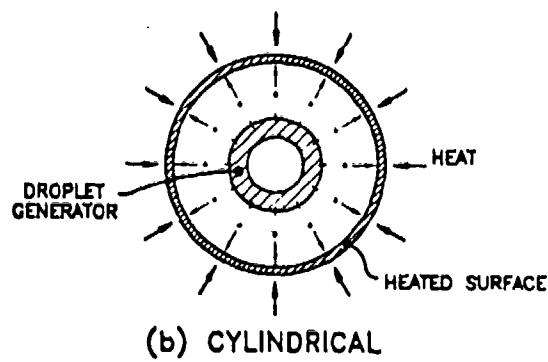
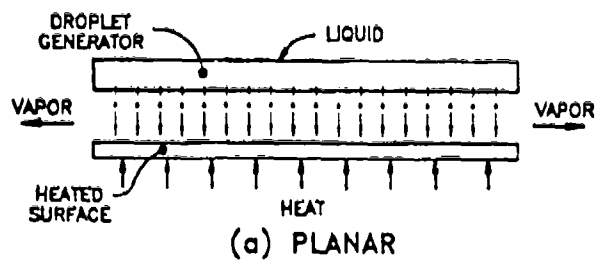


Figure 5.4. EXAMPLE DROPLET IMPINGEMENT COOLING EVAPORATOR CONFIGURATIONS

### 5.1.3 DIC Evaporator Sizing

For a typical evaporator design, there are several known parameters:

- Working fluid,
- Operating pressure and temperature,
- Total heat load.

The designer usually needs to estimate the size of the evaporator (heat transfer area), trading off the temperature difference, considering operational needs, and staying within technology constraints.

The design methods described in this manual may be utilized in several ways. One potential design sequence would run as follows. First, several parameters would need to be specified:

- Working fluid, solid wall material, and operating pressure,
- Wall temperature (or wall-fluid temperature difference),
- Droplet velocity and diameter from droplet generator.

Next, an estimate or guess of the time interval between droplets is made. Based on this guess, the following items are calculated using the methods described in Section 5.2:

- Droplet spreading,
- Heat transfer coefficient and heat flux,
- Droplet evaporation time,
- Peak wall superheat,
- Maximum heat flux.

Using these results the designer (or the design software) needs to make several checks:

- Droplets are spreading (not splattering),
- The time interval between droplets is greater than the evaporation time,
- The peak wall temperature does not exceed the critical heat flux criterion.

If any of these items are not true, then operating parameters must be adjusted. Droplet spreading is governed by the droplet diameter and velocity. The time interval between drops should be lengthened if it is too short to prevent flooding. If critical heat flux is exceeded, the effective wall-fluid temperature difference or the droplet parameters should be adjusted.

If the checks are successfully passed, then the designer can compute the evaporator size. The droplet spreading can be used to predict the minimum spacing between droplet nozzles and coverage of the hot wall by the liquid film. For less than perfect coverage (depends on nozzle spacing), the actual average heat flux is adjusted by the area ratio. Then, using the known total heat load, the evaporator area can be calculated. Various energy and flow balance checks would also be advisable.

Performance of the evaporator can be improved or the size can be reduced by increasing the droplet spreading or by tuning the time interval between droplets to be exactly equal to the droplet evaporation time.

## 5.2 Design Methods

The heat transfer performance of DIC evaporators can be predicted by the design methods given in this section. These methods are implemented in the companion software, DROPEVAP. Equations are provided for computing the droplet impact and spreading, film evaporation, transient heatup of the solid surface, and critical heat flux. The limitations of these equations are also noted.

### 5.2.1 Equations for DIC Heat Transfer

**Droplet Impact and Spreading.** The spreading of a droplet into a thin film is expressed in terms of the droplet spread ratio,  $\beta$ , by:

$$\beta = \frac{D}{d} \quad (5-1)$$

where  $d$  is the diameter of the droplet and  $D$  is the diameter of the thin film spot. The initial film thickness prior to evaporation,  $\delta_0$ , is obtained from a straightforward geometric calculation:

$$\delta_0 = \frac{2}{3} \frac{d}{\beta^2} \quad (5-2)$$

To compute  $\beta$ , a theoretical model developed by Kurabayashi (1967) and modified by Yang (1975) is applied. This model relates the droplet spread ratio to the Weber and Reynolds numbers for the droplet and to the fluid viscosity evaluated at the droplet temperature ( $\mu_l$ ) and at the wall temperature ( $\mu_w$ ).

$$\frac{1}{2} We = \frac{3}{2} \beta^2 \left[ 1 + 3 \frac{We}{Re_d} \left( \frac{\mu_l}{\mu_w} \right)^{0.14} \left[ \beta^2 \ln \beta - \frac{\beta^2 - 1}{2} \right] \right] - 6 \quad (5-3)$$

Here the Weber number,  $We$ , and Reynolds number,  $Re_d$ , are defined as:

$$We = \frac{\rho_l V^2 d}{\sigma} \quad (5-4)$$

$$Re_d = \frac{d V \rho_l}{\mu_l} \quad (5-5)$$

The experimental data of Toda (1974) indicate that the Weber number for the droplet should be below 2160 or else the droplet may shatter on impact instead of spreading.

**Spatial Averaging.** To arrive at the average heat transfer on the cooled surface, the "packing" of the thin film spots must be considered. Figure 5.5 illustrates two packing arrangements, a triangular and a square lattice. The wetted area fraction,  $\gamma$ , immediately following droplet impact can be calculated from:

$$\gamma = \left[ \frac{\text{area covered by film}}{\text{total area of the wall}} \right] \quad (5-6)$$

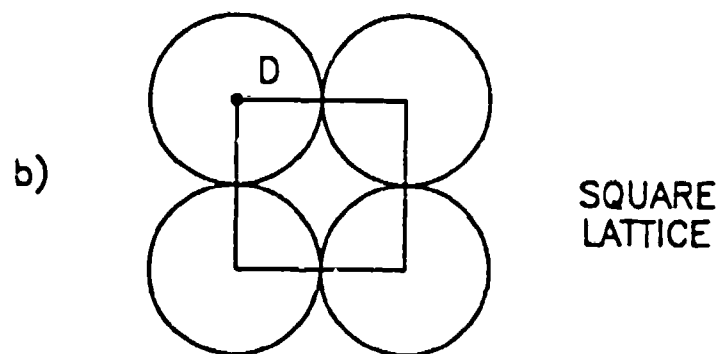
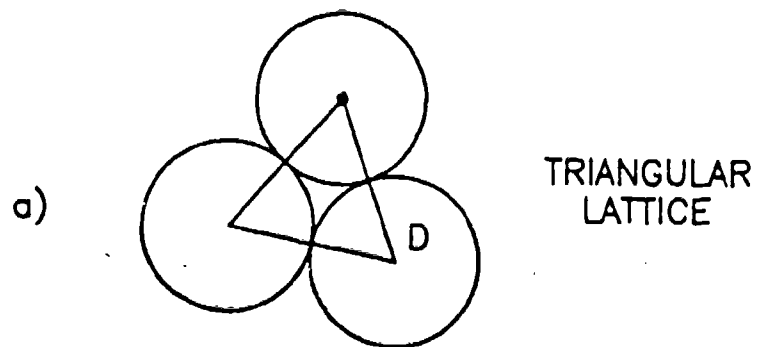


Figure 5.5. THIN FILM SPOT PACKING ARRANGEMENTS

For the extreme case of the thin film spots just touching,  $\gamma = 0.905$  for the triangular lattice and  $\gamma = 0.785$  for the square lattice. In general, the designer will leave some margin between thin film spots to allow for non-uniformity and tolerances. If the thin film spots overlap, the film may not completely evaporate before the arrival of the next droplet, and the surface may flood.

**Evaporation Time.** The evaporation time,  $t_{\text{evap}}$ , is the time required for the film to evaporate from the hot surface. It is an important parameter because it determines the minimum time interval between successive droplets that will not flood the surface. If the effective wall superheat,  $\Delta T_{\text{eff}}$ , and the initial film thickness,  $\delta_0$ , are known, the evaporation time for the film can be estimated by:

$$t_{\text{evap}} = \frac{1}{2} \left[ \frac{\rho_l h_{fg}}{k_l} \right] \left[ \frac{\delta_0^2}{\Delta T_{\text{eff}} (1 + A_r + B_r)} \right] \quad (5-7)$$

The time-averaged heat flux will be calculated using the ratio of the evaporation time to the time between droplets  $\eta$ :

$$\eta = \frac{t_{\text{evap}}}{t_{\text{drop}}} \quad (5-8)$$

**Heat Transfer Coefficient.** Three heat transfer resistances govern the heat transfer in DIC evaporators: conduction resistance in the liquid film, evaporation resistance (kinetic transport at the liquid-vapor interface), and conduction resistance in the solid. The relative strength of these three resistances can be evaluated in terms of ratios. The ratio of the characteristic thermal resistance of the solid to the initial thermal resistance of the liquid film is:

$$A_r = \left[ \frac{k_l \rho_l h_{fg}}{k_s \rho_s c_s \Delta T_{\text{eff}}} \right]^{\frac{1}{2}} \quad (5-9)$$

and the ratio of the evaporation resistance to the initial thermal resistance of the liquid film is:

$$B_r = \left[ \frac{k_l}{\delta_0} \right] R_{\text{evap}} \quad (5-10)$$

$$R_{\text{evap}} = \left[ \frac{T_{\text{sat}}^{3/2} (2\pi)^{0.5} R_g}{2 \rho_g h_{fg}^2} \right] \quad (5-11)$$

The effect of the liquid and evaporation resistances can be incorporated into an equation for the heat transfer coefficient:

$$h_{\text{dic}} = \gamma \frac{\eta k_l}{\delta_0} \left[ \frac{1}{B_r + 1/2} \right] \quad (5-12)$$

Here  $\gamma$  and  $\eta$  represent the spatial and temporal averaging. Note that in the limit of a very small evaporation resistance,  $B_r$  goes to zero and the heat transfer coefficient becomes solely a function of the liquid film resistance. Typically the solid resistance is small ( $A_r$  much less than 1), and it is reasonable to neglect it. If the solid resistance is important, a transient conduction solution must be carried out (see peak wall superheat below).



**Average Heat Flux and Wall Temperature.** Two heat transfer boundary conditions may be considered in design of the DIC evaporator: constant wall temperature and constant wall heat flux. The two representations are closely related by the heat transfer coefficient:

$$T_w = \Delta T_{\text{eff}} + T_{\text{sat}} = \frac{q''}{h_{\text{dic}}} + T_{\text{sat}} \quad (5-13)$$

$$q'' = h_{\text{dic}} \Delta T_{\text{eff}} = h_{\text{dic}} (T_w - T_{\text{sat}}) \quad (5-14)$$

Note that both the heat transfer coefficient and heat flux are spatially and temporally averaged. With the effective wall superheat, these form a self-consistent set of average parameters.

**Peak Wall Superheat.** As shown in Figure 5.3, the wall surface temperature is not constant with time but fluctuates with the arrival and evaporation of droplets. In evaluating whether the critical heat flux is exceeded, the peak wall superheat  $\Delta T_{\text{peak}}$  must be estimated. A transient solution to the conduction equation must be carried out.

Figure 5.6 illustrates the solution strategy. The time-dependent conduction equation for one-dimensional heat transfer is:

$$\frac{\partial^2 T}{\partial z^2} = \frac{1}{\alpha_s} \frac{\partial T}{\partial t} \quad (5-15)$$

where  $\alpha_s$  is the thermal diffusivity of the solid wall material. This equation is solved numerically subject to boundary and initial conditions. A distance  $L_{ss}$  is selected that is sufficiently deep in the solid so that the temperature is steady at that point. At the liquid-solid interface, the heat transfer resistance of the liquid film and of evaporation is coupled to the solid wall model. The time-dependent film thickness,  $\delta$ , is computed by:

$$\frac{\partial \delta}{\partial t} = \frac{1}{\rho_l h_{fg}} \left[ \frac{T(0) - T_{\text{sat}}}{\delta(t)/k_l + R_{\text{evap}}} \right] \quad (5-16)$$

where  $R_{\text{evap}}$  is the evaporation resistance.

The initial temperature profile is guessed (usually a linear variation), then the equations are solved for a series of droplet impacts. After a sufficient number of droplet impacts have been modelled, the temperature field in the solid well away from the surface reaches a steady state (i.e., at  $L_{ss}$  or beyond), and the temperature field near the surface assumes a stable, repeating, oscillatory behavior.

**Critical Heat Flux.** The critical heat flux for a DIC evaporator occurs when bubbles nucleate, grow, and disrupt the film. This mode of heat transfer is inherently less efficient than simple film evaporation and reduces the performance of the device. The wall superheat at critical heat flux is calculated from the model of Davis and Anderson (1966):

$$\Delta T_{\text{CHF}} = \left[ \frac{8 \alpha_s T_{\text{sat}}}{h_{fg} k_l \rho_g} \right]^{0.5} \quad (5-17)$$

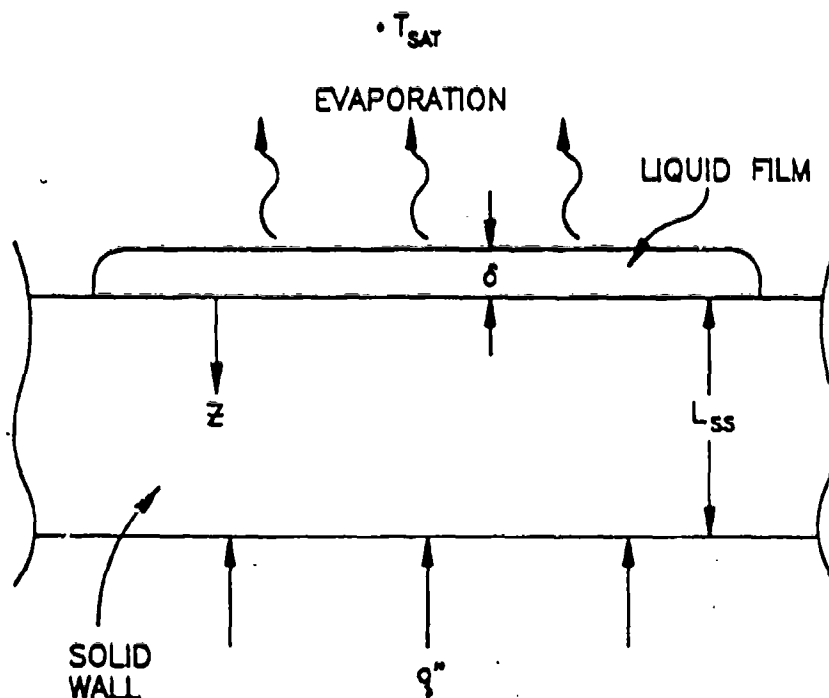


Figure 5.6. TRANSIENT WALL HEAT TRANSFER SOLUTION

When this superheat is reached, the heat transfer prediction methods outlined above become invalid, since film disruption is not considered. In general, the DIC evaporator should be designed so that this limit is not exceeded. As shown in the experimental data in Section 5.4, however, the evaporator performance appears to degrade gracefully rather than catastrophically when this limit is exceeded. Thus, performance near the limit may not be dangerous for many applications.

**Maximum Heat Flux.** The maximum attainable heat flux in the DIC evaporator may be calculated from:

$$q''_{max} = h_{dic} \Delta T_{CHF} \left[ \frac{\Delta T_{eff}}{\Delta T_{peak}} \right] \quad (5-18)$$

This equation predicts the maximum heat flux based on the margin between the effective and peak superheats. Implicit in this equation is the assumption that the evaporator is already running with the droplet interval equal to the droplet evaporation time ( $\eta = 1$ ). Note that the performance can also be improved by maximizing the fraction of wetted area ( $\gamma$ ) consistent with avoiding droplet interaction and surface flooding.

### 5.2.2 Limitations

The design equations of Section 5.2.1 are based on several simplifying assumptions.

- The droplet spreads instantaneously on impact. In general, spreading is an order of magnitude faster than evaporation.
- The droplet spreads to form a thin even film, not a lens-shaped drop. Lens-shaped droplets require much more complex analysis due to multi-dimensional effects.
- The thermal capacity of the droplet (sensible heat addition) is negligible compared to its latent heat.
- Heat transfer in the solid and liquid are one-dimensional.
- The thermal resistance of the solid is neglected in calculating the heat transfer coefficient. A method for transient calculation of the solid resistance is outlined, however.

### 5.3 Dimensionless Design Charts

The DIC evaporator design calculations can be performed using dimensionless charts for estimating key parameters. The following information is needed in order to use the dimensionless charts:

#### Fluid Properties

- $\rho_l$  Liquid Density
- $\mu_l$  Liquid Viscosity
- $\mu_w$  Liquid Viscosity (at Wall Temperature)
- $k_l$  Liquid Thermal Conductivity
- $\rho_g$  Gas Density
- $k_g$  Gas Thermal Conductivity
- $R_g$  Gas Constant
- $h_{fg}$  Heat of Vaporization
- $\sigma$  Surface Tension

#### Droplet Parameters

- $V$  Droplet Velocity
- $d$  Droplet Diameter

#### Wall Superheat or Heat Flux

- $\Delta T_{eff}$  or  $q''$  Effective Superheat or Average Heat Flux

The heat transfer performance of the evaporator can be predicted using the above information.

**Droplet Spreading.** Figure 5.7 plots the droplet spread ratio  $\beta$  (Equation 5-1) as functions of the Weber number (Equation 5-4), Reynolds number (Equation 5-5), and viscosity ratio. If the Weber number exceeds 2160, droplets will tend to shatter rather than to spread into an even thin film, and the heat transfer analysis will not apply.

The thin film spot diameter  $D$  and initial film thickness  $\delta_0$  are calculated from the droplet spread ratio using Equations 5-1 and 5-2 respectively. The average wetted area fraction,  $\gamma$ , will depend on the geometry of the evaporator and droplet generator. Note that the thin films created by the individual droplets should not overlap or the surface may flood.

**Evaporation Time and Wall Heat Transfer.** Figure 5.8 gives the droplet evaporation time as a function of the ratio of solid to liquid resistance,  $A_r$  (Equation 5-9), and the ratio of evaporation to liquid resistance,  $B_r$  (Equations 5-10 and 5-11). The dimensionless evaporation time,  $\theta_{\text{evap}}$ , is defined as:

$$\theta_{\text{evap}} = \frac{k_l \Delta T_{\text{eff}} t_{\text{evap}}}{\rho_l h_{fg} \delta_0^2} \quad (5-19)$$

Wall heat transfer is calculated using Equations 5-12 and 5-13 or 5-14.

**Peak Wall Superheat.** Figure 5.9 shows the ratio of peak to effective superheat as a function of the ratio of solid to liquid resistance,  $A_r$  (Equation 5-9), and the ratio of evaporation to liquid resistance,  $B_r$  (Equations 5-10 and 5-11), for conditions where the droplet interval is equal to the evaporation time ( $\eta = 1$ ).

## 5.4 Validation

Only one set of heat transfer data currently exists for a DIC evaporator. These data are from proof-of-concept tests performed at Creare using water as the working fluid (Valenzuela and Drew, 1987). Comparison calculations have been performed using the companion DROPEVAP software, which implements the design methods described in Section 5.2.

Figure 5.10 compares the calculated heat fluxes with measured values from the tests at various superheats. DROPEVAP correctly captures the trend in the data, but over predicts the heat transfer coefficient by up to a factor of two. For this set of tests, the parameter  $A_r$  is approximately 0.2, indicating that the solid resistance is small. The test report does mention that the nozzle on the droplet generator tended to discharge several small droplets rather than one larger droplet. The total volume of the multiple droplets was used to predict the effective droplet diameter of 91 microns used in the data comparisons. This represents one possible cause for the overprediction of the heat transfer.

In Figure 5.10, the data indicate that bubble nucleation (critical heat flux) occurs at wall superheats of 30 to 40 K with an attendant reduction in heat transfer. The models of DROPEVAP predict critical heat flux at a wall superheat of approximately 40 K, in good agreement with the data.

Future tests for a prototype DIC evaporator are planned, but data are not currently available for validation.

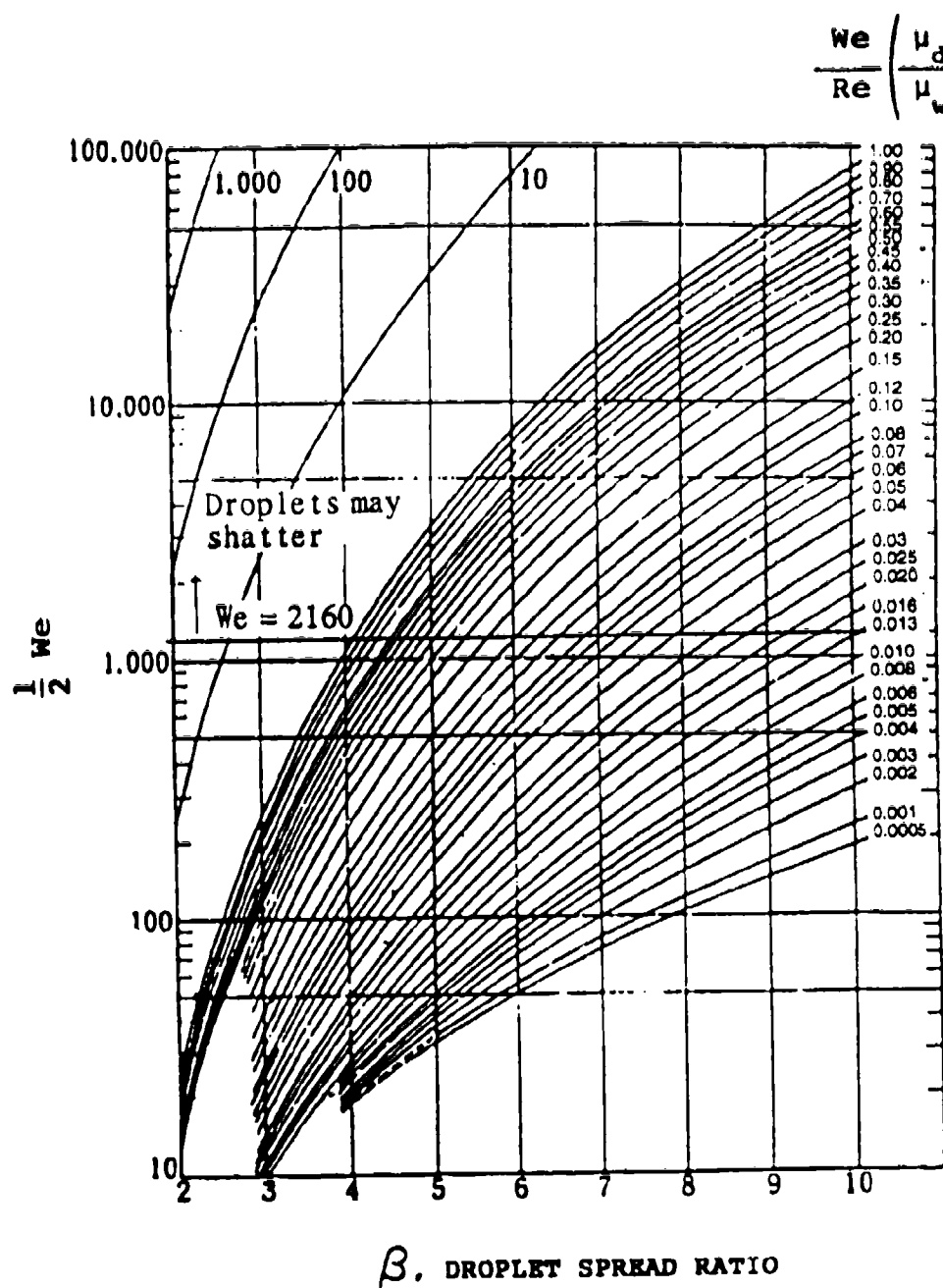


Figure 5.7. VARIATION OF DROPLET SPREAD RATIO WITH IMPACT PARAMETERS (YANG, 1975)

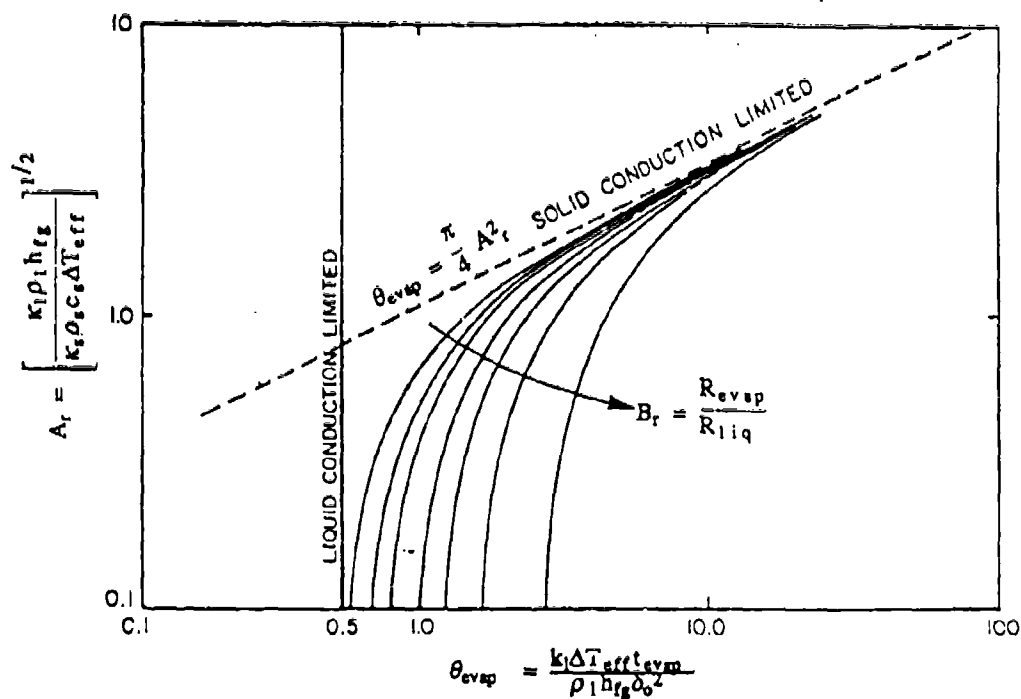


Figure 5.8. SIMULTANEOUS EFFECT OF SOLID, LIQUID AND EVAPORATION RESISTANCES ON THE EVAPORATION TIME

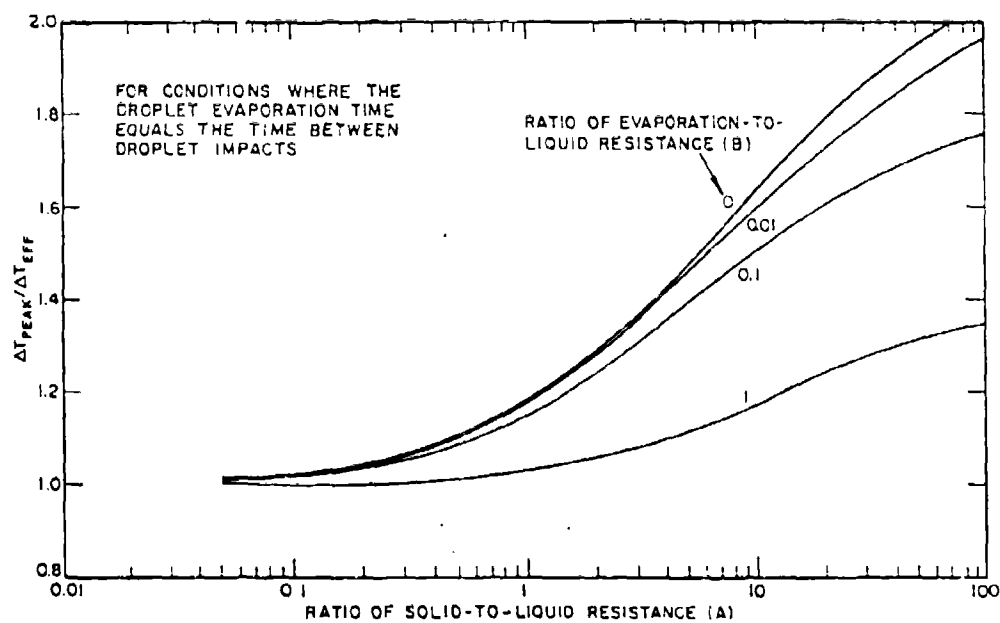


Figure 5.9. VARIATIONS OF PEAK WALL SUPERHEAT WITH HEAT TRANSFER RESISTANCE

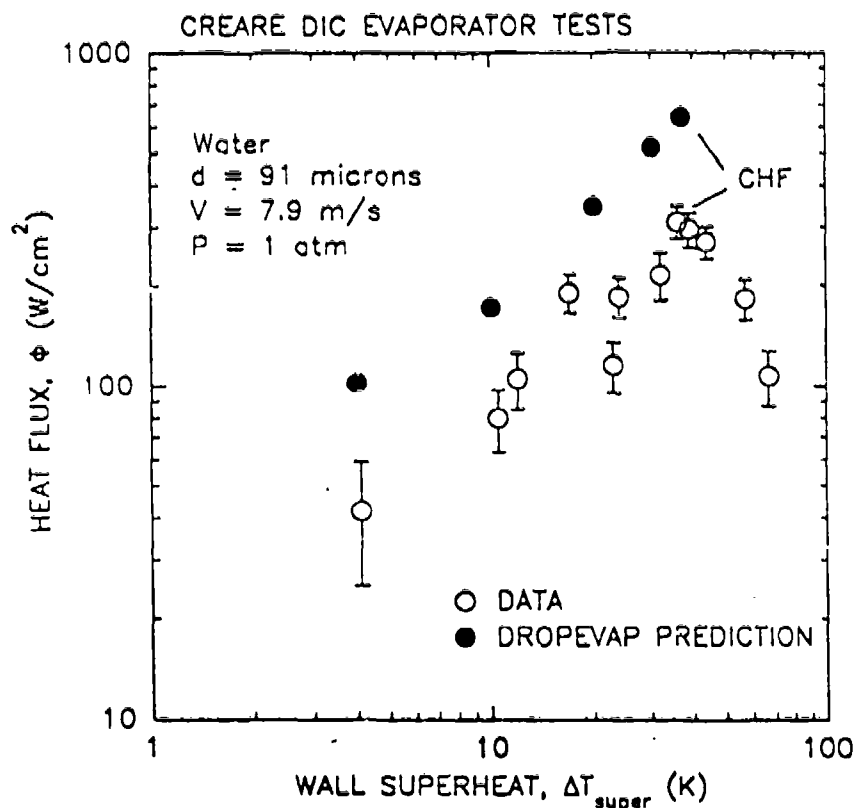


Figure 5.10. VALIDATION COMPARISON OF DESIGN METHODS VERSUS CREARE DIC DATA

### 5.5 References for Droplet Impingement Cooling

Barry, J.J., Crowley, C.J. and Ent, R.S.; "SOFTWARE MAINTENANCE MANUAL FOR THE DROPEVAP PROGRAM: DROPLET EVAPORATOR PERFORMANCE"; Creare CPD-244, Rev. 1.0, May 1991.

Kurabayashi, T., Karacawa, T. and Iida, K.; *Impact of Liquid Droplets on a Solid Surface*; Preprint No. 175, JSME, September 1967, pp. 153-156.

Yang, W.-J.; *Theory on Vaporization and Combustion of Liquid Drops of Pure Substances and Binary Mixtures on Solid Surfaces*; Inst. Space Aero. Sci., U. Tokyo, Rept. No. 535, November 1975.

Toda, S.; *A Study of Mist Cooling (2nd Report: Theory of Mist Cooling and Its Fundamental Experiments)*; Heat Transfer Japanese Research, 3(1), 1974, pp. 1-44.

Valenzuela, J.A. and Drew, B.C.; "HIGH HEAT FLUX DROPLET IMPINGEMENT HEAT TRANSFER"; Creare TM-1190, September 1987.

## 6 CONDENSERS: Vapor Shear

Condensers transfer heat between two-phase heat transport systems and spacecraft heat rejection systems such as radiators and interface heat exchangers. The condenser allows for controlled condensation of the two-phase working fluid so that heat can be efficiently and reliably removed from the two-phase loop. The condenser should be small and lightweight, have small pressure losses, and operate regardless of the spacecraft acceleration. In a shear condenser tube, shear forces due to high velocity vapor flow are much larger than body forces. Vapor shear propels the condensate through the condenser.

This section of the design manual provides heat transfer and pressure drop design methods for shear condenser tubes. Heat transfer design ensures that the liquid is completely condensed and exits the tube with the proper subcooling. Pressure drops must be calculated to size the capillary evaporators for mechanical pumps which circulate the fluid in the two-phase loop. The methods described here are used in the MICROCON program (Izensen, Martin, and McDonald, 1992).

These methods focus on the heat transfer and pressure drop within a single shear condenser tube. Heat transfer outside the tube is modelled in a simple and general way to simplify the design data requirements. Convective or radiative boundary conditions are both possible.

Section 6.1 describes the applications of the condenser design methods. These are primarily condensing radiators and interface heat exchangers in thermal control systems on spacecraft.

Section 6.2 summarizes the analysis approach and the design methods. A condenser tube is broken into a large number of segments. In each segment the flow regime is calculated from the known inlet conditions. The flow regime determines the constitutive relations to be used for heat transfer, pressure drop, and void fraction in that segment.

Section 6.3 presents the overall calculation method used in MICROCON to calculate the heat transfer and pressure drop in a shear condenser tube. A step-by-step procedure describes the sequence of calculations to march through a condenser and calculate the performance in each segment.

Section 6.4 presents the detailed equations for calculating the heat transfer coefficient in a shear condenser. Methods are presented for each flow regime which occurs in the condenser tube. Condensation in the annular flow regime is a key phenomenon which affects the condensing length and the pressure drop. Several alternative models are presented for the annular flow regime, along with recommendations based on model validation against experimental data.

Section 6.5 gives the detailed equations for calculating the void fraction in each flow regime. The interfacial friction factor is a key parameter for calculating the void fraction in the annular flow regime.

Section 6.6 presents the detailed equations for calculating the pressure drop in a shear condenser. The pressure drop calculation also depends on the flow regime in the segment. A key parameter is the interfacial friction factor in the annular flow regime. Several alternative methods are presented for calculating the interfacial shear ratio in the annular regime, along with recommendations based on validation against experimental data.



Section 6.7 presents dimensionless design maps for heat transfer and pressure drops in shear condensers. These maps allow a user who is unfamiliar with details of the theory to quickly calculate the condensing length and pressure drop by hand. An example illustrates how to model heat transfer in a condensing radiator.

Finally, Section 6.8 compares heat transfer and pressure loss calculations with data from various condenser tests. Data from several sources validate the MICROCON analysis.

## 6.1 Applications

The design methods provide key calculations for the development and design of shear condensers for thermal management of spacecraft. The primary applications are:

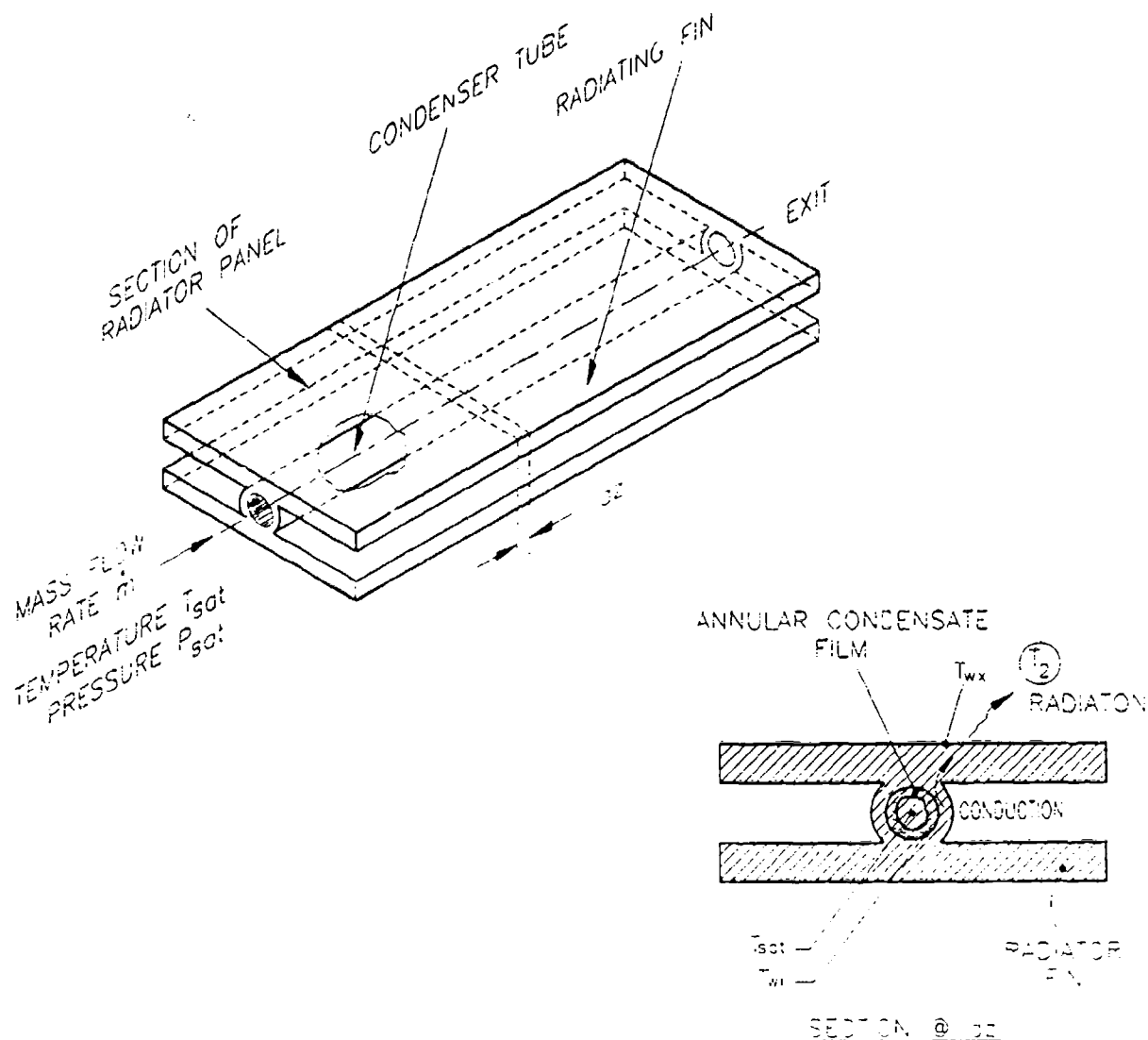
- Design of condensing radiators,
- Design of interface heat exchangers,
- Interpretation of test data.

Flexible boundary conditions permit solution of a range of design problems.

**Design of Condensing Radiators.** Figure 6.1 is a schematic of one tube in a shear condenser with attached fins which radiate heat directly to space. High quality vapor enters the tube from the left and subcooled liquid exits the tube to the right. As vapor condenses inside the tube, it gives up the heat of vaporization to the surrounding structure, in which it travels by conduction to the radiating surface. The heat leaves the spacecraft by radiation from the surface.

The condenser design methods calculate the heat transfer and pressure loss within the radiating shear condenser. For a condensing radiator the problem is solved with a radiation boundary condition and a heat sink temperature which is appropriate for the radiator's orientation (facing deep space, the sun, etc.). The designer must provide an effective "wall thickness" and thermal conductivity to model in one dimension the temperature drop from the condensing surface, through the radiator structure, to the radiating surface. These design methods do not include the radiating fin efficiency or view factor. Those effects are lumped into the effective thickness, as explained in Section 6.3.1. Given a specified mass flow rate, the designer uses the methods presented in the following sections to calculate the heat transfer and pressure drop in the condenser tube. Or, if the available pressure drop is specified, methods are presented to calculate the heat transfer and mass flow rate through the tube.

**Design of Interface Heat Exchangers.** Figure 6.2 is a schematic of an interface heat exchanger in which the condensing fluid in a two-phase thermal bus transfers heat to evaporators in the heat rejection system. In this case, secondary temperatures are constant and the heat flux varies along the length of the tube. The secondary evaporators are typically parts of heat pipe radiators (see Fredley and Warren, 1990). The design methods presented here apply to the condenser tube in this system as well. The designer specifies a secondary coolant temperature equal to the saturation temperature in the evaporator, and a secondary heat transfer coefficient which accounts for the superheat required to evaporate the secondary fluid. As in the case of the radiating condenser, the designer must provide effective values for the thermal conductivity and thickness of the condenser wall to model, in an equivalent one-dimensional fashion, the temperature losses in the heat exchanger structure.



### THERMAL MODEL

Condensation  $T_{sat} - T_{wi} = \frac{q'}{hP_i}$

Conduction  $T_{wi} - T_{wx} = \frac{q'}{P_i} \left[ \frac{t_w}{k_w} \right]_{eff}$

Radiation  $T_{wx}^4 - T_2^4 = \frac{q'}{\sigma_o \epsilon P_2} + \frac{q''_{env}}{\sigma_o \epsilon}$

Figure 6.1. THERMAL MODEL FOR A CONDENSING RADIATOR

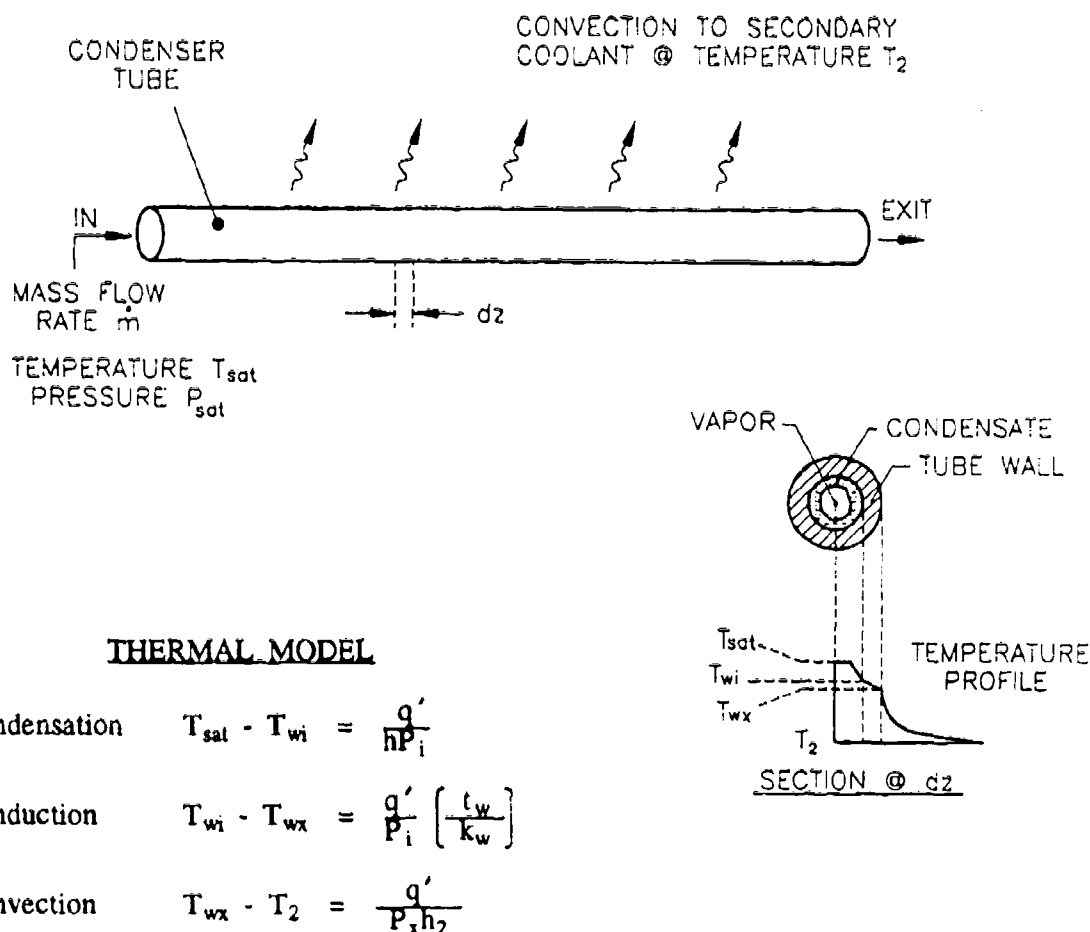


Figure 6.2. THERMAL MODEL FOR AN INTERFACE CONDENSER

High shear condensers are still at an early stage of development and most of the available data come from tests conducted on the ground. In these tests, the condenser is typically cooled by a single-phase heat exchanger with a high capacity rate, which approximates a constant-temperature boundary condition. In MICROCON, secondary heat transfer can be modeled with a constant secondary temperature and a single-phase heat transfer coefficient.

**Interpretation of Test Data.** Detailed results of the design calculations are useful for interpreting the results of shear condenser tests. For example, the designer can easily perform calculations using several different constitutive models for the interfacial vapor/liquid shear stress of the heat transfer coefficient in the annular condensing film. Comparing the calculated results with test data can show which constitutive models are most appropriate to calculate condensing length and pressure drop for that condenser. The calculations can be used to extrapolate from ground tests to a space environment, indicating whether condenser performance is the same in both cases. Calculated values of the quality and void fraction along the length of the tube provide detailed information to supplement experimental data.

General Requirements. The design methods for shear condensers apply if the following conditions are met:

- Operation is steady state,
- The spacecraft acceleration is less than 2 g,
- The secondary temperature is constant,
- Heat rejection is by radiation or convection,
- The tube has a constant diameter or constant rate of taper,
- The concentration of non-condensable gases is negligible.

The condenser tube may be one of many, parallel tubes, as in a condensing radiator panel. However, the methods presented have do not address flow distribution in the inlet and outlet plena or potential flow instability due to parallel channel effects.

## 6.2 Summary of Methods

The design methods are based on a mechanistic analysis of the heat transfer and flow in a shear condenser tube. Typically the condensing fluid experiences a sequence of flow regimes (annular, slug, etc.) as it flows from the inlet to the outlet of the condenser. The flow regime depends on the flow quality which, in turn, depends on the amount of heat transfer. The processes which govern heat and momentum transfer are different in each flow regime. The design methods can be used in a numerical procedure (such as the MICROCON program) to calculate the heat transfer in a shear condenser tube. Or, the analysis can be simplified for several important cases to create dimensionless design maps which allow quick hand calculations.

Boundary Conditions. Condenser design requires boundary conditions for heat transfer and fluid flow. There are two basic options for each type of boundary condition which may be used in any combination.

There are two possible heat transfer boundary conditions:

- Convection to secondary coolant at temperature  $T_2$ , or
- Radiation to a heat sink at temperature  $T_2$ .

Convective boundary conditions apply for the design of interface heat exchangers on spacecraft and are also commonly used for ground tests of shear condensers. The heat transfer model in this case includes temperature drops due to condensation heat transfer inside the tube, conduction heat transfer in the solid heat exchanger structure, and single-phase convective heat transfer to the secondary coolant. Radiation boundary conditions apply to condensing radiators on spacecraft. The heat transfer model for these boundary conditions includes temperature drops due to condensation, conduction through the solid structure, and radiation from the outer radiator surface.

For the flow boundary conditions, there are two possibilities:

- Specified mass flow rate, or
- Specified total pressure drop.

In a problem with a specified mass flow rate, the condenser performance is calculated using a straightforward "marching" scheme. The condenser is broken up into a large number of segments. Heat transfer and pressure loss are calculated in each segment, and the exit conditions from one segment become the inlet conditions for the next. The overall inlet conditions to the condenser are the inlet conditions to the first segment.

Iterative calculations are required for the case of a specified pressure drop. Iterations begin with a first estimate for the mass flow rate based on some simplifying assumptions. Then the pressure drop is calculated by marching through the condenser once using the same procedure as for a specified flow rate problem. The calculated pressure drop is compared to the specified pressure drop. The mass flow rate estimate is modified based on this comparison and the pressure drop is calculated again. Iterations continue until the calculated and specified pressure drops agree to within 0.1%.

**Flow Regimes in Shear Condensation.** Figure 6.3 illustrates one tube in a shear condenser. High quality vapor enters one end, condenses inside the tube, and leaves as single-phase liquid. The vapor flow decreases and the liquid flow increases from the inlet to the outlet due to condensation. As a result, the flow regime changes as the local flows pass through critical transition points along the length of the tube.

In general, the sequence of flow regimes from the condenser inlet to the outlet will be:

1. Annular,
2. Slug,
3. Bubbly, and
4. Single-phase.

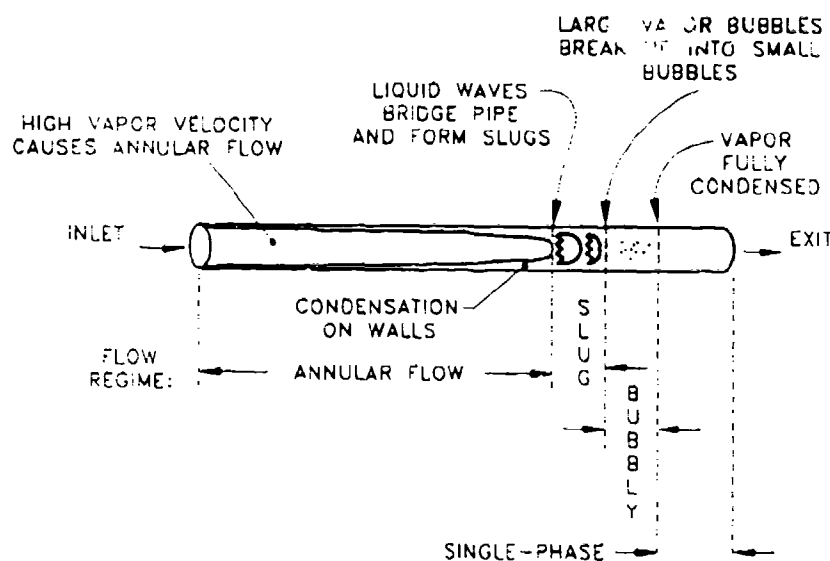


Figure 6.3. A SINGLE TUBE IN A SHEAR CONDENSER

Most of the condensation and pressure losses occur in the annular flow regime, so shear condensers can be characterized as operating mainly in annular flow. The lengths of the slug and bubbly regimes are typically very short compared to the overall tube length. The length of the single-phase section depends on the degree of outlet subcooling which is desired. High subcooling requires a long single-phase section.

The flow regime describes the physical configuration of the vapor and liquid in a two-phase flow. In annular flow, vapor flows in the center of the condenser and liquid flows in an annular film on the tube wall. Annular flow occurs at high qualities and void fractions. When there is too little vapor to support annular flow, slug flow begins. In slug flow, vapor flows in bullet-shaped bubbles in the center of the tube, separated by liquid slugs. As more vapor condenses, the bubbles grow shorter and the slugs grow longer. Eventually the large bubbles break up, and the bubbly regime begins. Ultimately all the vapor condenses and single-phase liquid remains.

The flow regime within a segment is calculated by a set of simple criteria based on the local void fraction. These approximate regime calculations are accurate for spacecraft accelerations less than 0.01 g or small diameter tubes operated horizontally on the ground (see Section 1 for methods to calculate the transition to stratified flow, where the condenser methods are no longer valid). The flow regime determines the basic configuration of the vapor and liquid phases. As a result, the heat transfer, pressure drop, and void fraction calculations all depend on the local flow regime.

**Condensation Heat Transfer.** The rate of heat transfer from the condenser tube depends on the local flow regime, quality, and void fraction, as well as the external boundary conditions. The design methods incorporate different relations for the heat transfer rate depending on the local flow regime. The design methods include more than one option for calculating the heat transfer in the annular flow regime (along with a recommendation based on comparison with experimental data). The optional methods allow the designer to assess the sensitivity of the design to the choice of the heat transfer model, and enable comparison with multiple models when evaluating test data.

The relative amounts of liquid and vapor flow at any position along the condenser tube are described by the thermodynamic quality. The quality is defined as the ratio of the mass flow rate of the vapor phase, measured at a particular point along the condenser tube, to the total mass flow rate through the condenser:

$$x \equiv \dot{m}_{\text{vap}} / \dot{m}_{\text{tot}} \quad (6-1)$$

where  $x$  = the quality,  
 $\dot{m}_{\text{vap}}$  = mass flow rate of vapor (kg/s),  
 $\dot{m}_{\text{tot}}$  = total mass flow rate (vapor + liquid) (kg/s).

The quality is a measure of the amount of energy removed from the fluid by condensation. An energy balance between any two points in the condenser tube relates the change in quality to the linear heat transfer rate from the condenser:

$$q' = \frac{\dot{m} h_{fg} \Delta x}{\Delta z} \quad (6-2)$$

where

$q'$	= heat transfer per unit length (W/m),
$h_{fg}$	= latent heat of evaporation (J/kg),
$\Delta x$	= change in quality over length $\Delta z$ ,
$\Delta z$	= a distance along the condenser tube (m).

Figure 6.4 shows typical results of heat transfer calculations for a shear condenser tube, illustrating the variation in fluid quality along the length of an ammonia condenser. Decreasing quality along the length of the tube indicates increasing liquid flow due to condensation. Negative quality at the exit indicates subcooling. The figure also shows the void fraction, which decreases with the quality and determines the flow regime in the condenser. The rate of change of quality along the length of the tube depends on the local heat transfer coefficient, which depends on the local flow regime.

In the annular flow regime, the Nusselt number for condensation may be calculated by any one of three methods:

- Rohsenow, Webber, and Ling (1956),
- Soliman, Schuster, and Berenson (1968),
- Shah (1979).

Based on comparison of model results with experimental data, we recommend the method of Rohsenow, Webber, and Ling. This method contains a mechanistic treatment of heat transfer through a turbulent liquid film. The method of Soliman, Schuster, and Berenson and the method of Shah include empirical correlations for the local heat transfer coefficient.

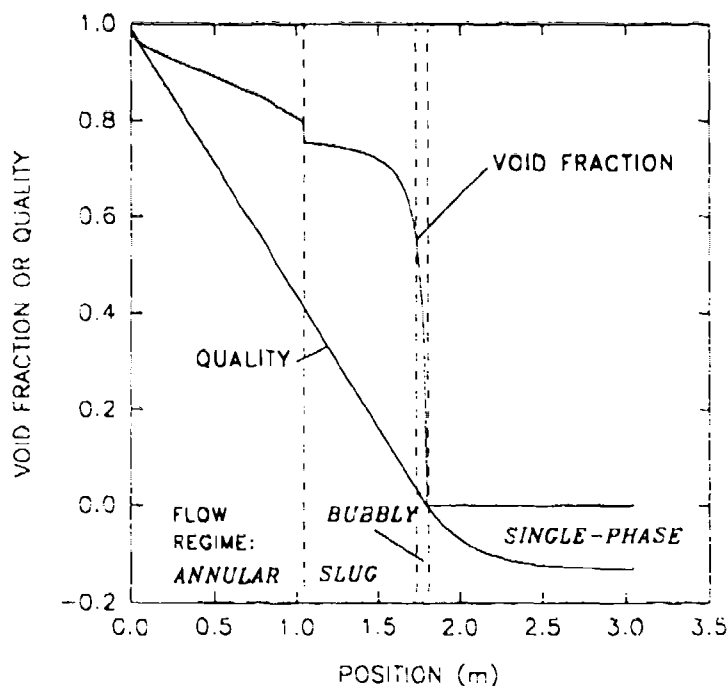


Figure 6.4. QUALITY AND VOID FRACTION PROFILES IN A SHEAR CONDENSER

In the slug flow regime, heat transfer is calculated based on a mechanistic analysis of heat transfer to alternating liquid slugs and the liquid film surrounding the Taylor bubbles. An empirical "mixing coefficient" is incorporated to match the high heat transfer rates observed in the slug regime during ground tests.

Bubbly condensation is modelled as a homogeneous flow. The heat transfer coefficient is calculated using single-phase correlations, except that the fluid properties used in these correlations are weighted averages of the vapor and liquid properties.

**Void Fraction.** The void fraction is a key parameter which is equal to the local, time-averaged area fraction of the condenser tube occupied by the vapor phase. Heat transfer and pressure losses depend strongly on the void fraction. The void fraction calculation, in turn, depends on the local flow regime.

In the annular regime, the void fraction is calculated by balancing the pressure losses in the vapor core and the liquid film. The key parameter in this calculation is the friction factor ratio,  $(f_i/f_{wg})$ , which is equal to the ratio of interfacial shear stress to the wall shear stress which would occur if the vapor phase were flowing alone in the condenser. The friction factor ratio is calculated using empirical correlations which depend on the local void fraction. The method of Chen (1989) has been found to give best agreement with pressure drop measurements in microgravity tests of shear condensers (see Section 6.8). Designers may also wish to compare results with Wallis's correlation (Wallis, 1969) or with bounding calculations in which  $f_i/f_{wg}$  is set to a constant value.

The void fraction in the slug regime is calculated using a drift-flux model. A homogeneous model is used in the bubbly regime. Section 3.2 of the manual describes the drift flux model in detail.

**Pressure Losses in Condensation.** The total pressure drop through the condenser is the sum of pressure drops due to friction, liquid deceleration, body forces, and taper (if any). Friction is usually the largest contributor to the total pressure drop, and the amount of friction depends strongly on the local flow regime. The design methods call for different methods to calculate the frictional pressure loss in each regime. Pressure losses due to fluid deceleration and body forces depend on the local void fraction, and thus these calculations will vary depending on the model chosen for void fraction in the annular regime (see below).

Figure 6.5 shows pressure drop profiles calculated for an ammonia condenser tube. In this case (simulating a ground test of a horizontal tube) the body forces are negligible, the tube has no taper, and the pressure drop is mainly due to friction in the annular flow regime. Fluid deceleration reduces the pressure drop by about 15% from the amount calculated from friction alone.

Generally, in shear condensers the frictional pressure drop dominates and occurs primarily in the annular flow regime. The frictional pressure loss in the annular flow regime is calculated based on analysis of the forces acting on the gas phase of the fluid. A key parameter for this calculation is the ratio of the interfacial friction factor to the wall friction factor for single-phase gas  $(f_i/f_{wg})$ . This factor is calculated using correlations which depend on the local void fraction. The design methods software recommends a correlation and allows the user to use other correlations as well, as described below.

As the vapor condenses into liquid, its velocity decreases because the liquid density is so much higher than the vapor. This fluid deceleration gives rise to a pressure recovery in the condenser tube which decreases the total pressure drop. The pressure recovery in a segment depends only on the quality and void fraction at the inlet and exit.



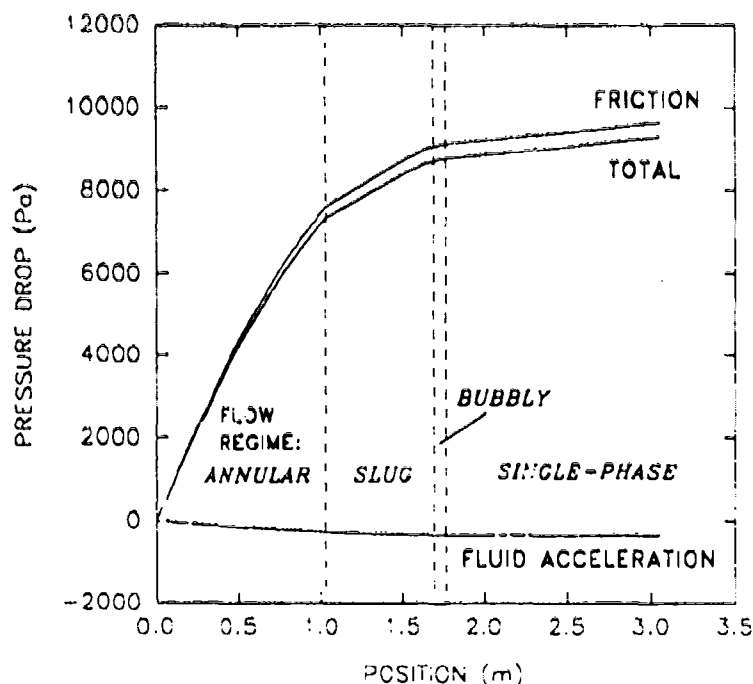


Figure 6.5. PRESSURE DROP PROFILES IN A SHEAR CONDENSER

Pressure losses due to body forces are generally negligible if the spacecraft acceleration is less than 0.01 g or if the tube operates horizontally on the ground.

**Dimensionless Design Maps.** Dimensionless design maps are useful because they show the general dependencies and scaling relationships for condenser design. The maps allow quick hand calculations for scoping analysis or verification of computer code results.

The design methods include dimensionless design maps for heat transfer and pressure losses in the annular flow regime. Methods are presented for modelling a condensing radiator using MICROCON. The heat transfer maps allow quick calculation of the condensing length, and the pressure drop maps enable estimation of the total pressure drop. Because turbulent film condensation depends on many fluid parameters (inlet Reynolds number, Prandtl number, and liquid/vapor ratios of viscosity and density), the dimensionless maps are provided for several specific fluids which are of prime interest for spacecraft thermal management.

### 6.3 Calculation Procedure for a Shear Condenser Tube

This section describes the overall procedure for calculating heat transfer and pressure drop in a shear condenser tube.

The calculations described here make up a numerical procedure in which the tube is broken up into a large number of small segments, which are analyzed in sequence. The MICROCON program performs these calculations. The basic sequence of calculations is:

- Determine the inlet conditions to a segment,
- Calculate the flow regime in the segment,
- Calculate heat transfer in the segment,
- Calculate the void fraction at the exit of the segment,

- Calculate the pressure drop in the segment,
- Proceed with the next segment.

The inlet conditions to each segment are known from the condenser inlet conditions or from the previous segment calculation. Flow regime is calculated from the inlet conditions. Heat transfer and pressure losses in the segment are calculated using the problem boundary conditions and constitutive relationships for the appropriate flow regime.

Figure 6.6 is a flow chart which details the steps in a condenser tube calculation. The basic calculations for each segment appear in the center of the flow chart. The segment calculations are sequenced and controlled by two program loops. The inner loop performs segment calculations in sequence from the inlet to the exit of the condenser tube, passing exit conditions from one segment as inlet conditions to the next. The outer loop performs iterative calculations for the entire tube for problems in which the flow boundary condition is a specified pressure-drop.

The remainder of this section describes the calculation procedure in detail.

### 6.3.1 Boundary Conditions

Design methods are provided for several different thermal and flow boundary conditions. Heat transfer calculations can use either convective or radiative boundary conditions. Either the mass flow rate or the total pressure drop across the condenser tube may be specified.

**Thermal Boundary Conditions.** Table 6.1 summarizes the thermal boundary conditions for the shear condenser analysis. Most of the parameters required for the two cases are the same, except that in the radiative case the secondary coolant temperature is replaced with a heat sink temperature, and the secondary heat transfer coefficient is replaced with the emissivity of the radiating surface. The user has the option of including a value for absorbed orbital average heat flux ( $q''_{env}$ ) if the sink temperature does not already account for it. If  $T_2$  does account for the absorbed heat flux, then use  $q''_{env} = 0$ .

Table 6.1. THERMAL BOUNDARY CONDITIONS FOR SHEAR CONDENSER ANALYSIS			
BOUNDARY CONDITION	REQUIRED PARAMETERS	DESCRIPTION	UNITS
CONVECTION	$T_2$	Secondary coolant temperature	K
	$h_2$	Secondary heat transfer coeff.	W/m <sup>2</sup> -K
	$P_x$	Tube external perimeter	m
	$t_w$	Tube wall equivalent thickness	m
	$k_w$	Tube wall thermal conductivity	W/m-K
RADIATION	$T_2$	Heat sink temperature	K
	$\epsilon$	Emissivity of radiating surface	---
	$P_x$	Tube external perimeter	m
	$t_w$	Tube wall equivalent thickness	m
	$k_w$	Tube wall thermal conductivity	W/m-K
	$q''_{env}$	Absorbed orbital average heat flux	W/m <sup>2</sup>

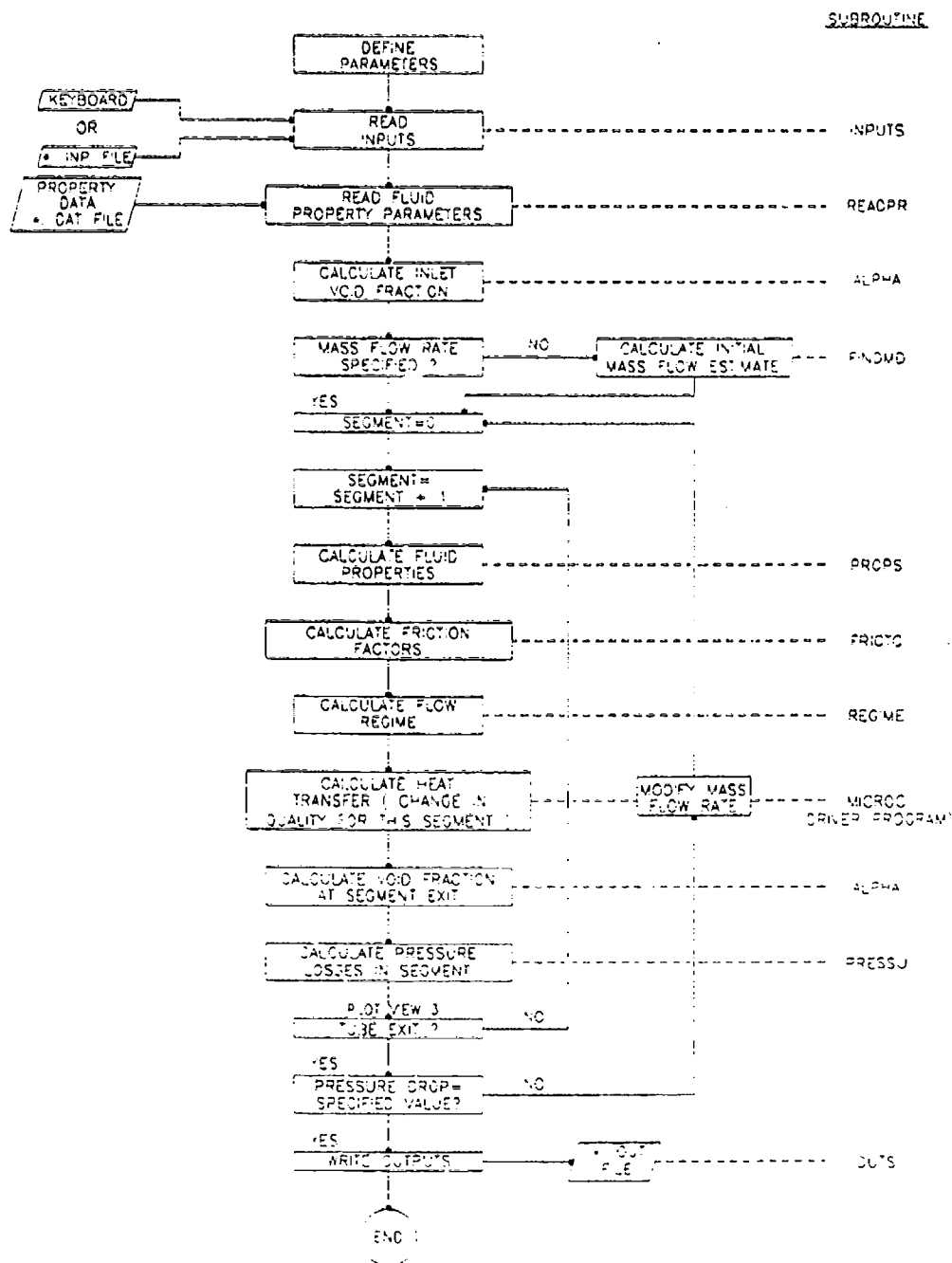


Figure 6.6. STEPS IN A CONDENSER TUBE CALCULATION

The equivalent wall thickness,  $t_w$ , requires some explanation.  $t_w$  is the thickness for which a one-dimensional calculation of heat transfer across the wall at a given temperature drop produces the same result as a more precise calculation. It is equal to the actual wall thickness if the condenser is a thin-walled tube. For complex two-dimensional structures, the designer must first calculate the conduction heat transfer from the inside of the condenser tube to the heat removal surface. Then  $t_w$  is calculated by:

$$t_w = \frac{k_w P_i \Delta T_w}{q} \quad (6-3)$$

where  $k_w$  = thermal conductivity of the wall structure (W/m-K),  
 $P_i$  = internal perimeter of the condenser tube (m),  
 $\Delta T_w$  = temperature drop across the wall in the 2D calculation (K), and  
 $q$  = heat transfer rate per unit tube length (W/m).

For a spacecraft radiator,  $\Delta T_w$  is the difference in temperature between the wall inside temperature and the effective, average radiating temperature,  $T_x$ .  $T_x$  should account for the radiating fin efficiency and the view factor of the radiator panel. Section 6.7 shows how to model the boundary conditions of a condensing radiator.

**Flow Boundary Conditions.** Table 6.2 summarizes the possible flow boundary conditions. Either the mass flow rate ( $\dot{m}$ ) or the total pressure drop ( $\Delta P_{tot}$ ) may be specified.

### 6.3.2 Preliminary Calculations

Before beginning the calculations for successive segments in the condenser, several global parameters must be calculated. Note that for cases in which the condenser geometry is not constant, such as a tapered-tube condenser, these parameters must be recalculated for every segment.

**Hydraulic Diameter,  $D_h$ .** The hydraulic diameter is defined as:

$$D_h = \frac{4A}{P_i} \quad (6-4)$$

where  $A$  = cross sectional area for fluid flow (m<sup>2</sup>),  
 $P_i$  = internal perimeter of the condenser tube (m).

Table 6.2. FLOW BOUNDARY CONDITIONS FOR SHEAR CONDENSER ANALYSIS			
BOUNDARY CONDITION	REQUIRED PARAMETERS	DESCRIPTION	UNITS
FLOW RATE	$\dot{m}$	Mass flow rate	kg/s
PRESSURE DROP	$\Delta P_{tot}$	Total pressure drop	Pa

**Dimensionless Segment Length,  $\Delta z^*$ .** The dimensionless segment length is the actual segment length,  $\Delta z$ , divided by the hydraulic diameter of the tube:

$$\Delta z^* = \frac{\Delta z}{D_h} \quad (6-5)$$

**Mass Flux Ratio,  $R_c$ .** The mass flux ratio is a dimensionless number which characterizes the condensation. It is proportional to the ratio of condensing mass flux to the mass flux flowing through the tube.

$$R_c = \frac{4(T_{sat} - T_2)k_l}{G h_{fg} D_h} \quad (6-6)$$

where

$T_{sat}$	=	saturation temperature (K),
$T_2$	=	secondary temperature (K),
$k_l$	=	thermal conductivity of liquid (W/m-°C),
$G$	=	mass flux through condenser (kg/m <sup>2</sup> -s),
$h_{fg}$	=	heat of vaporization (J/kg).

**Liquid-Only Reynolds Number,  $Re_{lo}$ .** This is the Reynolds number calculated as if all fluid in the tube were in the liquid phase.

$$Re_{lo} = \frac{G D_h}{\mu_l} \quad (6-7)$$

where  $\mu_l$  = viscosity of the liquid phase (kg/m-s).

**Liquid Prandtl Number,  $Pr_l$ .** This is the Prandtl number of the liquid phase.

$$Pr_l = \frac{\mu_l c_{pl}}{k_l} \quad (6-8)$$

where  $c_{pl}$  = specific heat of the liquid phase (J/kg-K).

**Liquid-Only Nusselt Number,  $Nu_{lo}$ .** This is the Nusselt number calculated as if all fluid were in the liquid phase.

$$Nu_{lo} = \begin{cases} 0.023 Re_{lo}^{0.8} Pr_l^{0.4} & (Re_{lo} > 1500) \\ 3.66 & (Re_{lo} \leq 1500) \end{cases} \quad (6-9)$$

### 6.3.3 Segment Calculations

Within each segment there are four basic calculations:

- Flow regime,
- Heat transfer,
- Void fraction, and
- Pressure drop.

This section covers the general procedure for calculating the change in fluid quality and pressure within each segment. The detailed constitutive relationships which are used to calculate the heat transfer coefficient, pressure drop, and void fraction depend on the flow regime in the segment. These regime-dependent calculations are covered in Sections 6.4 (condensing heat transfer coefficient), 6.5 (pressure drop), and 6.6 (void fraction).

**Flow Regime.** The flow regime is calculated at the inlet of each segment. The simplified flow regime criteria, applicable for spacecraft accelerations less than 0.01g, or small-diameter, horizontal tubes, are:

0.80	$\leq \alpha < 1.00$	$\Rightarrow$	ANNULAR
0.45	$\leq \alpha \leq 0.80$	$\Rightarrow$	SLUG
0.00	$< \alpha \leq 0.45$	$\Rightarrow$	BUBBLY
	$\alpha \leq 0.00$	$\Rightarrow$	SINGLE-PHASE

**Heat Transfer.** Heat transfer in a segment is calculated with the following procedure:

1. Calculate the Nusselt number,
2. Calculate the fluid temperature,
3. Calculate the change in fluid quality.

1.) Calculate the Nusselt number. The Nusselt number calculation depends on the local flow regime in the segment, as well as the choice of constitutive model. This calculation is detailed in Section 6.4. The result of this calculation is the Nusselt number for condensation,  $Nu_c$ :

$$Nu_c \equiv \frac{h_c D_h}{k_l} \quad (6-10)$$

where

$h_c$	= heat transfer coefficient for condensation (W/m <sup>2</sup> -K),
$D_h$	= hydraulic diameter of the condenser tube (m),
$k_l$	= thermal conductivity of the liquid phase (W/m-K).

2.) Calculate the fluid temperature. The fluid temperature is equal to the saturation temperature if vapor and liquid are both present in the segment. After the vapor has completely condensed, the temperature of the single-phase liquid drops due to further cooling.

Calculate fluid temperature by:

$$T_f = \begin{cases} T_{sat}(P) & x \geq 0.0 \\ T_{sat}(P) + \frac{x h_{fg}}{c_{pl}} & x < 0.0 \end{cases} \quad (6-11)$$

Where

$T_f$	= local fluid temperature (K),
$T_{sat}$	= saturation temperature corresponding to local pressure (K),
$p$	= local pressure (Pa),
$x$	= fluid quality at the inlet to the segment (-),
$h_{fg}$	= latent heat of vaporization (J/kg),
$c_{pl}$	= heat capacity of the liquid phase (J/kg-K).

When the quality is negative, the second equation in 6-11 produces a subcooled temperature.

3.) Calculate the change in fluid quality. The change in fluid quality in a segment depends on the amount of heat transfer. The heat transfer calculation depends on whether the boundary condition is convective or radiative heat transfer.

For the convective boundary condition, the change in quality is calculated by:

$$\Delta x = \frac{R_c \Delta z^*}{\frac{1}{Nu_c} + \frac{k_l t_w}{k_w D_h} + \frac{P_i k_l}{P_x h_2 D_h}} \times \frac{T_f - T_2}{T_{sat} - T_2} \quad (6-12)$$

The denominator of the first term contains three terms, corresponding to the heat transfer resistances in the condensate film, tube wall, and external heat transfer. The second term in Equation 6-12 is equal to 1.0 in the two-phase region of the condenser and decreases in the single-phase region as the liquid becomes subcooled and approaches the secondary temperature.

The radiative boundary condition leads to a non-linear equation for the heat transfer rate, so calculating the change in quality is not as simple. Two equations must be solved simultaneously to calculate the heat transfer by equating the heat transfer inside the condenser to the heat removed by radiation. The heat removed by radiation is:

$$q' = P_2 \sigma_o \epsilon (T_x^4 - T_2^4) - P_2 q''_{env} \quad (6-13)$$

where

- $q'$  = heat transfer per unit length of condenser (W/m),
- $q''_{env}$  = absorbed orbital average heat flux (W/m<sup>2</sup>),
- $P_2$  = total perimeter for radiation (m),
- $\sigma_o$  = Stefan-Boltzmann constant ( $5.67 \times 10^{-8}$  W/m<sup>2</sup>-K<sup>4</sup>),
- $\epsilon$  = emissivity of the radiator surface (-),
- $T_x$  = average effective temperature of the radiator surface (K).

The heat removed by condensation inside the condenser tube and conduction through the surrounding structure is:

$$q' = \frac{T_f - T_x}{\frac{1}{h_c P_i} + \frac{t_w}{k_w P_i}} \quad (6-14)$$

The only unknowns in Equations 6-13 and 6-14 are  $q'$  and  $T_x$ , the average effective temperature of the radiator surface. These two equations must be solved for these two variables. In the MICROCON program, an initial estimate for  $q'$  is calculated using Equation 6-13 assuming that  $T_x$  is equal to  $T_f$ . Then a bisection search is used to calculate the value of  $q'$  for which  $T_x$  calculated from both equations is equal.

Once  $q'$  has been calculated for the radiator, the change in quality is:

$$\Delta x = \frac{q' \Delta z}{m h_{fg}} \quad (6-15)$$

where  $\Delta z$  = segment length (m).

**Void Fraction.** Once the quality at the segment exit is known, the next step is to calculate the void fraction. The exit quality is calculated by subtracting the change in quality ( $\Delta x$ ) from the inlet quality. The void fraction at the segment exit is then calculated from the exit quality depending on the local flow regime. The regime-dependent methods for calculating the void fraction are detailed in Section 6.5

**Pressure Drop.** The pressure drop in the segment is now calculated based on the average quality and void fraction. The results of these calculations are four pressure drop components which are summed to yield the overall pressure drop in the segment:

$$\Delta P = \Delta P_f + \Delta P_a + \Delta P_g + \Delta P_t \quad (6-16)$$

where

$\Delta P$	=	total pressure drop in the segment (Pa),
$\Delta P_f$	=	pressure drop due to friction (Pa),
$\Delta P_a$	=	pressure drop due to fluid deceleration (Pa),
$\Delta P_g$	=	pressure drop due to body forces (Pa),
$\Delta P_t$	=	pressure drop due to taper of the condenser tube (Pa).

Calculation of each component of the pressure drop depends on the local flow regime. These calculations are detailed in Section 6.6.

#### 6.3.4 Calculation of the Entire Condenser Tube

Segment calculations are performed in sequence to calculate the performance of an entire condenser tube. There are two basic steps in the tube calculation:

- 1.) Calculate inlet conditions to the first segment,
- 2.) Calculate each segment in the condenser.

Inlet conditions for the entire tube are calculated from program inputs such as the inlet quality and mass flow rate. The inlet conditions for each segment are either the tube inlet conditions or the exit conditions from the previous segment.

**Number of Segments.** We recommend that the condenser be modeled with at least 100 segments so that the conditions in each segment are relatively constant.

**Inlet Conditions to the Condenser Tube.** The total mass flow rate and the quality at the inlet of the condenser tube are known inputs to the problem. (See Table 6.1). The void fraction at the inlet is calculated assuming annular flow. Fluid properties at the inlet are calculated for saturated liquid and vapor at the inlet pressure.

**Calculate Each Segment in the Condenser.** Once the inlet conditions to the condenser tube have been calculated, each segment is calculated in turn. Fluid properties are recalculated at the inlet of each segment. The flow regime and heat transfer in the segment are evaluated based on the inlet quality and void fraction. Next the exit quality is calculated from the amount of heat transfer. The void fraction at the exit of the segment is then calculated based on the exit void fraction and the local flow regime. The average quality and void fraction in the segment are calculated based on the inlet and outlet values, and the pressure drop in the segment is calculated based on these average values.



### 6.3.5 Mass Flow Rate Iterations for Specified Pressure Drop

MICROCON contains procedures to calculate the mass flow rate through a condenser tube with a specified pressure drop. This iteration contains three basic steps:

- 1.) Estimate the mass flow rate,
- 2.) Calculate the pressure drop,
- 3.) Modify the mass flow rate.

A rough, initial estimate of the mass flow rate is made from the specified pressure drop based on some simplifying assumptions about the flow. Then the pressure drop through a condenser tube is calculated using the standard MICROCON procedures described in the previous sections. The calculated pressure drop is compared to the specified pressure drop. The mass flow rate is modified based on this comparison, and iterations continue until the calculated and specified pressure drops agree.

First Estimate of the Mass Flow Rate. The initial estimate of the mass flow rate is based on a simplified analysis of the pressure drop which assumes that:

- The void fraction is constant over the entire tube,
- The void fraction is equal to the inlet void fraction,
- Frictional pressure drop can be calculated with a simplified liquid-phase momentum balance, and
- The tube has no taper.

Under these assumptions, the friction pressure drop is:

$$\Delta P_f = 4 f_{wl} \frac{L}{D_h} \frac{(1-x_{in})^2}{(1-\alpha_{in})^2} \frac{G^2}{2\rho_l} = F_f G^2 \quad (6-17)$$

where

- $f_{wl}$  = liquid-only friction factor, assume  $f_{wl} = 0.005$ .
- $L$  = total length of the condenser tube (m),
- $x_{in}$  = inlet quality,
- $\alpha_{in}$  = void fraction at the inlet,
- $G$  = total mass flux (liquid and vapor phases) (kg/m<sup>2</sup>-s)
- $F_f \equiv 4 f_{wl} \frac{L}{D_h} \frac{(1-x_{in})^2}{(1-\alpha_{in})^2} \frac{1}{2\rho_l}$

The pressure drop due to body forces is estimated by:

$$\Delta P_g = - [ (1-\alpha_{in})\rho_l + \alpha_{in}\rho_g ] L a \cos\theta \quad (6-18)$$

where

- $a$  = spacecraft acceleration (m/s<sup>2</sup>),
- $\theta$  = angle between flow and body force vector vectors (rad).

The pressure drop due to fluid deceleration is calculated by:

$$\Delta P_a = \left[ 1 - \frac{x_{in}^2}{\alpha_{in}} \frac{\rho_l}{\rho_g} - \frac{(1-x_{in})^2}{1-\alpha_{in}} \right] \frac{G^2}{\rho_l} = F_a G^2 \quad (6-19)$$

where

$$F_a \equiv \left[ 1 - \frac{x_{in}^2}{\alpha_{in}} \frac{\rho_l}{\rho_g} - \frac{(1-x_{in})^2}{1-\alpha_{in}} \right] \frac{1}{\rho_l} \quad (6-20)$$

Then the mass flow rate is first estimated by:

$$G_{est} = \left[ \frac{(\Delta p_{tot} - \Delta p_g)}{F_f + F_a} \right]^{0.5} \quad (6-21)$$

where  $F_f$  and  $F_a$  are the frictional and acceleration pressure drop factors defined in Equations 6.17 and 6.20.

**Calculate the Pressure Drop.** Calculate the heat transfer and pressure drop along the entire condenser tube with a mass flux of  $G_{est}$  as described in Sections 6.4 through 6.6. The components of the pressure drop calculated in this procedure are  $\Delta P_{f,est}$  (friction),  $\Delta P_{a,est}$  (fluid deceleration),  $\Delta P_{g,est}$  (body forces), and  $\Delta P_{g,tap}$  (taper). The total estimated pressure drop is  $\Delta P_{tot,est}$ .

**Modify the Mass Flow Rate.** Calculate an improved estimate for the mass flux based on the pressure drop calculations. The calculation is based on the ratio of the pressure drop components calculated from the last estimate for the mass flux to the total pressure drop specified for the condenser tube:

$$G_{new} = G_{est} \left[ \frac{\Delta P_{tot} - \Delta P_{g,est} - \Delta P_{a,est}}{\Delta P_{f,est} + \Delta P_{g,est}} \right]^{0.5} \quad (6-22)$$

**Stop Iterations.** When the estimated pressure drop ( $\Delta P_{tot,est}$ ) is within 0.1% of the specified pressure drop, stop the iterations. The last value for  $G_{est}$  is the mass flux through the condenser tube.

## 6.4 Condensing Heat Transfer Coefficient

The change in quality in a segment (Section 6.3.3, equation 6-12 or 6-15) depends on the Nusselt number for condensation. A high Nusselt number corresponds to a large heat transfer coefficient and implies very effective heat transfer. The Nusselt number depends on the flow regime, since the heat transfer depends on the relative locations in a segment of the liquid and vapor phases. This section presents the methods used to calculate the Nusselt numbers for each flow regime in a shear condenser.

### 6.4.1 Annular Flow

Most heat transfer usually occurs in the annular flow regime because the vapor is much less dense than the liquid. As a result, the void fraction remains high even at low values of the quality. Because the annular regime is key to designing the condenser, the design methods for the annular regime are more detailed than for the other regimes. The first step is to calculate the dimensionless thickness of the liquid film. Thin films are laminar, while thick films are turbulent.

If the film is laminar, then the Nusselt number is calculated by a simple analysis of heat conduction across the liquid film. If the film is turbulent, then there are three options for calculating the condensing Nusselt number:

- Method of Rohsenow, et al. (1956),
- Method of Soliman, et al. (1963),
- Method of Shah (1979).

The method of Rohsenow, et al., is recommended and the alternate models are useful for sensitivity studies or detailed analysis of test data. The following paragraphs detail the calculations according to each method.

**Dimensionless Film Thickness.** The first step is to calculate the dimensionless film thickness, which characterizes the liquid flow. First calculate  $\delta$ , the actual film thickness:

$$\delta = \frac{D_h (1-\alpha)}{4} \quad (6-23)$$

where  $\delta$  = film thickness (m),  
 $D_h$  = hydraulic diameter of condenser tube (m),  
 $\alpha$  = local void fraction.

Next calculate the local velocity of the vapor:

$$u_g = \frac{G x}{\rho_g \alpha} \quad (6-24)$$

where  $u_g$  = velocity of the vapor (m/s),  
 $G$  = total mass flux (kg/m<sup>2</sup>-s),  
 $x$  = local thermodynamic quality (-).

Next calculate  $f_i/f_{wg}$ , the ratio of the interfacial friction factor to the friction factor calculated as if all fluid were vapor:

$$f_i/f_{wg} = A \alpha^B + C (1-\alpha)^D \quad (6-25)$$

where A, B, C, and D are empirical coefficients. The values of the coefficients depend on the model selected for the interfacial shear. Table 6.3 presents values for the empirical coefficients for several interfacial shear correlations. The method of Chen is recommended generally for design calculations if more accurate data is not available.

Calculate the Reynolds number for the vapor phase alone:

$$Re_g = \frac{G x D_h}{\mu_g} \quad (6-26)$$

Table 6.3. EMPIRICAL COEFFICIENTS FOR $f_i/f_{wg}$				
Correlation	Coefficient for $f_i/f_{wg} = A\alpha^B + C(1 - \alpha)^D$			
	A	B	C	D
Chen	1	0	6.8	0.39
Wallis	1	0	75	1
Duschatko	1	0	2.5	0.39
Smooth film	1	0	0	0
Rough film	10	0	0	0

Next calculate  $f_{wg}$ , the friction factor calculated for the vapor phase alone:

$$f_{wg} = \begin{cases} 0.046 \text{ Re}_g^{-0.2} & (\text{Re}_g > 1500) \\ 17 \text{ Re}_g & (\text{Re}_g \leq 1500) \end{cases} \quad (6-27)$$

Then calculate the wall shear:

$$\tau_w = f_{wg}(f_l/f_{wg}) \frac{\rho_g u_g^2}{2} \quad (6-28)$$

where  $\tau_w$  = wall shear (Pa).

The dimensionless film thickness is:

$$\delta^+ = \frac{\delta}{v_l} \left[ \frac{\tau_w}{\rho_l} \right]^{0.5} \quad (6-29)$$

where  $v_l$  = kinematic viscosity of the liquid (m<sup>2</sup>/s).

The value of  $\delta^+$  indicates whether the liquid flow is laminar or turbulent:

$$\delta^+ < 6 \quad \Rightarrow \text{laminar film,} \quad (6-30)$$

$$\delta^+ \geq 6 \quad \Rightarrow \text{turbulent film.} \quad (6-31)$$

If the film is laminar, calculate the Nusselt number according to the laminar film section below. If the film is turbulent, calculate the Nusselt number according to one of the three turbulent film models detailed in the paragraphs following the laminar film discussion.

Nusselt Number for Laminar Films. In a laminar liquid film, heat transfer is accomplished by conduction across the film. In this case, the Nusselt number is calculated by:

$$\text{Nu}_c = \frac{D_h}{\delta} \quad (6-32)$$

Method of Rohsenow. The method of Rohsenow is recommended for turbulent films. It is the most mechanistic of the three annular condensation models and has been qualified through comparison with condenser test data. In this method, the Nusselt number depends on the dimensionless film thickness.

First calculate the factor  $F_2$ , which depends on  $\delta^+$ . For low values of  $\delta^+$  (between 6.0 and 30), use this equation:

$$F_2 = 5 \text{ Pr}_l + 5 \ln \left[ 1 + \text{Pr}_l \left( \frac{\delta^+}{5} - 1 \right) \right] \quad (\text{for } 6 \leq \delta^+ \leq 30) \quad (6-33)$$

where  $\text{Pr}_l$  is the Prandtl number of the liquid phase.

For high values of  $\delta^+$ , use this equation:

$$F_2 = 5 \text{Pr}_1 + 5 \ln(1 + 5\text{Pr}_1) + 2.5 \ln(3) \quad (\text{for } \delta^+ \geq 30) \quad (6-34)$$

Next calculate the condensing Nusselt number:

$$\text{Nu}_c = \delta^+ \frac{D_h}{\delta} \frac{\text{Pr}_1}{F_2} \quad (6-35)$$

Rohsenow et al. (1956) provide a detailed analysis leading to these equations.

Method of Soliman et al. In this method there is a single equation to calculate the condensing Nusselt number:

$$\text{Nu}_c = 0.036 \delta^+ \frac{D_h}{\delta} \text{Pr}_1^{0.65} \quad (6-36)$$

Soliman et al. (1968) explain the analysis and derive this equation.

Method of Shah. Shah's correlation is the most empirical of the three methods for turbulent liquid films. The equation for the Nusselt number is:

$$\text{Nu}_c = \text{Nu}_{lo} \left[ \frac{[(1-x)^{0.83} + 3.8x]^{0.76} (1-x)^{0.04}}{(P/P_{crit})^{0.38}} \right] \quad (6-37)$$

where

- $x$  = local thermodynamic quality,
- $P$  = the local fluid pressure (Pa),
- $P_{crit}$  = the critical pressure of the fluid (Pa),
- $\text{Nu}_{lo}$  = Nusselt number calculated as if all flow were liquid (Equation 6-9).

#### 6.4.2 Slug Flow

Slug flow typically follows the annular regime. In slug flow the vapor phase forms elongated bubbles which are located centrally in the pipe. The liquid phase forms slugs which separate the bubbles and also a film surrounding the bubbles. The design methods include an ad-hoc model for heat transfer in the slug flow regime. Heat transfer is modeled as a time-averaged combination of single-phase heat transfer from the liquid slugs and condensation of the vapor bubbles. An empirical enhancement factor is recommended to model developing flow effects which greatly increase the rate of heat transfer to the slugs.

Figure 6.7 illustrates the vapor and liquid flow pattern in the slug regime. Bubbles of length  $L_b$  are separated by slugs of length  $L_s$ . The total length of a slug plus a bubble is  $L_{tot}$ . As vapor condenses, the bubbles grow shorter. The average velocity of the liquid in the slugs is the total volumetric flux,  $j$ . The bubbles are surrounded by a liquid film which is essentially motionless because there is almost no shear acting on it (the pressure drop in a bubble is close to zero). Thus the bubble velocity  $u_b$  is equal to  $j/(1-m)$ , where  $m$  is the area fraction of the liquid film.

Heat transfer in the slug regime is controlled by convective heat transfer from the liquid slugs. Heat transfer from the slugs is quite efficient because the slugs are dominated by turbulent mixing and convective heat transfer. As a slug flows through the condenser tube, it continually "scoops up" the liquid film which surrounds the bubble in front of the slug. This

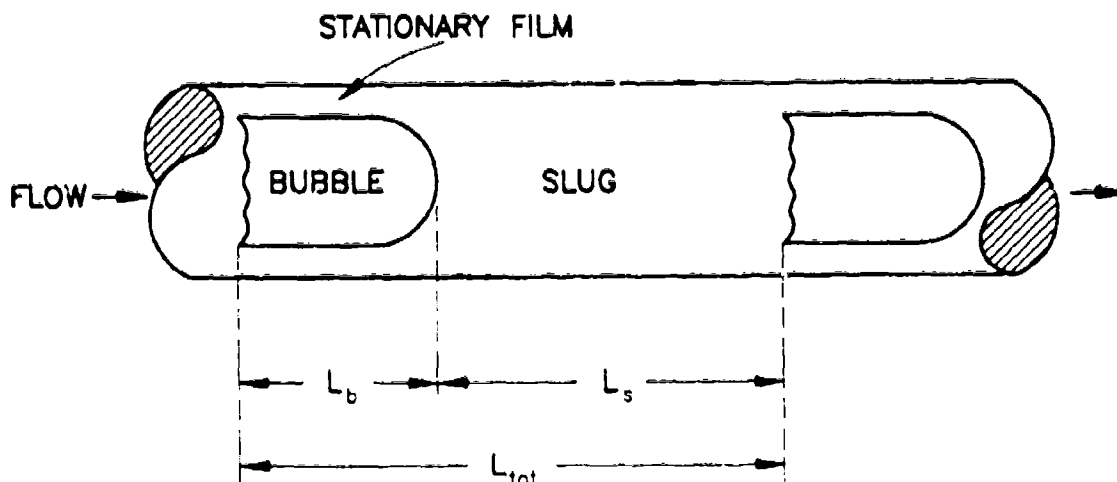


Figure 6.7. SLUG FLOW REGIME

film has been warmed by condensation from the bubble, and when it is scooped up, it is mixed with the liquid in the slug. Convective mixing due to developing flow leads to high rates of heat transfer which lower the temperature of the slug. Thus the film which trails off the back side of the slug is subcooled and causes condensation of the bubble behind the slug.

The procedure for calculating heat transfer in the slug flow regime is:

- 1.) Calculate the ratio of bubble to slug length,
- 2.) Calculate the Nusselt number for the slugs,
- 3.) Calculate the Nusselt number for the bubbles,
- 4.) Calculate the average Nusselt number.

These steps are explained in detail below.

1.) Calculate the ratio of bubble to slug length. The ratio of the bubble length to the total length of a bubble plus an adjacent slug depends only on the local flow quality and the vapor/liquid density ratio:

$$\frac{L_b}{L_{tot}} = \frac{x}{x + \frac{\rho_g}{\rho_l}(1-x)} \quad (6-38)$$

2.) Calculate the Nusselt number for the slugs. First a Nusselt number is calculated as if the flow in the slug were fully developed. Later this Nusselt number will be increased by an empirical factor to account for flow development and mixing effects which significantly increase the heat transfer. First calcu' the total volumetric flux:

$$j = G \left[ \frac{x}{\rho_g} + \frac{1-x}{\rho_l} \right] \quad (6-39)$$

where  $G$  = total mass flux ( $\text{kg}/\text{m}^2\text{-s}$ ).

Next calculate the Reynolds number for the liquid in the slug:

$$Re_s = \frac{G(1-x)D_h}{\mu_l} \quad (6-40)$$

Then the Nusselt number for the liquid slug, calculated as if the flow were fully developed, is:

$$Nu_s = \begin{cases} 0.023 Re_s^{0.8} Pr_l^{0.4} & (Re_s > 1500) \\ 3.66 & (Re_s \leq 1500) \end{cases} \quad (6-41)$$

3.) Calculate the Nusselt number for the bubbles. The heat transfer from the "bubbles" in the slug regime is typically much less than from the liquid slugs. Since the vapor does not touch the wall of the condenser tube, heat transfer occurs from the liquid in the film which surrounds the bubble. These films are almost always in laminar flow and heat transfer is governed by conduction through the film. As a result, heat transfer in the film is not very efficient.

Heat transfer in the liquid film depends on the cross-sectional area occupied by the liquid film. The ratio of film area to total area is denoted "m" and is almost always equal to 0.16:

$$m = 0.16 \quad (6-42)$$

More precise methods for calculating m can be found in Wallis (1969). But since the heat transfer to the film has little effect on the overall rate of heat transfer, we recommend using the constant value.

The Nusselt number for heat transfer from the film is then calculated as if the film were a steady, fully developed flow:

$$Nu_b = \frac{2}{1 - (1-m)^{0.5}} \quad (6-43)$$

4.) Calculate the average Nusselt number. Heat transfer from the condenser tube is dominated by the convective heat transfer from the liquid slugs. Thus the overall Nusselt number for condensation in the slug regime is calculated by weighting the slug heat transfer coefficient by the ratio of slug length to the total length of the slug plus a bubble.

$$Nu = \phi^2 Nu_s \left[ 1 - \frac{L_b}{L_{tot}} \right] + Nu_b \frac{L_b}{L_{tot}} \quad (6-44)$$

$\phi^2$  is an empirical constant which accounts for the effects of flow development and mixing. We recommend:

$$\phi^2 = 12 \quad (6-45)$$

Heat transfer data from slug condensation in ground tests (Crowley and Sam, 1991) indicate that condensation in the slug regime occurs much more quickly than can be calculated based on fully developed flow in the slugs. Calculations with an empirical factor of 12 match the condensing lengths measured in these experiments.

### 6.4.3 Bubbly Flow

In the bubbly flow regime, the flow is modeled as homogeneous. Heat transfer is calculated using single-phase relationships with the fluid properties modified to account for the presence of vapor bubbles in the liquid.

Calculate Average Fluid Properties. The density and viscosity of the two-phase bubbly mixture are calculated as weighted averages of the single-phase vapor and liquid values. The two-phase density is:

$$\rho_m = \alpha \rho_g + (1-\alpha) \rho_l \quad (6-46)$$

The two-phase viscosity is calculated by:

$$\mu_m = \left[ \frac{x}{\mu_g} + \frac{1-x}{\mu_l} \right]^{-1} \quad (6-47)$$

Calculate the Two-Phase Reynolds Number. The two-phase Reynolds number is based on the total volumetric flux and the average density and viscosity. The total volumetric flux is:

$$j = G \left[ \frac{x}{\rho_g} + \frac{1-x}{\rho_l} \right] \quad (6-48)$$

The two-phase Reynolds number is:

$$Re_m = \frac{\rho_m j D_h}{\mu_m} \quad (6-49)$$

Calculate the Two-Phase Nusselt Number. The two-phase Nusselt number for condensation is now calculated with standard relations used for single-phase heat transfer:

$$Nu_c = \begin{cases} 0.023 Re_m^{0.8} Pr_l^{0.4} & (Re_m > 1500) \\ 3.66 & (Re_m \leq 1500) \end{cases} \quad (6-50)$$

### 6.4.4 Single-Phase Liquid Flow

Heat transfer from subcooled, single-phase liquid is calculated using standard relations from the literature.

$$Nu_c = \begin{cases} 0.023 Re_{lo}^{0.8} Pr_l^{0.4} & (Re_{lo} > 1500) \\ 3.66 & (Re_{lo} \leq 1500) \end{cases} \quad (6-51)$$



## 6.5 Void Fraction

The void fraction is equal to the fraction of the condenser tube cross section which is occupied by vapor. It is a key parameter because it determines the velocities of the liquid and vapor phases. Calculation of the void fraction depends on the local flow regime.

### 6.5.1 Annular Flow

In the annular flow regime, the void fraction is calculated based on a momentum balance between the vapor and liquid phases. The quality in a segment is known from heat transfer calculations. Based on the quality, the volumetric fluxes of both the liquid and vapor phases are known, so liquid-only and vapor-only friction factors can be calculated. Then the void fraction can be calculated from these known quantities.

The first step is to calculate the vapor-only friction factor. First calculate the Reynolds number based on vapor-only flow in the segment:

$$Re_g = \frac{G \times D_h}{\mu_g} \quad (6-52)$$

where  $x$  is the average void fraction in the segment (in MICROCON, the value of the quality at both the inlet and exit are known before beginning the void fraction calculation).

Next calculate the friction factor based on vapor-only flow:

$$f_{wg} = \begin{cases} 0.046 Re_g^{-0.2} & Re_g \geq 1500 \\ 16/Re_g & Re_g < 1500 \end{cases} \quad (6-53)$$

The second step is to calculate the friction factor for liquid-only flow. Calculate the liquid-only Reynolds number by:

$$Re_l = \frac{G (1-x) D_h}{\mu_l} \quad (6-54)$$

where  $x$  is the average void fraction in the segment. Next calculate the friction factor based on liquid-only flow:

$$f_{wl} = \begin{cases} 0.046 Re_l^{-0.2} & Re_l \geq 1500 \\ 16/Re_l & Re_l < 1500 \end{cases} \quad (6-55)$$

Finally, the void fraction is calculated with the pressure balance relationship for annular flow. By setting the pressure loss due to liquid friction on the condenser wall equal to the pressure loss due to vapor friction with the liquid interface, a relationship can be derived between the void fraction and the quality. The void fraction is calculated by solving this relationship for  $\alpha$ :

$$\frac{(1-\alpha)^2}{\alpha^{2.5}} \frac{f_l}{f_{wg}} = \left[ \frac{1-x}{x} \right]^2 \frac{f_{wl}}{f_{wg}} \frac{\rho_g}{\rho_l} \quad (6-56)$$

where

$x$	$\equiv$ the local quality,
$\rho_l$	$\equiv$ density of the liquid phase (kg/m <sup>3</sup> ),
$\rho_g$	$\equiv$ density of the vapor phase (kg/m <sup>3</sup> ),
$\alpha$	$\equiv$ the local void fraction, and
$\frac{f_l}{f_{wg}}$	$\equiv$ the interfacial shear ratio.

Note that the left-hand side of Equation (6-56) depends only on the local void fraction, since  $f_l/f_{wg}$  is typically correlated as a function of the void fraction only. In MICROCON,  $f_l/f_{wg}$  is calculated by:

$$f_l/f_{wg} = A \alpha^B + C (1-\alpha)^D \quad (6-57)$$

where A, B, C, and D are empirical coefficients. There is a single value of  $\alpha$  between 0 and 1.0 which satisfies Equation 6-56.

Since Equation 6-56 is nonlinear, there is no explicit solution for the void fraction as a function of the quality. In MICROCON,  $\alpha$  is determined iteratively using a bisection search.

## 6.5.2 Slug Flow

In the slug flow regime, the void fraction is calculated based on a drift-flux model for the flow. Wallis (1969) explains the derivation of these models in detail; here we simply present the calculations recommended for condenser design. In the drift flux model, there are two empirical coefficients,  $C_{os}$  and  $k_s$ . For these regime calculations,  $C_{os}$  is approximated as a constant. The  $k_s$  coefficient depends on body forces which may be acting on the condenser:

$$C_{os} = 1.3 \quad (6-58)$$

$$k_s = \begin{cases} 0.35 & \theta > \pi/2 \\ 0.0 & \theta = \pi/2 \\ -0.35 & \theta < \pi/2 \end{cases} \quad (6-59)$$

where  $\theta$  is the angle (measured in radians) between the flow vector and the body forces vector. Figure 6.8 illustrates these two vectors.

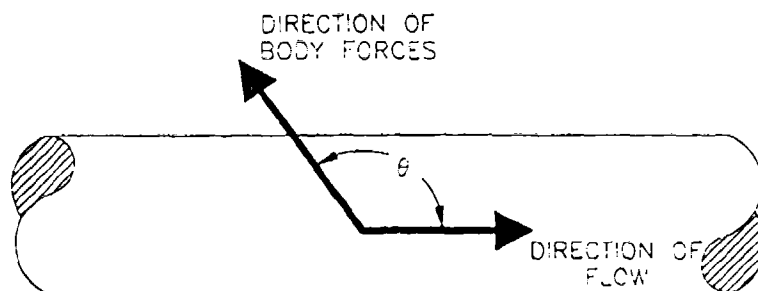


Figure 6.8. ANGLE BETWEEN CONDENSING FLOW AND BODY FORCES

Next calculate the ratio of vapor to liquid volumetric fluxes,  $M$ :

$$M = \frac{(1-x)\rho_g}{x\rho_l} \quad (6-60)$$

Then calculate the volumetric flux of the vapor phase,  $j_g$ :

$$j_g = \frac{Gx}{\rho_g} \quad (6-61)$$

Calculate a Froude number based on the volumetric flux of the vapor phase,  $F_g$ :

$$F_g = \frac{j_g \rho_g^{0.5}}{[a D_h (\rho_l - \rho_g)]^{0.5}} \quad (6-62)$$

Finally, calculate the void fraction with this equation:

$$\alpha = \frac{1}{C_{os}(1+M) + \frac{k_g}{F_g(\rho_l/\rho_g)^{0.5}}} \quad (6-63)$$

### 6.5.3 Bubbly Flow

The void fraction in the bubbly flow regime is also calculated based on a drift flux model for the flow. The two empirical coefficients have different values in this regime:

$$C_{ob} = 1.2 \quad (6-64)$$

$$k_b = \begin{cases} 1.4 & \theta > \pi/2 \\ 0.0 & \theta \leq \pi/2 \end{cases} \quad (6-65)$$

where  $\theta$  is the angle between the flow vector and the body forces vector.

First calculate ratio of volumetric fluxes ( $M$ ) and the vapor volumetric flux ( $j_g$ ):

$$M = \frac{(1-x)\rho_g}{x\rho_l} \quad (6-66)$$

$$j_g = \frac{Gx}{\rho_g} \quad (6-67)$$

(These are the same relations used in the slug flow regime).

Next calculate a Kutateladze number based on the vapor volumetric flux:

$$K_g = \frac{j_g \rho_g^{0.5}}{[a \sigma (\rho_l - \rho_g)]^{0.25}} \quad (6-68)$$

Finally, calculate the void fraction:

$$\alpha = \frac{1}{C_{ob}(1+M) + \frac{k_b}{K_g(\rho_l/\rho_g)^{0.5}}} \quad (6-69)$$

#### 6.5.4 Single-Phase Liquid Flow

In the single-phase liquid flow regime, the void fraction is always zero.

### 6.6 Pressure Drop

This section presents the detailed relations for calculating the pressure drop in each segment of a shear condenser. There are four contributions to the pressure drop:

- Friction,
- Fluid acceleration (or deceleration),
- Body forces, and
- Taper of the condenser tube.

Calculation of the pressure drop due to friction depends on the local flow regime. Pressure drops due to deceleration, body forces, and tube taper are calculated the same way regardless of the flow regime. The total pressure drop in each segment is the sum of the four component pressure drops.

#### 6.6.1 Total Pressure Drop

Calculate the total pressure drop in a segment by summing the four components of the pressure loss:

$$\Delta P = \Delta P_f + \Delta P_g + \Delta P_a + \Delta P_t \quad (6-70)$$

where

$\Delta P$	= total pressure drop (Pa),
$\Delta P_f$	= pressure drop due to friction (Pa),
$\Delta P_g$	= pressure drop due to body forces (Pa),
$\Delta P_a$	= pressure drop due to fluid acceleration (Pa),
$\Delta P_t$	= pressure drop due to taper of the condenser tube (Pa).

The following sections provide the detailed equations for calculating the pressure drop components.

#### 6.6.2 Pressure Drop Due to Friction

Friction is usually the largest single component of the pressure drop. It is also highly dependent on the flow regime. The following paragraphs present the equations to calculate the frictional pressure drop in the annular, slug, bubbly, and single-phase liquid flow regimes. In MICROCON the frictional pressure drop in each segment of the condenser is calculated based on the average void fraction in the segment.

**Frictional Pressure Drop in Annular Flow.** The frictional pressure drop in the annular flow regime is typically the largest single contribution to the total pressure drop in the condenser. This is because the gas velocity in the core is highest in this regime. Pressure drops are calculated using the vapor-phase momentum equation.

First calculate the Reynolds number for the vapor phase:

$$Re_g = \frac{G \times D_h}{\mu_g} \quad (6-71)$$

where  $x$  is the average void fraction in the segment (in MICROCON, the value of the quality at both the inlet and exit are known before beginning the pressure drop calculation).

Next calculate the friction factor based on vapor-only flow:

$$f_{wg} = \begin{cases} 0.046 Re_g^{-0.2} & Re_g \geq 1500 \\ 16/Re_g & Re_g < 1500 \end{cases} \quad (6-72)$$

The pressure drop in annular flow depends on the frictional shear stress between the vapor phase and the liquid phase, which depends on the interfacial friction factor,  $f_i$ . The interfacial friction factor is calculated by multiplying  $f_{wg}$  by the ratio of interfacial to vapor-only friction factors,  $f_i/f_{wg}$ . In MICROCON the ratio of friction factors is calculated based on the void fraction:

$$f_i/f_{wg} = A \alpha^B + C (1-\alpha)^D \quad (6-73)$$

where A, B, C, and D are empirical constants. Table 6.3 lists values for the constants determined by several researchers for several correlations and bounding approaches. We recommend the Chen correlation for designs when more specific data are not available.

Compute the frictional component of the pressure loss in the segment using this equation:

$$\Delta P_f = \frac{4}{D_h} f_{wg} \frac{f_i}{f_{wg}} \frac{x^2}{\alpha^{2.5}} \frac{G^2}{2\rho_g} \Delta z \quad (6-74)$$

**Frictional Pressure Drop in Slug and Bubbly Flow.** Frictional pressure losses in the remaining regimes are usually quite small compared to the annular regime. Most condensation has already occurred, and the velocity of the remaining vapor is small. Pressure drops are calculated using homogeneous flow models for the liquid-phase momentum equation.

First calculate the Reynolds number for the liquid phase:

$$Re_l = \frac{G (1-x) D_h}{\mu_l} \quad (6-75)$$

where  $x$  is the average void fraction in the segment (in MICROCON, the value of the quality at both the inlet and exit are known before beginning the pressure drop calculation).

Next calculate the friction factor based on liquid-only flow:

$$f_{wl} = \begin{cases} 0.046 \text{ Re}_l^{-0.2} & \text{Re}_l \geq 1500 \\ 16/\text{Re}_l & \text{Re}_l < 1500 \end{cases} \quad (6-76)$$

Calculate the two-phase multiplier based on a homogeneous flow model:

$$\phi^2 = \frac{1 + x(\rho_l/\rho_g - 1)}{[1 + x(\mu_l/\mu_g - 1)]^{0.25}} \quad (6-77)$$

Calculate the frictional pressure drop:

$$\Delta P_f = \frac{4}{D_h} f_{wl} \phi^2 (1-x)^2 \frac{G^2}{2\rho_l} \quad (6-78)$$

Frictional Pressure Drop in Single-Phase Liquid Flow. For subcooled liquid, the frictional pressure drop is calculated using standard techniques for single-phase flow.

First calculate the Reynolds number for the liquid flow:

$$\text{Re}_l = \frac{G D_h}{\mu_l} \quad (6-79)$$

Next calculate the friction factor for the liquid flow:

$$f_{wl} = \begin{cases} 0.046 \text{ Re}_l^{-0.2} & \text{Re}_l \geq 1500 \\ 16/\text{Re}_l & \text{Re}_l < 1500 \end{cases} \quad (6-80)$$

Finally calculate the pressure drop:

$$\Delta P_f = \frac{4}{D_h} f_{wl} \frac{G^2}{2\rho_l} \Delta z \quad (6-81)$$

### 6.6.3 Pressure Drop Due to Body Forces

Pressure losses due to body forces may arise if the spacecraft undergoes a significant acceleration. The pressure loss depends on the magnitude and direction of the acceleration, the liquid and vapor densities, and the void fraction.

The direction of acceleration is defined by the angle between the body force vector and a vector which points in the direction of flow in the condenser. Figure 6.8 illustrates the two vectors and the angle,  $\theta$ . On a spacecraft, the body force vector points in a direction opposite the spacecraft acceleration. For  $\theta = 0$ , the flow is with the body force, and there is a negative pressure drop. Thus the pressure drop due to body forces is proportional to  $-\cos\theta$ .

The pressure drop due to body forces is calculated based on the local void fraction:

$$\Delta P_g = - [\alpha \rho_g + (1-\alpha) \rho_l] a \cos \theta \Delta z \quad (6-82)$$

where  $\alpha$  is the average void fraction in the segment.

#### 6.6.4 Pressure Drop Due to Fluid Acceleration

As fluid condenses, its velocity decreases, and there is a pressure recovery. The pressure recovery is equal to the difference between the momentum fluxes leaving and entering the segment. The calculation depends only on the total mass flux, liquid and vapor densities, and the void fractions and qualities at both ends of the segment.

The pressure drop due to fluid acceleration is:

$$\Delta P_a = G^2 \left[ \frac{x_o^2}{\alpha_o \rho_g} + \frac{(1-x_o)^2}{(1-\alpha_o) \rho_l} - \frac{x_i^2}{\alpha_i \rho_g} - \frac{(1-x_i)^2}{(1-\alpha_i) \rho_l} \right] \quad (6-83)$$

where

$x_o$	= quality at the segment exit,
$\alpha_o$	= void fraction at the segment exit,
$x_i$	= quality at the inlet to the segment, and
$\alpha_i$	= void fraction at the inlet to the segment.

#### 6.6.5 Pressure Drop Due to Taper of the Condenser Tube

Some condensers may have a taper which results in additional pressure losses. A tapered tube has dimensions which decrease in the direction of condensation. The purpose of the taper is to maintain high vapor velocities, which increase the shear on the liquid film to keep it thin and enhance heat transfer. Taper has been found to have only marginal heat transfer benefits, nevertheless MICROCON has an option to calculate pressure losses in a tapered condenser tube.

The degree of taper in the tube is described by an input parameter to the MICROCON code. The input parameter is the rate of change of flow area per unit length of condenser tube,  $dA/dz$ .

In tapered condenser tubes each segment has a different cross-sectional area. In MICROCON, the local flow area, mass flux, and tube perimeter are recalculated in each segment. The pressure loss due to the taper is calculated based on the local value of the mass flux.

$$\Delta P_t = G^2 \left[ \frac{x^2}{\alpha \rho_g} + \frac{(1-x)^2}{(1-\alpha) \rho_l} \right] \left[ \frac{dA}{dz} \right] \Delta z \quad (6-84)$$

where

$G$	= the local mass flux (kg/m <sup>2</sup> /s),
$x$	= average quality in the segment,
$\alpha$	= average void fraction in the segment,
$\frac{dA}{dz}$	= the degree of taper, rate of change of flow area per unit length (m), and
$\Delta z$	= length of the segment.

## 6.7 Dimensionless Design Charts for Condensing Radiators

This section presents design charts to solve three common design problems for condensing radiators:

- 1.) Calculate the effective one-dimensional wall thickness for a radiator panel,
- 2.) Determine the tube length required for condensation and subcooling in the radiator, and
- 3.) Calculate the pressure drop in a condensing radiator.

The design charts are based on simplified models of condenser behavior and are presented in dimensionless form. The charts are useful for obtaining quick estimates and to verify numerical calculations.

### 6.7.1 Modelling Condensing Radiators with MICROCON

The external boundary conditions used by these design methods are flexible enough to model heat transfer in a condensing radiator panel. This example shows how to calculate the effective wall thickness,  $t_{eff}$  (Eq. 6-3), which simulates a radiator panel.

**Required Parameters.** Figure 6.9 illustrates a section of a condensing radiator panel and the key geometrical parameters. To calculate the effective one-dimensional wall thickness for a radiator panel, you will need to know:

- $T_{sat}$ , the saturation temperature of the condensing fluid (K),
- $T_2$ , the effective heat rejection temperature (K) (including effects of absorbed heat flux),
- $P_i$ , the internal perimeter of the condenser tube (m),
- $k_f$ , the thermal conductivity of the condensing liquid (W/m-K),
- $k_{fin}$ , the thermal conductivity of the radiator fins (W/m-K),
- $t_{fin}$ , the effective thickness of the radiator fins for heat conduction (m),
- $b$ , one-half the pitch between condenser tubes (m),
- $n$ , the number of actively radiating sides (1 or 2),
- $F$ , the view factor for the radiator, and
- $\epsilon$ , the emissivity of the radiating surface.

Note that for this analysis, the effective heat rejection temperature ( $T_2$ ) must account for the absorbed orbital average heat flux. So for these calculations we assume  $q''_{env} = 0$ .

**Calculation Procedure.** There are five steps to calculate  $t_{eff}$ :

- 1.) Calculate the fin parameter,  $B$ ,
- 2.) Calculate the fin efficiency,  $\eta_f$ ,
- 3.) Calculate the linear heat transfer rate,  $q'$ ,
- 4.) Calculate the effective average panel temperature,  $T_{wx}$ ,
- 5.) Calculate the effective one-dimensional wall thickness,  $t_{eff}$ .

Calculate the fin parameter  $B$  with this equation:

$$B = \left[ \frac{4F\sigma_0\epsilon T_{sat}^3}{t_{fin}k_{fin}} \right]^{0.5} \quad (6-85)$$



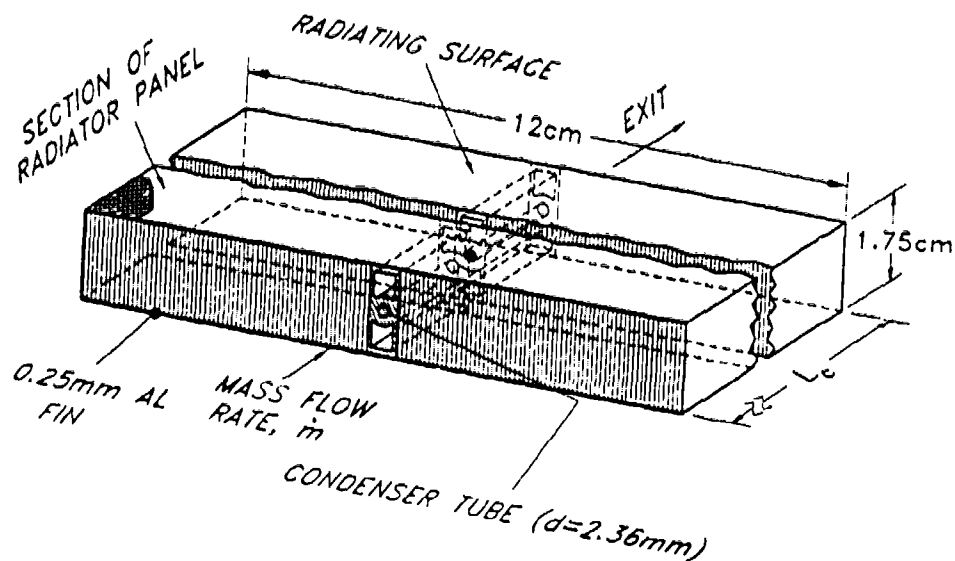


Figure 6.9. SECTION OF A CONDENSING RADIATOR PANEL

Then the fin efficiency,  $\eta$ , is:

$$\eta = \frac{\tanh(bB)}{bB} \quad (6-86)$$

The fin efficiency is then used to calculate the linear heat transfer rate:

$$q' = 2nbF\eta\sigma_o\epsilon(T_{sat}^4 - T_2^4) \quad (6-87)$$

Next calculate  $T_{wx}$ , the effective average temperature on the surface of the radiator:

$$T_{wx} = \left[ \frac{q'}{2nb\sigma_o\epsilon} + T_2^4 \right]^{0.25} \quad (6-88)$$

(The view factor,  $F$ , does not appear in this equation because MICROCON does not include a view factor in its calculations.)

Finally, use the average panel temperature to calculate the effective one-dimensional wall thickness,  $t_{eff}$ :

$$t_{eff} = k_{fin} \frac{P}{q} (T_{sat} - T_{wx}) \quad (6-89)$$

**Example.** Calculate the effective one-dimensional wall thickness for the condensing radiator shown in Figure 6.9. The condensing fluid is ammonia at a temperature of 300 K. The radiating condenser has the following parameters:

- $T_{\text{sat}} = 300 \text{ K},$
- $T_2 = 233 \text{ K},$
- $P_i = \pi \times 2.36 \times 10^{-3} \text{ m} = 7.414 \times 10^{-3} \text{ m},$
- $k_{\text{fin}} = 220 \text{ W/m}^2\text{-K}$  (corresponding to aluminum),
- $t_{\text{fin}} = 2 \times 0.25 \text{ mm} = 0.50 \times 10^{-3} \text{ m},$
- $b = 0.06 \text{ m},$
- $n = 2,$
- $F = 1.0$
- $\varepsilon = 0.80.$

The effective thickness of the radiator fins ( $t_{\text{fin}}$ ) is twice the thickness of a single fin. This would be true even if only one side of the panel were actively radiating, because both sides of the panel would still contribute to heat conduction from the condenser tube.

$$\begin{aligned}
 B &= \left[ \frac{4F\sigma_0\varepsilon T_{\text{sat}}^3}{t_{\text{fin}}k_{\text{fin}}} \right]^{0.5} \\
 &= \left[ \frac{4(1.0)(5.67 \times 10^{-8} \text{ W/m}^2\text{-K}^4)(0.8)(300 \text{ K})^3}{(0.50 \times 10^{-3} \text{ m})(220 \text{ W/m-K})} \right]^{0.5} \\
 &= 6.673 \text{ m}^{-1}
 \end{aligned}$$

$$\begin{aligned}
 \eta &= \frac{\tanh(bB)}{bB} \\
 &= \frac{\tanh[(0.06 \text{ m})(6.673 \text{ m}^{-1})]}{(0.06 \text{ m})(6.673 \text{ m}^{-1})} \\
 &= 0.950
 \end{aligned}$$

$$\begin{aligned}
 q' &= 2nbF\eta\sigma_0\varepsilon(T_{\text{sat}}^4 - T_2^4) \\
 &= 2(2)(0.06 \text{ m})(1.0)(0.950)(5.67 \times 10^{-8} \text{ W/m}^2\text{-K}^4)(0.8) \left[ (300 \text{ K})^4 - (233 \text{ K})^4 \right] \\
 &= 53.3 \text{ W/m}
 \end{aligned}$$

$$\begin{aligned}
 T_{\text{wx}} &= \left[ \frac{q'}{2nb\sigma_0\varepsilon} + T_2^4 \right]^{0.25} \\
 &= \left[ \frac{53.3 \text{ W/m}}{2(2)(0.06 \text{ m})(5.67 \times 10^{-8} \text{ W/m}^2\text{-K}^4)(0.8)} + (233 \text{ K})^4 \right]^{0.25} \\
 &= 297.594 \text{ K}
 \end{aligned}$$

$$\begin{aligned}
 t_{\text{eff}} &= k_{\text{fin}} \frac{P_1}{q} (T_{\text{sat}} - T_{\text{vc}}) \\
 &= (220 \text{ W/m-K}) \frac{7.414 \times 10^{-3} \text{ m}}{53.3 \text{ W/m}} (300 \text{ K} - 297.594 \text{ K}) \\
 &= \underline{0.0736 \text{ m}}
 \end{aligned}$$

So to use MICROCON to calculate condensation in the fin shown in Figure 6.9, use these input parameters:

- Radiation boundary condition,
- Heat sink temperature of ( $T_2$ ) 233 K,
- Panel emissivity of 0.8,
- Secondary perimeter ( $P_2$ ) =  $2nb = 0.24 \text{ m}$ ,
- Wall conductivity of 220 W/m-K, and
- Effective wall thickness of 0.0736 m.

**Analytical Basis.** The rate of heat transfer per unit length of the condenser tube ( $q'$ ) is determined almost entirely by the radiation and conduction resistance of the radiator panel. The thermal resistance of the panel is summarized by the fin efficiency,  $\eta$ . The heat transfer resistance due to condensation is insignificant compared to the thermal resistance of the panel (typically no more than 5%, even for tube diameters down to 2 mm). As a result,  $q'$  is very nearly constant throughout the two-phase section of the condenser.

Figure 6.10 illustrates analysis of heat transfer in the radiator panel. The temperature inside the condenser tube is equal to  $T_{\text{sat}}$ . The temperature at the end of the fin farthest from the condenser tube is somewhat less, depending on the balance between heat conduction in the fin and radiation heat transfer from the surface. This temperature gradient is accounted for in the thermal model through the fin efficiency,  $\eta$ . Equation 6-86 for the fin efficiency is derived from a linearized analysis of the differential equation which describes the heat transfer in the fin:

$$\frac{d^2T}{dx^2} = \frac{n\sigma_o\epsilon}{k_{\text{fin}} t_{\text{fin}}} (T^4 - T_2^4) \quad (6-90)$$

in which  $x$  is the distance from the condenser tube and  $T(x)$  is the local temperature in the radiator panel. So if the thermal resistance of the condensate film and the condenser tube itself are negligible (which is the case for 300 K radiators), the linear heat transfer rate is given by:

$$q' = 2nbF\eta\sigma_o\epsilon(T_{\text{sat}}^4 - T_2^4) \quad (6-87)$$

in which "2nb" is the total external perimeter for radiation,  $F$  is the view factor, and  $\eta$  accounts for the temperature drop in the panel.

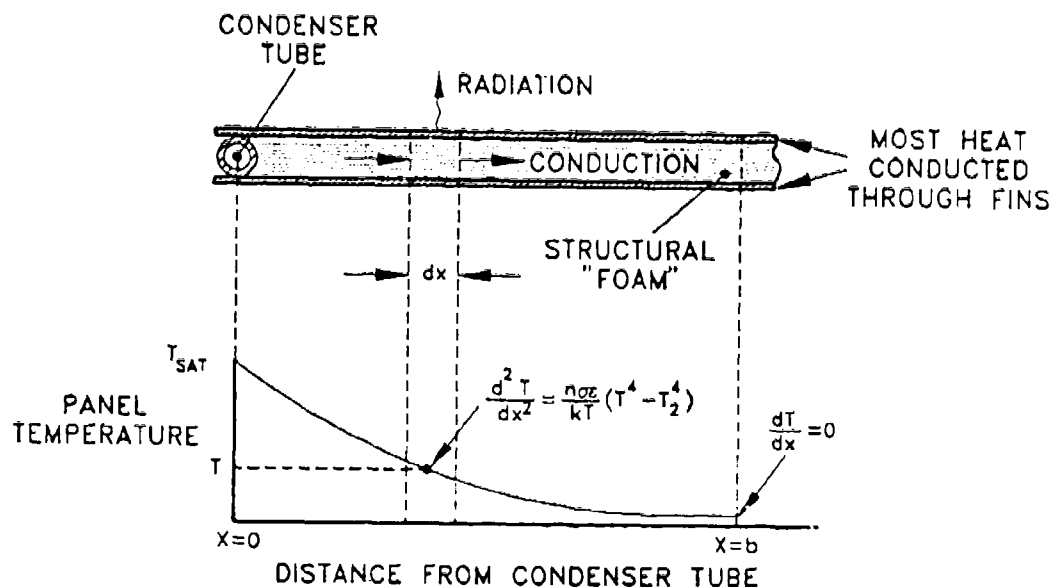


Figure 6.10. ANALYSIS OF HEAT TRANSFER IN A RADIATOR PANEL

Since  $q'$  can be calculated from known radiator parameters, the problem is to calculate the effective, one-dimensional wall thickness which simulates the radiator panel for MICROCON. We use Equations 6-13 and 6-14 from these design methods:

$$q' = P_2 \sigma_0 \epsilon (T_{wx}^4 - T_2^4) \quad (6-13)$$

$$q' = \frac{k_w}{t_w} P_1 (T_{wi} - T_{wx}) \quad (6-14)$$

where  $t_w$  is the same as  $t_{eff}$  in this discussion,  $q''_{env}$  is zero, and we have neglected the internal resistance of the condensing fluid. The thermal conductivity in Equation 6-14,  $k_w$ , is equal to the fin conductivity,  $k_{fin}$ . These are the equations which MICROCON uses to calculate  $q'$  for problems with a radiative boundary condition.  $T_{wx}$  is the average effective temperature of the radiator panel. Since  $q'$  is known, we can solve Equation 6-13 for  $T_{wx}$ :

$$T_{wx} = \left[ \frac{q'}{2nb\sigma_0\epsilon} + T_2^4 \right]^{0.25}$$

where  $P_2$  is equal to  $2nb$ . Then use Equation 6-14 to solve for  $t_{eff}$ , assuming that  $T_{wi} \equiv T_{sat}$ :

$$t_{eff} = t_w = k_{fin} \frac{P_1}{q} (T_{sat} - T_{wx}) \quad (6-91)$$

## 6.7.2 Estimates for Condensing Length

In condensing radiators which operate near 300 K, the largest resistance to heat transfer is usually the one due to thermal radiation outside the condenser. In this case the heat transfer rate is constant along the length of the condenser and independent of the condensation phenomena inside. Thus the designer can easily determine the tube length required to condense and subcool the fluid.

**Required Parameters.** To calculate the tube length for condensation and subcooling, you will need to know:

- $\eta$ , the fin efficiency calculated using Eq. 6-86,
- $x_i$ , the quality at the inlet to the condenser tube.
- $\dot{m}$ , the mass flow rate through the condenser tube (kg/s).
- $h_{fg}$ , the heat of evaporation of the fluid (J/kg),
- $c_p$ , the specific heat of the liquid (J/kg-K),
- $P_2$ , the radiating area per unit length of the condenser tube (m),
- $\epsilon$ , the emissivity of the radiating surface,
- $T_{sat}$ , the temperature of the condensing fluid (K),
- $T_{sub}$ , the subcooled temperature at the condenser exit (K), and
- $T_2$ , the ultimate temperature for heat rejection (K).

**Total Condenser Length.** The condenser must be long enough to condense all the vapor and produce liquid with a specified subcooling. The total length is the sum of the length required for condensation and the length required for subcooling:

$$L_{tot} = L_c + L_{sub} \quad (6-92)$$

where

- $L_{tot}$  = total condenser length (m),
- $L_c$  = condensing length (m), and
- $L_{sub}$  = subcooling length (m).

The paragraphs which follow provide equations to calculate the condensing and subcooling lengths.

**Condensing Length.** The condensing length,  $L_c$ , is the length of condenser tube required to reduce the fluid quality from  $x_i$  to 0. The condensing length is calculated by:

$$L_c = \frac{\dot{m} h_{fg} x_i}{\eta P_2 \sigma_o \epsilon (T_{sat}^4 - T_2^4)} \quad (6-93)$$

This equation is derived from an energy balance on the condenser, in which the heat rejection due to radiation is balanced by the energy lost by the fluid in condensation. Temperature drops due to condensation and conduction through the radiator structure are assumed to be negligible.

**Subcooling Length.** The additional tube length required to subcool the single phase liquid,  $L_{sub}$ , is estimated by:

$$L_{sub} = \frac{1}{4} \frac{\dot{m} c_p}{\eta P_2 \sigma_o \epsilon} \left[ \frac{1}{T_{sub}^3} - \frac{1}{T_{sat}^3} \right] \quad (6-94)$$

This equation is derived from an energy balance on a differential length of the condenser, in which the heat rejection due to radiation is balanced by the sensible heat lost by the subcooled liquid. The differential relation is integrated from the saturation temperature to the desired subcooling to obtain the subcooling length. For this simple estimate we assume that the temperature for ultimate heat rejection is small compared to the radiator temperature so that heat radiated into the condenser is much less than the heat radiated away. If  $T_2/T_{\text{sub}} \leq 0.56$ , then subcooling lengths calculated this way will be accurate to within 10%.

**Example.** Suppose we wish to calculate the tube length required to fully condense a vapor stream entering the condensing radiator shown in Figure 6.9. The condenser has the following operating conditions and fluid properties:

- $\eta = 0.95$ ,
- $x_i = 1.0$ ,
- $\dot{m} = 5 \times 10^{-5} \text{ kg/s}$ ,
- $h_{fg} = 1.16 \times 10^6 \text{ J/kg}$ ,
- $c_p = 4838 \text{ J/kg} \cdot \text{K}$ ,
- $P_2 = 0.24 \text{ m}$ ,
- $\epsilon = 0.80$ ,
- $T_{\text{sat}} = 300 \text{ K}$ ,
- $T_{\text{sub}} = 290 \text{ K}$ , and
- $T_2 = 120 \text{ K}$ .

The condensing length is:

$$\begin{aligned}
 L_c &= \frac{\dot{m} h_{fg} x_i}{\eta P_2 \sigma_0 \epsilon (T_{\text{sat}}^4 - T_2^4)} & (6-95) \\
 &= \frac{(5 \times 10^{-5} \text{ kg/s}) (1.16 \times 10^6 \text{ J/kg}) (1.0)}{(0.95)(0.24 \text{ m}) (5.67 \times 10^{-8} \text{ W/m}^2 \cdot \text{K}^4) (0.8) [(300 \text{ K})^4 - (120 \text{ K})^4]} \\
 &= \underline{0.711 \text{ m}}
 \end{aligned}$$

The subcooling length is:

$$\begin{aligned}
 L_{\text{sub}} &= \frac{1}{4} \frac{\dot{m} c_p}{\eta P_2 \sigma_0 \epsilon} \left[ \frac{1}{T_{\text{sub}}^3} - \frac{1}{T_{\text{sat}}^3} \right] & (6-96) \\
 &= \frac{(5 \times 10^{-5} \text{ kg/s}) (4838 \text{ J/kg} \cdot ^\circ\text{C})}{4(0.95)(0.24 \text{ m}) (5.67 \times 10^{-8} \text{ W/m}^2 \cdot \text{K}^4) (0.8)} \left[ \frac{1}{(290 \text{ K})^3} - \frac{1}{(300 \text{ K})^3} \right] \\
 &= \underline{0.023 \text{ m}}
 \end{aligned}$$

So the total required condenser length is:

$$L_{\text{tot}} = L_c + L_{\text{sub}} = 0.711 \text{ m} + 0.023 \text{ m} = \underline{0.734 \text{ m}} \quad (6-97)$$

### 6.7.3 Design Charts for Pressure Drop

This section presents universal design charts to estimate the pressure drop in a shear condenser. Since the heat transfer rate from a condensing radiator is fixed by the temperature and ratio of radiating to internal heat transfer areas, the main problem in condenser design is estimating the pressure loss in a condenser tube.

The main component of the total pressure drop is typically the frictional pressure loss in the annular condensation regime. Only in this regime does the vapor have high velocities resulting in a high pressure gradient.

The method presented in this section applies only to non-tapered condenser tubes.

**Required Parameters.** The pressure drop depends on a large number of parameters. To simplify the design charts, we have eliminated explicit dependence on fluid properties and present charts which are specific to several fluids which are of most interest for spacecraft thermal management. Four design charts are provided to estimate pressure drop for the following fluids:

- Ammonia ( $\text{NH}_3$ ),
- R11,
- R114, and
- R22.

These refrigerants have good heat transfer properties at a temperature of 300 K and are the most likely candidates for spacecraft systems or ground testing.

You will also need to know:

- $\dot{m}$ , the mass flow rate in the condenser (kg/s)
- $L_c$ , the condensing length (m), calculated for an inlet quality of 1.0,
- $\rho_g$ , the vapor density ( $\text{kg/m}^3$ ),
- $\mu_g$ , the viscosity of the vapor ( $\text{kg/m-s}$ ),
- $h_{fg}$ , the heat of condensation of the fluid (J/kg),
- $A$ , the cross sectional area of the condenser tube ( $\text{m}^2$ ), and
- $D_h$ , the hydraulic diameter of the condenser tube (m).

The condensing length,  $L_c$ , should be calculated using the methods described in the previous section (Equation 6-93).

Finally, select a method for calculating the ratio of interfacial to wall shear,  $f_i/f_{wg}$ . Design curves are presented for five methods:

- |                              |   |
|------------------------------|---|
| • Correlation of Wallis:     | $f_i/f_{wg} = 1 + 75(1-\alpha)$ ,         |
| • Correlation of Chen:       | $f_i/f_{wg} = 1 + 6.8(1-\alpha)^{0.39}$ , |
| • Correlation of Duschatko:  | $f_i/f_{wg} = 1 + 2.5(1-\alpha)^{0.39}$ , |
| • Constant high shear:       | $f_i/f_{wg} = 10$ , and                   |
| • Constant smooth interface: | $f_i/f_{wg} = 1.0$ .                      |

Calculation Procedure. First calculate  $G$ , the total mass flux through the condenser tube:

$$G = \frac{\dot{m}}{A} \quad (6-98)$$

Next calculate  $Re_g$ , the Reynolds number for vapor flow at a quality of 1.0:

$$Re_g = \frac{G D_h}{\mu_g} \quad (6-99)$$

Next refer to Figures 6.11 (a) through (d). Select the figure corresponding to the desired condensing fluid. Locate the design curve on this figure which corresponds to the desired method to calculate  $f_i/f_{wg}$ . Locate the y-coordinate of this point, which is denoted  $\Delta P^*$ .

Finally, calculate the actual pressure drop:

$$\Delta P = \frac{G^2}{2\rho_g} \frac{L_c}{D_h} \Delta P^* \quad (6-100)$$

**Example.** Estimate the pressure drop in the ammonia radiator. Use all the input values from the previous examples, plus values for the flow area in the condenser tube and the density and viscosity of ammonia vapor at 300 K:

- $A = \pi/4 \times (0.00236 \text{ m})^2 = 4.37 \times 10^{-6} \text{ m}^2$ ,
- $\rho_g = 8.26 \text{ kg/m}^3$ ,
- $\mu_g = 1.02 \times 10^{-5} \text{ kg/m-s}$ .

First calculate the mass flux,  $G$ :

$$G = \frac{\dot{m}}{A} = \frac{5 \times 10^{-5} \text{ kg/s}}{4.37 \times 10^{-6} \text{ m}^2} = 11.4 \text{ kg/m}^2\text{-s} \quad (6-101)$$

Next calculate the Reynolds number for all-vapor flow:

$$Re_g = \frac{G D_h}{\mu_g} = \frac{(11.4 \text{ kg/m}^2\text{-s})(0.00236 \text{ m})}{1.02 \times 10^{-5} \text{ kg/m-s}} = 2638 \quad (6-102)$$

Next refer to Figure 6.11. Using the Chen correlation for  $f_i/f_{wg}$ , locate the dimensionless pressure drop corresponding to a vapor-only Reynolds number of 6245. The result is:

$$\Delta P^* = 0.065 \quad (6-103)$$

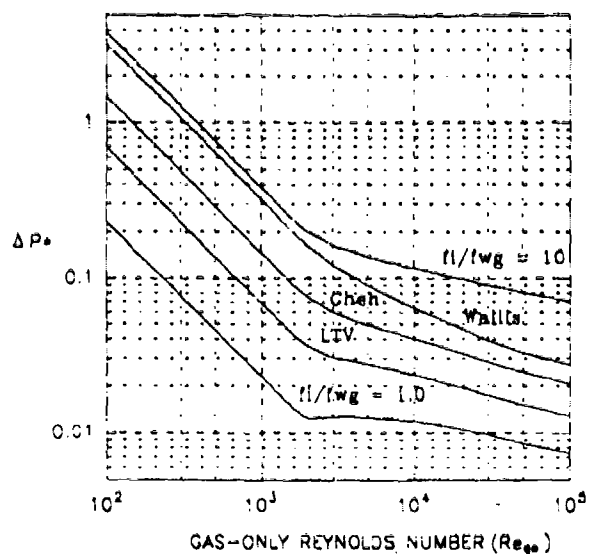
Finally, calculate the actual pressure drop:

$$\begin{aligned} \Delta P &= \frac{G^2}{2\rho_g} \frac{L_c}{D_h} \Delta P^* \quad (6-104) \\ &= \frac{(11.4 \text{ kg/m}^2\text{-s})^2}{2 (8.26 \text{ kg/m}^3)} \times \frac{0.711 \text{ m}}{0.00236 \text{ m}} \times 0.065 \\ &= 7.87 \text{ Pa} \times 301 \times 0.065 \\ &= \underline{154 \text{ Pa}} \end{aligned}$$



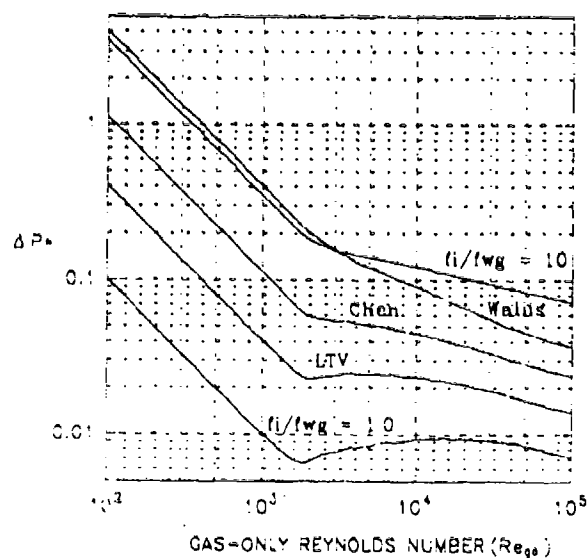
(a)

FLUID: AMMONIA AT 300 K



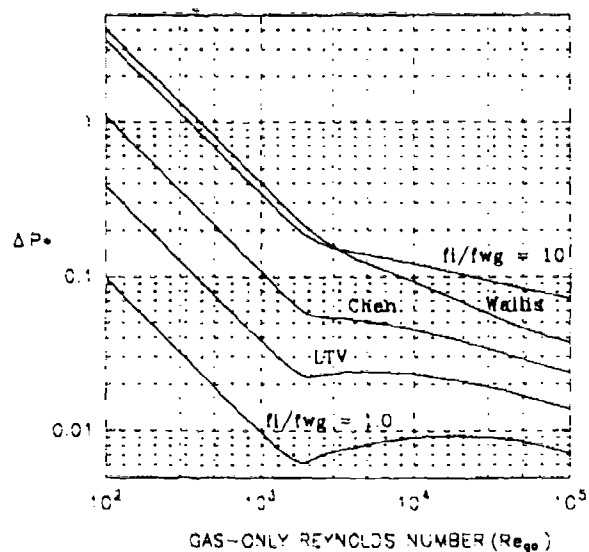
(b)

FLUID: R22 AT 300 K



(c)

FLUID: R114 AT 337 K



(d)

FLUID: R11 AT 351 K

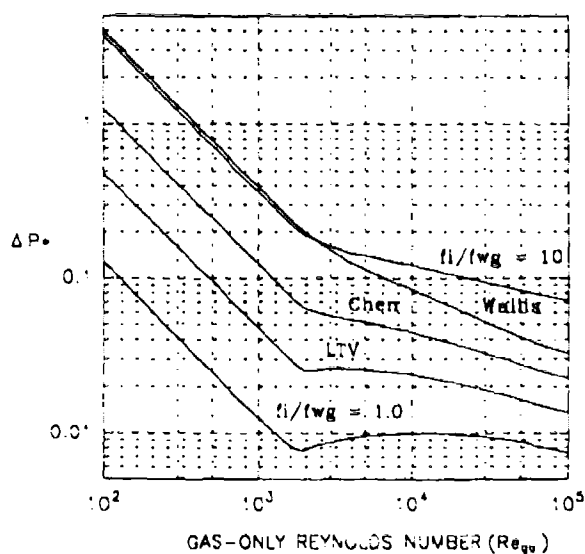


Figure 6.11. DESIGN MAPS FOR PRESSURE DROPS IN SHEAR CONDENSERS

Selection of the  $f_i/f_{wg}$  correlation is a key choice in the condenser design. Chen's correlation for  $f_i/f_{wg}$  leads to a predicted pressure drop of 154 Pa for the ammonia radiator. Table 6.4 presents the results of this calculation using alternate correlations for  $f_i/f_{wg}$ . For this problem, the Duschatko correlation may be more appropriate, since it was derived from ammonia condensation tests in small-diameter tubes. The Duschatko correlation leads to a predicted pressure drop of only 73 Pa. Since  $f_i/f_{wg}$  has such a strong effect on the calculated pressure drop, and mechanistic methods are not available to calculate  $f_i/f_{wg}$ , the designer is cautioned to choose carefully. Ideally the correlation for  $f_i/f_{wg}$  should be based on data from tests which closely approximate the design problem.

**Analytical Basis.** The calculation for the frictional pressure drop is based on the vapor-phase momentum equation for annular flow. The pressure drop due to friction in the vapor phase is equal to the dynamic pressure of the vapor ( $\rho_g u_g^2/2$ ) multiplied by an interfacial friction factor ( $f_i$ ) and the ratio of vapor cross sectional area to interfacial perimeter ( $4/D_i$ , where  $D_i$  is the diameter of the vapor core):

$$\frac{dP_f}{dz} = - \frac{4}{D_i} f_i \frac{\rho_g u_g^2}{2} \quad (6-105)$$

where  $u_g$  = the vapor velocity (m/s),  
 $f_i$  = the interfacial friction factor, and  
 $D_i$  = diameter of the vapor core (m).

In annular flow, the vapor core diameter is equal to the total tube diameter multiplied by the square root of the void fraction:

$$D_i = D_b \sqrt{\alpha} \quad (6-106)$$

Also, the vapor velocity is equal to the vapor superficial velocity ( $j_g = Gx/\rho_g$ ) divided by the void fraction:

$$u_g = \frac{G x}{\rho_g \alpha} \quad (6-107)$$

Table 6.4. CALCULATED PRESSURE DROP DEPENDS STRONGLY ON $f_i/f_{wg}$	
CORRELATION For $f_i/f_{wg}$	CALCULATED PRESSURE DROP
Chen	154 Pa
Duschatko	73 Pa
Wallis	308 Pa
$f_i/f_{wg} = 10$	355 Pa
$f_i/f_{wg} = 1.0$	36 Pa

The interfacial friction factor is equal to the product of 1) the friction factor for vapor-only flow ( $f_{wg}$ ), which is calculated using single-phase relationships and the vapor superficial velocity ( $j_g = Gx/\rho_g$ ), multiplied by 2) the ratio of interfacial to wall shear ( $f_i/f_{wg}$ ):

$$f_i = f_{wg} \times f_i/f_{wg} \quad (6-108)$$

Substitute Equations 6-106 through 6-108 into Equation 6-105 to obtain:

$$\frac{dP}{dz} = - \frac{4}{D_h} f_{wg} \frac{f_i}{f_{wg}} \frac{x^2}{\alpha^{2.5}} \frac{G^2}{2\rho_g} \quad (6-109)$$

Multiply by  $dz/dx$ , the tube length required per unit decrease in quality:

$$\frac{dP}{dz} \frac{dz}{dx} = \frac{dP}{dx} = - \frac{4}{D_h} f_{wg} \frac{f_i}{f_{wg}} \frac{x^2}{\alpha^{2.5}} \frac{G^2}{2\rho_g} \frac{dz}{dx} \quad (6-110)$$

$dz/dx$  is calculated from the condensation length:

$$\frac{dz}{dx} = \frac{-L_c}{\Delta x} = -L_c \quad (6-111)$$

since  $L_c$  for this analysis is calculated for  $x_i = 1.0$ . Substitute Equation 6-111 into 6-110 and rearrange to obtain:

$$\frac{dP}{\frac{G^2}{2\rho_g} \frac{L_c}{D_h}} = 4 f_{wg} \frac{f_i}{f_{wg}} \frac{x^2}{\alpha^{2.5}} dx \quad (6-112)$$

Finally, integrate this equation from the inlet quality ( $x_i = 1.0$ ) to the quality at which the flow regime changes to slug ( $x_s$ ):

$$\Delta P^* = \frac{\Delta P}{\frac{G^2}{2\rho_g} \frac{L_c}{D_h}} = 4 \int_{1.0}^{x_s} f_{wg} \frac{f_i}{f_{wg}} \frac{x^2}{\alpha^{2.5}} dx \quad (6-113)$$

This is the same as Equation 6-100 used to calculate the frictional pressure drop. Note that the entire integrand is a function of only the quality, the liquid/vapor density ratio, and the inlet Reynolds number. The integral has been evaluated numerically and the results are displayed graphically in Figure 6.11.

## 6.8 Validation of Methods

The design methods have been validated through comparison with tests of a shear condenser at Creare and published experimental data. Five experimental systems have been modelled using MICROCON, and the results have been compared with the test data. Four of the tests were run under Earth normal gravity with heat transfer, and the fifth is an adiabatic test in microgravity. There are no data from microgravity tests with heat transfer that are suitable for comparison.

### 6.8.1 Overall Conclusions for Validation

- Pressure drop calculations agree with reported pressure drops within experimental uncertainty for all cases where annular flow dominates. The pressure drops calculated for one case with very short or nonexistent annular flow sections (and a very low overall pressure drop) show larger errors.
- Heat transfer results agree very well with Creare ground test data and are within 20% of data from Bae.
- Heat transfer in the slug and bubbly regimes is higher than current analytical models predict. MICROCON includes an empirical coefficient ( $\phi^2$ ) to simulate high heat transfer coefficients for slug condensation. (See Section 6.4.2)

### 6.8.2 Experiments Used for Validation

Test results from five experiments are used to qualify the MICROCON program:

- LTV (heat transfer, 1-g),
- Sundstrand (adiabatic, microgravity),
- Creare (heat transfer, 1-g),
- Bae (heat transfer, 1-g),
- GE Astro Space (heat transfer, 1-g).

Table 6.5 lists the primary test parameters in these experiments. Note that all these tests have a convective heat transfer boundary condition. However, the LTV tests have a very large external resistance to heat transfer which simulates the heat transfer in a condensing radiator.

**LTV, 1-G Condensation of Ammonia.** LTV Aerospace and Defense Co. tested shear condenser tubes with ammonia as part of the effort to develop condensing radiators for Space Station Freedom (Duschatho, 1991). Figure 6.12 is a schematic of the test facility. Saturated ammonia vapor enters the tube from the left and condenses inside the tube. Liquid ammonia exits to the right. Cooling is provided by trichloroethylene flowing at a high velocity through a large-diameter cooling tube.

Figure 6.13 is a cross-section of the condenser and cooling tubes. The tubes are coupled by metal standoffs which provide a high, fixed thermal resistance between the ammonia and the coolant. Since the coolant flow rate is very high, its temperature changes very little. Heat transfer is controlled almost entirely by conduction through the standoffs, which have a much higher thermal resistance than the internal resistance of the condensing ammonia. Thus, these tests are characterized by a constant rate of heat transfer along the condenser tube, which simulates a radiation boundary condition at a temperature of 300 K.

Key test measurements are: ammonia flow rate, condenser tube temperature, and overall pressure drop in the condenser tube. The ammonia flow rate is measured by a liquid flow meter located downstream from exit of the condenser tube. The temperature of the condenser tube is measured by thermocouples located along the length. The condensing length is indicated by the position of the thermocouple which first detects a subcooled temperature. A differential pressure transducer measures the pressure drop from the inlet to the exit of the condenser tube.

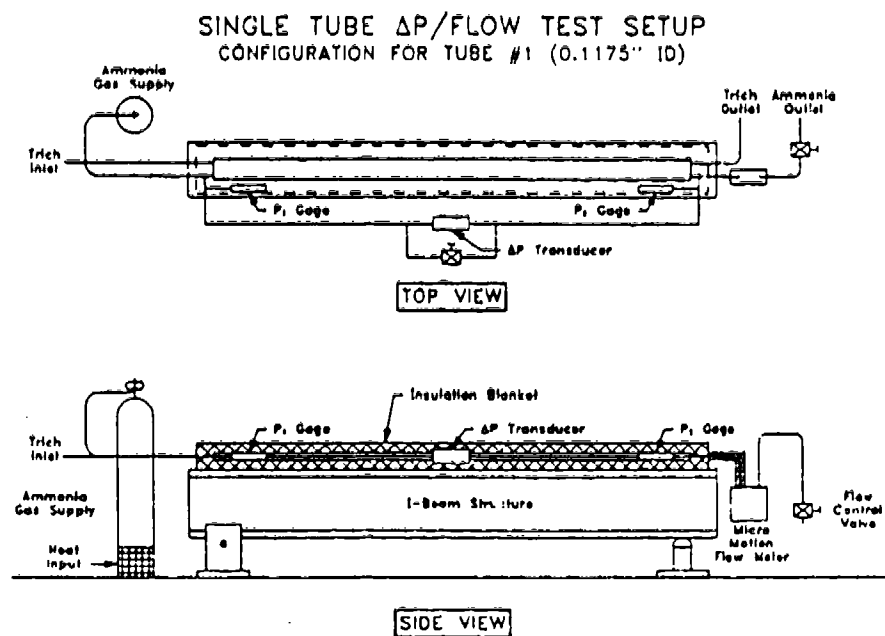


Figure 6.12. LTV's AMMONIA SHEAR CONDENSER

### TEST APPARATUS CROSS SECTION

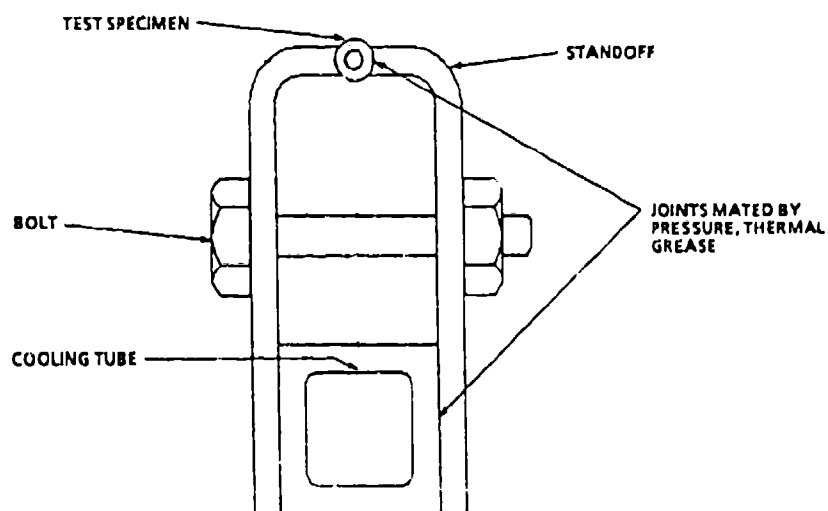


Figure 6.13. SHEAR CONDENSER TEST SPECIMEN AND COOLING ARRANGEMENT

Sundstrand, Microgravity Data With No Condensation. The only microgravity data suitable for comparison comes from an adiabatic experiment performed by Sundstrand (Chen, et al., 1989). The experiment was flown aboard the NASA KC-135 under reduced gravity conditions during Keplerian flight trajectories. Figure 6.14 shows the experimental apparatus used for the tests. Saturated, two-phase Refrigerant-114 flows through a 72-inch straight section. There are pressure taps at each end of the test section. The difference between the pressures measured at each end of the test section is reported, along with the mass flux, vapor quality, pressure, and average acceleration for each test run. Most of the Sundstrand data were taken during annular flow. Slug flow, however, was observed at qualities from 0.05 to 0.10.

Creare, Condensation of R-11 at 1-g. Creare tested a high shear condenser to demonstrate two-phase thermal management components for spacecraft (Crowley and Sam, 1991). This facility was operated both on the ground and aboard the KC-135 aircraft, but the data from the aircraft tests are dominated by transient effects and are not suitable for validating the MICROCON design methods. Figure 6.15 is a schematic diagram of the facility. Refrigerant-11 flows inside 0.634 cm (inner) diameter pipes with cooling water flowing on the outside. Condensation occurs in six segments (condensers and subcoolers) for a total length of 1.8 m (5.9 feet).

The average temperature of the cooling water in each of the segments is recorded independently. The pressure drop is measured across the first three segments and across the second three segments. The quality at the outlet of each section is also reported, derived from the heat transfer measured in the coolant motor.

Bae, Condensation of R-22 at 1-g. Bae, et al., performed experiments in 1-g similar to the Creare tests (Bae, et al., 1969). Figure 6.16 is a diagram of the experimental system. Two-phase Refrigerant-22 flows through a condenser with six sections, for a total length of 5.49 m (18 feet). The R-22 flows inside pipes, with cooling water flowing on the outside of the pipes. The mass flux and saturation temperature are recorded for each tests. The R-22 temperature is measured at the inlet to each section and the cooling water temperature is measured at the outlet of each section. The pressure drop across each section is measured and reported as well.

GE Astro Space, Condensation of Ammonia at 1-g. Fredley and Warren (1990) present ground test data for an ammonia interface heat exchanger. Figure 6.17 shows the configuration of the condenser. The ammonia condenser consists of a helical flow path wrapped around the evaporator of a cylindrical heat pipe. Vapor with a quality of approximately 1.0 enters from the left, flows through the helical condenser path, and condenses as heat flows to the heat pipe evaporator. Subcooled liquid exists from the right. During ground tests, the axis of the condenser helix was horizontal, and condensate puddled at the bottom of the heat exchanger.

The reported test data consist of temperature measurements from thermocouples fastened to the outside walls of the condenser. Thermocouples were located on both the top and bottom of the heat exchanger to detect differences in temperature which indicate puddling. The measured pressure drops are not reported.

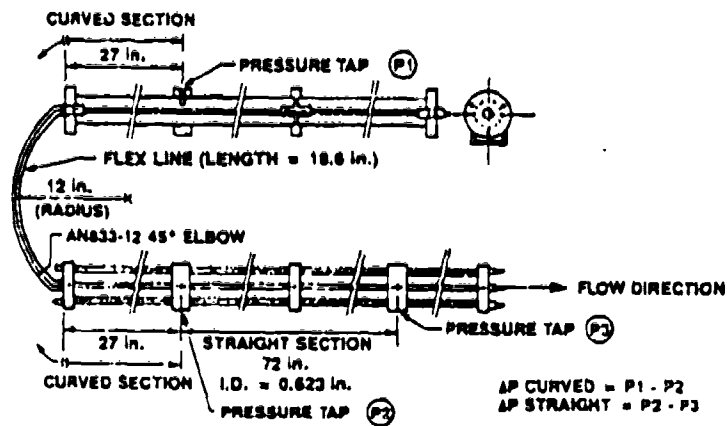


Figure 6.14. SUNDSTRAND TEST FACILITY

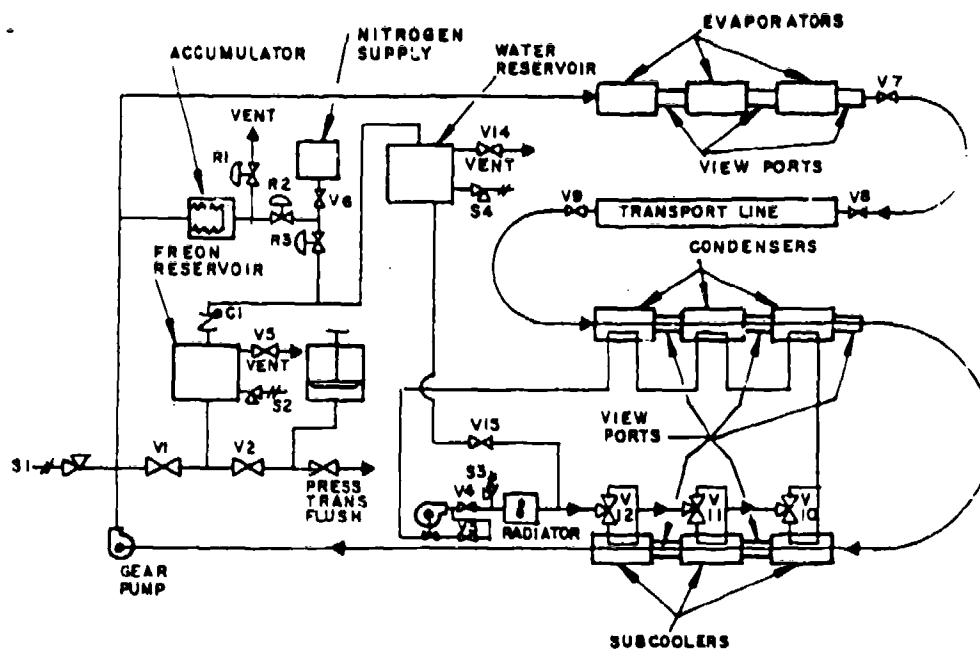


Figure 6.15. CREARE TEST FACILITY

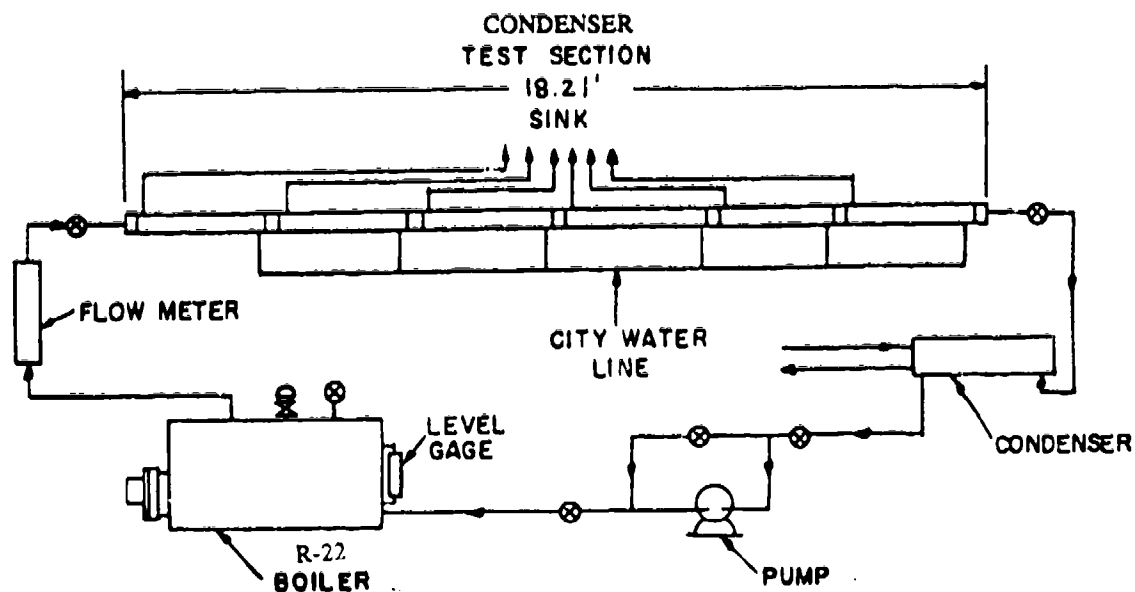


Figure 6.16. BAE ET AL. TEST FACILITY

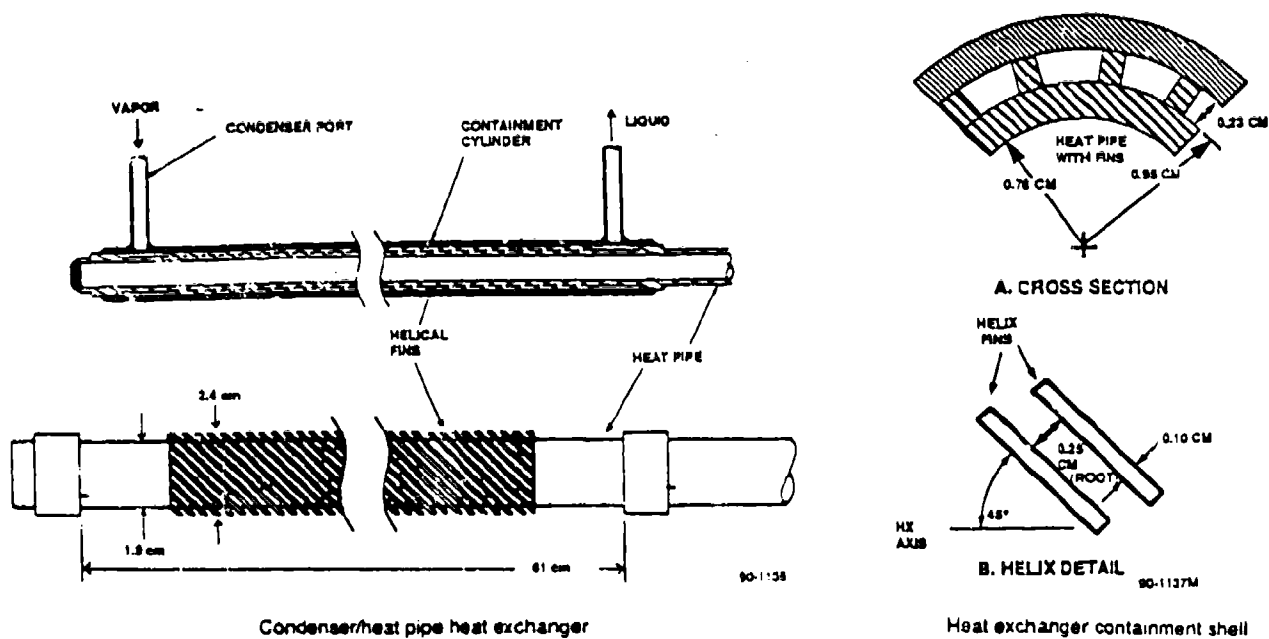


Figure 6.17. AMMONIA INTERFACE HEAT EXCHANGER  
(Fredley and Warren, 1990)



### 6.8.3

### Comparison of Data With MICROCON Calculations

MICROCON calculations agree well with the experimental data. Pressure drops are generally accurate to 15% for the cases of most interest, and outlet qualities are predicted to within 15% (with one exception). These results are achieved using various models for the interfacial shear ratio and the default model (Rohsenow's) for the Nusselt number. Table 6.6 summarizes the comparisons between MICROCON calculations and the test data. When the MICROCON predictions are not within 20% for the pressure drop, they are still within the error bands on the experimental data.

**LTV 1-g Condenser Experiments.** These tests validate the pressure drop models for condensation under conditions which are prototypical for spacecraft radiators. Predictions are accurate for a range of tube sizes, mass flow rates, and condensing lengths in which the pressure drop varies by over two orders of magnitude. Overall level of agreement is within 20% for smaller tubes with higher pressure drops (up to 10 psid). Agreement is within 35% for tests in larger diameter tubes in which the pressure drop is only a few inches of water.

Figure 6.18 shows comparisons between measured pressure drops (symbols) and MICROCON calculations (solid and dashed lines). Pressure drops are compared as a function of the mass flow rate for condensers with diameters of 1.1 mm, 1.8 mm, and 2.4 mm with condensing lengths of 1.8 and 3.0 meters. The condensing lengths are fixed in these tests by adjusting the subcooling of the secondary coolant.

For the MICROCON calculations we used LTV's recommended dependence of  $f_i/f_{w2}$  on the local void fraction (Duschatko, 1991). However, we did not vary the  $f_i/f_{wg}$  correlation with the size of the condenser tube, which LTV also recommends. Even without this refinement the agreement between test data and calculated pressure drops is good.

**Sundstrand 1-g Adiabatic Experiments.** These tests validate pressure drop models for annular flow in microgravity. In Section 3 of this manual we have already compared data from this experiment with the pressure drop methods in MICROP, but here we compare with the methods in the MICROCON program. In the experiment there is no heat transfer, so MICROCON was run with no secondary subcooling. The Chen correlation is used for the interfacial shear ratio ( $f_i/f_{wg}$ ). Pressure drops for the experiment have been calculated for a number of different inlet qualities. Figure 6.19 shows the measured and calculated pressure drops as a function of the inlet quality. Very good agreement between the calculations and the measurements is achieved, with all calculated pressure drops falling within the error bands on the measured data.

**Creare 1-g Condenser Experiments.** The Creare tests provide data to validate heat transfer and pressure drop models over all flow regimes. Figures 6.20 and 6.21 compare MICROCON calculations with heat transfer and pressure drop data reported by Crowley and Sam (1991). In these tests, the internal convective resistance in the condenser controls the rate of heat transfer. Figure 6.20 compares the measured and calculated thermodynamic quality along the length of the condenser tube. With the Wallis model for interfacial shear and Rohsenow's model for condensation heat transfer, the condensing length is predicted to within 20% for Run 30, in which the inlet quality is high (0.80). However for Run 4, in which the inlet quality was only 0.20, the condensing length is over predicted by about 40%.

# MICROCON CALCULATIONS FOR LTV TESTS

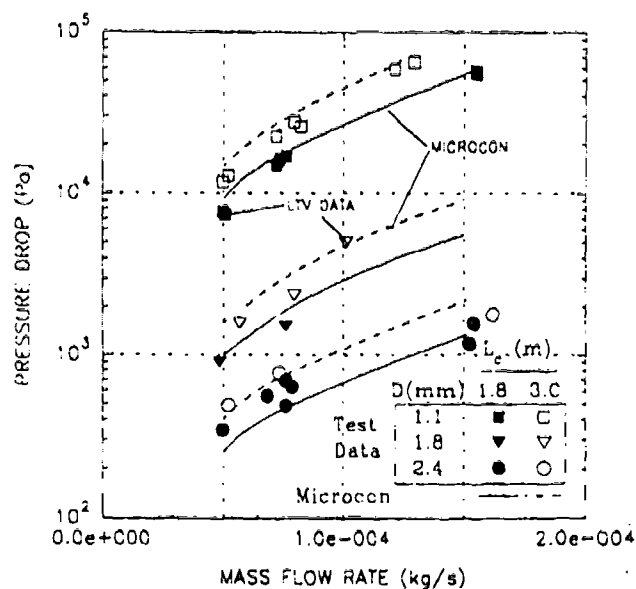


Figure 6.18. COMPARISON WITH LTV CONDENSER DATA

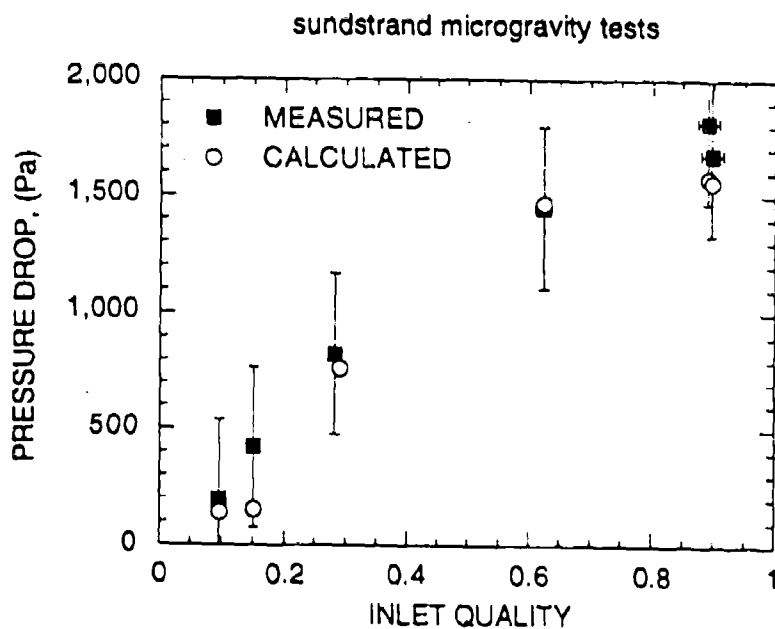


Figure 6.19. COMPARISON WITH SUNDSTRAND DATA

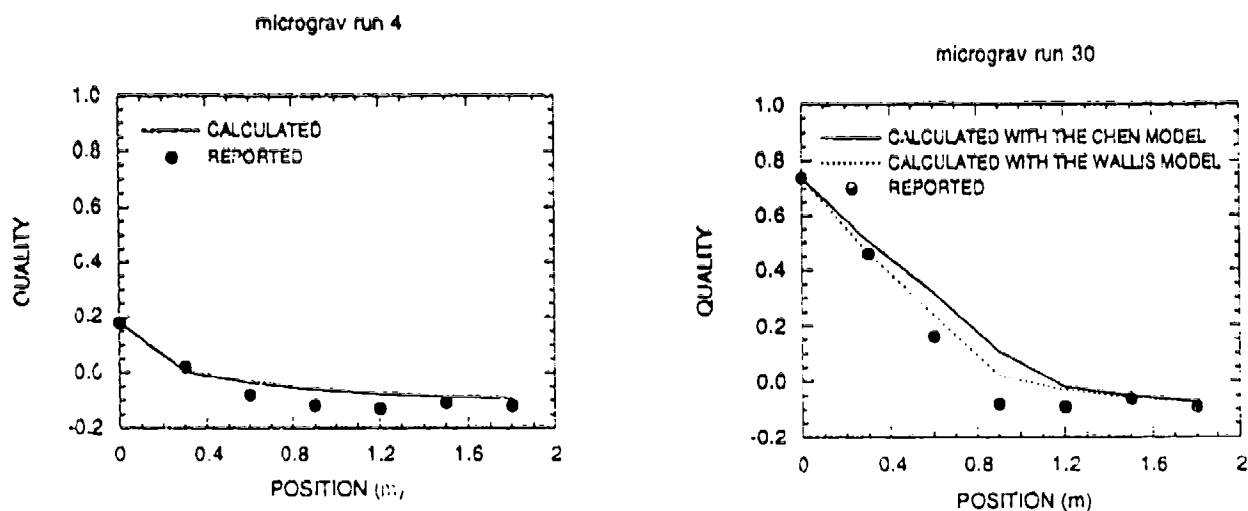


Figure 6.20. COMPARISON OF HEAT TRANSFER CALCULATIONS WITH CREARE DATA

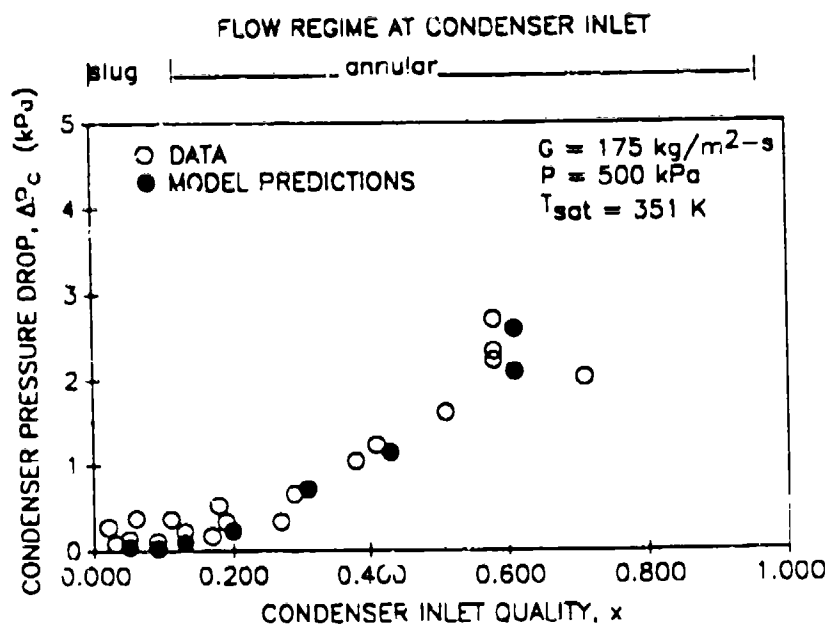


Figure 6.21. COMPARISON OF PRESSURE DROP CALCULATIONS WITH CREARE DATA

Figure 6.21 compares pressure drop as a function of the inlet quality to the condenser. Model predictions (filled circles) match the test data (open circles) well, particularly at high inlet qualities, which are of most practical interest.

It is these tests which show extremely high rates of heat transfer in the slug condensation regime. Observations during the tests indicate that the complete transition from annular to single-phase flow occurs within a single 30-cm condenser segment. The heat transfer rate must have been extremely high due to efficient mixing in the liquid slugs. Based on this data, an empirical factor is included for calculating heat transfer in the slug regime. The factor increases the heat transfer coefficient (calculated for fully-developed flow) to account for developing flow and mixing in the liquid slugs. Section 6.4.2 explains this calculation in detail.

**Bae 1-g Condenser Experiments.** These data validate pressure drop and heat transfer models for the annular flow regime. Bae, et al., conducted condensing experiments with R-22 in horizontal pipes with annular flow (Bae, et al., 1959). Figures 6.22 and 6.23 show the quality as a function of position along the pipe for, respectively, the experiments designated Run 2 and Run 6. The calculated quality correlates well with the measured quality.

There are six sections to the condenser. The temperature of the primary fluid is measured at the beginning of each section. Secondary coolant temperature and flow rate is measured at the outlet of each section, and the temperature difference of the secondary coolant is measured for each section. The pressure drop in each segment is also reported.

The secondary coolant temperatures yield an estimate of the average secondary temperature for each segment. The secondary heat transfer coefficient for input to MICROCON is taken from Bae's report.

Since the parameters are known for each segment separately, and since the secondary coolant temperature changes between the segments, the MICROCON code solves each segment separately, with the calculated output quality of one section used as the input quality for the next section. Chen's correlation for  $f/f_{wg}$  and Rohsenow's model for heat transfer are used in the calculations.

**GE Astro Space 1-g Ammonia Condenser.** Figure 6.24 compares MICROCON calculations with data reported by Fredley and Warren (1990). To calculate the wall temperatures from the MICROCON results, the local condensation ( $dx/dz$ ) was used to calculate a local heat flux. The local heat flux was then used to estimate the wall temperature using the heat transfer coefficient for the heat pipe evaporator. Calculations predict the general trends in the wall temperature, but over predict the condensing length by 50%. The analysis under predicts the heat transfer in these tests because of liquid puddling in the low elevations of the condenser. Cooler temperatures measured on the bottom wall of the condenser indicate a puddle of condensate. Since the vapor must flow through the stagnant liquid, the heat transfer efficiency of the tube is enhanced compared to the calculations, which do not model the liquid pool.

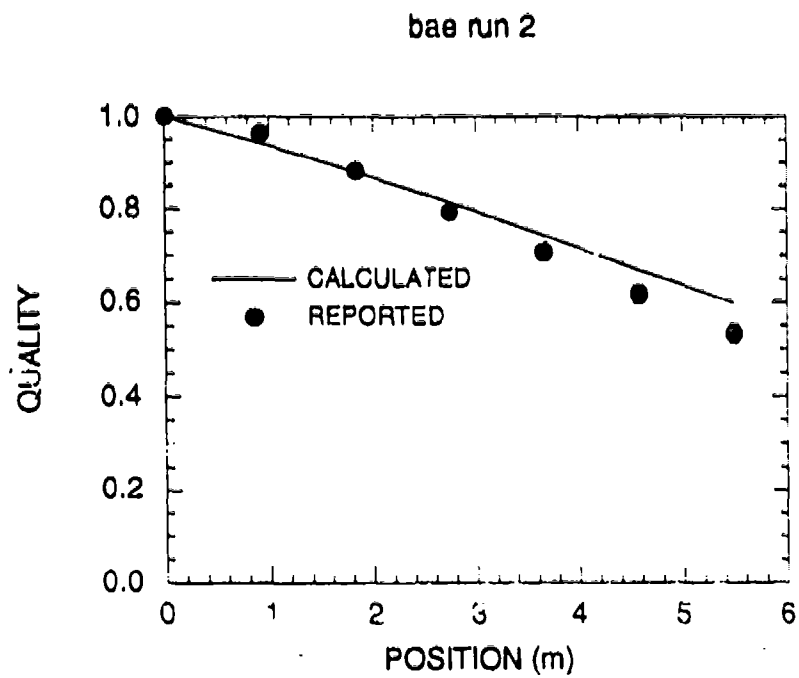


Figure 6.22. COMPARISON WITH BAE ET AL., RUN 2

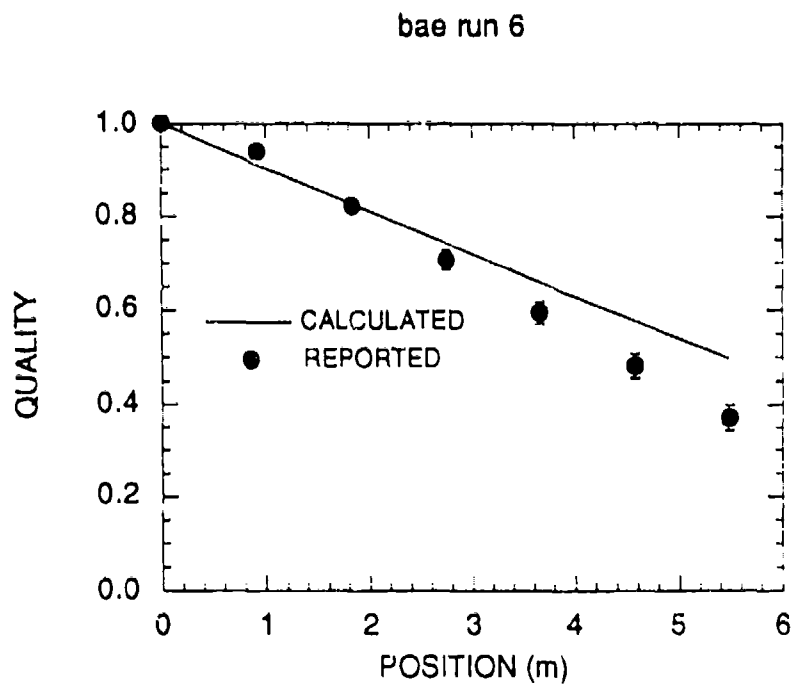


Figure 6.23. COMPARISON WITH BAE ET AL., RUN 6

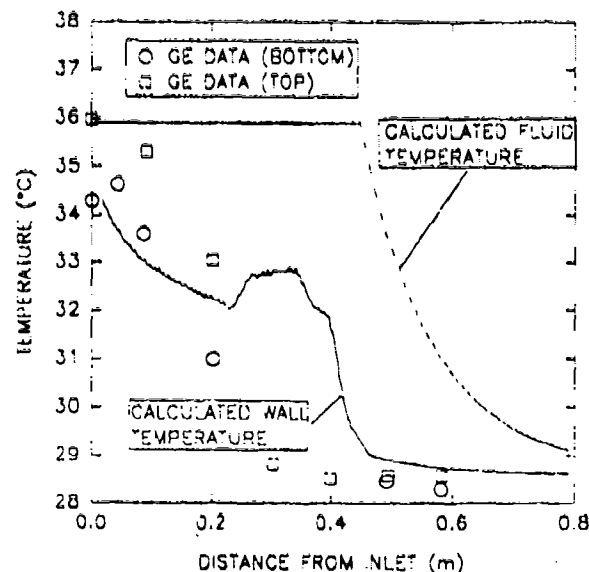


Figure 6.24. COMPARISON WITH HEAT TRANSFER DATA FROM AN AMMONIA INTERFACE HEAT EXCHANGER

## 6.9 References for Vapor Shear Condensers

Bae, S., et al.; *Refrigerant Forced-Convection Condensation Inside Horizontal Tubes*; Report No. DSR 79760-64 Department of Mech. Engineering, Engineering Projects Laboratory, Massachusetts Institute of Technology, Cambridge, Massachusetts, November 1969.

Chen, I., et al.; *An Experimental Study and Prediction of a Two Phase Pressure Drop in Microgravity*; AIAA 89-0074, 26th Aerospace Sciences Meeting, Reno, Nevada, January 1989.

Chen, I-Y, Downing, R.S., Keshoch, E. and Al-Sharrit, M.M.; *"An Experimental Study and Prediction of a Two-Phase Pressure Drop in Microgravity"*; AIAA Paper 89-0074, January 1989.

Crowley, C.J. and Sam, R.G.; *"MICROGRAVITY EXPERIMENTS WITH A SIMPLE TWO-PHASE THERMAL SYSTEM"*; PL-TR-91-1059, Prepared for Phillips Laboratory, Kirtland AFB, Prepared by Creare Inc., Hanover, New Hampshire, December 1991.

Daubert, T.E. and Danner, R.D.; *"DATA COMPILATION TABLES OF PROPERTIES OF PURE COMPOUNDS"*; Design Institute for Physical Property Data, American Institute of Chemical Engineers, August 1984.

Duschatko, J.; "CONDENSATE TUBE  $\Delta P$  TEST SUMMARY"; LTV Aerospace and Defense Co.; October 1, 1991.

Fredley, J.E. and Warren, P.H.; *Final Design and Testing of a Low-Pressure Drop Heat Exchanger with Integral Heat Pipe*; Thermophysics and Heat Transfer Conference, AIAA/ASME, Seattle, Washington; 18-20 June, 1990.

Hill, W.S. and Best, F.R.; "DEFINITION OF TWO-PHASE FLOW BEHAVIORS FOR SPACECRAFT DESIGN"; AFK-0062-FM-8933-418; Prepared by Creare Inc., Hanover, New Hampshire, for the U.S. Air Force Albuquerque, New Mexico, AFWL/AWYS, June 1991.

Izenson, M.G., Martin, C.M. and McDonald, M.M.; "MICROCON PROGRAM: HIGH VAPOR SHEAR CONDENSATION"; Creare CPD-242, Software Maintenance Manual, Prepared for Phillips Laboratory, Edwards AFB, California, 1992.

National Institute of Standards; "DIPPR DATA COMPILATION OF PURE COMPOUND PROPERTIES, NIST STANDARD REFERENCE DATABASE 11, U.S."; Department of Commerce, May 1990.

Rohsenow, W.M., Webber, J.H. and Ling, A.T.; "Effect of Vapor Velocity on Laminar and Turbulent-Film Condensation"; Transactions of the ASME, V.78, 1956, pp. 1637-1643.

Shah, M.M.; "A General Correlation for Heat Transfer During Film Condensation Inside Pipes"; International Journal of Heat and Mass Transfer, V.22, April 1979, pp. 547-555.

Soliman, M., Schuster, J.R., and Berenson, P.J.; "A General Heat Transfer Correlation for Annular Flow Condensation"; Journal of Heat Transfer, V.90(2), pp. 267-276, May 1968.

Wallis, G.B.; *One-Dimensional Two-Phase Flow*; McGraw Hill, Inc., 1969.

## 7 CONDENSERS: Capillary Grooves

Capillary condensers are heat rejection elements for heat pipes or thermal management systems such as capillary pumped loops. The condensation rate for a capillary surface depends on the amount of liquid that can be pumped from the surface. The heat transfer coefficient depends on the shape of the condensate film which covers the surface, and the conduction heat transfer through the film. These processes occur at the scale of the capillary microstructure, which is typically 10 to 100 microns (0.5 to 5 thousandths of an inch).

This section of the design manual provides methods to calculate the performance of capillary condensers. There are three calculation methods:

- Methods to calculate the friction factor in liquid-filled grooves,
- Methods to calculate the capillary area needed for a given application,
- Methods to calculate the condensation heat transfer coefficient on a grooved surface.

The friction factor in a capillary groove must be calculated to find the pressure gradient, which can be integrated over the length of the groove to yield the flow (or heat transfer) capacity. The condensation heat transfer coefficient relates the temperature drop across the condenser to the heat flux. This temperature drop is often a major contribution to the thermal resistance of a heat pipe.

### 7.1 Introduction

The heat transfer coefficient for capillary condensation is determined by heat conduction across the liquid condensate film which coats the surface. Figure 7.1 shows a sectional view of condensation in a rectangular capillary groove. Liquid in the groove is under suction which draws the condensate in from adjacent crests. The film is thinnest at the corner of the crest, and this is where the heat transfer resistance is the lowest and the condensation rate is the highest. The heat flux in the corner is much greater than the average heat flux, resulting in a significant temperature drop. This temperature drop determines the heat transfer coefficient.

The detailed shape of the capillary groove can strongly influence the performance. For example, Figure 7.2 shows that a deep rectangular groove has approximately a constant friction factor, because changing the meniscus angle does not much affect the overall flow. In contrast, the flow area in a shallow groove depends strongly on the meniscus angle. Large suction results in a small meniscus angle which increases the pressure gradient and reduces the flow capacity. For each set of methods, detailed descriptions are given for determining the performance of surfaces with rectangular, trapezoidal, and triangular groove cross-sections. In addition, the performance of a contoured fin condenser is also modelled.

Section 7.2 gives the methods for calculating the pressure drops in rectangular, triangular, and trapezoidal grooves. Sections 7.3 through 7.4 give methods for calculating the heat transfer coefficients on rectangular and contoured fins. Sections 7.5 and 7.6 give the methods for sizing capillary condensers.



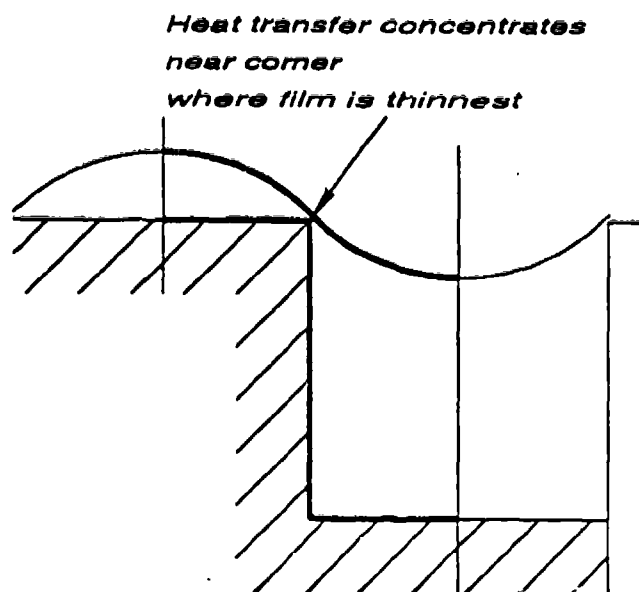
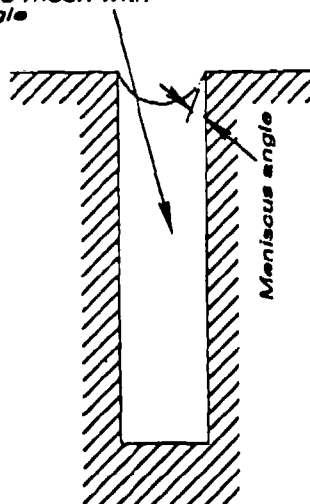


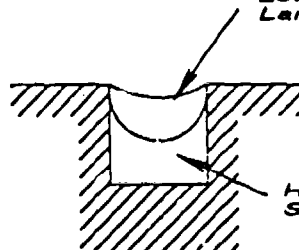
Figure 7.1. HEAT TRANSFER IN A RECTANGULAR GROOVE

Flow area and pressure drop  
do not change much with  
meniscus angle



Deep Groove  
Large aspect ratio

Low suction, high meniscus angle  
Large flow area, low pressure gradient



High suction, low meniscus angle  
Small flow area, high pressure drop

Shallow groove  
Small aspect ratio

Figure 7.2. GROOVE GEOMETRY STRONGLY AFFECTS THE  
FRICTION IN A CAPILLARY GROOVE

## 7.2 Pressure Gradient in Capillary Grooves

Calculations of the flow in a grooved surface condenser require a prediction of the pressure gradient in the fluid inside the grooves. This gradient is a function of the fluid properties, groove geometry and the meniscus shape. As an example, the rectangular geometry is shown in Figure 7.3. The relevant parameters for this geometry are:

- Groove half width (W). This is the characteristic length used to normalize other geometrical dimensions,
- Groove depth (d),
- Groove aspect ratio ( $\alpha \equiv d/2W$ ),
- Groove longitudinal coordinate (z),
- Reduced area due to the meniscus curvature ( $A_m$ ),
- Flat meniscus area ( $A_o$ ),
- Meniscus contact angle ( $\gamma$ ),
- Fluid dynamic viscosity ( $\mu$ ),
- Flow velocity averaged over the nominal groove area ( $V_g^o$ ).

**Calculation Procedure.** The friction factors in capillary grooves were obtained by solving numerically the Navier-Stokes equations for laminar flows in grooves of different geometries. The three geometries considered here are: rectangular grooves, triangular grooves and trapezoidal grooves. Figures 7.4 through 7.6 show calculated dimensionless velocity contours for three sample grooves. The dimensionless velocity is given by:

$$v^* = \frac{v}{(dP/dz)(W^2/\mu)} \quad (7-1)$$

The volumetric flow rate of the condensate over the groove cross-section was obtained by integrating the flow velocity over the cross-section area bounded by the wetted perimeter and the meniscus curve. The results are expressed in terms of a dimensionless pressure gradient defined as:

$$\left[ \frac{dP}{dz} \right]^* = \frac{(dP/dz)}{\mu V_g^o / D_h^2} \quad (7-2)$$

where  $V_g^o$  and  $D_h$  are the averaged liquid velocity and hydraulic diameter for a nominal groove with a flat meniscus. The results can also be expressed in terms of a friction factor, K, defined from:

$$\frac{dP}{dz} = \frac{K}{2Re D_h} \rho V_g^2 \quad (7-3)$$

where  $D_h$  and  $V_g$  are the actual hydraulic diameter and averaged liquid velocity and  $Re$  is the Reynolds number for the liquid flowing in the groove.

ASPECT RATIO  $\alpha = \frac{d}{2W}$

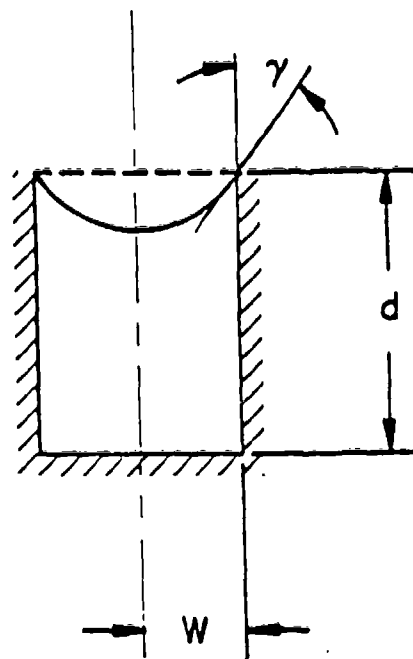


Figure 7.3. GEOMETRY FOR A RECTANGULAR GROOVE

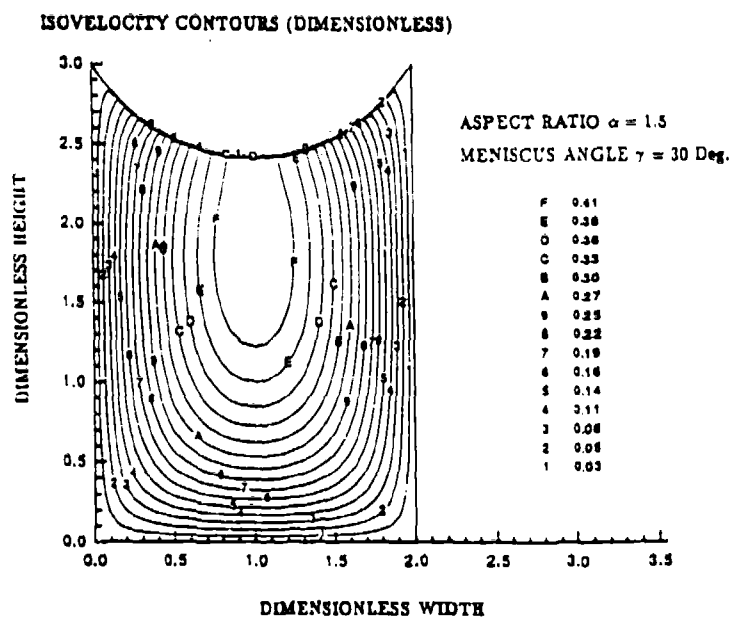


Figure 7.4. DIMENSIONLESS VELOCITY PROFILES IN RECTANGULAR GROOVE

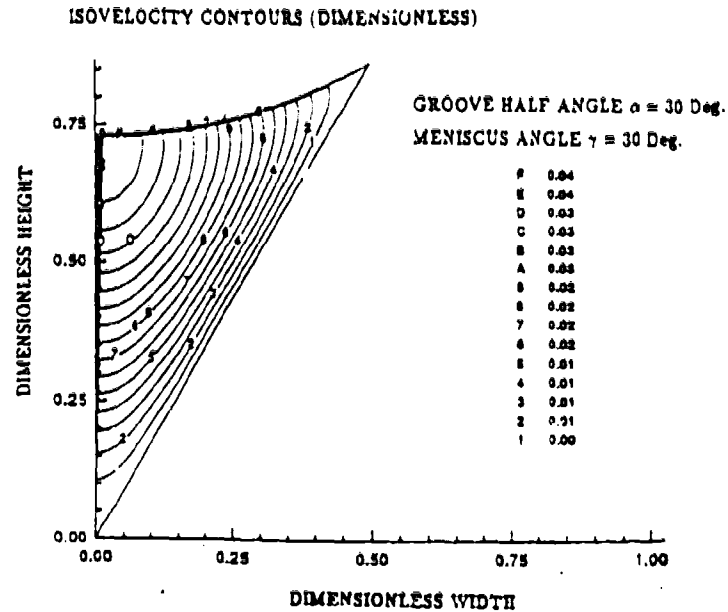


Figure 7.5. DIMENSIONLESS VELOCITY PROFILES IN TRIANGULAR GROOVE

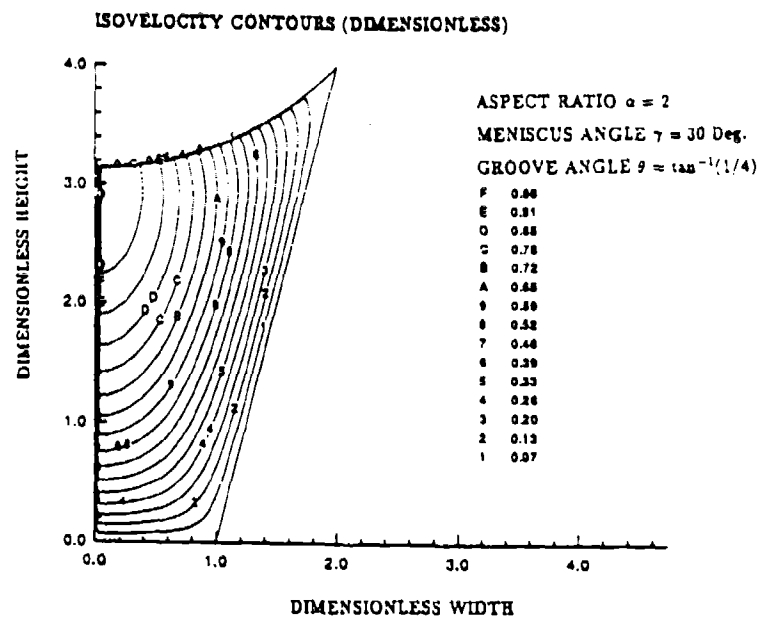


Figure 7.6. DIMENSIONLESS VELOCITY PROFILES IN TRAPEZOIDAL GROOVE

Using the relationships above, the pressure gradient may also be expressed as:

$$\frac{dP}{dz} = \frac{K}{2} \frac{\mu V_g}{D_h} = \left[ \frac{dP}{dz} \right]^* \frac{\mu V_g^0}{D_g^2} \quad (7-4)$$

In these methods, we focus on the dimensionless pressure gradient, rather than the friction factor. The local pressure gradient may be expressed either as a function of the friction factor, the local Reynolds number and the local hydraulic diameter, or as a function of the dimensionless pressure drop and the channel-averaged liquid velocity and hydraulic diameter. Since these channel-averaged or nominal (flat-meniscus) values may be calculated easily, the dimensionless pressure gradient gives the local pressure drop with only a single table lookup.

Since the friction factor and average flow rate are a function of the groove cross-section shape, a two-dimensional boundary-fitted general coordinate code was written to solve the normalized Poisson equation to obtain the factors. The resulting friction factors,  $K$ , were built into a computerized data base. This data base is part of the MICROCAP software suite, and is contained in the files RECTNG.DAT, TRIANG.DAT, and TRAPZDL.DAT. These data are functions of groove aspect ratio ( $\alpha$ ) and the meniscus contact angle ( $\gamma$ ). For given ( $\alpha, \gamma$ ), a bicubic spline is used to interpolate the corresponding friction factor.

### 7.2.1 Pressure Gradient in Rectangular Grooves

This section describes the procedure for calculating the local pressure gradient in rectangular grooves with a uniform curvature vapor-liquid interface. The rectangular geometry is shown in Figure 7.3. The relevant parameters are:

- Groove half width ( $W$ ). This is the characteristic length used to normalize other geometrical dimensions,
- Groove depth ( $d$ ),
- Groove aspect ratio ( $\alpha \equiv d/2W$ ),
- Groove longitudinal coordinate ( $z$ ),
- Area reduction due to the meniscus curvature ( $A_m$ ),
- Flat meniscus area ( $A_o$ ),
- Meniscus contact angle ( $\gamma$ ),
- Fluid dynamic viscosity ( $\mu$ ),
- Flow velocity averaged over the nominal groove area ( $V_g^0$ ).

The overall procedure is summarized as follows:

- 1) Calculate flat meniscus groove area:

$$A_o = 2Wd \quad (7-5)$$

- 2) Calculate flow area reduction due to meniscus curvature:

$$A_m = W^2 \left[ \frac{\frac{\pi}{2} - \gamma}{\cos^2(\gamma)} - \tan(\gamma) \right] \quad (7-6)$$

- 3) Calculate flow area:

$$A = A_o - A_m \quad (7-7)$$

- 4) Calculate hydraulic diameters:

$$D_g = \frac{2A_o}{(W + d)} \quad (7-8)$$

$$D_h = \frac{2A}{(W + d)} \quad (7-9)$$

- 5) Use a bicubic spline to interpolate the friction factor  $K$  from the rectangular groove data base.
- 6) Calculate normalized pressure gradient:

$$\left[ \frac{dP}{dz} \right]^* = \frac{K}{2} \left[ \frac{D_g}{D_h} \right]^3 \quad (7-10)$$

Results of these calculations are presented in Figure 7.7.

The predictions of this section may be directly compared with other solutions presented in the literature for the limiting case of a fully filled groove. For this case, the rectangular groove solutions from Kays and London (1984) may be used. For the case of an open channel flow, the friction factor must be compared to that of a channel with twice the height, so the free surface of the open channel and the symmetry line of the closed channel have the same boundary condition. Figure 7.8 shows the good agreement between the solutions in Kays and London and those obtained using the methods of this section. Note that, in accordance with Kays and London, this figure gives the Fanning friction factor, rather than the Darcy friction factor used in our results. The Darcy friction factor, when multiplied by four, gives the Fanning friction factor.

In addition, these methods were compared to the calculations from Hwangbo and McEver (1987). The authors of this paper expressed their results in terms of a groove hydraulic factor  $2D_g^2 A/K$ . Comparison of their results to those produced using the methods of this section show good agreement between the two solutions.

### 7.2.2 Pressure Gradient in Triangular Grooves

This section describes the procedure for calculating the local pressure gradient in triangular grooves with a uniform curvature vapor-liquid interface. The triangular geometry is shown in Figure 7.9. The relevant parameters are:

- Groove side length ( $W$ ). This is the characteristic length used to normalize other geometrical dimensions,
- Groove depth ( $d$ ),
- Groove half angle ( $\alpha$ ),
- Groove longitudinal coordinate ( $z$ ),

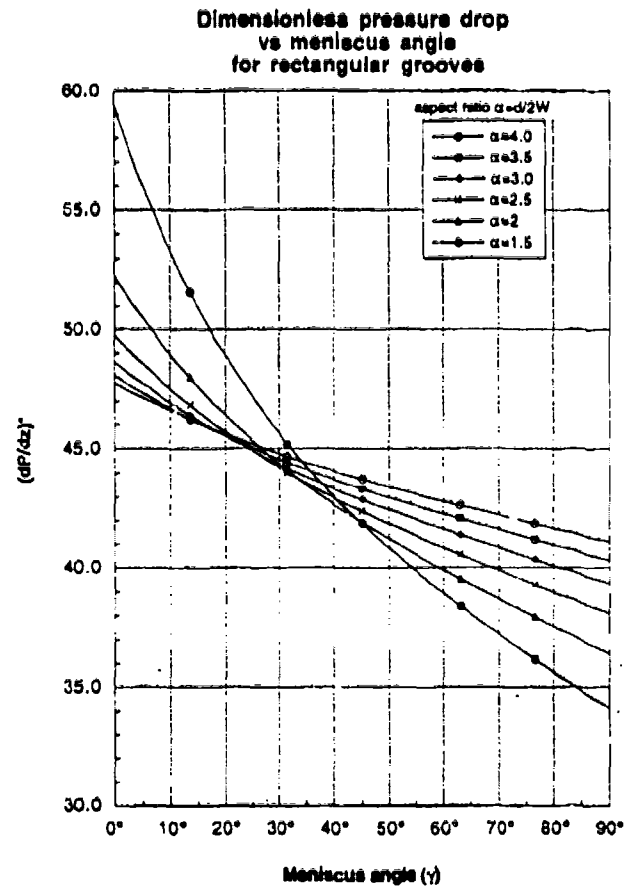


Figure 7.7. DIMENSIONLESS PRESSURE GRADIENT IN RECTANGULAR GROOVES

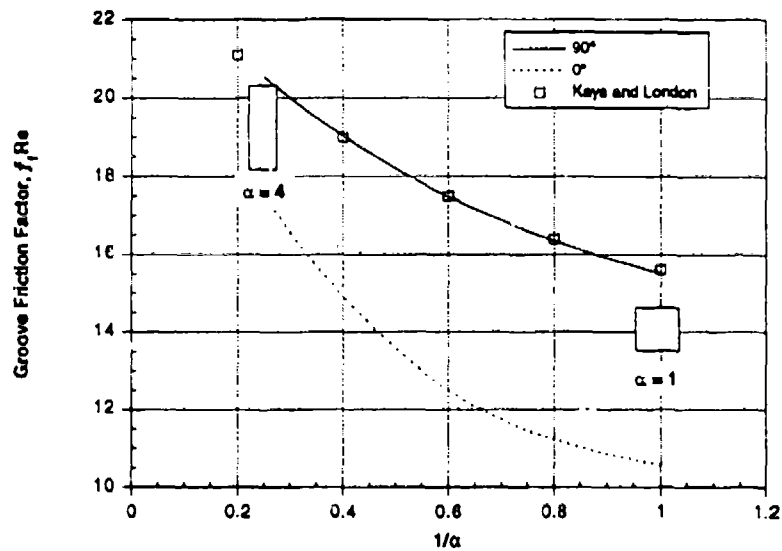


Figure 7.8. PRESSURE DROP IN RECTANGULAR GROOVES

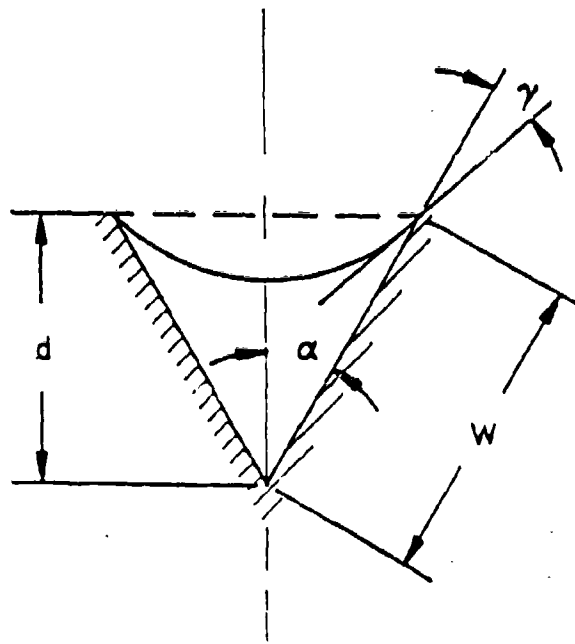


Figure 7.9. GEOMETRY FOR A TRIANGULAR GROOVE

- Area reduction due to the meniscus curvature ( $A_m$ ),
- Flat meniscus area ( $A_o$ ),
- Meniscus contact angle ( $\gamma$ ),
- Fluid dynamic viscosity ( $\mu$ ),
- Flow velocity averaged over the nominal groove area ( $V_g^c$ ).

**Calculation Procedure.** The procedure for calculating the frictional pressure drop is the same as that in the rectangular groove. The same computer code was used to solve the normalized Poisson equation and obtain the friction factors to build up the data base. We also compared our results with those obtained from a semi-analytical solution by Ayyaswami, et al. (1981). The agreement is within 0.3%. These data are functions of groove half angle ( $\alpha$ ) and the meniscus contact angle ( $\gamma$ ). For given ( $\alpha, \gamma$ ), a bicubic spline is used to interpolate the corresponding friction factor. The overall procedure is summarized as follows:

- 1) Calculate the groove height:

$$d = W \cos(\alpha) \quad (7-11)$$

- 2) Calculate flat meniscus groove area:

$$A_o = d^2 \tan(\alpha) \quad (7-12)$$



- 3) Calculate flow area reduction due to meniscus curvature:

$$A_m = d^2 \tan^2(\alpha) \left[ \frac{\frac{\pi}{2} - \gamma - \alpha}{\cos^2(\gamma + \alpha)} - \tan(\gamma + \alpha) \right] \quad (7-13)$$

- 4) Calculate flow area:

$$A = A_o - A_m \quad (7-14)$$

- 5) Calculate hydraulic diameters:

$$D_h^* = \frac{2A_o \cos(\alpha)}{d} \quad (7-15)$$

$$D_h = \frac{2A \cos(\alpha)}{d} \quad (7-16)$$

- 6) Use bicubic spline to interpolate the friction factor  $K$  from the triangular groove data base.  $K$  is a function of  $\alpha$  and  $\gamma$ .
- 7) Calculate normalized pressure gradient:

$$\left[ \frac{dP}{dz} \right]^* = \frac{K}{2} \left[ \frac{D_h^*}{D_h} \right]^3 \quad (7-17)$$

Results of these calculations are shown in Figure 7.10 which illustrates the dimensionless pressure gradient in triangular grooves of various aspect ratios.

### 7.2.3 Pressure Gradient in Trapezoidal Grooves

This section describes the procedure for calculating the local pressure gradient in trapezoidal grooves with a uniform curvature vapor-liquid interface. The geometry is shown in Figure 7.11. The relevant parameters are:

- Groove base half width ( $W$ ). This is the characteristic length used in the subroutine to normalize other geometrical dimensions,
- Groove depth ( $d$ ),
- Groove aspect ratio ( $\alpha \equiv d/2W$ ),
- Groove base angle  $\theta = \tan^{-1}(1/4)$ ,
- Groove longitudinal coordinate ( $z$ ),
- Area reduction due to the meniscus curvature ( $A_m$ ),
- Flat meniscus area ( $A_o$ ),
- Meniscus contact angle ( $\gamma$ ),
- Fluid dynamic viscosity ( $\mu$ ),
- Flow velocity averaged over the nominal groove area ( $V_g$ ).

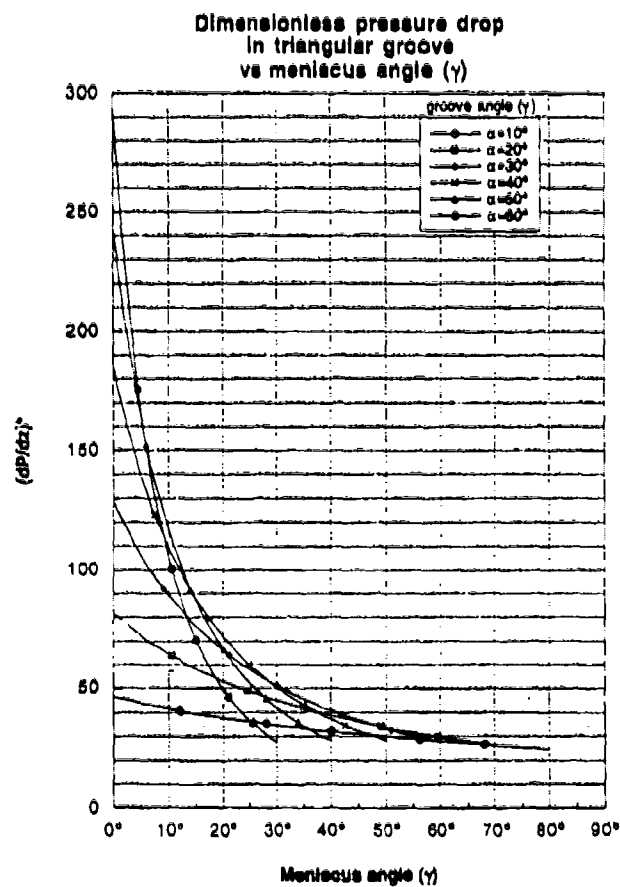


Figure 7.10. DIMENSIONLESS PRESSURE GRADIENT IN TRIANGULAR GROOVES

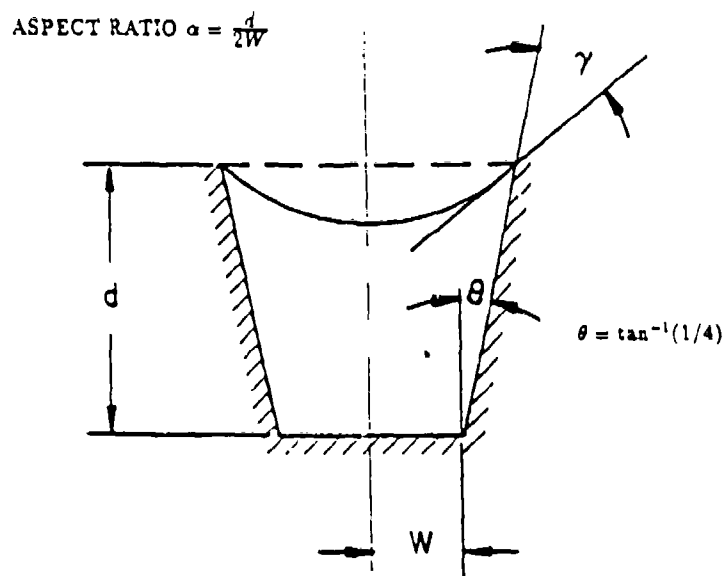


Figure 7.11. GEOMETRY FOR A TRAPEZOIDAL GROOVE

**Calculation Procedure** The procedure for calculating the frictional pressure drop is the same as that for the rectangular groove. The normalized Poisson equation was first solved and the solution used to obtain the friction factor  $K$  to build up the data base. The data are functions of groove aspect ratio ( $\alpha$ ) and the meniscus contact angle ( $\gamma$ ). For given ( $\alpha, \gamma$ ), a bicubic spline is used to interpolate the corresponding friction factor. The overall procedure is summarized as follows:

- 1) Calculate groove height:

$$d = 2\alpha W \quad (7-18)$$

- 2) Calculate flat meniscus groove area:

$$A_o = 2Wd[1 + \alpha \tan(\theta)] \quad (7-19)$$

- 3) Calculate flow area reduction due to meniscus curvature:

$$A_m = \left[ \frac{W(1 + 2\alpha \tan(\theta))}{\sin\left(\frac{\pi}{2} - \gamma - \theta\right)} \right]^2 \left[ \frac{\pi}{2} - \gamma - \theta \right] - W^2[1 + 2\alpha \tan(\theta)]^2 \cot\left[\frac{\pi}{2} - \gamma - \theta\right] \quad (7-20)$$

- 4) Calculate flow area:

$$A = A_o - A_m \quad (7-21)$$

- 5) Calculate hydraulic diameters:

$$D_g = \frac{2A_o}{W + \frac{d}{\cos(\theta)}} \quad (7-22)$$

$$D_h = \frac{2A}{W + \frac{d}{\cos(\theta)}} \quad (7-23)$$

- 6) Use bicubic spline to interpolate the friction factor  $K$  from the triangular groove data base.  $K$  is a function of  $\alpha$  and  $\gamma$ .
- 7) Calculate normalized pressure gradient:

$$\left[ \frac{dP}{dz} \right]^* = \frac{K}{2} \left[ \frac{D_g}{D_h} \right]^3 \quad (7-24)$$

Results of these calculations are shown in Figure 7.12 which shows the dimensionless pressure gradient in trapezoidal grooves of various aspect ratios.

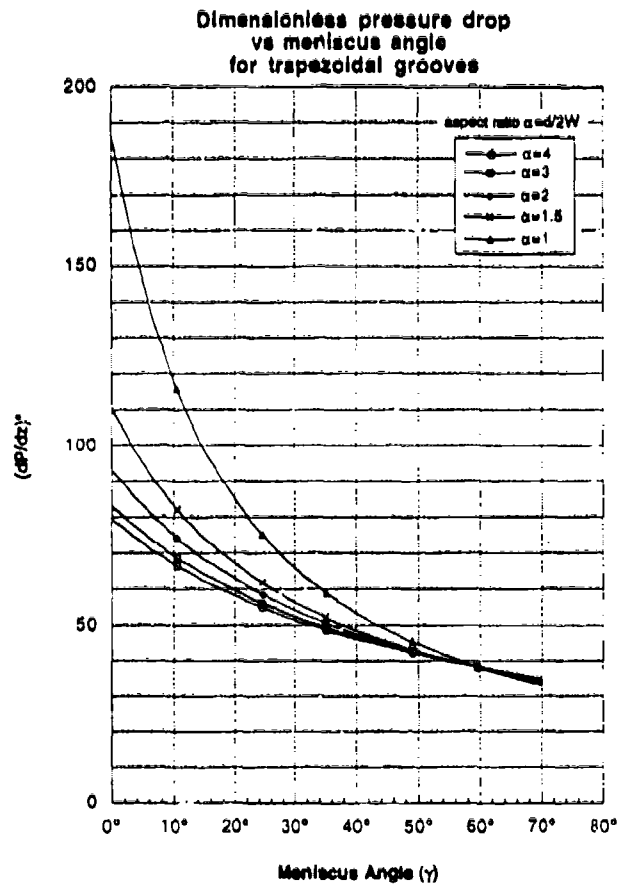


Figure 7.12. DIMENSIONLESS PRESSURE GRADIENT IN TRAPEZOIDAL GROOVES

### 7.3 Heat Transfer Coefficients on Rectangular Fins

This section describes the procedure for calculating the local heat transfer coefficient on a rectangular fin. The fin geometry is shown in Figure 7.13. The fin is assumed to have infinite thermal conductivity. The relevant parameters are:

- Groove half pitch ( $W$ ).
- Vapor temperature ( $T_v$ ).
- Wall temperature ( $T_w$ ).
- Fluid conductivity ( $k_f$ ).
- Fluid kinematic viscosity ( $\nu$ ).
- Fluid surface tension ( $\sigma$ ).
- Latent heat of fluid ( $h_{fg}$ ).

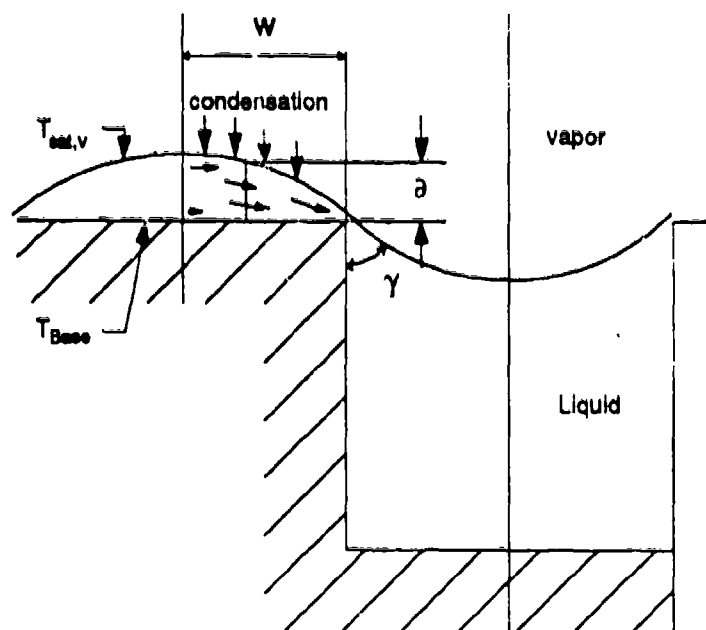


Figure 7.13. GEOMETRY FOR A FLAT TOP FIN

**Calculation Procedure.** To determine the condensation heat transfer coefficient, we make the following approximations:

- The film surface is at the saturation temperature of the vapor,  $T_v$ .
- Acceleration forces may be neglected,
- The meniscus shape is in the form of two circular arcs,
- Heat transfer through the film is one-dimensional,
- The fin has infinite thermal conductivity.

With these approximations, the solution strategy is to guess a film minimum thickness  $\eta$ , calculate the condensation mass flux, and determine the total pressure drop from the fin top center to the center of the groove. This pressure drop is compared to the local capillary head available, and the minimum film thickness varied until the calculated pressure drop matches the capillary head.

The solution procedure for a given meniscus angle begins with a guess of the minimum film thickness. The meniscus angle and the film thickness are used to calculate the meniscus geometry under the assumption that both meniscii are circular arcs. Beginning at the fin top center, two equations are integrated to find the local pressure and mass flow at various points along the fin top and side. These equations account for the mass addition due to condensation:

$$\frac{dm}{dx} = \frac{k_f(T_w - T_v)}{\delta h_{fg}} \quad (7-25)$$

and the local pressure gradient in the film:

$$\frac{dP}{dx} = \frac{vm}{\delta^3} \quad (7-26)$$

The equations are integrated from the top center of the fin around the corner to the bottom of the meniscus in the groove. The pressure difference between these two points is calculated and compared to the available capillary head,

$$\Delta P = \frac{\sigma}{R_1} + \frac{\sigma}{R_2} \quad (7-27)$$

where  $R_1$  and  $R_2$  are the radii of curvature on the fin top and in the groove. The result of this comparison is fed into a root-finding routine and used to modify the guess for the minimum film thickness until a match is achieved between the pressure drop calculated from the film flow equations and that calculated from the surface tension forces. These calculations can be repeated for a number of meniscus angles to determine the local heat transfer coefficient over the entire length of the condenser.

Figure 7.14 shows the heat transfer coefficient in ammonia versus fin pitch for various sub-coolings (from a  $30^\circ$  meniscus angle). Figure 7.15 shows the variation of heat transfer coefficient with meniscus angle for the same conditions.

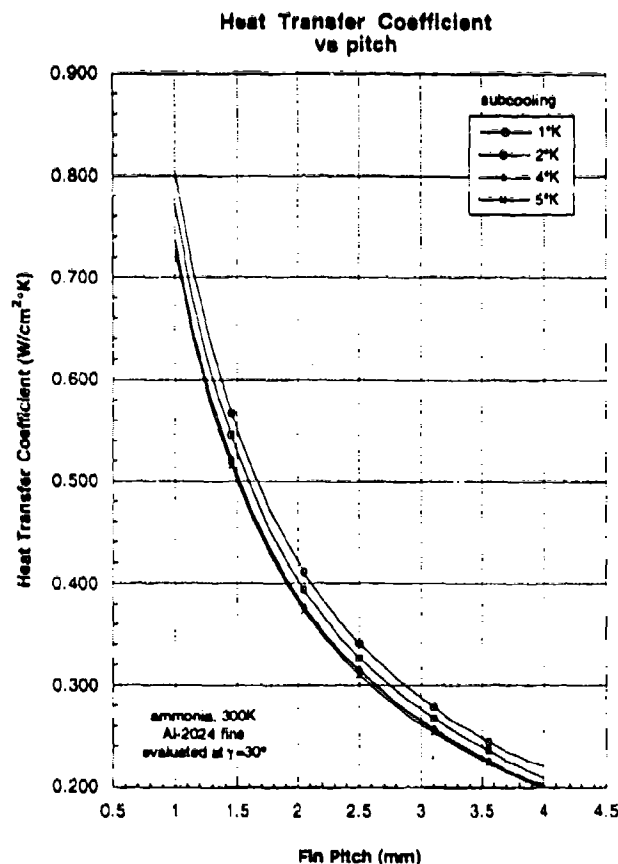
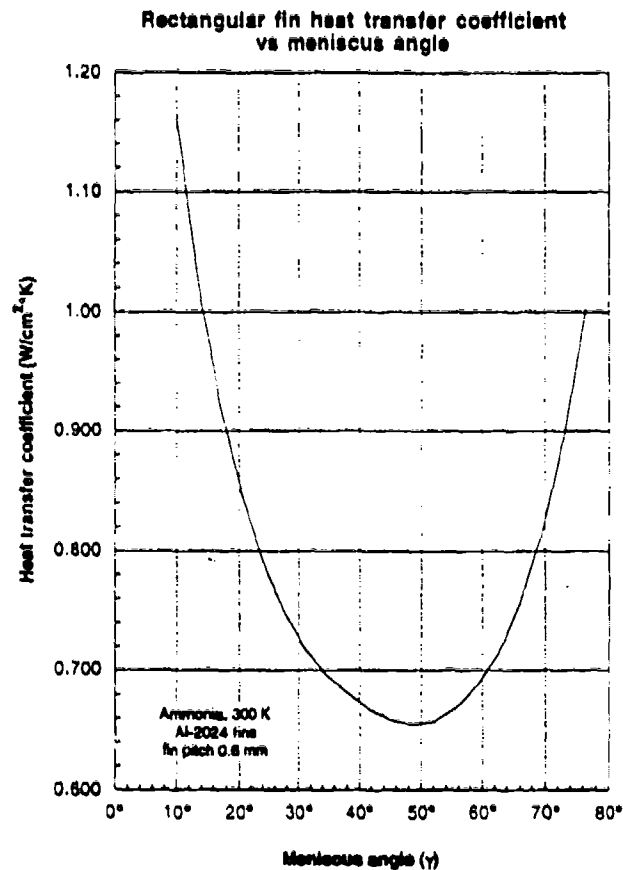


Figure 7.14. FLAT TOP FIN HEAT TRANSFER COEFFICIENT VERSUS FIN PITCH



**Figure 7.15. FLAT TOP FIN HEAT TRANSFER COEFFICIENT VERSUS MENISCUS ANGLE**

**Limitations of the Method.** The assumptions used to derive these equations do not hold when the film thickness is large. This occurs on the fin top at small meniscus angles, and on the fin side at large angles. However, the condensation rate in these areas is small due to the large film thickness, so the error in the total condensation rate is also small. Nonetheless, the methods of this section are of greatest accuracy at intermediate angles.

For angles near 45°, the film thickness at the fin corner becomes only a few tens of microns. For these small film thicknesses, most of the heat transfer occurs at the fin corner, leading to very high temperature gradients in this area. Near the fin corner, the thermal resistance of the fin itself may become comparable with the film resistance. For these cases, a more accurate model would take into account the conduction resistance in the fin.

Local condensation heat transfer coefficients are difficult to measure accurately, and few are reported in the literature. Our results are consistent with the heat transfer coefficients reported in Alario, et al. (1981).

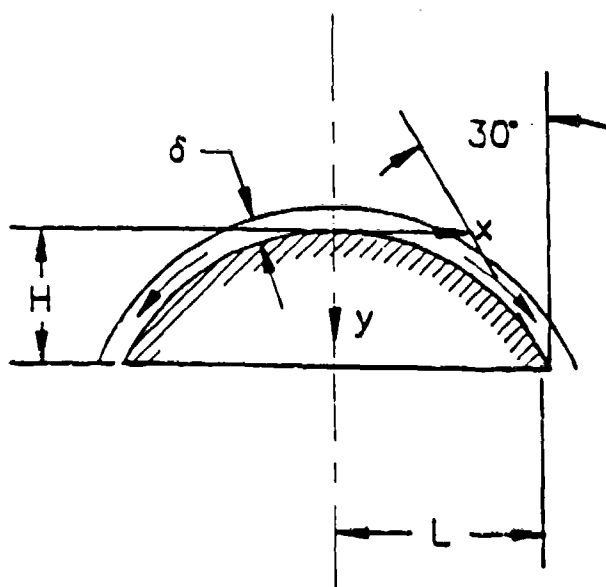
#### 7.4 Heat Transfer Coefficients on Contoured Fins

This section describes the procedure for calculating the local heat transfer coefficients on a contoured fin. In this approach, the condensate is driven from the top of the fins to the troughs between the fins by capillary forces resulting from a gradual increase in the radius of curvature of the fin surface. The fin geometry is displayed in Figure 7.16. The fin surface contour is given by:

$$\frac{y}{H} = \cosh \left[ \frac{x}{H} \right] - 1 \quad (7-28)$$

with the fin half pitch  $L = 1.32H$ . As described by Valenzuela and Drew (1989), this geometry provides a good compromise between performance and manufacturability of the condenser surface. The relevant parameters are:

- Fin half pitch (L),
- Fin height (H),
- Vapor temperature ( $T_v$ ),
- Wall temperature ( $T_w$ ),
- Wall conductivity ( $k_w$ ),
- Fluid conductivity ( $k_f$ ),
- Fluid kinematic viscosity ( $\nu$ ),
- Fluid surface tension ( $\sigma$ ),
- Latent heat of fluid ( $h_{fg}$ ).



$$\frac{y}{H} = \cosh \left( \frac{x}{H} \right) - 1$$

$$L = 1.38 H$$

$\delta \approx$  FILM THICKNESS

Figure 7.16. GEOMETRY FOR THE CONTOURED FIN



**Calculation Procedure.** The calculation procedure is based on the model described by Valenzuela and Drew (1989). They obtained an analytical solution for the condensation on the contoured fin under the assumption of constant wall temperature. The effect of the wall conduction resistance was then estimated using a 1-D conduction solution. Their solution can be implemented by the procedure given below:

- 1) Calculate the uniform wall temperature heat transfer coefficient:

$$h_{fb} = 1.06 \left[ \frac{k_1}{L} \right]^{0.75} \left[ \frac{h_{fg} \sigma}{v(T_v - T_w)} \right]^{0.25} \quad (7-29)$$

- 2) Calculate the fin efficiency:

$$\eta = 0.574 \int_0^{1.32} \frac{dx}{\frac{1}{\cosh(x)} + \frac{h_{fb} H [2 - \cosh(x)]}{1.32 k_w}} \quad (7-30)$$

- 3) Calculate the 1-D conduction heat transfer coefficient:

$$h_{cb} = \eta h_{fb} \quad (7-31)$$

- 4) Calculate the actual heat transfer coefficient:

$$h_b = \frac{1}{2} [h_{cb} + h_{fb}] \quad (7-32)$$

- 5) Calculate the Nusselt number:

$$Nu = \frac{h_b L}{k_1} \quad (7-33)$$

- 6) Calculate the curve length of the contoured surface:

$$S = H \sinh \left[ \frac{L}{H} \right] \quad (7-34)$$

- 7) Calculate the condensate thickness:

$$\delta = \frac{k_1 S}{h_{fb} L} \quad (7-35)$$

Figure 7.17 shows the calculated heat transfer coefficient in ammonia versus fin pitch for various sub-coolings.

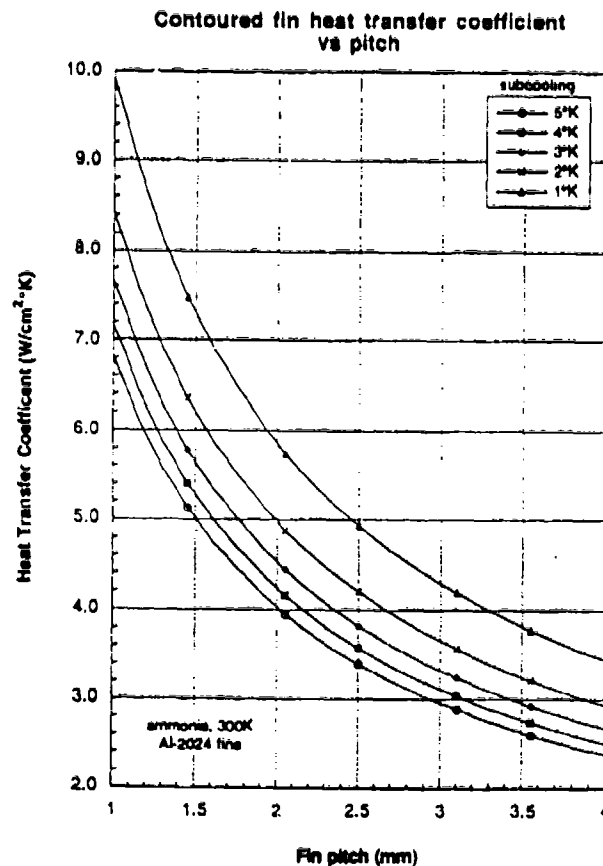


Figure 7.17. CONTOURED FIN HEAT TRANSFER COEFFICIENT VERSUS FIN PITCH

### 7.5 Internally Drained Condenser (IDC)

This section describes the procedure for calculating the local performance and geometry of an internally drained condenser. This high performance capillary condenser was developed at Creare under contract NAS9-17989. The geometry is illustrated in Figure 7.18. The internally drained condenser consists of a series of shaped fins separated by thin liquid drainage grooves. The fin shape has a constantly varying curvature, with the radius of curvature increasing monotonically from the crest of the fin to the drainage groove. Vapor condenses on the fins, forming a thin liquid film which has approximately the same radius of curvature as the fin surface. The varying curvature of the vapor-liquid interface produces a surface pressure gradient from crest to trough, moving the liquid in that direction. The relevant parameters are:

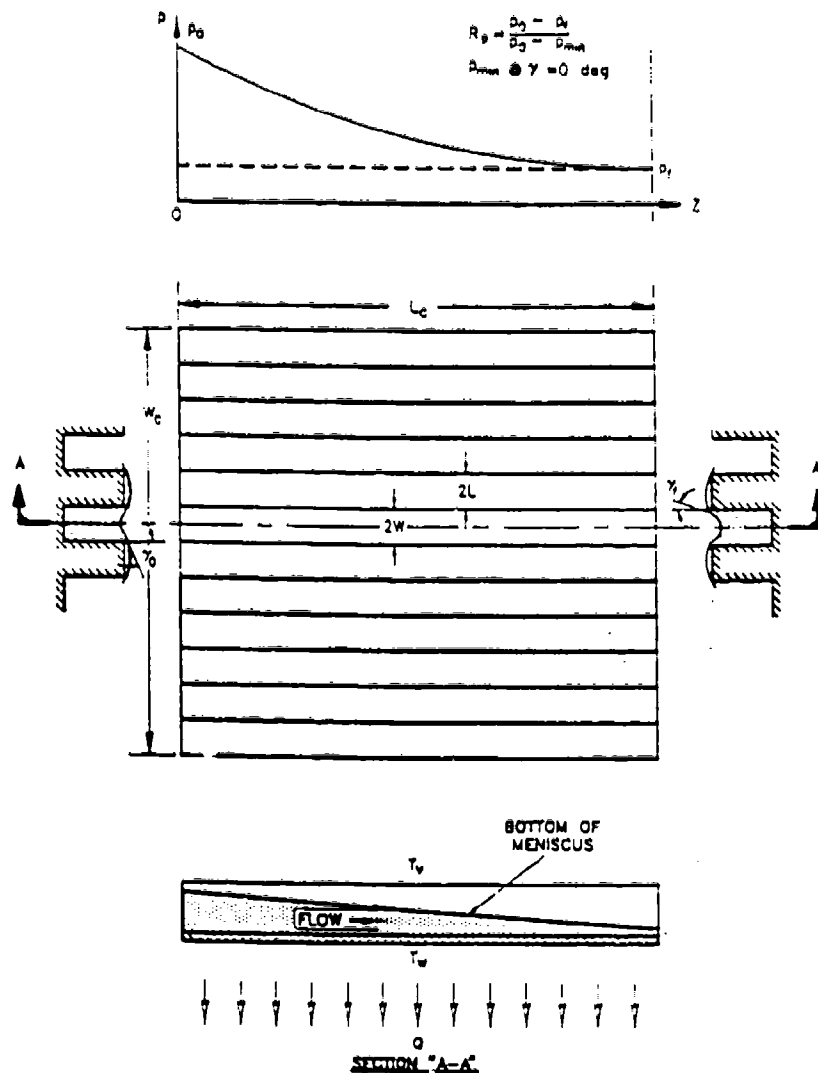


Figure 7.18. GEOMETRY FOR AN INTERNALLY DRAINED CONDENSER

- Condenser length ( $L_c$ ),
- Fin half pitch ( $L$ ),
- Drainage groove half base width ( $W$ ),
- Drainage groove depth ( $d$ ),
- Drainage hole diameter ( $D$ ),
- Vapor temperature ( $T_v$ ),
- Wall temperature ( $T_w$ ),
- Total condensation rate ( $Q_c$ ),
- Wall conductivity ( $k_w$ ),
- Liquid conductivity ( $k_l$ ),
- Liquid kinematic viscosity ( $\nu$ ),
- Liquid surface tension ( $\sigma$ ),
- Latent heat of fluid ( $h_{fg}$ ).

**Calculation Procedure.** The calculation procedure is based on the model described in Valenzuela and Drew (1989). The model accounts for temperature drops in the condensate film and in the wall portion above the bottom of the drainage grooves. The temperature at the bottom of the drainage grooves is assumed to be uniform throughout the surface of the condenser. The drainage network is sized to fully utilize the available capillary pumping. The model can be implemented using the procedure given below:

- 1) Assume the fin base temperature is equal to the wall temperature:

$$T_b = T_w \quad (7-36)$$

- 2) Calculate the heat transfer coefficient,  $h_b$ , on the contoured fin, as described above.
- 3) Calculate heat flux:

$$q'' = h_b(T_v - T_b) \quad (7-37)$$

- 4) Calculate the drainage hole pitch:

$$P = \frac{[-a_{12} + (a_{12}^2 + 4a_{11}a_{13})^{1/2}]}{2a_{11}} \quad (7-38)$$

where

$$a_{11} = \frac{3L\mu q''}{W^3 \rho h_{fg} d} \quad (7-39)$$

$$a_{12} = \frac{20.37 L^2 \mu q''}{D^4 \rho h_{fg}} \quad (7-40)$$

$$a_{13} = 0.134 \sigma / W \quad (7-41)$$

- 5) Calculate the fin base temperature:

$$T_b = T_w + \frac{Pq''d}{k_w(P + D)} \quad (7-42)$$

- 6) Iterate steps 2 to 5 until the fin base temperature converges to 0.1% of sub-cooling.
- 7) Calculate the condenser area and width:

$$A_c = \frac{Q_c}{q''} \left[ \frac{L + W}{L} \right] \quad (7-43)$$

$$W_c = A_c / L_c \quad (7-44)$$

## 7.6 Grooved Surface Condensers

The procedures given in this section allow the design of grooved surface condensers with three different groove cross-sections: rectangular, trapezoidal and triangular.

The first step in the procedure is to estimate the maximum available capillary head. The maximum capillary head is obtained by varying the meniscus from the user-specified initial meniscus contact angle to zero degrees, followed by receding the meniscus height down to certain limits. There is no gain in the total capillary head for a rectangular groove as the meniscus recedes, therefore meniscus receding is necessary only in triangular and trapezoidal grooves. For these calculations, the designer specifies the total pressure drop in the grooves as a fraction of the maximum available capillary head.

### 7.6.1 Rectangular Grooves

The relevant parameters for the rectangular groove are:

- Condenser length ( $L_c$ ),
- Fin half pitch ( $L$ ),
- Drainage groove characteristic length ( $W$ ),
- Drainage groove aspect ratio ( $\alpha$ ),
- Vapor temperature ( $T_v$ ),
- Wall temperature ( $T_w$ ),
- Total condensation rate ( $Q_c$ ),
- Fluid kinematic viscosity ( $\nu$ ),
- Fluid surface tension ( $\sigma$ ),
- Latent heat of fluid ( $h_{fg}$ ),
- Initial meniscus angle ( $\gamma_o$ ),
- User-specified initial meniscus angle ( $\gamma_o$ ),
- Terminal meniscus angle ( $\gamma_f$ ),
- User-specified ratio of maximum pressure drop ( $R_p$ ),
- User-specified heat transfer coefficient ( $h_b$ ).

**Calculation Procedure.** The model assumes that the rate of condensate flowing into the groove is not influenced by the change of meniscus angle, and the temperature difference  $T_v - T_w$  is constant throughout the length of the groove. the groove is sized to utilize the available capillary pumping head by a ratio of  $R_p$  ( $0 < R_p < 1$ ). The model can be implemented following the procedure given below:

- 1) Calculate or specify the heat transfer coefficient,  $h_b$  (see Sections 7.3 and 7.4).
- 2) Obtain the condensate flow rate per unit groove length:

$$\dot{m} = \frac{2h_b(W + L)(T_v - T_w)}{h_{fg}} \quad (7-45)$$

- 3) Calculate the maximum available capillary head for the given initial meniscus angle,  $\gamma_0$ :

$$\Delta P_{\max} = \frac{\sigma}{W} [1 - \cos(\gamma_0)] \quad (7-46)$$

- 4) Calculate the terminal meniscus angle:

$$\gamma_t = \cos^{-1}[R_p(1 - \cos \gamma_0) + \cos \gamma_0] \quad (7-47)$$

- 5) With initial condition  $z = 0$  at  $\gamma = \gamma_0$ , solve the following differential equation to obtain the desired groove length  $z = L_c$  at  $\gamma = \gamma_t$ :

$$\frac{d(z^2)}{d\gamma} = - \left[ \frac{2\sigma}{v_m W} \right] \left[ \frac{2AD_f^2}{K} \right]^* \sin(\gamma) \quad (7-48)$$

In the equation  $\left[ \frac{2AD_f^2}{K} \right]^*$  is a dimensionless hydraulic factor. It is a function of  $\alpha$  and  $\gamma$ . A fairly comprehensive data base has been calculated and built into a lookup table. This table is part of the MICROCAP software suite, and is contained in the files RECQV.DAT, TRIQV.DAT, and TRAPQV.DAT. In the course of solving the differential equation given above, the corresponding hydraulic factor at each  $(\alpha, \gamma)$  is obtained through a bicubic spline interpolation.

- 6) Calculate the condenser area and width:

$$W_c = 2 \left[ \frac{Q_c}{mh_{fg} L_c} \right] (L + W) \quad (7-49)$$

$$Ac = L_c W_c \quad (7-50)$$

Figure 7.19 shows the maximum dimensionless heat transfer per fin for a rectangular groove. This curve is calculated by setting the allowed pressure drop to the maximum available in the groove.

### 7.6.2 Triangular Grooves

The relevant parameters for the triangular groove are:

- Condenser length ( $L_c$ ),
- Fin half pitch ( $L$ ),
- Drainage groove characteristic length ( $W$ ),
- Groove half angle ( $\alpha$ ),
- Vapor temperature ( $T_v$ ),
- Wall temperature ( $T_w$ ),
- Total condensation rate ( $Q_c$ ),
- Fluid kinematic viscosity ( $\nu$ ),
- Fluid surface tension ( $\sigma$ ),

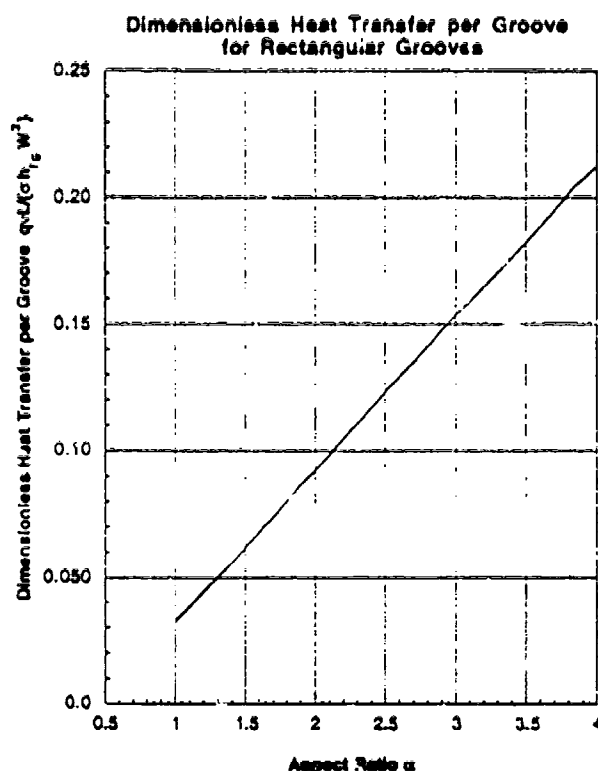


Figure 7.19. DIMENSIONLESS HEAT TRANSFER PER GROOVE FOR A RECTANGULAR GROOVE

- Latent heat of fluid ( $h_{fg}$ ),
- Initial meniscus angle ( $\gamma_0$ ),
- User-specified initial meniscus angle ( $\gamma_0$ ),
- Terminal meniscus angle ( $\gamma_f$ ),
- User-specified ratio of maximum pressure drop ( $R_p$ ),
- User-specified heat transfer coefficient ( $h_b$ ).

Calculation Procedure. The assumptions are the same as those for the rectangular groove. In the triangular groove, we allow the meniscus to recede down to one-tenth initial groove side length. The calculation procedure is summarized as follows:

- 1) Calculate or specify the heat transfer coefficient,  $h_b$  (see Sections 7.3 and 7.4).
- 2) Obtain the condensate flow rate per unit groove length:

$$\dot{m} = \frac{2h_b(L + W \sin \alpha)(T_y - T_w)}{h_{fg}} \quad (7-51)$$

- 3) Calculate  $\tilde{R}_p$ , the pressure ratio which indicates the meniscus has receded:

$$\tilde{R}_p = \frac{\sin(\frac{\pi}{2} - \alpha) - \sin(\frac{\pi}{2} - \alpha - \gamma_o)}{10 \sin(\frac{\pi}{2} - \alpha) - \sin(\frac{\pi}{2} - \alpha - \gamma_o)} \quad (7-52)$$

- 4) If  $R_p < \tilde{R}_p$ , the desired pressure drop can be achieved without meniscus receding. In this case, the calculation procedure is:

- Calculate the terminal meniscus angle:

$$\gamma_f = \frac{\pi}{2} - \alpha - \sin^{-1}(c_{11}) \quad (7-53)$$

$$c_{11} = \sin\left(\frac{\pi}{2} - \alpha - \gamma_o\right) \quad (7-54)$$

$$+ R_p \left[ 10 \sin\left(\frac{\pi}{2} - \alpha\right) - \sin\left(\frac{\pi}{2} - \alpha - \gamma_o\right) \right]$$

- With initial condition  $z = 0$  at  $\gamma = \gamma_o$ , solve the following differential equation to obtain the desired groove length  $z = L_c$  at  $\gamma = \gamma_f$ :

$$\frac{d(z^2)}{d\gamma} = - \left( \frac{2\sigma W^3}{\nu m \sin(\alpha)} \right) \left( \frac{2AD_h^2}{K} \right)^* \cos\left(\frac{\pi}{2} - \alpha - \gamma\right) \quad (7-55)$$

The dimensionless hydraulic factor  $\left[ \frac{2AD_h^2}{K} \right]^*$  for triangular grooves at the corresponding  $(\alpha, \gamma)$  is obtained from the lookup table during the course of integrating the above differential equation.

- Go to step 6 to calculate the condenser size.

- 5) If  $R_p > \tilde{R}_p$ , in addition to varying  $\gamma$  from  $\gamma_o$  to 0, meniscus receding is also required to achieve the desired pressure drop. In this case, the calculation procedure is:

- Calculate the terminal groove side length  $W_f$ :

$$W_f = \frac{W}{c_{12}} \quad (7-56)$$

$$c_{12} = 10R_p + (1 - R_p) \frac{\sin\left(\frac{\pi}{2} - \alpha - \gamma_o\right)}{\sin\left(\frac{\pi}{2} - \alpha\right)} \quad (7-57)$$

- Set  $\gamma_f = 0$ , then solve Equation (7-55) by marching the meniscus angle from  $\gamma_o$  to  $\gamma_f$ , while  $W$  remains fixed.



- Solve the following differential equation to obtain the final groove length  $L_c$  by receding the groove side length from  $W$  to  $W_f$ , while holding  $\gamma_f = 0$ :

$$\frac{d(z^2)}{dW} = - \left( \frac{2\sigma}{\nu m \sin(\alpha)} \right) \left( \frac{2AD_h^2}{K} \right)^* \sin \left( \frac{\pi}{2} - \alpha - \gamma_f \right) W^2 \quad (7-58)$$

- 6) Calculate the condenser area and width:

$$W_c = 2 \left( \frac{Q_c}{m h_{fg} L_c} \right) (L + W \sin(\alpha)) \quad (7-59)$$

$$A_c = L_c W_c \quad (7-60)$$

### 7.6.3 Trapezoidal Grooves

The relevant parameters for the triangular groove are:

- Condenser length ( $L_c$ ),
- Fin half pitch ( $L$ ),
- Drainage groove characteristic length ( $W$ ),
- Groove aspect ratio ( $\alpha$ ),
- Vapor temperature ( $T_v$ ),
- Wall temperature ( $T_w$ ),
- Total condensation rate ( $Q_c$ ),
- Fluid kinematic viscosity ( $\nu$ ),
- Fluid surface tension ( $\sigma$ ),
- Latent heat of fluid ( $h_{fg}$ ),
- Initial meniscus angle ( $\gamma_0$ ),
- Terminal meniscus angle ( $\gamma_f$ ),
- User-specified initial aspect ratio ( $\alpha_0$ ),
- User-specified initial meniscus angle ( $\gamma_0$ ),
- User-specified ratio of maximum pressure drop ( $R_p$ ),
- User-specified heat transfer coefficient ( $h_b$ ).

**Calculation Procedure.** The assumptions are the same as those in the rectangular groove. In the calculation, the terminal aspect ratio is set to be 0.625 where the trough of the meniscus is very close to the groove base. The calculation procedure is given below:

- 1) Calculate or specify the heat transfer coefficient,  $h_b$  (see Sections 7.3 and 7.4).
- 2) Obtain the condensate flow rate per unit groove length:

$$\dot{m} = \frac{2h_b[(L + W(1 + 0.5\alpha))(T_v - T_w)]}{h_{fg}} \quad (7-61)$$

- 3) Calculate  $\bar{R}_p$ , the pressure ratio which indicates the meniscus has receded:

$$\bar{R}_p = \frac{\sin(\frac{\pi}{2} - \theta) - \sin(\frac{\pi}{2} - \theta - \gamma_o)}{\left(\frac{1 + 2\alpha_o \tan \theta}{1.3125}\right) \sin(\frac{\pi}{2} - \theta) - \sin(\frac{\pi}{2} - \theta - \gamma_o)} \quad (7-62)$$

- 4) If  $R_p < \bar{R}_p$ , the desired pressure drop can be achieved without meniscus receding. In this case, the calculation procedure is:

- Calculate the terminal meniscus angle:

$$\gamma_f = \frac{\pi}{2} - \theta - \sin^{-1}(c_{21}) \quad (7-63)$$

$$c_{21} = (1 - R_p) \sin\left(\frac{\pi}{2} - \theta - \gamma_o\right) \quad (7-64)$$

$$+ R_p \sin\left(\frac{\pi}{2} - \theta\right) \left(\frac{1 + 2\alpha_o \tan \theta}{1.3125}\right)$$

- With initial condition  $z = 0$  at  $\gamma = \gamma_o$ , solve the following differential equation to obtain the desired groove length  $z = L_c$  at  $\gamma = \gamma_f$ :

$$\frac{d(z^2)}{d\gamma} = \quad (7-65)$$

$$\left(\frac{2\sigma W^3}{\nu m}\right) \left(\frac{2AD_h^2}{K}\right)^* \left(\frac{-1}{1 + 2\alpha_o \tan \theta}\right) \cos\left(\frac{\pi}{2} - \theta - \gamma\right)$$

The dimensionless hydraulic factor  $\left[\frac{2AD_h^2}{K}\right]^*$  for trapezoidal grooves at each corresponding  $(\alpha_o, \gamma)$  is obtained from the lookup table during the course of integrating the above differential equation.

- Go to step 6 to calculate the condenser size.

- 5) If  $R_p > \bar{R}_p$ , in addition to varying  $\gamma$  from  $\gamma_o$  to 0, meniscus receding is also required to achieve the desired pressure drop. In this case, the calculation procedure is:

- Calculate the terminal aspect ratio  $\alpha_f$ :

$$\alpha_f = 2 \left( \frac{1}{c_{22}} - 1 \right) \quad (7-66)$$

$$c_{22} = \frac{R_p}{1.3125} + \left( \frac{1 - R_p}{1 + 2\alpha_o \tan \theta} \right) \left[ \frac{\sin(\frac{\pi}{2} - \theta - \gamma_o)}{\sin(\frac{\pi}{2} - \theta)} \right] \quad (7-67)$$

- Set  $\gamma_f = 0$ , then obtain the groove length  $L_{c1}$  by integrating Equation (7-66) over the meniscus angle from  $\gamma_o$  to  $\gamma_f$ , while  $\alpha_o$  remains fixed.

- With initial condition  $z = L_{c1}$  at  $\alpha = \alpha_o$  and  $\gamma = 0$ , solve the following differential equation to obtain the final groove length  $L_c$  by receding the groove aspect ratio from  $\alpha_o$  to  $\alpha_{min} = 0.625$ :

$$\frac{d(z^2)}{d\alpha} = -4 \left( \frac{\sigma W^3}{\nu \dot{m}} \right) \left( \frac{2AD_h^2}{K} \right)^* \sin \left( \frac{\pi}{2} - \theta \right) \left[ \frac{\tan \theta}{(1 + 2\alpha \tan \theta)^2} \right] \quad (7-68)$$

- 6) Calculate the condenser area and width:

$$W_c = 2 \left( \frac{Q_c}{\dot{m} h_{fg} L_c} \right) \left[ L + W \left( 1 + \frac{\alpha_o}{2} \right) \right] \quad (7-69)$$

$$A_c = L_c W_c \quad (7-70)$$

Figure 7.20 shows the dimensionless heat transfer rate per groove for a trapezoidal groove. This curve is calculated by setting the allowed pressure drop to the maximum available in the groove.

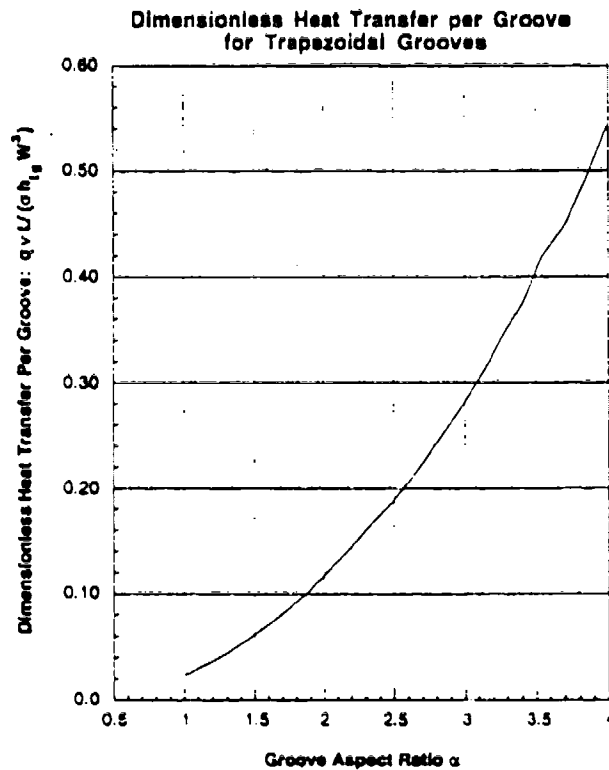


Figure 7.20. DIMENSIONLESS HEAT TRANSFER RATE PER GROOVE FOR A TRAPEZOIDAL GROOVE

## 7.7 References for Capillary Groove Condensers

Alario, J., Haslett, R., and Kosson, R.; *"The Monogroove High Performance Heat Pipe"*; AIAA Paper No. 81-1156, 1981.

Ayyaswamy, P.S., Catton, I., and Edwards, D.K.; *"Capillary Flow in Triangular Grooves"*; I. Appl. Mech., Vol. 43(2), pp. 332.

Hwangbo, H. and McEver, W.S.; *"Liquid Flow Analysis in the Evaporator Grooves of the Cold Plate"*; I. Thermo. and Heat Transfer, Vol. 2, pp. 172-179.

Kays and Landon; Compact Heat Exchangers; McGraw-Hill, NY, 1984.

Valenzuela, J.A. and Drew, B.C.; *"Internally Drained Condensers for Spacecraft Thermal Management"*; AIAA Paper No. 89-1725, June 1989.

## 8 PUMPS: Two-Phase Degradation

This section of the Design Manual discusses methods used in predicting centrifugal pump performance, including degradation resulting from two-phase operation. These methods can be used for predicting steady-state pump performance under a variety of operating conditions. Transient pump performance may also be predicted.

Much of the work concerning pump two-phase performance stems from studies conducted for the nuclear industry. A primary concern in these studies was assuring that sufficient cooling capability be provided for the reactor core, even during loss-of-coolant-accidents (LOCAs). These postulated events involve a break in the primary reactor cooling loop. This could lead to water flashing to steam and thus the possibility of two-phase conditions at the primary coolant pump. The pump itself would also affect the rate of system depressurization by retarding the blowdown flow rate.

This work may also be applied to any system in which pump behavior can affect overall system performance, including spacecraft two-phase thermal management systems. The Air Force is developing a mechanical pump for a pump-assist capillary loop for example. This could include instances in which the pump behavior would directly impact the system, for example, a loss of pump power. Changes in system operating conditions such as a change in spacecraft acceleration or the system heat load can directly impact the pump performance. The use of these methods in a transient calculation could then predict the impact of these changes on overall system performance.

Section 8.1 will present an introduction to pump performance, including an introduction to pump performance parameters and a discussion of two-phase effects.

Section 8.2 will introduce the calculation methods used to predict pump performance. The design methods rely heavily on empirical data from two-phase pump performance tests. Homologous relationships and "degradation multipliers" are used to scale the empirical data to predict two-phase performance.

The use of the dimensionless, homologous relations for predicting pump performance will be outlined step-by-step in Section 8.3. This discussion follows the same steps utilized in the accompanying computer code. This will allow the designer either to make a quick check without the need for computer modelling, or can serve as a means of verifying computational results.

Section 8.4 gives validation results, comparing transient two-phase pump data with the pump performance as calculated using these methods.

### 8.1 Introduction

During a system transient the flow through a pump may change direction. The rotating speed and torque may also reverse in some cases. Fluid entering the pump may contain vapor which decreases the head and torque. Design methods for transient operation must encompass all possible combinations of these operating conditions.

### 8.1.1 Four Quadrant Operation

The important parameters describing pump performance are:

- Rotational speed,  $N$ ,
- Volumetric flow rate,  $Q$ ,
- Head,  $H$ ,
- Hydraulic torque,  $T$ .

Typically, speed and flow rate are used to predict both head and torque. During pump operation any of the quantities may be either positive or negative. Positive values are used for normal pump operation. This implies four modes (or quadrants) of operation with speed and flow rate being both positive and negative. These four quadrants are shown quantitatively by Swift (1982) in Figure 8.1. A more qualitative representation is given by Fox (1977) and is shown in Figure 8.2. A brief discussion of each of these operating zones follows.

Quadrant 1 is referred to as the normal pumping quadrant. Both direction of rotation and flow rate are positive. Pump torque and head are typically positive (Shown as Zone P1 in Figure 8.2). Pump head and torque can also become negative (Zones D1 and T1).

Quadrant 2 is the energy dissipation quadrant. The flow rate reverses, while the direction of pump rotation remains positive. Both head and torque are positive in this quadrant (Zone D2).

Quadrant 3 is the normal turbine quadrant. In this zone both flow rate and rotation are reversed. Typically in this quadrant, both torque and head are positive (Zone T2). Torque may also be negative, shown as Zone D3.

Finally, Quadrant 4 is referred to as the reverse pump quadrant. Torque is always negative in this quadrant. Pump head may be either positive (Zone P2) or negative (Zone D4). Pump operation in the fourth quadrant is rarely seen.

### 8.1.2 Two-Phase Effects

The general effect of two-phase flow on pump performance is to produce a significant degradation in both head and torque with increasing void fraction. The fluid mechanics behind two-phase flow behavior are quite complex and not fully understood. This has led to the use of empirical data to predict two-phase behavior. Runstadler (1976) does provide a detailed discussion of many of the factors which do influence two-phase performance. In summary, some of the more important factors are:

- Phase slip; that is, differing superficial velocities between the gas and liquid phases.
- Flow regime effects, for example, the dispersed bubble regime exhibits no slip between gas and liquid phases, whereas the annular regime exhibits large differences between the phase superficial velocities.
- The low acoustic velocity in a two-phase fluid implies that shock waves and flow choking may become important factors.

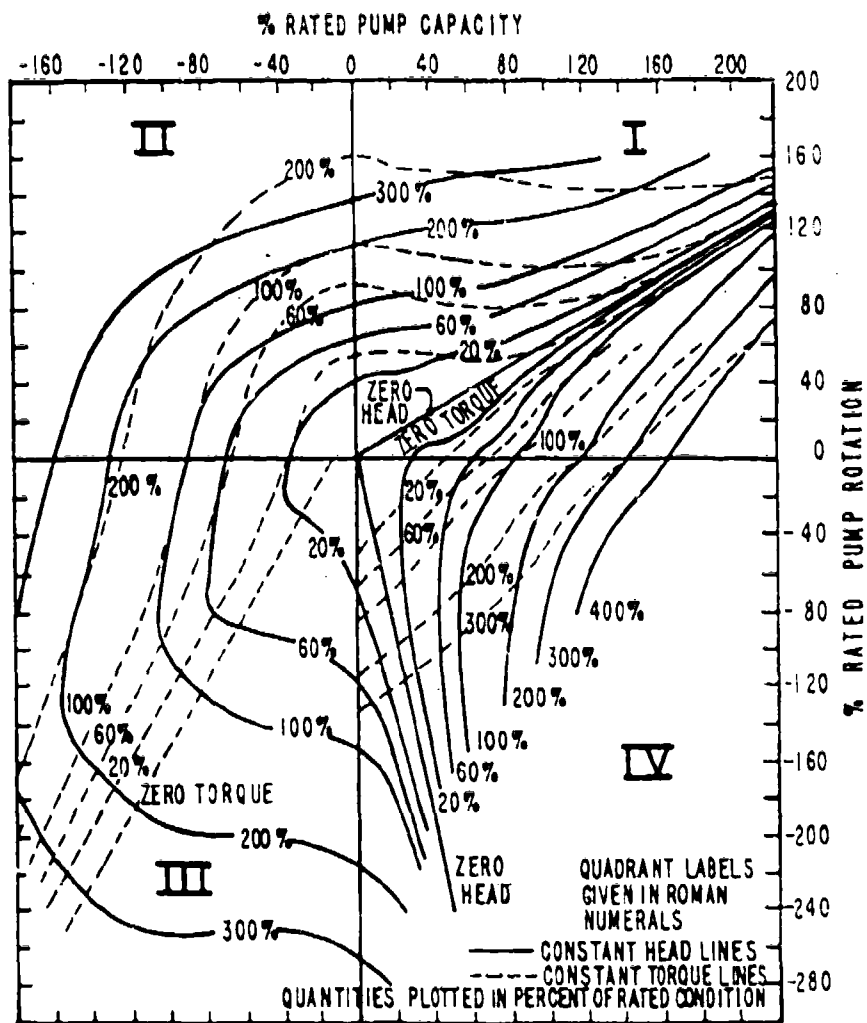
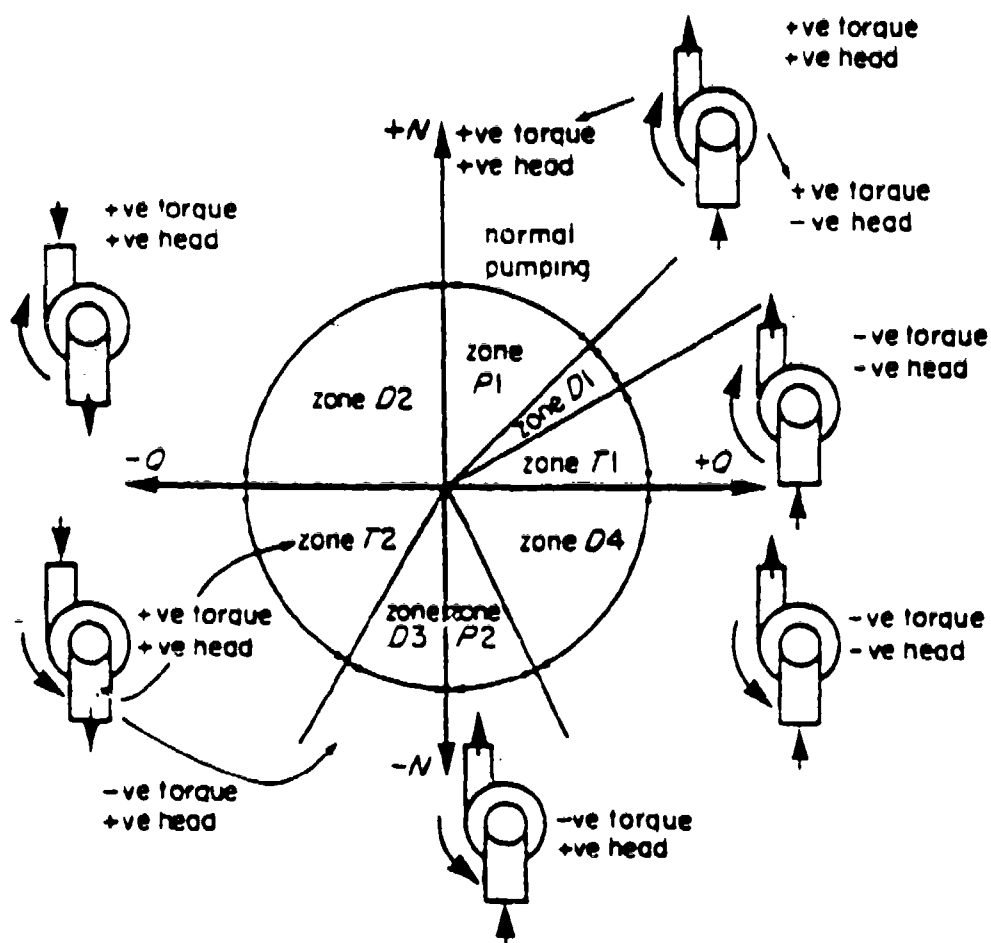


Figure 8.1. FOUR QUADRANT CHARACTERISTICS FOR TYPICAL CENTRIFUGAL PUMP



Positive torque, positive head, positive  $N$  and positive  $O$  are all as for normal pumping

Figure 8.2. OPERATING ZONES OF TYPICAL CENTRIFUGAL PUMP



- The three-dimensional pressure field within the impeller passages acting along with body forces from centrifugal and Coriolis effects produce regions of flow stall and separation, which in turn affects the flow regime at pump discharge.

Due to the complexity of the underlying physics of this problem, a mechanistic model is unavailable. The methods presented in the following section employ empirical data to predict both head and torque degradation. The flow is assumed to be homogeneous; that is, flow regime effects will not be considered. By making this assumption, void fraction alone is sufficient to describe the two-phase fluid state.

## 8.2 Design Methods for Pump Two-Phase Performance

Pump analytical models employ homologous flow relationships to predict head and torque behavior from empirical data given the pump speed and flow rate. Empirical data are required for both single-phase and fully-degraded two-phase operation. Two-phase performance predictions are based on the void fraction of the flow entering the pump, which is then used to determine both head and torque degradation factors.

### 8.2.1 Pump Scaling Relationships

The performance of geometrically similar pumps follows a well-known set of pump scaling relationships (Runstadler, 1976). The acquisition of empirical data for pump behavior has typically relied upon testing of model pumps. These scaling, or similarity, relations are then used to predict the performance of full-size pumps. Table 8.1 shows the basic scaling relationships.  $D$  can be used to represent any pump linear dimension (usually the impeller diameter), and the subscripts 1 and 2 refer to different pumps. Alternatively, the subscripts can designate the same pump at different operating points. When used to predict operating points for a single pump, the dimension,  $D$ , drops out of the equation.

Table 8.1. SCALING RELATIONSHIPS FOR CENTRIFUGAL PUMPS		
Flow Rate $Q$ :	$\frac{Q_1}{Q_2} = \frac{N_1 D_1^3}{N_2 D_2^3}$	(8-1)
Head $H$ :	$\frac{H_1}{H_2} = \frac{N_1^2 D_1^2}{N_2^2 D_2^2}$	(8-2)
Torque $T$ :	$\frac{T_1}{T_2} = \frac{N_1^2 D_1^5}{N_2^2 D_2^5}$	(8-3)
Specific Speed:	$N_s = \frac{N \sqrt{Q}}{(gH)^{3/4}}$	(8-4)

The pump specific speed has no fundamental physical significance. It does serve as a useful index of pump type. Geometrically similar pumps which obey these scaling relationships will have the same specific speed, implying that characteristic data from a given pump can be used to predict the performance of other pumps with the same specific speed.

In the recommended methods, pump performance parameters are normalized. The normalized performance parameters are:

$$\text{Pump Speed, } N: \quad \omega = N/N_r \quad (8-5)$$

$$\text{Flow Rate, } Q: \quad q = Q/Q_r \quad (8-6)$$

$$\text{Head, } H: \quad h = H/H_r \quad (8-7)$$

$$\text{Torque, } T: \quad \beta = T/T_r \quad (8-8)$$

The subscript "r" refers to rated pump conditions.

### 8.2.2 Pump Dimensionless Homologous Relations

Figure 8.1 presented curves of dimensionless pump performance. From a computational viewpoint, this is a rather unwieldy representation. To further simplify pump characteristic data, the similarity relations (Equations 8-1 through 8-4) given above can be combined to collapse the information in Figure 8.1 into four curves, one for each quadrant of pump operation. This procedure can be used in describing both pump head and torque. Figures 8.3 and 8.4 present data in terms of the following dimensionless, homologous relations:

$$h/q^2 \text{ vs. } \omega/q \quad \text{or} \quad h/\omega^2 \text{ vs. } q/\omega \text{ and,} \quad (8-9)$$

$$\beta/q^2 \text{ vs. } \omega/q \quad \text{or} \quad \beta/\omega^2 \text{ vs. } q/\omega. \quad (8-10)$$

These data curves show the measured performance of a primary coolant pump in a 50 MW LOFT pressurized water reactor test facility (Los Alamos National Laboratory, 1986).

### 8.2.3 Two-Phase Multipliers

As previously noted, the physics involved in two-phase pump operation is quite complex and not fully understood. The recommended design methods use pump characteristic data for two extreme operating conditions: fully degraded two-phase and single-phase operation. Fully degraded operation refers to poor pump performance which is observed for a wide range of void fractions between 0 and 1.0. Single-phase operation occurs when the void fraction is equal to 0.0 or 1.0. These data will be combined through the use of "degradation multipliers" to produce two-phase performance characteristics as a continuous function of void fraction. This approach works well for first quadrant pump operation. Data on two-phase pump performance outside of the normal pumping quadrant is limited, and results of this analysis outside of that quadrant should be avoided when possible.

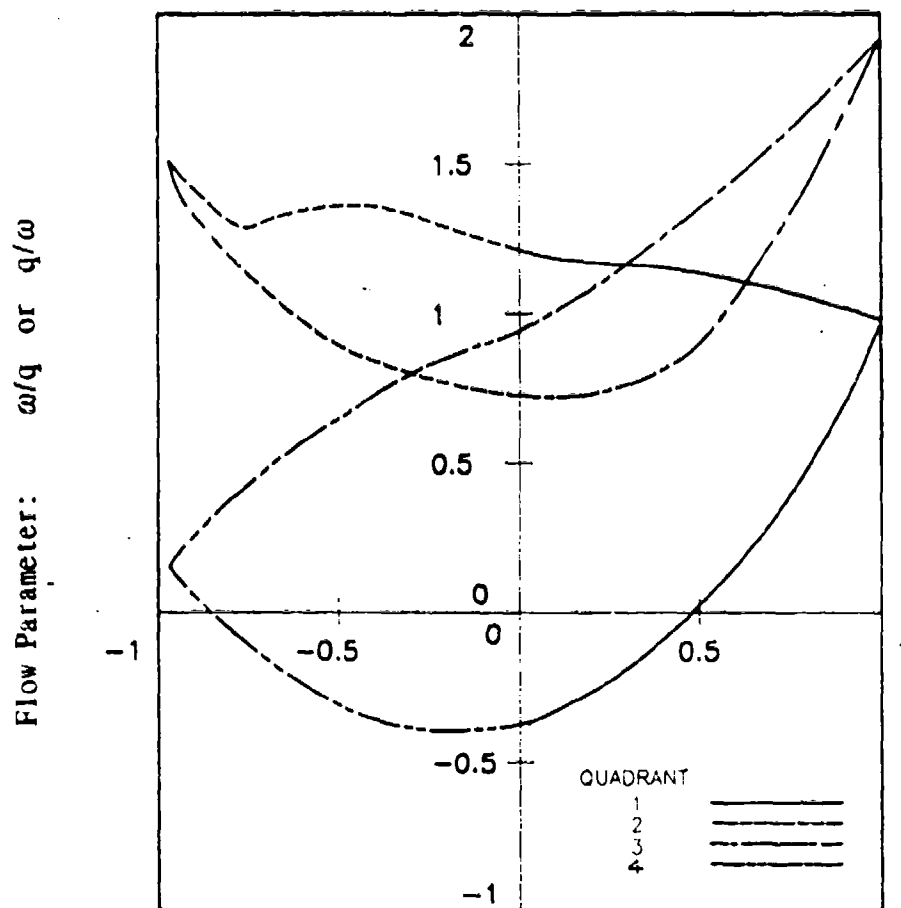


Figure 8.3. PUMP HEAD CHARACTERISTICS

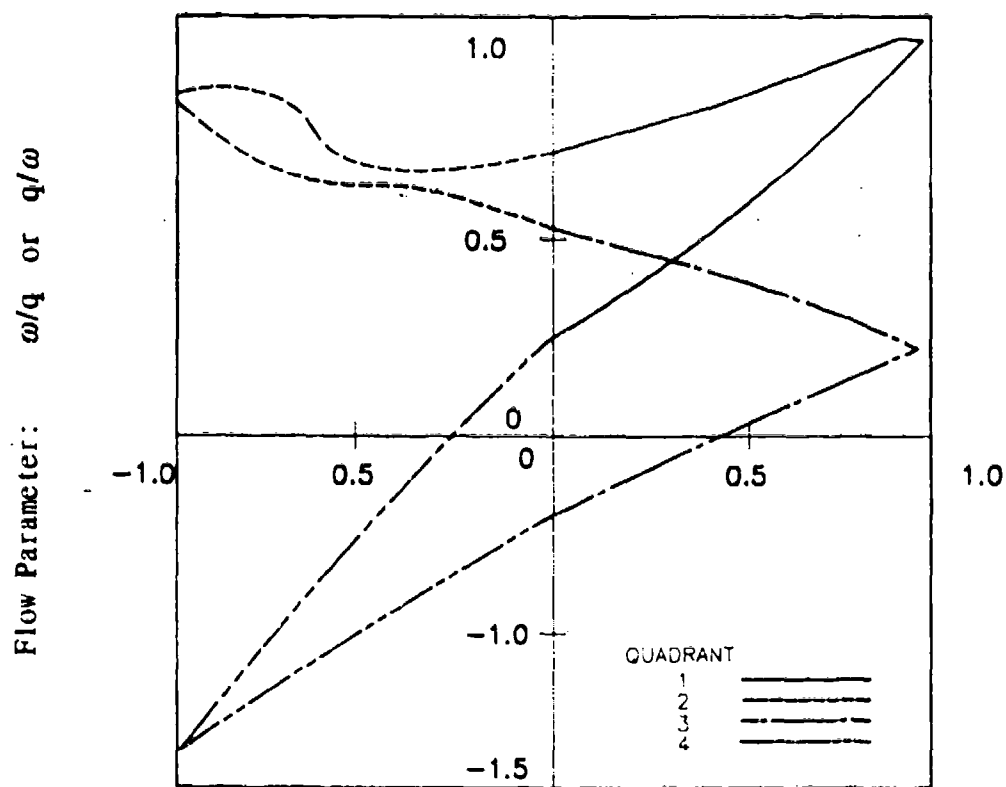


Figure 8.4. PUMP TORQUE CHARACTERISTICS

The same homologous relations described above are used for fully degraded two-phase pump operation. These curves describe the "worst case" scenario, i.e., that point at which pump head and torque have been completely degraded. For other values of void fraction, the actual pump performance falls somewhere in between the results for single-phase and fully degraded two-phase performance. This performance can be quantified through the use of degradation multipliers as follows:

$$h = h_{1\phi} - M_h (h_{1\phi} - h_{2\phi}), \text{ and} \quad (8-11)$$

$$\beta = \beta_{1\phi} - N_\beta (\beta_{1\phi} - \beta_{2\phi}). \quad (8-12)$$

The multipliers,  $M_h$  and  $N_\beta$ , are defined as functions of void fraction and are required data for this analysis. Figures 8.5 and 8.6 present degradation multiplier curves measured for the LOFT pump, whose head and torque characteristics are shown in Figures 8.3 and 8.4.

#### 8.2.4 Transient Calculations

These models may also be used to describe transient pump operation. At any instant, steady-state characteristics represent the transient behavior. That is, at any point in time, pump speed and flow rate (along with void fraction if two-phase) can be used to find the pump head and torque at that time.

Pump transients may also involve the calculation of the rate of change in pump speed. For example, the coast-down transient may be of interest on drive motor trip. As the input torque from the motor goes to zero, the pump is slowed by the action of the hydraulic torque along with friction and the bearing and windage torques. This is shown pictorially in Figure 8.7. This analysis lumps the bearing and windage torques together as  $T_b$  and considers the frictional torque as  $T_f$ . Both of these torques are proportional to the square of the pump speed. Proportionality constants,  $C_f$  and  $C_b$ , (obtained from pump manufacturers) are then used to calculate the resulting torques:

$$T_f = C_f \frac{N |N|}{N^2} \quad (8-13)$$

$$T_b = C_b \frac{N |N|}{N^2} \quad (8-14)$$

These values, along with the moment of inertia for the pump,  $I$  (also obtainable from pump manufacturers), can then be used to find the rate of change in pump speed:

$$\frac{dN}{dt} = \frac{-(T + T_f + T_b)}{I} \quad (8-15)$$

Multiplying this by the magnitude of the time step, and adding the result to the speed from the previous time step, provides the new pump speed.

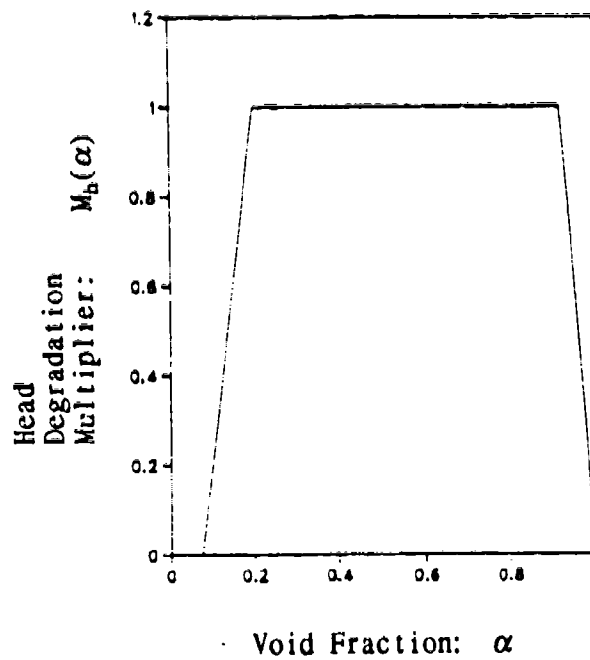


Figure 8.5. HEAD DEGRADATION MULTIPLIER CURVE

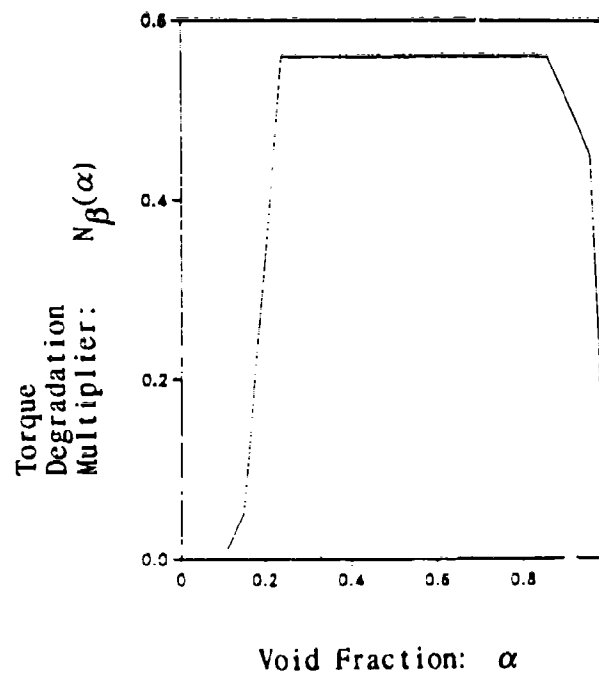
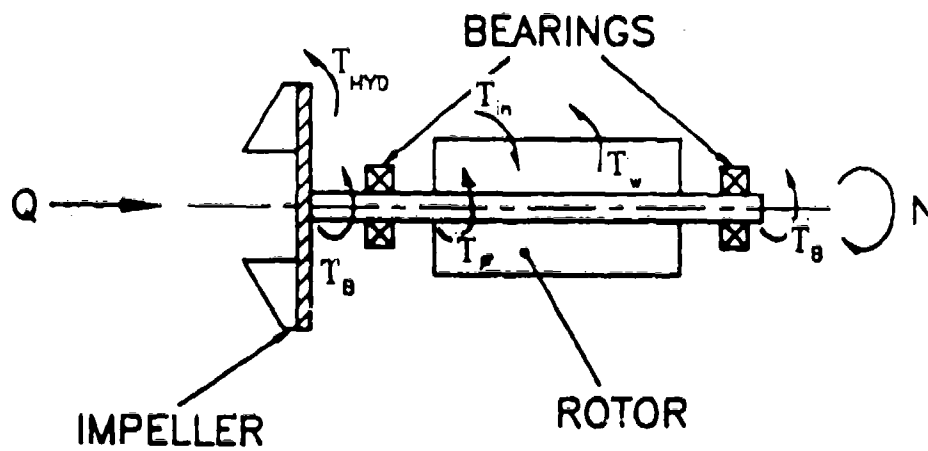


Figure 8.6. TORQUE DEGRADATION MULTIPLIER CURVE



$$\frac{dN}{dt} = \frac{\sum T_L}{\sum L}$$

Figure 8.7. ELEMENTS OF PUMP DYNAMICS

### 8.2.5 Limitations of These Methods

The primary limitation of these methods is heavy dependence on pump characteristic data. It is often difficult to find data for all four quadrants of pump operation, especially for the fourth quadrant. In order to derive two-phase performance, these data are also required for two-phase operation, but these data are also not commonly available.

This model does not include a means of calculating the motor input torque. Thus, calculation of the rate of change in pump speed is only applicable in cases where the motor is not operating. The motor torque depends on the current, voltage, rotating speed, and motor efficiency. A system model is required which provides the proper boundary conditions to the motor. Motor characteristics are required which show the mechanical power (torque vs. speed) as a function of the input power. These data are extremely application and pump specific, so the general design methods recommended in the manual do not address them.

Finally, a number of simplifying assumptions were made in the implementation of the two-phase pump models. The flow is assumed to be homogeneous, that is, the effect of various flow regimes is not included. This allows the two-phase characteristics to be specified by the input of void fraction alone. In addition, the model has been found to be most effective in the first quadrant (normal pump operation). Models have not been validated in the other quadrants, though it is common practice (e.g., in nuclear safety analysis) to use these models since they are the best available.

### 8.3 Use of Dimensionless Performance Charts

This section of the manual shows how to apply the recommended methods to determine pump performance. The characteristic data presented in this section apply to a pump with a specific speed,  $N_s = 1.22$  (3335 in  $\text{rpm-gpm}^{0.5}\text{-ft}^{-0.75}$ ). These data apply for any geometrically similar pump (that is, any pump with the same specific speed).

Obtain Inputs. The user must supply the rated conditions of operation:

- Pump speed,  $N_r$ ,
- Flow rate,  $Q_r$ ,
- Head,  $H_r$ ,
- Torque,  $T_r$ , and
- Fluid Density,  $\rho_r$

In all, 10 sets of data are required to model a single pump. Pump characteristic data are needed in the form of homologous, dimensionless curves for:

- Single and two-phase head (4 curves each), and
- Single and two-phase torque (4 curves each).

Degradation multipliers as a function of void fraction are required for:

- Pump head, and
- Pump torque.



are: In addition to the operating characteristics, other required data for the pump of interest

- Torque coefficients,  $C_f$  and  $C_b$ , and
- Pump moment of inertia,  $I$ .

Finally, to describe the operating point of interest:

- Pump speed,  $N$ ,
- Flow rate,  $Q$ , and
- Void fraction,  $\alpha$ .

are required. The void fraction is used to determine the effective density of the two-phase mixture by:

$$\rho_m = (1-\alpha)\rho_l + \alpha\rho_g \quad (8-16)$$

Normalize Inputs. The input values of speed and flow rate are next normalized as defined in Equations 8-5 and 8-6:

$$q = Q/Q_r \text{ and} \quad (8-5)$$

$$\omega = N/N_r \quad (8-6)$$

Calculate Pump Head. The single-phase pump head is first found using the homologous characteristic curves shown in Figure 8.8. The choice of curve uses the following logic:

if  $|\omega| > |q|$  and  $\omega > 0$  then use Curve 1, else  
 if  $|q| > |\omega|$  and  $q > 0$  then use Curve 2, else  
 if  $|q| > |\omega|$  and  $q < 0$  then use Curve 3, else  
 if  $|\omega| > |q|$  and  $\omega < 0$  then use Curve 4.

Figure 8.11 shows the choice of characteristic data curves on a plot of  $\omega$  vs.  $q$ . If Curves 1 or 4 are used, then the value obtained from the figure is:

$$h/\omega^2,$$

this can be multiplied by  $\omega^2$  to obtain the single- phase pump head,  $h_{1\phi}$ .

If Curves 2 or 3 are used, then the value obtained is:

$$h/q^2$$

and this is multiplied by  $q^2$  to obtain the single- phase pump head,  $h_{1\phi}$ .

This same process can be used to derive the two-phase pump head,  $h_{2\phi}$ , using Figure 8.9.

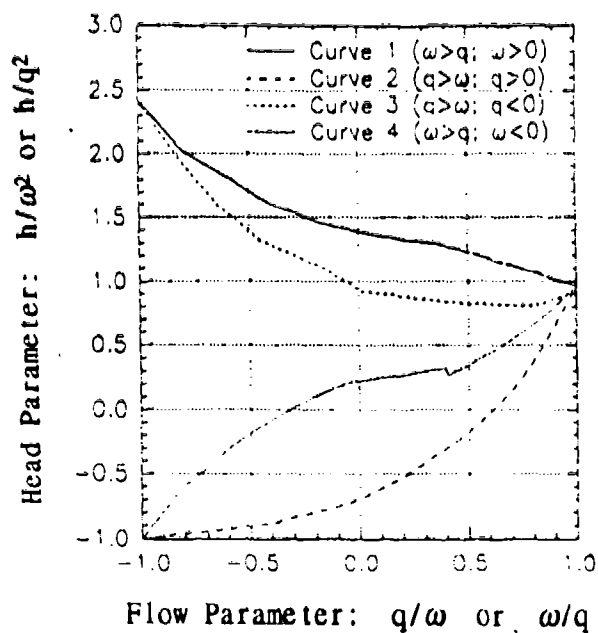


Figure 8.8. SINGLE-PHASE HEAD

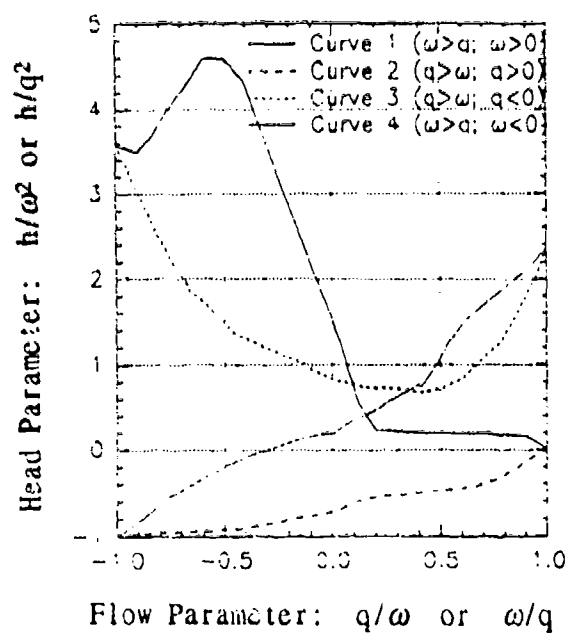


Figure 8.9. TWO-PHASE HEAD

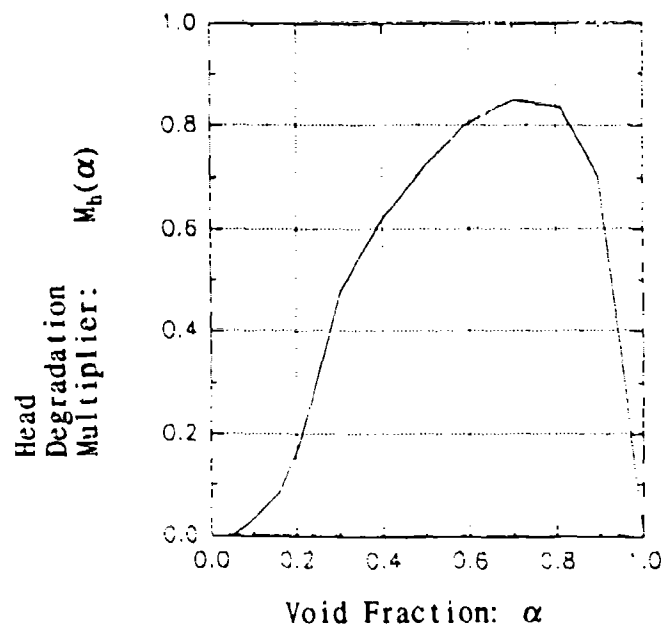


Figure 8.10. HEAD DEGRADATION MULTIPLIER

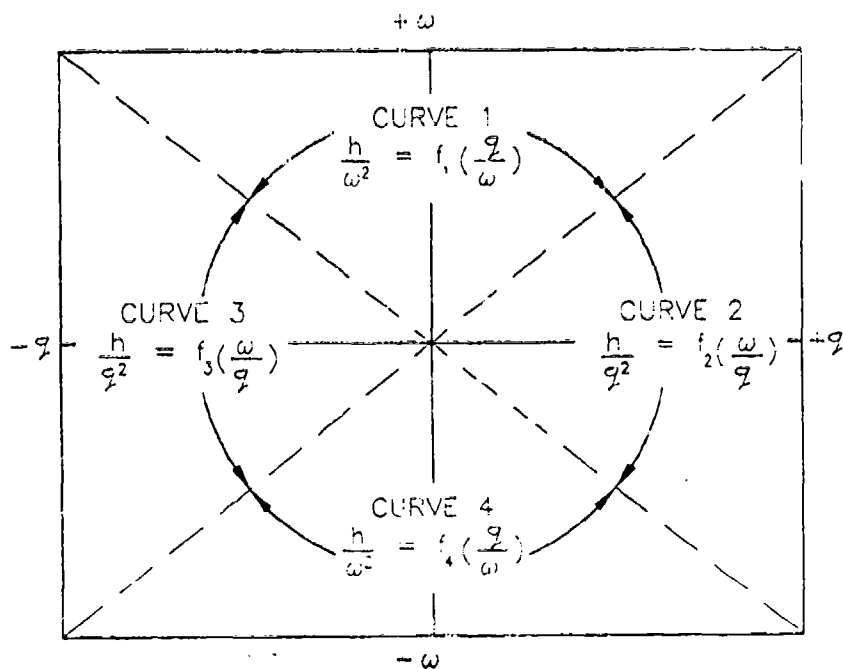


Figure 8.11. CHOICE OF HEAD CHARACTERISTIC CURVES

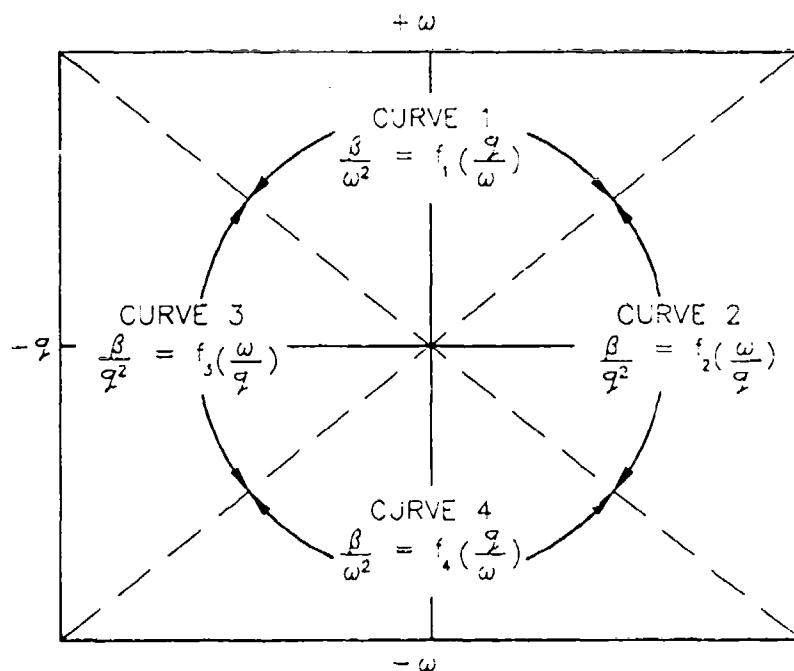


Figure 8.12. CHOICE OF TORQUE CHARACTERISTIC CURVES

Finally, the two-phase head degradation multiplier can be obtained using Figure 8.10. This value is needed to determine the effective pump head using Equation 8-11:

$$h = h_{1\phi} - M_h (h_{1\phi} - h_{2\phi}). \quad (8-11)$$

**Calculate Pump Torque.** The pump torque is also derived using the homologous, dimensionless pump characteristic curves in the same fashion as pump head. Figure 8.13 presents these data for single-phase pump torque. The data curves are selected in the same way as in the case of pump head, as illustrated in Figure 8.12. Two-phase data were unavailable for pump torque, therefore a value of zero should be assumed:

$$\beta_{2\phi} = 0.0 \quad (8-17)$$

The data for the torque two-phase degradation multiplier are given in Figure 8.14. This value can be used to obtain pump torque from Equation 8-12:

$$\beta_r = \beta_{1\phi} - N_\beta (\beta_{1\phi} - \beta_{2\phi}) = \beta_{1\phi} (1 - N_\beta) \quad (8-12)$$

where the subscript "r" indicates that this value is the actual pump torque only if the two-phase fluid has the same density as the rated pump fluid. Otherwise, the pump torque must be adjusted to account for the density difference between the pumped fluid and the rated fluid:

$$\beta = \beta_r (\rho_m / \rho_r). \quad (8-18)$$

**Re-Dimensionalize.** The values obtained for pump head and torque are next re-dimensionalized using the rated values and Equations 8-7 and 8-8:

$$T = \beta T_r \text{ and} \quad (8-7)$$

$$H = h H_r \quad (8-8)$$

**Calculate the Rate of Change in Pump Speed.** The torque coefficients,  $C_f$  and  $C_b$  are used to determine the frictional and bearing and windage torques with Equations 8-13 and 8-14:

$$T_f = C_f \frac{N |N|}{N^2} \text{ and} \quad (8-13)$$

$$T_b = C_b \frac{N |N|}{N^2} \quad (8-14)$$

Finally, the rate of change in pump speed is given by Equation 8-15:

$$\frac{dN}{dt} = \frac{-(T + T_f + T_b)}{I} \quad (8-15)$$

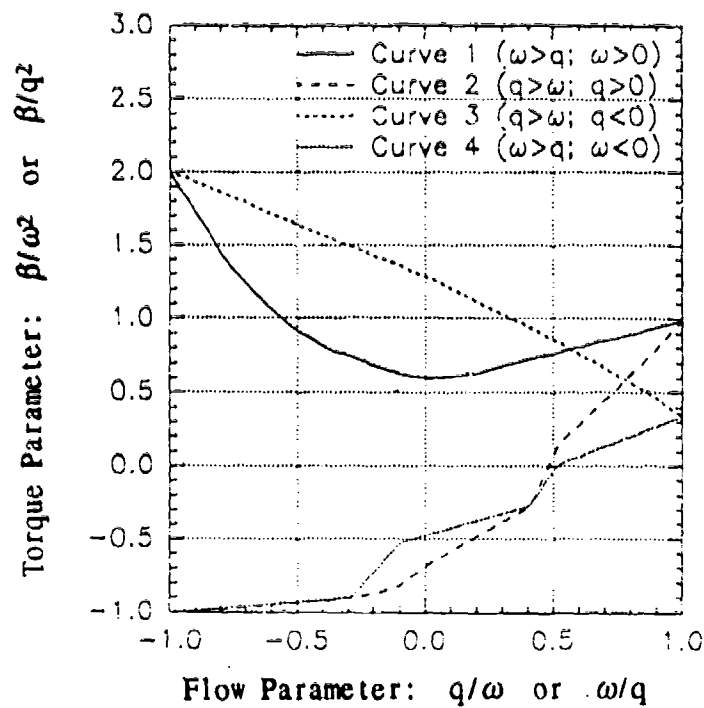


Figure 8.13. SINGLE-PHASE TORQUE

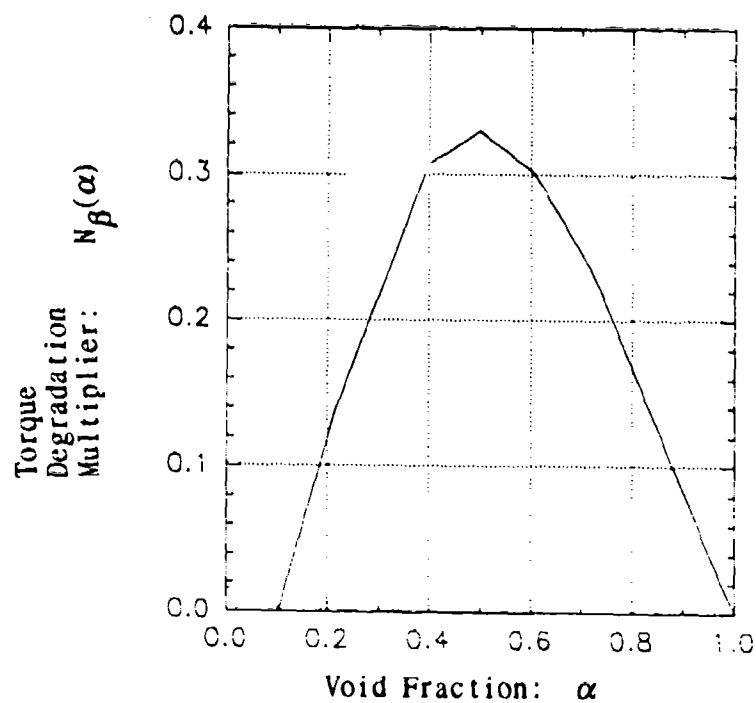


Figure 8.14. TORQUE DEGRADATION MULTIPLIER

#### 8.4 Validation of Design Methods

The design methods for pumps have been validated by comparing calculations with experimental data reported by Swift (1982). These methods successfully predict two-phase operation in the first quadrant for inlet void fractions ranging from 0 to 0.94.

The validation data used were obtained from 1/20 scale pump testing performed at Creare. The test program was intended to improve understanding of pump two-phase phenomena occurring in light water reactors during a loss-of-coolant-accident. The actual pump tested is a 1/20 scale model of a primary coolant pump found in a light water reactor. The model pump operates at the following rated conditions:

$$\begin{aligned}Q_r &= 1.38 \times 10^{-2} \text{ m}^3/\text{s} \\H_r &= 753 \text{ N-m/kg} \\N_r &= 1885 \text{ rad/sec}\end{aligned}$$

$$N_s = 1.54 \quad (4200 \text{ rpm-gpm}^{0.5}\text{-ft.}^{-0.75})$$

A schematic of the pump test facility is shown as Figure 8.15. In performing the transient tests, initial pump operating conditions were set and allowed to stabilize. The blowdown valve was then opened at the same time that the pump return line was closed. This converted the system from a closed, recirculating loop to an open loop discharging to atmosphere through the blowdown orifice. Operating conditions were not changed once the transient was initiated.

Figure 8.16 shows the results of the system transient along with the predicted pump performance. Pump inlet void fraction is shown as well. The pump characteristic data used for this comparison were also from the LOFT pump. Characteristic data for this pump were presented in the preceding sections. This pump operates at the following rated conditions:

$$\begin{aligned}Q_r &= 0.315 \text{ m}^3/\text{sec} \\H_r &= 942 \text{ N-m/kg} \\N_r &= 370 \text{ rad/sec}\end{aligned}$$

$$N_s = 1.22 \quad (3300 \text{ rpm gpm}^{0.5} \text{ ft.}^{-0.75})$$

The specific speeds,  $N_s$ , for these two pumps are somewhat different, however the data comparison against actual pump head is quite good. Unfortunately, test data were unavailable for pump hydraulic torque from these tests. This validation task underscores the difficulty in obtaining pump characteristic data. The greatest handicap in the use of these methods is obtaining pump operating data for all four quadrants for both single- and two-phase pump characteristics.

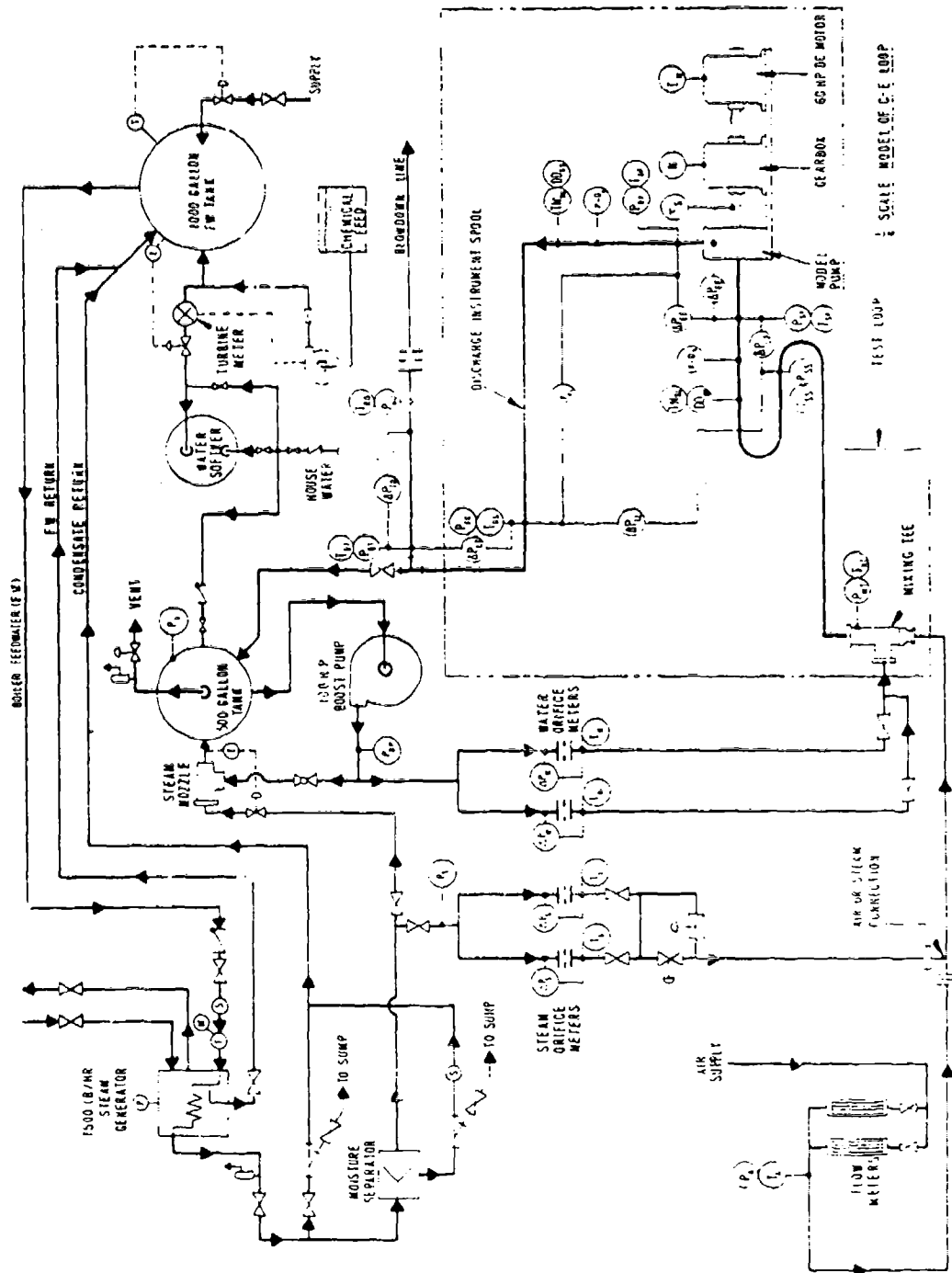


Figure 8.15. SCHEMATIC OF EPRI/CREARE TWO-PHASE PUMP TEST FACILITY

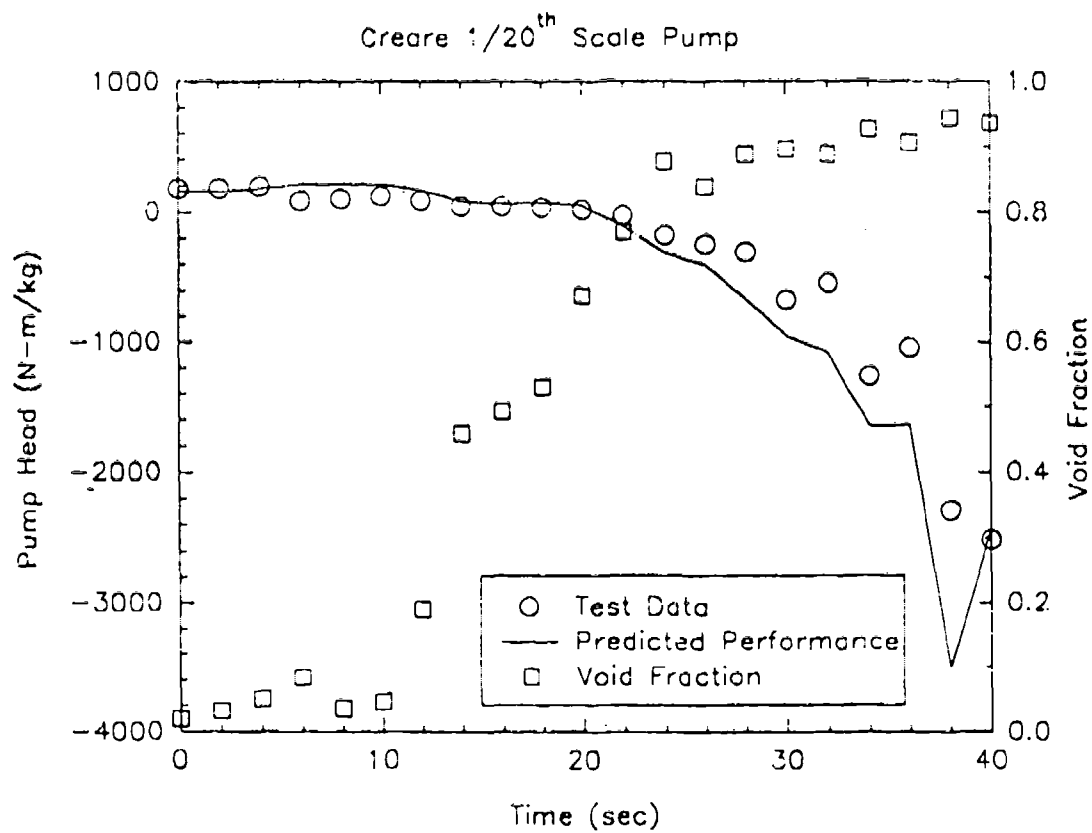


Figure 8.16. COMPARISON OF PREDICTED RESULTS WITH TEST DATA FOR PUMP HEAD



## 8.5 References for Two-Phase Degradation in Pumps

Cudlin, J.J. and Parks, C.E.; "1/3 SCALE AIR-WATER PUMP PROGRAM, ANALYTICAL PUMP PERFORMANCE MODEL"; EPRI NP-160, Prepared by Creare, Inc., Hanover, NH, Prepared for EPRI, Palo Alto, CA, October 1977.

Fox, J.A.; Hydraulic Analysis of Unsteady Flow in Pipe Networks; John Wiley & Sons, New York, NY, 1977.

Kamath, P.S. and Swift, W.L.; "TWO-PHASE PERFORMANCE OF SCALE MODELS OF A PRIMARY COOLANT PUMP"; EPRI NP-2578, Prepared by Creare, Inc., Hanover, NH, Prepared for EPRI, Palo Alto, CA, September, 1982.

Los Alamos National Laboratory; "TRAC-PF1/MOD1: AN ADVANCED BEST-ESTIMATE COMPUTER PROGRAM FOR PRESSURIZED WATER REACTOR THERMAL-HYDRAULIC ANALYSIS"; NUREG/CR-3858, U.S. Nuclear Regulatory Commission, July 1986, pp. 169-182, 311-325, 602-603.

Runstadler, P.W. Jr.; "REVIEW AND ANALYSIS OF STATE-OF-THE-ART OF MULTIPHASE PUMP TECHNOLOGY"; EPRI NP-159, Prepared by Creare, Inc., Hanover, NH, Prepared for EPRI, Palo Alto, CA, February, 1976.

Runstadler, P.W. Jr. and Dolan, F.X.; "1/20 SCALE MODEL PUMP TEST PROGRAM PRELIMINARY TEST PLAN"; EPRI NP-292, Prepared by Creare, Inc., Hanover, NH, Prepared for EPRI, Palo Alto, CA, February, 1977.

Runstadler, P.W. Jr. and Dolan, F.X.; "1/20 SCALE MODEL PUMP TEST PROGRAM FACILITY DESCRIPTION REPORT"; EPRI NP-293, Prepared by Creare, Inc., Hanover, NH, Prepared for EPRI, Palo Alto, CA, November, 1977.

Swift, W.L.; "MODEL PUMP PERFORMANCE PROGRAM - DATA REPORT"; EPRI NP-2379, Prepared by Creare, Inc., Hanover, NH. Prepared for EPRI, Palo Alto, CA, May, 1982.

Wylie, E.B. and Streeter, V.L.; Fluid Transients; McGraw-Hill, Inc., New York, NY, 1978.

## APPENDIX A FLUID PROPERTY ROUTINES

### A.1 Introduction

The various pieces of software developed under this program all share a common set of fluid property routines. These routines are based upon work performed by the Design Institute for Physical Property Data (DIPPR). (See Daubert & Danner, 1984; NIST, 1990.) This data compilation includes constant properties for a fluid (molecular weight, gas constant, critical temperature and pressure) as well as coefficients for determining temperature dependent thermodynamic and transport properties. These coefficients are used in a set of standard equations to calculate the required properties.

### A.2 Use of the DIPPR Routines

Prior to accessing any of the fluid property functions, the coefficients for the fluid of interest must first be read into the program and placed in COMMON blocks for passing to the actual property functions. This is done by calling the subroutine READPR. This subroutine takes an integer argument specifying the fluid to be used. Table A.1 outlines the available fluids, their corresponding data file name and the integer value to be passed to READPR.

The data files listed in Table A.1 contain some constant fluid properties as well as the coefficients used in determining the temperature dependent properties. Table A.2 shows the format of a fluid data file. Note that the annotations are not part of the file. The actual file consists solely of the numbers shown.

This approach allows for easy expandability of the fluid properties package. Adding a new fluid requires only the creation of an additional data file and a minor change in the subroutine READPR to attach an integer value to the appropriate data file name.

The file PROPS.FOR contains the functions which evaluate the fluid properties, as well as the subroutine which returns the constant properties. The subroutine is accessed as follows:

Table A.1. AVAILABLE FLUIDS		
Integer	Fluid	Data File
1	Water	WATER.DAT
2	Freon R-11	R11.DAT
3	Freon R-12	R12.DAT
4	Ammonia R-717	NH3.DAT
5	Air	AIR.DAT
6	Freon R-114	R114.DAT
7	Ethanol	ETHANOL.DAT
8	Toluene	TOLUENE.DAT

Table A.2. FLUID PROPERTY DATA FILE FOR AMMONIA (NH3.DAT)							
17.031,	488.1862,	405.65,	1.1277E+07				MW, R <sub>gas</sub> , T <sub>crit</sub> , P <sub>crit</sub>
3.5430E+00,	2.5471E-01,	4.0565E+02,	2.8870E-01,		195.41,	405.65	Liquid Density
9.0451E+01,	-4.6690E+03,	-1.1601E+01,	1.7183E-02,	1.0000E+00,	195.41,	405.65	Sat. Press.
3.0094E+06,	-4.3692E+04,	2.4114E+02,	-5.8560E-01,	5.2953E-04,	195.41,	385.15	Liquid Cp
3.3480E+04,	4.8200E+04,	9.5189E+02,	-3.0100E+04,	1.0560E+03,	100.00,	1500.00	Vapor Cp
-6.7430E+00,	5.9830E+02,	-7.3410E-01,	-3.6900E-27,	1.0000E+01,	195.41,	393.15	Liq. Visc.
4.1855E-08,	9.8060E-01,	3.0800E+01,	0.0000E+00,		195.41,	1000.00	Gas Visc.
9.1200E-02,	1.1028E+00,	0.0000E+00,	0.0000E+00,	0.0000E+00,	195.41,	405.65	Surf. Tens.
1.5600E-02,	-1.9900E+01,	-5.0500E+06,	-2.5330E+18,	3.8700E+20,	200.00,	700.00	Gas Dens.
1.1606E+00,	-2.2840E-03,	0.0000E+00,	0.0000E+00,	0.0000E+00,	220.05,	400.05	Liq Cond.
3.1523E+07,	3.9140E-01,	-2.2890E-01,	2.3090E-01,	0.0000E+00,	195.41,	405.65	Latent Heat
A	B	C	D	E	T <sub>min</sub>	T <sub>max</sub>	Property
Coefficients (A-E)					Valid Temperature Range		

CALJ, GETVAL (MW, RG, TCRIT, PCRT)

where:

MW            Molecular Weight (kg/kg-mole)  
 RG            Gas Constant (J/kg-K)  
 TCRIT        Critical Temperature (K)  
 PCRT        Critical Pressure (Pa)

### A.3 Error Trapping and Handling

All of the functions and subroutines found within the property routines contain some checking for errors. In general this assures that the inputs received by the function are valid. There are a number of error conditions which all or many of the functions check. These conditions will first be outlined. This is followed by a discussion of each function and any error conditions which apply to it.

#### A.3.1 General Error Messages

Each of the functions in the file PROPS.FOR first checks to see if the input value of temperature is within the range of the fit for the given property and fluid. A list of these temperature limitations is given in Table A.3. If the input temperature is outside of those limits the error message:

\*\*\* Temperature out of range in FUNCTION, T = <value>

where FUNCTION is the name of the individual function (e.g., DENSEF, VISCGR...) and value is the value of temperature input. If this occurs, the evaluation of the property function is allowed to proceed; however, the user should be aware that the actual value calculated may be inaccurate in that case.

Table A.3. VALID TEMPERATURE RANGES OF FLUID PROPERTY CORRELATIONS									
Property	Temperature (K)	Fluid							
		Water	R-11	R-12	Ammonia	Air	R-114	Ethanol	Toluene
$\rho_l$	$T_{min}$	273.16	162.04	115.15	195.41	59.15	179.15	159.05	178.18
	$T_{max}$	506.00	471.20	384.95	405.65	132.45	418.85	516.25	591.79
$\rho_g$	$T_{min}$	323.64	235.60	245.00	200.00	118.15	209.40	258.13	295.90
	$T_{max}$	3236.4	2356.0	480.00	700.00	248.15	2094.0	2581.3	2959.0
$c_{pl}$	$T_{min}$	273.15	162.04	160.00	195.41	75.00	180.00	158.50	178.18
	$T_{max}$	560.00	365.00	370.00	385.15	115.00	410.00	399.82	420.00
$c_{pg}$	$T_{min}$	100.00	88.71	99.82	100.00	100.00	273.15	100.00	200.00
	$T_{max}$	1500.0	1500.0	1500.0	1500.0	3000.0	1500.0	873.15	1500.0
$h_{fg}$	$T_{min}$	273.16	162.04	115.15	195.41	59.15	179.15	159.05	178.18
	$T_{max}$	647.13	471.20	384.95	405.65	132.45	418.85	516.25	591.79
$\sigma$	$T_{min}$	273.16	162.04	115.15	195.41	---	179.15	273.15	178.18
	$T_{max}$	647.13	471.20	384.95	405.65	---	418.85	513.15	591.79
$\mu_g$	$T_{min}$	373.15	248.15	250.00	195.41	80.00	230.00	200.00	273.15
	$T_{max}$	1073.1	996.97	575.00	1000.0	2000.0	500.00	1000.0	873.15
$\mu_l$	$T_{min}$	273.15	170.00	170.00	195.41	60.00	179.15	240.00	200.00
	$T_{max}$	643.15	470.00	380.00	393.15	130.00	400.00	513.15	453.15
$k_l$	$T_{min}$	273.15	170.00	150.00	220.05	60.00	179.15	213.15	178.18
	$T_{max}$	633.15	471.20	363.15	400.05	130.00	410.00	350.00	513.15
$P_{sat}$	$T_{min}$	273.16	162.04	115.15	195.41	78.80	179.15	159.05	178.18
	$T_{max}$	647.13	471.20	384.95	405.65	132.45	418.85	516.25	591.79

All of the functions which calculate liquid properties (DENSEF, SPHTF, SURTEN, VISCF and TCONDf) include a check to insure that the input temperature is less than or equal to the critical temperature of the fluid. If the temperature is above that limit at which liquid can not exist, the message:

\*\*\* Liquid phase does not exist at this temperature \*\*\*  
 T = <value>, T critical = <value>

is printed. The function is assigned a value of -1, and control is returned to the calling routine. The routine which called the function can then check for this condition.

### A.3.2 List of Routines and Specific Errors

The subroutine READPR (IFLUJD) reads in the coefficients for each fluid. It includes a check for existing fluid codes. If the input integer is not valid, it is assigned a value of -1 and control is returned to the calling routine. Currently, valid fluid codes are the integers 1-8 inclusive.

Liquid Density. The function DENSF (T) evaluates the liquid density using an equation of the form:

$$\text{DENSF} = [A/B^{**}(1.+(1.-T/C)^{**D})] \times \text{MW} \quad (\text{A-1})$$

Temperature is input in degrees Kelvin, and the density is returned in kg/m<sup>3</sup>. In addition to checking for temperature within the range of the fit, DENSF checks to see that the input temperature is less than the critical temperature.

Gas Density. The function DENSG (T,P) calculates the gas density using the second virial coefficient in the equation of state. This is expressed as the quadratic

$$\text{DENSG} = (-1. + \text{SQRT}(1. + 4. * \text{VIR2} * P / (\text{RG} * T))) / (2. * \text{VIR2}) \quad (\text{A-2})$$

The second virial coefficient, VIR2, has been fit using the equation:

$$\text{VIR2} = A + B/T + C/T^{**3} + D/T^{**8} + E/T^{**9} \quad (\text{A-3})$$

This function takes both pressure (Pa) and temperature (K) as arguments and returns the gas density in kg/m<sup>3</sup>. A number of error conditions are considered in this function. First, if the temperature is less than the critical temperature a check is made to ascertain that the gas phase does exist. If the input pressure is greater than the saturation pressure then the message:

\*\*\* Gas phase does not exist at this pressure \*\*\*  
P = <value>, Psat = <value>

is printed and the function is assigned a value of -1. The function next checks to see if the ideal gas law will be used or if the second virial coefficient is to be included in the equation of state. The ideal gas law is used if the value of the discriminant in the above quadratic is less than zero or if the input temperature is outside of the range of the fit for the virial coefficient. Typically, this will produce the message:

\*\*\* Ideal gas law used for gas density \*\*\*

However, in the special case where the temperature is close to the critical temperature ( $0.9 < T/T_{\text{crit}} < 1.05$ ) the message:

\*\*\* WARNING: Ideal gas law being used \*\*\*  
\*\*\* Inaccurate for T close to T critical \*\*\*  
T = <value>, T critical = <value>

is displayed. For most temperatures outside of this range, the ideal gas law should provide an accurate value for the gas density.

Liquid Specific Heat. The liquid specific heat in the function SPHTF (T) is given by the equation:

$$\text{SPHTF} = [A + B * T + C * T^{**2} + D * T^{**3} + E * T^{**4}] / \text{MW} \quad (\text{A-4})$$

Temperature is input in degrees Kelvin, and the specific heat is returned in J/kg-K. This function checks for temperature within bounds and less than the critical temperature of the fluid.

Gas Specific Heat. The gas specific heat in the function SPHTG (T) is calculated as:

$$\text{SPHTG} = [A + B*((C/T)/\text{SINH}(C/T))^{**2} + D*((E/T)/\text{COSH}(E/T))^{**2}] / \text{MW} \quad (\text{A-5})$$

Again, temperature is input in degrees Kelvin, and specific heat has units of J/kg-K. This function checks only for temperature within the range of the fit.

Latent Heat of Vaporization. The latent heat of vaporization in the function ENTHFG (T) is calculated using the equation:

$$\text{ENTHFG} = [A*(1.-\text{TR})^{**}(B+C*\text{TR}+D*\text{TR}^{**2}+E*\text{TR}^{**3})] / \text{MW} \quad (\text{A-6})$$

The reduced temperature, TR, is equivalent to the input temperature (K) divided by the critical temperature. The result has units of J/kg. In addition to checking for temperature within the bounds of the fit, this function checks to see if the temperature is greater than the critical temperature. The message:

\*\*\* Liquid-vapor transition not possible at this temp \*\*\*  
T = <value>, T critical = <value>

is printed if that is the case. The function is assigned a value of -1.

Surface Tension. Surface tension at the liquid/vapor interface is expressed by the function SURTEN (T) as:

$$\text{SURTEN} = A*(1.-\text{TR})^{**}(B+C*\text{TR}+D*\text{TR}^{**2}+E*\text{TR}^{**3}) \quad (\text{A-7})$$

The reduced temperature, TR, is equal to  $T/T_{\text{crit}}$ . Temperature is input in degrees Kelvin, and surface tension is returned with units of N/m. This function checks for temperature both within the range of the fit and less than the critical temperature. In addition, SURTEN checks for the fluid code for air. A fit does not exist for this fluid due to a lack of data. The message:

\*\*\* Surface tension unavailable for air \*\*\*

is printed and a value of -1 is returned to the calling routine if surface tension is requested for air.

Gas Viscosity. The gas viscosity is calculated in the function VISCg (T) using the equation:

$$\text{VISCg} = A*T^{**B}/(1.+C/T+D/T^{**2}) \quad (\text{A-8})$$

Viscosity is given in kg/m-s with temperature specified in degrees Kelvin. This function checks for temperature within the range of the fit.

Liquid Viscosity. Liquid viscosity is specified VISCf (T) as:

$$\text{VISCf} = \text{EXP}(A + B/T + C*\text{ALOG}(T) + D*T^{**E}) \quad (\text{A-9})$$

Given temperature in degrees Kelvin, viscosity is returned with units of kg/m-s. VISCFC checks to see that the input temperature is both within the range of the fit and less than the critical temperature.

Liquid Thermal Conductivity. The liquid thermal conductivity is found by the function TCONDf (T) using the equation:

$$TCONDf = A + B*T + C*T**2 + D*T**3 + E*T**4 \quad (A-10)$$

It is given in W/m-K, and temperature is input in degrees Kelvin. This function traps for temperature outside the range of the fit or greater than the critical temperature.

Saturation Pressure. The saturation pressure of the fluid is given in the function PSCALC (T) by the equation:

$$PSCALC = EXP(A+B/T+C*ALOG(T)+D*T**E) \quad (A-11)$$

Temperature is input in degrees Kelvin, and pressure is returned in Pascals. PSCALC looks to see that the input temperature is within the range of the fit and less than the critical temperature. If the temperature is greater than the critical temperature, the message:

\*\*\* Liquid-vapor transition not possible at this temp \*\*\*  
T = <value>, T critical = <value>

is printed and a value of -1.0 is returned to the calling routine.

Saturation Temperature. The saturation temperature at a given pressure is found in the function TSCALC (P) by solving the equation shown above in PSCALC for temperature. An implementation of Newton's method of root finding is used by this routine. This routine checks for temperature within the range of the fit. It also checks for pressure greater than the critical pressure. If that is the case, the message:

\*\*\* Liquid-vapor transition not possible at this pressure \*\*\*  
P = <value>, P critical = <value>

is printed, and the function is assigned a value of -1. Pressure is input to the function in Pascals, and temperature returned in degrees Kelvin.

#### A.4 Validation of Curve Fit Coefficients

The validity of these property routines has been confirmed by comparing the results with various published sources. (ASME, 1967; ASHRAE, 1986, 1989, Jasper, 1972; Mattheson Gas Products, 1971; Reid & Smith, 1951; Starling, 1973; Vargaftik, 1975) The results of these comparisons are shown as Figures A.1 through A.10. Data from the DIPPR routines are shown as solid lines. In some cases, the fit has either been altered or extended for greater range. If this is the case, the new fit has been shown as a dashed line. Data from the various sources are shown as symbols on the plots. A discussion of the results for each fluid property follows.

**Liquid Density.** With the exception of water, all of the fits (Figure A.1) show good agreement with published data. The fit for water has been extended to a higher temperature, with some small sacrifice in accuracy at the low end of the temperature range. The fit was extended to a temperature of 506 K, an increase from the previous value of 333.15 K.

**Gas Density.** The plot shown for gas density (Figure A.2) gives the density values for saturation conditions. Many of these plots show a problem as the temperature approaches the critical value. The point of discontinuity on these plots occurs where the routine switches over to using the ideal gas law when the value of the discriminant in the quadratic equation used becomes less than zero. As noted previously, the gas density function, DENS<sub>G</sub>, identifies this condition and warns the user of the potential inaccuracies.

**Liquid Specific Heat.** Two of the fluorocarbon refrigerants, R-12 and R-114 have been refit for this property (Figure A.3). R-12 was refit in order to increase the valid temperature range. The reported values for R-114 did not agree well with published sources, thus a new fit was performed to better match the available data.

**Gas Specific Heat.** In general, these fits (Figure A.4) showed good agreement with data. The curve fit for ethanol was slightly modified in order to better match the data at high temperatures. Its range was also slightly reduced, but is still within the range of most potential uses ( $T < 873.15$  K).

**Heat of Vaporization.** With the exception of air, all fluids showed good agreement between the DIPPR results and published sources (Figure A.5). Air was refit in order to better match the data at low temperatures. The range of the fit was not changed.

**Surface Tension.** For many of the fluids, limited surface tension data were available (Figure A.6). This fit does not apply to air due to the lack of any data. Ethanol was the only fluid which was refit; its range was extended upward to higher temperatures. The remaining fluids matched data available.

**Gas Viscosity.** These results showed good agreement with the data (Figure A.7). The fit for toluene was extended upward to higher temperatures.

**Liquid Viscosity.** These results (Figure A.8) also showed good agreement with the data. For this property, the fits for both ethanol and toluene were redone in order to include higher temperatures.

**Liquid Thermal Conductivity.** For this property, only the fits for water and ammonia remain unchanged (Figure A.9). The curve fit coefficients were recalculated for R-11, R-12, R-114 and ethanol in order both to better match the available data and to extend the range of applicability. The coefficients for air and toluene were altered in order to extend the range of temperatures.

**Vapor Pressure.** The check of this function (Figure A.10) also serves to confirm the validity of the routine for calculating the saturation temperature, as both the coefficients and equations are shared by the two functions. The DIPPR routines showed good agreement with data for all of the fluids considered here.



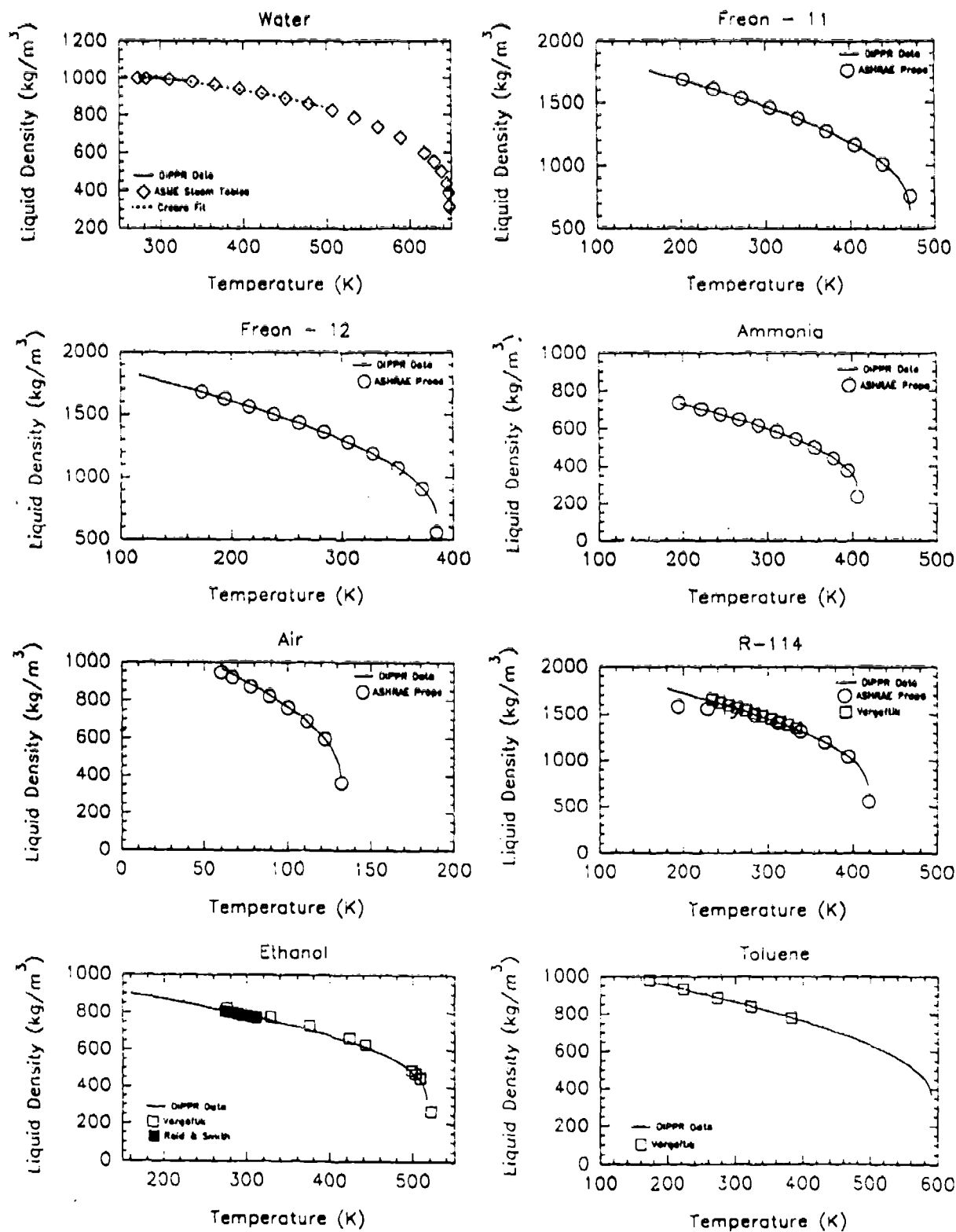


Figure A.1. LIQUID DENSITY

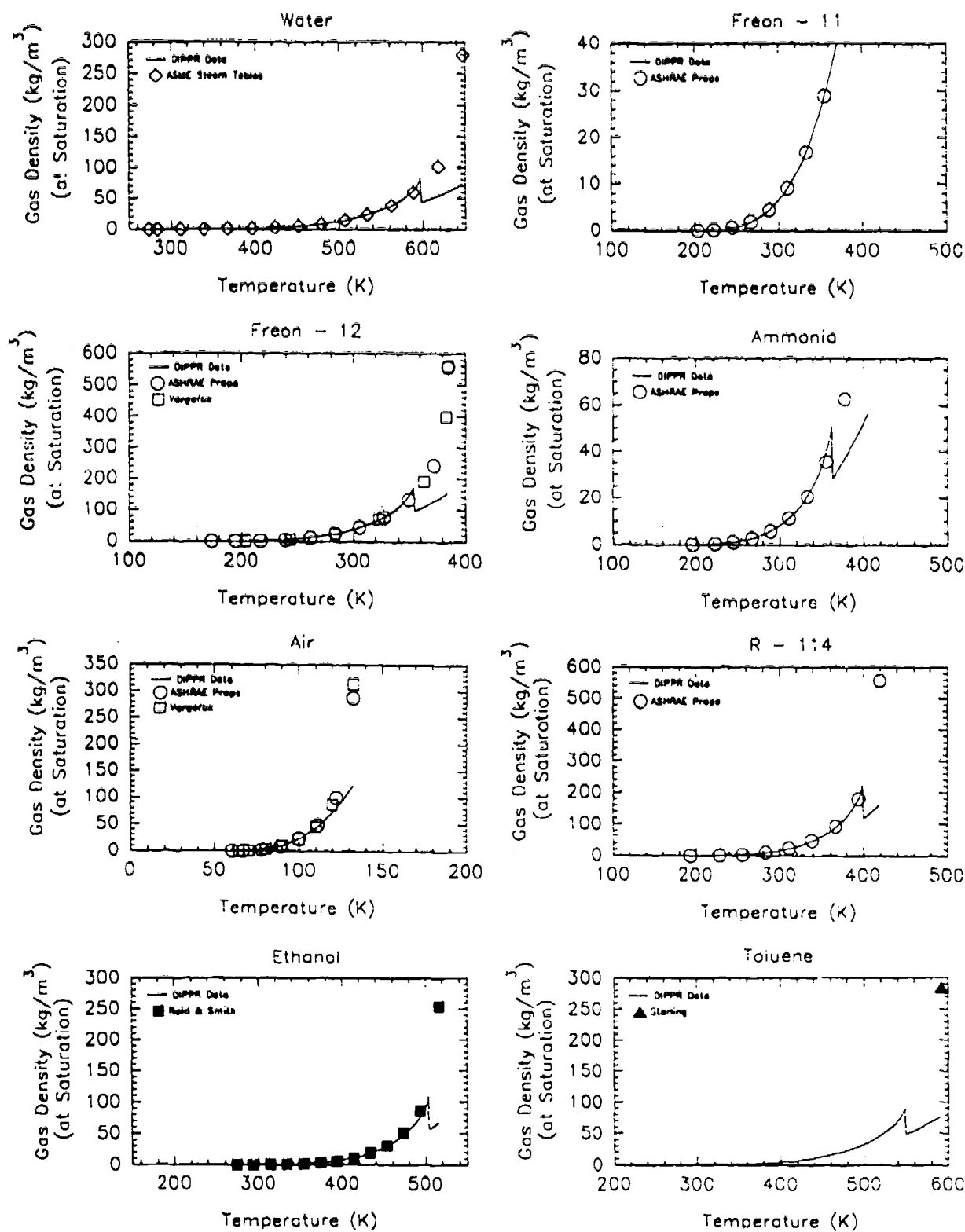


Figure A.2. GAS DENSITY

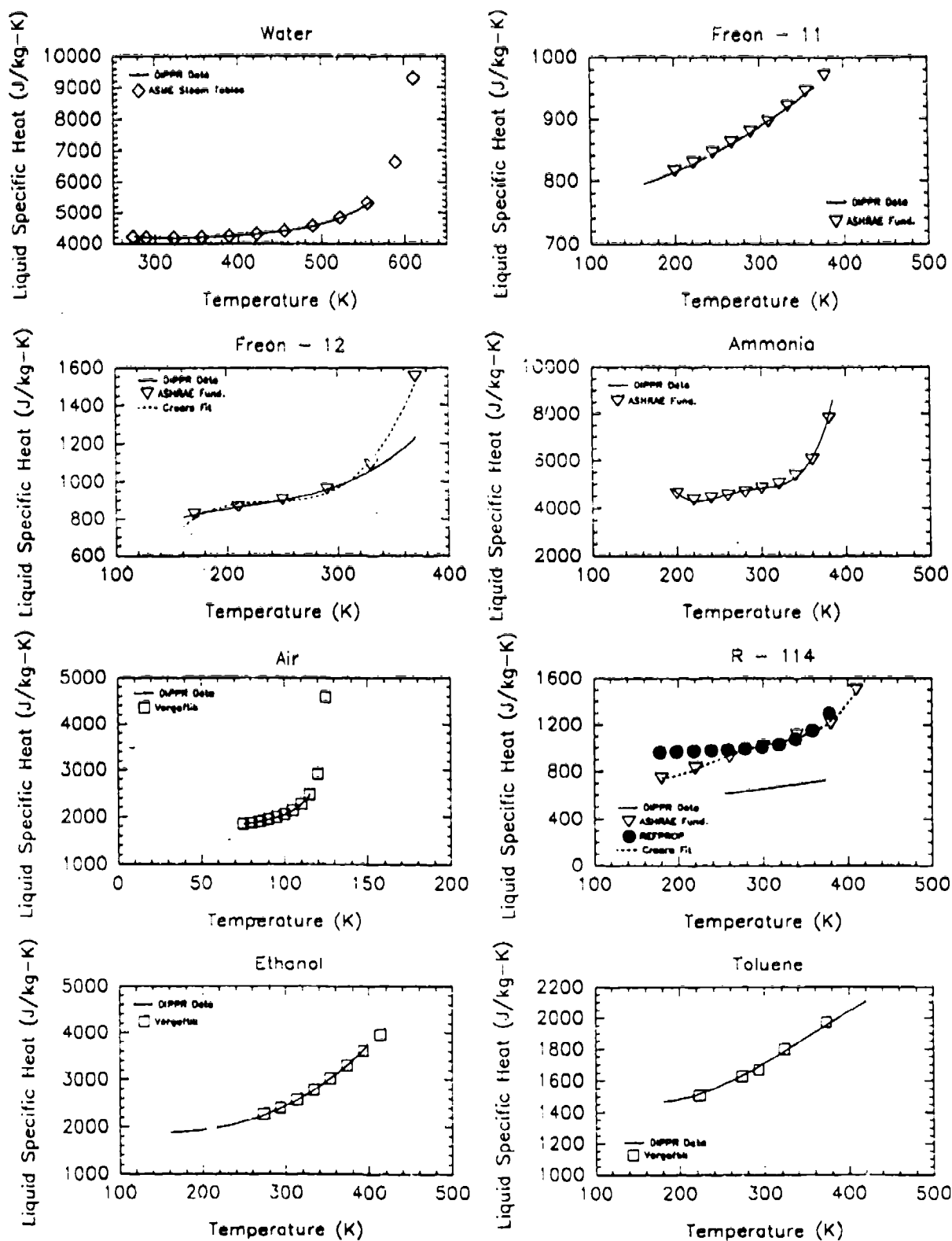


Figure A.3. LIQUID SPECIFIC HEAT

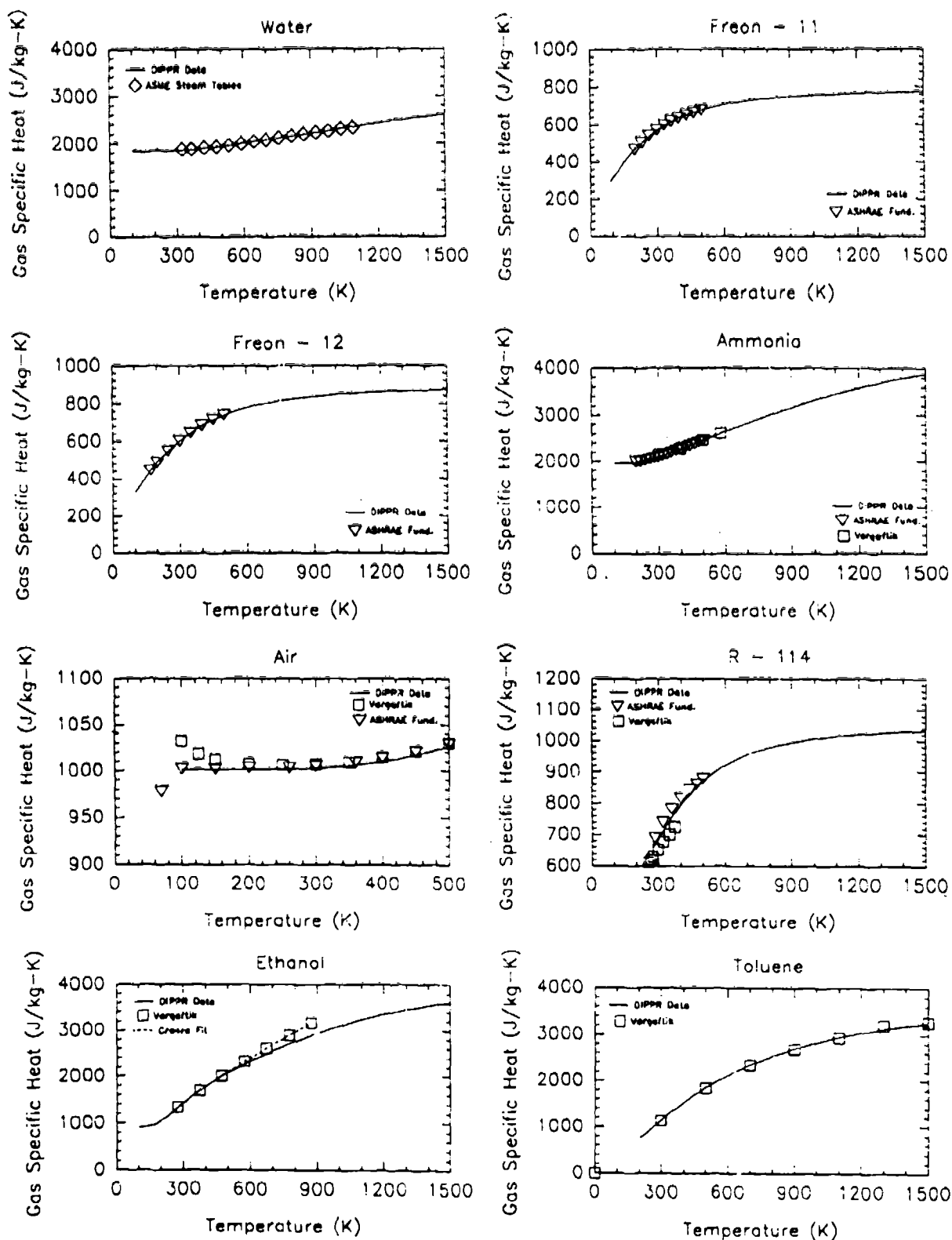


Figure A.4. GAS SPECIFIC HEAT

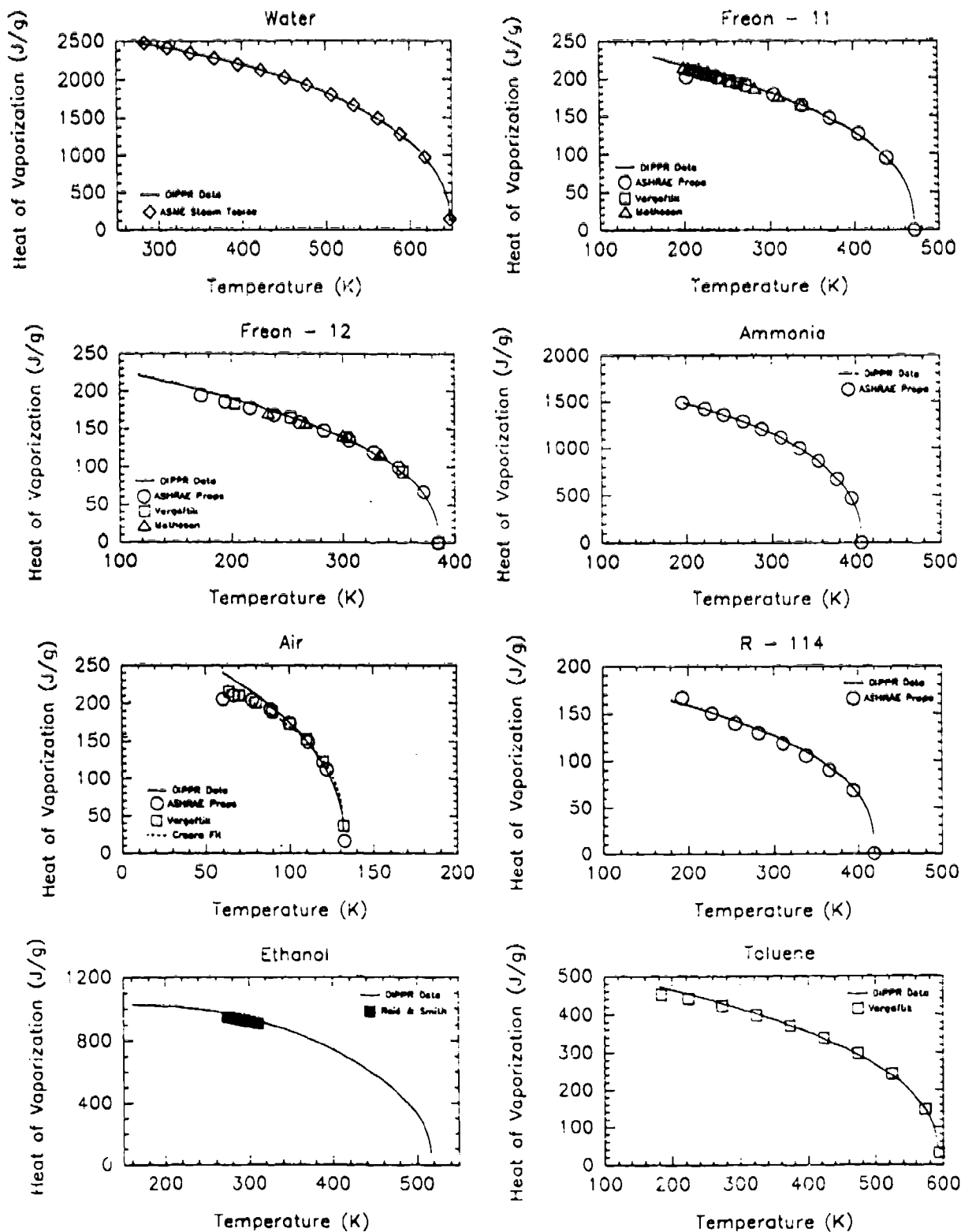


Figure A.5. HEAT OF VAPORIZATION

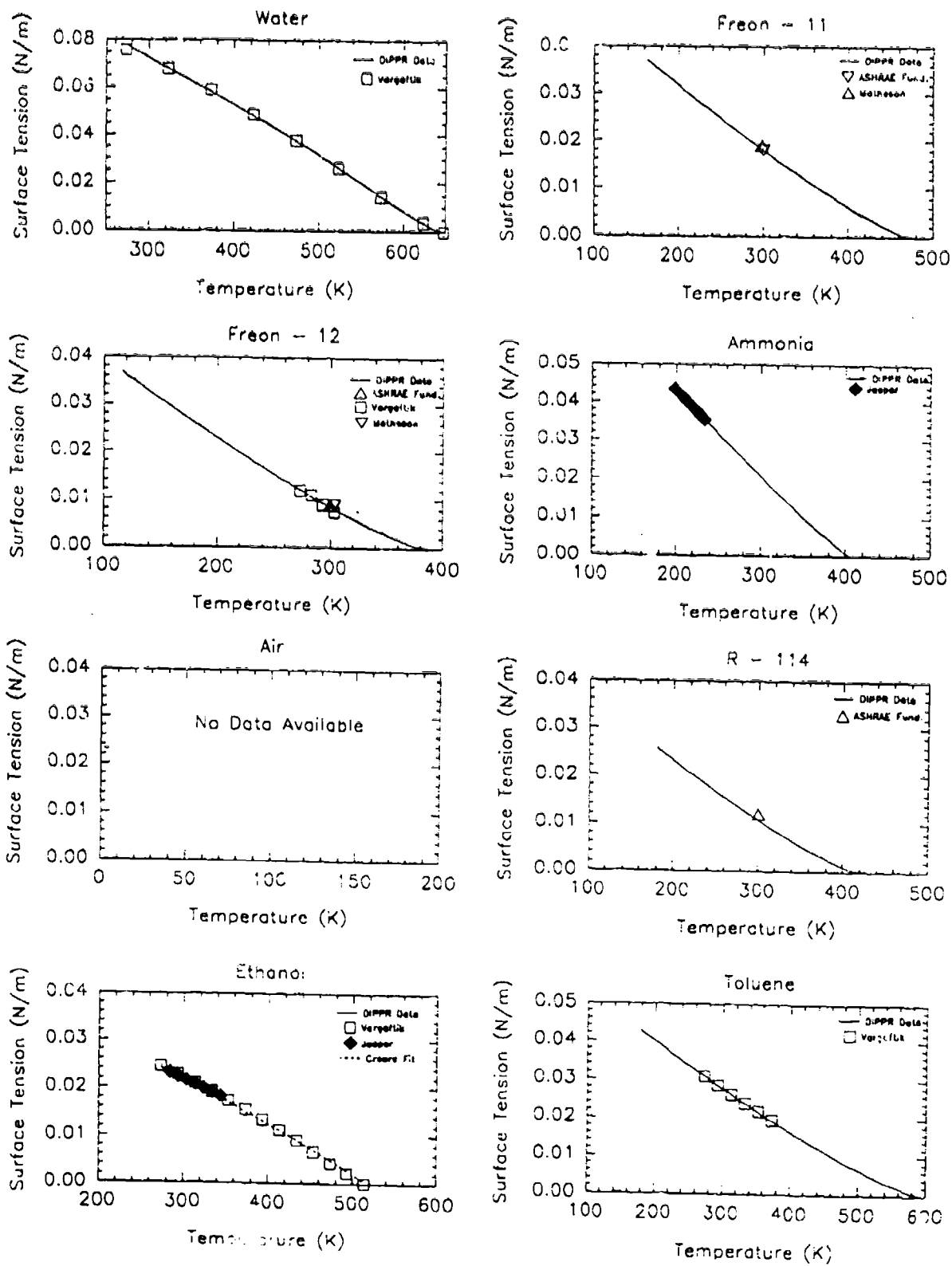


Figure A.6. SURFACE TENSION

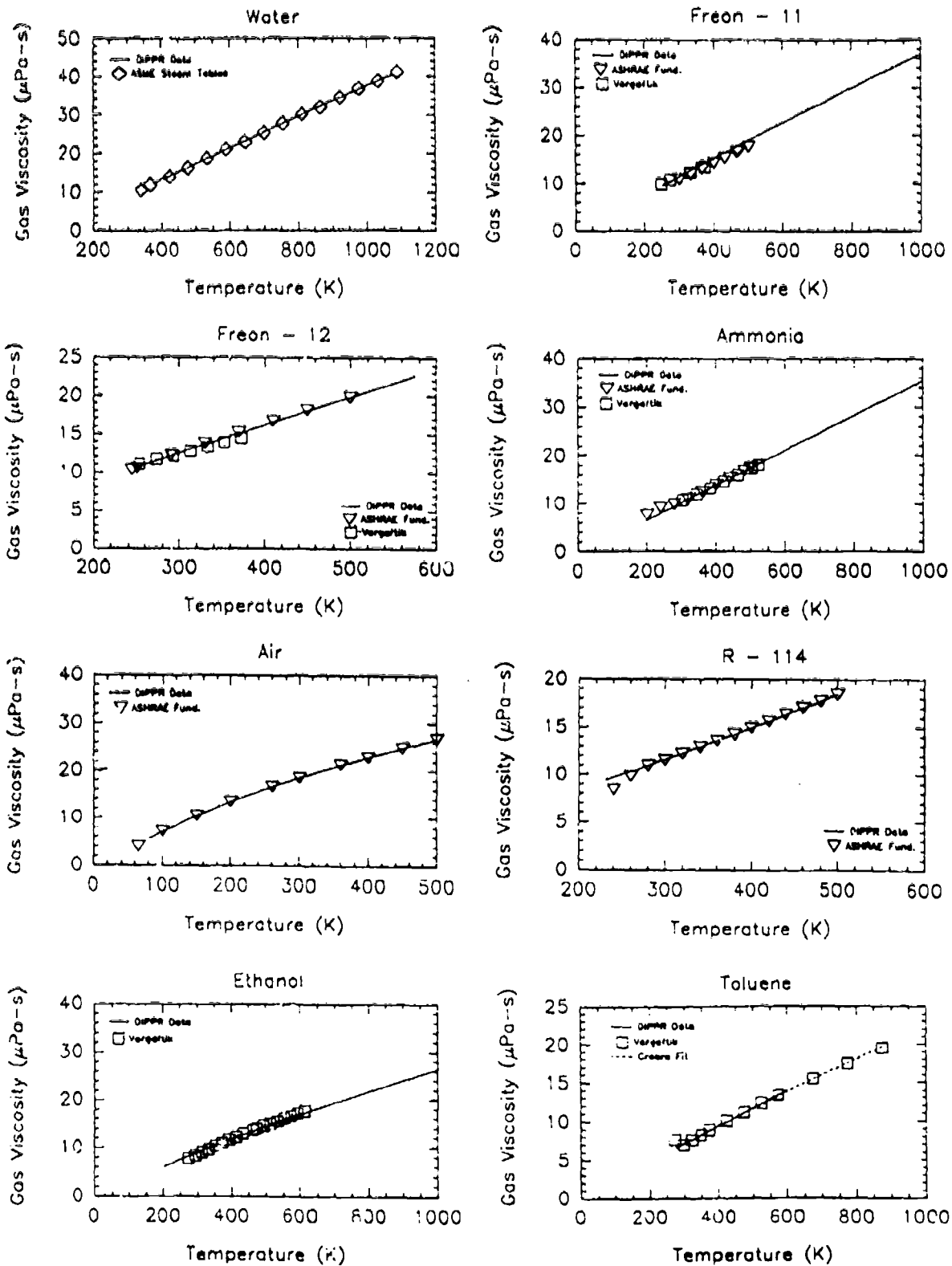


Figure A.7. GAS VISCOSITY

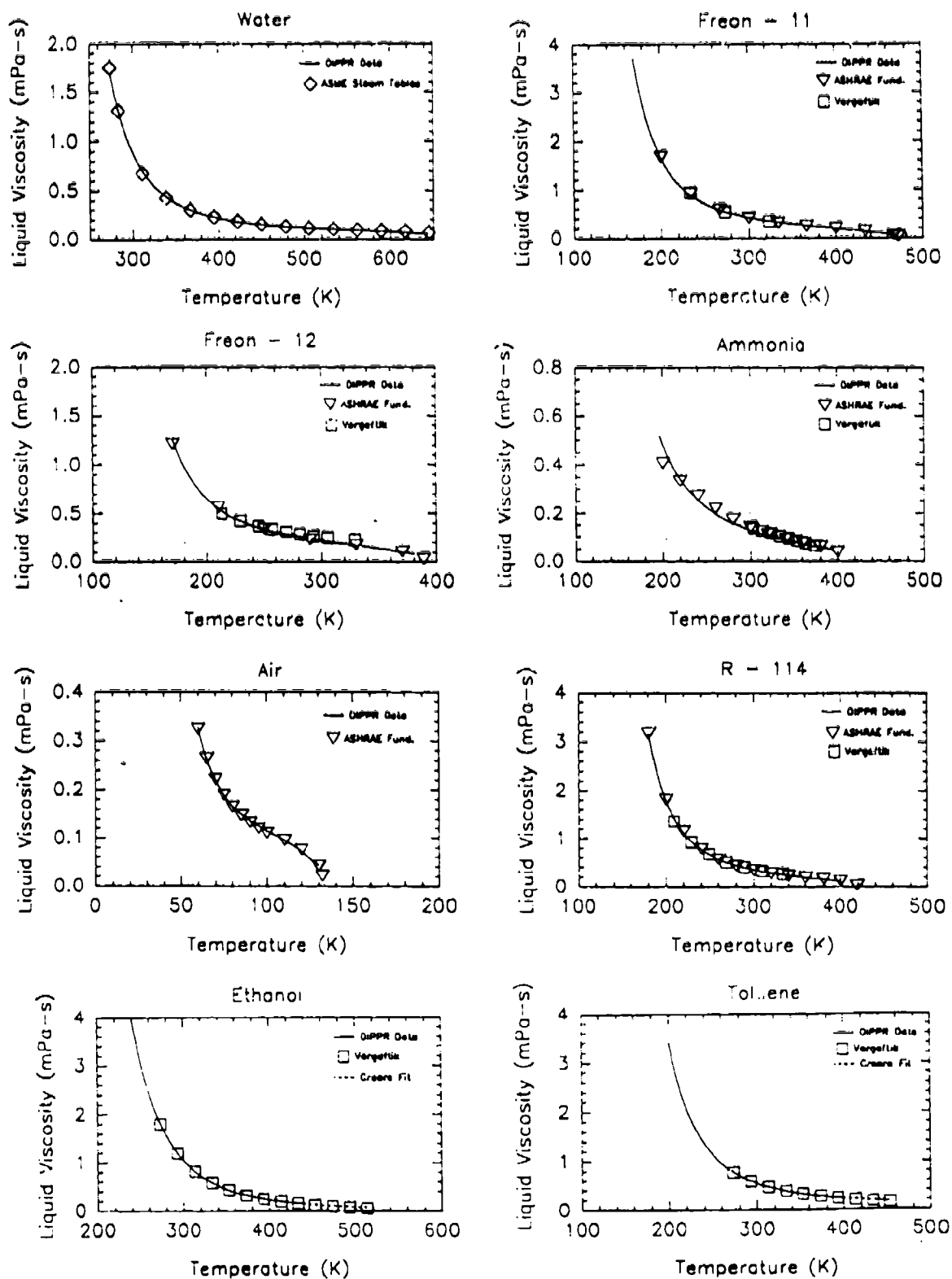


Figure A.8. LIQUID VISCOSITY



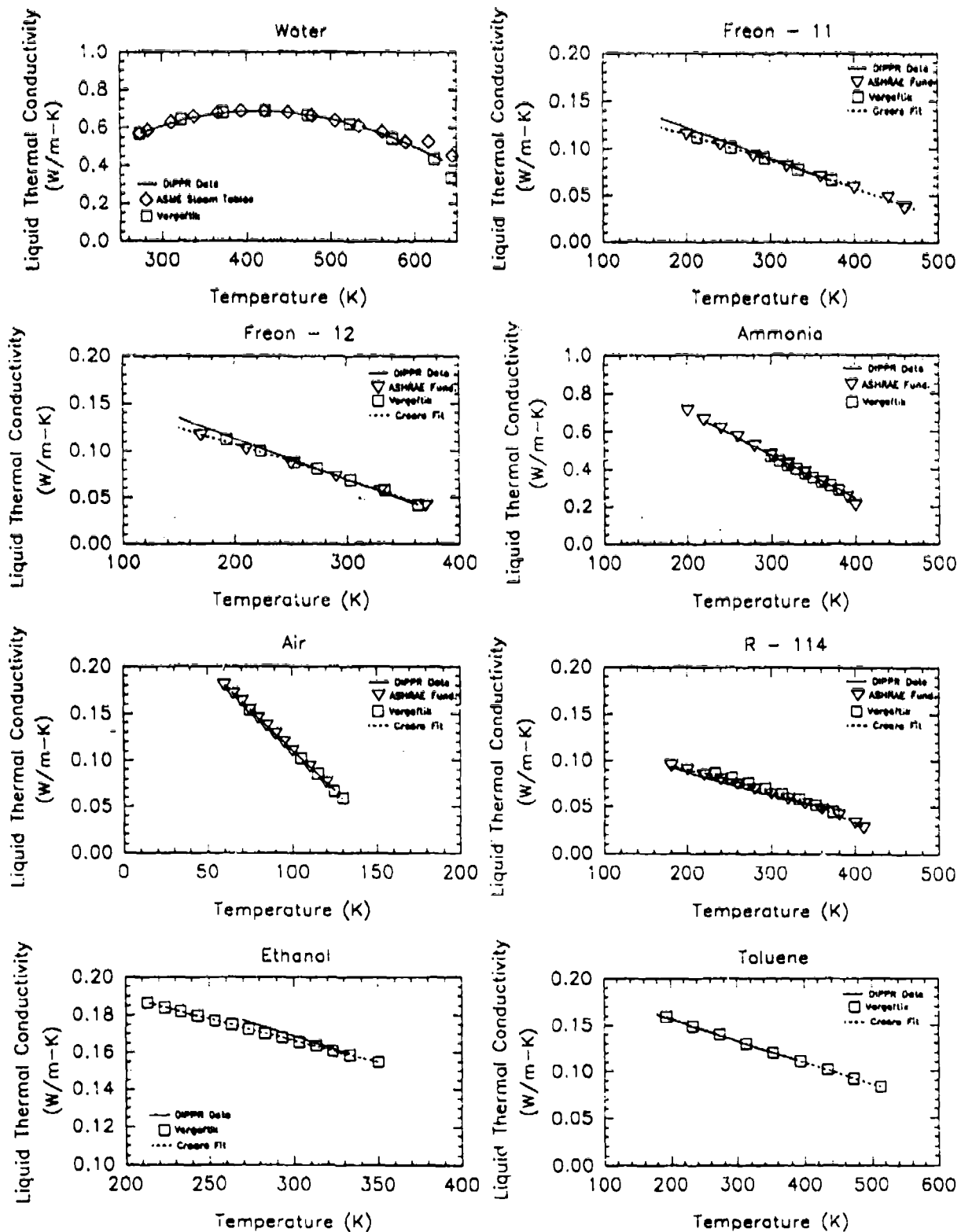


Figure A.9. LIQUID THERMAL CONDUCTIVITY

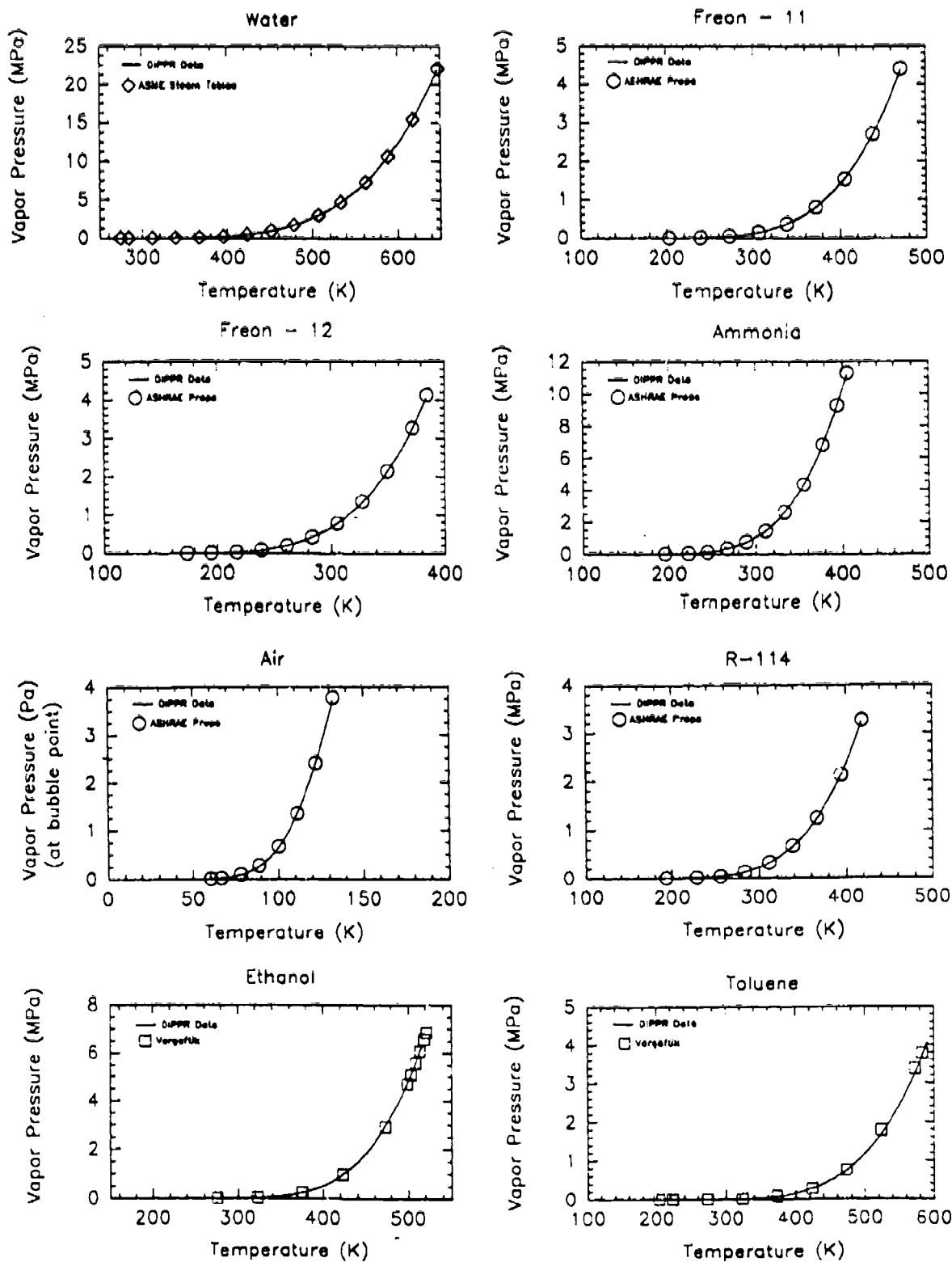


Figure A.10. VAPOR PRESSURE

## A.5 References for Fluid Property Routines

Anon., 1967 ASME Steam Tables; American Society of Mechanical Engineers; New York, 1967.

Anon., 1989 ASHRAE Handbook Fundamentals SI Edition; American Society of Heating; Refrigerating and Air Conditioning Engineers, Inc., 1989.

Anon., ASHRAE Thermodynamic Properties of Refrigerants; American Society of Heating; Refrigerating and Air Conditioning Engineers, Inc., 1986.

Anon., Matheson Gas Products; Matheson Gas Data Book, East Rutherford, NJ, 1971.

Anon., National Institute of Standards; DIPPR Data Compilation of Pure Compound Properties, NIST Standard Reference Database 11, U.S. Department of Commerce, May, 1990.

Daubert, T.E. and Danner, R.D.; Data Compilation Tables of Properties of Pure Compounds; Design Institute for Physical Property Data, American Institute of Chemical Engineers, 1984.

Jasper, J.J.; "The Surface Tension of Pure Liquid Compounds"; J. Phys. Chem. Ref. Data; Vol. 1, No. 4, 1972.

Reid, R.C. and Smith, J.M.; "Thermodynamic Properties of Ethyl Alcohol"; Chemical Engineering Progress; Vol. 47, No 8, Aug., 1951, pp. 415-418.

Starling, K.E.; Fluid Dynamic Properties for Light Petroleum Systems; Gulf Publishing Co., Houston, 1973.

Vargaftik, N.B.; Tables on the Thermophysical Properties of Liquids and Gases; Hemisphere Publishing Corp., 1975.

## **APPENDIX B REFERENCES FOR DESIGN METHODS SOFTWARE**

Barry, J.J. and Ent, R.S.; "FCEVAP PROGRAM: FORCED CONVECTION EVAPORATORS"; Software Maintenance Manual, PL-TR-92-3003, Vol. 3, Prepared for Phillips Laboratory, OL-AC, PL/VTPT, Edwards AFB, Contract F04611-90-C-0004, Prepared by Creare Inc., Hanover, NH, May 1992.

Barry, J.J. and Ent, R.S.; "DROPEVAP PROGRAM: DROPLET EVAPORATOR PERFORMANCE"; Software Maintenance Manual, PL-TR-92-3003, Vol. 4, Prepared for Phillips Laboratory, OL-AC, PL/VTPT, Edwards AFB, Contract F04611-90-C-0004, Prepared by Creare Inc., Hanover, NH, May 1992.

Crowley, C.J., Wallis, P.N., and Ent, R.S.; "MICROREG PROGRAM: FLOW REGIMES IN MICROGRAVITY"; Software Maintenance Manual, PL-TR-92-3003, Vol. 1, Prepared for Phillips Laboratory, OL-AC, PL/VTPT, Edwards AFB, Contract F04611-90-C-0004, Prepared by Creare Inc., Hanover, NH, May 1992.

Crowley, C.J., Wallis, P.N., and Ent, R.S.; "MICROP PROGRAM: PRESSURE DROPS IN MICROGRAVITY"; Software Maintenance Manual, PL-TR-92-3003, Vol. 2, Prepared for Phillips Laboratory, OL-AC, PL/VTPT, Edwards AFB, Contract F04611-90-C-0004, Prepared by Creare Inc., Hanover, NH, May 1992.

Ent, R.S. and Izenzon, M.G.; "PUMPS PROGRAM: TWO-PHASE PUMP PERFORMANCE"; Software Maintenance Manual, PL-TR-92-3003, Vol. 7, Prepared for Phillips Laboratory, OL-AC, PL/VTPT, Edwards AFB, Contract F04611-90-C-0004, Prepared by Creare Inc., Hanover, NH, May 1992.

Izenzon, M.G., Martin, C.M. and McDonald, M.M.; "MICROCON PROGRAM: HIGH VAPOR SHEAR CONDENSATION"; Software Maintenance Manual, PL-TR-92-3003, Vol. 5, Prepared for Phillips Laboratory, OL-AC, PL/VTPT, Edwards AFB, Contract F04611-90-C-0004, Prepared by Creare Inc., Hanover, NH, May 1992.

Valenzuela, J.A., Perng, C.Y., Martin, J.L. and Ent, R.S.; "MICROCAP PROGRAM: CAPILLARY CONDENSATION CALCULATIONS"; Software Maintenance Manual, PL-TR-92-3003, Vol. 6, Prepared for Phillips Laboratory, OL-AC, PL/VTPT, Edwards AFB, Contract F04611-90-C-0004, Prepared by Creare Inc., Hanover, NH, May 1992.